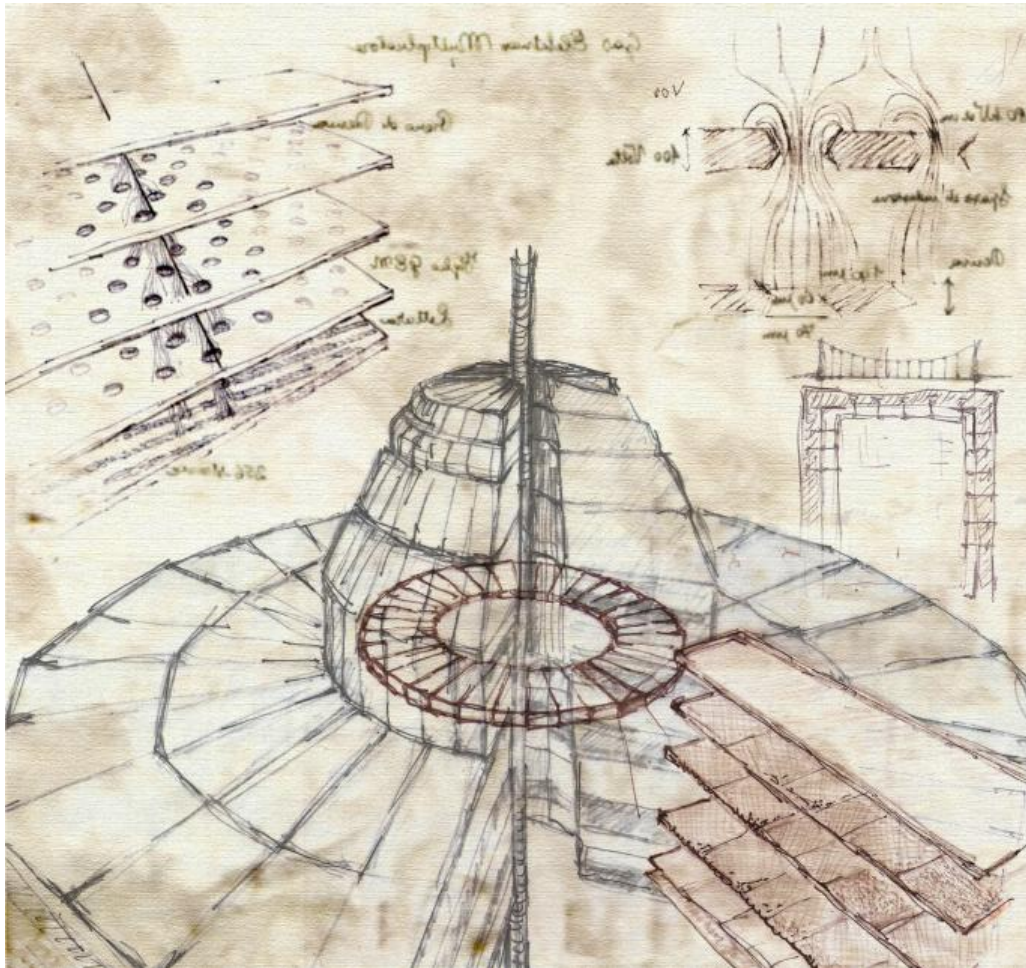


**Triple-Gas Electron Multiplier technology for
future upgrades of the CMS experiment:
construction and certification of the CMS
GE1/1 detectors and longevity studies**

Francesco Fallavollita



Tesi per il conseguimento del titolo



Università di Pavia

Università degli Studi di Pavia
Dipartimento di Fisica



Istituto Nazionale di Fisica Nucleare
SEZIONE DI PAVIA

DOTTORATO DI RICERCA IN FISICA - XXXI CICLO

**Triple-Gas Electron Multiplier technology for
future upgrades of the CMS experiment:
construction and certification of the CMS
GE1/1 detectors and longevity studies**

Francesco Fallavollita

Submitted to the Graduate School of Physics in partial
fulfillment of the requirements for the degree of

DOTTORE DI RICERCA IN FISICA

DOCTOR OF PHILOSOPHY IN PHYSICS

at the

University of Pavia

University Supervisor: Prof. Paolo Vitulo

Cover: Drawings of the elements of CMS detector, in the style of Leonardo da Vinci [CMS Collection: CMS-PHO-OREACH-2009-001].

Triple-Gas Electron Multiplier technology for future upgrades of the CMS experiment: construction and certification of the CMS GE1/1 detectors and longevity studies

Francesco Fallavollita

Ph.D Thesis - University of Pavia

Pavia, Italy, January 2019

To my parents

I am among those who think that science has great beauty. A scientist in his laboratory is not a mere technician: he is also a child placed before natural phenomena which impress him like a fairy tale. We would not allow it to be believed that all scientific progress can be reduced to mechanisms, machines, gearings, even though such machinery also has its own beauty. Neither do I believe that the spirit of adventure runs any risk of disappearing in our world.

If I see anything vital around me, it is precisely that spirit of adventure, which seems indestructible and is akin to curiosity [· · ·].

(Marie Curie Skłodowska, 1937)

List of Figures

2.1	General view of the CERN accelerator complex and location of its main experiments [5].	8
2.2	Pictures of the superconducting magnets in the LHC tunnel (left) and its cross-section (right) [3].	10
2.3	Form of potential V as a function of ϕ on the complex plane [16]	14
2.4	Cross section and event rates of several processes as a function of the center-of-mass energy of proton-(anti) proton collisions [18].	16
2.5	The Feynman diagrams for the main production mechanisms of the Higgs boson: (a) <i>gluon-gluon fusion</i> ; (b) <i>vector boson fusion (VBF)</i> ; (c) <i>associated with vector boson</i> ; (d) <i>associated with pairs of top quarks</i> [18].	17
2.6	(a) Higgs production cross section and (b) branching ratios as a function of the Higgs mass at the center-of-mass energy $\sqrt{s} = 7, 8, 14 \text{ TeV}$ [19].	18
2.7	The LHC main experiments: ATLAS, CMS, ALICE and LHCb	20
3.1	Overall view of CMS detector.	22
3.2	The CMS coordinate system.	23
3.3	A schematic view of the CMS solenoid (left), and the photograph of the CMS magnet and the return yoke with the barrel muon chambers installed at the Underground Experimental Cavern (right).	24
3.4	Overview of the CMS inner tracking system [26].	25
3.5	CMS pixel detector: (left) 3D-dimensional view and (right) photo of the detector [26].	25
3.6	CMS Electromagnetic calorimeter: (left) $PbWO_4$ ECAL crystals with photodetectors attached a barrel crystal with APD capsule (top) and an endcap crystal with a VPT (bottom), and (right) General CMS ECAL layout: Barrel Super Module (yellow), Endcap crystal (green) and Preshower detectors (pink) [29]. 27	

3.7	A quadrant of the CMS detector with locations of the calorimeters: hadron barrel (HB), endcap (HE), outer (HO) and forward (HF) [32].	28
3.8	Longitudinal view of one quarter of the present CMS Muon Spectrometer [33].	29
3.9	Illustration of the Drift Tube Chamber: (left) schematic view of a DT chamber and (right) the one section of the DT with electric field [33].	30
3.10	Illustration of the Cathode Strip Chamber: (left) the layout of a CMS CSC with local chamber coordinates and (right) the cross-sectional view of the gas gap in a CSC, with a schematic illustration of the gas ionization avalanche and induced charge distribution on the cathode strips [33].	32
3.11	Pictures of the CSC chambers installed at CMS detector [33].	32
3.12	Principle scheme of a double-gap RPC chamber [33].	33
3.13	The architecture of the CMS Trigger System [35].	35
3.14	Architecture of the Level 1 Trigger [36].	36
3.15	Schematic representation of a HLT menu in CMS and of the HLT paths in it [37].	37
3.16	The LHC upgrade schedule [38].	38
3.17	Expected LHC instantaneous and integrated luminosity as a function of time up to 2037. Dates for long-shutdowns (LS) periods are also marked [38]	39
3.18	A high-pileup events (yellow) with some reconstructed vertices (green) [39]	40
3.19	Simulated trigger efficiency as a function of the η number of layers numbers of RPCs [34].	46
3.20	A quadrant of the CMS Muon Spectrometer, showing DT chambers (yellow), RPC (light blue), and CSC (green). The locations of new forward muon detectors for HL-LHC phase are contained within the dashed box and indicated in red for GEM stations (ME0, GE1/1, and GE2/1) and violet for improved RPC stations (RE3/1 and RE4/1) [34].	47
4.1	Multi-Wire Proportional Chambers : (Left) Principle of construction and definition of the parameters in a multiwire proportional chamber. A set of parallel anode wires is mounted symmetrically between two cathode planes. (Right) Electric field equipotentials and field lines in a multiwire proportional chamber. The effect on the field due to a small displacement of one anode wire is also shown [41].	50
4.2	Micro Strip Gas Chamber: (Left) Schematic overview of the Micro Strip Gas Chamber. (Right) Picture of the anode and cathode strips.	51

LIST OF FIGURES

4.3	Rate capability of the MWPC and MSGC technologies manufactured on substrates with different values of bulk or surface resistivity.	52
4.4	Damage caused by a discharge in a MSGC.	53
4.5	Schematic overview (Figure 4.5a) and electron microscope picture (Figure 4.5b) of a section of typical GEM electrode, $T = 50 \mu m$ thick Kapton foil, clad on each side with a $t = 5 \mu m$ copper layer. The holes pitch is $P = 140 \mu m$ and the external and internal diameter are $D = 70 \mu m$ and $d = 50 \mu m$, respectively. Schematic overview (Figure 4.5c) and electron microscope picture (Figure 4.5d) of the cross-section of a bi-conical hole of a GEM-foil [55].	54
4.6	Measured effective gas gain and real gas gain of GEMs operated in Ar/CO_2 (70/30) with different metal hole diameters [55]. It should be noted that, since fraction of the multiplying electrons is lost on the lower electrode of the GEM-foil, the effective gas gain, defined as ratio of the detected charge to the primary ionization charge, is lower than the real gas gain of the amplification stage, shown in the figure.	55
4.7	Electron transparency as a function of drift electric field in a single-GEM detector operated in Ar/CO_2 (70/30) for different GEM geometry, labeled as pitch/hole diameter [55].	56
4.8	Charging-up effect as a function of time at X-ray photons flux of about $10^4 Hz/mm^2$ for three different shapes of the GEM-holes [55].	57
4.9	Schematics of a single-GEM detector: E_D and E_I are the drift and the induction electric fields, while h_D , h_I are the drift and induction gaps; ΔV_{GEM} is the voltage difference applied to the two copper electrodes of the GEM-foil [58].	58
4.10	Schematic overview (not in scale) of a single-GEM detector operation together with the 2D map of electric field lines (red) and equipotential lines (green) in proximity of the GEM-holes. . . .	59
4.11	Collection efficiency as a function of drift electric field in a single-GEM detector operated in Ar/CO_2 (70/30) for two different method of measurement: integral current or pulse with two time constants [58].	60
4.12	Currents on the various electrodes of a single-GEM detector as a function of the induction electric field: I_S is the current on the readout pads, I_T and I_B the current on the upper and lower copper layer of the GEM-foil, and I_D the current of the cathode electrode [58].	61
4.13	Effective gas gain and discharge probability as a function of voltage in a single-, double- and triple-GEM detectors in Ar/CO_2 (70/30) gas mixture [55].	65

4.14	Schematics of a triple-GEM detector: E_D , E_{T1} , E_{T2} and E_I are the drift, the first and the second transfer and the induction electric fields respectively; g_D , g_{T1} , g_{T2} and g_I are the drift, the two transfer and the induction gaps respectively [55].	65
4.15	Currents on the various electrodes of a double-GEM detector as a function of the transfer electric field: I_D current on the cathode electrode, I_{T1} and I_{B1} current respectively on the upper and lower electrodes of the first GEM-foil, I_{T2} and I_{B2} current respectively on the upper and lower electrodes of the second GEM-foil and I_S current on the readout pads [55].	66
5.1	A quadrant of the muon system, showing DT chambers (yellow), RPC (light blue), and CSC (green). The new GEM detector station, GE1/1, is indicated in red [69].	74
5.2	L1 muon trigger rate at a luminosity of $2 \times 10^{34} \text{ cm}^{-2}\text{s}^{-1}$ as a function of p_T threshold. With the addition of GE1/1, the bending angle between ME1/1 and GE1/1 stations can be used and the trigger rate is greatly reduced [69].	75
5.3	Principle of operation of a triple-GEM detector and definition of drift, transfer, and signal induction gap regions within the detector. The table on the right gives the actual gap configuration in the GE1/1 detector. The table also list typical values for electric potentials on the top and bottom of each GEM-foil and typical values for voltages and electric fields across the four gaps (blue) and the three GEM-foils (red) if the nominal potential of 3200 V for operation in Ar/CO_2 (70 : 30) is applied to the drift electrode.	79
5.4	Design of the readout board for the long detector GE1/1-VI-L. (Left) outer side of the readout board showing the traces from vias to Panasonic connectors. (Right) inner side that faces into the gas volume opposite to the third GEM-foil. The circular structures on each strip are vias that connect the strips to the outside of the board.	80
5.5	(Top left) Exploded view of a single GE1/1 detector showing the Drift and Readout board, the GEM-foil stack, the electronics, the cooling system and the protection cover. (Bottom left). Example of an assembled super-chamber. (Right) Mechanical overview of the GE1/1 station with both long and short GE1/1 detectors.	81
5.6	GE1/1 detectors mass production chain. Together with the production and quality control phase are listed the production site and/or the industrial companies in charge of the GE1/1 mass production.	83
5.7	Exploded view of the mechanical design of a GE1/1 triple-GEM detector and its main assembly components.	84

LIST OF FIGURES

5.8	Mechanical design of the GE1/1 Drift Board	85
5.9	Left: Picture of the GE1/1 the Drift Board. Right: Close view of the wider base of the GE1/1 drift board showing the HV distribution circuit traces and pads for the spring-loaded pins that make the electrical connections to the GEM-foils. The pad for $10\text{ M}\Omega$ protective resistor and the pads for the $100\text{ k}\Omega$ resistor and 330 pF capacitor of the decoupling RC circuit are shown. Holes to fix Pull-Outs against the board are also shown.	86
5.10	Mechanical design of the External Frame	87
5.11	Left: Picture of the external frame. Right: Close view of the section of the external frame showing the groove in the frame, O-ring in and out of its groove and notches in the inner side of the frame to accommodate the Pull-Outs	87
5.12	Mechanical design of the Internal Frame	88
5.13	Left: Close view of the section of the Figure 5.12. Right: Shapes and mechanical structure of different pieces of the internal frames. Ten pieces per frame combine together and surround all round the periphery of the GEM-foils stack.	89
5.14	Schematic comparison of procedures for fabrication of a double-mask GEM-foils (left) and a single-mask GEM-foils (right) [70] [71].	90
5.15	Left: Design of GEM-foil for GE1/1 detector. Right: Close view of the section of foil showing the small holes for alignment pins which are used during the assembly procedures of the GE/1 detectors, large holes to allow the passage of screws through them and to attach the foil to internal frames, plus-shaped slits for stretching nuts and HV Sectors.	91
5.16	Mechanical design of the Readout Board.	91
5.17	Left: Outer side of GE1/1 readout board showing 24 ($i\eta$, $i\phi$) readout sectors with each sector mounted with a male Panasonic adopter for signal readout. The board has also two holes at the opposite corners which allow to mount the two gas plugs. Also, there are machined holes on the periphery of the board which allow the passage of closing screws to fix the board against detector structure. Middle: Inner side of the drift board showing the readout strips. Right: Close view showing the readout strips on the inner side and Panasonic connector on the outer side of the board.	92
5.18	Mechanical design of the gas plug fixed against the readout board.	93
5.19	Exploded view of the mechanical design of a CMS GE1/1 triple-GEM detector showing the schematic flow of the assembly procedure.	94
5.20	Schematic overview of the HV circuit and the twelve HV-pins on the drift board.	94

5.21	Sliced view showing the spring loaded mechanism of the twelve HV-pins and their position on the drift board with respect to the GEM-foils.	95
5.22	Magnified view of one of the HV-pins showing the GEM-foils stack, the 3 mm, 1 mm, 2 mm, 1 mm internal frames, the powerin pad of the second GEM-foil, the single HV-pin pressed against powering pad of the second GEM-foil and the readout board.	95
5.23	(left) High voltage circuit arrangement on the drift board showing the twelve HV-pins. The heights of each set of HV-pins are in accordance with the position of the respective GEM-foils and are mounted on the drift board in that specific order so that they can properly reach the three GEM-foils. Their spring-loaded design allows for continuous contact with the corresponding pads of the GEM-foil. (right) HV divider circuit diagram for the 3/1/2/1 mm gap configuration and corresponding connections to GE1/1 detector electrodes.	96
5.24	Pictures of the process of laying the first GEM-foil on a Plexiglas base with the 3mm internal frames in position.	97
5.25	(top) Picture of the GEM-foil cleaning procedure using adhesive roller, which removes dust particles of micron level effectively by its strong sticking capacity. (bottom) Picture of the leakage current test measurement using MEGGER MIT420 insulation tester.	98
5.26	Mechanical structures of the four different internal frames which are stacked together to maintain the gap configuration of 3/1/2/1 mm in GE1/1 detector, showing the positioning of the brass inserts, grooves for the stretching nuts and positions of fastening screws.	99
5.27	Pictures of the various assembly steps for the stack formation procedure.	100
5.28	(top) Pictures of the placement of the GEM-foils stack on the drift board. (bottom) Picture of the GEM-foils stack on drift board and fixation of drift board against Jig by means of Aluminium bars.	101
5.29	Magnified view of the section of the GE1/1 detector with GEM-foils stack tensioned against the pull-outs mounted onto the drift board and surrounded by outer frame having O-ring on its grooves. The active chamber volume is ready to be closed with the readout board.	102
5.30	(top) Closing of the GE1/1 triple-GEM detector with the readout board. (bottom) The final assembled detector on the Quality Control line.	103
5.31	Schematic overview of the mechanical stretching method of the GEM-foils in the CMS GE1/1 detector.	104

LIST OF FIGURES

5.32	Picture of the mechanical stretching method during the GE1/1 detector assembly	105
5.33	Schematic overview of the quality assurance and quality control procedures of the GE1/1 detectors.	106
5.34	Pictures of the initial inspection and qualification procedures of the external frame and the Vito O-ring. The width and depth of the grooves along periphery of the external frame are accurately measured using an high resolution digital caliper and a mechanical dial indicator as well as the external diameter dimensions of the O-ring.	107
5.35	Pictures of the initial inspection and qualification procedures of the readout board. In order to check the flatness of the readout board, its height is accurately measured in several points along its perimeter with respect to the plane of the optical table using an high resolution digital caliper.	108
5.36	Pictures of the QC1 connectivity test setup.	109
5.37	Microscopy photos of the readout strips showing some examples of defects and short circuits between the readout strips.	109
5.38	Schematic cross section of a GEM-foil and its equivalent resistive circuit.	110
5.39	Preparation of the GEM-foil and installation on the FR4 frame.	112
5.40	Cleaning of the GEM-foil with an anti-static roll in order to remove any possible dust particle deposited on the foil.	112
5.41	Schematic view of the QC2 fast test setup (acceptance test I).	113
5.42	Picture of the QC2 fast test on a GEM-foil (acceptance test I).	113
5.43	Paschen Curve obtained for helium, neon, argon, hydrogen and nitrogen, using the expression for the breakdown voltage as a function of the parameters A , B and γ , the second Townsend coefficient [72].	115
5.44	Schematic view of the QC2 long test setup (acceptance test II).	116
5.45	Picture of the QC2 long test setup at CMS-GEM QA/QC facility.	116
5.46	Results from the QC2 long leakage current test of a rejected GEM-foil: voltage and current delivered by the power supply as a function of time in dry nitrogen environment with an ambient average temperature of $22.4\text{ }^{\circ}\text{C}$ and ambient relative humidity equal to 7.9%.	118
5.47	Results from the QC2 long leakage current test of an approved GEM-foil: voltage and current delivered by the power supply as a function of time in dry nitrogen environment with an ambient average temperature of $21.9\text{ }^{\circ}\text{C}$ and ambient relative humidity equal to 6.1%.	119
5.48	Picture of the QC2 post-assembly test setup on a GE1/1 detector.	120
5.49	QC3 gas leak test experimental setup.	121

5.50	Result from the calibration of the gas system installed in the QC3 Gas Leak Stand. The over-pressure is stable over the entire gas leak test, with negligible fluctuations within 1% of its initial value. The pressure drop is modeled by the function $P_m(t) = P_0 \times \exp(-t/\tau)$ which provides a gas leak time constant $\tau \sim 10^4 \text{ hr}$, demonstrating a perfect gas tightness of the entire gas system under test.	123
5.51	Results from the QC3 Gas Leak Test on the GE1/1-X-S-CERN-0002 detector. The pressure drop is modeled by the function $P_m(t) = P_0 \times \exp(-t/\tau)$ which provides a gas leak time constant $\tau \sim 6 \text{ min}$	124
5.52	Results from the QC3 Gas Leak Test on the GE1/1-X-S-CERN-0004 detector. The pressure drop is modeled by the function $P_m(t) = P_0 \times \exp(-t/\tau)$ which provides a gas leak time constant $\tau \sim 25 \text{ hr}$	125
5.53	Results from the QC3 Gas Leak Test on the GE1/1-X-L-CERN-0004 detector. The pressure drop is modeled by the function $P_m(t) = P_0 \times \exp(-t/\tau)$ which provides a gas leak time constant $\tau \sim 29 \text{ hr}$	126
5.54	Top panel: Results from the QC3 Gas Leak Test on the GE1/1-X-L-CERN-0001 detector. The pressure drop is modeled by the function $P_m(t) = P_0 \times \exp(-t/\tau)$ which provides a gas leak time constant $\tau \sim 18 \text{ hr}$. Bottom panel: Residual data after subtraction of fit. The residuals appear randomly scattered around zero indicating that the proposed model describes the data well.	128
5.55	Gas volume leakage rate $dV(t)/dt$ as a function of the working condition, i.e. the over-pressure P_0 in a GE1/1 detector during the operation in the Muon Spectrometer of the CMS experiment for several possible values of the gas leak time constant τ , i.e. for different acceptance limit of the QC3 gas leak test.	130
5.56	Gas volume leakage rate $dV(t)/dt$ as a function of the gas leak time constant τ for several possible values of the over-pressure P_0 in a GE1/1 detector during the operation in the Muon Spectrometer of the CMS experiment.	131
5.57	Examples of damage assembly components identified as potential gas leak sources in the GE1/1 detectors.	131
5.58	QC4 HV test experimental setup.	132
5.59	QC4 HV test overview of the detector with the Panasonic-to-LEMO and the 50Ω terminations.	132
5.60	QC4 HV test magnified view of the sample point on the drift PCB board showing the RC circuit used to decouple the signal from HV when the detector is read from the bottom of the third GEM foil.	133

LIST OF FIGURES

5.61	Results from the QC4 HV Test on the GE1/1-X-S-CERN-0004 detector. Top: current through the HV divider as a function of the applied voltage. The linear fit to the experimental data provides an equivalent resistance $R_{equiv.} \sim 4.99 M\Omega$, resulting in a deviation of about 0.4% with respect to the expected value ($R = 5.01 \pm 0.02 M\Omega$). Bottom: intrinsic noise rate N_{noise} as a function of the applied voltage: $N_{noise} \sim 6.4 \times 10^{-3} Hz/cm^2$ at 4.9 kV.	135
5.62	Results from the QC4 HV Test on the GE1/1-X-L-CERN-0004 detector. Top: current through the HV divider as a function of the applied voltage. The linear fit to the experimental data provides an equivalent resistance $R_{equiv.} \sim 4.96 M\Omega$, resulting in a deviation of about 1% with respect to the expected value ($R = 5.01 \pm 0.02 M\Omega$). Bottom: intrinsic noise rate N_{noise} as a function of the applied voltage: $N_{noise} \sim 5.3 \times 10^{-3} Hz/cm^2$ at 4.9 kV.	136
5.63	QC5 readout sectorization and APV mapping. The dark grey flat cable represent the HDMI connectors on the output of the master APVs. This mapping is valid for both Short and Long detectors.	137
5.64	Close view of an APV25 Front-End ASICs plugged on the detector.	137
5.65	Picture of the GE1/1 detector inside of the X-ray station.	138
5.66	QC5 Schematic view of the optimum grounding for QC5 Gas Gain Calibration Test. The orange line represents copper ribbon.	139
5.67	QC5 effective gas gain data acquisition setup.	141
5.68	Close view of the Panasonic-to-LEMO adapter with a 50 k Ω protective resistor for the rate measurement.	141
5.69	Close view of the Panasonic-to-LEMO adapter for the readout current measurement.	142
5.70	Results from the QC5 - Effective Gas Gain Measurement on the GE11-X-S-CERN-0004 assembled with GEM-foils based on the single-mask photolithography technique produced by the CERN PCB Workshop. The detector under test has been operated in Ar/CO_2 (70/30) gas mixture and irradiated by a 22 keV photons X-ray from an X-ray tube with an interaction rate of $\sim 3.2 kHz$	144
5.71	Results from the QC5 - Effective Gas Gain Measurement on the GE11-X-L-CERN-0004 assembled with GEM-foils based on the single-mask photolithography technique produced by the CERN PCB Workshop. The detector under test has been operated in Ar/CO_2 (70/30) gas mixture and irradiated by a 22 keV photons X-ray from an X-ray tube with an interaction rate of $\sim 4.0 kHz$	145

-
- 5.72 Picture of the experimental setup for the QC5 response uniformity test showing the X-ray generator, the DAQ stations (left) and the inside of the copper box with the electronics in place on the GE1/1 detector (right). 147
- 5.73 Schematic overview of the experimental setup for the QC5 response uniformity test showing the DAQ electronics and the trigger line. 147
- 5.74 Raw data of an APV25 triggered by an X-ray photons. The acquisition window contains 12 samples delayed by 25 ns. Each sample includes the ADC values of all the 128 strips, fired or not by the particles. The average number of strips fired by a 8 keV X-ray is ~ 3 (cluster size) at a gas gain of 600. 148
- 5.75 QC5 picture of the HDMI cable connected to its APV25 hybrid. 149
- 5.76 Schematic overview of the GE1/1 detector built in the analysis code. The η -partitions are divided in 96 slices. For each slice, the maximum cluster charge for all the events occurring in this slice is added to a charge histogram related to the energy deposited by the particles. 151
- 5.77 Top: Example of energy spectrum from a slice (four strips) of the GE1/1 triple-GEM detector under test operated at an average gain around 600 with Ar/CO_2 (70/30) fully illuminated by a 22 keV X-ray. The solid line represents a fit to the experimental data using a Cauchy distribution to model the copper fluorescence photopeak plus a fifth order polynomial that models the background. Bottom: The mean of the copper fluorescence spectrum extracted from the fit of each slice is assigned to coordinate point of the slice in the local coordinates of the detector. 152
- 5.78 Top: Distribution of fitted photopeak positions obtained from GE1/1 triple-GEM detector under test: the experimental points represent each photopeak position and the solid line is a Gaussian fit to the data. The response uniformity for this detector is $R.U. = 6.6 \pm 0.3\%$. Bottom: Map of the detector response (i.e. the normalized photopeak energy) across the detector under test. 153
- 5.79 Summary of QC3 - gas leak tests performed on the long GE1/1 detectors (top) and short GE1/1 detectors (bottom) assembled at the CERN production and quality control site. The horizontal dashed line shows the QC3 acceptance limit in terms of the gas leak time constant $\tau \approx 3.04$ hr, which corresponds to a maximum acceptable gas leak rate of about 7 mBar/hr. 155

LIST OF FIGURES

5.80	Summary of QC4 - HV tests performed on the long GE1/1 detectors assembled at the CERN production and quality control site: the percentage variation of resistance $\Delta R/R \times 100\%$ (top) and the intrinsic noise rate R_{noise} at applied voltage of 4.9 kV (bottom) are shown as a function of the detectors serial number. The horizontal dashed lines shows the QC4 acceptance limits.	157
5.81	Summary of QC4 - HV tests performed on the short GE1/1 detectors assembled at the CERN production and quality control site: the percentage variation of resistance $\Delta R/R \times 100\%$ (top) and the intrinsic noise rate R_{noise} at applied voltage of 4.9 kV (bottom) are shown as a function of the detectors serial number. The horizontal dashed lines shows the QC4 acceptance limits.	158
5.82	MIP detection efficiency (left) and time resolution (right) of a triple-GEM detector in CMS configuration as a function of the detector gas gain, for a Ar/CO ₂ (70/30) gas mixture and 3/1/2/1 mm gap configuration [82] [83].	160
5.83	Summary of QC5 - Effective Gas Gain Measurements performed on the Long GE1/1 detectors (top) and Short GE1/1 detectors (bottom) assembled at the CERN production and quality control site. The effective gas gain has been measured in a Ar/CO ₂ (70/30) gas mixture on the reference readout sector ($i\eta, i\phi$) = (4, 2) at an applied voltage of 3102 V (660 μ A divider current equivalent).	164
5.84	Summary of QC5 - Response Uniformity Measurements performed on the Long GE1/1 detectors (top) and Short GE1/1 detectors (bottom) assembled at the CERN production and quality control site. The response uniformity has been measured in a Ar/CO ₂ (70/30) gas mixture at an effective gas gain of ~ 600 .	165
5.85	Summary of QC5 - Average Effective Gas Gain Measurements performed on the Long GE1/1 detectors (top) and Short GE1/1 detectors (bottom) assembled at the CERN production and quality control site.	167
5.86	LS2 - GE1/1 detectors mass production trend. The black solid line shows the level of current production rate, whereas the blue dashed line shows the expected detectors based on the average production rates achieved during the GE1/1 Slice Test experience. The red dotted line shows the actual number of validated detectors at different production sites (latest data as at 31 th August 2018).	168
6.1	Example of SEM micrographs of a clean gold plated tungsten wire (a) and damaged wires (b, c, d) used in a Multi-Wire Proportional Chambers after sustained irradiation, showing a different type of polymer deposits on the wire surface [87].	174

6.2	Example of <i>Classical Aging</i> of a wire chamber exposed to an X-rays flux from a <i>Cu</i> -target X-ray tube at a rate of about 1.4 MHz/cm . The detector has been operated at a gas gain of $\sim 2 \times 10^4$ and has been flushed with the <i>Ar/CH₄</i> (90/10) gas mixture. The curve represents the variation of the relative gas gain normalized with the initial value as a function of the accumulated charge per unit wire length (<i>C/cm</i>). The energy spectrum of the X-ray source has been performed at different value of accumulated charge to quantify the the energy resolution loss [88].	175
6.3	Schematic of the mechanism leading to the Malter effect [90].	176
6.4	Example of SEM micrographs of GEM holes of a triple-GEM detector, showing the etching induced by <i>HF</i> acid [105].	178
6.5	Schematic overview of the experimental setup for the outgassing studies showing the outgassing box that contains the material under test and the Single Wire Proportional Counter (SWPC) placed downstream [90].	182
6.6	Result of the longevity studies at the GIF facility: normalized and corrected anode current as a function of the accumulated charge. The detector under test is a GE1/1 triple-GEM detector of the 4 th generation operated in <i>Ar/CO₂/CF₄</i> (45/15/40) gas mixture at an initial gas gain of 2×10^4 [90].	184
6.7	Result of the longevity studies at the GIF++ facility: normalized and corrected anode current as a function of the accumulated charge. The detector under test is a GE1/1 triple-GEM detector of the 4 th generation operated in <i>Ar/CO₂</i> (70/30) gas mixture at an initial gas gain of 2×10^4 [90].	185
6.8	Result of the longevity studies at the GIF++ facility. Left: Typical ADC spectrum of the GIF++ facility of ¹³⁷ Cs. The experimental data have been fitted by a Landau distribution, convoluted with a normal distribution. Right: energy resolution as a function of the accumulated charge. The detector under test is a GE1/1 triple-GEM detector of the 4 th generation operated in <i>Ar/CO₂</i> (70/30) gas mixture at an initial gas gain of 2×10^4 [90].	186
6.9	Floor plan of the GIF++ facility [116].	187
6.10	(a) Schematic structure of the irradiator at GIF++ facility with angular correction aluminium filters and independent filter systems at both sides. (b) On both sides a set of independently movable and remotely controlled attenuation lead filters and collimator frames permits to fine tune the intensity of emitted photons. (c) Each set of 3×3 movable attenuation filters, with 27 combinations of filters, leads to 24 different attenuation factors between 1 and 46415 [116].	188

LIST OF FIGURES

6.11 Simulated photons current in air [$cm^{-2}s^{-1}$] in xz plane at $y = 0.0$ m; attenuation filters system at factor 1 [116]. 189

6.12 Absorbed dose rate in air [$\mu Gy/h$] in xz plane at $y = 0.0$ m of the facility [116]. 190

6.13 Figure A: The detector under test is a GE1/1 triple-GEM detector of the 4th generation operated in Ar/CO_2 (70/30) gas mixture at an initial gas gain of 2×10^4 . Figure B: close lateral view of the external frame. The frame is fixed to the PCB with vertical screws. Figure C: close view of the gas input [90]. 191

6.14 Results from the QC3 Gas Leak Test on the aged GE1/1 triple-GEM detector. The pressure drop is modeled by the function $P_m(t) = P_0 \times exp(-t/\tau)$. The parameter P_0 is a constant that takes into account the initial overpressure of the detector. The parameter τ is the gas leak time constant and quantifies how fast the overpressure inside the detector decreases as a function of the time. The exponential fit to the experimental data provides a gas leak time constant $\tau \sim 6$ min. 192

6.15 Results from the QC4 HV Test on the aged GE1/1 triple-GEM detector. Left: current through the HV divider as a function of the applied voltage. The linear fit to the experimental data provides an equivalent resistance $R_{equiv} \sim 5.00$ M Ω , resulting in a deviation of about 0.2% with respect to the expected value ($R = 5.01 \pm 0.02$ M Ω). Right: intrinsic noise rate R_{noise} as a function of the applied voltage: $R_{noise} \sim 1.3 \times 10^{-3}$ Hz/cm² at 4.9 kV. 193

6.16 Comparison between the effective gas gain of the GE1/1 triple-GEM detector measured before (black dots) and after (red dots) the 2015/2016 longevity test campaign. 194

6.17 (Figure 6.17a) Example of energy spectrum from a slice (four strips) of the GE1/1 triple-GEM detector under test operated at an average gain around 600 with Ar/CO_2 (70/30) fully illuminated by a 22 keV X-ray. The solid line represents a fit to the experimental data using a Cauchy distribution to model the copper fluorescence photopeak plus a fifth order polynomial that models the background. (Figure 6.17b) The mean of the copper fluorescence spectrum extracted from the fit of each slice is assigned to coordinate point of the slice in the local coordinates of the detector. (Figure 6.17c) Distribution of fitted photopeak positions obtained from GE1/1 triple-GEM detector under test: the experimental points represent each photopeak position and the solid line is a Landau fit to the data. The response uniformity for this detector is $R.U. = 7.6 \pm 0.5\%$. (Figure 6.17d) Map of the detector response (i.e. the normalized photopeak energy) across the detector under test. 195

6.18	Schematic drawing of the CMS triple-GEM stand designed in aluminium bosh-profiles for the longevity studies at GIF++ facility.	196
6.19	LabVIEW-software interface for the N1470 CAEN power supply to control and monitor the high voltages and current of detector. It is possible to see the high voltage real-time monitoring (top right) and the current real-time monitoring (bottom right). . . .	197
6.20	Schematics of the gas system in the GIF++ facility. The whole gas inlet line is made of stainless-steel tubes, while the exhaust gas line is made of polypropylene tubes (not hygroscopic). . . .	198
6.21	Picture of the longevity test at GIF++ facility. The GE1/1 triple-GEM detector is placed directly in front of the ^{137}Cs source irradiator. The DAQ electronics is placed below the detector structure and is protected inside the lead shielding box. The entire system is connected to the DAQ station via USB cables.	199
6.22	Scheme of the electronic chain and data acquisition system used during the longevity test at GIF++ facility.	199
6.23	LabVIEW-software interface for the KEITHLEY 6487 pico-ammeters to control and monitor the anode current on the R/O sectors under irradiation. The software has been developed to read a maximum of four pico-ammeters at the same time. It is possible to see the anode current real-time monitoring for the R/O sector $i\eta = 7; i\varphi = 2$ (top left) and for the R/O sector $i\eta = 2; i\varphi = 2$ (top right), as defined in Section 5.2.2.	200
6.24	Schematic representation of the analysis steps for the longevity studies.	201
6.25	Ambient parameters versus time (The accuracy is $\pm 0.2\text{ }^\circ\text{C}$ for temperature, $\pm 2\%$ for relative humidity, and $\pm 2\text{ mBar}$ for atmospheric pressure).	202
6.26	Result of the 2017/2018 longevity test campaigns at the GIF++ facility: the normalized anode current and the ratio temperature over pressure of the gas mixture as a function of time. The large fluctuations of the anode current are essentially correlated to the variations of the environmental conditions.	203
6.27	Correlation plot: measured and normalized anode current as a function of the ratio temperature over pressure. A best fit to the data with the Equation 6.5 gives for the slope parameter B the value of $\sim 56.22\text{ mBar}/^\circ\text{C}$. The dependence can be used in the experiment to actively correct the value of the measured anode current in order to maintain it constant in varying ambient conditions.	204

LIST OF FIGURES

- 6.28 Correlation plot: logarithm value of the measured and normalized anode current as a function of the logarithm value of the pressure. A best fit to the data with the Equation 6.8 gives for the slope parameter F_1 the value of -5.93 and for the mean values of the inverse of pressure $\langle 1/P_i \rangle$ the value of $\sim 0.001 \text{ mBar}^{-1}$. The dependence has been used in the experiment to actively correct the value of the measured anode current in order to maintain it constant in varying ambient conditions. . 205
- 6.29 Correlation plot: logarithm value of the measured and normalized anode current, already corrected in order to remove fluctuations due to the pressure changes, as a function of the logarithm value of the temperature. A best fit to the data with the Equation 6.10 gives for the slope parameter F_2 the value of -0.756 and for the mean values of the temperature $\langle T_i \rangle$ the value of $\sim 22.0 \text{ }^\circ\text{C}$. The dependence has been used in the experiment to actively correct the value of the measured anode current in order to maintain it constant in varying ambient conditions. . . 206
- 6.30 Result of the longevity studies at the GIF++ facility: accumulated charge per unit of detector area (mC/cm^2) as a function of time. Different slopes account for different attenuation factors during data taking. 207
- 6.31 Result of the longevity studies at the GIF++ facility: normalized and corrected anode current as a function of the accumulated charge. The detector under test is a GE1/1 triple-GEM detector of the 4th generation operated in Ar/CO_2 (70/30) gas mixture at an initial gas gain of 2×10^4 208
- 6.32 Result of the 2015/2016 and 2017/2018 longevity test campaigns at the GIF++ facility: normalized and corrected anode current as a function of the accumulated charge. No gas gain degradation is observed. The detector under test is a GE1/1 triple-GEM detector of the 4th generation operated in Ar/CO_2 (70/30) gas mixture at an initial gas gain of 2×10^4 209
- 6.33 Scanning Electron Microscope (SEM) picture of double-mask korean GEM-foil, the top layer (left) and the bottom layer (right). The outer diameters of the hole are 68-72 μm . (design goal = 70 μm) and the inner diameter is 48-52 μm . (design goal = 50 μm); the hole pitch is 140 μm 210
- 6.34 The detector under test is a triple-GEM detector equipped with korean GEM-foils based on the double-mask photolithography technique produced by the Mecaro company and operated in Ar/CO_2 (70/30) gas mixture at an initial gas gain of 2×10^4 . . 211

6.35 Results from the QC3 Gas Leak Test for the triple-GEM detector assembled with korean GEM-foils. The pressure drop is modeled by the function $P_m(t) = P_0 \times \exp(-t/\tau)$. The parameter P_0 is a constant that takes into account the initial overpressure of the detector. The parameter τ is the gas leak time constant and quantifies how fast the overpressure inside the detector decreases as a function of the time. The exponential fit to the experimental data provides a gas leak time constant $\tau \sim 25 \text{ hr}$. 212

6.36 Results from the QC4 HV Test for the triple-GEM detector assembled with korean GEM-foils. Left: current through the HV divider as a function of the applied voltage. The linear fit to the experimental data provides an equivalent resistance $R_{equiv} \sim 4.97 \text{ M}\Omega$, resulting in a deviation of about 0.8% with respect to the expected value ($R = 5.01 \pm 0.02 \text{ M}\Omega$). Right: intrinsic noise rate R_{noise} as a function of the applied voltage: $R_{noise} \sim 9.2 \times 10^{-3} \text{ Hz/cm}^2$ at 4.9 kV. 213

6.37 Results from the QC5 - Effective Gas Gain Measurement on the triple-GEM detector assembled with GEM-foils based on the double-mask photolithography technique produced by the Mecaro company. The detector under test has been operated in Ar/CO_2 (70/30) gas mixture and irradiated by a 22 keV photons X-ray from an X-ray tube with an interaction rate of 1.5 kHz. 214

6.38 (Figure 6.38a) Example of energy spectrum from a slice (four strips) of the triple-GEM detector under test operated at an average gain about 600 with Ar/CO_2 (70/30) fully illuminated by a 22 keV X-ray. The solid line represents a fit to the experimental data using a Cauchy distribution to model the copper fluorescence photopeak plus a fifth order polynomial that models the background. (Figure 6.38b) The mean of the copper fluorescence spectrum extracted from the fit of each slice is assigned to coordinate point of the slice in the local coordinates of the detector. (Figure 6.38b) Distribution of fitted photopeak positions obtained from GE1/1 triple-GEM detector under test: the experimental points represent each photopeak position and the solid line is a Gaussian fit to the data. The response uniformity for this detector is $R.U. = 16.4 \pm 0.4\%$. (Figure 6.38d) Map of the detector response (i.e. the normalized photopeak energy) across the detector under test. 215

6.39 Result of the longevity studies at the GIF++ facility: accumulated charge per unit of detector area (mC/cm^2) as a function of time. Different slopes account for different attenuation factors during data taking. 216

- 6.40 Result of the longevity studies at the GIF++ facility: normalized and corrected anode current as a function of the accumulated charge; no gas gain degradation is observed. The detector under test is a triple-GEM detector assembled with korean GEM-foils based on the double-mask photolithography technique developed by the Mecaro company and operated in Ar/CO_2 (70/30) gas mixture at an initial gas gain of 2×10^4 . . 217
- 6.41 The detector under test is a GE1/1 triple-GEM detector of the 10th generation operated in Ar/CO_2 (70/30) gas mixture at an initial gas gain of 2×10^4 for the longevity studies at the CMS-GEM QA/QC facility. 219
- 6.42 Results from the QC4 HV Test on the GE1/1 triple-GEM detector. Left: current through the HV divider as a function of the applied voltage. The linear fit to the experimental data provides an equivalent resistance $R_{equiv} \sim 4.98 M\Omega$, resulting in a deviation of about 0.4% with respect to the expected value ($R = 5.01 \pm 0.02 M\Omega$). Right: intrinsic noise rate R_{noise} as a function of the applied voltage: $R_{noise} \sim 4.7 \times 10^{-3} Hz/cm^2$ at 4.9 kV. 220
- 6.43 Results from the QC5 - Effective Gas Gain Measurement. Left: Schematic overview of the CMS GE1/1 triple-GEM detector readout board showing the readout sectors under test for the effective gas gain measurement (red circle). Right: Example of QC5 - Effective Gas Gain measurement performed on the readout sector $i\eta = 4, i\phi = 2$ of the GE11-X-S-CERN-0002 detector. 221
- 6.44 Results from the QC5 - Effective Gas Gain Measurement showing the gas gain values for the thirteen readout sector of the GE11-X-S-CERN-0002 detector at an applied voltage of 3390 V (676.6 μA divider current equivalent) as a function of spatial location. 222
- 6.45 Results from the Energy Resolution Measurement. Left: ^{109}Cd energy spectrum taken with the GE11-X-S-CERN-0002 detector at an applied voltage of 3390 V (676.6 μA divider current equivalent). The solid line represents a fit to the experimental data using a sum of two gaussians distribution, to model the copper fluorescence photopeak and the Ar escape peak, plus a fifth order polynomial that models the background. The energy resolution (FWHM value of the photopeak divided by the mean value μ) is 17.2%. Right: Energy resolution as a function of spatial location for the GE11-X-S-CERN-0002 detector at an applied voltage of 3390 V (676.6 μA divider current equivalent). 223

- 6.46 (Figure 6.46a) Example of energy spectrum from a slice (four strips) of the GE1/1-X-S-CERN-0002 detector under test operated at an average gain around 800 with Ar/CO_2 (70/30) fully illuminated by a 22 keV X-ray. The solid line represents a fit to the experimental data using a Cauchy distribution to model the copper fluorescence photopeak plus a fifth order polynomial that models the background. (Figure 6.46b) The mean of the copper fluorescence spectrum extracted from the fit of each slice is assigned to coordinate point of the slice in the local coordinates of the detector. (Figure 6.46c) Distribution of fitted photopeak positions obtained from GE1/1 triple-GEM detector under test: the experimental points represent each photopeak position and the solid line is a Gaussian fit to the data. The response uniformity for this detector is $R.U. = 3.4 \pm 0.2\%$. (Figure 6.46d) Map of the detector response (i.e. the normalized photopeak energy) across the detector under test. 224
- 6.47 (left) Picture of the AMPTEK mod. Mini-X X-ray Tube with the main specifications shown in the table. (right) Energy spectrum of the X-ray emitted by the Ag-target X-ray tube operated at tube voltage of 50kV and a tube current of 25μA. It has been registered with a CdTe detector [121]. 225
- 6.48 Schematic overview of the X-ray copper box showing the detector under test irradiated by the silver X-ray source. 225
- 6.49 The schematic overview of the gas system used during the X-ray longevity test at the CMS-GEM QA/QC facility. The whole gas line is made of stainless-steel tubes. 226
- 6.50 Pictures of the longevity test stand showing the X-ray generator in front of the detector under test (left) and the detector equipped with the readout electronics (right). 226
- 6.51 Schematic overview of the X-ray copper box showing the detector under test irradiated by the silver X-ray source. The X-ray generator has been initially placed at ~ 80.0 cm from the detector under test and ~ 32.5 cm from the floor of the X-ray copper box 228
- 6.52 AMPTEK miniX X-ray iso-power curve: the tube current and the voltage must be set in accordance with this curve in order to avoid severely damage of the device [80]. 229
- 6.53 Anode current measured on the irradiated readout sector $i\eta = 6$, $i\phi = 2$ at different operating point of the X-ray tube. The X-ray generator has been placed at ~ 80.0 cm from the detector under test and ~ 32.5 cm from the floor of the X-ray copper box. The GE1/1-X-S-CERN-0002 detector has been operated in Ar/CO_2 (70/30) gas mixture at gas gain of 2×10^4 230

6.54	Anode current measured on the irradiated readout sector $i\eta = 6$, $i\phi = 2$ at different positions of the X-ray tube from the detector under test. The experimental data are modeled by the function $I_{anode} = A \times r^B$. The X-ray generator settings have been selected at 40 kV and 100 μA (black dots) and at 50 kV and 70 μA (blue dots). The GE1/1-X-S-CERN-0002 detector has been operated in Ar/CO ₂ (70/30) gas mixture at gas gain of 2×10^4	231
6.55	Schematic overview of the X-ray copper box showing the detector under test irradiated by the silver X-ray source. The X-ray generator has been placed at ~ 12.0 cm from the detector under test and ~ 32.5 cm from the floor of the X-ray copper box . . .	232
6.56	Anode current flow map in the final configuration of the X-ray settings: tube powering current of 70 μA , tube powering voltage of 40 kV and distance between the X-ray tube and the detector of 12 cm. The GE1/1 triple-GEM detector has been operated in Ar/CO ₂ (70/30) gas mixture at an initial gas gain of 2×10^4 .	234
6.57	Measured interaction rates with and without the copper attenuator at different current settings for the X-ray generator at 10 cm from the detector under test. The measured rate without copper attenuators clearly shows the pile-up effect on the preamplifier stage from starting ~ 50 kHz. The GE1/1-X-S-CERN-0002 detector has been operated in Ar/CO ₂ (70/30) gas mixture at an initial gas gain of 2×10^4	235
6.58	(left) Interaction rate measured as a function of the inverse square distance between the X-ray tube and the detector. The experimental data are modeled by the function $R = A \times \frac{1}{r^2} + B$. (right) Measured and extrapolated interaction rates at different current settings for the X-ray generator at 10 cm from the detector under test.	236
6.59	Scheme of the electronic chain and data acquisition system used during the longevity test at CMS-GEM QA/QC facility.	237
6.60	(top) Correlation between the anode current of the GE1/1-X-S-CERN-0002 detector and the atmospheric pressure during the entire irradiation test (~ 5 months). (bottom) Normalized anode current ($I_{meas.}$) of the GE1/1-X-S-CERN-0002 detector under test, over the irradiation period (~ 1 month). I_{real} is the normalized and corrected anode current after the applying the correction expressed in Equation 6.6. All the data points have been normalized with the initial value of the anode current.	238
6.61	Result of the longevity studies at the CMS-GEM QA/QC facility: accumulated charge per unit of detector area (mC/cm^2) as a function of time for the irradiated $i\eta = 6, i\phi = 2$	239

-
- 6.62 Accumulated charge per unit of detector area as a function of time in two different periods of continuous irradiation. The linear fit to the experimental data provides the average integrated charge rate: $R(Q_{int})_{X-ray} = 5.5 \pm 0.1 \text{ mC/cm}^2 \cdot \text{day}$ 240
- 6.63 Result of the longevity studies at the CMS-GEM QA/QC facility: normalized and corrected anode current as a function of the accumulated charge for the irradiated sector $i\eta = 6, i\phi = 2$. The GE1/1-X-S-CERN-0002 has been operated in Ar/CO_2 (70/30) gas mixture at an initial gas gain of 2×10^4 241
- 6.64 Result of the longevity studies at the CMS-GEM QA/QC facility: accumulated charge per unit of detector area (mC/cm^2) as a function of time (6.64a, 6.64c) and normalized and corrected anode current as a function of the accumulated charge (6.64b, 6.64d) for the readout sectors $i\eta = 6, i\phi = 1$ (top) and $i\eta = 6, i\phi = 3$ (bottom). 242
- 6.65 Effective gas gain measurement as a function of the divider current performed on the readout sectors $i\eta = 6, i\phi = 2$ for different accumulated charge value: 0 mC/cm^2 , 326.06 mC/cm^2 (safety factor ~ 1.2), 570.31 mC/cm^2 (safety factor ~ 2.0) and 874.16 mC/cm^2 (safety factor ~ 3.1). 243
- 6.66 Results from the effective gas gain measurement campaign. Effective gas gain measurements performed every week (i.e. every about 30 mC/cm^2 of accumulated charge) on the readout sectors $i\eta = 6, i\phi = 2$ for the selected HV divider current $I_{divider} = 660 \mu A$ (left) and $I_{divider} = 680 \mu A$ (right). 244
- 6.67 Results from the energy resolution measurement campaign. Top: ^{109}Cd energy spectrum taken with the GE11-X-S-CERN-0002 detector at an applied voltage of 3390 V ($676.6 \mu A$ divider current equivalent). The solid line represents a fit to the experimental data using a sum of two gaussians distribution, to model the copper fluorescence photopeak and the Ar escape peak, plus a fifth order polynomial that models the background. The energy resolution (FWHM value of the photopeak divided by the mean value μ) is 17%. Bottom: Energy resolution as a function of accumulated charge for the readout sectors $i\eta = 6, i\phi = 2$ at an applied voltage of 3390 V ($676.6 \mu A$ divider current equivalent). 246
- 6.68 Results of the effective gas gain and the energy resolution measurements campaign: effective gas gain and the energy resolution measurements campaign performed every week (i.e. every about 30 mC/cm^2 of accumulated charge) on the readout sectors $i\eta = 6, i\phi = 1$ (top) and $i\eta = 6, i\phi = 3$ (bottom). 247

LIST OF FIGURES

6.69	Results from the response uniformity measurement campaign. The detector under test is a GE11-X-S-CERN-0002 detector operated in Ar/CO_2 (70/30) gas mixture at an effective gas gain of ~ 600	248
6.70	Results from the response uniformity measurement campaign. The detector under test is a GE11-X-S-CERN-0002 detector operated in Ar/CO_2 (70/30) gas mixture at an effective gas gain of ~ 600	248
6.71	Results from the response uniformity measurement campaign. The detector under test is a GE11-X-S-CERN-0002 detector operated in Ar/CO_2 (70/30) gas mixture at an effective gas gain of ~ 600	249
6.72	Results from the response uniformity measurement campaign. The detector under test is a GE11-X-S-CERN-0002 detector operated in Ar/CO_2 (70/30) gas mixture at an effective gas gain of ~ 600	249
6.73	Results from the response uniformity measurement campaign. The detector under test is a GE11-X-S-CERN-0002 detector operated in Ar/CO_2 (70/30) gas mixture at an effective gas gain of ~ 600	250
6.74	Result from the response uniformity measurement campaign showing the response uniformity of the detector under irradiation test, normalized to the initial value, as a function of the accumulated charge. The detector under test is a GE11-X-S-CERN-0002 detector operated in Ar/CO_2 (70/30) gas mixture at an initial gas gain of 2×10^4	251
7.1	A 3D Catia schematic overview for the T8 beam-line on the PS East Experimental Area hall showing the position of the IRRAD and CHARM facilities along the T8 beam-line [132].	256
7.2	FLUKA Monte Carlo geometry simulations of the experimental area, cut at beam-height. The racks 1 to 13 are the regions that correspond to the test position. The grey and brown plates are concrete and iron movable bloks of shielding respectively [132].	257
7.3	An example plot of the radiation spectra seen at the R1 test position for the facility configuration copper-O000. The artificial lower thresholds seen for electrons and photons at ~ 1 MeV is due to the threshold settings used for the FLUKA Monte Carlo simulations and is not strictly a physical phenomena [137].	258
7.4	An example plot of the dose (left) and high energy hadrons fluence (right) normalised per day inside the experimental area at beam height. (1.5×10^{15} protons per day) [132].	259
7.5	Voltage distribution in the triple-GEM detector prototype under test at CHERM facility.	261

7.6 Principle of operation of the triple-GEM tedector prototype and definition of drift, transfer, and signal induction gap regions within the detector. The columns on the right give the actual gap sizes in the detector. They also list typical values for electric potentials on the seven electrodes and typical values for voltages and electric fields across the four gaps blue) and the three GEM-foils (red) if the nominal potential of 3275 V in Ar/CO_2 (70/30) is applied to the drift cathode (696.8 μA divider current equivalent). 262

7.7 Schematic overview of the experimental set-up used for the effective gas gain measurement on the 10 cm \times 10 cm triple GEM detector prototype. 263

7.8 Measured particle interaction rate (black dots) and the effective gas gain (blue dots) as function of the voltage difference applied to the drift cathode V_{Drift} . The detector under test is a single-mask GEMs in tripple stack configuration of 10 cm \times 10 cm operated in Ar/CO_2 (70/30) gas mixture. 264

7.9 Schematic overview of the experimental set-up used for the energy resolution measurement on the 10 cm \times 10 cm triple GEM detector prototype. 264

7.10 ^{55}Fe energy spectrum taken with single-mask GEMs in tripple stack configuration of 10 cm \times 10 cm operated in Ar/CO_2 (70/30) gas mixture at an $V_{Drift} = 3275 V$ (696.8 μA divider current equivalent). The solid line represents a fit to the experimental data using a sum of two gaussians distribution, to model the main photopeak and the Ar escape peak, plus a fifth order polynomial that models the background. The energy resolution ($FWHM$ value of the main photopeak divided by the mean value μ) is $25.9 \pm 0.1\%$ 265

7.11 Layout of CHARM configuration with copper target with shielding (copper-CIIC). The position used during the discharge probability test campaign is highlighted in green. 266

7.12 Particles lethargy spectra obtained by Fluka simulation for the CuCIIC configuration in the R3 test position, i.e. the available particle fluence for the configuration copper-CIIC in the R3 test position normalized over primary Protons On (copper-)Target (POT) [137]. 266

7.13 Simulated energy spectra for different background particles considering CMS-FLUKA Phase-2 geometry and an instantaneous luminosity of $5 \times 10^{34} cm^2 s^{-1}$ for the upgrade ME0 detector [140]. 267

7.14 Schematic overview of the gas system used during the irradiation test at CHARM facility. The whole gas line is made of stainless-steel tubes. 268

LIST OF FIGURES

7.15	Pictures of the experimental set-up for the discharge probability studies at CHARM facility. The triple-GEM detector prototype is placed in the R3 test location and the copper target in the shielding configuration copper-CIIC has been selected.	268
7.16	Scheme of the electronic chain and data acquisition system used during the discharge probability studies at CHARM facility. . .	270
7.17	Average counting rate per spill from the lower electrode of the third GEM-foil as a function of the voltage difference applied to the drift cathode V_{Drift} measured by the triple-GEM detector under irradiation test at CHARM facility a discriminator threshold value of 500 mV. The average counting rate inside the spill (black dots) has been corrected by the average counting rate outside the spill and the average net counting rate per spill (blue dots) has been obtained. The working point corresponding to a $V_{Drift} = 3350 V$ (712.8 μA divider current equivalent) has been used to calculate the discharge probability.	273
7.18	Average net counting rate per spill from the lower electrode of the third GEM-foil as a function of the applied discriminating threshold at working point corresponding to a $V_{Drift} = 3350 V$ (712.8 μA divider current equivalent). The point corresponding to a threshold value of 500 mV has been used to calculate the triple-GEM neutron sensitivity.	274
7.19	Result of the discharge probability studies at the CHARM facility: accumulated charge per unit of detector area (mC/cm^2) as a function of time. The detector under irradiation test integrated about 0.9 mC/cm^2 after ~ 120 hours of continuous irradiation of sustained operation in the harsh mixed-radiation fields, which represents about 1.5 years of operation in GE1/1 environment at the HL-LHC.	277
7.20	Comparison of effective gas gains of the triple-GEM detectors under test at the CHARM facility in pre- and post-irradiation conditions with the irradiated electronics.	278
A.1	Plan of the Clean Room installed at the CMS-GEM QA/QC facility at CERN.	286
A.2	The view of the CMS-GEM QA/QC facility at CERN.	287
A.3	The internal view of the Clean Room installed at the CMS-GEM QA/QC facility at CERN.	287
A.4	The view of the assembly zone in the Clean Room installed at the CMS-GEM QA/QC facility at CERN.	288
A.5	The view of the QC2 Long - Current Leakage Test in the Clean Room installed at the CMS-GEM QA/QC facility at CERN. . .	288
A.6	Plan of the GEM Laboratory installed at the CMS-GEM QA/QC facility at CERN.	289

A.7	The view on the QC3/4 stands in the CMS-GEM QA/QC facility at CERN.	290
A.8	The view on the QC5 stands in the CMS-GEM QA/QC facility at CERN.	290

List of Tables

2.1	Main parameters of the LHC and its beam [3].	9
2.2	Fundamental particles in the Standard Model [15].	12
2.3	Fundamental Interactions in the Standard Model [15].	12
3.1	The main characteristics of the CMS sub-detectors and their functions [33], [34].	22
3.2	Parameters of the CMS superconducting solenoid.	24
5.1	Material budget for a GE1/1 triple-GEM station [69].	77
5.2	Specifications and parameters for the technical design and operation of the CMS GE1/1 detector [69].	78
5.3	Main industrial partners involved in the CMS-GE1/1 project.	82
5.4	Technical specifications and parameters of Short and Long GE1/1 detectors.	85
5.5	Timeline for the GE1/1 assembly and commissioning.	106
5.6	Typical QC2 fast summary table for an accepted GEM-foil.	114
5.7	Summary status of the LS2-GE1/1 detectors mass production in the different production and quality control sites involved in the CMS-GE1/1 project (latest data as at 31 th August 2018).	169
6.1	Physical Properties of gases at normal temperature and pressure (NTP): E_x and E_i are the excitation and ionization energy, respectively, n_p and n_t are the number of primary electron-ion pairs per cm and the total number of electron-ion pairs per cm, respectively, W_i is the average energy required to produce one electron-ion pair in the gas, $\langle dE/dx \rangle_{MIP}$ is the most probable energy loss by a minimum ionizing particle (MIP) [84].	172
6.2	Expected background components and their corresponding hit rates in the <i>GE1/1</i> , <i>GE2/1</i> , and <i>ME0</i> detectors. The total accumulated charge is calculated from the total hit rate at a typical detector gas gain of 2×10^4 after 10 HL-LHC years which correspond an effective exposure time of about 6×10^7 s [69].	173

6.3	Outgassing test campaign results showing the list of the materials under test, their role in the detector, and the effect of their presence on the irradiated Single Wire Proportional Counter [90].	183
6.4	Configurations which maximize the anode current in the GE1/1-X-S-CERN-0002 detector for the X-ray generator placed at 80cm from the irradiated detector. The anode current has been measured from the readout sector $i\eta = 6$, $i\phi = 2$.	229
6.5	The two intermediate working settings for which the anode current has been measured on the readout sector $i\eta = 6$, $i\phi = 2$.	233
6.6	The final working settings for which the anode current has been measured on the readout sector $i\eta = 6$, $i\phi = 2$.	233
7.1	Different type of particles with the relative contribution for the configuration copper-CIIC in the R3 test position. <i>HEH</i> refers to "High Energy" Hadrons, i.e. all hadron particles with energy above 20 <i>MeV</i> [137].	267
7.2	Expected number of discharges in GE1/1, GE2/1, and ME0 triple-GEM detectors after ten years of operation at HL-LHC.	276

Contents

List of Figures	i
List of Tables	xxvi
1 General Introduction	1
2 Large Hadron Collider	7
2.1 Large Hadron Collider	7
2.2 LHC Main Characteristics	10
2.3 The Physics at the LHC	11
2.3.1 The Standard Model	11
2.3.2 Electroweak Symmetry Breaking in the Standard Model	12
2.3.3 Search for Higgs Boson at LHC	15
2.3.3.1 Phenomenology	15
2.3.3.2 Discovery of Higgs Boson at LHC	19
2.4 LHC Experiments	19
3 The CMS Experiment	21
3.1 Overall Design	21
3.2 The Superconducting Magnet	23
3.3 Tracker System	24
3.4 Calorimeter System	26
3.5 CMS Muon Spectrometer	28
3.5.1 Drift Tube	30
3.5.2 Cathode Strip Chambers	31
3.5.3 Resistive Plate Chamber	33
3.6 CMS Trigger Systems	34
3.6.1 Level-1 Trigger	34
3.6.2 High-Level Trigger	36
3.7 Overview of CMS Upgrade Project	37
3.7.1 Schedule of the Upgrades	38
3.7.2 Motivation	39

3.7.3	Overview of the expected CMS upgrades during the technical stop, LS2, and LS3	41
3.8	Overview of the Phase-2 Upgrade of CMS Muon Spectrometer	43
3.8.1	The Upgrade of the Existing Muon Stations	44
3.8.2	New Stations in the innermost region of the CMS forward Muon Spectrometer	46
4	The Gas Electron Multiplier	49
4.1	Introduction	49
4.2	The GEM Technology	53
4.2.1	Influence of GEM-hole diameter	55
4.2.2	Influence of GEM-hole pitch	56
4.2.3	Influence of GEM-hole shape	56
4.3	The single-GEM detector	57
4.3.1	Drift and induction electric fields	59
4.3.2	Drift and induction region thickness	62
4.3.3	GEM-foil voltage	62
4.4	The triple-GEM detector	64
4.4.1	Transfer electric field effect	66
4.4.2	Transfer region thickness	67
4.4.3	GEM-foils voltage in a triple-GEM detector	68
4.4.4	Time performance in a triple-GEM detector	69
4.4.5	The signal formation in a triple-GEM detector	70
5	The Assembly, Quality Control and Commissioning of the GE1/1 detectors	73
5.1	The GE1/1 detectors for the CMS-GEM project	73
5.1.1	Description of the GE1/1 project	73
5.1.2	GE1/1 detector requirements	76
5.1.3	GE1/1 detector overview	77
5.1.4	Mass production of the GE1/1 detectors	79
5.2	GE1/1 detector components and design	84
5.2.1	GE1/1 technical design	84
5.2.2	Drift Board design	85
5.2.3	External Frame Design	86
5.2.4	Internal Frame Design	87
5.2.5	GEM Foil design and production technology	88
5.2.6	Readout Board design	91
5.2.7	Gas Distribution System	92
5.3	Description of the assembly procedure	93
5.3.1	Drift Board Preparation	93
5.3.2	GEM Stack Assembly	96
5.3.3	Detector Construction	99
5.3.4	Stretching Mechanism	100

5.4	Requirements for GE1/1 Quality Assurance/Quality Control assessment	104
5.4.1	Overview of the QA/QC	104
5.4.2	QC1 - GE1/1 Detectors Components Inspection and Read-out Board Connectivity Test	107
5.4.3	QC2 - Leakage Current Test	110
5.4.3.1	GEM-foil preparation and cleaning	111
5.4.3.2	QC2 fast: GEM acceptance test I	111
5.4.3.3	QC2 long: GEM acceptance test II	114
5.4.3.4	QC2 post-assembly in clean room	118
5.4.3.5	QC2 fast in dry gas	120
5.4.4	QC3 - Gas Leak Test in CO_2	120
5.4.5	QC4 - HV Test in CO_2	130
5.4.6	QC5 - Gas Gain measurement in Ar/CO_2 (70/30)	134
5.4.6.1	Preparation and installation of the GE1/1 detector	137
5.4.6.2	Effective gas gain measurement	138
5.4.6.3	Description of the experimental setup	140
5.4.6.4	Procedure of the QC5 effective gas gain measurement	141
5.4.6.5	Results of the QC5 effective gas gain measurement	142
5.4.6.6	Response Uniformity	143
5.4.7	Summary of QA/QC test results at CERN	154
5.4.7.1	QC3 - Gas Leak Test in CO_2	154
5.4.7.2	QC4 - HV Test in CO_2	156
5.4.7.3	QC5 - Gas Gain Measurement in Ar/CO_2 (70/30)	159
5.4.8	LS2 - GE1/1 Detector Production Status	166
6	Long-term operation study	171
6.1	Introduction	171
6.1.1	Aging phenomena of gaseous detectors	173
6.1.2	Past experience on the aging of GEM-based detector	179
6.1.3	Motivation for additional aging studies	185
6.2	Triple-GEM Aging Studies at GIF++ facility	187
6.2.1	The GIF++ facility at CERN for aging studies	187
6.2.2	Aging Test on triple-GEM technology for the ME0 project of the GIF++ facility	190
6.2.2.1	The CMS GE1/1 triple-GEM detector under test and quality control	190
6.2.2.2	The CMS GE1/1 triple-GEM detector at GIF++ facility	196
6.2.2.3	Data acquisition and analysis procedure	198
6.2.2.4	Aging Test Results for CERN GEM-foils	206
6.2.3	Aging Test on triple-GEM technology for GE2/1 project	208

6.2.3.1	Introduction	208
6.2.3.2	The triple-GEM detector with korean GEM-foils quality control	211
6.2.3.3	Aging Test Results on Korean GEM-foils	216
6.3	Triple-GEM Aging Studies at CMS-GEM QA/QC facility with X-ray source	218
6.3.1	Aging Test on triple-GEM technology for ME0 project	218
6.3.1.1	GE1/1 detector under test and quality control	218
6.3.1.2	Experimental setup	222
6.3.1.3	X-ray generator set-up and working parameters definition	227
6.3.1.4	Data acquisition and analysis procedure	235
6.3.1.5	Aging Test Results for CERN GEM-foils	239
7	Discharge Probability Studies in triple-GEM detectors	253
7.1	Introduction	253
7.2	Discharge probability studies on triple-GEM technology at CHARM facility	255
7.2.1	The CHARM facility at CERN	255
7.2.2	The triple-GEM detector prototype under test and characterization	258
7.2.2.1	Effective gas gain measurement	260
7.2.2.2	Energy resolution measurement	262
7.2.3	The triple-GEM detector prototype at the CHARM facility	263
7.2.4	The data acquisition system and discharge monitoring at the CHARM facility	269
7.2.5	Measurement of the discharge probability	272
7.2.5.1	Expected number of discharges during detector operation	275
7.2.5.2	Effects of the discharges on the detector operation	276
8	General conclusions	279
A	CMS-GEM QA/QC facility in CERN	285
	Bibliography	289
	Acknowledgements	301

Chapter 1

General Introduction

This Doctoral Thesis takes place in the framework of the upgrade of the Muon System of the Compact Muon Solenoid (CMS) experiment, one of the two general-purpose detectors measuring proton-proton and heavy-ion collisions at the Large Hadron Collider (LHC) at CERN laboratory, in Geneva. To extend the sensitivity for new physics searches, a major upgrade of the LHC machine has been decided and is being prepared, the High Luminosity LHC (HL-LHC). The instantaneous luminosity of LHC is expected to exceed the nominal value and reach $2.5 \times 10^{34} \text{ cm}^{-2}\text{s}^{-1}$, after the second Long Shutdown (LS2) foreseen in 2019-2020. A further increase is planned during the third Long Shutdown (LS3) in 2024-2026, up to $5 \times 10^{34} \text{ cm}^{-2}\text{s}^{-1}$, i.e. a yield five times greater than the initially design value of the current LHC. The increase of the energy and luminosity during the future upgrades of the LHC machine will deeply affect the performance of the CMS Muon System due to the harsh background environment and the high pile-up.

The CMS collaboration is currently improving the Muon System to maintain the high level of performance achieved during the first period of operation (Run 1) also in the challenging environment of the high-luminosity LHC. The Muon System of CMS experiment was originally designed as a highly hermetic and redundant system that employs three gas-based detectors: Drift Tubes (DTs), Cathode Strip Chambers (CSCs), and Resistive Plate Chambers (RPCs). It was designed to operate in the initial LHC environment with an instantaneous luminosity up to $10^{34} \text{ cm}^{-2}\text{s}^{-1}$, and provided excellent triggering, muon identification, timing, and momentum measurement achieved during the entire Run 1 period. Precision measurements and Level 1 (L1) triggering are provided by Drift Tubes in the barrel, covering acceptances up to $|\eta| < 1.2$, and Cathode Strip Chambers in the endcaps covering $1.0 < |\eta| < 2.4$. Additionally, Resistive Plate Chambers provide redundant trigger and coarse position measurement in both barrel and endcap regions, but were not implemented beyond $|\eta| > 1.6$ due to concerns about their capability to handle the high background particle rates. This imposes severe restriction on the gaseous detection technology

that can be used: new detector requirements include a high rate capability $O(MHz/cm^2)$, a good spatial resolution $O(100 \mu m)$ for tracking, a good time resolution for triggering, and in addition, radiation hardness.

In order to cope with very high operation condition, high pile-up and background environment in particular in the forward region, the CMS Collaboration is planning to install a detector based on the Gas Electron Multiplier (GEM) technology to upgrade the CMS Muon System, instrumenting the non-redundant CMS high η region with detectors that could withstand the hostile environment and high luminosity rates at the LHC and its future upgrades. GEMs are gas-based detectors, characterized by a detection efficiency more than 98% even for rate exceeding few MHz/cm^2 , high spacial resolution of order $\sim 100 \mu m$, and good time resolution of order ~ 8 and $\sim 5 ns$ at the efficiency plateau for Ar/CO_2 (70/30) and $Ar/CO_2/CF_4$ (45/15/40) gas mixture, respectively. Additionally, the gas gain is observed to be stable up to a several MHz/cm^2 of incident particle rate by demonstrating that the triple-GEM detectors have a high rate capability and will be suitable to operate in the forward muon region of CMS experiment, where a maximum rate on the order of $50 kHz/cm^2$ is expected. Despite being invented just in 1997 by F. Sauli, the triple-GEM technology has become a widely used detection technology for high-rate experiments like COMPASS, LHCb or TOTEM and are foreseen for new experiments or upcoming upgrades, such as the CMS Muon System or the ALICE TPC upgraded.

The triple-GEM detectors are approved to instrument two forward region of the Muon System of the CMS experiment at $1.6 < \eta < 2.4$, called GE1/1 and GE2/1 station during the second and third Long Shutdown, respectively. The GE1/1 and GE2/1 detectors are "super-chambers", each made of a double layer of trapezoidal triple-GEM detector. They will cover slightly more than 10° in GE1/1 station and 20° in GE2/1 station, overlapping in φ just like the corresponding CSC detectors in ME1/1 and ME2/1 stations, complementing them and providing redundancy and enhanced triggering and tracking capabilities in the region which currently suffering from the highest background rates and a non uniform magnetic field. Therefore, 36 super-chambers will be installed for the GE1/1 station and 18 for the GE2/1 station in each muon endcap in order to ensure the full azimuthal coverage. In order to gain first operational experience with the new subsystem and also to demonstrate the integration of GE1/1 detectors into the trigger, a demonstrator, consisting of five GE1/1 super-chambers, has already been installed in CMS during the year-end technical stop 2016/2017. In addition to GE1/1 and GE2/1 station, the ME0 station is approved to be instrumented with triple-GEM detector. Indeed, with pixel tracking extension close to $\eta < 4$ and the replacement of the endcap of the electromagnetic and hadronic calorimeters during the third Long Shutdown, comes the opportunity to extend the muon coverage beyond the present limit of $\eta < 2.4$ with the addition of a muon gas-based detector installed in a space of $\sim 30 cm$ freed behind the new end-cap calorimeters. The ME0 detector

station comprises 36 module stacks (18 per endcap), each composed of six layers of triple-GEM detectors, compared to the two-layer design of GE1/1 and GE2/1, covering the region $2 < \eta < 2.8$, in order to allow proper rejection of neutron background, particularly intense in that region. The large η coverage foreseen would lead to an improvement of the acceptance, with a consequent boost in the signal over noise ratio in the signature with muons, especially with the multiple-muon final states, and better hermeticity for signature without muons.

The Doctoral Thesis subject has been proposed by the CMS GEM Collaboration and three main research projects have been conducted in this context:

The first project, conducted in the framework of the LS2 GE1/1 detector mass production, is focused on the production and quality control of the triple-GEM detectors for the CMS-GE1/1 station, to be installed in the CMS Muon System during the second Long Shutdown in 2019/2020. The aim of the LS2 GE1/1 detector mass production is to assemble, certify and characterize the CMS GE1/1 triple-GEM detectors using the large amount of data acquired during the 18 months of quality certification tests at the CERN production site. The Quality Assurance (QA) and the Quality Control (QC) are key elements to ensure the delivery of fully efficient GE1/1 detectors yielding their best performance when installed in the Muon Spectrometer of the CMS experiment. The final detector quality and performance depend on the production quality and on the accuracy of the detector assembly procedures. For this reason, a standardized QA and QC protocol for the GE1/1 chamber and super-chamber assembly and certification has been carefully prepared for each level of the mass production in order to prevent any mechanical or electrical issues that might affect the detector performance. The quality control tests involve all the principal GE1/1 detector components and focus on the following main aspects: Gas Tightness, Electric Test, Noise, Effective Gas Gain and Response Uniformity Measurement.

The second project has been focused on the long-term operation of triple-GEM detectors, in particular the study of the aging phenomena. The innermost region of the forward CMS Muon Spectrometer is characterized by a harsh environment, primarily composed by neutrons and photons. Aging is one of the most critical limitations of the use of gaseous detectors in strong radiation environments; it includes all the processes that lead to a significant and permanent degradation of the detection performances: gain drop, non-uniformity, dark current, discharge, etc. Long-term operation in high-intensity experiments of the HL-LHC era not only demands extraordinary radiation hardness of construction materials and gas mixtures but also very specific and appropriate assembly procedures and quality checks during detector construction and testing. For this reason, it will be of primary importance the analysis of the behavior of the new detectors in neutrons and gamma fields, in order to verify the proper operation in such a huge environment. To evaluate the potential

detector performance deterioration over the lifetime of an experiment, detector prototypes are subject to accelerated aging tests performed at a higher instantaneous radiation rate. Similarly to several gaseous detector, the triple-GEM detector might be subject to aging effect when operating in a high-rate environment. For this reason, several aging tests of full size CMS-GE1/1 triple-GEM detectors have been carried out in parallel at CERN Gamma Irradiation Facility (GIF++), using for the irradiation an intense 14 TBq (2015) ^{137}Cs source emitting 662 keV γ -rays, and at the CMS-GEM QA/QC Lab. using as irradiation source a 22 keV X -rays source. Both detectors are operated with Ar/CO_2 (70/30) gas mixture at an effective gas gain of 2×10^4 . The aim of this aging test campaign is to validate the triple-GEM technology developed for the CMS-GE1/1 project, using large GEM-foils based on the single-mask photolithography technique produced by the CERN PCB workshop, also for CMS-ME0 project which is expected to integrate an accumulated charge of $283\text{ mC}/\text{cm}^2$ in 10 years of HL-LHC. An additional aging test on the triple-GEM technology based on the double-mask photolithography technique developed by the Mecaro company (Korea) has been carried out in parallel at GIF++ facility. The detector is operated with Ar/CO_2 (70/30) gas mixture at an effective gas gain of 2×10^4 . The large GEM-foils based on the double-mask technique are not yet tested from the aging point of view. The aim of this aging test campaign is to validate the large GEM-foils based on the double-mask photolithography technique produced by the Mecaro company for CMS-GE2/1 project by integrating a minimum of charge per unit area of about $9\text{ mC}/\text{cm}^2$, which represent a 10 years of the total GE2/1 operation at HL-LHC with a safety factor three, and future applications.

The third project included a systematic investigation of the discharge probability with the triple-GEM detectors under neutron irradiation in Ar/CO_2 (70/30) gas mixture. Still on the subject of the capability of the new detectors of working in intense neutrons and photons environment, the CMS-GEM Pavia group performed several neutron tests at CERN CHARM (Cern High energy Accelereator Mixed Field facility): it provides neutrons, produced in spallation reaction of the Proton Synchrotron (PS) beam with a copper target, with an energy spectrum similar to CMS Muon System, for an integrated flux of about 10^5 - $10^6\text{ n}/\text{cm}^2 \cdot \text{s}$ in the irradiation position. The aim of these neutron tests has been the study of neutron sensitivity and neutron-induced discharge probability of a triple-GEM detector irradiated by neutrons. These measurements have been crucial in the choice of technology to be installed on the detector in order to preserve adequate detector performance and its discovery potential in high luminosity environment of the HL-LHC era.

The aging and the discharge probability studies have been performed in the framework of an R&D activity on detectors for the innermost region of the forward muon spectrometer of the CMS experiment. These long-term operation test campaigns have demonstrated the robustness and the radiation hardness of the triple-GEM technology, which could tolerate the radiation dose fore-

seen in 10 HL-LHC years of operation in the ME0 environment of the CMS experiment. Therefore, the triple-GEM technology, based on the single-mask photolithography technique produced by the CERN PCB workshop, is fully validated for CMS-ME0 upgrade project. The results obtained during the three years of Ph.D. have been contributed to the success of the CMS-ME0 upgrade project and its approval by the CMS and LHCC Collaboration.

Chapter 2

Large Hadron Collider

By colliding the two oppositely directed beams of charged particles with high-energy in a circular accelerator, it is possible to reconstruct similar conditions which were at the first moments of life of our Universe. The higher the energy, the farther we can see in the past, the more likely, we can observe the exotic interactions and discover the new physics laws. Large Hadron Collider (LHC) and its experiments were built by the European Organization for Nuclear Research (CERN) [1] from 1998 to 2008. They are the unique objects and one of the greatest achievements of human engineering. Since 2008, the development of high-energy physics has been determined by the results obtained in the experiments at the LHC. The LHC and its experiments allowed scientists to verify the predictions of the elementary particles physics theories, by finding the evidence of the existence of the long-theorized Higgs boson and by searching the large family of new particles predicted by the theory of supersymmetry as well.

2.1 Large Hadron Collider

The *Large Hadron Collider* (LHC) [2] [3] [4] [5] is a proton-proton superconducting accelerator and collider installed in the existing 26.7 km tunnel that was constructed between 1984 and 1989 to host the *Large Electron Positron* (LEP) collider [6] [7] [8]. The LEP tunnel has eight straight sections and eight arcs and lies between 45 m and 170 m below the surface. The approval of the LHC project was given by the CERN Council in December 1994. At that time, the plan was to build a machine in two stages starting with a center-of-mass energy of 10 TeV (be upgraded later to 14 TeV), but later it was approved the construction of the 14 TeV machine in a single stage.

The choice of proton beams is mainly dictated by the following considerations [2] [3]:

- hadron allow to explore a wide range of energies with fixed-energy beams:

they are the natural choice for a discovery machine. This is because of the fact that protons are not elementary particles, and in hard collisions, the interaction involves their constituents (quarks and gluons), which carry only a fraction of the proton energy;

- protons due to their higher mass imply a smaller energy loss from synchrotron radiation with respect to electrons, since in a circular collider of radius R , the energy loss per turn is proportional to $(E/m)^4/R$, where E and m are the energy and mass of the particles accelerated, respectively.

Since only a fraction of the proton energy contributes to the hard scattering, the center-of-mass energy of the beam must be much higher than the mass of the particle that has to be produced. It can be noted that the Higgs cross section increases steeply with the center-of-mass energy, while the total cross section remains almost constant. It is clear that the highest center-of-mass energy should be used.

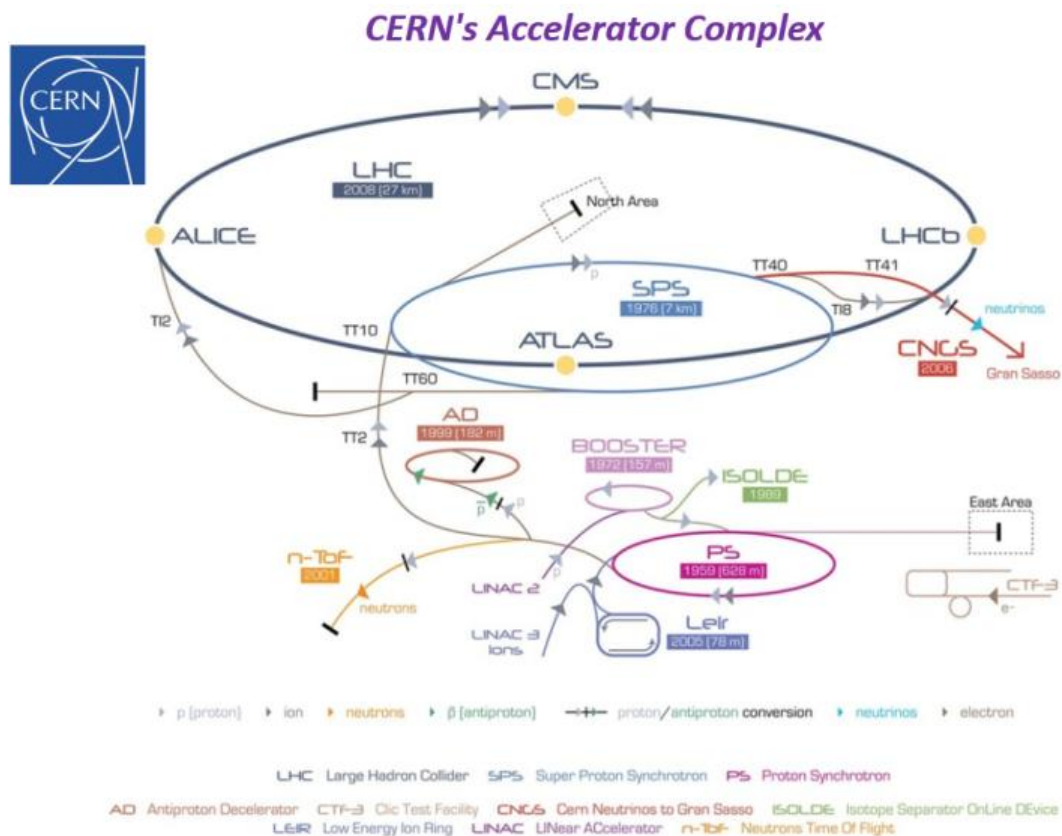


Figure 2.1: General view of the CERN accelerator complex and location of its main experiments [5].

Before begin injected to the LHCs main ring, the charged particles beams are gradually accelerated in the different stages of the CERN accelerating complex

2.1. Large Hadron Collider

(see Figure 2.1). First of all, protons are extracted from hydrogen stored in a gas cylinder by stripping orbiting electrons from the atoms. At this early stage, the protons have an energy around 100 keV and are pulsed every $100 \mu\text{s}$. They enter the 30 m long linear accelerator called Linac2, where they acquire an energy of 50 MeV . Protons are then injected into the Proton Synchrotron Booster (PSB), a four ring synchrotron that accelerates single bunches up to 1.4 GeV . Two bunches of protons are transferred to the Proton Synchrotron (PS), the oldest CERN accelerator still in service. In the PS, the large PSB bunches are split into smaller bunches and accelerated to 28 GeV , before being split again to achieve the final 25 ns bunch spacing that will be maintained up to the LHC. The last step of pre-acceleration is made by the 6.9 km Super Proton Synchrotron (SPS), where the beams reach the injection energy of 450 GeV . The SPS is filled with 3 to 4 cycles of the PS (out of the 11 that would fit), as it is not capable of accelerating more than 4×10^{13} protons at a time. After acceleration, the proton bunches are then transferred to the LHC ring for acceleration up to 7 TeV . It takes 12 cycles of the SPS in order to fill the LHC. The LHC rings can contain up to 2808 bunches moving in opposite directions. Every second a proton bunches cross the 27-kilometer ring of 11000 times. Before the particles collide in the four main interaction points (ATLAS [9], CMS [10], ALICE [11], and LHCb [12]), they will circulate around the ring about 5 hr 24 min.

In addition, when LHC operates as a heavy ion accelerator, lead ions are first accelerated by the linear accelerator LINAC 3, and the Low-Energy Ion Ring (LEIR) is used as an ion storage and cooler unit. The ions then are further accelerated by the PS and SPS before being injected into LHC ring, where they will reach an energy of 2.76 TeV per nucleon (or 5.75 TeV per lead ion). The main parameters of the LHC machine and the particle beams are presented in Table 2.1.

Parameters	p-p collisions	Pb-Pb collisions
Center-of-mass energy (TeV)	14	1148
Number of particles per bunch	$1.1 \cdot 10^{11}$	$\sim 8 \times 10^7$
Number of bunches	2808	608
Design luminosity ($\text{cm}^{-2}\text{s}^{-1}$)	10^{34}	2×10^{27}
Bunch length (mm)	53	75
Beam radius at interaction point (μm)	15	15
Time between collisions (ns)	25	124.75×10^3
Bunch crossing (MHz)	40.08	0.008
Dipole field (T)	8.3	8.3

Table 2.1: Main parameters of the LHC and its beam [3].

To hold and focus the particles inside LHC vacuum tubes, 1632 superconducting magnets were installed (see Figure 2.2a). In order to achieve a center-of-mass energy of $\sqrt{s} = 14 \text{ TeV}$ and luminosity of $10^{34} \text{ cm}^{-2}\text{s}^{-1}$, these magnets must be cooled up to 1.9 K . It is the temperature at which helium becomes



Figure 2.2: Pictures of the superconducting magnets in the LHC tunnel (left) and its cross-section (right) [3].

superfluid. After that, the magnets can create a magnetic field of $8.3 T$. The innovative design of two-in-one magnets allows both transport tubes of beams to be located in a single cryostat (see Figure 2.2b), which significantly reduces the size and cost. The total amount of helium, about 96 tons, allow to cool the LHC accelerator with a mass of 37000 tons. Thus, the LHC is one of the largest cryogenic systems in the World.

2.2 LHC Main Characteristics

The most important performance parameters of LHC are the beam energy and the luminosity.

The energy available for the production of new effects is the most significant feature. It is chosen based on the physical tasks which must be solved during the operation LHC. The range of LHC physics tasks is very wide and a brief description will be given in the Section 2.4, where the main LHC experiments and their main tasks will be presented. In the LHC collides two opposite beams which have the energy depend on the operation phase of the collider. The total energy at the collisions determines as the center-of-mass energy (\sqrt{s}) which depends on the energies E_1 and E_2 of the particles of the two beams and of their momenta \vec{p}_1 and \vec{p}_2 . Taking into account that the LHC is a collider, then $\vec{p}_1 = -\vec{p}_2$. The center-of-mass energy is given by:

$$\sqrt{s} = \sqrt{(E_1 + E_2)^2 - (\vec{p}_1 + \vec{p}_1)^2} = \sqrt{(E_1 + E_2)^2} \quad (2.1)$$

The collider's luminosity \mathcal{L} is the second most important parameter. The number of colliding particles increases with increasing luminosity. The instantaneous luminosity is defined as the number of collisions per unit time and cross-sectional area of the beams:

$$\mathcal{L} = \frac{N_1 N_2 n_b f_{rev}}{A} \quad (2.2)$$

2.3. The Physics at the LHC

where N_1 and N_2 are the number of particles in the two colliding bunches, A is the overlap area of the two bunches transverse to the beam, n_b is the number of bunches in one beam, and f_{rev} is the revolution frequency of one bunch (with a design value of 11245 Hz). At the LHC proton-proton collisions $N_1 = N_2 = N_p$, and, since the area of overlap is difficult to measure directly in an accelerator, for a Gaussian beam distribution \mathcal{L} can be written as:

$$\mathcal{L} = N_p^2 n_b f_{rev} \frac{\gamma}{4\pi\epsilon_n\beta^*} F \quad (2.3)$$

where γ is the relativistic Lorentz factor, ϵ_n is the normalized transverse beam emittance (with a design value of $3.75 \mu\text{m}$), β^* is the so-called betatron function at the interaction point [13], and F is the geometric luminosity reduction factor due to the crossing angle at the interaction point.

The luminosity integrated over a time period refers to the number of bunch crossings during this period. It is often expressed in inverse femtobarn fb^{-1} . The integrated luminosity multiplied by the interaction cross-section gives the total number of events produced during a time period. This parameter characterizes the efficiency of obtaining physical information from the LHC.

$$R \equiv \frac{dN}{dt} = \mathcal{L}\sigma \quad (2.4)$$

The first year LHC operated at $\mathcal{L} \sim 6 \times 10^{33} \text{ cm}^{-2}\text{s}^{-1}$, center-of-mass energy $\sqrt{s} = 7 \text{ TeV}$ and integrated a luminosity of 5.1 fb^{-1} . The gradual increase of the luminosity has led to the fact that by 2017, it reached the value $\mathcal{L} \sim 1 \times 10^{34} \text{ cm}^{-2}\text{s}^{-1}$ and nowadays the center-of-mass energy is $\sqrt{s} = 14 \text{ TeV}$ with an integrated luminosity of 100 fb^{-1} . Such a high luminosity is necessary to study the extremely rare events with a small cross-section which characterizes the new physics [14].

2.3 The Physics at the LHC

The LHC at CERN is the most powerful particle accelerator in the World at the moment. It operates at 14 TeV center-of-mass energy, and a design luminosity of $10^{34} \text{ cm}^{-2} \text{ s}^{-1}$. This energy and luminosity values are needed in order to investigate a range of energy (mass) never explored before and to confirm or deny the Standard Model theory. The main goal of LHC is to study the physics of elementary particles, such as Higgs boson, at the highest energies accessible to the accelerators.

2.3.1 The Standard Model

The Standard Model (SM) is a theory that describes all the elementary particles actually known and the forces (except for the gravity) between them [15]

[16] [17]. It describes matter as composed by fermions (half-integer spin particles), divided into main groups: leptons including electrons, muons, taus and the related neutrinos, and quarks. In Table 2.2 a classification of SM fermions is given.

Fermions	1 st Fam.	2 st Fam.	3 st Fam.	Charge	Interactions
Quarks	u	c	t	$+2/3$	All
	d	s	b	$-1/3$	
Leptons	e	μ	τ	-1	Weak, E.M.
	ν_e	ν_μ	ν_τ	0	Weak

Table 2.2: Fundamental particles in the Standard Model [15].

In the SM the interactions between particles are described as an exchange of bosons, the mediators of fundamental forces. Bosons are integer spin particles that mediate the fundamental interactions. In particular, the SM describes only three of the four known forces: electromagnetic, weak and strong. Gravitation is not described by SM because is not relevant at the scale of distance common in the particle physics. The fundamental interactions are described in Table 2.3.

	Electromagnetic	Weak	Strong
Quantum	Photon (γ)	W^\pm and Z	Gluons
Mass GeV/c^2	0	80-90	0
Coupling Constant	$\alpha(Q^2 = 0) \approx 1/137$	$G_F \approx 1.2 \times 10^{-5} GeV^{-2}$	$\alpha_s(m_Z) \approx 0.1$
Range (cm)	∞	10^{-6}	10^{-13}

Table 2.3: Fundamental Interactions in the Standard Model [15].

The Standard Model describes these interactions with two gauge theories:

- the theory of the electroweak interaction, or Electroweak Standard Model, that unifies the electromagnetic and the weak interaction;
- the theory of strong interactions or Quantum Chromodynamics (QCD).

2.3.2 Electroweak Symmetry Breaking in the Standard Model

The Quantum Electrodynamics is based on the invariance of the QED Lagrangian for local gauge transformation with respect to the $U(1)$ symmetry group [15] [16]. This symmetry leads to the existence of the photon, that is the massless field vector of the electromagnetic interaction. If we extend the symmetry to the group $SU(2) \times U(1)$ we can unified the weak and electromagnetic interactions in a single one, it will be the electroweak interaction. There

2.3. The Physics at the LHC

are two quantum numbers associated to this interaction: the weak isospin (I) and (Y) that satisfy the relation:

$$Q = I_3 + \frac{Y}{2} \quad (2.5)$$

where I_3 is the third component of the weak isospin and Q is the electric charge. The request of invariance for local gauge transformations with respect to the $SU(2) \times U(1)$ group introduces four massless vector fields $W_\mu^{1,2,3}$ and B_μ that couple to fermions with two coupling constants g and g' . In order to have the physical field, we have to re-organize the four massless fields in a linear combination. This gives us two charged bosons:

$$W_\mu^{1,2,3} = \sqrt{\frac{1}{2}}(W_\mu^1 \pm iW_\mu^2) \quad (2.6)$$

while the neutral bosons γ and Z correspond to

$$A_\mu = B_\mu \cos\theta_W + W_\mu^3 \sin\theta_W \quad (2.7)$$

$$z_\mu = -B_\mu \sin\theta_W + W_\mu^3 \cos\theta_W \quad (2.8)$$

The two neutral bosons are obtained by mixing the neutral fields W_μ^3 and B_μ with a rotation defined by Weinberg angle θ_W . In particular, the A_μ field is identified with the electromagnetic field tensor. The unification can be done if the two coupling constants are equal:

$$g \sin\theta_W = g' \cos\theta_W = e \quad (2.9)$$

that represents the electromagnetic unification.

The four bosons obtained are massless. If we try to introduce a mass term for the gauge bosons in the $SU(2) \times U(1)$ Lagrangian, we will destroy the invariance of local gauge transformations. In order to keep the mass, we have to use the Brout-Englert-Higgs (BEH) mechanism, that permits to have massive fermions, W^\pm and Z leaving the photon γ massless. The BEH mechanism introduces the Higgs field, a doublet of complex scalar field:

$$\phi = \begin{pmatrix} \phi^+ \\ \phi^0 \end{pmatrix} = \sqrt{\frac{1}{2}} \begin{pmatrix} \phi_1 + i\phi_2 \\ \phi_3 + i\phi_4 \end{pmatrix} \quad (2.10)$$

where the ϕ^+ and ϕ^0 are the charged and neutral fields, ϕ_1, ϕ_2, ϕ_3 and ϕ_4 are complex of the scalar fields.

The Lagrangian of this field must be invariant under $SU(2) \times U(1)$ local gauge transformations and include a potential term

$$\mathcal{L}_{Higgs} = (D_\mu \phi)^\dagger (D^\mu \phi) - V(\phi) \quad (2.11)$$

where

$$V(\phi) = -\mu^2 \phi^\dagger \phi + \lambda (\phi^\dagger \phi)^2 \quad (2.12)$$

and D_μ is the covariant derivative for local gauge transformations. The potential written above depends on the pure imaginary parameter μ and the real and positive parameter λ . By minimizing $V(\phi)$, the fundamental state of the system is obtained.

At $\lambda > 0$ and $\mu^2 < 0$, we have a lowerly limited Lagrangian density and a minimum of the potential that is not unique, but an infinite set of minimum points dislocated on a circumference on the complex plane, as shown in the Figure 2.3.

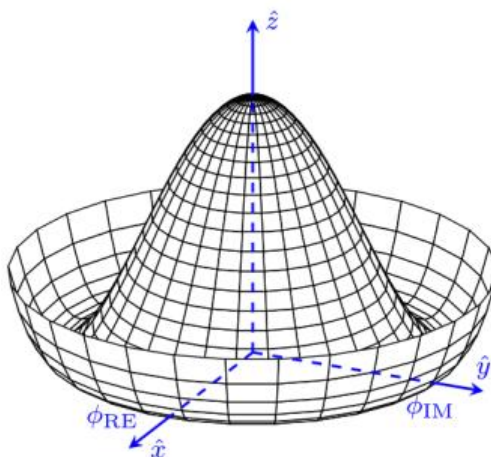


Figure 2.3: Form of potential V as a function of ϕ on the complex plane [16]

Under these conditions ($\lambda > 0$ and $\mu^2 < 0$) the potential has a minimum for

$$\phi^\dagger \phi = \frac{1}{2}(\phi_1^2 + \phi_2^2 + \phi_3^2 + \phi_4^2) = \frac{\mu^2}{2\lambda} \equiv \frac{v^2}{2} \quad (2.13)$$

The minimum is not found for ϕ_i but for a manifold of value: this effect is called *spontaneous symmetry breaking*. The coupling between boson fields and the non-zero vacuum value of the Higgs field gives masses to the bosons. An important result is that the fundamental state of the potential doesn't have the same symmetry properties as the Lagrangian while the minimum of Higgs field is invariant for $U(1)$ transformations. This means that the electromagnetic symmetry remains unbroken and photon remains massless.

Using the Higgs mechanism, we have three massive gauge bosons, corresponding to nine degrees of freedom. Since the initial number of independent fields is ten (three massless bosons \times two polarization states + four real ϕ_i fields), one additional scalar gauge boson should appear as a real particle. This "new"

boson is called Higgs boson and his mass depend on v and λ . The value is related to the boson masses by the relation:

$$\begin{aligned} m_{W^\pm} &= \frac{1}{2}gv \\ m_Z &= \frac{gv}{2\cos\theta_W} \end{aligned} \tag{2.14}$$

However, the λ parameter is a characteristic of the field ϕ and we cannot determine it from other constrains: this implies that the Higgs mass can not be obtained theoretically. The fermion masses are generated with a similar mechanism, but like free parameters of the theory (6 masses of quarks and 3 for leptons, assuming neutrinos to be massless). This brings the number of free parameters of Standard Model to 17, the others are 4 parameters of Cabibbo-Kobayashi-Maskawa matrix that describes the mixing of quark flavours, the coupling g and g' , the parameter of the Higgs vacuum expectation value and the Higgs mass. Nowadays, the parameters have been determined from experimental results and in 2012 the Higgs boson experimental mass close to 125 GeV has been observed by the ATLAS and CMS experiments.

2.3.3 Search for Higgs Boson at LHC

The LHC is providing p-p collisions at high center-of-mass energy. The search for the Standard Model Higgs boson is one of the major physics goals at this collider. But the production of the SM Higgs boson is a very rare process at the LHC, largely dominated by the production of quarks and gluons. The cross-section of the different processes as a function of the center-of-mass energies in proton-(anti) proton collisions are shown in Figure 2.4. Taking into account this, it is clear that the production of $b\bar{b}$ -pairs are the dominant process while the production of gauge or Higgs bosons is several orders of magnitude smaller.

2.3.3.1 Phenomenology

The main mechanisms of the Higgs boson production at LHC in the proton-proton collisions are presented below:

- *gluon – gluon fusion* ($gg \rightarrow H$), is a dominant mechanism regulated by strong interaction. The leading order includes a heavy-quark loop with the main contribution given by the top quark, as shown in the Feynman diagram in Figure 2.5a. It also is the main Higgs production mode at the LHC and represents about 87% of the total Higgs production at the center-of-mass energy $\sqrt{s} = 14 \text{ TeV}$ and for the Higgs mass around $m_H = 125 \text{ GeV}$.
- *vector boson fusion* (VBF) ($q\bar{q} \rightarrow qqVV \rightarrow qqH$) is the second most dominant production mode at the LHC. This production mechanism

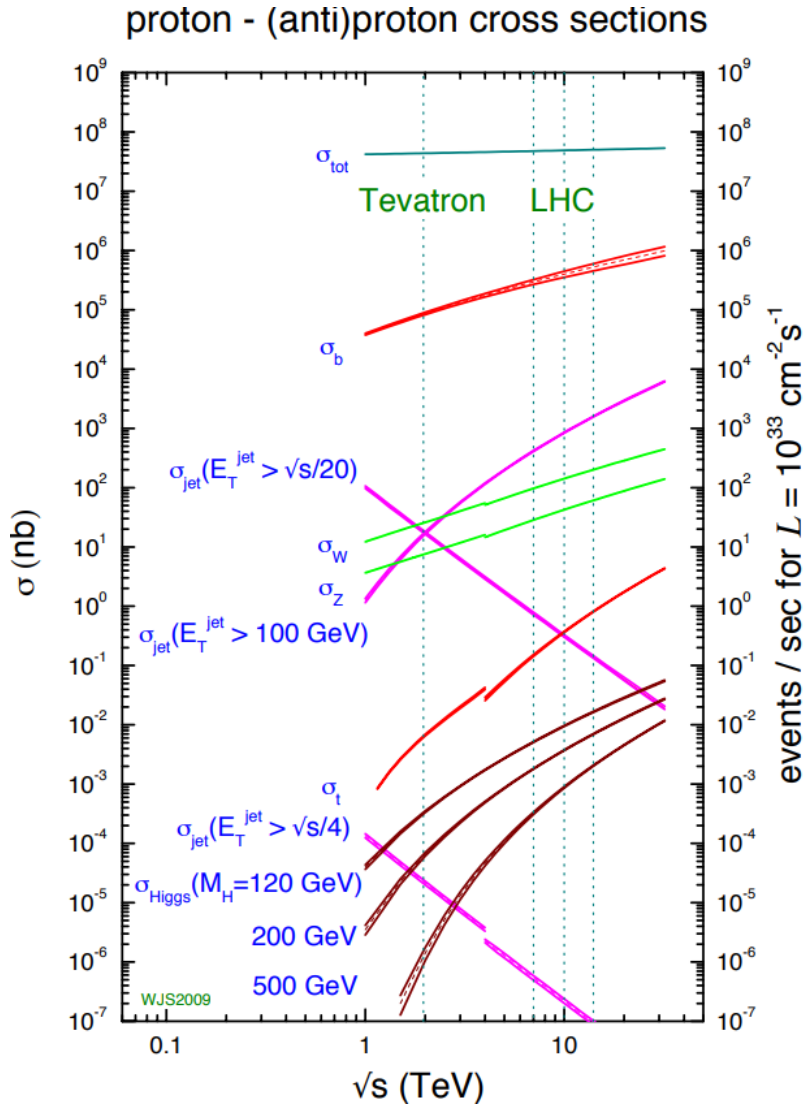


Figure 2.4: Cross section and event rates of several processes as a function of the center-of-mass energy of proton-(anti) proton collisions [18].

occurs as the scattering between two $q\bar{q}$ with weak boson (W^\pm and Z) exchange in the t-channel and with the Higgs boson radiated off the weak-boson propagator. The main characteristic of this process, as shown in the corresponding Feynman diagram in Figure 2.5b, is the production of two small angle jets. The Higgs VBF production cross section is somewhat smaller ($\sim 20\%$) than the gluon fusion one.

- *associated with vector boson* ($q\bar{q} \rightarrow V^* \rightarrow VH$, see in Figure 2.5c) production, called Higgsstrahlung, is the most promising channel (about 5% of the overall Higgs production). This channel is the associate production Higgs with virtual boson decays into a real boson W^\pm or Z for $m_H < 135 \text{ GeV}$, where the bb -decay is dominant. This is due to the

2.3. The Physics at the LHC

possibility to trigger on the leptonic decay of the vector boson.

- *associated with top quarks* ($gg/q\bar{q} \rightarrow Ht\bar{t}/b\bar{b}ab$, see in Figure 2.5d). This channel is radiated off one of the two tops in the $q\bar{q}$, gg s-channel or off the top propagator in the gg t-channel. It can be important in the low-mass region at high luminosity LHC condition. In this production mode represents about 1% of the total Higgs production at the center-of-mass energy $\sqrt{s} = 14 \text{ TeV}$.

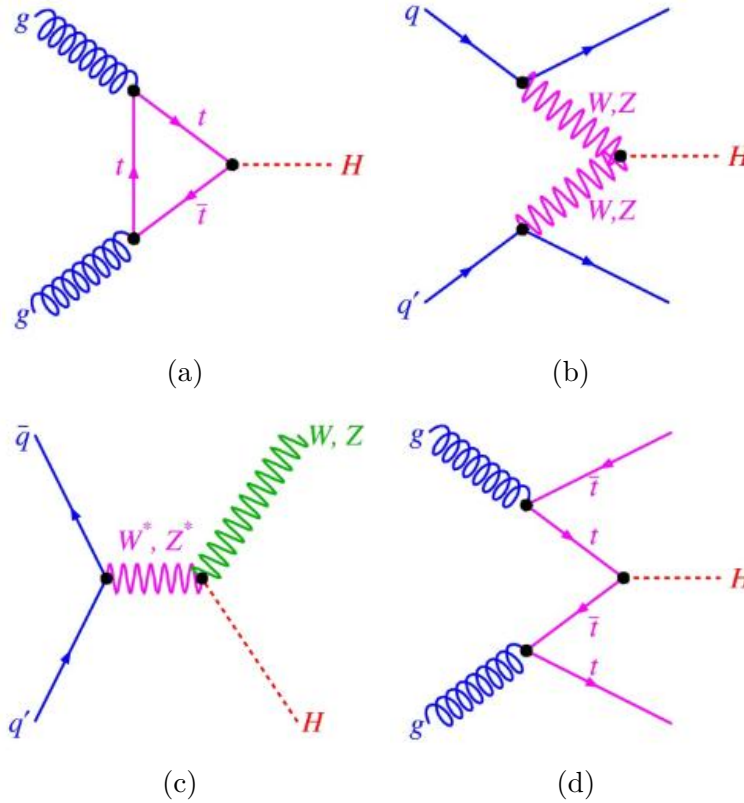
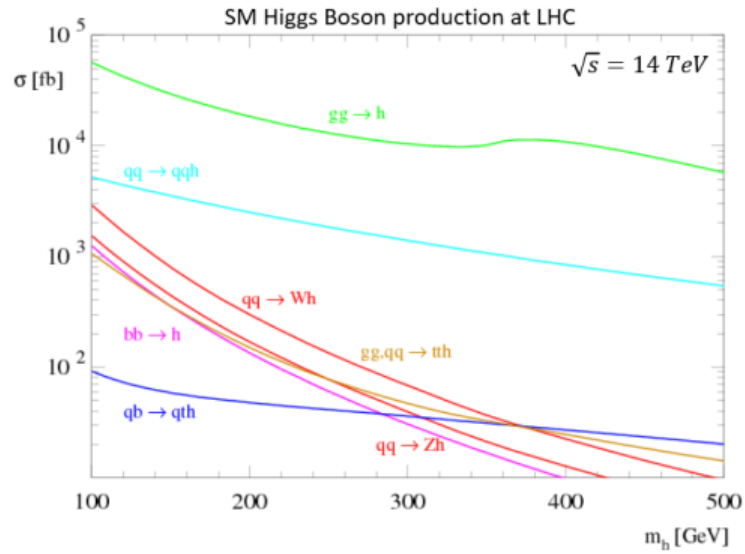
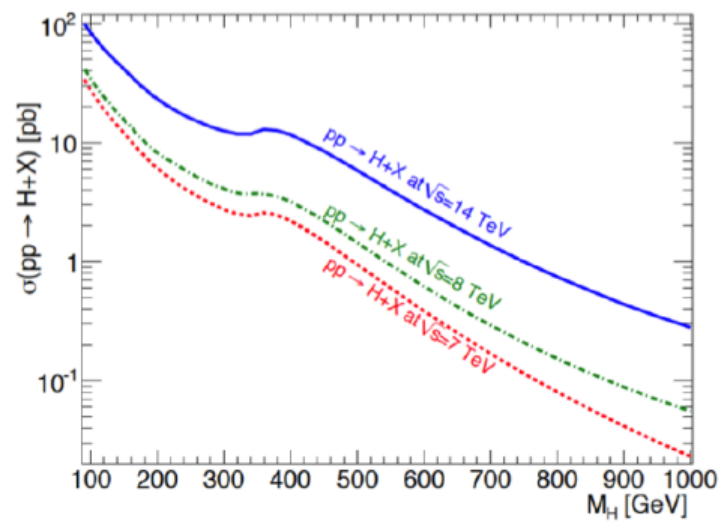


Figure 2.5: The Feynman diagrams for the main production mechanisms of the Higgs boson: (a) *gluon-gluon fusion*; (b) *vector boson fusion (VBF)*; (c) *associated with vector boson*; (d) *associated with pairs of top quarks* [18].

The Higgs boson is an unstable particle and therefore can only be revealed through its decay products. The branching ratio is defined for a possible decay channel, such as the probability of decaying in that particular decay channel with respect to the total probability of decay in all permissible channels. The branching ratio and the cross-section at $\sqrt{s} = 14 \text{ TeV}$ of the various decay modes of the SM Higgs boson are shown in Figure 2.6. At the leading order, according to the Standard Model, the Higgs boson can decay into: $H \rightarrow \gamma\gamma$; $H \rightarrow WW^*$ or $\rightarrow ZZ^*$; $H \rightarrow 2l$ ($l = \mu, \tau$); $H \rightarrow b\bar{b}$ or $H \rightarrow gg$ and etc.



(a)



(b)

Figure 2.6: (a) Higgs production cross section and (b) branching ratios as a function of the Higgs mass at the center-of-mass energy $\sqrt{s} = 7, 8, 14 \text{ TeV}$ [19].

2.3.3.2 Discovery of Higgs Boson at LHC

On July 2012 in the 36th Conference on High Energy Physics (ICHEP 2012, Australia) ATLAS and CMS experiments announced the discovery of a new, neutral particle of mass of about 125 GeV. The properties of the new particle were shown to be consistent with those predicted for the SM Higgs boson. Thus, with the discovery of the Higgs boson, the picture appears complete: all fundamental constituents of the Standard Model have been realized in nature, and the major task of the Large Hadron Collider and its detectors was achieved.

Results were received by using data samples collected by the CMS and ATLAS during the first operation of the LHC at the integrated luminosities of 5.1 fb^{-1} and $\sqrt{s} = 7 \text{ TeV}$ and 19.7 fb^{-1} at $\sqrt{s} = 8 \text{ TeV}$. The search was performed in the six different decays: $\gamma\gamma$, ZZ , W^+W^- , $\tau^+\tau^-$, bb and $\mu^+\mu^-$ and the five different production modes, where the boson produced in vector boson constitutes two very distinguishable final states [20] [21]. Each experiment produced an observation compatible with the predictions of production and decay of a SM Higgs boson. ATLAS and CMS each observed a significance of 5.9 and 5.8 standard deviations respectively. Both of these experiments saw the highest contribution to this measurement from the $ZZ^* \rightarrow 4l$ and $\gamma\gamma$ final states, which also correspond to the two final states with the highest resolution on the mass of this newly discovered particle. A combination of ATLAS and CMS results in these channels was performed to provide a combined measured mass of the Higgs boson of $m_H = 125.09 \pm 0.21(\text{stat.}) \pm 0.11(\text{syst.}) \text{ GeV}$ [21]. The joint ATLAS and CMS results were used to produce observations of the vector boson fusion production process and for the $H \rightarrow \tau^+\tau^-$ decay process of 5.4 and 5.5 standard deviations, respectively.

2.4 LHC Experiments

In June 1995, the LHC Committee approved the construction of two new detectors designed to operate on the accelerator: ATLAS (A Toroidal LHC ApparatuS) and CMS (Compact Muon Solenoid). The general principles of operation of the ATLAS and CMS experiments are the same and aim at detailed studies of the known physics and search for new physics beyond the SM. They maximally cover the space around the interaction point of colliding proton beams (so-called 4π detectors). The decision to build two detectors for physical research was related to the need for the confirmation of each discovery by independent experiments. Independently created experiments should ensure the reliability of the obtained physical results. Each detector has its own area of intersection beams called interaction point (IP). There are four such areas at the LHC. Two of them are designed for ATLAS and CMS detectors (IP1 and IP5). The two remaining ones are intended for other experiments such as ALICE (A Large Ion Collider Experiment) and LHCb (The Large

Hadron Collider beauty experiment), IP2 and IP8 respectively. In the ALICE experiment, a study over lead-ion collisions is done in order to improve the understanding of the quark-gluon plasma, which is postulated to have existed during the early universe. The LHCb experiment is specialized in studying the bottom-quark physics and CP violation in order to better understand the matter-antimatter asymmetry in the universe. The schematic views of the LHC main experiments are shown in Figure 2.7.

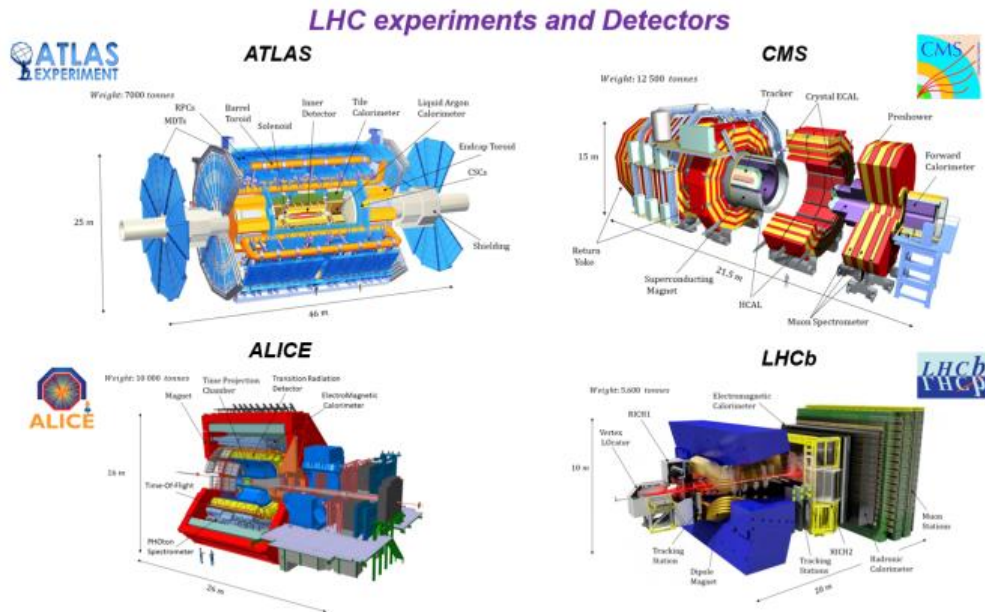


Figure 2.7: The LHC main experiments: ATLAS, CMS, ALICE and LHCb

In addition to the four main experiments, single-purpose experiments such as TOTEM (TOTAL Elastic and diffractive cross section Measurement), which is installed near ATLAS and CMS respectively, LHCf (The Large Hadron Collider forward) and MoEDAL (Monopole and Exotic Detector At the LHC) were designed. LHCf aims at studying particle showers close to the beam pipe in order to test models of particle showers as present in astroparticle physics. TOTEM is measuring up to high pseudorapidity in order to study the total cross section of proton collisions. MoEDAL is designed to directly search for magnetic monopoles and other highly ionizing stable or metastable particles arising in various theoretical scenarios beyond the Standard Model. More details about these experiments can be found in [22], [23], [24] and [25].

Chapter 3

The CMS Experiment

The Compact Muon Solenoid (CMS) is one of the four main experiments and a multi-purpose apparatus operating at the Large Hadron Collider. Its scientific goals are to describe the features of all known particles, including the latest discovered Higgs boson, as well as search for new physics beyond the Standard Model at the TeV energy scale. The CMS experiment is a worldwide collaboration that includes more than 4300 scientists and engineers from 186 institutes and 42 countries.

3.1 Overall Design

The CMS detector system, located at the underground cavern (IP 5) near Cessy in France, is in shape of a cylindrical barrel closed by two endcap disks, with a full length of $\sim 21 m$, a diameter of $\sim 15 m$ and a total weight of about 14000 tonnes. Its main distinguishing features are a compact solenoid with the high magnetic field of $3.8 T$.

The CMS detector is designed to follow the traditional scheme of the sub-detectors location: the first layer (close to the interaction point) is an inner tracking detector followed by Electromagnetic and Hadronic Calorimeters and Muon Spectrometer on the outside. All detector components were chosen to meet the LHC physics programme requirements. In Table 3.1 the main characteristics of the CMS sub-detectors and their functions are presented. The overall view of the CMS detector is shown in Figure 3.1 where we can distinguish the barrel region and the endcap stations.

The CMS coordinate frame is a right-handed system where the x -axis pointing radially inward that is, toward the center of the LHC ring, the y -axis points upwards and the z -axis is parallel to the beam and points toward the Jura mountains from LHC Point 5. Reconstruction algorithms, however, use a spherical coordinate system based on the radial distance $R = \sqrt{x^2 + y^2}$ from the z -axis, the azimuthal angle ϕ with respect to the y -axis and polar angle θ

Sub-detector	Composition	Functions	Main characteristics
Inner tracker	silicon strip and pixel detectors	the charged particles momentum measuring and reconstruction of their trajectory	isolated track efficiency $\varepsilon > 95\%$ within jets $\varepsilon \sim 90\%$; primary vertex resolution: 10-20 μm ; p_T resolution: $\Delta p_T/p_T = 1\%$ (0.1 TeV), 10% (TeV); coverage $\eta < 2.5$
Electromagnetic Calorimeter	PbWO ₄ crystals	high precision measurements of the electrons and photons	energy resolution: $(\frac{\sigma}{E})^2 = (\frac{2.7\%}{\sqrt{E}})^2 + (\frac{245}{E})^2 + 0.55\%$ (barrel); $(\frac{\sigma}{E})^2 = (\frac{3.7\%}{\sqrt{E}})^2 + (\frac{245}{E})^2 + 0.55\%$ (endcap); coverage $\eta < 3$;
Hadron Calorimeter	Cu-Zn scintillators	hadrons energy measurement and the indirect measurement of the presence of non-interacting, uncharged particles such as neutrinos	energy resolution: $(\frac{\sigma}{E})^2 = (\frac{98\%}{\sqrt{E}})^2 + 4.5\%$ (barrel); coverage $\eta < 3$;
Muon Spectrometer	gaseous detectors	precise muon detection and identification	efficiency $\varepsilon \sim 90\%$ $\Delta p_T/p_T = 8-15\%$ (0.01 TeV)/20-40% (TeV) coverage $\eta < 2.4$

Table 3.1: The main characteristics of the CMS sub-detectors and their functions [33], [34].

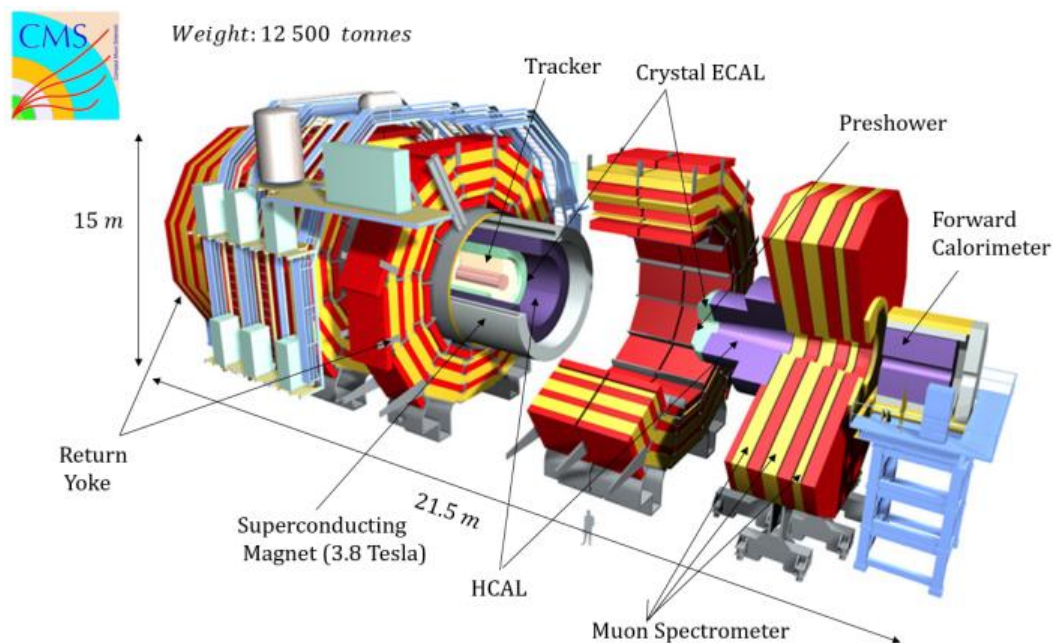


Figure 3.1: Overall view of CMS detector.

with respect to the beam line. However, taking into account that the particles produced by proton collisions are strongly pressed to the collision axis and distributed over the angle θ very unevenly, it is customary to use a different, more convenient, kinematic variable called *pseudorapidity* (η). The η value is determined by the formula [33], [34]:

$$\eta = -\ln\left(\tan\frac{\theta}{2}\right) \quad (3.1)$$

3.2. The Superconducting Magnet

The benefit of this kinematic value is that hadrons generated in proton collisions are much more uniformly distributed in velocity than in angle θ , which makes the analysis of a complex event easier and more clearly. The CMS coordinate system is shown in Figure 3.2.

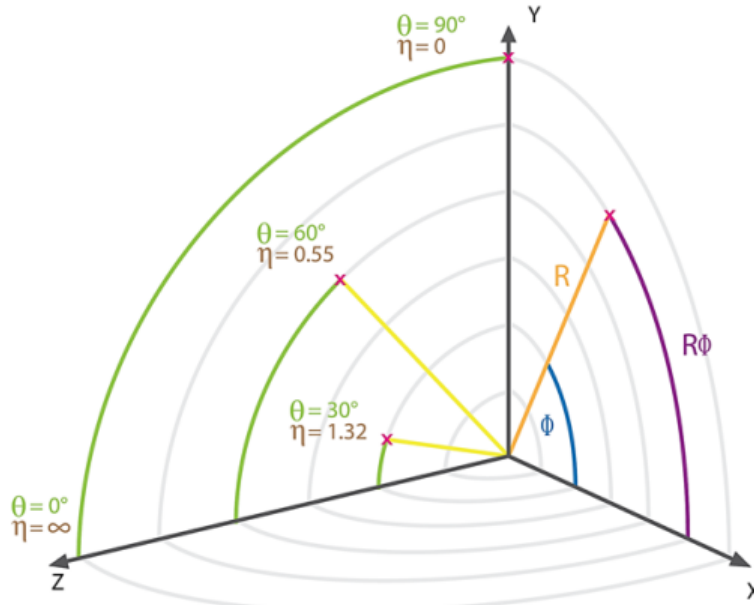


Figure 3.2: The CMS coordinate system.

3.2 The Superconducting Magnet

A magnetic field is essential for identifying the particles emerging from collisions: it curves their trajectory allowing to calculate their momentum and to establish whether they have a positive or negative charge. The stronger the field and the larger the volume on which it acts, the higher the resolution of the detector.

The heart of the CMS detector is the magnet, which consists of a 12.5 m long, 6 m inner diameter, 3.8 T superconducting solenoid and of a 12000 tons, 1.5 m thick iron yoke. Various detectors are located both inside the bore of the magnet coil (inner tracker, calorimetry) and outside the coil into the gaps of the segmented return yoke (muon detection). In Figure 3.3 a schematic view of the CMS solenoid is shown as well as the picture of the steel return yoke and muon chambers around the magnet are presented. Other main parameters of the CMS superconducting magnet are given in Table 3.2 [33], [34].



Figure 3.3: A schematic view of the CMS solenoid (left), and the photograph of the CMS magnet and the return yoke with the barrel muon chambers installed at the Underground Experimental Cavern (right).

Parameter	Value
Magnetic length	12.5 m
Free bore diameter	5.9 m
Number of turns	2168
Central magnetic induction	3.8 T
Maximum induction on conductor	4.6 T
Nominal current	19.1 kA
Average inductance	14.2 H
Stored energy	2.6 GJ
Operating temperature	4.5 K

Table 3.2: Parameters of the CMS superconducting solenoid.

3.3 Tracker System

The main goal of the inner tracker is to reconstruct high- p_T charged particles (electrons and muons) tracks in the region $|\eta| < 2.5$ with high efficiency and good momentum resolution, to measure their impact parameter and to reconstruct secondary vertices [26] [27] [28]. It surrounds the interaction point and features high granularity and fast response, as in the LHC design luminosity of $10^{34} \text{ cm}^{-2} \text{ s}^{-1}$ there will be on average about 1000 particles from more than 20 overlapping proton-proton interactions traversing the tracker for each bunch crossing. The trajectories can, therefore, be identified reliably and attributed to the correct bunch crossing. Tracker has a cylinder shape with 5.4 m long, 2.4 m of the diameter. The magnetic field (3.8 T) is maintained throughout all the volume of the tracker system. The CMS tracker is constructed using the two type of detector technologies: pixel and microstrip. A general overview of the CMS tracker system is given in Figure 3.4, with its subsystems Pixel, Tracker Inner Barrel (TIB) and Tracker Inner Disks (TID), Tracker Outer

3.3. Tracker System

Barrel (TOB) and Tracker Endcaps (TEC).

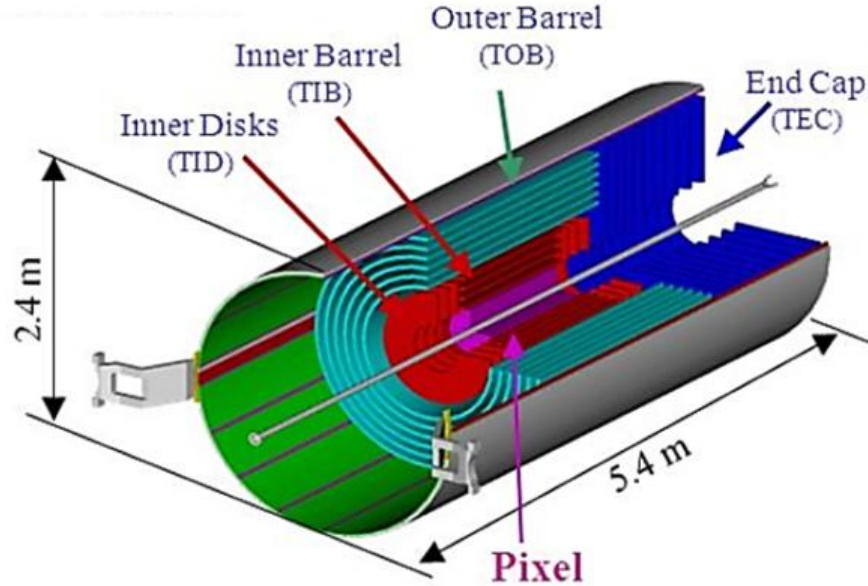


Figure 3.4: Overview of the CMS inner tracking system [26].

Pixel Detector. The inner pixel detector is installed within a distance of 20 cm from the beam pipe. It provides high-resolution three-dimensional measurements for the charged track reconstruction. Its excellent resolution allows the measurement of track impact parameter, the identification of b and t -jets and the reconstruction of vertices in the 3D-dimensions. In overall, the pixel detector consists of three barrel layers (BPix) with two endcap disks (EPix) on each side of the barrel as shown in Figure 3.5a. The 53 cm long BPix layers are located at mean radii of 4.4, 7.3, and 10.2 cm. The EPix disks extending from 6.1 to 15.0 cm in radius are placed on each side at $z = \pm 34.5$ cm and $z = \pm 46.5$ cm [26] [27].

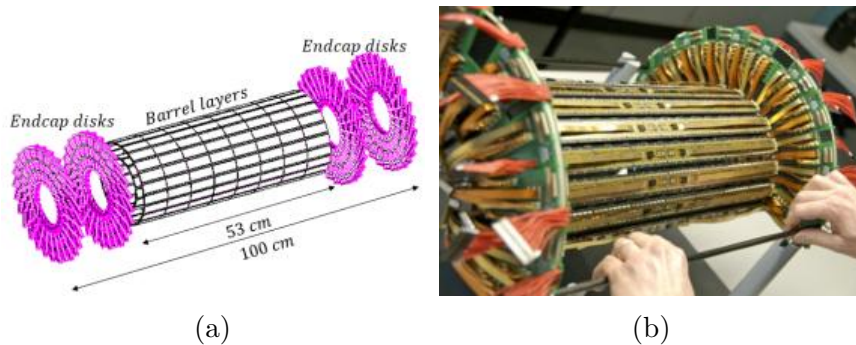


Figure 3.5: CMS pixel detector: (left) 3D-dimentional view and (right) photo of the detector [26].

It covers an area of about 1 m^2 and consists of 1440 segmented silicon sensor modules with a total of 66 million readout channels with size $100\text{ }\mu\text{m}$ by $150\text{ }\mu\text{m}$ which are implemented into 285 mm thick n-type bulk and p-type backside. They are oriented with the smaller pitch in the azimuthal direction in the barrel and in the radial direction in the disks. The range $-2.5 < |\eta| < 2.5$ covered by the pixel detector matches the acceptance of the central tracker. The spatial resolution of the pixel detector is in the range of $15 - 20\text{ }\mu\text{m}$ [26] [27].

Microstrip Detector. In addition to the pixel detectors, the inner tracker is composed of several layers of silicon microstrip detectors: four-layer Tracker Inner Barrel (TIB), six-layer tracker outer barrel (TOB) and on each side three-disk Tracker Inner Disks (TID) and nine-disk Tracker Endcaps (TEC). The full tracker consists of about 15148 microstrip detectors, with a pitch size ranging from $80\text{ }\mu\text{m}$ to $180\text{ }\mu\text{m}$. Some of the modules are composed by two detectors mounted back to back with the strips rotated by 100 mrad . These double-sided ("stereo") modules also provide a measurement in the coordinate orthogonal to the strips [26] [27].

3.4 Calorimeter System

In accordance with the standard layout, in the CMS detector two types of calorimeters were installed: the internal (electromagnetic) and the external (hadron). In particular, the first one measures the energy of electrons and photons, while the second one measures the energy loss by all the hadrons (i.e. jets formed by the quark hadronization).

Electromagnetic calorimeter. The CMS electromagnetic calorimeter (CMS ECAL) [29] [30] [31] is a hermetic homogeneous calorimeter made of lead tungstate crystals ($PbWO_4$). The ECAL subdetector covers the pseudorapidity range $|\eta| < 3.0$ with 61200 $PbWO_4$ crystals in the barrel, read out by Avalanche Photodiodes (APDs) (see Figure 3.6a (top)), and 7324 crystals in the endcap region, read out by Vacuum Phototriodes (VPTs) (see Figure 3.6a (bottom)).

The use of high-density crystals such as $PbWO_4$ allows the design of a calorimeter which is fast, has fine granularity and is radiation resistant. One of the driving criteria in the design was the capability to detect the decay into two photons of the Higgs boson $H \rightarrow \gamma\gamma$. This capability was enhanced by the good energy resolution provided by a homogeneous crystal calorimeter.

In order to avoid cracks, crystals are mounted slightly turned, so that the crystal axes make a 3° angle with respect to the direction of the nominal interaction point in both the azimuthal ϕ and η projections. The length of the crystals is 230 mm in the barrel and 220 mm in the endcaps, corresponding to $25.8 X_0$ and $24.7 X_0$ respectively. Crystals are trapezoidal, with a square front

3.4. Calorimeter System

face of $22 \times 22 \text{ mm}^2$ in the barrel and $30 \times 30 \text{ mm}^2$ in the endcaps, matching the Moliere radius. All crystals are collected in a matrix forming the so-called Super Module and Supercrystal.

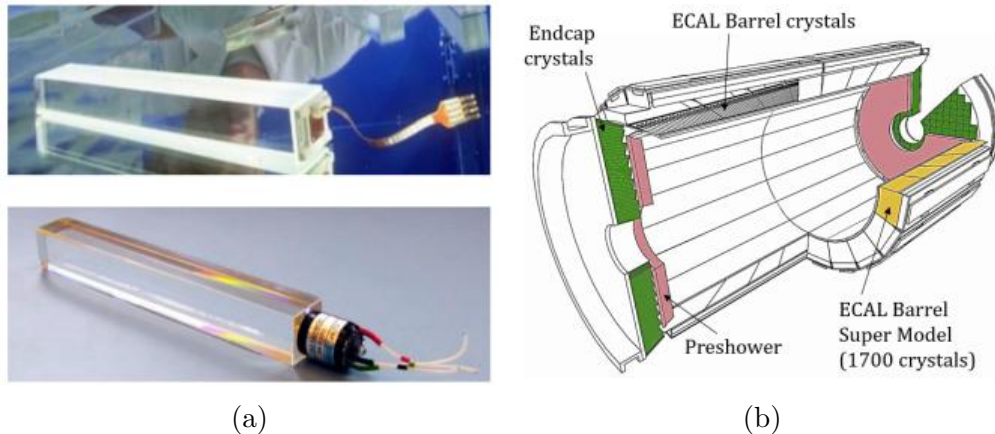


Figure 3.6: CMS Electromagnetic calorimeter: (left) $PbWO_4$ ECAL crystals with photodetectors attached a barrel crystal with APD capsule (top) and an endcap crystal with a VPT (bottom), and (right) General CMS ECAL layout: Barrel Super Module (yellow), Endcap crystal (green) and Preshower detectors (pink) [29].

In addition to the barrel and endcap crystals, the Preshower detector has been installed, consisting of two lead radiators and two planes of silicon strip detectors, with a total of $3 X_0$. The principal aim of the CMS Preshower detector is to identify neutral pions in the endcaps within a fiducial region $1.653 < |\eta| < 2.6$. It also helps the identification of electrons against minimum ionizing particles, and improves the position determination of electrons and photons with high granularity, providing a good measurement of two-photon invariant mass. The CMS ECAL layout is shown in Figure 3.6b.

Hadron calorimeter. The CMS hadron calorimeter (CMS HCAL) [32] measures the energy of the hadrons jets created by the proton-proton interaction. It plays a main role in the identification of neutrinos and exotic particles that do not interact with the detector and whose signature is a non zero transverse energy balance. Due to the fact that the HCAL is placed inside the magnet, materials with short interaction lengths need to be used. Therefore, the main materials, from which the HCAL is made, are the scintillator and the layers of the absorber, mainly brass. The innermost and outermost ones are made of stainless steel whereas the others also consist of brass. A good hermiticity is also requested in order to accurately measure the transverse missing energy.

The HCAL consists of a barrel region up to $|\eta| < 1.3$ (Hadron Barrel, 5.4 to $10.6 \lambda_I$), an endcap region up to $|\eta| < 3$ (Hadron Endcap) and a forward region further down the beam pipe at 11.2 m that increases the coverage up to $|\eta| < 5.2$ (Hadron Forward). The limited space for stopping power in the

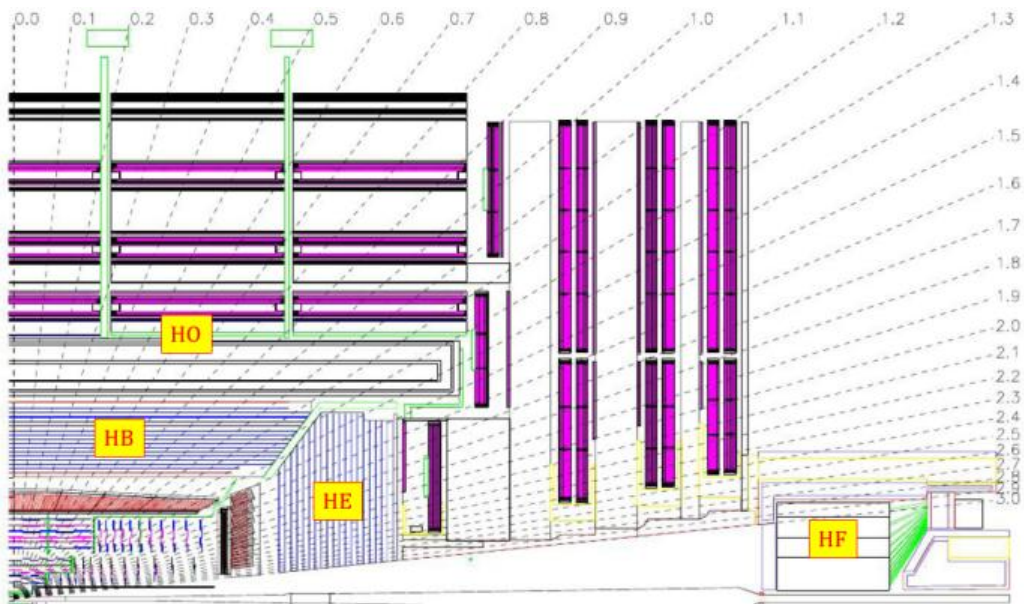


Figure 3.7: A quadrant of the CMS detector with locations of the calorimeters: hadron barrel (HB), endcap (HE), outer (HO) and forward (HF) [32].

barrel region is overcome with an additional calorimeter outside the solenoid up to $|\eta| < 1.3$ (Hadron Outer) that uses the coil and a 19.5 cm layer of steel yoke as the absorber [32]. Figure 3.7 shows the quadrant of the CMS detector with locations of the calorimeters: hadron barrel (HB), endcap (HE), outer (HO) and forward (HF).

In addition, between the brass absorber plates with $\approx 5\text{ cm}$ for HB, $\approx 8\text{ cm}$ for HF, the scintillator tiles with a segmentation depending on η from $\Delta\eta \times \Delta\phi = 0.087 \times 0.087$ to 0.17×0.17 produce the optical signal that embedded wavelength-shifting fibers take to hybrid photodiodes [32]. The total amount of light summed over the layers of tiles within a given region is a measure for the passing particle energy.

3.5 CMS Muon Spectrometer

Muon detection is a powerful tool for recognizing signatures of interesting processes over the very high background rate expected at the LHC with full and high luminosity. For example, the predicted and confirmed decay of the Standard Model Higgs boson into ZZ or ZZ^* , which in turn decay into 4 leptons, has been called "gold plated" for the case in which all the leptons are muons. This example and others from SUSY models emphasize the discovery potential of muon final states and the necessity for wide angular coverage for muon detection. Therefore, as is implied by the experiment middle name, the detection of muons is of central importance to CMS: precise and robust muon measurement was a central theme from its earliest design stages. The muon

3.5. CMS Muon Spectrometer

spectrometer has 3 functions: muon identification, momentum measurement, and triggering. Good muon momentum resolution and trigger capability are enabled by the high-field solenoidal magnet and its flux-return yoke. The latter also serves as a hadron absorber for the identification of muons.

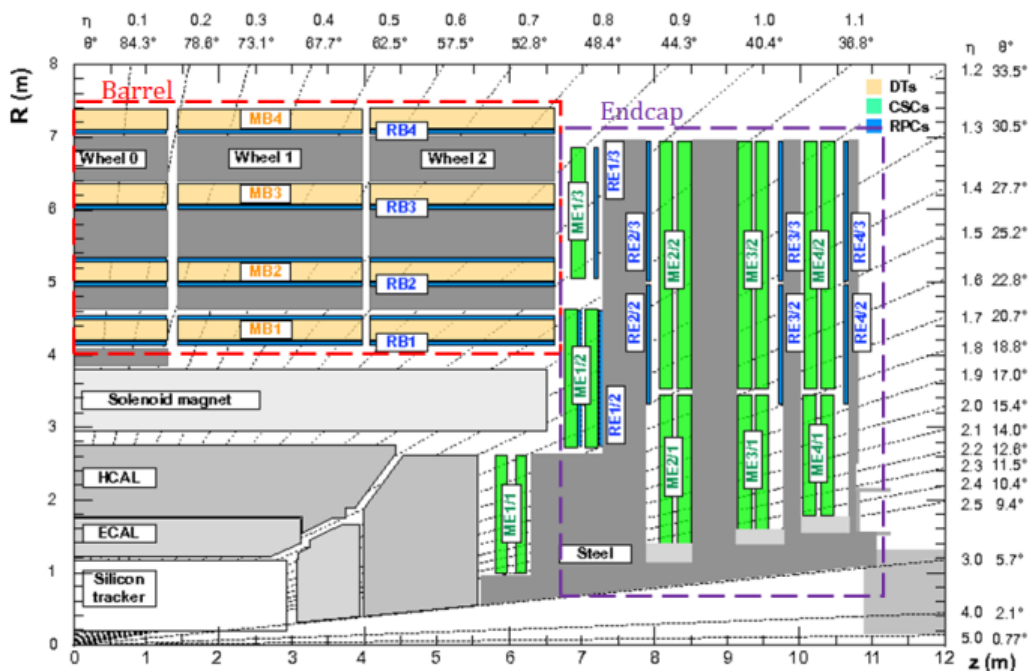


Figure 3.8: Longitudinal view of one quarter of the present CMS Muon Spectrometer [33].

The CMS Muon Spectrometer [33] [34] has been designed to have the capability of reconstructing the momentum and charge of muons over the entire energy range of the LHC. Due to the shape of the solenoid magnet, the muon spectrometer is naturally divided in the cylindrical barrel part and two planar endcap regions. Nowadays, three types of gaseous detector are installed for muon identification, the total surface coverage is around 25000 m^2 . The layout of the CMS Muon Spectrometer is presented in Figure 3.8 The gas ionization technology was chosen since the detectors must be relatively inexpensive, reliable and robust.

In the barrel region, where the neutron-induced background is small, the muon rate is low, and the 3.8 T magnetic field is uniform and mostly contained in the steel yoke, drift chambers with standard rectangular drift cells are used. The barrel Drift Tube (DT) chambers cover the pseudorapidity region $|\eta| < 1.2$ and are organized into four stations which are labeled MB1, MB2, MB3, and MB4 in Figure 3.8. In the two endcap regions of CMS, where the muon rates and background levels are high and the magnetic field is large and non-uniform, the muon system uses Cathode Strip Chambers (CSC). With their fast response

time, fine segmentation and radiation resistance, CSC's identify muon in the range $0.9 < |\eta| < 2.4$. There are four stations of CSCs, which are named ME1, ME2, ME3 and ME4 as shown in Figure 3.8, in each endcap, with chambers positioned perpendicular to the beam line and displaced between the flux return plates. In both the barrel and endcap regions ($|\eta| < 1.9$), a third system, composed by Resistive Plate Chamber (RPC) (marked as RB1, RB2, RB3 and RB4 - for barrel and RE1, RE2, RE3 and RE4 - for endcap) is present. This type of detector provides an independent measurement for triggering purposes with a coarser space resolution but a fast time response for unambiguous assignment. All the above muon detectors contribute to the Level-1 Trigger System, providing independent and complementary sources of the information.

3.5.1 Drift Tube

In the barrel the muon detector does not operate in particularly demanding conditions [33] since the occupancy in this region is low and the magnetic field is well contained in the iron plates of the magnet return yoke. For this reason, the Drift Tubes (DT) [33] was chosen. DT system covers the region $|\eta| < 1.2$ and consists of 4 coaxial stations (MB1 to MB4), forming concentric wheels (*Wheel 0*, *Wheel ± 1* , *Wheel ± 2*) which are segmented in 12 sectors around the beam line (total of 250 DT chamber).

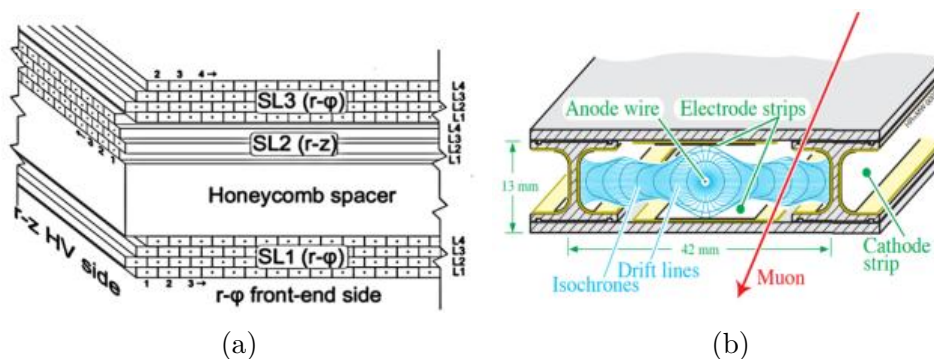


Figure 3.9: Illustration of the Drift Tube Chamber: (left) schematic view of a DT chamber and (right) the one section of the DT with electric field [33].

The basic detector element is a drift tube cell, whose section is shown in Figure 3.9a. Cells have a size of $42 \text{ mm} \times 13 \text{ mm}$. A layer of cells is obtained by two parallel aluminum planes and by "I" - shaped aluminum beams which define the boundary of the cells and serve as cathodes. I-beams are insulated from the planes by a 0.5 mm thick plastic profile. The anode is a $50 \mu\text{m}$ stainless steel wire placed in the center of the cell. Additional field shaping is obtained with two positively-biased insulated strips, glued on the planes in correspondence to the wire. Typical voltages are $+3.6 \text{ kV}$, $+1.8 \text{ kV}$ and -1.2 kV for the wires, the strips, and the cathodes, respectively [33].

In addition, the four staggered layers of parallel cells constitute a *Super Layer* (SL), which allows to resolve the left-right ambiguity of a single layer and provides the measurement of a two-dimensional segment (see 3.9a). Also, it measures the bunch crossing time using a generalization of the mean-timer technique: this permit to originate a segment that does not need any external input (trigger). A chamber is composed by two SL measuring the $r - \phi$ coordinates, with the wires parallel to the beam line, and an orthogonal SL measuring the $r - z$ coordinates. The latter is not presented in the outermost MB4 station because MB4 only has the 8 layers measuring the ϕ coordinate [33].

The DT are gaseous detectors and their working principle is based on the produced ionization of the gas volume of the detector caused by the passing of a charged particles (see 3.9b). The used gas mixture is a Ar/CO_2 (85/15) which provides good quenching properties and a saturated drift velocity, of about $5.6 \text{ cm}/\mu\text{s}$. The maximum drift time is, therefore, $\sim 375 \text{ ns}$, i.e. 15 bunch crossing. A single cell has an efficiency of about 99.8% and a resolution of $\sim 180 \mu\text{m}$ [33].

3.5.2 Cathode Strip Chambers

The Cathode Strip Chamber (CSC) [33] is one of a type of the gaseous particle detectors, combining cathode strips running along η , and perpendicular anode wires measuring the η coordinate. These multi-wire proportional chambers have the good spatial and time resolution and can operate at high occupancy levels and in the presence of the large inhomogeneous magnetic field. For this reason, they were adopted for the endcap region. General view and picture of the CSC chambers are shown in Figure 3.10 and Figure 3.11.

CMS CSC system uses of 540 chambers covering the endcap region of $0.9 < |\eta| < 2.4$. CSC chambers are arranged in four disks (stations) placed between the iron disks of the yoke (see Figure 3.8) and directed perpendicular to the beam line. The innermost station consists of three concentric rings (ME1/1, ME1/2 and ME1/3), the first being closer to the interaction point. The other stations are composed by two disks only (ME2/1, ME2/2, ME3/1, and ME3/2). The rings are formed by 18 or 36 trapezoidal chambers with two different sizes covering either 10° or 20° in the azimuthal angle ϕ direction with a small overlap in ϕ (the exception of the outermost ring of ME1/1).

CSC chamber consists of 6 gas gaps 9.5 mm thick (see Figure 3.10), each composed by an array of anode wires between two cathode planes. The wires are held at a potential value from 2.9 kV to 3.6 kV . One of the cathode planes is segmented into strips orthogonal to the wires, disposed in the radial direction to measure the ϕ -coordinate. The strip pitch range is $8.4\text{-}16 \text{ mm}$ and the distance between wires is $2.5\text{-}3.16 \text{ mm}$ depending on their location in the chamber. The avalanche produced by crossing particle in the $Ar/CO_2/CF_4$ (40/50/10) gas volume induces a charge in several adjacent strips. A precise

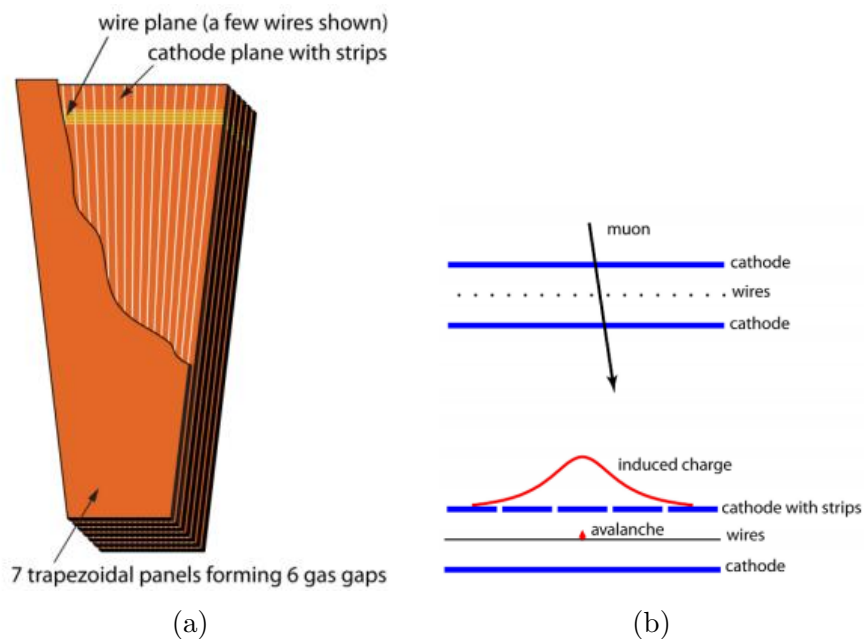


Figure 3.10: Illustration of the Cathode Strip Chamber: (left) the layout of a CMS CSC with local chamber coordinates and (right) the cross-sectional view of the gas gap in a CSC, with a schematic illustration of the gas ionization avalanche and induced charge distribution on the cathode strips [33].

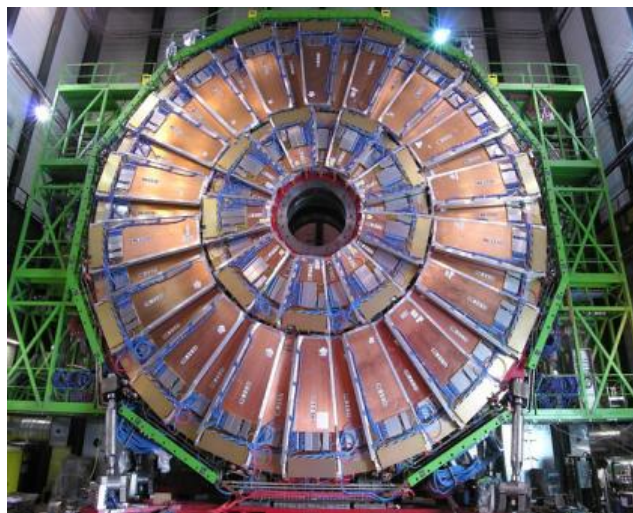


Figure 3.11: Pictures of the CSC chambers installed at CMS detector [33].

spatial measurement is obtained by interpolating the strip signals achieving a resolution of about $50 \mu m$. The r coordinate is measured by the wires which, to reduce the number of channels, are read out in groups of 5 to 16 with a resolution of $0.5 cm$ [33].

3.5.3 Resistive Plate Chamber

The Resistive Plate Chamber (RPC) [33] is the third type of gaseous detector installed both in the barrel (along with DTs) and endcap regions (along with CSCs), covering $|\eta| < 1.9$ (see Figure 3.8). A total of 1056 RPC detectors with total active area of $3500 m^2$ is used in the CMS Muon Spectrometer. The RPC system is complementary to the DT and CSC systems and adds robustness and redundancy to the muon trigger. In the barrel region the RPC system is distributed in five wheels (*Wheel 0, Wheel $\pm 1, Wheel \pm 2$*) around the beam pipe. Each wheel is divided into 12 sectors, covering the full azimuthal dimension. Each sector consists of four layers of DTs and six layers of RPCs, with a total of 480 RPC stations: the first four are attached to each side of MB1 and MB2, and the other two are attached to MB3 and MB4 DT chambers. Each barrel RPC station is composed of two or three adjacent RPC partitions, called “*rolls*”, making a total of 1020 rolls for the barrel RPC system. This geometry difference is driven by the need to have the adjustable trigger on muons with different transverse momentum p_T . The endcap region has 576 trapezoidal shapes of chambers, covering 10° of the azimuthal angle. RPC chambers are installed in 8 disks (4 for the positive side and 4 for the negative side from the interaction point). Endcap RPCs are divided in 3η -partitions or in the total of 3 rolls.

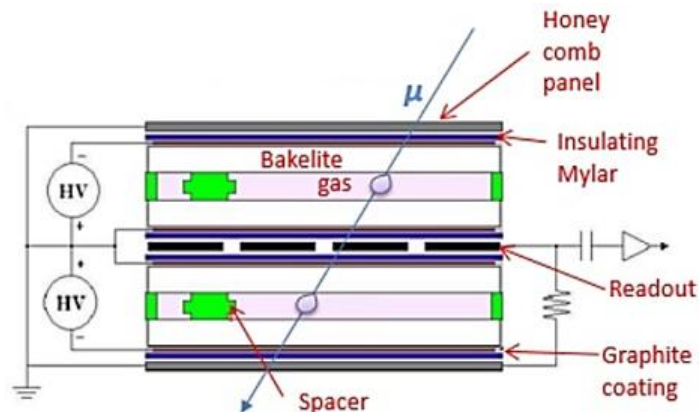


Figure 3.12: Principle scheme of a double-gap RPC chamber [33].

The RPCs used by CMS are double-gap chambers composed by four $2 mm$ thick HPL (*High Pressure Laminate*) planes externally coated with graphite, as shown in Figure 3.12. Insulated copper strips are placed in the middle, to

collect the signal induced in the gas mixture 95.2% $C_2H_2F_4$ (*tetrafluoroethane*), 4.5% $i - C_4H_{10}$ (*isobutane*) and 0.3% SF_6 (*sulphur hexafluoride*) by crossing particles. The readout strips have different geometry depending on which part of the system they are in: the barrel chambers have rectangular shaped strips, while in the endcap chambers their shape is trapezoidal. The pitch of the strips depends on the distance to the beam pipe varying from 1.5 *cm* for the innermost stations to 4 *cm* for the outermost stations.

The two innermost electrodes are kept at -9.6 *kV* and the RPCs operate in "*avalanche*" mode, rather than in the more common for this technology "*streamer*" mode, obtained with a lower electric field and allowing to sustain higher rates. However, in this case, the gas multiplication is reduced, and improved electronic amplification is required. The two-gap design is adopted to increase the charge induced on the strips. The spatial resolution provided by RPC is limited by the strip pitch but are characterized by an excellent time resolution, of the order of few nanoseconds.

3.6 CMS Trigger Systems

The LHC delivers proton-proton collisions at a rate of 40 *MHz* and the data produced by the CMS experiment are orders of magnitudes too large to be stored. The typical size of one event recorded by the CMS detector is about 1 *MB*, and it would be technically impossible to stream about 40 *TB/s* to disk. However, even if possible, the added scientific value would be questionable since most of the events only contain low-energy glancing collisions rather than inelastic hard scattering processes. The required reduction of the event rate is achieved by the so-called trigger system [35] [36] [37]. The aim of the trigger is the selection of potentially interesting events and the reduction of the rate to a manageable value of a few hundred *Hz*. While most high energy physics experiments use three trigger levels, the CMS trigger system implements a two-stage (Figure 3.13), rate reduction which provides additional flexibility. The first is the Level-1 (L1) [36] trigger, which is largely based in Field Programmable Gate Arrays (FPGAs) and Application Specific Integrated Circuits (ASICs), and therefore uses the coarse and crude information to reduce the rate from 40 *MHz* to 100 *kHz*. The second is the High-Level Trigger (HLT) [37], which is a software-based system, implemented in computing facility with approximately 16000 CPU cores, that reduces the L1 trigger rate to a viable level for storage of about 100 *Hz*.

3.6.1 Level-1 Trigger

The Level 1 Triggers (L1) are hardware based online triggers, meaning that they decide whether to save the events or not, directly after they have been recorded by the detector. In fact, the decision has to be made within 3-4 μs after each collision, because the data saved in the buffer are overwritten after

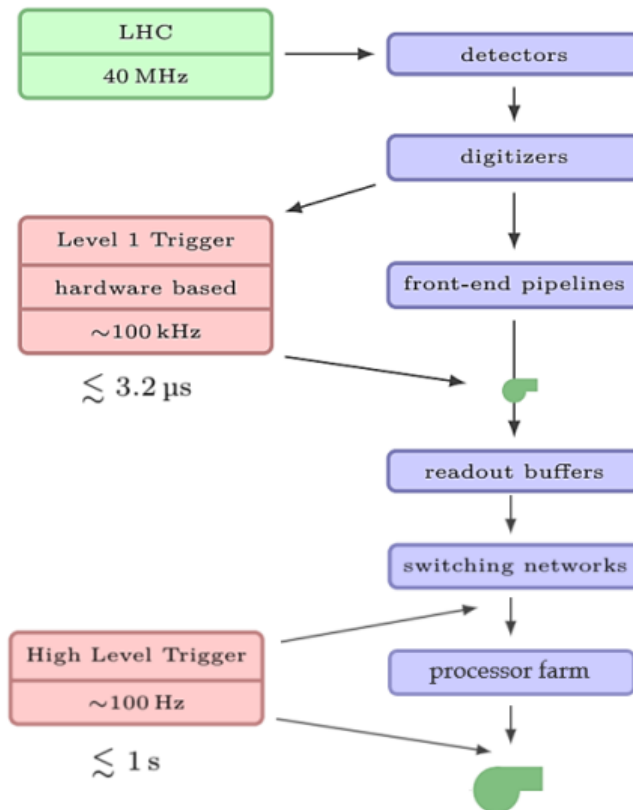


Figure 3.13: The architecture of the CMS Trigger System [35].

this period. The L1 triggers lead to a reduction of the event rate from 40 MHz to 100 kHz , which is low enough to be saved and transferred to a computer facility.

A schematic of the architecture of the Level 1 Trigger is shown in Figure 3.14 and consists of the following components:

- The Calorimeter trigger preserves the local energy sums from the ECAL, HCAL and HF individual readout cells or towers and reconstructed candidates of electrons, photons, taus, and jets. This information is the Trigger Primitive Generator (TPG) which is transferred to the Regional Calorimeter Trigger (RCT), which identifies electrons, γ s, τ s and hadron jets candidates. The formed trigger primitives with sums of transverse energy from RCT are sent to the Global Calorimeter Trigger (GCT), where the best four candidates from each category go to the last step in the L1 hierarchy, i.e. the L1 Global Trigger.
- The Muon Trigger which is focused on μ preselecting. Information from DT, CSC, and RPC is used to drop events with low-quality muons. The trigger information from the different muon chambers is sent to the Global Muon Trigger (GMT). Then the Global Muon Trigger collects,

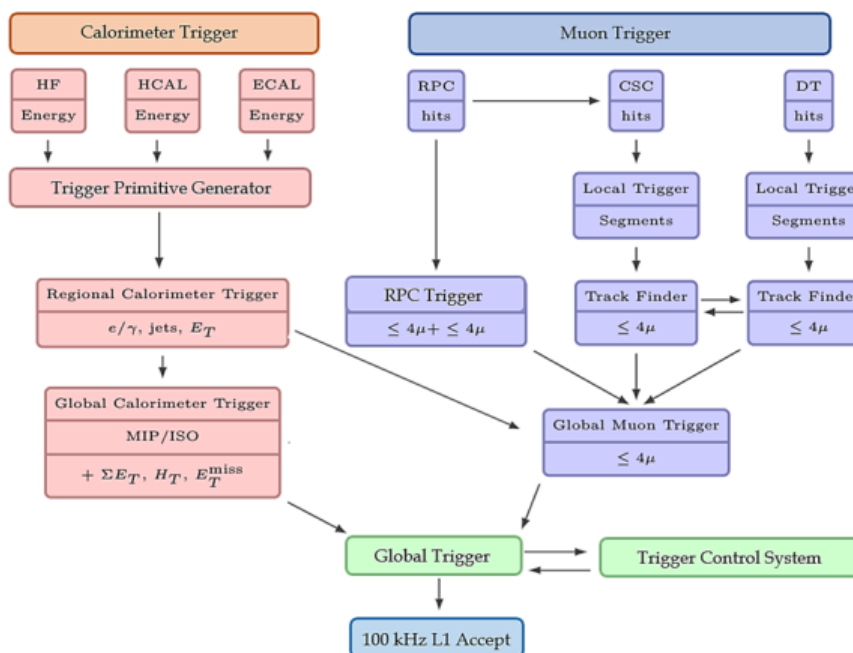


Figure 3.14: Architecture of the Level 1 Trigger [36].

combines and converts the information from all three systems into the same η , ϕ , and p_T scale in order to correlate the muon tracks. Finally, estimates only the four best muon objects and sends them to the L1 Global Trigger.

- The Global Trigger is the last step in the L1 Trigger architecture. It decides whether to reject or accept the event information received from the GCT and GMT to be further analyzed at the HLT. This decision is based on the various algorithms and readiness of the sub-detectors and the DAQ system, which is in turn determined by the Trigger Control System (TCS).

3.6.2 High-Level Trigger

The High-Level Trigger (HLT) is implemented software running on a farm of commercial computers which includes about 16000 CPU cores and reduces the L1 Trigger output rate to the sustainable level of storage and physics analysis of about 100 Hz . The HLT software consists of a streamlined version of the offline reconstruction algorithms.

The HLT menu in CMS has a modular structure, which is graphically depicted in Figure 3.15. The HLT modular design is such that it allows logically independent trigger path, which to a large extent could be run in parallel. Each trigger path is the sequence of software modules and classified based on their function, there are reconstruction modules (*producers*) and filtering modules (*filters*). The latter usually accept or reject events based on the properties

designed. All the system of CMS detector requires upgrades to preserve the efficiency, resolution, and background rejection of the detector at the higher luminosity. The scientific goals now ahead of the LHC experiments concern precision Higgs studies and the search for new physics; both motivations bring indeed a powerful demand for higher luminosities.

3.7.1 Schedule of the Upgrades

In order to open full physics potential, the LHC needs to be upgraded gradually, both the accelerator complex and its experiments. There are two major aspects of the LHC upgrade: the increase of the center-of-mass energy and the increase of the instantaneous luminosity to search very rare physics phenomena. The summary of the present schedule of the LHC upgrade with the various shutdowns and the expected improvements of the beam performance is shown in Figure 3.16 and the projected LHC instantaneous and integrated luminosity as a function of time up to 2037 in Figure 3.17.

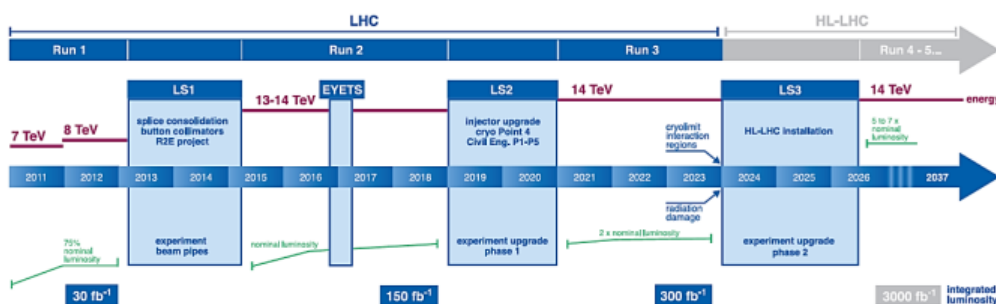


Figure 3.16: The LHC upgrade schedule [38].

The LHC is currently in its first cycle, called Phase-I [38]. The first upgrade was successfully performed during Long Shutdown 1 (LS1) between 2013 and 2014: the magnet interconnections were improved that allowed to increase the center-of-mass energy from 7 TeV to 13 and soon 14 TeV . Moreover, the bunch-spacing has been reduced to 25 ns and luminosity reached the design value of $10^{34} cm^{-2}s^{-1}$ with 25 pile-up interactions. After LS1, the LHC Run-2 was started and the operation was continued until the integrated luminosity of $150 fb^{-1}$. The second long shutdown (LS2) will take place starting from beginning 2019 to the end of 2020. The accelerators will stop again to upgrade the injector chain in order to increase the luminosity up to $2 \times 10^{34} cm^{-2}s^{-1}$. The LHC is expected to start the Run 3 in 2021 and operate continuously until $300 fb^{-1}$. Also, this period will be used to upgrade all detectors for running at this new value of luminosity and at an expected average pile-up of 50. During the LS2, CMS experiment foresees to replace the pixel detector and to upgrade the trigger as well. Finally, the next phase of planned LHC operation called High Luminosity LHC (HL-LHC) or Phase-II [39] will begin with the third Long Shutdown (LS3) in the period from 2024 to middle of 2026,

3.7. Overview of CMS Upgrade Project

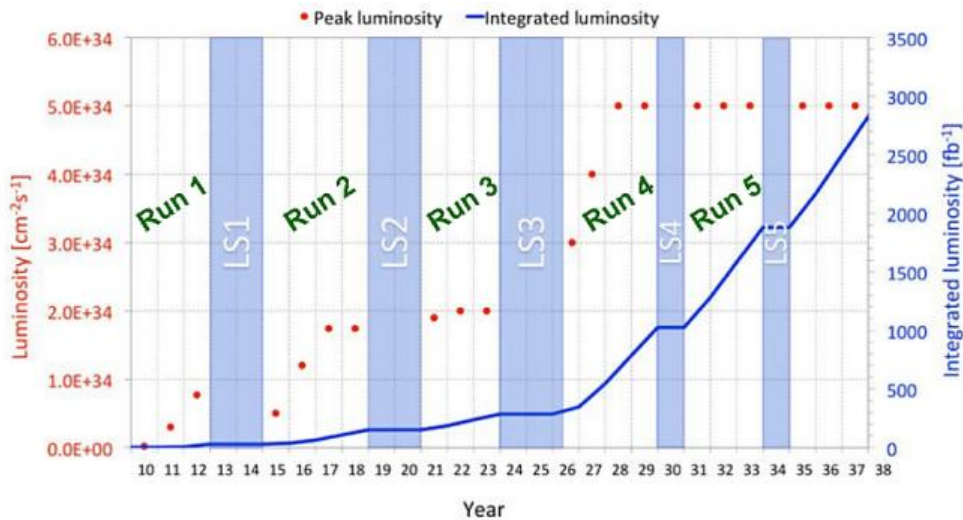


Figure 3.17: Expected LHC instantaneous and integrated luminosity as a function of time up to 2037. Dates for long-shutdowns (LS) periods are also marked [38]

where the machines and detectors will be upgraded to allow for pp running at a luminosity of $5 \times 10^{34} \text{ cm}^{-2}\text{s}^{-1}$ and the expected average pile-up of 140. In the HL-LHC program, the accelerator machines will continuously operate with the aim of integrating a total luminosity of 3000 fb^{-1} . In particular, the CMS will completely replace the tracking detector and will make many other changes to sub-detectors and the trigger and data acquisition systems.

The upgrades of the LHC and its experiments will be allowed to investigate the properties of the the Higgs boson: it will be measured up to the highest achievable precision, including its self-coupling, while additional Higgs bosons and exotic decays will found or excluded. At the higher luminosity, the search for supersymmetric particles will be intensified and the precision of top and electroweak measurements will continuously improve. All CMS upgrades are designed to enable these physics goals by not only mitigating the effects of radiation damage and higher luminosity but by maintaining the existing performance of the detector in key areas relative to the data taking at 13 TeV . The upgrade activities foreseen involves muon detectors, hadron calorimeters, the pixel detector, the trigger and data acquisition, and the beam radiation monitoring and the luminosity measurement system.

3.7.2 Motivation

During the Phase-I and Phase-II periods, the peak luminosity is expected to exceed the design value by a factor of two and three, respectively. After that, a series of problems must be solved to operate successfully throughout these periods. All these challenges are related to high background environment to which all CMS subsystems will be exposed to. In the CMS detector, the most of

the occurring interactions classify as "soft" because they are dominated by the non-perturbative regime. It means, that they do not make high mass states nor they are considered for the search of the electroweak and Beyond the Standard Model (BSM) physics. High mass states, called "hard" collisions, produce very rarely. For a successful analysis, the CMS detector must distinguish with a sufficient efficiency between "soft" and "hard" collisions. The "pile-up" is the occurrence of many proton-proton interactions in a single crossing corresponding to 25 ns . As an example, in Figure 3.18 a high-pile-up event with some reconstructed vertices is shown. The presence of such pile-up makes the discrimination between types of collisions more difficult. Thus, at the high luminosity, CMS L1 trigger performance will degraded continuously. The Muon Spectrometer and the hadron calorimeters upgrades will be aimed to preserve the L1 trigger capability.

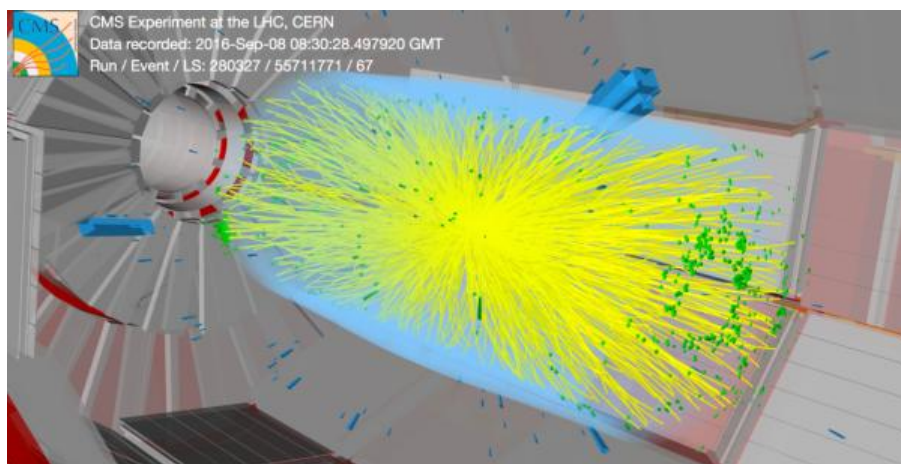


Figure 3.18: A high-pileup events (yellow) with some reconstructed vertices (green) [39]

When the pile-up occurs in the same crossing as the interesting triggered event, it is called "in-time pile-up". On the contrary, when there is signal contamination from preceding or following crossings, we speak of "out-of-time pile-up". This is caused by the intrinsic response of the sensor, or because the electronics takes longer than the 25 ns bunch crossing interval. The contamination is unlikely if the occupancy of a given channel is small: increasing the segmentation of a detector is, therefore, one way to counteract out-of-time pileup.

Also, the integrated luminosity will be affected by the resolution and efficiency of the detector. Ionizing radiations is one of the main sources of detectors damage. The development of radiation hard or radiation tolerant sensors and electronics is a major Research and Development (R&D) effort for experiments installed at LHC. Most CMS detectors can sustain the integrated luminosity of Phase-I with at most slight degradation. But for Phase-II, the replacement of damaged detectors operated during Phase-I will be necessary.

3.7. Overview of CMS Upgrade Project

It is also worth noting other effects, not related with pp-collision which can be a motivation for upgrade studies.

- *Cosmic rays:* The cosmic rays are continuously passing through the detector. Occasionally, they will occur in time with a trigger and may be overlaid on the event and be recorded as part of the crossing data. Some may pass through the pixel detector and be close enough to beam spot to mimic genuine tracks from interactions.
- *Beam halo:* Machine-induced secondary particles are produced in showers which are initiated by collisions of the beam with the material of the beam pipe or collimator. In addition to these scattering processes, charged particles are deflected by the magnetic field of the beam optics. These so-called beam halo particles are one of the main sources of beam background at the LHC. These particles are especially troublesome for large area systems such as the muon detectors.
- *Beam-gas interactions:* The protons in one of the beams can hit a residual gas molecule inside the vacuum pipe and interact with them. The collision products may reach the detector a direct path or may strike other material producing more secondaries that eventually reach the detector.
- *The residual radiation:* The particles passing through CMS can activate the elements of the detector producing various radionuclides. Their decay products may cause signals in some detectors.

All these effects also worsen the operation trigger and affect the quality of the identification and reconstruction of the rare events.

3.7.3 Overview of the expected CMS upgrades during the technical stop, LS2, and LS3

The basic goal of the CMS experiment upgrade is to maintain the excellent performance of the detector subsystems in terms of efficiency, resolution, and optimize the reconstruction of the particles at higher luminosities.

Tracker. The CMS pixel detector is the innermost sub-detector, located close to the collision point. This detector provides important information to reconstruct the tracks and vertices of charged particles. The present pixel detector was designed to work efficiently at maximum instantaneous luminosity up to $1 \times 10^{34} \text{ cm}^{-2} \text{ s}^{-1}$ only and cannot operate for HL-LHC program. The upgrade plan of the pixel systems will be executed during Phase-I and Phase-II. During the Phase-I, the upgrade of the pixel tracker was focused on the replacement of the present pixel detector during the end of year technical stop

of 2016/2017. Due to the fact that the entire tracker will suffer significant radiation damage by LS3, the tracker must be completely replaced for Phase-II. The granularity of both the outer tracker and the pixel systems will be increased by a factor 4. In the outer tracker, the lengths of silicon sensor strips will be shortened without modifying the pitch. Design improvements will lead to a much lighter outer tracker, improving, therefore, the p_T resolution and providing a lower rate of γ -conversions. Moreover, the module design will provide track-stub information to the L1 trigger at 40 MHz for tracks with $p_T > 2 \text{ GeV}/c$, ensuring meaningful power rejection at the earliest stage of the event selection. The pixel system will implement smaller pixels and thinner sensors for improved impact parameter resolution and better two-track separation. The system coverage will be extended to almost $|\eta| = 4$, thanks to the addition of up to 10 additional pixel disks in each of the forward regions [39].

Calorimeters. The hadron calorimeter upgrades for Phase-I was planned to modify the HCAL Barrel (HB), the HCAL Endcap (HE) and the HCAL Forward (HF). HF was designed to measure hadronic energy from jets in the region of $3.0 < |\eta| < 5$. HF calorimeter is a Cherenkov calorimeter comprised of a steel absorber through which quartz fibers are run to collect the Cherenkov light. The light from the quartz fibers is then sent to Photomultiplier Tubes (PMTs) from which an electric signal is produced that is read out and digitized by the front-end electronics. During Run 1, anomalous signals were identified caused by muons or particle showers producing Cherenkov light in the windows of the PMTs. These produce unwanted signals, which are difficult to reject at increasing luminosity. In order to provide a more robust method of rejection, the Phase I upgrade of the HF calorimeter has been done. The upgrade was made in two steps: a replacement of the current phototubes with a multi-anode version which has a thinner window and the replacement of the front-end electronics responsible for the readout. The main problem of the HE and HB is related to the operation of the Hybrid Photodiode which was chosen for their magnetic field tolerance and gain greater than 2×10^3 . In this case, the high voltage applied to these devices led to electrical discharges, which are a source of high-amplitude noise and a risk to the longevity of the HPDs themselves. For this reason, the Collaboration decided to substitute them, together with their electronics, with Silicon Photomultiplier (SiPM). For Phase-II the replacement of the electromagnetic and hadronic endcap calorimeters has been also planned due to the possibility of the radiation damage by LS3. The new calorimeter is called the High Granularity Calorimeter. It includes excellent transverse and longitudinal segmentation, allowing detailed three-dimensional images of particle showers. Its electromagnetic sensor consists of 28 tungsten plates interleaved with silicon sensors as the active material. The sensors have pads of size around 1.0 cm^2 . This section has $25 X_0$ and one hadron interaction length (λ). The hadronic part has a front section comprising 12 stainless steel plates interleaved with silicon sensors for a depth of 3.5λ . This covers the hadronic shower maximum measurement. It is followed by a backing hadron calorimeter

of similar design to the current endcap hadronic calorimeter detector, brass plates interleaved with plastic scintillating tiles read out with a wavelength shifting fiber, to provide an overall depth of $\sim 10\lambda$ for the full calorimeter [39].

Beam radiation instrumentation and luminosity measurement system. The Beam Radiation Instrumentation and Luminosity control (BRIL) of the CMS experiment are responsible for measuring: luminosity, machine induced background and beam timing. BRIL systems also provide active protection in case of intense beam loss events and give various inputs to the CMS trigger system. In order to ensure reliable luminosity and beam background monitoring for HL-LHC, all the installed beam monitoring devices for Phase-II that are located in high radiation environments close to the beam pipe will be completely replaced due to radiation damage. In this upgrade activity, the beam radiation protection system will be modernized by new polycrystalline diamond sensors and the Machine Induced Background (MIB) and Luminosity measuring systems in the Pixel volume will also be changed [39].

Trigger. Concerning the Level-1 trigger: the electronics for the calorimeter trigger, muon trigger, and the global trigger are planned to be improved. For this aim, during the Phase-I the high bandwidth optical links for most of the data communication between trigger cards was installed, and modern, large FPGAs and large memory resources for the trigger logic were used. Using optical links allows to change the architecture very faster, while large FPGAs allow algorithms to evolve as needed. For Phase-II, the latency of the current L1 trigger will be increased from $3.4 \mu\text{s}$ to $12.5 \mu\text{s}$ to provide sufficient time for the hardware track reconstruction and matching of tracks to muons and calorimeter information. Due to this increasing time information readout, the front-end electronics in some present sub-detectors must be upgraded. Taking into account the expected performance of the trigger with track information, the proposed L1-trigger acceptance rate is 500 kHz for beam conditions yielding 140 pileup. This will allow CMS to maintain thresholds comparable to those that will be used in a typical Phase-I trigger menu. To retain comparable performance in beam conditions that result in 200 pileup, the L1 rate must increase to 750 kHz , and so all detectors will have readout capabilities compatible with this possibility. To satisfy these trigger requirements, the Muon system readout electronics in the CSCs and in the DT readout should be upgraded as well [39].

3.8 Overview of the Phase-2 Upgrade of CMS Muon Spectrometer

The muon detectors play a central role in CMS. Muon particles detection is a powerful tool for recognizing signatures of interesting physics processes over the high background rates at the LHC, such as Higgs boson decay $H \rightarrow 4\mu$ and B -meson decay $B \rightarrow 2\mu$. The Muon Spectrometer has three main functions:

- muon triggering;
- muon identification;
- momentum measurement.

Good muon momentum resolution is provided by the high spatial resolution of the detector and the high magnetic field of the superconducting solenoidal magnet and its flux-return yoke. Thus, the CMS muon system was designed to measure the momentum and charge of muons over a large kinematic range. During the next HL-LHC program, the CMS Muon Spectrometer is to preserve the present muon triggering and reconstruction capabilities which were achieved at the Run-1. In order to reach these aims, it will be necessary to mitigate the efficiency loss due to the aging effect of the existing detectors and to improve the offline reconstruction resolution. In addition, a new Track Trigger, which would match candidate tracks with p_T in the inner tracker to muons at L1 Trigger, will require ultra-high purity muon triggering with low thresholds for a very low fake rate.

3.8.1 The Upgrade of the Existing Muon Stations

As described in Section 3.5, the CMS Muon Spectrometer consists of three types of gaseous detectors: Cathode Strip Chambers, Drift Tubes, and Resistive Plate Chambers. While operating very well at the designed luminosity of LHC, upgrades are foreseen for each of the subsystems, necessary to guarantee its role of muon triggering and tracking also in the HL-LHC phase.

Cathode Strip Chambers. The CSC upgrade plans are focused on electronics, in particular foreseeing the replacement of cathode front-end boards (CFEB) on inner chambers in order to handle the increased L1 trigger latency and rate. The CFEB use analog charge storage within custom Switched Capacitor Array (SCA) chips (ASICs) that sample at 50 *ns* intervals and contain a depth of 96 cells. These boards are used on all CSCs except ME1/1 chambers which, in 2013-2014, have undergone an upgrade of the front- and back-end electronics to improve rate capability and performance at higher luminosity. With the increased L1 trigger latency (up to 12.5 *ms*) and rate (up to 750 *kHz*) that is planned for HL-LHC CMS operation, the 108 inner CSC chambers (ME2/1, ME3/1, and ME4/1) will fill the SCA cells; consequently, no additional data can be stored, causing readout inefficiency. Therefore, the CFEBs will be replaced by boards similar to the "digital" DCFEBs that have already been installed on the ME1/1 chambers. These boards flash-digitize the data continuously and store them in large digital buffers, resulting in zero dead-time and the capability to handle latencies well beyond the current specification. They also send their output data on 3.2 *Gb/s* optical links, as compared to 1 *Gb/s* achievable on the copper output cables of the CFEBs; the

higher output data capability of the DCFEBs is important to handle the HL-LHC and CMS L1 trigger conditions. Some additional elements of the CSC data acquisition system, namely the Data Acquisition Motherboards (DMBs) and Detector-Dependant Units (DDUs) that connect to the DCFEBs will be replaced as well in order to handle the high data throughput using the fast optical links. Due to the fact, that new electronics will consume more power, the LV system will be redesigned. Higher background rates and the need for a more accurate monitoring of CSC currents will also imply an incremental upgrade for the present HV system [34] [39].

Drift Tube. DTs modernizations are also focused on electronics. It is known that DT electronics will need replacement due to limited radiation tolerance of some components; this replacement also gives the opportunity to increase the trigger rate capability and performance, and improve maintainability. Each DT chamber houses the L1 Trigger and Readout electronics in an aluminum profile, called a Minirate, which hosts the time digitization logic and the logic for the L1 trigger primitive generation. During HL-LHC the survival of this system is not guaranteed, and will not be able to cope with increasing the Level 1 trigger acceptance rate beyond 300 kHz . In order to increase their reliability and improving their performance, the DT upgrade will focus in moving them to the Underground Control Room where the environment is more congenial. Moreover, this replacement will allow the implementation of full time (and therefore space) resolution and to provide complete chamber information in the DT trigger system, with improved performance in terms of rate reduction and better matching with the tracker at the Level 1 trigger [34] [39].

Resistive Plate Chambers. During LS1 the fourth RPC endcap station was instrumented in the η region up to $|\eta| = 1.6$. One of the more important requirements of the muon trigger is the achieving of the good enough resolution to identify high- p_T tracks. With the RPC trigger requiring segments in at least three stations, the endcap system did not have the necessary redundancy to control the trigger rate at the increased luminosity while preserving high trigger efficiency. The addition of the fourth layer called RE4 helped to provide the finer timing and redundancy to the corresponding CSC station and preserved a low- p_T threshold [34] [39].

Figure 3.19 shows the simulated trigger efficiency as a function of η is shown in case of the present 3 layers compared to the result for a 4-layer system. The advantage in extending the detector to include the fourth station is clearly evident. RE4 has been installed on the back of the YE3 yoke during LS1, mounted independently of the CSC chambers.

For Phase-II, CMS RPC Collaboration have planned two important upgrades:

- on the existing RPC chamber, which will be continuously operated until the end of 2026, the link system must be replaced.

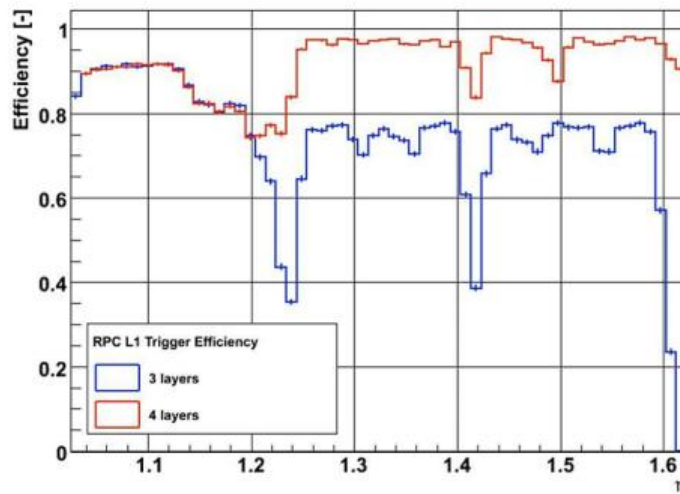


Figure 3.19: Simulated trigger efficiency as a function of the η number of layers numbers of RPCs [34].

- on additional set of new RPC detector will be installed in the high- η regions.

3.8.2 New Stations in the innermost region of the CMS forward Muon Spectrometer

In the region $1.5 < |\eta| < 2.4$ the muon system currently consists of four stations of CSC only. It is the only region of the muon detector that lacks redundant coverage despite being a challenging region for muons in terms of backgrounds and momentum resolution. To maintain good L1 muon trigger acceptance in this region it is therefore proposed to enhance these four stations with additional chambers that make use of new detector technologies with higher rate capability, as originally proposed by the design of CMS.

The CMS Collaboration is planning to install a detector based on the Gas Electron Multiplier (GEM) technology that could withstand the hostile environment and high luminosity rates at the LHC and its future upgrades. GEMs are gas-based detectors, characterized by a detection efficiency more than 98% even for rate exceeding few MHz/cm^2 , high spacial resolution of order $\sim 100 \mu m$, and good time resolution of order ~ 8 and $\sim 5 ns$ at the efficiency plateau for Ar/CO_2 (70/30) and $Ar/CO_2/CF_4$ (45/15/40) gas mixture, respectively. Additionally, the gas gain is observed to be stable up to a several MHz/cm^2 of incident particle rate by demonstrating that the GEM detectors have a high rate capability and will be suitable to operate in the forward muon region of CMS experiment, where a maximum rate on the order of $150 kHz/cm^2$ is expected.

Triple-GEM detectors are approved to instrument two forward regions at $1.6 <$

3.8. Overview of the Phase-2 Upgrade of CMS Muon Spectrometer

$\eta < 2.4$ (see Figure 3.20), called GE1/1 and GE2/1 station during the second and third Long Shutdown, respectively. The GE1/1 and GE2/1 detectors are "super-chambers", each made of a double layer of trapezoidal triple-GEM detector. They will cover slightly more than 10° in GE1/1 station and 20° in GE2/1 station, overlapping in φ just like the corresponding CSC detectors in ME1/1 and ME2/1 stations, complementing them and providing redundancy and enhanced triggering and tracking capabilities in the region which currently suffering from the highest background rates and a non uniform magnetic field. Therefore, 36 super-chambers will be installed for the GE1/1 station and 18 for the GE2/1 station in each muon endcap in order to ensure the full azimuthal coverage. In order to gain first operational experience with the new subsystem and also to demonstrate the integration of GE1/1 detectors into the trigger, a demonstrator, consisting of five GE1/1 super-chambers, has already been installed in CMS during the year-end technical stop 2016/2017 [34] [39].

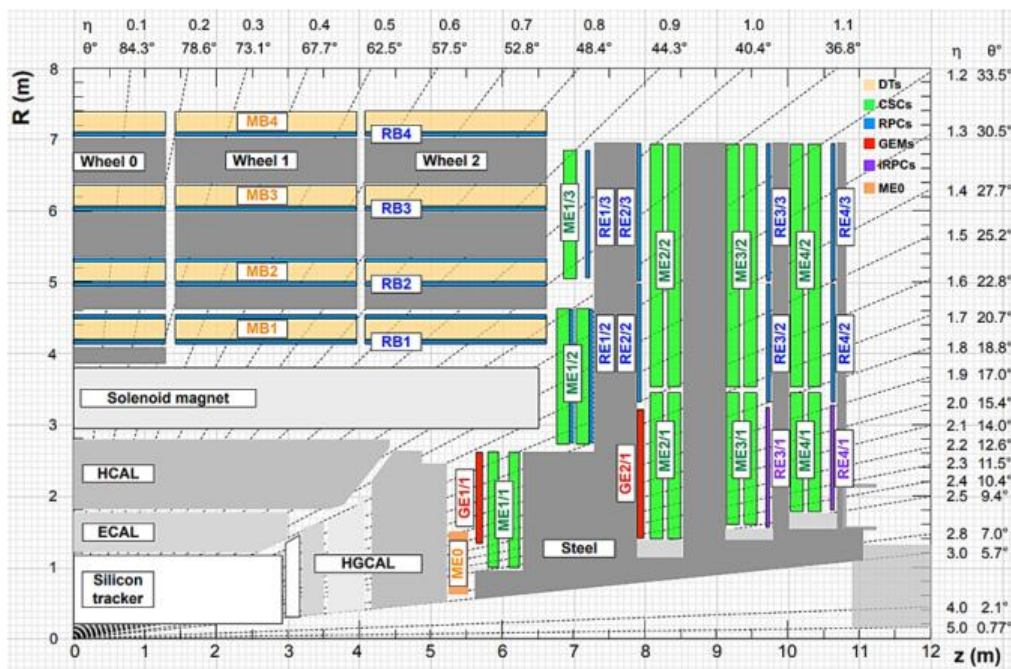


Figure 3.20: A quadrant of the CMS Muon Spectrometer, showing DT chambers (yellow), RPC (light blue), and CSC (green). The locations of new forward muon detectors for HL-LHC phase are contained within the dashed box and indicated in red for GEM stations (ME0, GE1/1, and GE2/1) and violet for improved RPC stations (RE3/1 and RE4/1) [34].

In addition to GE1/1 and GE2/1 station, the ME0 station is approved to be instrumented with triple-GEM detectors. Indeed, with pixel tracking extension close to $\eta < 4$ and the replacement of the endcap of the electromagnetic and hadronic calorimeters during the third Long Shutdown, comes the opportunity to extend the muon coverage beyond the present limit of $\eta < 2.4$ with the addition of a muon gas-based detector installed in a space of ~ 30 cm freed

behind the new end-cap calorimeters. The ME0 detector station comprises 36 module stacks (18 per endcap), each composed of six layers of triple-GEM detectors, compared to the two-layer design of GE1/1 and GE2/1, covering the region $2 < \eta < 2.8$, in order to allow proper rejection of neutron background, particularly intense in that region. The large η coverage foreseen would lead to an improvement of the acceptance, with a consequent boost in the signal over noise ratio in the signature with muons, especially with the multiple-muon final states, and better hermeticity for signature without muons. The technical details of the CMS Muon System upgrade for Phase-II can be found at [34] [39].

Chapter 4

The Gas Electron Multiplier

4.1 Introduction

The introduction of the Multi-Wire Proportional Chambers (MWPCs) by G. Charpak in 1968 [40] radically changed the physics of particle detectors. With its good space-resolution and rate capability, and the possibility to electronically record signals generated by the passage of the charged particle in the sensitive gas volume, the MWPCs became the workhorse for many particle detectors in high-energy physics. Furthermore, these detectors have come into widespread use in several fields, such as astroparticle physics, nuclear medicine and industrial diagnostic.

A MWPC consists of a set of thin, parallel and equally spaced anode wires, symmetrically sandwiched between two parallel cathode planes. Figure 4.1a shows a schematic cross-section of a multiwire proportional chamber. For proper operation, the wire spacing S is typically 2 mm , while the gap l , i.e. the distance between the wire plane and the cathode plates, is three or four times larger. By applying a negative potential to the cathode planes, the anode being grounded, an electric field develops as indicated by the electric field equipotentials and field lines shown on Figure 4.1b.

When filled with the appropriate gas mixture, an ionizing particle crossing the detector active gas volume releases primary electrons that will drift along the field lines until they approach the anode wire. Close to the anode wires, the field strength increases so as to trigger an avalanche multiplication process: the primary electrons become energetic enough to ionize the gas mixture, and in turn grow exponentially in numbers. Because of the pattern structure of the anode wire plane, the spatial resolution can be evaluated by $\sigma = \text{pitch}/\sqrt{12}$, where the pitch is defined by the distance between the anode wires. With a typical pitch of the anode wires of 2 mm , the spatial resolution is of the order of $0.5\text{-}1\text{ mm}$. Additionally, the spatial resolution can be improved by combining several layers of MWPCs with different orientations and segmented cathode plates with a fine pitch. The typical time resolution is of the order

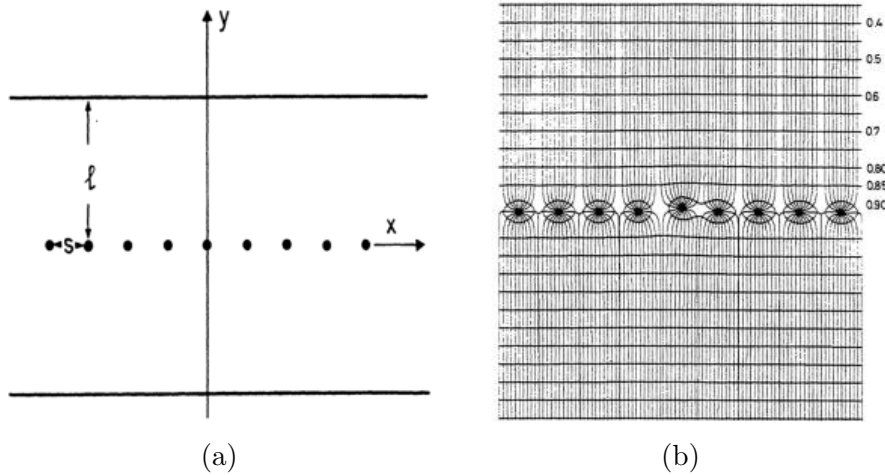


Figure 4.1: Multi-Wire Proportional Chambers : (Left) Principle of construction and definition of the parameters in a multiwire proportional chamber. A set of parallel anode wires is mounted symmetrically between two cathode planes. (Right) Electric field equipotentials and field lines in a multiwire proportional chamber. The effect on the field due to a small displacement of one anode wire is also shown [41].

of 10 ns in Ar/CO_2 (70/30) gas mixture [41]. In the CMS experiment, a variant of the MWPC, the CSCs, are used for the L1 trigger and the muon reconstruction in the forward region of the CMS Muon System. Large sizes MWPCs can be produced with a relatively inexpensive materials and very precise wire geometry. Moreover, the mechanical and electrostatic forces in the inner structure can induce a displacement of the anode wires that lead to a distortion of the electric field and thus affect the quality of the gas gain uniformity.

With the advent of the new high luminosity accelerator machines, the MWPCs have shown several limitations concerning the capacity to tolerate the very high particle fluxes foreseen. The rate capability in the MWPCs is mainly affected by the low drift velocity of the positively-charged ions from the anode wire towards the cathode electrode. When a MWPC is subjected to a high flux rate of particles, the ions produced in the avalanche multiplication process around the anode wire could generate a positive space charge such as to distort the electric field. The net effect is a significant decrease of the detector gas gain leading to a detection efficiency loss. For a MWPC the maximum rate capability, depending on the detector geometry (wire pitch, anode-cathode wire distance), is generally below $1 MHz/cm^2$ [41]. Additionally, the MWPCs are rather susceptible to aging phenomena when they are subjected to high particle flux rate. Indeed, the creation and deposit on the anode wires of thin insulating layers due to the polymerization of organic molecules and/or pollutants present inside the detector gas volume, lead to enormously reduce the life-time of the detector.

4.1. Introduction

In order to overcome this issue, i.e. to drain the positively-charged ions, the anode wire spacing and/or the anode-cathode gap should be reduced to minimize the the space charge buildup around the anode wires. Typically, below 1 *mm* wire spacing and below 2 *mm* anode-cathode gap, the operation of the MWPCs becomes particularly unstable due to the electrostatic instabilities arising from the mechanical tolerances.

A new generation of gas-based detectors, collectively named micro-pattern gaseous detectors (MPGD), allows to overcome the rate capability and aging problems of the MWPCs. The first example of a micro-pattern detector is the Micro-Strip Gas Chamber (MSGC), designed by A. Oed in 1988 [42] [43]. The detector geometry is planar: the anode and cathode are both placed on the same plane and consist of thin metal strips alternately deposited on an insulating substratum which acts as a support. The upper electrode, called drift electrode, is used to define the drift region. A further electrode behind the insulating substratum, called back-plane, is generally segmented as orthogonal readout strips giving the second coordinate (see Figure 4.2).

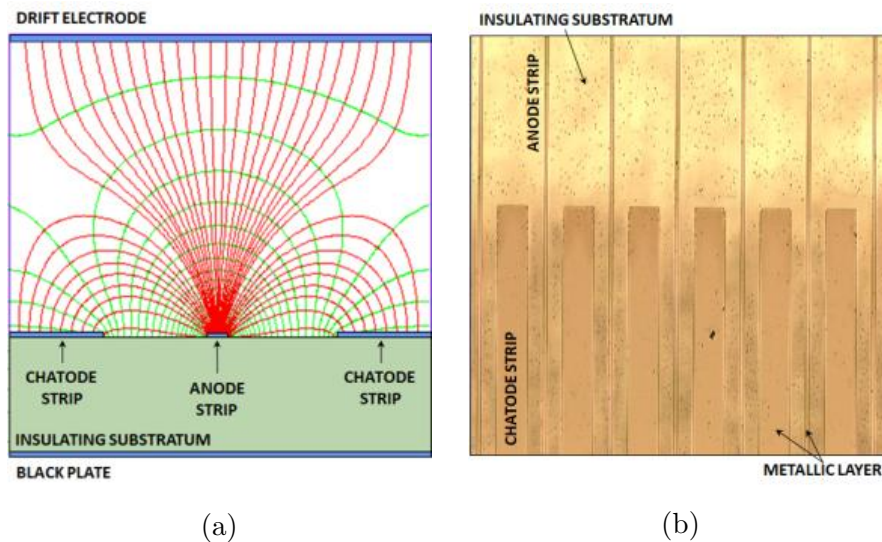


Figure 4.2: Micro Strip Gas Chamber: (Left) Schematic overview of the Micro Strip Gas Chamber. (Right) Picture of the anode and cathode strips.

The strips, alternatively connected to positive and negative voltage, act as a multi-anode proportional chamber. The electrons, produced by a charged particle crossing the detector in the drift region, move towards the anode strips where they are multiplied. The ions produced in the avalanche multiplication process are mainly collected in the neighbouring cathode strips typically 100 μm distant from the anode strips. The modern photolithographic techniques, the same used for the production of multi-layer printed boards, allow to produce 0.3-0.5 μm thick anode and cathode strips with 100 μm of pitch, resulting in an improved rate capability and space-resolution by more than one order of magnitude compared to the previous MWPCs.

However, operating instabilities have been observed in the MSGCs due to the so-called charging-up of the insulating support. Indeed, when these device are subject to high particle flux, a fraction of the multiplication ions could be collected on the insulating support without neutralizing itself. The charge accumulation on the surface of the insulating support leads to the distortion of the electric field between the anode and cathode strips with a consequent rate dependent gas gain drop. The charging-up effect could be minimized using a slightly conducting supports, and rate capability up to 100 MHz/cm^2 could be achieved (see Figure 4.3) [44] [45].

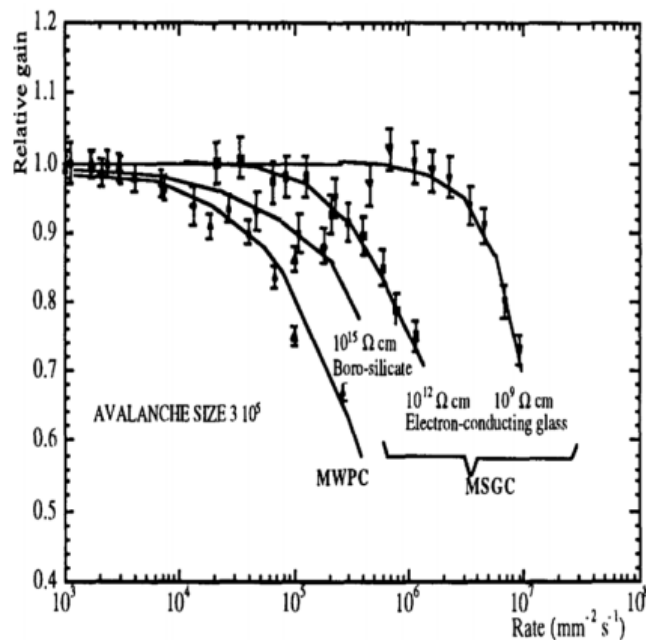


Figure 4.3: Rate capability of the MWPC and MSGC technologies manufactured on substrates with different values of bulk or surface resistivity.

Additionally, the MSGCs appeared rather susceptible to aging and discharge phenomena. Long-term studies have shown a slight degradation of the detection performances due to the formation of polymers in the avalanche multiplication process. However, with the proper choice of the detector materials and gas mixture, a long-term operation up to integrated charge above 100 mC/cm of strip, has been demonstrated [46]. On the other hand, the MSGCs appear to be extremely susceptible to irreversible degradation due to destructive discharges. The discharge could permanently damage the strips leading in the time to an increased dead channels with a consequent efficiency loss (see Figure 4.4). The discharge damages represent a serious limitation to the use of the MSGCs in the new high luminosity accelerator machines, where among the particles to be detected, heavily ionizing particle, such as nuclear fragments, gamma and neutron, are also present. Therefore, a compromise value of gas gain allowing proper detection of minimum ionization particles (M.I.P.) and at

the same time avoiding discharge damages triggered by the crossing of heavily ionizing particles, could not be possible.

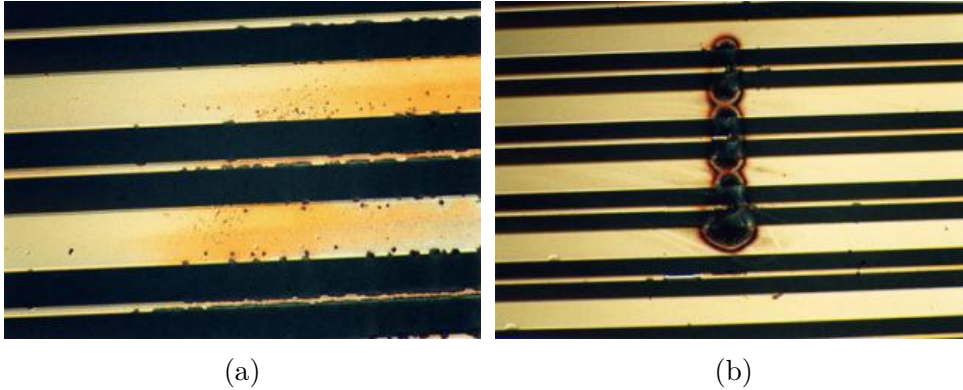


Figure 4.4: Damage caused by a discharge in a MSGC.

The problems highlighted by the studies of the MWPCs and MSGCs resulted in a large effort devoted to the development of new and more rugged micro-pattern gaseous detector. Over the last two decades, many of such MPGDs have been developed: the microgap chamber (MGC) [47], the Microdot [48], the "Compteur á Trous" (CAT) [49], the MicroMesh Gas Chamber (MicroMeGas) [50], the Micro-Groove [51] and the WELL [52] detectors.

Among the most recent developments in the micro-pattern gaseous detectors field, the Gas Electron Multiplier (GEM) proposed in the 1997 by F. Sauli [53], represents the object of this Doctoral Thesis. Compared to the other micro-pattern gaseous detectors, in the GEM-base detector the conversion, the amplification and the signal induction regions are physically separate resulting in greater freedom in the readout geometry. Additionally, as will be presented in the following paragraphs, the possibility to share the multiplication in more amplification stage allows to drastically minimize the problems related to the aging and discharge damage.

4.2 The GEM Technology

The Gas Electron Multiplier (GEM) technology consists in a $50\ \mu\text{m}$ thick Kapton foil, clad on each side with a $5\ \mu\text{m}$ thin copper layer and chemically perforated with a high density of holes. Each GEM-hole is characterized by a bi-conical structure with an external diameter of $70\ \mu\text{m}$ and internal diameter of $50\ \mu\text{m}$ and a pitch of $140\ \mu\text{m}$ [54] [55] (see Figure 4.5).

The GEM-holes represent the active part of a GEM-based detector acting as a multiplication channel for the electrons released by ionizing radiation in the gas mixture. Applying a suitable potential difference of 300-500 V between the two copper surfaces, an high electric field up to $\sim 100\ \text{kV/cm}$ is established

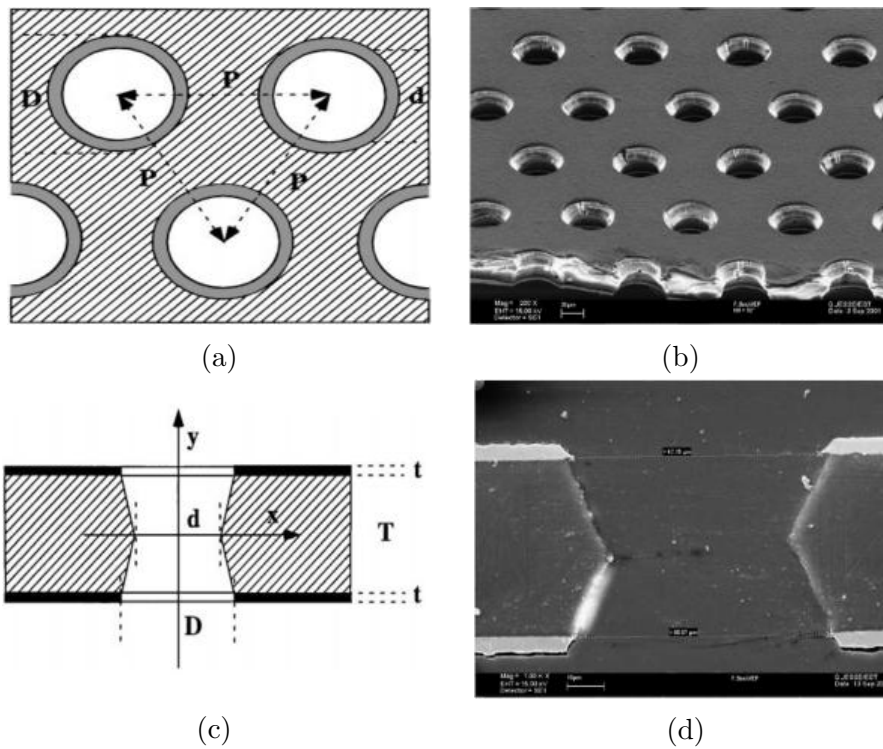


Figure 4.5: Schematic overview (Figure 4.5a) and electron microscope picture (Figure 4.5b) of a section of typical GEM electrode, $T = 50 \mu\text{m}$ thick Kapton foil, clad on each side with a $t = 5 \mu\text{m}$ copper layer. The holes pitch is $P = 140 \mu\text{m}$ and the external and internal diameter are $D = 70 \mu\text{m}$ and $d = 50 \mu\text{m}$, respectively. Schematic overview (Figure 4.5c) and electron microscope picture (Figure 4.5d) of the cross-section of a bi-conical hole of a GEM-foil [55].

4.2. The GEM Technology

inside the holes. In this region, an electron could acquire enough energy to ionize the gas molecules and triggering an avalanche multiplication process. The reachable gas gain with a single GEM-foil could be greater than 10^3 .

The GEM-foils manufacturing technology is realized using the conventional photolithography technique for standard printed circuit boards [56] (see Section 5.2.5). The choice of geometrical parameters of a GEM-foil, such as the GEM-holes diameter, pitch and shape (conical, biconical, cylindrical, etc.) are a compromise between the manufacturing technique and the proper operation of the detector [55] [57] [58].

4.2.1 Influence of GEM-hole diameter

In order to achieve a higher gas gain, the electric field lines density in the amplification channel could be increased by raising the voltage difference between the upper and lower GEM-electrodes, or by reducing the GEM-hole diameter. A diameter-reduction leads generally to an increase in the gas gain as it improves the multiplication electric field inside the hole. Figure 4.6 shows the correlations between the effective gas gain of the GEM-foils and the hole diameter, measured at equal electric fields conditions and gas mixture.

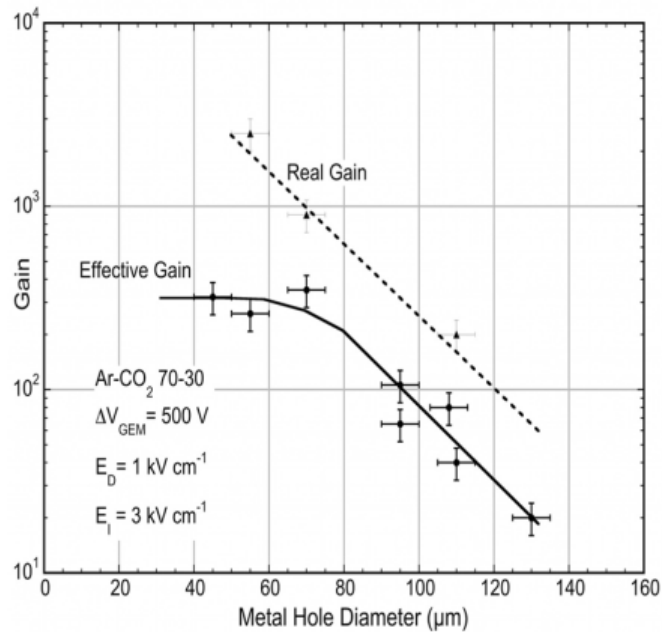


Figure 4.6: Measured effective gas gain and real gas gain of GEMs operated in Ar/CO_2 (70/30) with different metal hole diameters [55]. It should be noted that, since fraction of the multiplying electrons is lost on the lower electrode of the GEM-foil, the effective gas gain, defined as ratio of the detected charge to the primary ionization charge, is lower than the real gas gain of the amplification stage, shown in the figure.

A gas gain saturation effect is observed for hole diameter below $\sim 70 \mu\text{m}$ which is due to the increasing losses of electrons in the avalanche multiplication process to the lower GEM electrode (see Section 4.3.3). The saturation effect, whilst limiting the possible gas gain enhancement, has the very positive effect of reducing substantially the dependence of the detector gas gain from the precision of the GEM manufacturing procedures.

4.2.2 Influence of GEM-hole pitch

The GEM-hole pitch does not play a direct role on the gas gain behavior, but when combined with the hole diameter, affect the collection efficiency of the electrons released in the upper volume of the GEM-foil into the holes. The collection efficiency is correlated with the so-called electron transparency: it gives a measure of the electrons losses crossing a hole due to different effects, and plays an important role in the detection performances (see Section 5.2.5). At this level, it is possible to deduce that a high electron transparency is achieved with a small GEM-hole pitch, as shown in Figure 4.7.

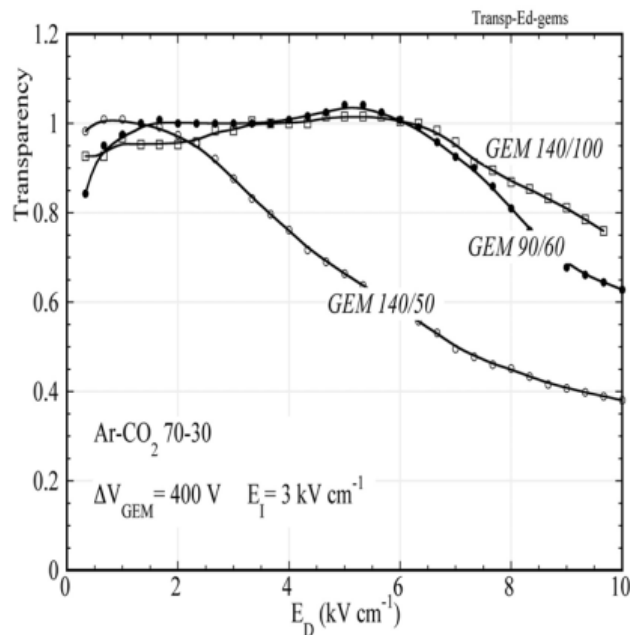


Figure 4.7: Electron transparency as a function of drift electric field in a single-GEM detector operated in Ar/CO_2 (70/30) for different GEM geometry, labeled as pitch/hole diameter [55].

4.2.3 Influence of GEM-hole shape

The GEM-hole shape, which essentially depends on the GEM-foils manufacturing technology, is correlated with the short-term charging-up effect, generally observed in gas-based detectors that use high surface resistivity substrates as

4.3. The single-GEM detector

active parts. Such effect consists in the accumulation of a fraction of the positive ions, generated in the avalanche multiplication process, on the insulating Kapton surface by producing an alteration of the multiplication electric field inside the holes. The GEM-hole geometry which best minimizes the charging-up effect is the cylindrical shape, as shown in Figure 4.8. However, considering the difficulties in the manufacture of the GEM-foils with a cylindrical hole shape, it was decided to produce the GEM-foils with a biconical hole shape through single or double-mask photolithography technology. The choice of a GEM-hole bi-conical shape is a compromise between a good production yield and a limited charging-up effect with respect to the GEM-hole conic shape [55].

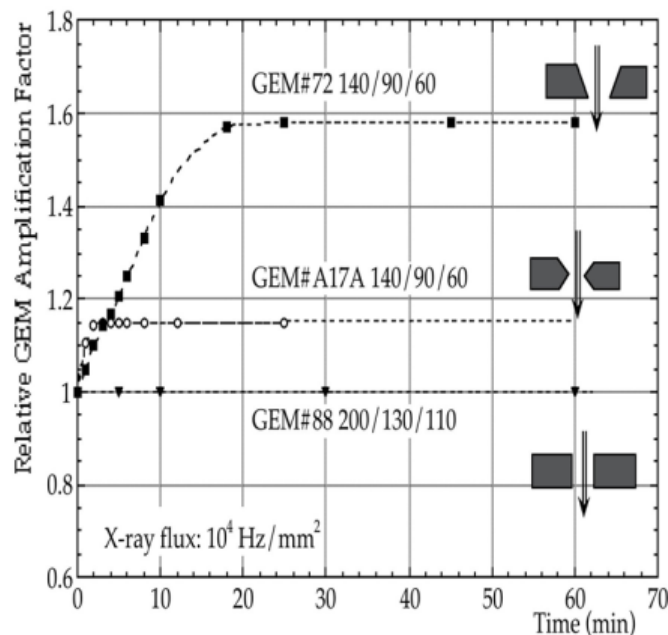


Figure 4.8: Charging-up effect as a function of time at X-ray photons flux of about 10^4 Hz/mm^2 for three different shapes of the GEM-holes [55].

4.3 The single-GEM detector

The simplest gas detector based on GEM technology is the single-GEM [55] [58], which consists of one GEM foil sandwiched between two flat parallel electrodes. The upper electrode acts as a cathode while the lower electrode as an anode or a signal collecting electrode. The Figure 4.9 shows a schematic cross section of a single-GEM detector.

A voltage difference is applied between the electrodes and the GEM-foils in order to generate three electric fields above, below and cross the GEM-foil:

- The drift electric field, E_D , is generated between the upper surface of the GEM-foils and the cathode electrode;

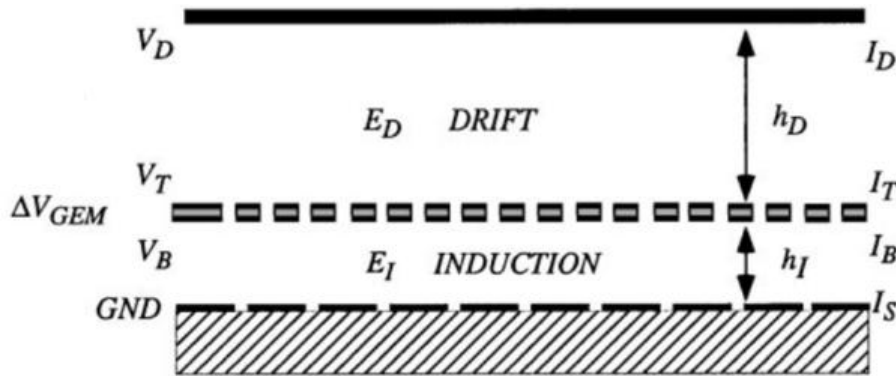


Figure 4.9: Schematics of a single-GEM detector: E_D and E_I are the drift and the induction electric fields, while h_D , h_I are the drift and induction gaps; ΔV_{GEM} is the voltage difference applied to the two copper electrodes of the GEM-foil [58].

- The induction electric field, E_I , is generated between the lower surface of the GEM-foils and the anode electrode;
- The amplification field, E_A , is generated across the GEM-holes.

The two corresponding regions are called *drift gap* and *induction gap* respectively and in each of the two regions the resulting electric field is essentially uniform.

When a single-GEM detector is filled with the appropriate gas mixture, a charged particle crossing the detector gas volume releases primary electron-ion pairs. Following the drift electric field lines, positively charged ions migrate to the cathode, while the electrons move towards GEM-holes where they are multiplied. Some of the electrons from the multiplication are partly collected on the lower side of the GEM-foil. The most of the multiplication electrons are transferred to the induction region contributing to the formation of an induced current signal on the anode, which is generally constituted by a simple and cheap printed circuit board (PCB), whose readout structure can be easily adapted to the experimental requirements by using strips or pads of arbitrary shapes connected to the front-end electronics. Typically the fraction of the multiplication electrons that are transferred in the induction region is $\sim 50\%$ and this fraction depends on the electric field inside the GEM-hole and electric field below the GEM-foil [55] [58]. Similarly, the multiplication ions are mainly collected on the upper side of the GEM-foil instead of drifting towards the cathode leaving the GEM-hole from charges in a relatively short time, few μs (see Figure 4.10).

A major difference in comparison to the other gaseous detectors is the electronic nature of the signal induced on the anode of the GEM-based detectors, i.e. the induced signal is purely due to the motion of the multiplication electrons in the induction region. Therefore, taking into account the high electron

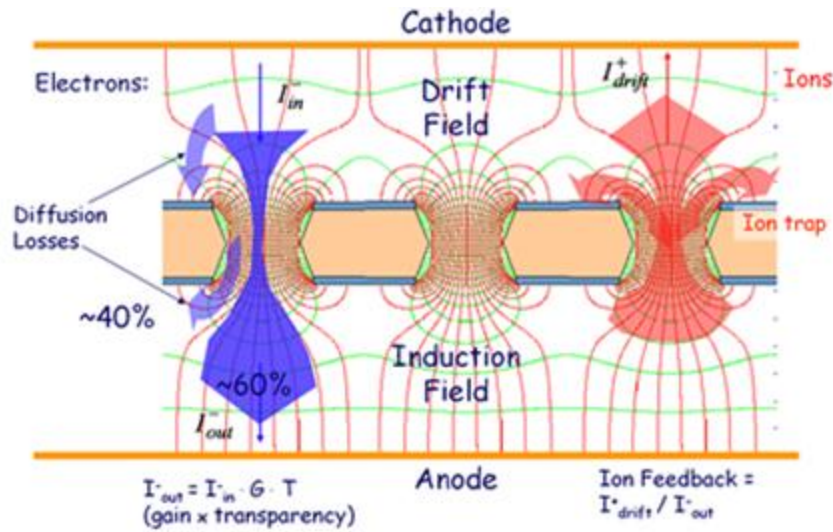


Figure 4.10: Schematic overview (not in scale) of a single-GEM detector operation together with the 2D map of electric field lines (red) and equipotential lines (green) in proximity of the GEM-holes.

mobility, the induced signal is fast and is not affected by the ballistic deficit typical of the other gaseous detectors, such as the multi-wire chambers where the pulse signal on the electrodes is formed by induction due to the movement of ions.

The major parameters that affect the performance of the single GEM detector with defined geometry of a GEM-foil and the gas mixture, typically Ar/CO_2 (70/30) or $Ar/CO_2/CF_4$ (45/15/40) [55] [58], are:

- The electric fields in the drift and the induction region;
- The thickness of the drift and induction region.
- The voltage difference applied between the electrodes of the GEM-foil;

4.3.1 Drift and induction electric fields

The study of the electric fields structure in a GEM-based detector, in various geometries, gas mixture and electric fields conditions, is typically carried out through several simulation softwares, such as GARFIELD [59] and MAXWELL [60]. The Maxwell simulation software is an engineering program which allows to build the 3D geometry of a detector, taking into account all the detector material properties, while the Garfield simulation software is the common framework used for the simulation the particle detectors that use gas and semi-conductors as sensitive medium. The electric field lines in the drift and induction regions are similar to those of a parallel plate capacitor with an increasing field line density near the holes, as shown in Figure 4.10.

Drift electric field effect. The aim of the drift electric field is to transfer the primary electrons produced by the ionization particles in the drift region and focus them into the GEM-holes. The effect of the drift electric field can be evaluated in Figure 4.11, showing the relative amplitude of the signal induced on the readout board as a function of the drift field, deduced from a measurement of current and from pulse height with two shaping times (100 ns and $1\ \mu\text{s}$) [58].

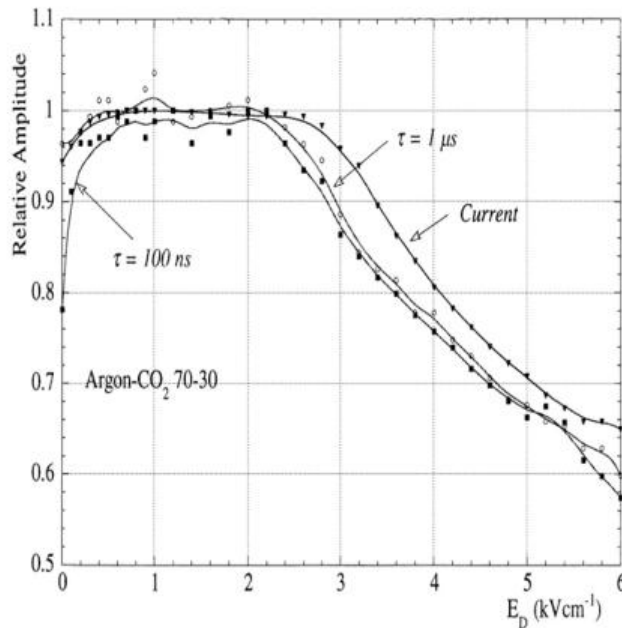


Figure 4.11: Collection efficiency as a function of drift electric field in a single-GEM detector operated in Ar/CO_2 (70/30) for two different method of measurement: integral current or pulse with two time constants [58].

For relatively low drift electric field values ($< 0.5\text{ kV/cm}$), a decrease in the amplitude of the signal induced on the readout board is observed. This is due to the concomitance of the recombination effects (due to the large diffusion) and the low electron drift velocity as can be deduced from the two curves with different shaping times. For intermediate drift electric field values ($\sim 1\text{--}3\text{ kV/cm}$), the amplitude of the signal reaches a plateau and then decreases again for higher values. The latter effect is due to the fact that an increasingly consistent fraction of the drift field-lines ends on the upper side of the GEM-foil rather than focusing into the holes, which leads the primary electrons to be directly collected on the upper electrode of the GEM-foils. The above dispersive effects are correlated to the so-called *collection efficiency* which will be discussed in detail in Section 4.3.3. The value of the drift electric field is generally in the range ($\sim 1\text{--}3\text{ kV/cm}$); for a given gas mixture and GEM-foil geometry, the value of the drift electric field is chosen in order to optimize both the collection efficiency and the electron drift velocity. For example, in

4.3. The single-GEM detector

the Ar/CO_2 (70/30) gas mixture the typical value of the drift electric field is $\sim 2 \text{ kV/cm}$ [58].

Induction electric field effect. The aim of the induction electric field is to extract the multiplied electrons from the GEM-holes and to transfer them towards the anode. Figure 4.12 shows the electron current induced on the lower electrode of the GEM (I_B) and on readout pad (I_S), together with the sum (I_{TOT}), as a function of the induction electric field [58]. The drift electric field was fixed to 1 kV/cm to ensure full collection efficiency in GEM holes.

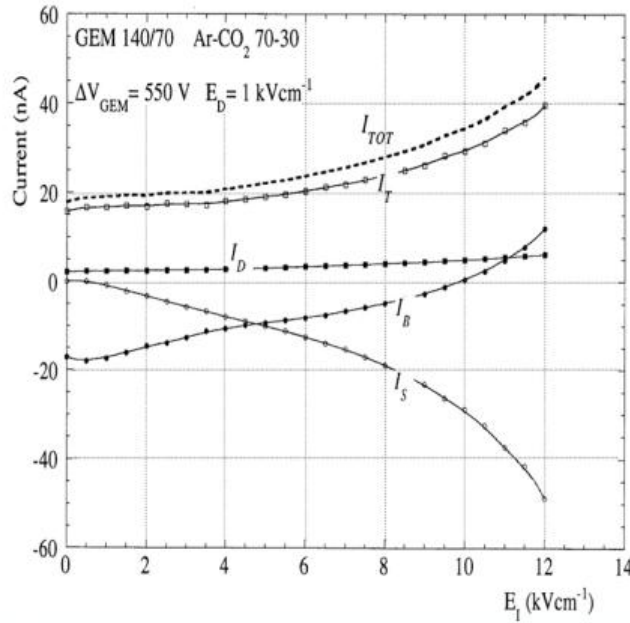


Figure 4.12: Currents on the various electrodes of a single-GEM detector as a function of the induction electric field: I_S is the current on the readout pads, I_T and I_B the current on the upper and lower copper layer of the GEM-foil, and I_D the current of the cathode electrode [58].

A very low value of the induction electric field, or at the null limit, does not allow the multiplication electrons to be effectively transported toward the readout board. In this case, the electrons are still extracted from the GEM-holes thanks to the electric field present inside the holes themselves, but they are completely collected on the lower electrode of the GEM-foil due to the fact that the field-lines end on the latter electrode ($I_B = \text{maximum}$) and the induced signal is vanishing (Ramo's theorem [67]): the induced signal on the readout pads is null ($I_S = 0$). By incrementing the induction electric field (E_I), the fraction of current collected on the readout pads (I_S) increases to the detriment of the current collected on the lower electrode of the GEM-foil (I_B). At very high induction field ($E_I > 8 \text{ kV/cm}$), discharges on the anode can occur due to the high electric field in proximity to the edges of the readout electrode.

Independently by the gas mixture used, a compromise value of the induction electric field of $\sim 5kV/cm$ allows to collect a large fraction ($\sim 50\%$) of the total charge on the readout board.

4.3.2 Drift and induction region thickness

Drift region. The geometry of drift region is chosen in order to ensure an high intrinsic detection efficiency. For a charged particle, the number of electrons clusters created has a Poisson distribution with an average value depending on the energy of the particle crossing the detector and the gas mixture.

A 3 mm thickness gap guarantees, for standard gas mixture used in High Energy Physics gas-based detectors, a sufficient number of electron-ion clusters to achieve a full particle detection of minimum ionizing tracks; a wider drift gap could leave the detection efficiency unchanged, but at the same time it could increase the pile-up effects at very high particle rate as well as the ageing rate: the total charge integrated by the detector depends linearly on the value of the primary charge released in the drift gap [55] [58].

Induction region. The geometry of induction region is chosen in order to optimize the signal fraction collected by the amplifier. In a GEM-based detector, the signal amplitude is proportional to the ratio between the electron drift velocity and the induction gap thickness (see Section 4.4.5). Such consideration suggests the use of a fast gas mixture and a small thickness for the induction gap. On the other hand, a sub-millimetric gap is not advised because it would require a high mechanical tolerance in order to avoid discharges on the readout board and/or gas gain disuniformity on the entire detector area.

4.3.3 GEM-foil voltage

As discussed previously, the voltage difference between the two electrodes of a GEM-foil would be such that to generate an high electric field inside the holes in order to develop avalanche multiplication processes. Therefore, the voltage difference, V_{GEM} , defines the intrinsic gas gain of a GEM-foil:

$$G_{intrinsic} = exp \left(\int [\alpha(x) - \eta(x)] \delta x \right) \quad (4.1)$$

where $\alpha(x)$ and $\eta(x)$ are respectively the first Townsend [61] and the attachment coefficient in the path δx . Both of these coefficients are dependent on the electric field and gas mixture. Due to the high electric field inside the holes ($\sim 100 kV/cm$), the attachment coefficient becomes negligible and the previous formula can be rewritten:

$$G_{intrinsic} \propto e^{\langle \alpha \rangle \cdot V_{GEM}} \quad (4.2)$$

where $\langle \alpha \rangle$ is the average of the first Townsend coefficient along the electron path through the hole.

4.3. The single-GEM detector

Generally, the intrinsic gain of a single-GEM detector can reach value of the order of 10^3 . However, only a fraction of the multiplication electrons generated inside the holes is transferred to the anode. Therefore, due to the dispersive effects, the effective gas gain is generally lower than the intrinsic gas gain. These dispersive effects are strongly related to the value of the electric fields above and below the GEM-foil and the voltage difference between the two electrodes of the GEM-foil.

For a GEM-based detector it is possible to define the following parameters:

1. *collection efficiency* (ϵ^{coll}):

$$\epsilon^{coll} = \frac{\text{electrons collected in the holes}}{\text{electrons produced above the holes}} \quad (4.3)$$

It represents the ratio between the number of electrons entering the GEM-hole and the number of primary electrons generated above the GEM-foil. The collection efficiency is related to the electron diffusion phenomena and the field-line defocusing effects above the GEM-foil [62]. Because of these two phenomena, some of the primary electrons are collected on the upper electrode of the GEM-foil or hit the Kapton surface inside the hole before starting the multiplication. As previously mentioned, this effect could be reduced decreasing the drift electric field or increasing the electric field inside the hole [55] [58].

In case of electronegative gas mixtures, additional primary electrons losses can occur before the multiplication process due to recombination phenomena. For example, for the $Ar/CO_2/CF_4$ (45/15/40) gas mixture, the electric field in the vicinity of the hole (~ 10 kV/cm) can allow for a recombination of the primary electrons due to a high electron attachment with respect to the Townsend coefficient. For the $Ar/CO_2/CF_4$ (45/15/40) gas mixture, the defocusing effect and the capture on the Kapton are of the order of 20% and 5% respectively, while the electron attachment is about 10%, giving a total collection efficiency of 65% [63].

2. *extraction efficiency* (f^{extr}):

$$f^{extr} = \frac{\text{electrons extracted from the holes}}{\text{electrons produced in the holes}} \quad (4.4)$$

It represents the ratio between the number of electrons extracted from the holes and transferred to the anode and the number of multiplication electrons produced inside the holes. Due to the diffusion phenomena, the multiplication electrons are not confined in the central region of the hole channel and therefore, especially for values of the electric field relatively low below the GEM-foils, the electrons could be collected on the lower electrode of the GEM-foil rather than being transferred to the anode.

Simulation studies have demonstrated that $\sim 3\%$ of the multiplication electrons are trapped at the hole surface due to the diffusion phenomena, $\sim 10\%$ are ion-captured in proximity of the hole exit. The remaining multiplication electrons, coming out from the hole, are either collected on the bottom electrode of the GEM-foil or transferred to the induction region. With an induction electric field set at 5 kV/cm in order to assure a safe detector operation, a fraction of $\sim 50\%$ of multiplication electrons are lost on the lower electrode of the GEM-foil and the other 50% move towards the readout electrode. A total extraction fraction of about 35% is obtained [63].

The definition of the collection and extraction efficiencies allows to define the *electron transparency* (T) of a GEM-foil and, therefore, to correlate the effective gas gain (G_{eff}) with the intrinsic gas gain (G_{intr}) of a GEM-based detector through the following relation:

$$G_{eff} = G_{intr} \times T = G_{intr} \times \epsilon^{coll} \times f^{extr} \quad (4.5)$$

The maximum effective gas gain reachable with a single-GEM detector is of the order of 10^3 . Higher gas gain, up to 10^4 - 10^5 , are reachable using multiple structures, realized assembling more than one GEM-foil at close distance one to each other.

4.4 The triple-GEM detector

A triple-GEM detector is a gas-based detector consisting of three GEM-foils cascaded and sandwiched between the cathode and anode electrodes. The use of triple-GEM detector allows to share the amplification in multiple cascaded stages in order to achieve very high gas gain already at relatively moderate voltages across individual GEM-foils. As a consequence, the risk of discharge occurring when a heavily ionizing particle enters the active gas volume, is strongly reduced (see Figure 4.13).

Figure 4.14 shows a schematic overview of a triple-GEM detector, together with the labelling defining the major geometrical and electrical parameters. The voltage difference applied across individual GEM-foils are called V_{GEM1} , V_{GEM2} , V_{GEM3} and their sum V_{GEM}^{tot} .

The description of the single-GEM detector allows to understand more clearly the operation of a triple-GEM detector. The first gap between the cathode electrode and the first GEM-foil is the drift region which acts as conversion gap. The last gap between the third GEM-foil and the anode electrode is the induction region where, after the multiplication process due to the multiple cascade amplification stages, the final charge induces a signal on the anode. For the electric fields and geometrical thickness of the drift and induction regions, the same considerations discussed for the single-GEM detector are

4.4. The triple-GEM detector

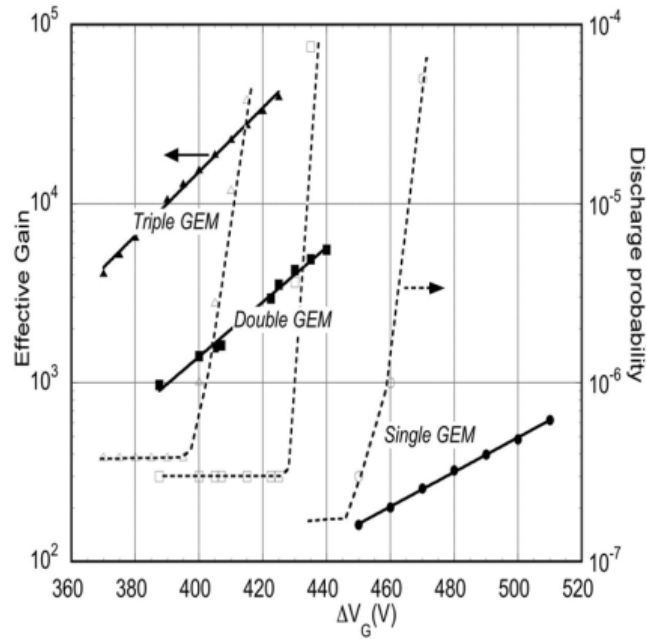


Figure 4.13: Effective gas gain and discharge probability as a function of voltage in a single-, double- and triple-GEM detectors in Ar/CO_2 (70/30) gas mixture [55].

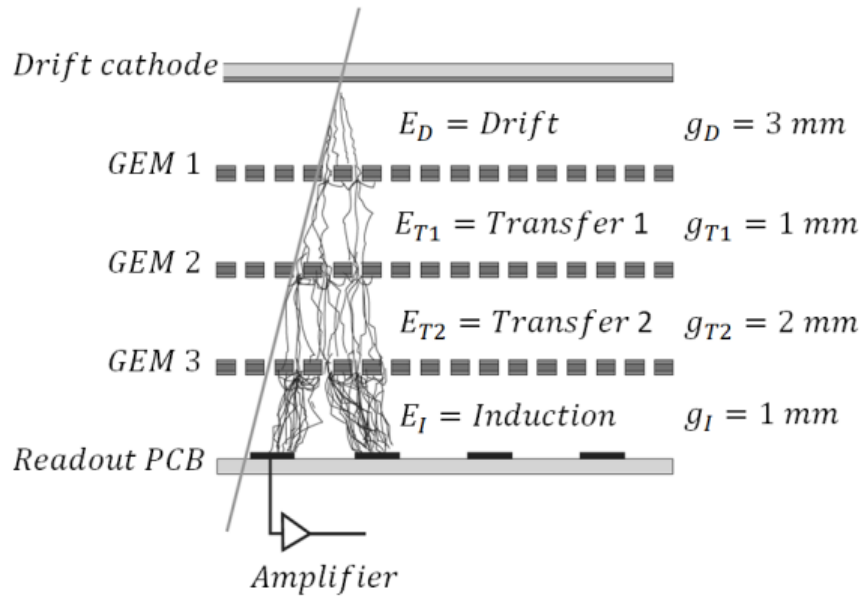


Figure 4.14: Schematics of a triple-GEM detector: E_D , E_{T1} , E_{T2} and E_I are the drift, the first and the second transfer and the induction electric fields respectively; g_D , g_{T1} , g_{T2} and g_I are the drift, the two transfer and the induction gaps respectively [55].

valid. The other two gaps, between two consecutive GEM foils, are called

transfer regions which act as an induction region if they are referred to the above GEM, while as a drift region if they are referred to the GEM below. Therefore, the choice of the transfer electric fields and the relative geometrical thickness requires additional considerations.

4.4.1 Transfer electric field effect

The aim of the transfer electric field is to transfer the multiplication electrons produced in the holes of the above GEM-foil and to focus them into the holes of the below GEM-foil. Therefore, the value of the transfer electric field should be chosen in order to optimize both the extraction efficiency from the upper GEM-foil and the collection efficiency to the lower GEM-foil. Figure 4.15 shows the electron current induced on the various electrodes of a double-GEM detector as a function of the transfer electric field operated in Ar/CO_2 (70/30) gas mixture for a given value of drift and induction electric fields ($E_D = E_I = 5 \text{ kV/cm}$). The same considerations on the transfer electric fields remain valid for a triple-GEM detector.

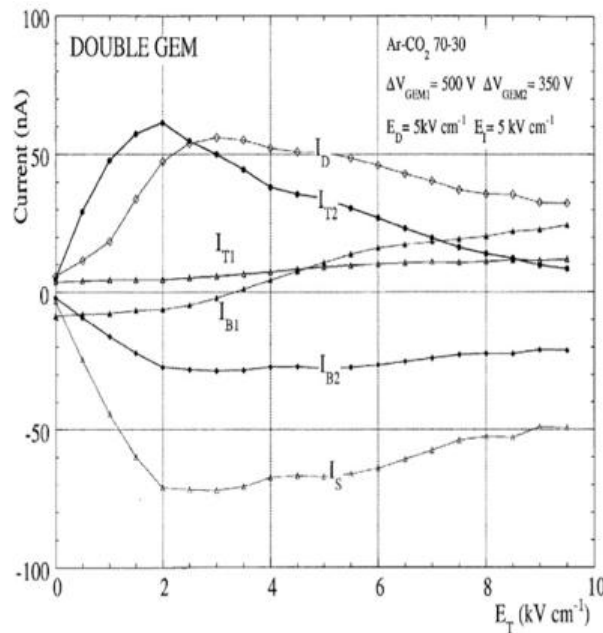


Figure 4.15: Currents on the various electrodes of a double-GEM detector as a function of the transfer electric field: I_D current on the cathode electrode, I_{T1} and I_{B1} current respectively on the upper and lower electrodes of the first GEM-foil, I_{T2} and I_{B2} current respectively on the upper and lower electrodes of the second GEM-foil and I_S current on the readout pads [55].

At very low value ($E_T < 2 \text{ kV/cm}$), the transfer electric field does not allow the multiplication electrons to be effectively transported toward the readout electrode. In this case, the electron current is affected by a low extraction

efficiency of the GEM-foils: the electrons are still extracted from the GEM-holes thanks to the electric field present inside the holes themselves, but they are completely collected on the lower electrode of the first GEM-foil due to the fact that the field-lines end on the latter electrode ($I_{B1} = \text{maximum}$, $I_{B2} = 0$) and the induced signal is vanishing ($I_S = 0$). By incrementing the transfer electric field ($E_T > 2 \text{ kV/cm}$), the fraction of current collected on the readout pads (I_S) increases to the detriment of the current collected on the lower electrode of the GEM-foils (I_{B1} and I_{B2}). At very high transfer field ($E_T > 6 \text{ kV/cm}$), the electron current is affected by a low collection efficiency of the GEM-foils. In this case, the multiplication electrons, coming from the above GEM-foil, are mainly collected on the upper electrode of the successive GEM-foil. For an Ar/CO_2 (70/30) gas mixture, a typical value for the transfer electric field is in the range of 3-5 kV/cm .

4.4.2 Transfer region thickness

In order to improve the time performance of the GEM-based detectors and to minimise the discharge probability, several studies have been performed for different geometrical thickness of the transfer region [55] [58] [64].

First transfer gap. In a triple-GEM detector, the gas ionization induced by a charged particle crossing the gas volume could occur in each of the four regions of the detector. The main difference between the primary electrons produced in the various region is the number of multiplication stages that they undergo along their drift towards the readout electrode: an electron generated in the drift region will pass through all the three amplification stage, while an electron produced in the first transfer region will only undergo the last two multiplication steps. Therefore, since the total ionization and the gas gain are subject to statistical fluctuations, the primary charge produced in the first transfer region, and amplified by the last two multiplication stages, could induce signals whose amplitude is large enough to be discriminated by the front-end electronics. Furthermore, depending on the drift velocity v_{drift} of the gas mixture used and the transfer region thickness g_t , this signal will be anticipated of the quantity $\Delta t = g_t/v_{drift}$ compared to the signal generated by the electron coming from the drift region. This effect is called *bi-gem* effect and it is particularly significant for the performance of the detector in term of time resolution since it leads to the broadening of the time distribution of the events. Several studies have been demonstrated that a significant reduction of the bi-GEM effect could be achieved by decreasing of the transfer region thickness to 1 mm [64].

Second transfer gap. As regarding the second transfer region, the bi-GEM effect is totally negligible, since the primary electrons generated in this region will pass through only one multiplication stage. Therefore, they could rarely give rise to a signal over the electronic threshold. However, the thickness of the second transfer region is strongly correlated to discharge phenomena.

The number of electron-ion pairs could exceed the Raether limit [65] and give rise to the transition from the avalanche to the streamer regime in the third multiplication stage and, finally, a discharge could develop. For the most gas-based detectors, the discharge effect can be reduced by adding a suitable amount of a quencher component to the gas mixture. On the other hand, the quantity and the type of the quenching gas are limited by the degradation of the detection performance due to ageing phenomena (see Section 6).

For a triple-GEM detector operated with a given gas mixture, the discharge probability can be minimized by increasing the thickness of the second transfer region. Since the transverse dimension of the electron clouds increases with the square root of the electron drift [41], a larger transfer region allows to increase the electron diffusion in this region. Consequently, the number of the holes involved in the multiplication process increase linearly with the thickness of a transfer region. Therefore, it is possible to use the diffusion to spread the electron cloud over more than a single hole, reducing the probability of reaching the Raether limit in a single hole of the third multiplication stage. A value of 2 mm for the second transfer region is a good compromise between the necessity to minimize the discharge probability and the mechanical constraints required by the muon system on the maximum size of the detector thickness [66].

4.4.3 GEM-foils voltage in a triple-GEM detector

As discussed in Section ..., the voltage difference applied between the two electrodes of each GEM-foil defines the intrinsic gas gain of the detector:

$$G_{intr} \propto \prod_{k=1}^3 e^{\langle \alpha \rangle \cdot V_{GEMk}} \propto e^{\langle \alpha \rangle \cdot \sum_{k=1}^3 V_{GEMk}} \quad (4.6)$$

where $V_{GEM}^{tot} = \sum_{k=1}^3 V_{GEMk}$ is the sum of the voltage differences on each GEM-foil and $\langle \alpha \rangle$ is the average of the first Townsend coefficient along the electron path through a hole [61]. As in the case of a single-GEM detector, the effective gas gain of a triple-GEM detector is less than the intrinsic gas gain due to several dispersive effects that decrease the number of multiplication electrons actually transferred from one GEM-foil to another. Together with the electric field in the various region, that define the total electron transparency T_{tot} of a triple-GEM detector, the effective gas gain is defined as:

$$G_{eff} = G_{intr} \cdot T_{tot} = \prod_{k=1}^3 e^{\langle \alpha \rangle \cdot V_{GEMk}} \cdot T_k = e^{\langle \alpha \rangle \cdot \sum_{k=1}^3 V_{GEMk}} \cdot \prod_{k=1}^3 \epsilon_k^{coll} \cdot f_k^{extr} \quad (4.7)$$

where ϵ_k^{coll} and f_k^{extr} are the collection efficiency and the extraction efficiency of the k^{th} GEM-foil.

As described by the equation 4.7, the effective gas gain of a triple-GEM detector is a function of the voltage difference applied to the three GEM-foils

only through their sum. Therefore, it is possible to unbalance these voltage differences in order to minimize the discharge probability in the last multiplication stage where the probability of reaching the Raether limit and triggering a discharge is higher. Indeed, keeping the sum of the three voltage differences constant, i.e. at a fixed gas gain, it is possible to increase the voltage applied on the first GEM-foil while reducing the one applied to third GEM-foil. In these conditions, the charge reached on the third GEM-foil is greater, but the diffusion effect allows to redistribute the electron cloud over a larger number of holes, reducing the discharge probability. The optimal configuration of the triple-GEM voltages that allows to minimize the discharges probability is: [64]

$$V_{GEM1} \gg V_{GEM2} \geq V_{GEM3} \quad (4.8)$$

Such configuration also allows to minimize the bi-gem effect, since the electrons generated in the first transfer region will be amplified with a lower gain compared to the case in which the triple-GEM voltage configuration is not unbalanced and, therefore, the resulting signals will be under the discrimination threshold of the detector front-end electronics. Finally, the electron transparency on the first GEM-foil will be slightly increased due to a reduction of the defocusing effect.

4.4.4 Time performance in a triple-GEM detector

The performance of a triple-GEM detector in terms of time resolution is strongly correlated with the statistical nature of the electron cluster which develops in the drift region. Therefore, the number of the electron clusters produced in the primary ionization depends on the type of the particle crossing the detector active volume (α , γ , π , protons, etc.), on its energy and the gas mixture used as sensitive medium.

The space-distribution of the cluster j created at distance x from the first GEM-foil is described by the Poisson statistics [41]

$$A_j^{\bar{n}}(x) = \frac{x^{j-1}}{(j-1)!} \bar{n}^j \cdot e^{-\bar{n}x} \quad (4.9)$$

where \bar{n} is the average number of electron clusters per unit length x . If one considers the first electron cluster produced closest to the upper electrode of the first GEM-foil ($j = 1$), the space-distribution can be rewrite as follows:

$$A_1^{\bar{n}}(x) = \bar{n} \cdot e^{-\bar{n}x} \quad (4.10)$$

with standard deviation (*r.m.s.*) is given by:

$$\sigma(x) = \frac{1}{\bar{n}} \quad (4.11)$$

For a given drift velocity (v_d) in the drift region, the previous equations allow to define the probability distribution of the arrival time on the first GEM-foil for the electron cluster j :

$$P_j(t_d) = A_j^{\bar{n}}(v_d \cdot t_d) \quad (4.12)$$

Specifically for the first electron cluster produced closest to the first GEM-foil ($j = 1$):

$$P_1(t_d) = \bar{n} \cdot e^{-\bar{n}v_d t_d} \quad (4.13)$$

Therefore, the intrinsic value of the time resolution of the detector if the first electron cluster is always detected is:

$$\sigma_1(t_d) = \frac{1}{\bar{n} \cdot v_d} \quad (4.14)$$

Equation 4.14 shows that the intrinsic value of the time resolution depends on the inverse of the product of the drift velocity and the specific primary ionization in the drift region. Therefore, in order to reach high time resolution, it is necessary to use gas mixtures with high drift velocity (v_d) and high primary ionization (\bar{n}).

Additionally, taking into account the limited collection efficiency of the first GEM-foil, the statistical fluctuations which affect the gas gain and the finite threshold of the front-end electronics, the signal induced by the first cluster could not be properly discriminated. Therefore, the successive pile-up of electron clusters is needed to generate an induced signal above the electronic threshold. The latter effect is the major limitation of the time resolution of the triple-GEM detector. In order to overcome or to minimize this issue, it is necessary to increase the single electron detection capability, using gas mixture characterized by a high drift velocity at a relative low value of drift electric field. As discussed in Section 4.3.3 a relative low value of drift electric field (2-3 kV/cm), allows to reach a large collection efficiency in the first amplification stage, thereby ensuring a high detection efficiency of the first electron cluster with consecutive significant improvement of the time performance of a triple-GEM detector.

4.4.5 The signal formation in a triple-GEM detector

The formation of the signal induced on the readout pads and/or strips in a GEM-based detector exclusively depends on the motion of the multiplication electrons in the induction region. Therefore, it can be considered that the induced signal formation starts as soon as the first multiplication electrons emerge from the lower electrode of the last amplification stage and stops when all of them are completely collected on the readout electrode.

4.4. The triple-GEM detector

The induced current I_k on the k^{th} electrode due to a moving charge q and velocity v_d , can be calculated using the Ramo's theorem [67]:

$$I_k = -\frac{q \vec{v}_d(x) \times \vec{E}_k(x)}{V_k} \quad (4.15)$$

where $\vec{E}_k(x)$ is the electric field created by raising the electrode k to the potential V_k . Therefore, if $V_k = 1$ V and all the other pads (or strips) are connected to ground, the Equation 4.15 can be rewritten as follows:

$$I_k = -q \vec{v}_d(x) \times \vec{E}_k^w(x) \quad (4.16)$$

where $\vec{E}_k^w(x)$ is the so-called *weighting field*.

In order to study the properties of a triple-GEM detector, a complete and detailed simulation of the detector has been performed taking into account all the relevant processes from the ionization mechanism up to the signal formation and electronic response [63]. In these studies, the $\vec{E}_k^w(x)$ behavior has been simulated and it results to be practically constant in the induction region meaning the electron drift velocity is uniform in the induction region. Therefore, these studies suggest that each multiplication electron emerging from the last GEM-foil induces a rectangular current signal in the nearest pad (or strips) with a width dependent on the time needed by the electron to cross the induction region:

$$i = -\frac{q}{t} = -\frac{qv_d}{x} \quad (4.17)$$

where x is the thickness of the induction region and v_d is the electron velocity in that region. Finally, in order to achieve an higher induced signals, the thickness of the induction region should be reduced and/or a fast gas mixture for induction electric field in the range 4.5-5.5 kV/cm should be used.

The Assembly, Quality Control and Commissioning of the GE1/1 detectors

5.1 The GE1/1 detectors for the CMS-GEM project

5.1.1 Description of the GE1/1 project

To extend the sensitivity for new physics searches, a major upgrade of the LHC machine has been decided and is being prepared, the High Luminosity LHC (HL-LHC). The instantaneous luminosity of LHC is expected to exceed the nominal value and reach $2.5 \times 10^{34} \text{ cm}^{-2}\text{s}^{-1}$, after the second Long Shutdown (LS2) foreseen in 2019. A further increase is planned during the third Long Shutdown (LS3) in 2024 - 2026, up to $5 \times 10^{34} \text{ cm}^{-2}\text{s}^{-1}$, i.e. a yield five times greater than the initially design value of the current LHC. The increase of the energy and luminosity during the future upgrades of the LHC machine will deeply affect the performance of the detectors in the CMS Muon System due to the harsh background environment and the high pile-up. As a consequence, a general upgrade of the present detectors and their electronics is mandatory.

The CMS collaboration is currently improving the Muon System to maintain the high level of performance achieved during the first period of operation (Run 1) also in the challenging environment of the high-luminosity LHC. The CMS Muon System was originally designed as a hermetic and redundant system that exploits three gaseous detection technologies. In the barrel, Drift Tubes (DT), covering acceptances up to covering acceptances up to $|\eta| < 1.2$, provide precision measurements and Level 1 (L1) triggering; in the endcaps the same role is played by Cathode Strip Chambers (CSC), covering the region $1.0 < |\eta| < 2.4$. Additionally, Resistive Plate Chambers (RPC) provide redundant trigger and coarse position measurement in both barrel and forward regions,

5. The Assembly, Quality Control and Commissioning of the GE1/1 detectors

but they were not implemented beyond $|\eta| > 1.6$, due to the high background rate expected that region. This imposes severe restriction on the gaseous detection technology that can be used: new detector requirements include a high rate capability $O(MHz/cm^2)$, a good spatial resolution $O(100 \mu m)$ for tracking, a good time resolution for triggering, and in addition, radiation hardness.

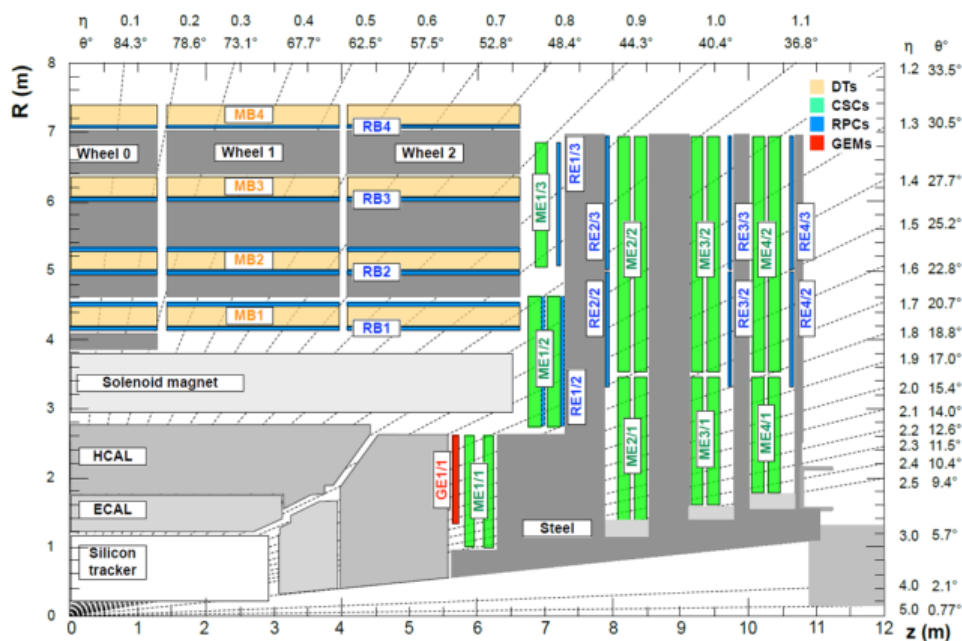


Figure 5.1: A quadrant of the muon system, showing DT chambers (yellow), RPC (light blue), and CSC (green). The new GEM detector station, GE1/1, is indicated in red [69].

In order to cope with very high operation condition, high pile-up and background environment in particular in the forward region of the CMS muon end-caps, the CMS Collaboration is planning to install detectors based on the Gas Electron Multiplier technology during the second Long Shutdown. The project is named GE1/1, where "G" stands for GEM, "E" for End-cap, the first "1" corresponds to the first muon station and the second "1" the first ring of the muon station (see Figure 5.1). In the GE1/1 Muon System, a pair of such GE1/1 detectors are combined in order to form the so-called GE1/1 "super-chamber" that provides two measurement planes in the muon endcap and optimizes the detection efficiency. Each super-chamber covers a $\sim 10^\circ$ sector so that 72 super-chambers are required (36 per each endcap of the CMS Muon System) to form a ring of superchambers that gives full azimuthal coverage. The superchambers alternate in ϕ between long ($1.55 < |\eta| < 2.18$) and short ($1.61 < |\eta| < 2.18$) versions. Each endcap holds 18 long and 18 short super-chambers, for a total of 144 detectors in all CMS Muon System. The GE1/1 station is currently undergoing construction. In order to gain first

5.1. The GE1/1 detectors for the CMS-GEM project

operational experience with the new subsystem and also to demonstrate the integration of GE1/1 detectors into the trigger, a demonstrator, consisting of five GE1/1 superchambers, has already been installed in CMS during the year-end technical stop 2016/2017.

The muon trigger rates are higher in the forward region where the bending of the track of the muon candidate in the magnetic field is small, the background is large and the redundancy is reduced since the pseudorapidity region $|\eta| > 1.6$ is instrumented with only the CSC detectors. These factors lead to muon momentum mismeasurement at the first level of trigger (L1), and as a consequence, the contribution to the trigger rate coming from the forward region is particularly large. The installation of GE1/1 in front of ME1/1 will create a large enough lever arm between GE1/1 and ME1/1 detector to enable a good measurement of the muon direction within the first station. Moreover, the added redundancy allows reducing the fraction of muons with unreconstructed segments in the first station, which in turn reduces the fraction of poorly measured muon candidates [69]. The consequence is an improvement of the L1 stand-alone muon trigger momentum resolution and a drastically reduction of its large contribution to the overall L1 muon trigger rate. The single muon trigger rate curves before and after the GE1/1 upgrade are shown in in Figure 5.2.

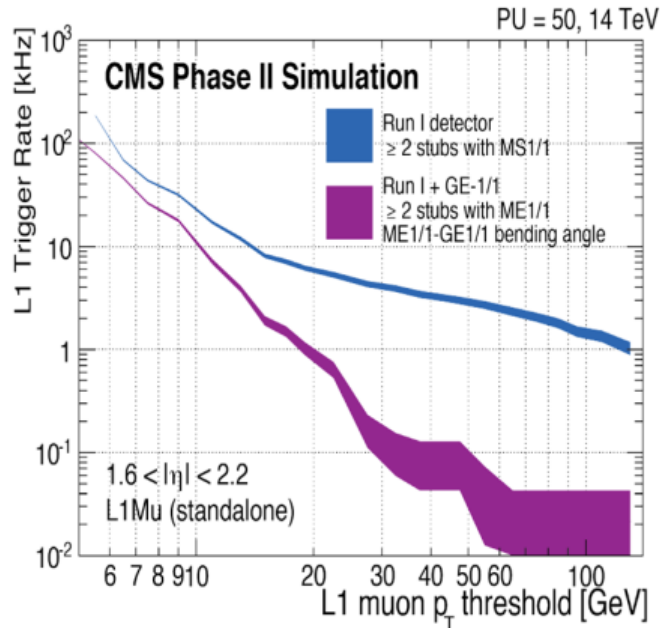


Figure 5.2: L1 muon trigger rate at a luminosity of $2 \times 10^{34} \text{ cm}^{-2} \text{ s}^{-1}$ as a function of p_T threshold. With the addition of GE1/1, the bending angle between ME1/1 and GE1/1 stations can be used and the trigger rate is greatly reduced [69].

5.1.2 GE1/1 detector requirements

The fundamental requirements on the detection performance that a GE1/1 detector have to fulfill in the CMS GE1/1 region are:

- Particle rate capability up to 4.5 kHz/cm^2 ;
- Detection efficiency higher than 97% for detecting minimum ionizing particles for each single GE1/1 detector;
- Angular resolution of $300 \text{ } \mu\text{rad}$ on $\Delta\Phi = \Phi_{GE1/1} - \Phi_{ME1/1}$;
- Timing resolution of 8-10 ns for a single GE1/1 detector;
- Gas gain uniformity of 30% across a detector and between detectors;
- GE1/1 detector must tolerate, without damages or performance losses, an integrated charge of $\sim 18 \text{ mC/cm}^2$;
- Discharge rate that does not impede performance or operation of the GE1/1 detector

The maximum expected background hit rates in the GE1/1 region is about 1.5 kHz/cm^2 for HL-LHC running at 14 TeV and $5 \times 10^{34} \text{ cm}^{-2}\text{s}^{-1}$. Multiplying with a safety factor of 3 then requires a hit-rate capability of 4.5 kHz/cm^2 . With 97.0% individual detector efficiency, a superchamber composed by two triple-GEM detectors logically OR-ed strip by strip will have an efficiency above 99.9%. A precision of $300 \text{ } \mu\text{rad}$ on the difference $\Delta\Phi = \Phi_{GE1/1} - \Phi_{ME1/1}$ of the angular muon positions measured in GE1/1 and ME1/1 is required to guarantee to the trigger to discriminate high- p_T muons from low- p_T muons reliably. A time resolution of about 8-10 ns is required in order to combine the timing information provided by a GE1/1 superchamber with timing provided by the CSC detectors, i.e. in order to reliably match GE1/1 hits to ME1/1 stubs in time when running with a 25 ns bunch crossing time at the HL-LHC. An uniform response of the detector ensure that there are no geometrical trigger or muon reconstruction biases. The intrinsic variation of the detector response due to the hole size variation at the manufacturing stage of the GEM-foils is about 5-8%. The detectors should not incur significant additional response non-uniformities due to any other factors. The response uniformity across all the sectors of a single GE1/1 detector should not exceed the 30% value in order to guarantee a stable operation efficiency $> 98\%$ and time resolution $< 10 \text{ ns}$. The GE1/1 detectors must be able to integrate a charge of 18 mC/cm^2 , which represents ten years of GE1/1 operation at the HL-LHC with a safety factor 3, at a gas gain of $\sim 2 \times 10^4$ and an average particle flux of $\sim 1.5 \text{ kHz/cm}^2$ for an average luminosity machine of $5 \times 10^{34} \text{ cm}^{-2}\text{s}^{-1}$.

In addition, several technical constraints and requirements need to be taken into account in the detector design. Since the GE1/1 station is placed in

5.1. The GE1/1 detectors for the CMS-GEM project

front of the ME1/1 station, a special care has to be taken in the detector design in order to reduce the material budget in such a way as to minimize the multiple scattering within the GE1/1 itself that could affect the muon track reconstruction in the GE1/1–CSC trigger. All components used for the detector construction have been selected in order to minimize this requirement. Clearly, these choices are a compromise between rigidity and low mass requirements. The detector materials and components have been also qualified for long term exposure to radiation and possible outgassing. The material budget of the GE1/1 detector station is shown on Table 5.1.

Layer	Material	Thickness (mm)
Protective cover	<i>Al</i>	1
Cooling pipe	<i>Cu</i> (filled with H_2O)	8 external \varnothing , 6 inner \varnothing
Cooling pads	<i>Cu</i>	1
GEB board	<i>Cu/FRA</i>	0.140/0.856
Readout board	<i>Cu/FRA/Cu</i>	0.035/3.2/0.035
Induction gap	<i>Ar/CO₂ (/CF₄)</i>	1
GEM 3	<i>Cu/polyimide/Cu</i>	0.005/0.050/0.005
Transfer gap 2	<i>Ar/CO₂ (/CF₄)</i>	2
GEM 2	<i>Cu/polyimide/Cu</i>	0.005/0.050/0.005
Transfer gap 1	<i>Ar/CO₂ (/CF₄)</i>	1
GEM 1	<i>Cu/polyimide/Cu</i>	0.005/0.050/0.005
Drift gap	<i>Ar/CO₂ (/CF₄)</i>	3
Drift board	<i>Cu/FRA/Cu</i>	0.035/3.2/0.035
	Total	20.585

Table 5.1: Material budget for a GE1/1 triple-GEM station [69].

Moreover, the major constraint for the GE1/1 station dimension is the space currently available between the end-cap of the hadronic calorimeter and ME1/1 station (see Figure 5.1). The GE1/1 detectors have been designed so that a superchamber, together the final electronics, cooling system, mechanical elements, etc, is less than 10 *cm* thick and will correctly fit into the available slot in the muon end-cap nose. Table 5.2 shows the technical specifications for the construction of the GE1/1 detectors and their operation in the Muon System of the CMS experiment.

5.1.3 GE1/1 detector overview

To increase redundancy and enhance the trigger and reconstruction capabilities, the CMS collaboration approved the installation of 144 GE1/1 detectors in both positive and negative end-caps of the Muon Spectrometer of the CMS experiment covering the pseudorapidity region $1.55 < \eta < 2.18$. Each GE1/1 detector consists of a trapezoidal gas volume containing a stack of three large trapezoidal GEM-foils placed at a relative distance of a few *mm* and embedded between a drift electrode and a readout board. Each GEM-foil consist of a layer of copper-clad kapton foils perforated with a high density of holes

5. The Assembly, Quality Control and Commissioning of the GE1/1 detectors

Specification/Parameter	GE1/1
Detector technology	Gaseous detector; micro-pattern gas detector (MPGD)
Charge amplification element	GEM foil (triple, cascaded, tensioned at $\approx 5 N/cm$)
Number of chambers in overall system	144 (72 in each endcap)
Chamber shape (active readout area)	Trapezoidal; opening angle 10.15°
Active area overlap in adjacent chambers	$2.6 mrad$ (corresponds to 5.7 readout strip pitches)
Short chamber dimensions (active vol.)	L: 106.1 <i>cm</i> (center line), W: (23.1 - 42.0) <i>cm</i> , D: 0.7 <i>cm</i>
Long chamber dimensions (active vol.)	L: 120.9 <i>cm</i> (center line), W: (23.1 - 44.6) <i>cm</i> , D: 0.7 <i>cm</i>
Total chamber thickness	D: 3.5 <i>cm</i>
Active readout area	0.345 m^2 (short ch.); 0.409 m^2 (long ch.)
Active chamber volume	2.6 liters (short ch.); 3 liters (long ch.)
Radial distance from beam line	130.2 <i>cm</i> (at inner edge of active readout area)
Geometric acceptance in η	1.61 - 2.18 (short ch.); 1.55 - 2.18 (long ch.)
Signal readout structure	Truly radial readout strips
Readout strip dimensions	230 μrad angular strip width; 463 μrad angular pitch
Number of η -segments in readout	8
Number of readout strips per η -segment	384
Number of readout strips per chamber	3072
Counting gas mixtures	Ar/CO_2 (70/30) or $Ar/CO_2/CF_4$ (45/15/40)
Nominal operational gas flow	1 chamber volume per hour
Number of gas inlets	1
Number of gas outlets	1
Nominal HV applied to drift electrode	3200 V (Ar/CO_2); 4000 V ($Ar/CO_2/CF_4$)
Nominal operational gas gain	$1-2 \times 10^4$
Demonstrated rate capability	100 MHz/cm^2

Table 5.2: Specifications and parameters for the technical design and operation of the CMS GE1/1 detector [69].

produced with the single-mask photolithographic technique (see Section 5.2.5). The GEM-holes are truncated double cones with the larger (outer) diameters around 70 μm and the smaller (inner) diameter around 50 μm ; they are spaced with a pitch of 140 μm in a hexagonal pattern. The electric field strength inside GEM-holes can be as high as 80 kV/cm . The thickness of the different regions in a GE1/1 triple-GEM detector have been optimized for the CMS application in order to ensure the best time resolution. The different regions in the CMS GE1/1 triple-GEM detectors are drift region of 3 *mm* between drift electrode and first GEM-foil, spaces of 1 *mm* and 2 *mm* in the electron transfer gaps between GEM-foils, and a 1 *mm* space in the signal induction region. The baseline gas mixture for operating the CMS triple-GEM detector is Argon (*Ar*) and Carbon Dioxide (CO_2) in proportion of 70% and 30%, respectively. The electrons produced by a charged particle passing through the detector due to primary ionization of the counting gas drift towards the GEM-holes and once they start to experience the very intense electric field in the holes, they acquire enough kinetic energy to produce secondary ionization in the gas. This produces an electron avalanche process, which induces an electrical signal on the readout board. A schematic overview of this operation principle is given in Figure 5.3, which also defines the drift gap, two transfer regions, and induction gap within the triple-GEM detector.

As shown in Figure 5.4, the readout board is divided into 8 partitions (or η -sectors) along the pseudorapidity coordinate, consisting of 384 copper strips

5.1. The GE1/1 detectors for the CMS-GEM project

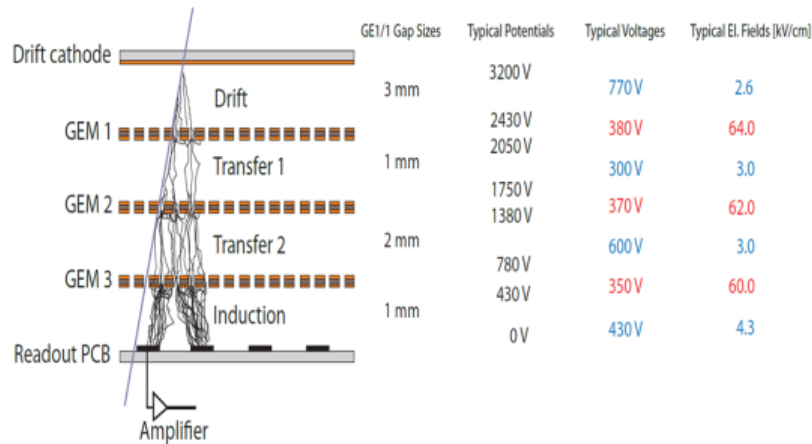


Figure 5.3: Principle of operation of a triple-GEM detector and definition of drift, transfer, and signal induction gap regions within the detector. The table on the right gives the actual gap configuration in the GE1/1 detector. The table also list typical values for electric potentials on the top and bottom of each GEM-foil and typical values for voltages and electric fields across the four gaps (blue) and the three GEM-foils (red) if the nominal potential of 3200 V for operation in Ar/CO_2 (70 : 30) is applied to the drift electrode.

with a trapezoidal shape. Additionally, each η -sector is divided into 3 partitions (or ϕ sectors) along the azimuthal coordinate, thus resulting in a total of 24 readout sectors for the whole detector active area. Each readout sector has a 128 signal-pins Panasonic connector outside of the active gas volume. The connection between the strips and the connectors is ensured by metallic vias running through the readout board.

Because of the mechanical constraints in the GE1/1 station, two versions of GE1/1 detectors are proposed in order to keep the maximum detection coverage. These include, the long detectors with a length of 120.9 cm and the short detectors with a length of 106.1 cm. In the GE1/1 station, two identical single GE1/1 detectors will be combined to form a "super-chamber" in order to provide an independent local pattern recognition and maximizes the detection efficiency. Each super-chamber covers a $\sim 10^\circ$ sector, therefore 36 super-chambers will be installed in each muon endcap in order to ensure the full azimuthal coverage. The super chambers will alternate in the azimuthal direction between the long and the short versions in order to fully exploit the available space as shown in Figure 5.5.

5.1.4 Mass production of the GE1/1 detectors

The GE1/1 detectors mass production has been optimized during years with many efforts from the research laboratories and the involved industries. The GE1/1 detector assembly and quality control take place at several produc-

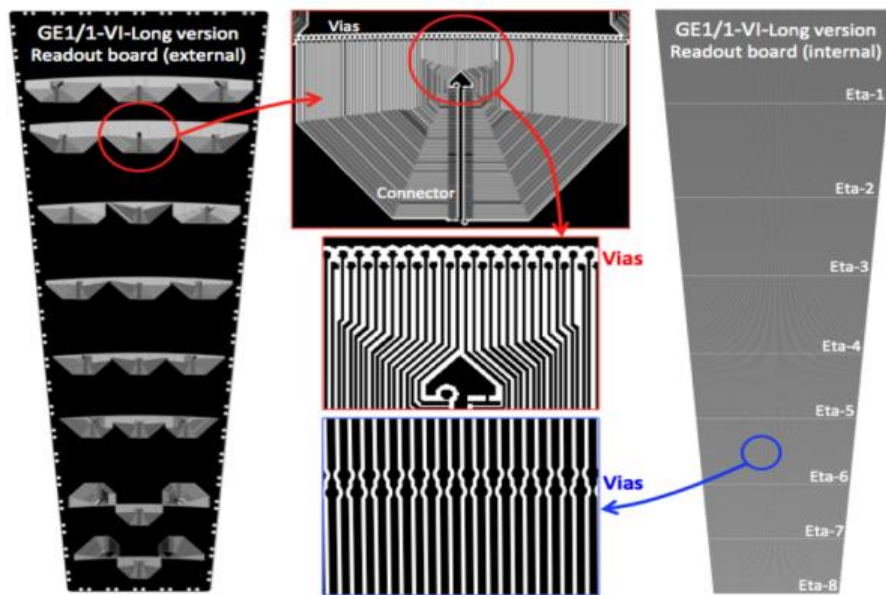


Figure 5.4: Design of the readout board for the long detector GE1/1-VI-L. (Left) outer side of the readout board showing the traces from vias to Panasonic connectors. (Right) inner side that faces into the gas volume opposite to the third GEM-foil. The circular structures on each strip are vias that connect the strips to the outside of the board.

tion sites. The central R&D laboratory and the production facility is based at CERN, as well as the GEM-foil production workshop. The CERN is the headquarters of the GE1/1 detectors mass production collaboration. Among the production and quality control sites, the CERN has implemented the most exhaustive quality control tests, since the production headquarters takes care of both raw material and integration of the GE1/1 detectors in the muon end-cap regions of the CMS experiment. Additionally, the CMS-GEM collaboration has identified other production and quality control sites on the basis of their past experience in detector construction and of the support from their home institute given to the GE1/1 project:

- Bhabha Atomic Research Center (BARC), Delhi University and Panjab University - India
- Florida Institute of Technology (FIT) - USA
- Ghent University (UGent) - Belgium
- INFN Laboratori Nazionali di Frascati (LNF) - Italy
- INFN Sezione di Bari and Bari University - Italy
- National Center for Physics (NCP) - Pakistan

5.1. The GE1/1 detectors for the CMS-GEM project

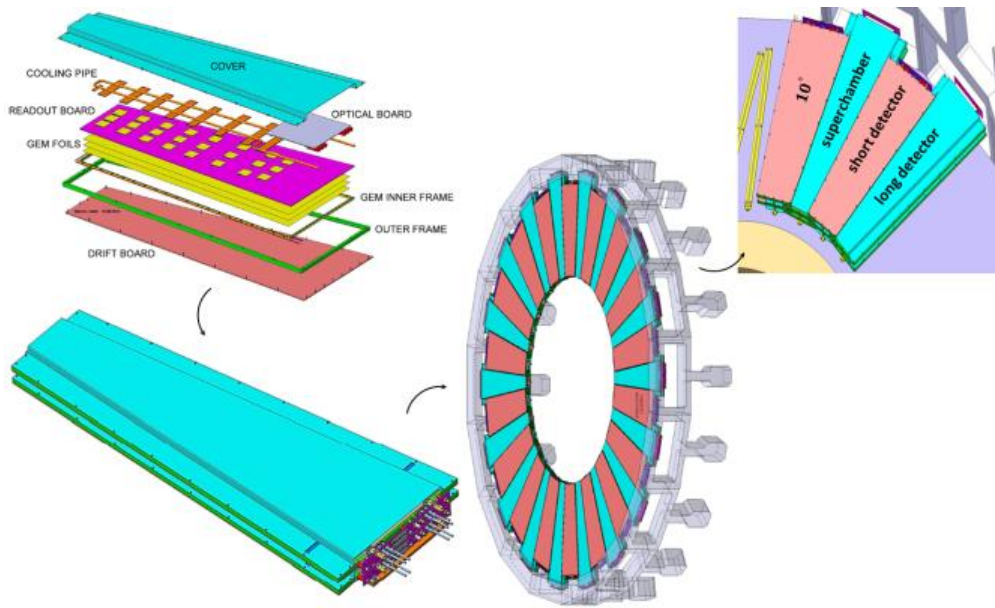


Figure 5.5: (Top left) Exploded view of a single GE1/1 detector showing the Drift and Readout board, the GEM-foil stack, the electronics, the cooling system and the protection cover. (Bottom left). Example of an assembled super-chamber. (Right) Mechanical overview of the GE1/1 station with both long and short GE1/1 detectors.

An additional satellite site at University of Aachen - Germany perform quality control test on the GE1/1 detectors assembled both at CERN and UGent production sites. The main industrial partners involved in the CMS-GEM project are listed in the Table 5.3.

Many other research institutes and industrial companies are involved in the the CMS-GEM project, namely Belgium, Bulgaria, China, Colombia, Egypt, Finland, France, Germany, Hungary, India, Italy, Korea, Pakistan, Qatar and USA. The full list of institutions and the corresponding collaborators can be found at [69]. Figure 5.6 shows the GE1/1 detectors mass production chain.

The GE1/1 detector components produced by industrial companies are delivered to CERN where they are inspected for manufacturing defects and tested. The visual inspection is the basis of the quality control process required to validate the detector assembly components. Additionally, the GEM-foils are tested for leakage current and the readout boards are checked with a dedicated testing system capable of identifying any possible short between strips or open strip-readout connections. Many other quality control are performed on the other detector components in order to ensure their integrity and the quality. Therefore, the CERN is the only production and quality control site that deals with detector components and their specifications: all other production sites receive only detector components within the specification.

The components passing the preliminary quality control are used for the as-

Suppliers	Detector Components
<i>MicroPack Pvt. Ltd.</i>	Drift and Readout PCBs
<i>Eltos S.p.A.</i>	Internal and External frames
<i>Mansner Oy Hienomekaniikka</i>	Pull-out
<i>Bossard Group</i>	Screws and Washers
<i>Angst & Pfister SA</i>	Vito O-ring
<i>Parker Legris</i>	Gas Plug
<i>Peninunsula</i>	Panasonic Connectors Assembly
<i>Hybrid SA</i>	HV Dividers
<i>Farnell/Mouser Electronics</i>	SMD components
<i>Fixtest</i>	High Voltage Pins
<i>Kerb-Konus/Titanox</i>	Brass Insert (Internal/Flanges)

Table 5.3: Main industrial partners involved in the CMS-GE1/1 project.

sembling at CERN production site and/or shipped to the other production and quality control sites. Upon receipt of the different detector assembly components, the production sites start the quality control procedure to identify possible damage that might have been incurred in the transport. Once the acceptance criteria are fulfilled, the production sites finalize the GE1/1 detector assembly procedures. Upon completion of the assembly, the GE1/1 detectors (built at CERN production site and externally at all production sites) are accurately tested in situ to ensure their proper and robust operation when installed in the CMS experimental. The quality control tests involve all the principal GE1/1 detector components and focus on the following aspect: *Gas Tightness, Electric Test, Noise, Effective Gas Gain and Response Uniformity Measurement*. The detectors that not ensure adequate performance have to be repaired or eventually substituted.

As for the external production, the GE1/1 detectors passing the intermediate quality control are send back to the CERN production site. The CERN, being the final recipient of the assembled detectors, has implemented additional quality controls to verify and test the performance of the received detectors as well as those of the detectors assembled directly at CERN production site. At this stage, the detectors are equipped with the latest CMS electronics, cooling system, mechanical elements, etc. Then, two GE1/1 single detectors are coupled together in order to fabricate a superchamber. Whereas the GE1/1 single detectors assembly and quality control are done by the different production sites, the assembly of the superchambers and the their quality control tests are performed at CERN exclusively. After the mechanical assembly of a superchamber, the relevant parameters (*Efficiency, Spatial and Time Resolution, Noise, Cluster Size, etc.*) are measured with a dedicated cosmic stand. Once this stage is completed, the superchamber is declared ready for final installation in the Muon Spectrometer of the CMS experiment.

The production of the GE1/1 detectors has started in April 2017 at CERN

5.1. The GE1/1 detectors for the CMS-GEM project

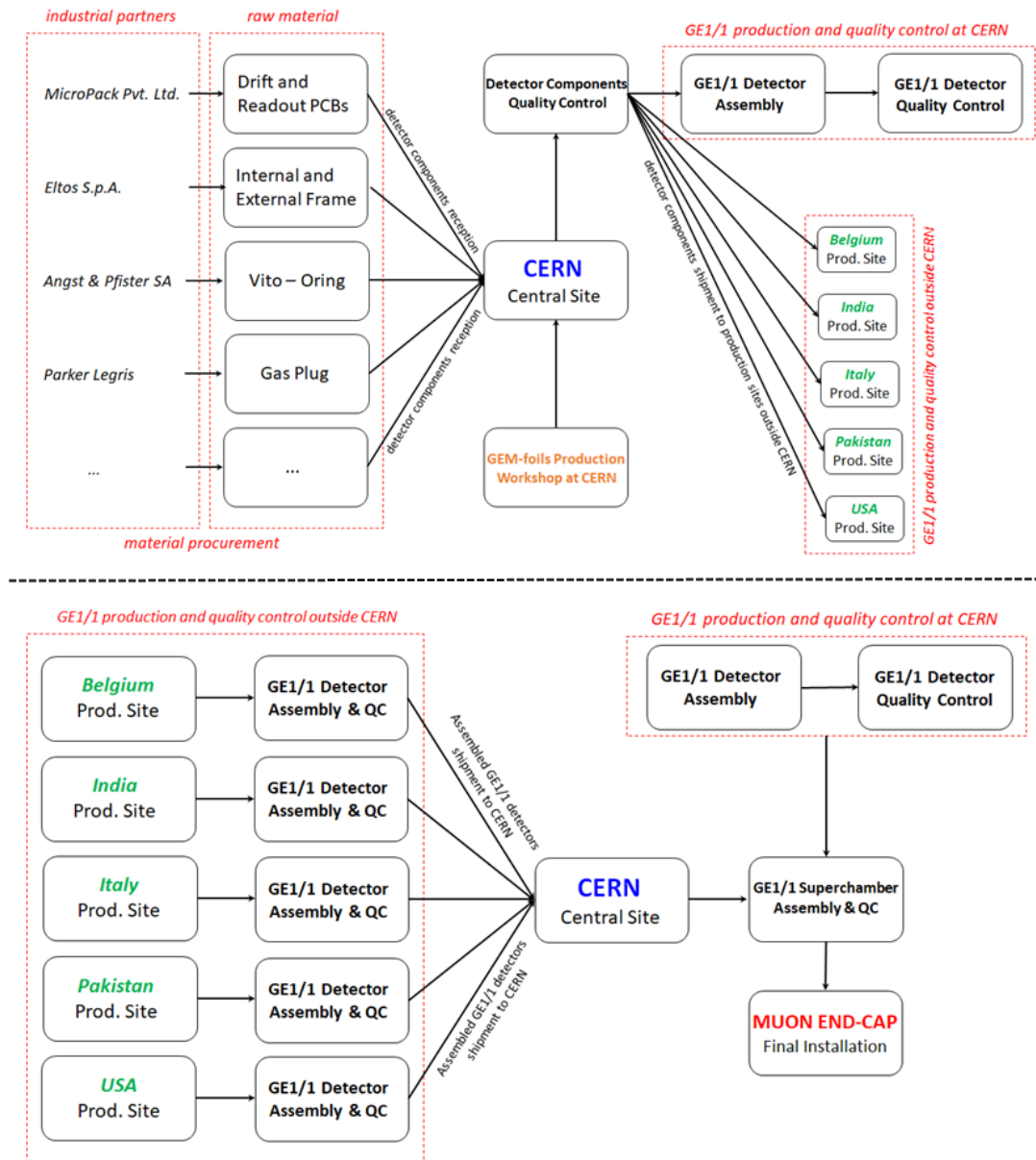


Figure 5.6: GE1/1 detectors mass production chain. Together with the production and quality control phase are listed the production site and/or the industrial companies in charge of the GE1/1 mass production.

production site and in Autumn 2017 at most production and quality control sites. Their installation in the Muon Spectrometer of the CMS experiment is planned to be ready in 2020 after the assembly and the validation of all the superchambers at CERN production site. Therefore, the GE1/1 detectors production and validation have to be completed within year 2019. Therefore, the mass production schedule has been designed in such way that the assembly and the quality control tests can be conducted in parallel in the several production sites. The detailed step-by-step description of the GE1/1 detectors

assembly and quality certification procedures is given in the Sections 5.3 and 5.4.

5.2 GE1/1 detector components and design

5.2.1 GE1/1 technical design

The CMS GE1/1 detector is a large trapezoidal triple-GEM detector. The detector itself consists of a trapezoidal gas volume containing a stack of three identical large area trapezoidal shaped GEM-foils embedded between a drift electrode and a readout board. The drift board, the readout board and the external frame define the gas volume. Two rubber O-ring placed in the groove of the external frame ensure the gas tightness. Figure 5.7 shows the exploded view of the mechanical design of a CMS GE1/1 triple-GEM detector and its main assembly components starting from bottom: drift board mounted all around with stainless steel pull-outs used for mechanical stretching of GEM-foils, 3 *mm* internal frame, first GEM-foil, 1 *mm* internal frame, second GEM-foil, 2 *mm* internal frame, third GEM-foil, 1 *mm* internal frame, first O-ring, external frame, second O-ring and the readout board.

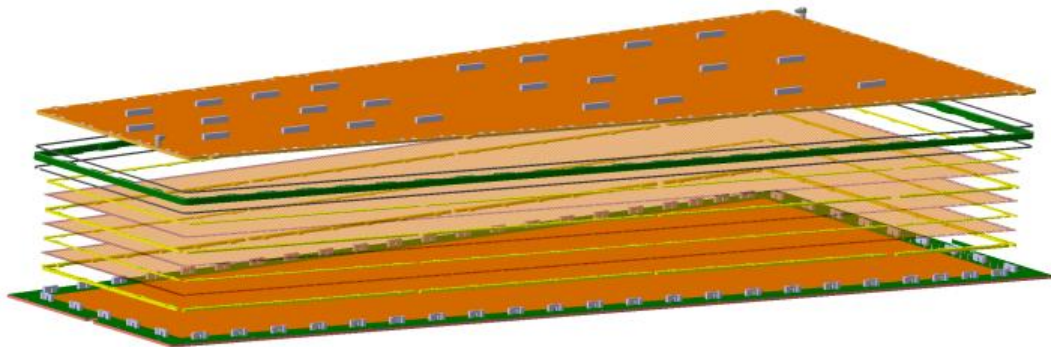


Figure 5.7: Exploded view of the mechanical design of a GE1/1 triple-GEM detector and its main assembly components.

Since very limited space available within the current mechanical structures of the forward region of the muon endcap at the CMS experiment, the CMS GE1/1 detectors are very compact in size. Furthermore, because of the mechanical constraints in the GE1/1 station, two versions of detectors have been designed in order to keep the maximum detection coverage: the *Long GE1/1* detectors with a length of 120.9 *cm* and the *Short GE1/1* detectors with a length of 106.1 *cm*. The technical specifications of the GE1/1 detectors for both short and long versions are shown in the Table 5.4. The design of the main assembly components is dealt with individually in the following sections.

5.2. GE1/1 detector components and design

Specification	Sort	Long
Chamber Shape	Trapezoidal	Trapezoidal
Chamber Dimensions	L: 106.1 <i>cm</i> , W: (23.1-42.0) <i>cm</i> , D: 0.7 <i>cm</i>	L: 120.9 <i>cm</i> , W: (23.1-44.6) <i>cm</i> , D: 0.7 <i>cm</i>
Chamber Thickness	3.5 <i>cm</i>	3.5 <i>cm</i>
Active readout area	0.345 <i>m</i> ²	0.409 <i>m</i> ²
Active chamber volume	2.6 liters	3 liters
Geometric acceptance in η	1.61-2.18	1.55-2.18

Table 5.4: Technical specifications and parameters of Short and Long GE1/1 detectors.

5.2.2 Drift Board design

The Drift Board is a Printed Circuit Board (PCB) that holds the trapezoidal drift electrode. The mechanical design of the drift board is shown in the Figure 5.8. The active area of the board is coated with a copper layer, which is in contact with the active gas volume of the detector. The Figure 5.9 shows the actual drift board (left) and the magnified view of its wider base (right).

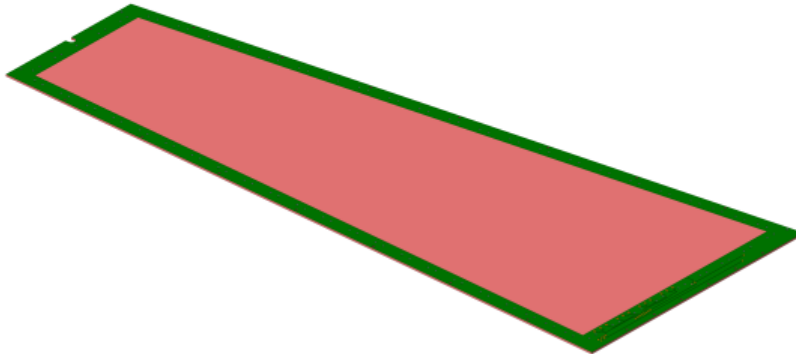


Figure 5.8: Mechanical design of the GE1/1 Drift Board

The board also houses the spring loaded High Voltage (HV) pins which are used to power the GEM-foils. Four pins are used to power each foil, two for the top of each foil and two for the bottom. The positions of the pins are defined corresponding to the HV pads on each foil. The HV pins corresponding to one foil are of the same height but vary in height from the pins of another foil. The height of the pins is calculated according to the height of the corresponding GEM foil from the drift board. Consequently there are 12 HV pins on the drift board positioned relevantly.

On the periphery of the board there are multiple through-holes to mount the stainless steel Pull-Outs on the board. These Pull-Outs are important parts of the mechanical stretching system of the GEM-foils. The details of the mechanical stretching technique is explained in Section 5.3.4. The other elements

on the drift board are the HV distribution circuit traces, a dedicated pad for a protective resistor and pads for a decoupling RC circuit. The $10\text{ M}\Omega$ protective resistor ensures the safety of the detector from electrical damage that could arise as a result of the high voltage of operation. The decoupling RC circuit consists of a $100\text{ k}\Omega$ resistor and a 330 pF capacitor. This RC circuit is used to decouple the signal from the HV signal when the readings are acquired from the bottom of the third GEM-foil.

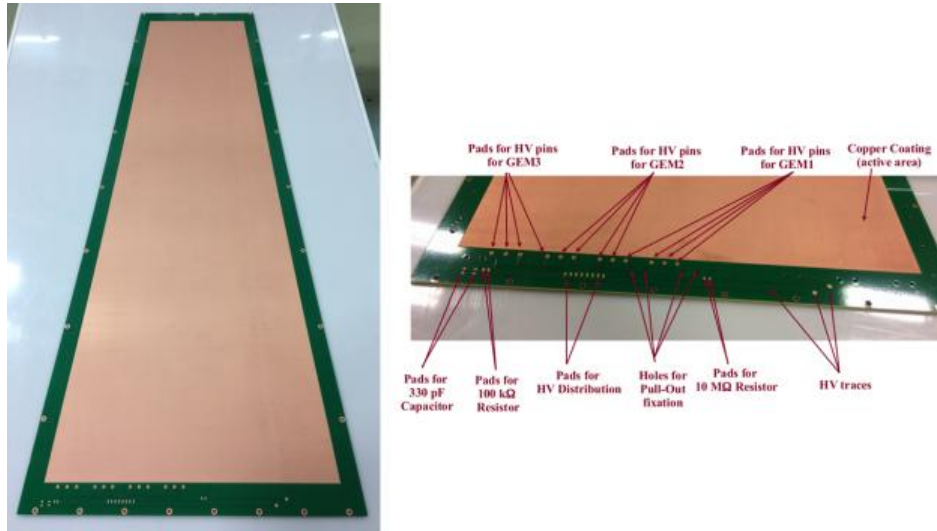


Figure 5.9: Left: Picture of the GE1/1 the Drift Board. Right: Close view of the wider base of the GE1/1 drift board showing the HV distribution circuit traces and pads for the spring-loaded pins that make the electrical connections to the GEM-foils. The pad for $10\text{ M}\Omega$ protective resistor and the pads for the $100\text{ k}\Omega$ resistor and 330 pF capacitor of the decoupling RC circuit are shown. Holes to fix Pull-Outs against the board are also shown.

5.2.3 External Frame Design

The external frame is a trapezoidal structure as shown in Figure 5.10 made of halogen-free glass-epoxy material and is machined from a single piece to minimize material non-homogeneity. The frame is primarily used to make the chamber gas tight, by closing in the active gas volume between the drift and readout boards. The Figure 5.11 shows the actual external frame (left) and the magnified view of of the section of the external frame (right).

The external frame also has a small groove along its periphery in order to accommodate the Viton O-ring that compresses between the drift and readout boards, thereby ensuring a greater degree of gas-tightness without damage or deformation to the frame or any other components. The frame also has notches all around to accommodate the Pull-Outs. A Nuvovern[®] polyurethane varnish coating is applied on the frame to seal in the particulates such that it does

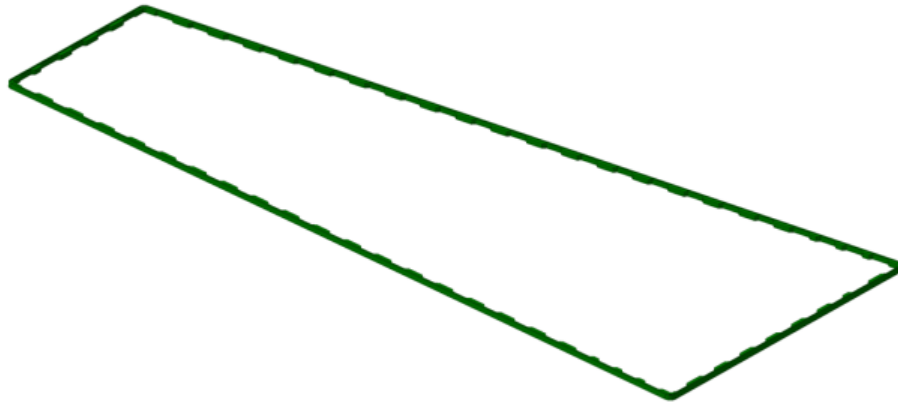


Figure 5.10: Mechanical design of the External Frame

not contaminate the detector with particulate matter during assembly and operation.

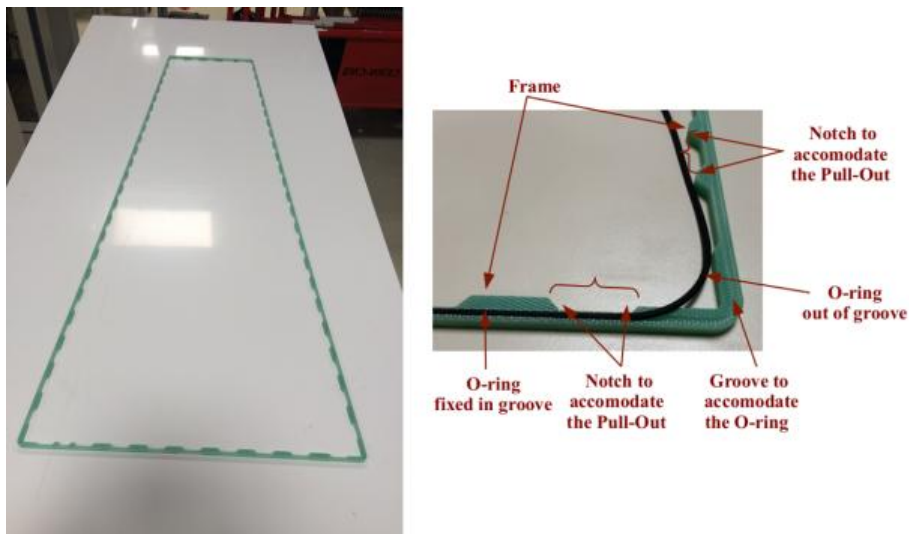


Figure 5.11: Left: Picture of the external frame. Right: Close view of the section of the external frame showing the groove in the frame, O-ring in and out of its groove and notches in the inner side of the frame to accommodate the Pull-Outs

5.2.4 Internal Frame Design

The internal frames are important components as they define the distances between the drift board, GEM-foils and readout board. There are four layers made of halogen-free epoxy glass. The thickness of each layer is 3 mm, 1 mm,

2 mm and 1 mm respectively and each layer is made of ten individual pieces as shown in Figure 5.12.

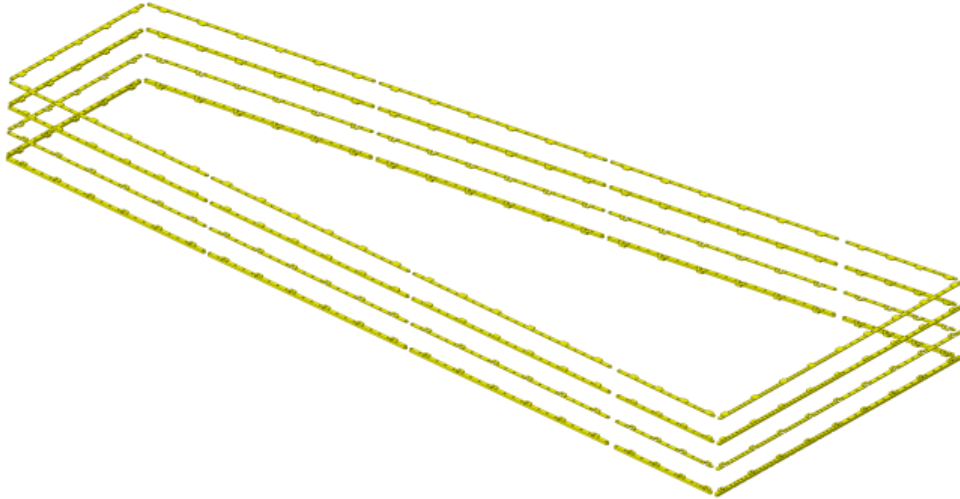


Figure 5.12: Mechanical design of the Internal Frame

The frames are coated with a Nuvovern[®] polyurethane varnish coating which ensures that no glass epoxy particulates are detached from the frames during the assembly which could contaminate the detector and/or the clean room. Such particulate on the GEM-foils is often responsible for sparks and electrical shorts in the holes and thus potentially causing damage to the GEM-foil. *M2* screws are used to couple the three GEM-foils on the the internal frames, screws are fixed all around the perimeter of the GEM-foils. Threaded *M2* brass inserts are fitted in the 3 mm frame to avoid loosening of macroscopic and microscopic epoxy glass particulates that could arise when screws pass through the frames during assembly procedures.

5.2.5 GEM Foil design and production technology

The GE1/1 detector uses three identical trapezoidal GEM-foils as shown in the Figure 5.15. The GEM-foils manufacturing technology is realized using conventional photolithography technique commonly employed by the printed circuit industry.

- **double-mask photolithography technique** [70] [71]. The double-mask photolithography process consists of applying a 15 μm -thick photoresistive layer on both sides of the copper-clad polyimide substrate.

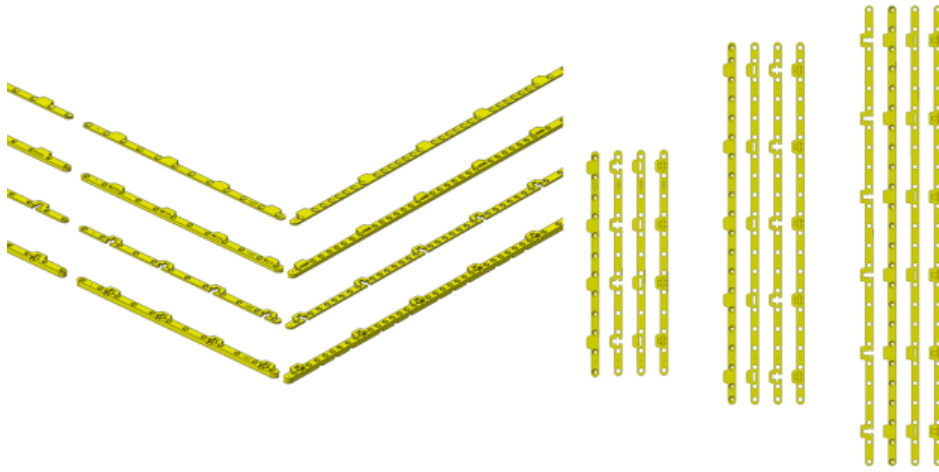


Figure 5.13: Left: Close view of the section of the Figure 5.12. Right: Shapes and mechanical structure of different pieces of the internal frames. Ten pieces per frame combine together and surround all round the periphery of the GEM-foils stack.

That the GEM-hole pattern is transferred onto by UV-light exposure through flexible masks. After development, the substrate can be etched with several solvent and acid bath (*wet-etching*), which removes copper from the holes, but not from where the photoresist still masks the copper. The next step is the etching of the polyimide substrate, for which the holes in the copper layers act as a mask.

To obtain a homogeneous hole geometry across the GEM-foil, it is imperative to keep the alignment error between top and bottom mask within $10\ \mu\text{m}$. As both the mask and the base substrate are flexible, the manual alignment is far from trivial, and when foil size exceed about $40\ \text{cm}$ this technique is hardly feasible anymore. A way of overcoming this alignment problem for larger GEM-foils is the use of single-mask photolithography.

- **single-mask photolithography technique** [70] [71]. In single-mask photolithography technique, the GEM-hole pattern is transferred only to one side of the copper-clad polyimide substrate. Therefore, any need for alignment is removed. The $15\ \mu\text{m}$ -thick photoresistive layer is developed and the hole pattern is used as a mask to chemically etch holes in the top copper cladding. After stripping the photoresist, the holes in the top copper cladding are in turn used as a mask to etch the polyimide. Then the bottom copper cladding is etched after the polyimide, using the holes in the polyimide as a mask. Finally, a second polyimide etching is performed from the bottom to transform the hole geometry and give the typical bi-conical shape. All GE1/1 detectors comprise GEM-foils produced with single-mask photolithography technique at CERN.

The photolithography process steps of the double-mask and the single-mask techniques, both developed by the CERN PCB Workshop [70] [71], are shown in Figure 5.14.

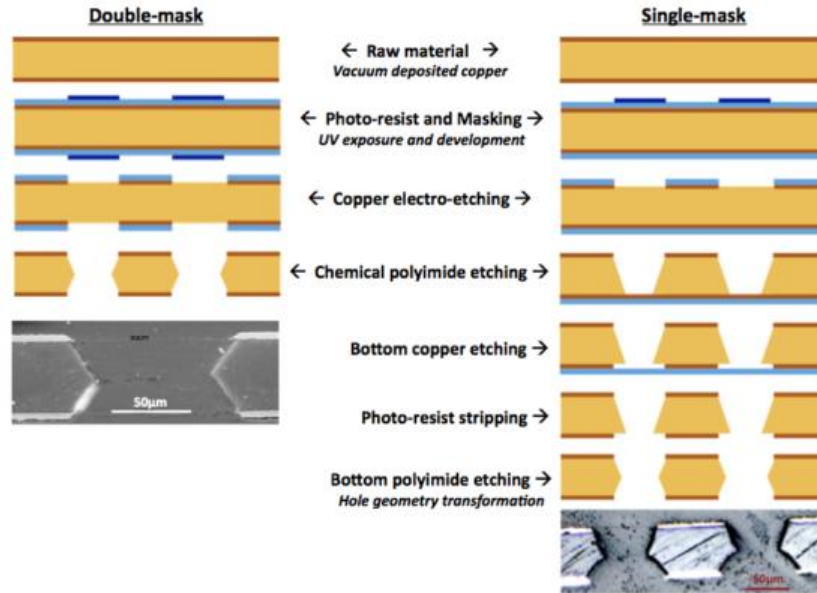


Figure 5.14: Schematic comparison of procedures for fabrication of a double-mask GEM-foils (left) and a single-mask GEM-foils (right) [70] [71].

The surface of the GEM-foil oriented towards the readout boards is a single continuous conductor whereas the other surface, oriented towards the drift board is segmented into sectors. These sectors are aligned parallel to the base of the trapezoid and the width of each sectors reduces when going from the short end to the wide end of the trapezoid. This is to ensure that the area of each sectors is approximately equal to 100 cm^2 . This segmentation restricts the amount of charge that can get generated during a discharge, thereby limiting the total energy of a discharge itself. Another advantage of segmentation is that even in extreme cases such as destructive discharge causing a short in one particular HV sector, only that sector is rendered useless and not the entire foil. This however bears the implication that each sector has to have a separate HV supply. This is dealt with by choosing a common connection point that receives the external HV supply and routing a HV trace from it along the periphery of the GEM foil. The common connection points are placed on the wide end of the foil and two connection points are added for redundancy. The HV trace is connected to each HV sector through $10 \text{ M}\Omega$ protection resistors that are mounted on the surface. These resistors limit the current supplied from HV supply, decouple the capacitance from all other HV sectors and to quench the discharge.

5.2. GE1/1 detector components and design

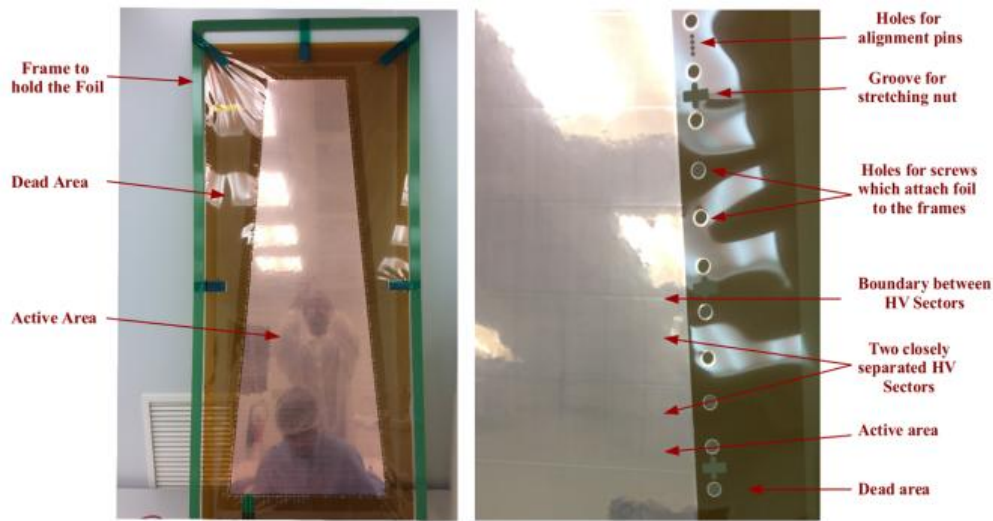


Figure 5.15: Left: Design of GEM-foil for GE1/1 detector. Right: Close view of the section of foil showing the small holes for alignment pins which are used during the assembly procedures of the GE1/1 detectors, large holes to allow the passage of screws through them and to attach the foil to internal frames, plus-shaped slits for stretching nuts and HV Sectors.

5.2.6 Readout Board design

The Readout Board is a trapezoidal shaped printed circuit board as shown in Figure 5.16.

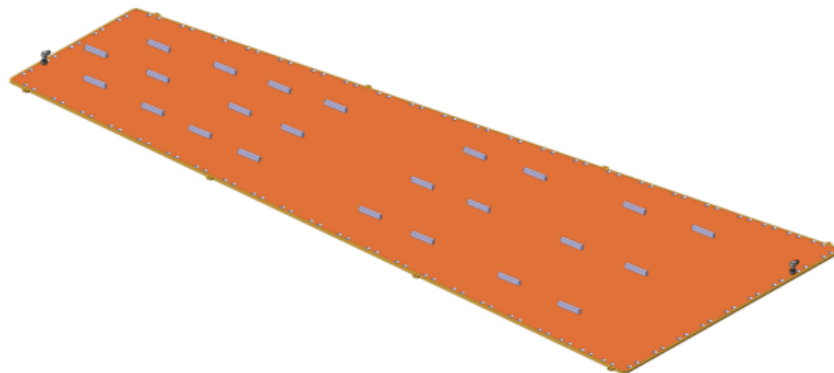


Figure 5.16: Mechanical design of the Readout Board.

The inner side of the readout board contains 3072 trapezoidal readout strips oriented radially along the longer side of the detector. The area covered by the strips is called the active area and it subtends an angle of 10.15° . This allows for an over lap of 2.6 mrad (5.67 strips) between the active area of subsequent detectors. The readout strips are connected through metalized vias to the

other side of the board, from which traces are routed to 8×3 partitions in $(i\eta, i\phi)$. Each $(i\eta, i\phi)$ sector contains 128 strips. The strip pitch increases from 0.6 mm at the shorter end of the detector to 1.2 mm at the wider end. The readout board also has two diagonally opposite holes on the corners to accommodate the gas plugs that will serve as the inlet and outlet respectively, as explained in Sec.5.2.7.

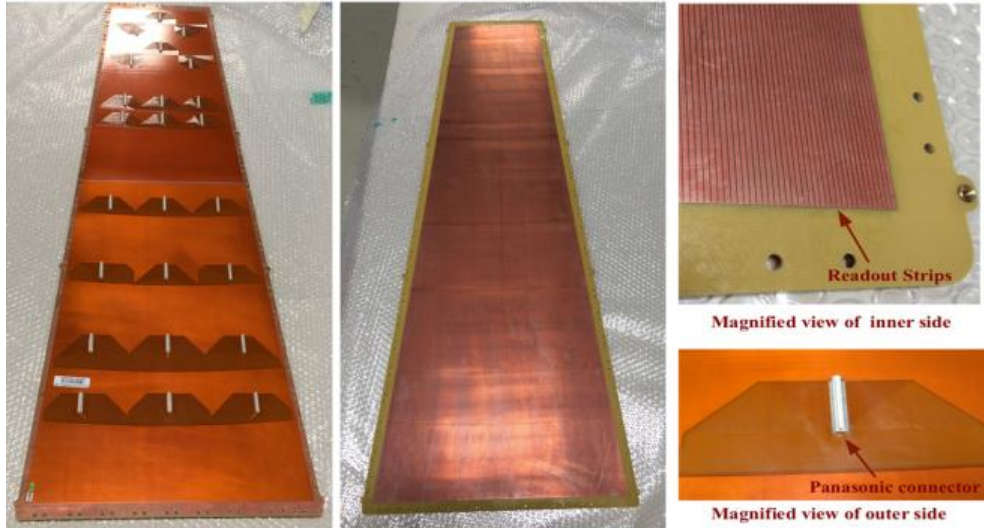


Figure 5.17: Left: Outer side of GE1/1 readout board showing 24 $(i\eta, i\phi)$ readout sectors with each sector mounted with a male Panasonic adopter for signal readout. The board has also two holes at the opposite corners which allow to mount the two gas plugs. Also, there are machined holes on the periphery of the board which allow the passage of closing screws to fix the board against detector structure. Middle: Inner side of the drift board showing the readout strips. Right: Close view showing the readout strips on the inner side and Panasonic connector on the outer side of the board.

5.2.7 Gas Distribution System

The gas distribution system on the GE1/1 chambers is a single inlet and single outlet system. As mentioned in the previous section the inlet and outlet gas plugs are mounted at diagonally opposite points on the readout board. Figure 5.18 show the mechanical design of the gas plug fixed against the readout board.

The gas mixture flows into the detector through the inlet diagonally. The gas distribution within the GEM-foils stack occurs by means of the holes in the foil and through the gaps in the internal frames.

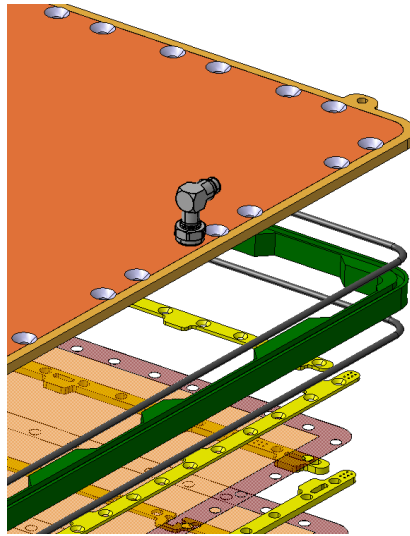


Figure 5.18: Mechanical design of the gas plug fixed against the readout board.

5.3 Description of the assembly procedure

The GEM technology heavily depends on the integrity of the GEM-foils and its precision-etched micron level holes. Even the smallest of particulate contaminant could become a source for irregular operation or could even cause unrepairable damage to the detector. Therefore, the assembly can only be performed within a clean room with a class-1000 rating at the very least. Tools with lubricated shafts, soldering equipment's that requires heating of volatile fluxes, motors and vacuum pipes with out-gassing oils, etc. are the main sources which could contaminate the detector and, thus, are forbidden in the assembly area. People performing the assembly strictly abide by the code of conduct within the clean room such as wearing aprons, dust-free gloves, facial masks, shoe covers, hair caps etc. Figure 5.19 shows a schematic overview of the critical steps to be performed during assembly and is a representation of the overall flow of the assembly procedure. Additional details and technical aspects on the assembly procedures of the CMS GE1/1 detectors can be found at [68] [69].

5.3.1 Drift Board Preparation

The drift board preparation includes the mounting of the stainless steel pull-outs and the soldering of twelve HV-pins in order to power each layer. Since this involves soldering and manual fastening of screws, there is high scope for contamination and thereby this step is carried out outside the clean room. The heights of each set of HV-pins are in accordance with the position of the respective GEM-foils and are mounted on the drift board in that specific order. Each pull-out is fastened to the drift board using two A2 stainless steel $M3 \times 6 \times 8$ screws with polyamide washers to ensure gas tight fastening. The

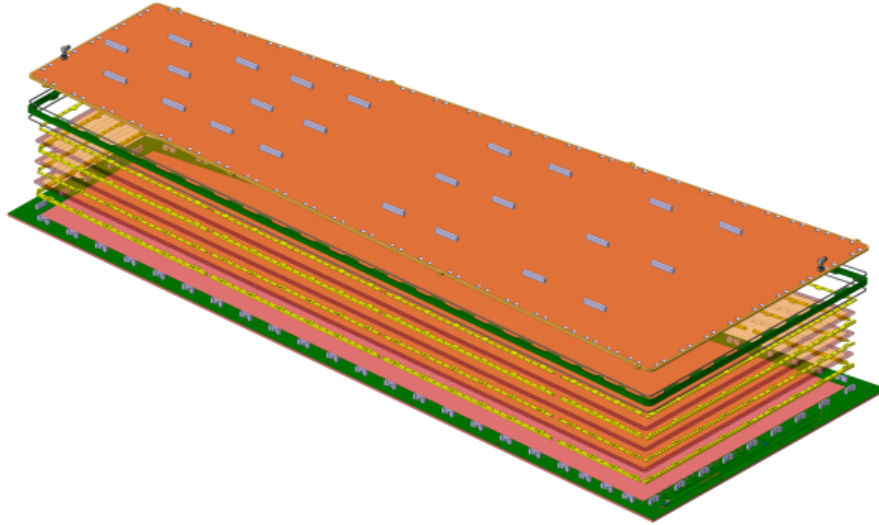


Figure 5.19: Exploded view of the mechanical design of a CMS GE1/1 triple-GEM detector showing the schematic flow of the assembly procedure.

surface mounted (SMD) $10\text{ M}\Omega$ protection resistance and the decoupling RC circuit consisting of the $100\text{ k}\Omega$ resistor and the 330 pF capacitor are mounted in their respective positions at this stage.

The HV-pins are soldered onto the drift board within the gas volume and designed to provide optimal and stable power supply to each foil. Their spring-loaded design allows for continuous contact with the corresponding pads of the GEM-foil when the foil is mounted on the stack. The HV circuit design on the drift board is shown in Figure 5.20.

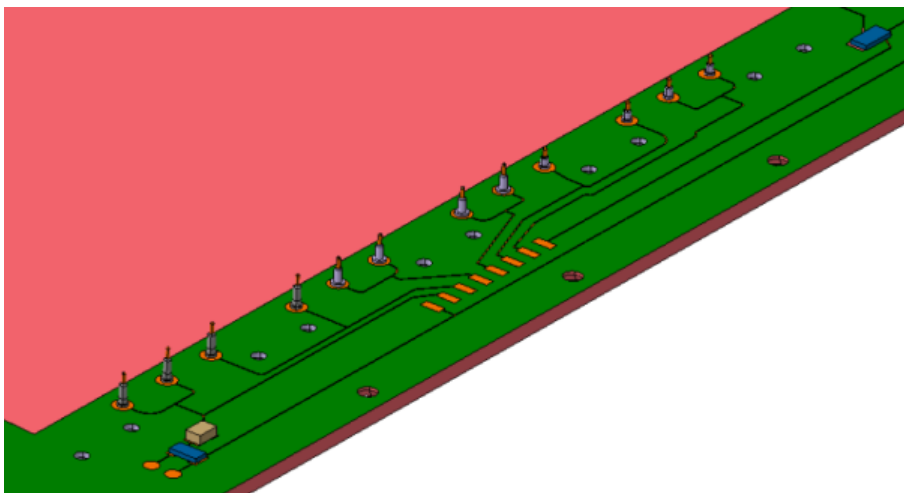


Figure 5.20: Schematic overview of the HV circuit and the twelve HV-pins on the drift board.

5.3. Description of the assembly procedure

The HV-pins are connected with pads outside the gas volume: these pads are designed to be used with both single channel and multi channel power supply. In case of a single channel power supply a resistive high voltage divider network is used to supply appropriate voltage distribution within the detector. Figures 5.21, 5.22 and 5.23a show the design and arrangement of the HV-pins on the drift board and their positions with respect to the GEM-foil stack. Figure 5.23b shows the HV divider circuit diagram for the 3/1/2/1 mm gap configuration.

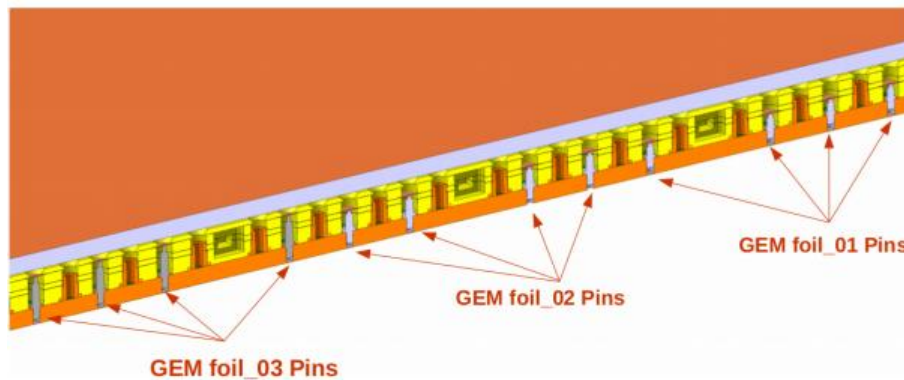


Figure 5.21: Sliced view showing the spring loaded mechanism of the twelve HV-pins and their position on the drift board with respect to the GEM-foils.

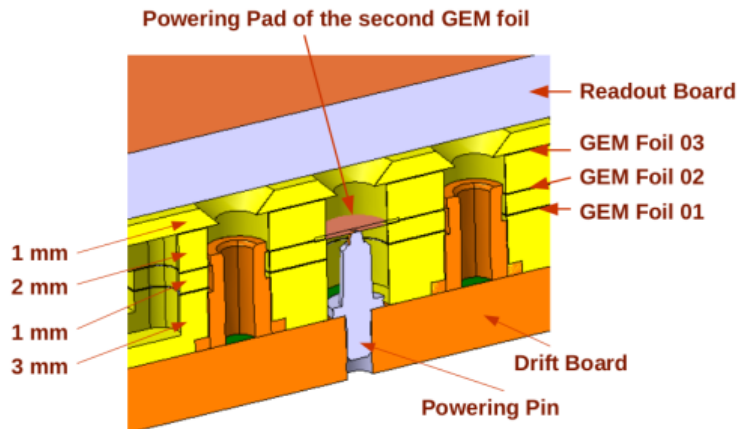


Figure 5.22: Magnified view of one of the HV-pins showing the GEM-foils stack, the 3 mm, 1 mm, 2 mm, 1 mm internal frames, the powerin pad of the second GEM-foil, the single HV-pin pressed against powering pad of the second GEM-foil and the readout board.

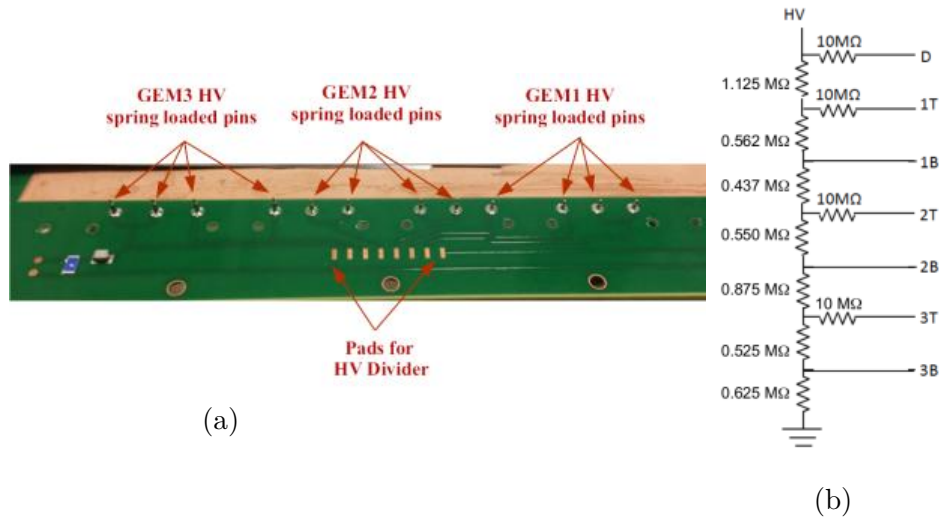


Figure 5.23: (left) High voltage circuit arrangement on the drift board showing the twelve HV-pins. The heights of each set of HV-pins are in accordance with the position of the respective GEM-foils and are mounted on the drift board in that specific order so that they can properly reach the three GEM-foils. Their spring-loaded design allows for continuous contact with the corresponding pads of the GEM-foil. (right) HV divider circuit diagram for the 3/1/2/1 mm gap configuration and corresponding connections to GE1/1 detector electrodes.

5.3.2 GEM Stack Assembly

The most important part of the assembly procedure is the preparing of the GEM-stack, which is a delicate process as it deals with the accurate alignment of the parts without any scope for contamination. This step is performed within the clean room. The alignment is done using alignment pins on a Plexiglas base. The alignment pins are placed at precise positions in correspondence to the alignment holes on the FR4 pieces which hold each GEM-foil with respect to themselves. The 10 pieces of the 3 mm internal frame are first placed in proper positions over the alignment pins before the first GEM-foil is placed as shown in Figure 5.24.

The GEM-foil has to be cleaned again as a precautionary measure just before aligning them on top of the first external frame layer. This is carried out using an anti-static adhesive roller which can remove dust with micron level precision as shown in Figure 5.25a). This step is followed by the leakage current test measurement using a MEGGER MIT420 insulation tester (see Figure 5.25b). In this step a 550 V potential difference is applied across the foils which produces a strong electric field, generally of the order of 70-100 kV/cm inside the GEM-holes. When the relative humidity (RH) of the assembly area is 30% or less, the maximum permissible leakage current is 35 nA for an applied potential difference of 550 V . Above 30% the leakage current increases drastically. Minor sparks may be observed during this procedure. This is caused small

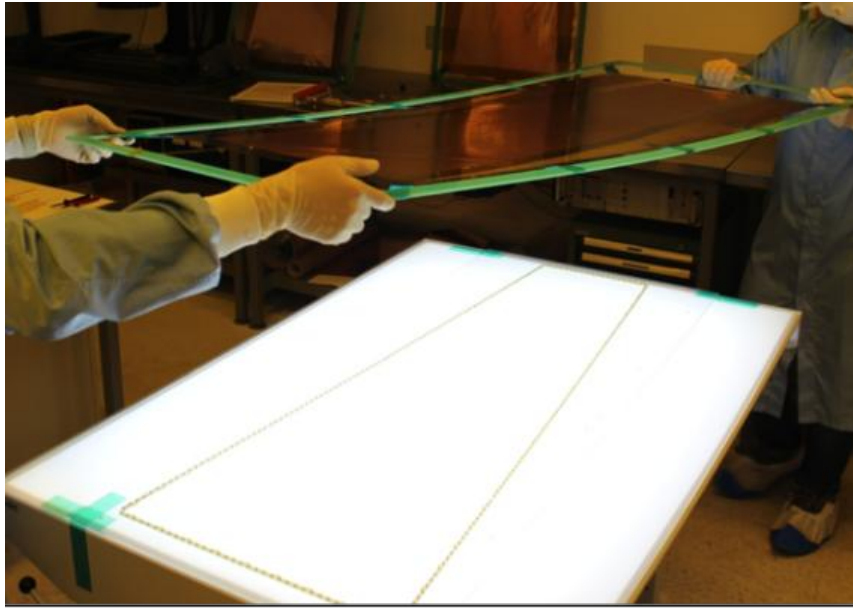
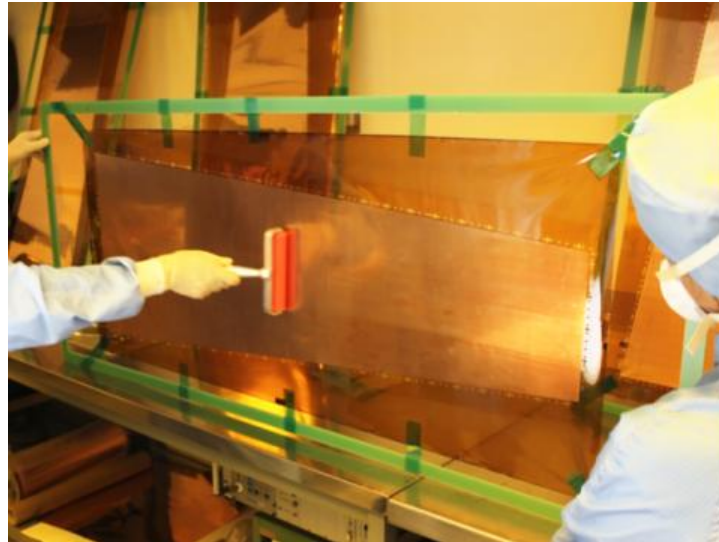


Figure 5.24: Pictures of the process of laying the first GEM-foil on a Plexiglas base with the 3mm internal frames in position.

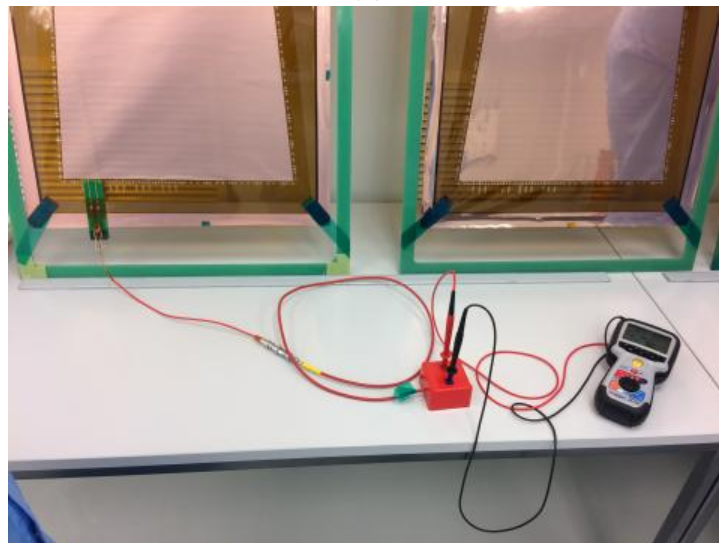
particulate matter trapped between the holes. The spark burns out the small particles and thus serves as a secondary cleaning procedure. Excessive rate of sparking however implies that the GEM-foils are contaminated with dust and the primary foil cleaning procedures are to be repeated. As a result of this test, the foils accumulate electrostatic charges and by virtue of this might start catching dust themselves. Also, if the GEM-foils on the stack happen to come in contact with each other prior to the stretching procedure, the accumulated energy might get released at the point-like contact, thereby leading to destructive discharges that might damage the integrity of either or both of the foils. For these reasons, the foils must be discharged after the leakage current test by shorting the top and bottom electrodes of the foil.

As a precautionary measure, the GEM-foils are stretched manually and fixed temporarily using tape between the stretched outer holding frame of the foil (which is cut out in a later step) and the Plexiglas base. This prevents the foils from sagging and coming in contact with each other during the aligning of the foils in the stack, prior to the implementation of the stretching procedure. The foils are aligned in the stack using the alignment holes and they are attached to the internal frames using a pattern of holes as seen in Figure 5.15. The foil stack is held in place by multiple $M2 \times 6$ screws, that run through all the internal frame segments and are tightened against the $M2$ brass inserts shown in Figure 5.26.

After the second GEM foil is placed on the stack followed by the 2mm frame, the stainless steel nuts are positioned in dedicated plus-shaped grooves of the internal frames at this point in the assembly, with their axes oriented per-



(a)



(b)

Figure 5.25: (top) Picture of the GEM-foil cleaning procedure using adhesive roller, which removes dust particles of micron level effectively by its strong sticking capacity. (bottom) Picture of the leakage current test measurement using MEGGER MIT420 insulation tester.

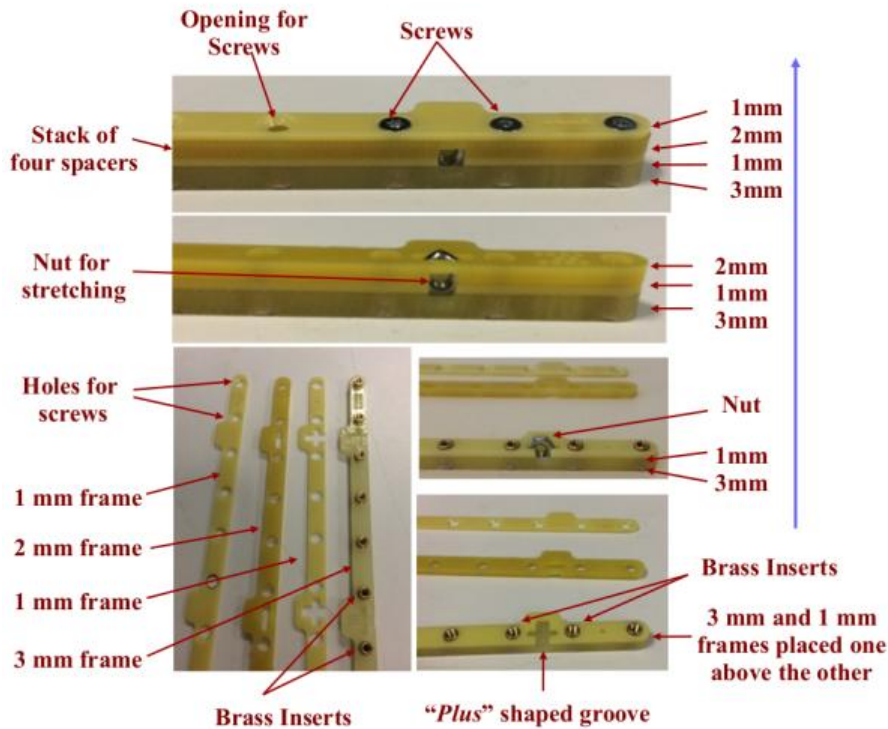


Figure 5.26: Mechanical structures of the four different internal frames which are stacked together to maintain the gap configuration of 3/1/2/1 mm in GE1/1 detector, showing the positioning of the brass inserts, grooves for the stretching nuts and positions of fastening screws.

pendicular to the axes of the brass inserts in the internal frame. The nuts together with the pull-out and dedicated screws form stretching mechanism (see Section 5.3.4). The GEM-foils stack consisting of three foils with desired 3/1/2/1 mm frames is finally formed by removing the dead area around the GEM-foils. The various steps explained above are shown in Figure 5.27 (the details of the GEM-foils stack assembly are further described in 5.3.3).

5.3.3 Detector Construction

The detector construction starts with the placement of the GEM-foils stack on the drift board as shown in Figures 5.28a. The drift board is fixed against the Jig by means of Aluminium bars which are tightened on the Jig with the help of fixation bolts as shown in the Figure 5.28b. The Jig keeps the drift board flat and prevents any kind of deformations that may occur during stretching procedure of GEM-foils stack or during the fixation of readout board against it. The stack is stretched against the pull-outs manually by applying a monitored torque. The stretching mechanism is dealt with in detail in the next section. After stretching, a connectivity check between the gaps and across the GEM-foils is performed by measuring the impedance using a MEGGER MIT420

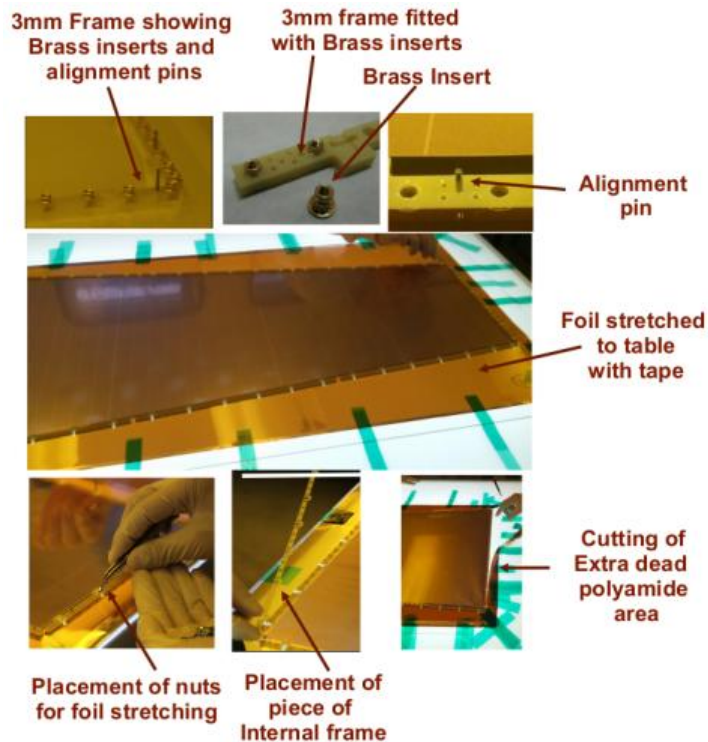


Figure 5.27: Pictures of the various assembly steps for the stack formation procedure.

insulation tester. The HV traces outside the gas volume on the drift board are used to apply a potential difference of 550 V in between the gaps and across the GEM-foils. At RH 30% an impedance of 100-150 GΩ is expected. At higher values of humidity, the impedance may have lower value.

The external frame with the O-ring is placed around the GEM-foils stack and the readout board is placed over the external frame. The readout board is tightened against the pull-outs using A2 stainless steel M3 × 6 × 8 screws sealed with polyamide washers. This causes the O-ring to deform and fill up the gaps forming a gas tight barrier. The final chamber is shown in Figure 5.30.

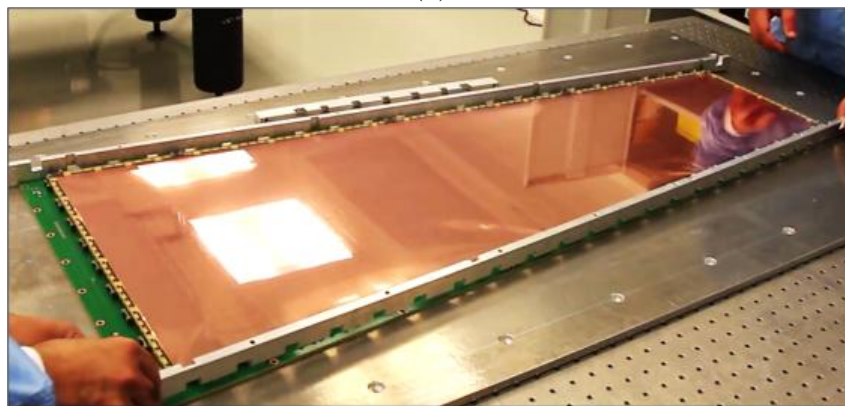
5.3.4 Stretching Mechanism

For the construction of GE1/1 prototype, the GEM foils have been initially thermally stretched during 24 hours at 37° in a special oven. Fiberglass spacer frames have been then glued onto the GEM-foils in order to fix and keep them separated at the correct distance in the triple-GEM configuration. These procedures used considerable amounts of glues and were therefore prone to possible contamination of the active gas volume due to the outgassing phenomena. Furthermore, the previous procedures were time-consuming process and

5.3. Description of the assembly procedure



(a)



(b)

Figure 5.28: (top) Pictures of the placement of the GEM-foils stack on the drift board. (bottom) Picture of the GEM-foils stack on drift board and fixation of drift board against Jig by means of Aluminium bars.

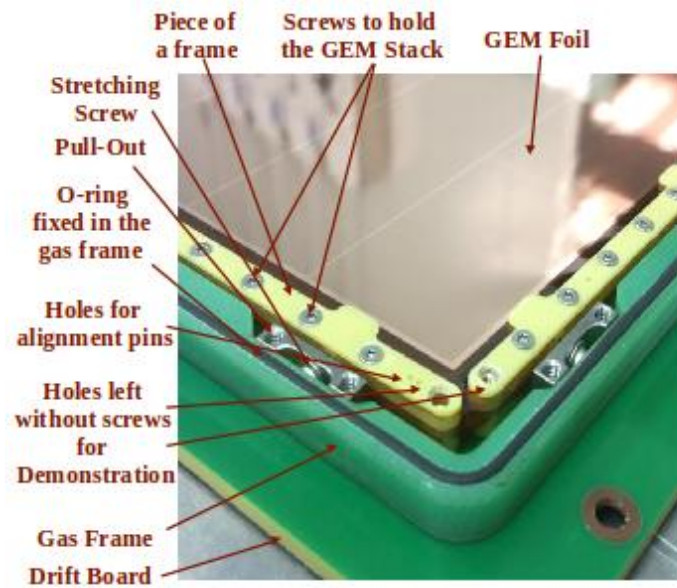


Figure 5.29: Magnified view of the section of the GE1/1 detector with GEM-foils stack tensioned against the pull-outs mounted onto the drift board and surrounded by outer frame having O-ring on its grooves. The active chamber volume is ready to be closed with the readout board.

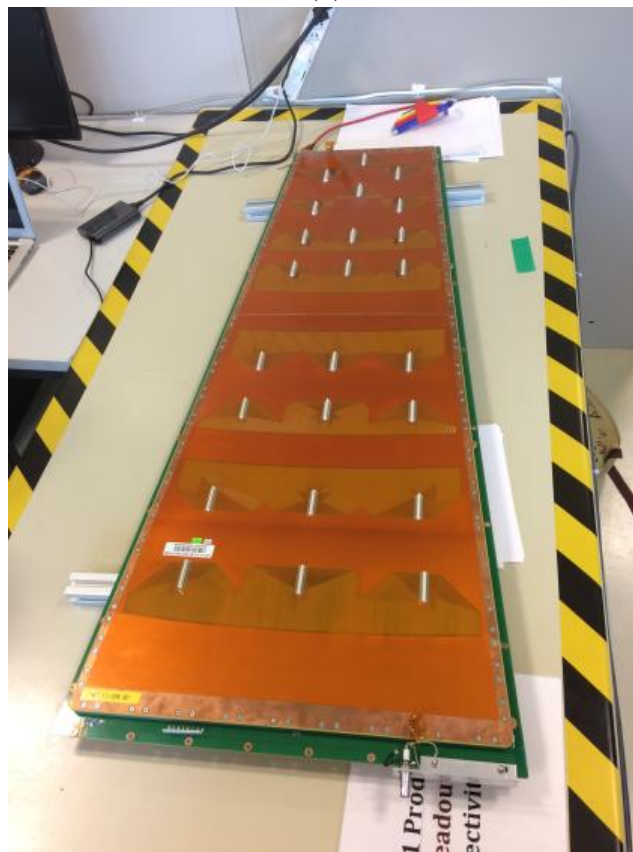
labour-intensive and therefore not well suited to the timescales required by the mass production. Alternative techniques have been tested to stretch GEM-foils including the stretching due to infrared heating lamps. After testing multiple stretching mechanisms, the mechanical stretching method has been chosen owing to significant reduction in time consumed for stretching as compared to the other methods considered. Since the detector is constructed without the need for gluing, the assembly time is reduced from a time dynamic of days to a few hours. The mechanical stretching technique is conceptually visualized in the Figure 5.31.

Once the stack is placed on the drift board, $M2.5 \times 8 \times 8$ screws are inserted around the periphery of the stack and are tightened manually into the perpendicular nuts that were previously placed into the grooves of the internal frame. These screws are manually tightened using a controlled and monitored torque of $8-10 \text{ cN} \cdot \text{m}$. Thus the GEM-foils are tensioned uniformly as the inner frame is being pulled outwards i.e. towards the pull-outs as shown in the Figure 5.32. The torque specifications are to be followed with as much precision as possible since the inherent tolerances of this method have an effect on the uniformity of the gas gain and the time response. Therefore, it is very important and crucial to ensure uniform stretching during assembly in order to achieve the uniform response from all over the detector.

5.3. Description of the assembly procedure



(a)



(b)

Figure 5.30: (top) Closing of the GE1/1 triple-GEM detector with the readout board. (bottom) The final assembled detector on the Quality Control line.

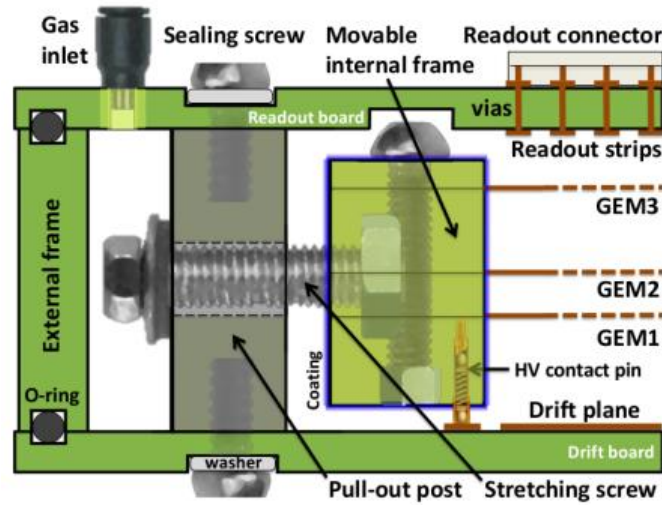


Figure 5.31: Schematic overview of the mechanical stretching method of the GEM-foils in the CMS GE1/1 detector.

5.4 Requirements for GE1/1 Quality Assurance/Quality Control assessment

5.4.1 Overview of the QA/QC

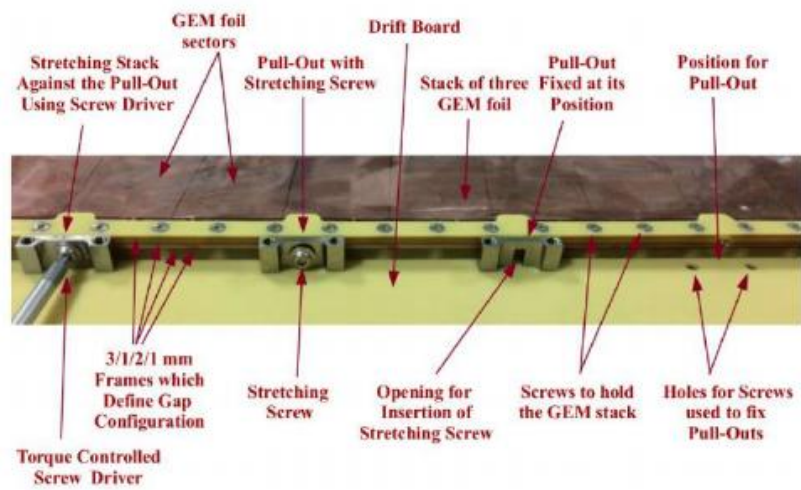
The Quality Assurance (QA) and the Quality Control (QC) are key elements to ensure the delivery of fully efficient GE1/1 detectors yielding their best performance when installed in the Muon Spectrometer of the CMS experiment. The final detector quality and performance depend on the production quality and on the accuracy of the detector assembly procedures. Standardized QA and QC procedures have been established in order to prevent any mechanical or electrical issues that might affect the detector performance. These procedures are identical as far as possible for all production and quality control sites.

Figure 5.33 shows a flow card with the general quality assurance and quality control procedures for the GE1/1 project. The overall process is divided into three major stages:

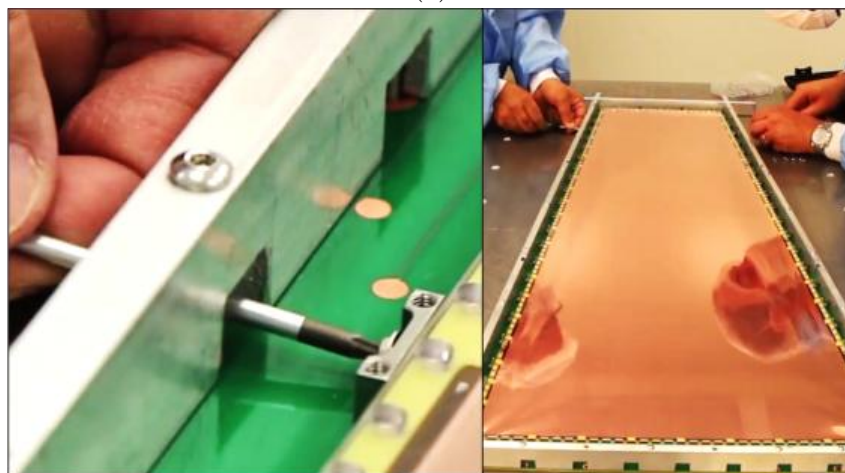
- assembly components production and quality control at CERN production site;
- assembly and quality control of single GE1/1 detectors at production sites;
- assembly and quality control of superchambers at CERN production site before delivery for installation at CMS Muon System.

The corresponding timeline is presented in Table 5.6. For each steps, the average time is expressed: these numbers are generally estimated and additional

5.4. Requirements for GE1/1 Quality Assurance/Quality Control assessment



(a)



(b)

Figure 5.32: Picture of the mechanical stretching method during the GE1/1 detector assembly

5. The Assembly, Quality Control and Commissioning of the GE1/1 detectors

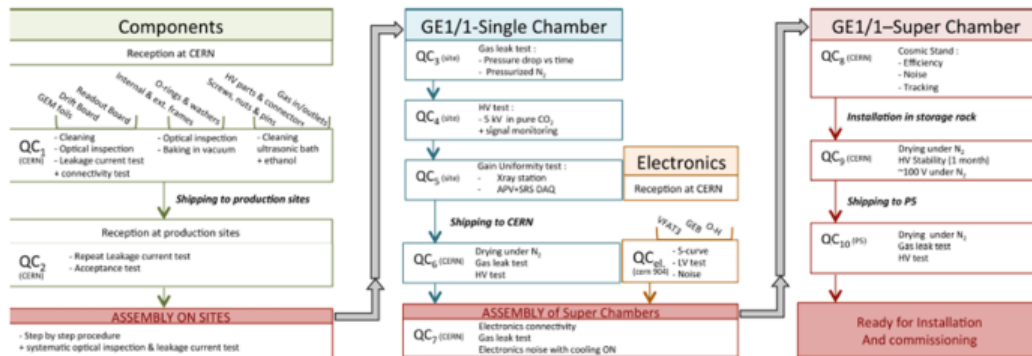


Figure 5.33: Schematic overview of the quality assurance and quality control procedures of the GE1/1 detectors.

delays may happen during the detector's assembly and quality control.

Quality Control	Expected time
QC1	2 days (all components)
QC2 + assembly	2 days
QC3	1 days
QC4	1 days
QC5	1 - 2 days
QC6	Until needed to assemble Superchamber
QC7	2 days
QC8	5 days
QC9	Waiting for installation
QC10	Quick test after transport

Table 5.5: Timeline for the GE1/1 assembly and commissioning.

In this section the main quality assurance and quality control procedures for the LS2 GE1/1 detectors implemented at CERN production site are described:

- Assembly component: QC1 - GE1/1 Detectors Components Inspection and Readout Board Connectivity Test
- GEM-foils: QC2 - Leakage Current Test;
- GE1/1 detector: QC3 - Gas Leak Test in CO_2 ;
- GE1/1 detector: QC4 - HV Test in CO_2 ;
- GE1/1 detector: QC5 - Gas Gain Calibration Test in Ar/CO_2 (70/30)

5.4.2 QC1 - GE1/1 Detectors Components Inspection and Readout Board Connectivity Test

All the GE1/1 detector components produced by industrial companies are delivered to CERN where they are immediately verified for defects and tested. Visual inspection is a commonly used method for quality assurance of the various detector components during the manufacturing and assembly. Therefore, after cleaning of all parts with the deionized water using ultrasonic baths or possible baking and sand blast procedures, an optical inspection of the main detector components is performed to ensure the integrity and the quality of the drift and readout board, internal and external frames, O-ring, gas inlets and outlets, etc. Some of the preliminary inspections and tests on detector components are described below:

Frame. An optical inspection is performed in order to identify possible cracks, mechanical unconformities and manufacturing defects on the epoxy glass structure of the internal and external frames. The dimensions of the frames are accurately measured using an high resolution digital caliper and a mechanical dial indicator, as well as the width and depth of the grooves along periphery of the external frame that will accommodate the Viton O-ring in order to ensure greater degree of the gas-tightness of the detector (see Figure 5.34a and 5.34b).

O-ring. An optical inspection and dedicated cleaning is performed in order to identify the integrity and the quality of the Vito O-ring. The external diameter dimensions are accurately measured using an high resolution digital caliper in order to ensure a correct coupling between the O-ring and the external frame and then to ensure a correct gas-tightness of the detector (see Figure 5.34c).

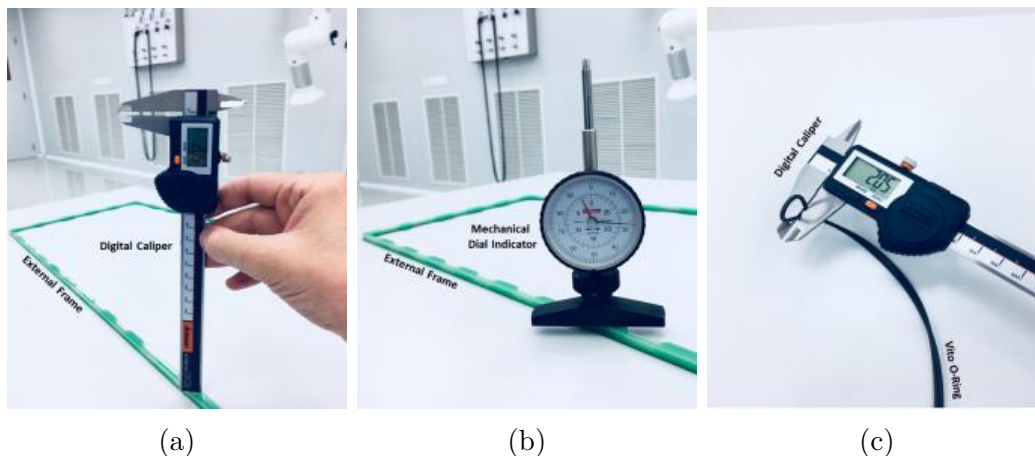


Figure 5.34: Pictures of the initial inspection and qualification procedures of the external frame and the Vito O-ring. The width and depth of the grooves along periphery of the external frame are accurately measured using an high resolution digital caliper and a mechanical dial indicator as well as the external diameter dimensions of the O-ring.

Drift Board. An optical inspection is performed in order to identify possible mechanical damage and surface anomalies on the drift electrode and PCB high voltage traces and pads. An high-pressure nitrogen gun is used to remove possible dust and/or processing residues on the drift board.

Readout Board. An initial inspection is performed to check the planarity of the readout board. The readout board under test is placed on a flat optical table (in horizontal position) and its possible bending is verified by measuring the height of the readout board in several points along its perimeter with respect to the plane of the optical table using an high resolution digital caliper (see Figure 5.35a and 5.35b). The test campaign results are reported in a dedicated summary table. Figure 5.35c shows an example of the heights measured in several points along the perimeter of a readout board under test using an high resolution digital caliper.

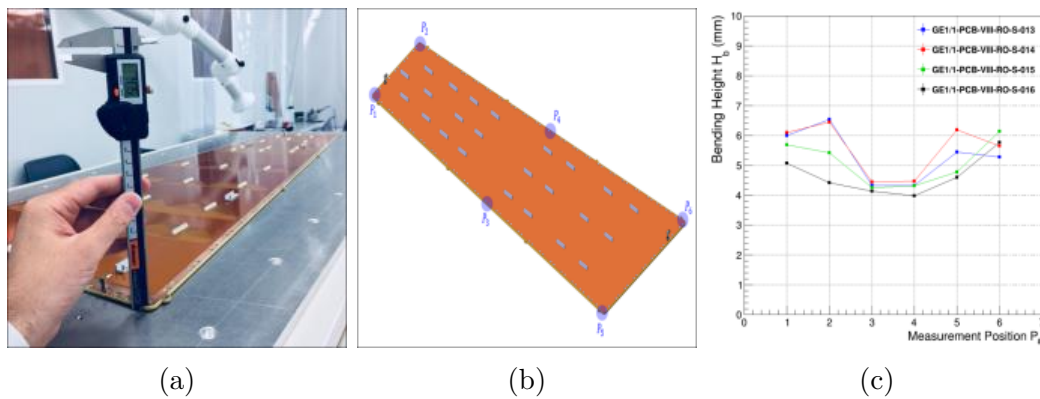


Figure 5.35: Pictures of the initial inspection and qualification procedures of the readout board. In order to check the flatness of the readout board, its height is accurately measured in several points along its perimeter with respect to the plane of the optical table using an high resolution digital caliper.

Additionally, an optical inspection is performed in order to identify possible macroscopic scratches and defects on the readout strips or Panasonic adopters for signal readout. However, it is not possible to verify the integrity and the quality of the readout board with a simple visual inspection because of the relatively small size of the readout strips and the large size of the readout board. A dedicated quality control test has been designed in order to inspect the readout board for possible shorts between strips or open strip-readout connections.

An automated testing system based on ARDUINO Mega 2560 microcontroller has been designed to simultaneously check all the strips in one readout sector. The ARDUINO platform is responsible for the data acquisition and system control. In order to perform the electrical test on the readout board, the testing system is plugged onto each Panasonic connector to check the continuity and/or possible shorts of the readout strips (see Figure 5.36).



Figure 5.36: Pictures of the QC1 connectivity test setup.

A signal is passed onto one of the pins of the Panasonic connector while the rest of the pins are simultaneously tested for a response. If a signal is detected in any of the neighbouring pins, this indicates the presence of a short circuit fault in the readout sector under test. This procedure is repeated for every pin on the connector. The readout board under test is rejected if more than 4 defects (short circuit) are identified in the whole readout board under test and/or more than 3 faulty channels inside the same connector. Figure 5.37 shows examples of short circuits and defects on the surface of the readout strips identified during initial inspection and qualification procedures of the readout board by using a digital microscope (specification: 2.0 *megapixel* resolution and 10× - 230× magnification range).



Figure 5.37: Microscopy photos of the readout strips showing some examples of defects and short circuits between the readout strips.

Once the acceptance criteria are fulfilled, complete assembly sets are used for the assembling at CERN production site and/or shipped to the other production and quality control sites.

5.4.3 QC2 - Leakage Current Test

The QC2 - leakage current test aims to determine the quality of a GEM-foil by measuring the maximum leakage current flowing on the surface of the GEM-holes. It is therefore mandatory to perform the QC2 test before, during and after the assembly of the GE1/1 detector. The GEM-foils are immediately verified after the reception at the CMS-GEM QA/QC facility at CERN. An optical inspection is first performed in order to identify macroscopic defects on the copper or Kapton layers, which could increase the probability of electrical breakdown and/or cause a direct electrical connection between the top and bottom sides of the foil. However, it is not possible to verify the integrity and the quality of the GEM-foils with a simple optical inspection because of the microscopic scale of the GEM-holes and the large size of the GEM-foils. A dedicated quality control test has been designed to this purpose.

When a voltage is applied across the GEM-foil, a current flows from its top to bottom due to the surface conductivity of the polyimide (Kapton) which is known as leakage current. The current cannot pass inside the polyimide, but a path of relatively low resistance exists over its surface. This is actually the interface between the polyimide surface and the gas as shown in Figure 5.38. This path has low resistance than the gas around the polyimide. This is more accurately called surface leakage current path. A small amount of leakage current flows over this path and can never be eliminated at all. The presence of dust, pollution deposits or defects, such as pieces of copper sticking out from the foil, could act as an electrical bridge between the top and bottom sides of the foil and provoke an increase the leakage current flowing through the polyimide surface. The leakage current also varies temporarily due to environmental changes like humidity, temperature, etc. Therefore, it is possible determinate the integrity and quality of the GEM-foils by measuring this leakage current.

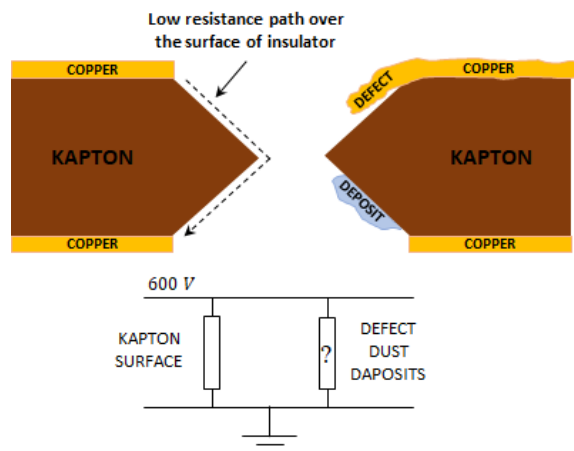


Figure 5.38: Schematic cross section of a GEM-foil and its equivalent resistive circuit.

The QC2 procedure is divided in five main steps in order to ensure the perfect functionality of the GEM-foils:

- GEM-foil preparation and cleaning;
- QC2 fast: GEM acceptance test I;
- QC2 long: GEM acceptance test II;
- QC2 post-assembly in clean room;
- QC2 fast in dry gas.

Each step has a specific procedure and output that will be described below.

5.4.3.1 GEM-foil preparation and cleaning

GEM-foils are delivered from CERN PCB Workshop to the CERN production sites (CMS-GEM QA/QC facility) in a sealed box to prevent any potential damage. To prevent contaminations that may compromise the GEM-foils performance, all operations during which the foils are exposed directly to the air must be carried out in clean room certified at least class 1000. The box itself must be cleaned before the opening phase to avoid contamination and/or deposition of dust on the GEM-foils. The GEM-foils have to be extracted one at a time by at least two trained operators who have to keep the foils well tensioned to avoid the formation of folds. The operators should not wear gloves but carefully wash their hands before starting the manipulation. In order to correctly test the foils and afterwards proceed with the detector assembly:

1. The GEM-foil is fixed to its dedicated frame with tape as shown on Figure 5.39. The support frame is realized with FR4, but aluminum or any other rigid, light and easily cleanable material could also be used.
2. The GEM-foil is cleaned with a dedicated anti-static and dust remover roll (see Figure 5.40) in order to remove any possible dust particle deposited on the foil during the delivery and the fixation on the frame.

5.4.3.2 QC2 fast: GEM acceptance test I

The first step of the acceptance test consists of applying voltage to the GEM-foil and measure the leakage current between the top and the bottom electrodes. The QC2 fast test is performed with a Multi Mega-ohmmeter (e.g. Insulation Tester MEGGER MIT485 by RECOM Electronic AG), also called Megger, connected to the GEM top and bottom HV pads (see Figure 5.41). The connection between the Megger and the GEM electrodes is done using custom HV clips shown on Figure 5.42. Since the surface conductivity of the GEM foil depends on the relative humidity of the environment, a meteo-station



Figure 5.39: Preparation of the GEM-foil and installation on the FR4 frame.



Figure 5.40: Cleaning of the GEM-foil with an anti-static roll in order to remove any possible dust particle deposited on the foil.

with temperature and humidity sensors is setup near the QC2 test stand. In order to obtain comparable results, the relative humidity in the clean room must be equal or less than 40%.

The procedure to perform the QC2 fast test is as follows:

1. The GEM-foil and its frame are placed in vertical position, for example against a wall of the clean room (see Figure 5.42).

5.4. Requirements for GE1/1 Quality Assurance/Quality Control assessment

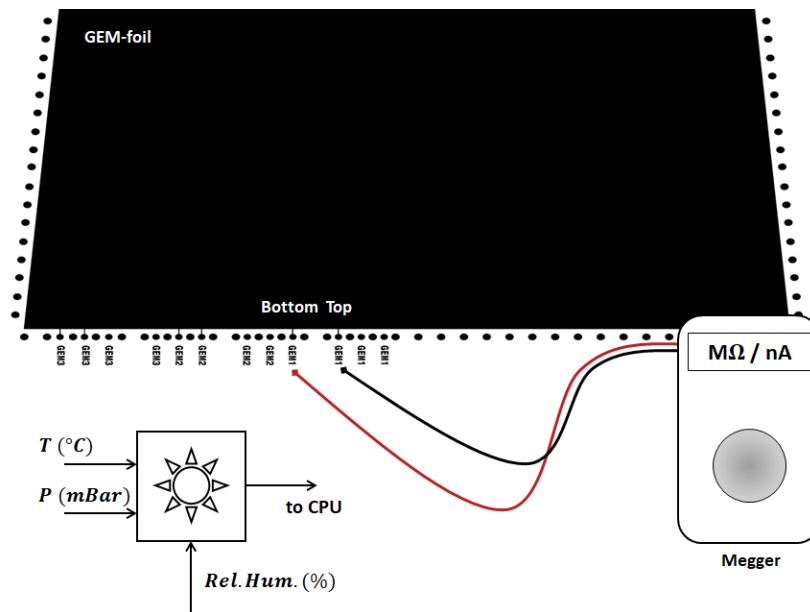


Figure 5.41: Schematic view of the QC2 fast test setup (acceptance test I).

2. The Megger is connected to the GEM HV pads with the custom HV clip (see Figure 5.42) and the high voltage is set to 550 V.

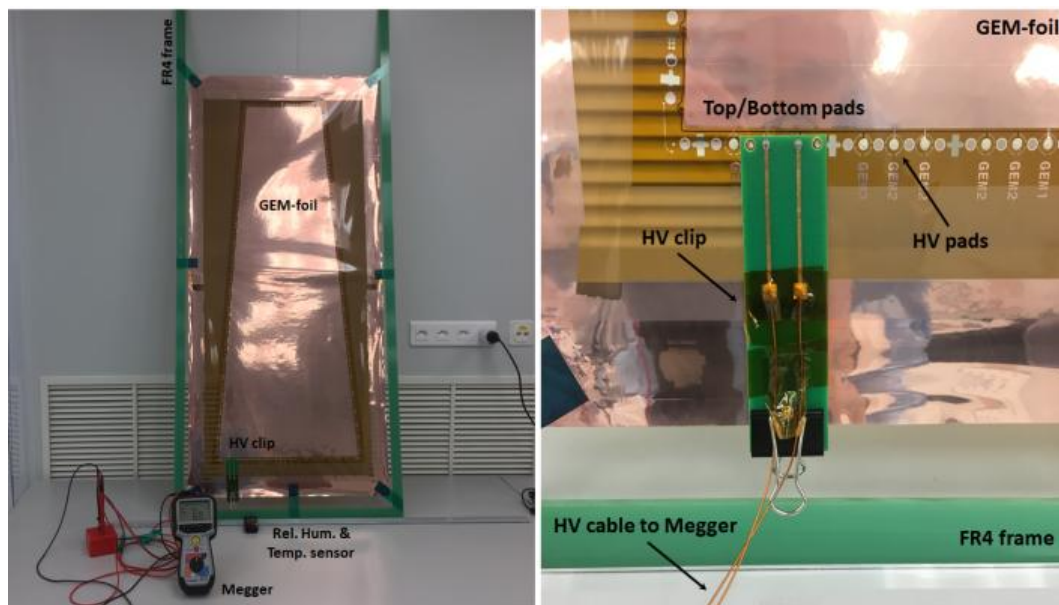


Figure 5.42: Picture of the QC2 fast test on a GEM-foil (acceptance test I).

3. The impedance of the GEM-foil is measured and the number of possible sparks is counted after 30 s and then every minutes over a period of 10 minutes.
4. The time, the applied voltage, the impedance of the foil, the leakage

current and the number of sparks are reported in a dedicated summary table.

Time [min]	Voltage [V]	Impedance [$G\Omega$]	Current [nA]	Sparks	Total Sparks
0.5	550	3.11	176	6	6
1	550	3.73	147	3	9
2	550	5.90	93	1	10
3	550	7.60	72	0	10
4	550	8.00	68	1	11
5	550	8.50	64	1	12
6	550	9.20	59	1	13
7	550	9.60	57	0	13
8	550	10.50	52	0	13
9	550	10.00	55	0	13
10	550	11.00	50	0	13

Table 5.6: Typical QC2 fast summary table for an accepted GEM-foil.

The GEM-foil is accepted if its impedance is above $10 G\Omega$ and the number of sparks is lower than 2 during the last two/three minutes of test. If the number of sparks exceeds this limit, the foil needs to be cleaned again with the anti-static roll. If the problem persists after several cleaning attempts, the foil has to be sent back to the production CERN PCB workshop and cleaned with de-ionized water in ultrasonic baths. Therefore, the QC2 fast acceptance test is performed at each step of the assembly procedure of the GE1/1 detectors to identify possible damages on the GEM-foils and to remove the dust that could have been produced during the mounting of the internal frame (see Section 5.4.3.1).

5.4.3.3 QC2 long: GEM acceptance test II

The second step of the acceptance test consists of measuring the high voltage long-term stability of the GEM-foils in a dry environment. The so-called QC2 long test is performed only at CERN production site before the shipment of the foils to other production sites. It consists of monitoring the leakage current and the possible sparks when the GEM-foil is subject to high voltage, typically up to $600 V$ during a period of 6-7 hour. The value of the voltage applied on the GEM-foil during the QC2 long test should be higher than the real operating voltage in order to have a large safety factor. However, this value should not exceed the breakdown voltage of the gas under the penalty of triggering self-sustained discharge in the gas. The breakdown voltage is the experimental value necessary to start a discharge in a gas between two electrodes. It is a combined function of the distance between the two electrodes, the composition of gas surrounding the electrodes and the gas pressure. The breakdown voltage V_b is described by the Paschen's law:

$$V_b = \frac{B \times pd}{\ln(A \times pd) - \ln[\ln(1 + \frac{1}{\gamma_{SE}})]} \quad (5.1)$$

where A and B are empirically calculated constants, γ_{SE} the second Townsend coefficient, p the gas pressure (*Torr*) and d the distance between the electrodes (*cm*). Therefore, knowing the product pd corresponding to the GEM-structure:

$$pd = \left(7.5 \times 10^2 \text{ [Torr]} (1 \text{ atmosphere})\right) \times \\ \times \left(5.0 \times 10^{-3} \text{ [cm]} (Polyimide \text{ thickness})\right) \approx 3.8 \text{ [Torr cm]}$$

it is possible to obtain the breakdown voltage in pure Nitrogen given by Paschen's curves. Typical breakdown curves for plane-parallel electrodes are shown in Figure 5.43.

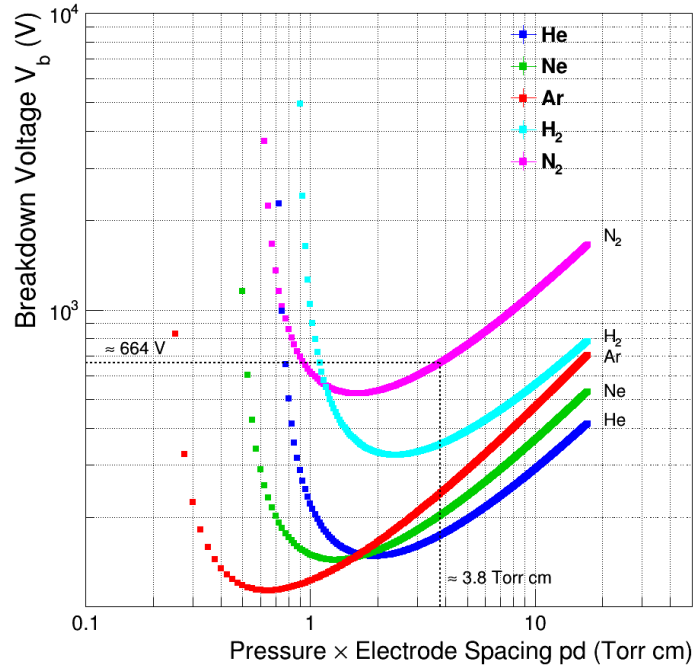


Figure 5.43: Paschen Curve obtained for helium, neon, argon, hydrogen and nitrogen, using the expression for the breakdown voltage as a function of the parameters A , B and γ , the second Townsend coefficient [72].

As shown on Figure 5.44, the GEM-foils under test are placed in a dedicated plexiglass box filled with pure nitrogen in order to control the polyimide surface conductivity and the breakdown voltage, and to reduce the relative humidity at the same time. The temperature and the humidity inside of the box are monitored using a professional Meteo-station and a dedicated LabVIEW-software that records the data every minutes over the entire test. The GEM-foils are powered using a programmable HV power supply (CAEN R1471HETD module) that has a current monitoring resolution of 50 pA . The QC2 long test experimental setup for leakage current measurements is shown on Figure 5.44.

5. The Assembly, Quality Control and Commissioning of the GE1/1 detectors

A picture of the QC2 long test setup at CMS-GEM QA/QC facility at CERN is shown on Figure 5.45.

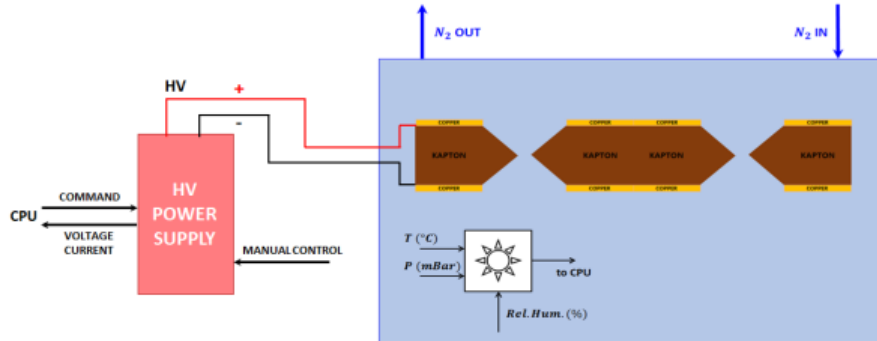


Figure 5.44: Schematic view of the QC2 long test setup (acceptance test II).

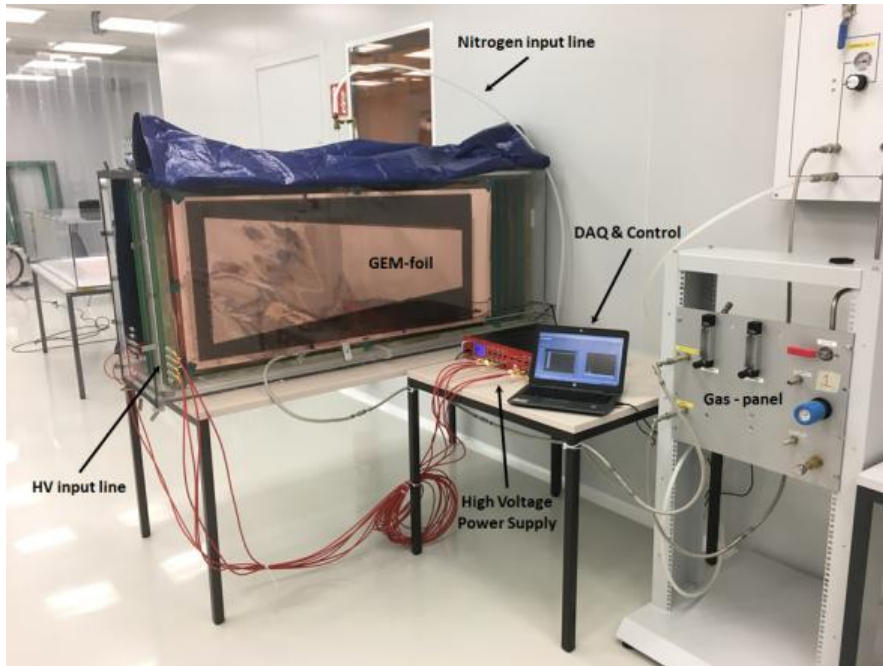


Figure 5.45: Picture of the QC2 long test setup at CMS-GEM QA/QC facility.

The procedure to perform the QC2 long test is as follows:

- The GEM-foils are cleaned with the anti-static roll in order to remove the possible dust particles deposited on the foils during the previous operations.
- The GEM-foils are carefully inserted into the HV box one at the time by keeping note of the serial number of the foils and batch.

5.4. Requirements for GE1/1 Quality Assurance/Quality Control assessment

- A custom clips is fixed to the HV pads to each foil (see Figure 5.42). A standard multimeter is used to check the connectivity between the custom clips and the SHV connectors outside of the nitrogen box.
- A Meteo-station is started by setting the recording rate to one measurement per minute and inserted it into the nitrogen box.
- The nitrogen flow rate is set to $50 L/hr$ and left it flush until the relative humidity inside of the nitrogen box is equal or lower than 7% (typically 48 hours).
- The manual control of the power supply is used to apply $600 V$ across the GEM-foils with a total ramping time of couple of seconds. Such technique allows to burn and blow away the possible dust particles trapped in the GEM-holes by non-destructive discharges. On the contrary, applying the same voltage with a long ramping time and/or applying a lower voltage could not be enough to burn the dust particles, could fix them to the holes, lead to a permanent contamination and/or trigger several discharge.
- after the previous cleaning procedure, the voltage applied on the GEM-foils is slowly ramped up to reach an operating voltage of $600 V$, by steps of $100 V$. After 1-2 hours of stabilization at the maximum voltage of $600 V$, the voltage is set to $100 V$ for several minutes, then back to $600 V$ and so on. The difference of current delivered by the power supply in these series of alternating voltages corresponds to the real leakage current of the foil. An automated test protocol has been developed using LabVIEW in order to measure the leakage current by applying these voltage cycles to the GEM-foils and monitoring their stability throughout this procedure.

The acceptance criteria for the QC2 long leakage current test correspond to a leakage current of about $3 nA$ and a total number of discharges lower than 3 when applying $600 V$ in pure nitrogen during the last 6 hours of test. Typical results from the QC2 long leakage current test can be seen on Figure 5.46 and Figure 5.47.

- Figure 5.46 show a typical leakage current test results of an rejected GEM-foil. In addition to the discharges observed during the time period of around 3 hours, the leakage current after stabilization was higher than $4.9 nA$, i.e. a leakage current approximately 5 times higher than the one allowed by the QC2 long acceptance criteria for the LS2 GE1/1 mass production.
- Figure 5.47 show a typical leakage current test results of an accepted GEM-foil. The leakage current after stabilization was about $0.5 nA$, in agreement with the QC2 long acceptance criteria for the LS2 GE1/1 mass production.

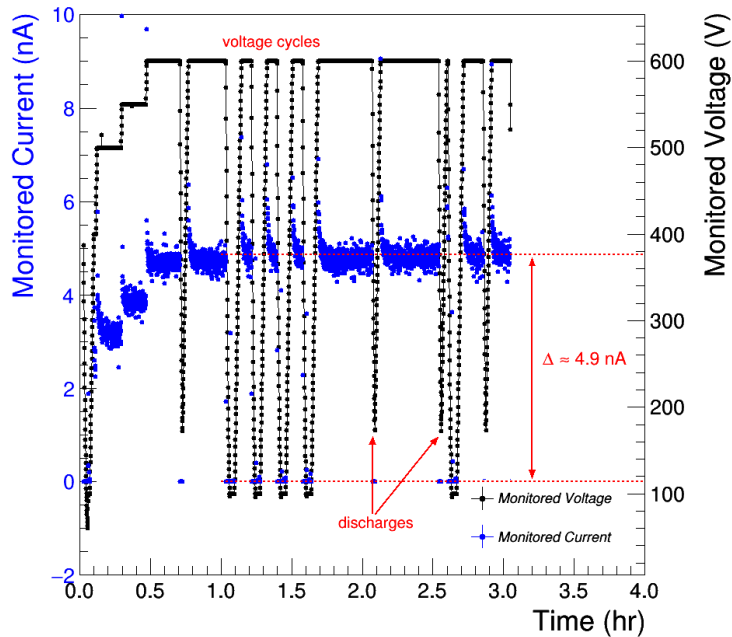


Figure 5.46: Results from the QC2 long leakage current test of a rejected GEM-foil: voltage and current delivered by the power supply as a function of time in dry nitrogen environment with an ambient average temperature of $22.4\text{ }^{\circ}\text{C}$ and ambient relative humidity equal to 7.9%.

5.4.3.4 QC2 post-assembly in clean room

After the GE1/1 detector is assembled, it is mandatory to check the impedance and the discharge rate of the GEM-foils before to move out the assembled detector from the clean room. As for the QC2 fast acceptance test, this test is carried out using a Multi Mega-ohmmeter (Megger). The voltage is applied on the pads of the HV distribution present on the Drift Board (Figure 5.48). Since this test is performed in air, it is necessary to measure the ambient temperature and the relative humidity in the vicinity of the detector. The procedure to perform the QC2 fast test on a GE1/1 detector is as follows:

1. The Megger is connected to the appropriate GEM HV pads by putting the negative pin on the top electrode and the positive pin on the bottom electrode (Example 1: to test first GEM-foil the negative pin of the Megger is connected to the GEM1 top pad and the positive pin to the GEM1 bottom pad. Example 2: to test the second transfer gap the negative pin of the Megger is connected to the GEM02 bottom pad and the positive pin to the GEM3 top),
2. The high voltage is set to 550 V on the Megger. The impedance and

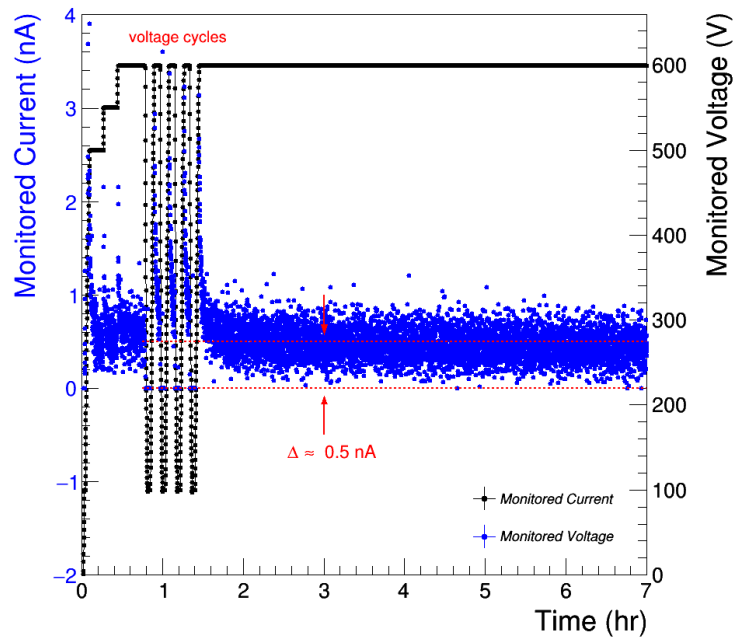


Figure 5.47: Results from the QC2 long leakage current test of an approved GEM-foil: voltage and current delivered by the power supply as a function of time in dry nitrogen environment with an ambient average temperature of $21.9\text{ }^{\circ}\text{C}$ and ambient relative humidity equal to 6.1%.

count the number of sparks are measured after 30 s and then every minute over a period of 10 minutes.

The detector is accepted if the impedance of all GEM-foils is above $10\text{ G}\Omega$ after few minutes and no sparks can be observed after 10 minutes. Similarly, the impedance of the gaps must reach $100\text{ G}\Omega$ or more after only few minutes, with no sparks. The impedance of the induction gap is measured by applying 550 V of potential difference between the high voltage pad of the lower electrode of the third GEM-foil and the signal pad of the Panasonic-to-LEMO adapter where all the 128 readout channels are grounded. An impedance of $100\text{ G}\Omega$ have to be measure over all the 24 readout connectors. If the impedance of the induction gap is lower than $100\text{ G}\Omega$, and/or if several discharges occur at 550 V , there might be a short circuit of a weak point caused by the bending of the readout board toward the third GEM-foil. In latter case the detector have to be disassembled and fixed.

After a GE1/1 detector passes this test, it can leave the clean room and mounted on the QC3 test stand to start the gas tightness measurement. The detectors that does not pass this step are not moved out of the clean room but immediately re-opened for further investigations. If the problem is identified

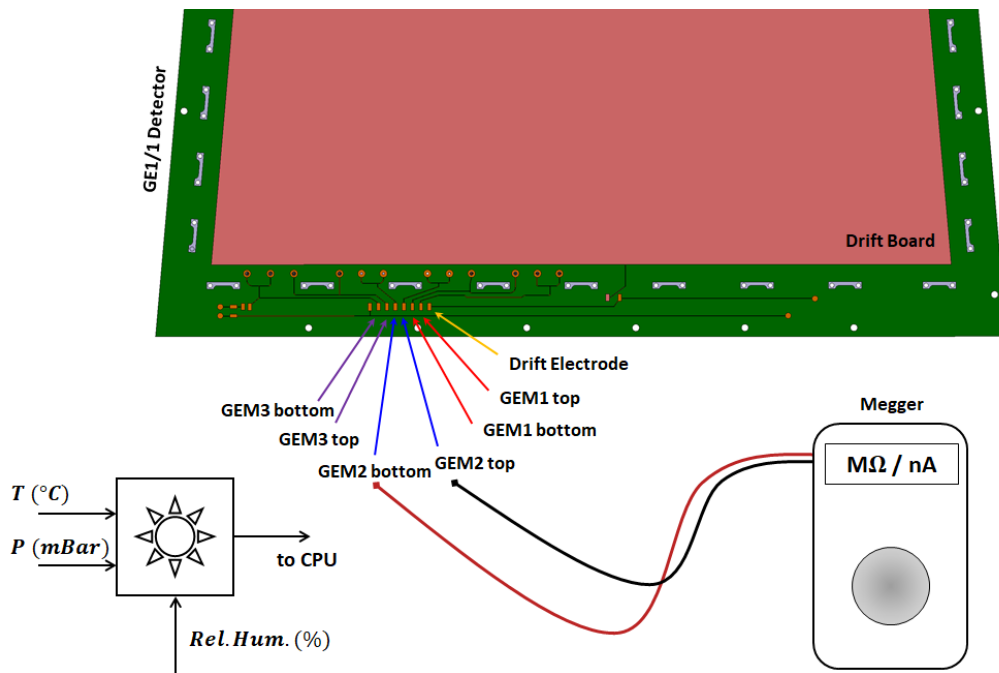


Figure 5.48: Picture of the QC2 post-assembly test setup on a GE1/1 detector.

and fixed, the QC2 fast test is performed again before the detector can move to the next QC step.

5.4.3.5 QC2 fast in dry gas

The QC2 fast test in dry gas is performed just before mounting the HV circuit on the detector. Moreover, it is usually the first step of every investigations or repairing protocols that start after a chamber showed a suspicious behavior (e.g. sparking at high gain, instability, high-rate spurious signal, etc.). To perform QC2 fast in dry gas, the GE1/1 detector must be flushed for at least 5 hours with pure CO_2 at a gas flow rate of 5 L/hr . The CO_2 gas is useful to dry out the GEM-foils, to prevent electron amplification and therefore to avoid the possible propagation of discharges. After the detector is flushed, the procedure is substantially identical for QC2 post assembly in clean room. However, the acceptance criteria are different in dry gas: the impedance of the GEM-foils should be above 20 $G\Omega$ after one minute with no repetitive discharges. Few discharges may occur after few seconds due to the deposition of dust on the GEM-foils. After the dust particles are blown away, the GEM should be completely quiet. Similarly, the impedance of the detector's gaps should be above 100 $G\Omega$ after few seconds, with no discharges.

5.4.4 QC3 - Gas Leak Test in CO_2

The QC3 gas leak test is the first quality control test performed on a new assembled GE1/1 detector and aims to identify possible gas leak and even-

5.4. Requirements for GE1/1 Quality Assurance/Quality Control assessment

tually measuring the gas leak rate by monitoring the drop of the internal over-pressure as a function of the time. The drift and readout PCB boards are closed with several hundred of screws, which can be possible openings to the external environment. Gas leaks are not only pointless waste of gas but also a source of possible pollution, humidity and unknown species from the external environment that could contaminate the active gas volume, react in the avalanche plasma, trigger the polymerization and lead a degradation of the performance of the detector.

A schematic overview of the QC3 gas system is shown in Figure 5.49 (top). The gas input is connected to a CO_2 gas line equipped with a pressure regulator with the output pressure being set to a maximum of 50 *mBar* millibars. The input flow meter, together with its manual valve, allows controlling the gas flow rate at the entrance of the detector while the output flow-meter allows to monitor the output flow and therefore to identify large leaks. The input and output valves are used to isolate the detector from the rest of the gas system during the gas leak test. The calibration of the gas system itself is done before connecting the detector, as indicated in Figure 5.49 (bottom). A digital pressure transducer is connected between the input and the output valves in order to monitor the over-pressure inside of the gas system only or of the detector + gas system. Additional atmospheric pressure and ambient temperature sensors are located nearby the test stand. All the sensors are then connected to a ARDUINO Mega 2560 microcontroller that is responsible for the data acquisition and slow control.

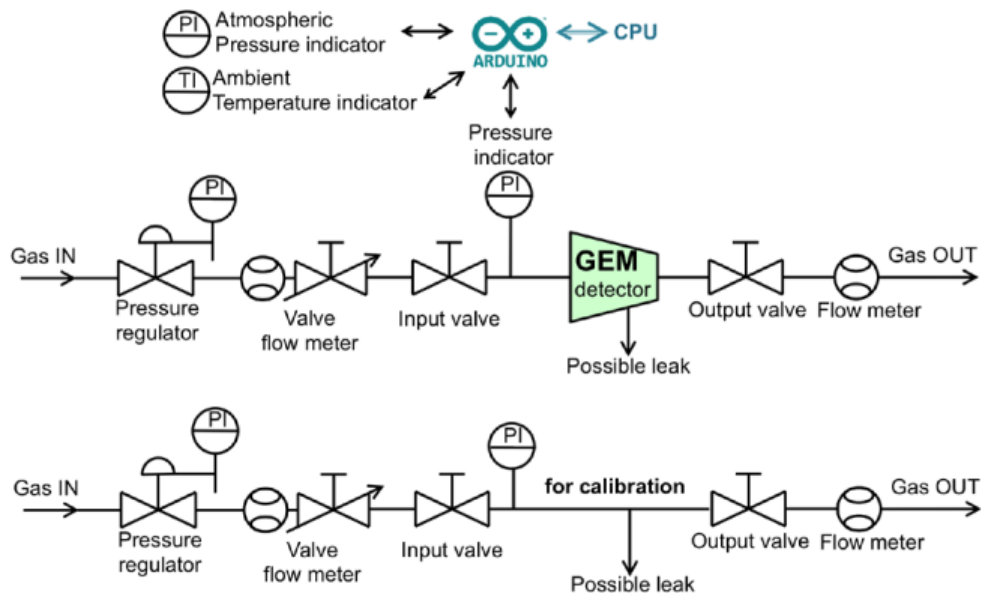


Figure 5.49: QC3 gas leak test experimental setup.

The QC3 gas leak test is divided into two stages:

- 1st stage: gas system calibration;

5. The Assembly, Quality Control and Commissioning of the GE1/1 detectors

- 2nd stage: detector + gas system gas tightness measurement.

The procedure to perform the calibration of the gas system proceeds as follows:

1. The input and the output lines of the gas system are connected together, as indicated on Figure 5.49 (bottom).
2. The input and the output valves of the gas system are opened and the manual valve of the input flow-meter is adjusted in order to allow the CO_2 to flow through the system.
3. The input gas flow rate is set to 5 L/hr . The output flow rate should be immediately visible on the output flow-meter.
4. the over-pressure in the gas system is set to about 25 $mBar$. In order to pressureze the gas system, the output valve of the gas system is closed and therefore the pressure inside the system begin to ramp up. As soon as the over-pressure reaches $\sim 25 mBar$, the input valve is closed. Then the valve of the input flow meter is also closed.
5. After the gas system pressurization, the DAQ system is started in order to monitor the drop of the internal over-pressure as a function of the time. The DAQ system records the data from the over-pressure inside the gas sytem and the environmental parameters (room temperature and atmospheric pressure) every minutes.

The gas system is validated if the pressure drop in the gas system does not exceed 1 $mBar$ per hour. Typical result from the calibration of the gas system can be seen on Figure 5.50.

After the gas system validation, the QC3 gas leak test is performed on the the GE1/1 detector. The procedures to perform the QC3 gas leak test on the GE1/1 detector are basically identical to the calibration procedure for the gas system:

1. The detector's gas inlet and outlet are connected to the gas system as indicated on Figure 5.49 (top).
2. The input and the output valves of the gas system are opened and the manual valve of the input flow-meter is adjusted in order to allow the CO_2 to flow through the detector under test.
3. The input gas flow rate is set to 5 L/hr . The output flow rate should be immediately visible on the output flow-meter.

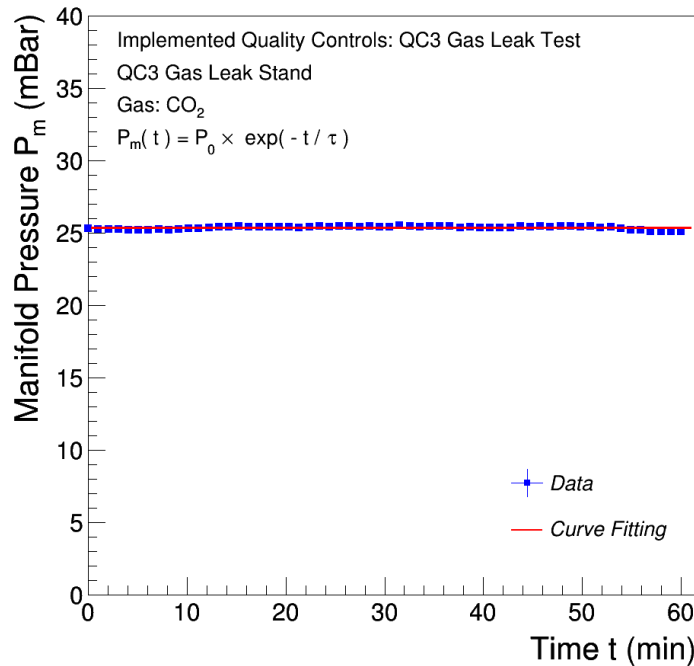


Figure 5.50: Result from the calibration of the gas system installed in the QC3 Gas Leak Stand. The over-pressure is stable over the entire gas leak test, with negligible fluctuations within 1% of its initial value. The pressure drop is modeled by the function $P_m(t) = P_0 \times \exp(-t/\tau)$ which provides a gas leak time constant $\tau \sim 10^4$ hr, demonstrating a perfect gas tightness of the entire gas system under test.

4. The over-pressure in the detector under test is set to about 25 mBar. In order to pressurize the detector, the output valve of the gas system is closed and therefore the pressure inside the detector begins to ramp up. As soon as the over-pressure reaches ~ 25 mBar, the input valve is closed. Then the valve of the input flow meter is also closed. Since the GE1/1 detectors cannot sustain over-pressure higher than 40-50 mBar, a safety relief valve is installed in the gas line in order to avoid irreparable damage to the detector under test.
5. After the detector pressurization, the DAQ system is started in order to monitor the possible drop of the internal over-pressure as a function of the time. The DAQ system records the data from the over-pressure inside the detector and the environmental parameters (room temperature and atmospheric pressure) every minutes.

The LS2 GE1/1 triple-GEM detector under test is validated if the pressure drop in the detector + gas system does not exceed 7 mBar per hour, i.e. ~ 0.12 mBar/min. Typical results from the QC3 gas leak test can be seen on

Figure 5.51, 5.52 and 5.53:

- Figure 5.51 shows an example of a GE1/1 detector (GE1/1-X-S-CERN-0002) which has not passed the QC3 gas leak test: ~ 32.5 minutes after the starting of the QC3 Gas Leak Test, the pressure drop was about 22.9 mBar resulting in a gas leak rate of $\sim 0.70 \text{ mBar}/\text{min}$, i.e. a gas leak rate approximately 6 times higher than the one allowed by the QC3 acceptance criteria for the LS2 GE1/1 mass production.

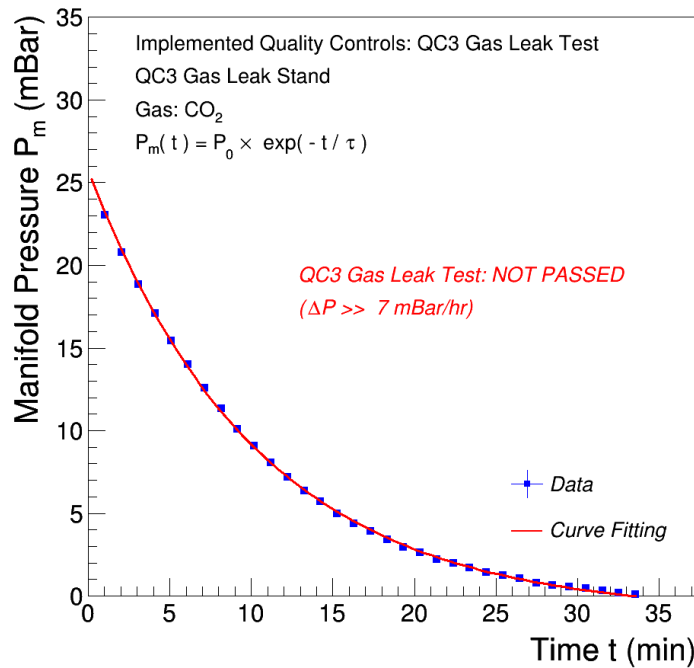


Figure 5.51: Results from the QC3 Gas Leak Test on the GE1/1-X-S-CERN-0002 detector. The pressure drop is modeled by the function $P_m(t) = P_0 \times \exp(-t/\tau)$ which provides a gas leak time constant $\tau \sim 6 \text{ min}$.

- Figure 5.52 shows an example of a short GE1/1 detector (GE1/1-X-S-CERN-0004) which has passed the QC3 gas leak test: ~ 60.0 minutes after the starting of the QC3 Gas Leak Test, the pressure drop was about 1.03 mBar resulting in a gas leak rate of $\sim 0.017 \text{ mBar}/\text{min}$, in agreement with the QC3 acceptance criteria for the LS2 GE1/1 mass production.
- Figure 5.53 shows an example of a long GE1/1 detector (GE1/1-X-S-CERN-0004) which has passed the QC3 gas leak test: ~ 60.0 minutes after the starting of the QC3 Gas Leak Test, the pressure drop was about 0.96 mBar resulting in a gas leak rate of $\sim 0.016 \text{ mBar}/\text{min}$, in agreement with the QC3 acceptance criteria for the LS2 GE1/1 mass production.

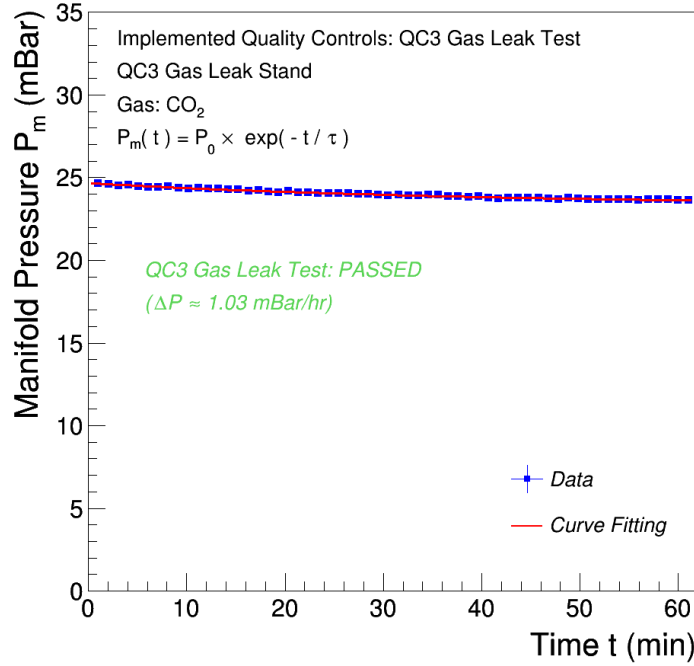


Figure 5.52: Results from the QC3 Gas Leak Test on the GE1/1-X-S-CERN-0004 detector. The pressure drop is modeled by the function $P_m(t) = P_0 \times \exp(-t/\tau)$ which provides a gas leak time constant $\tau \sim 25 \text{ hr}$.

As described previously, the idea of the QC3 gas leak test is to pressurize the detector under test up to 25 mBar of over-pressure and then close the gas volume with input and output valves. The over-pressure of 25 mBar is slightly above the expected value during the operation in the Muon Spectrometer of the CMS experiment. In case of gas leaks, the over-pressure in this volume drops down to zero with a time scale that depends on the leak rate and on the initial over-pressure. Knowing the density of the gas $\rho(t)$ inside the gas volume of the detector V_{det} :

$$\rho(t) = \frac{m(t)}{V_{det}} \quad (5.2)$$

where $m(t)$ is the mass of the gas, the density variation in case of gas leak can be calculated as follows:

$$\frac{d\rho(t)}{dt} = \frac{1}{V_{det}} \times \frac{dm(t)}{dt} \quad (5.3)$$

The $dm(t)/dt$, also called mass flow rate, can be expressed as follows:

$$\frac{dm(t)}{dt} = -S \times v \times \rho(t) \quad (5.4)$$

where S is the area of the leak, v the velocity of the gas escaping the system and the negative sign in the equation represents a loss of density.

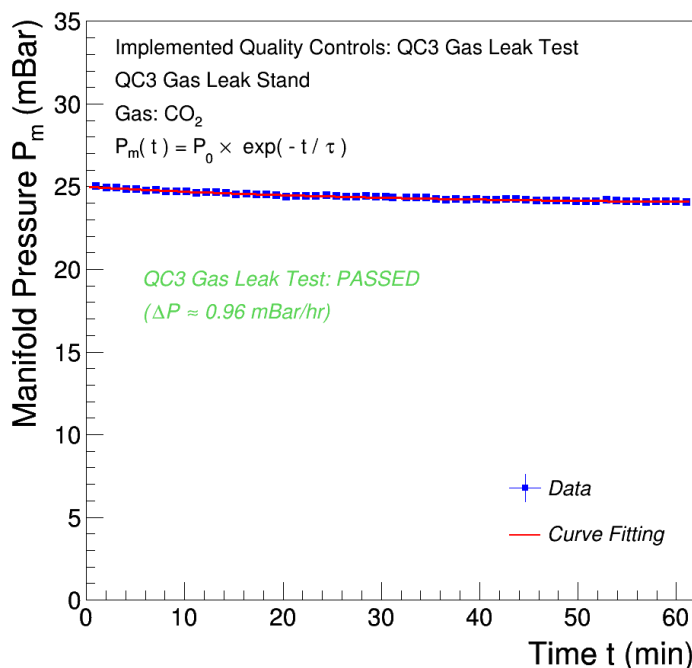


Figure 5.53: Results from the QC3 Gas Leak Test on the GE1/1-X-L-CERN-0004 detector. The pressure drop is modeled by the function $P_m(t) = P_0 \times \exp(-t/\tau)$ which provides a gas leak time constant $\tau \sim 29$ hr.

Fluid dynamics theory show that for very tiny orifices, the velocity of the gas escaping the system is approaches the sound velocity (*choked* or *sonicflow*) [73] and can be expressed as follows:

$$u = \sqrt{2(\gamma RT_{det.})/M} \quad (5.5)$$

where R is the ideal gas constant, $T_{det.}$ the absolute temperature inside the detector (considered constant), M the molar mass of the gas and γ the adiabatic coefficient ($\gamma = 5/3$ for noble gases). All these parameters are constant. Substituting back into the equation 5.3, the density variation in case of gas leak can be rewritten as follows:

$$\frac{d\rho(t)}{dt} = -\frac{S \times \sqrt{2(\gamma RT_{det.})/M}}{V_{det.}} \times \rho(t) \quad (5.6)$$

Considering the ideal gas law:

$$P(t)V_{det.} = n(t)RT_{det.} \quad (5.7)$$

where $n(t) = m(t)/M$ and $V_{det.} = m(t)/\rho(t)$, the density of the gas can be expressed as follows:

$$\rho(t) = P(t) \times \frac{M}{RT_{det.}} \quad (5.8)$$

Substituting back into the equation 5.6, the density variation can be rewritten in terms of over-pressure variation as follows:

$$\frac{dP(t)}{dt} = -\frac{S \times \sqrt{(\gamma RT_{det.})/M}}{V_{det.}} \times P(t) \quad (5.9)$$

Solving the differential equation, the over-pressure inside of the detector can be expressed as an exponential function of time:

$$P(t) = P_0 \times \exp\left(-\frac{S \times \sqrt{(\gamma RT_{det.})/M}}{V_{det.}} \times t\right) = P_0 \times \exp\left(-\frac{t}{\tau}\right). \quad (5.10)$$

where the parameter τ is the gas leak time constant related to the gas composition and characteristics of the gas leak. The gas leak time constant quantifies how fast the over-pressure inside the detector decreases as a function of the time.

Figure 5.54 show an example of a typical result from the QC3 gas leak test on a GE1/1 detector: ~ 60.0 minutes after the starting of the QC3 Gas Leak Test, the pressure drop was about 1.36 mBar resulting in a gas leak rate of $\sim 0.02 \text{ mBar/min}$, in agreement with the QC3 acceptance criteria for the LS2 GE1/1 mass production. The pressure drop is modeled by the function $P_m(t) = P_0 \times \exp(-t/\tau)$ which provides a gas leak time constant $\tau \sim 18 \text{ hr}$. The figure show also the residual plot, i.e. the deviation of each data point from the calculated exponential fit, in the subplot below the plot of the experimental data and the curve fitting. Plotting the residuals in this way gives a graphical representation of the goodness of the fit. Since the residuals fluctuate randomly about zero and do not show any overall upward or downward curvature, or any long wavelength oscillations, the proposed model would seem to describe the experimental data well.

Assuming that the volume of the detector $V_{det.}$ and the temperature inside it $T_{det.}$ are constants, the pressure inside the detector can be expressed as follows:

$$P(t) = P_{out} + P_0 e^{-\frac{t}{\tau}} \quad (5.11)$$

where P_{out} is the environmental pressure, P_0 the over-pressure inside the detector. As described previously, in order to estimate the gas particles loss rate, i.e. the lost moles rate, the gas mixture can be approximate to an ideal gas:

$$P(t) V_{det.} = n(t) R T_{det.} \quad (5.12)$$

Rearranging and differentiating implicitly the equation 5.12 with respect to time, the variation in the number of moles due to the gas leak can be rewritten as follows:

$$\frac{dn(t)}{dt} = \left(\frac{V_{det.}}{R T_{det.}}\right) \times \left(\frac{dP(t)}{dt}\right) = \left(-\frac{V_{det.}}{R T_{det.}}\right) \times \left(\frac{P_0}{\tau} e^{-\frac{t}{\tau}}\right) \quad (5.13)$$

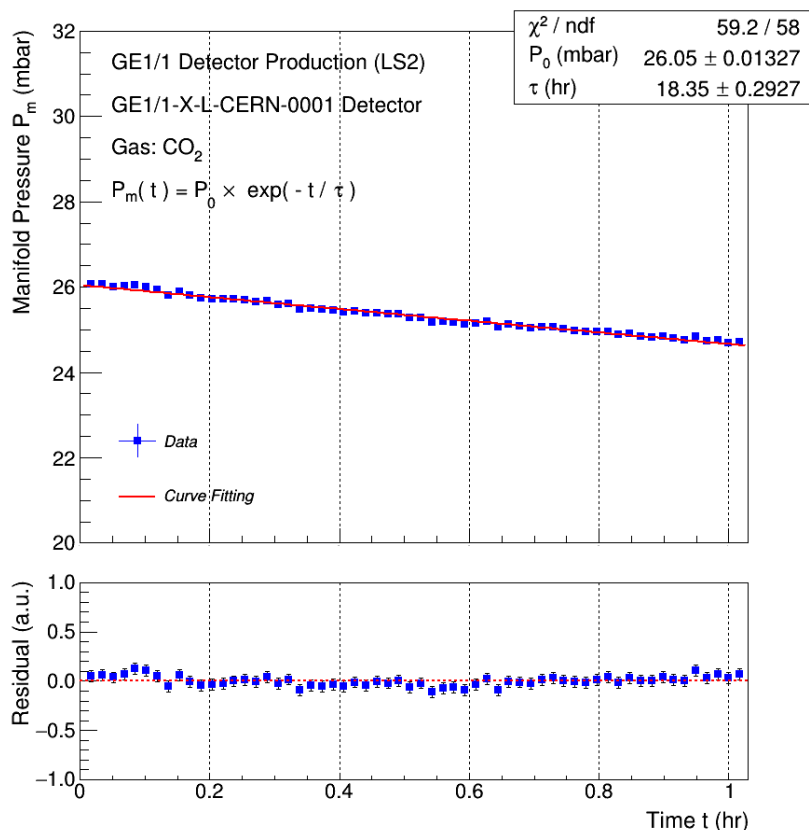


Figure 5.54: Top panel: Results from the QC3 Gas Leak Test on the GE1/1-X-L-CERN-0001 detector. The pressure drop is modeled by the function $P_m(t) = P_0 \times \exp(-t/\tau)$ which provides a gas leak time constant $\tau \sim 18 \text{ hr}$. Bottom panel: Residual data after subtraction of fit. The residuals appear randomly scattered around zero indicating that the proposed model describes the data well.

where the negative sign in the equation represents a loss of gas particles. The latter quantity is the only one needed in order to estimate the gas volume leakage from the detector. Therefore, the gas particles emitted outside the detector will occupy a certain volume depending on the environmental conditions outside the detector by following the ideal gas law:

$$\left(\frac{dV(t)}{dt} \right) P_{out} = \left(\frac{dn(t)}{dt} \right) R T_{out}, \quad (5.14)$$

where P_{out} and T_{out} are now the absolute pressure and absolute temperature outside the detector. Without loss of generality, it is reasonable to assume that the temperature inside the detector is the same as the outside environment,

then:

$$\frac{dV(t)}{dt} = \left(\frac{dn(t)}{dt} \right) \times \frac{R T_{det.}}{P_{out}}, \quad (5.15)$$

Substituting back into the equation 5.13, the gas volume leakage rate can be rewritten in terms of over-pressure variation as follows:

$$\frac{dV(t)}{dt} = \left(-\frac{V_{det.}}{P_{out}} \right) \times \left(\frac{P_0}{\tau} e^{-\frac{t}{\tau}} \right) \quad (5.16)$$

The maximum gas volume emitted per unit time by one GE1/1 detector as well as the expected volume released during the operation in the Muon Spectrometer of the CMS experiment (in latter case the over-pressure is constant) can be then estimated as follows:

$$\left. \frac{dV(t)}{dt} \right|_{t=0} = \left(-\frac{V_{det.}}{P_{out}} \right) \times \left(\frac{P_0}{\tau} \right) \quad (5.17)$$

For a short GE1/1 detector $V_{det.} \approx 2.6 L$, $\tau = 3.04 hr$ (calculated for a 7 mBar loss in 1 hr), $P_0 = 25 mBar$ and $P_{out} = 964 mBar$ (mean pressure in the Muon Spectrometer of the CMS experiment), the gas volume leakage rate is:

$$\left. \frac{dV(t)}{dt} \right|_{short} = -0.022 L/hr.$$

For a long GE1/1 detector $V_{det.} \approx 3.0 L$, $\tau = 3.04 hr$ (calculated for a 7 mBar loss in 1 hr), $P_0 = 25 mBar$ and $P_{out} = 964 mBar$ (mean pressure in the Muon Spectrometer of the CMS experiment), the gas volume leakage rate is:

$$\left. \frac{dV(t)}{dt} \right|_{long} = -0.026 L/hr.$$

Therefore, the equation 5.17 allows to predict the gas volume leakage rate $dV(t)/dt$ expected in a GE1/1 detector during the operation in the Muon Spectrometer of the CMS experiment as a function of the over-pressure P_0 of the system for a certain value of the acceptance limit of the QC3 gas leak test, i.e. the gas leak time constant τ (see Figure 5.55) or the use of the same equation allows one to predict the gas volume leakage rate expected in a GE1/1 detector during the operation in the Muon Spectrometer of the CMS experiment as a function of the acceptance limit of the QC3 gas leak test, i.e. the gas leak time constant, for a certain value of the over-pressure of the system. (see 5.56).

The major gas leak sources encountered in the GE1/1 detectors during the mass production phase were:

- Deformation, unusual position or absence of some polyamide washers on the drift and/or readout board;

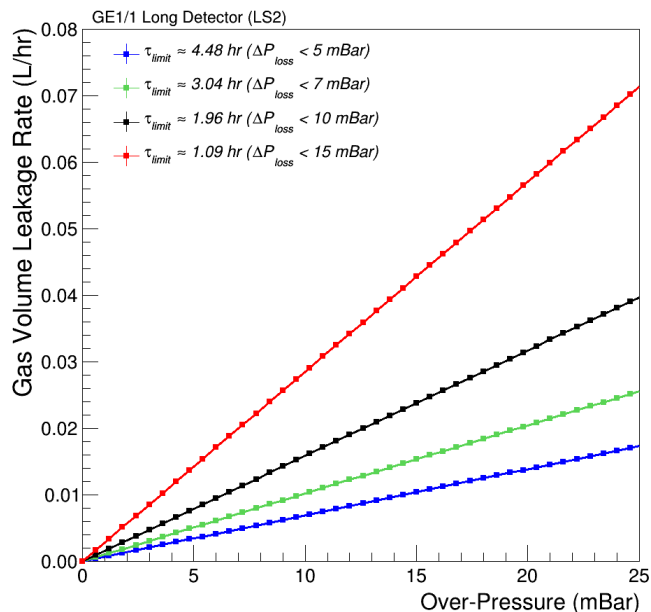


Figure 5.55: Gas volume leakage rate $dV(t)/dt$ as a function of the working condition, i.e. the over-pressure P_0 in a GE1/1 detector during the operation in the Muon Spectrometer of the CMS experiment for several possible values of the gas leak time constant τ , i.e. for different acceptance limit of the QC3 gas leak test.

- Not properly tightened screws on the drift and/or readout board;
- presence of gaps at the interface between the external frame and the drift and/or readout board;
- incompatibility between the O-ring and the external frame (e.g. due to the groove of the external frame wider and/or deeper than the size of the O-ring);
- compromised integrity of the gas inlet/outlet and/or external frames.

5.4.5 QC4 - HV Test in CO_2

The QC4 HV Test aims to determine the Current-Voltage curve of a GE1/1 detector, in order to identify possible malfunctions, defects in the HV circuit and intrinsic noise rate (i.e. pulses not produced by ionizing particle). The detector under test is connected to the gas system (see Figure 5.49) and flushed with pure CO_2 . Negative high voltage (V_{set}) is provided by a programmable HV power supply (CAEN N1470 model) that allows the user to control the current limit (I_{set}), the steps to ramp up and down the voltage, the maximum voltage, and the trip time. The HV power supply is able to deliver a current up to 1 mA

5.4. Requirements for GE1/1 Quality Assurance/Quality Control assessment

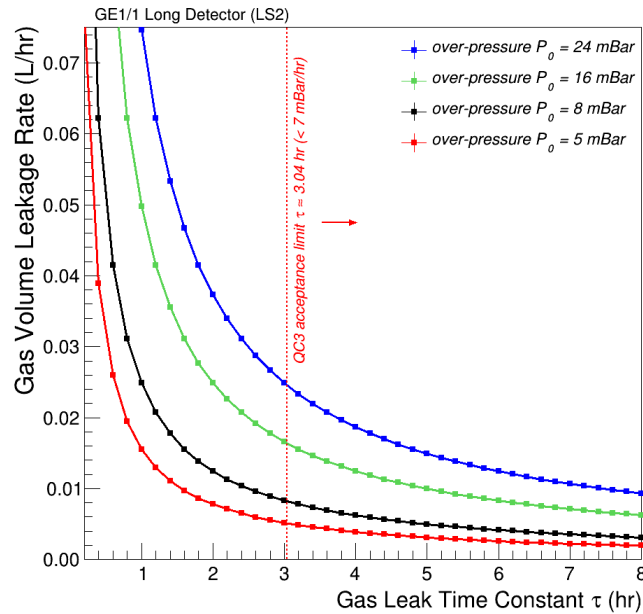


Figure 5.56: Gas volume leakage rate $dV(t)/dt$ as a function of the gas leak time constant τ for several possible values of the over-pressure P_0 in a GE1/1 detector during the operation in the Muon Spectrometer of the CMS experiment.



Figure 5.57: Examples of damage assembly components identified as potential gas leak sources in the GE1/1 detectors.

with a monitoring resolution of about 50 nA in order to identify possible leaks, sparks, or unusual current fluctuations. The QC4 HV test experimental setup for intrinsic noise measurements is shown on Figure 5.58. The readout of the detector is done using a charge sensitive pre-amplifier (ORTEC 142PC module) connected to the bottom electrode of the third GEM-foil. This connection is made through a decoupling RC circuit already present on the detector's drift board. The output of the pre-amplifier is then sent to an amplifier+shaper

5. The Assembly, Quality Control and Commissioning of the GE1/1 detectors

unit (ORTEC 474 model) and then to a discriminator (Lecroy 623A model). The resulting digital pulses go through a dual timer and then to a scaler unit for the rate measurement.

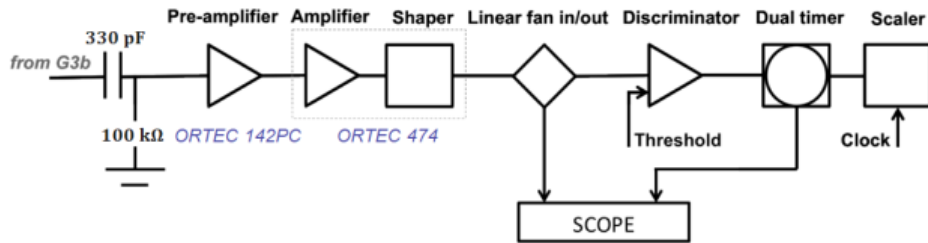


Figure 5.58: QC4 HV test experimental setup.

The procedure to perform the QC4 - HV Test is as follows:

1. The GE1/1 detector is connected to the gas system with pure CO_2 , the gas flow rate is setted to 5 L/hr and left it flush for at least 5 hours.
2. The Panasonic-to-LEMO adapters with the 50 Ω terminations are connected to all the readout sectors, as shown on Figure 5.59



Figure 5.59: QC4 HV test overview of the detector with the Panasonic-to-LEMO and the 50 Ω terminations.

3. The input wire of the pre-amplifier is soldered to the dedicated pad on the drift board in order to read the signal from the bottom of the third GEM-foil, by using the RC circuit to decouple the signal itself from high voltage, as shown on Figure 5.60.

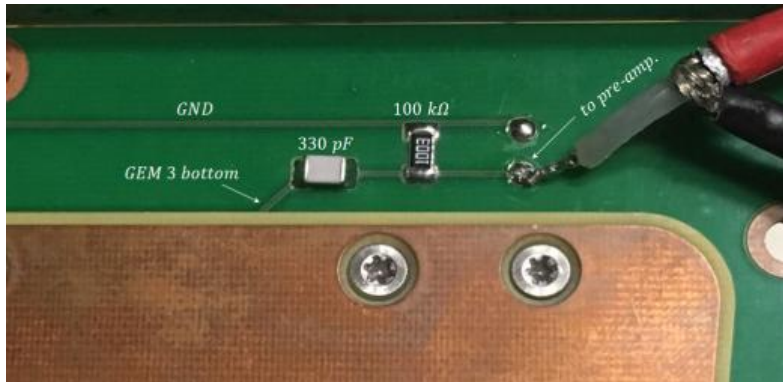


Figure 5.60: QC4 HV test magnified view of the sample point on the drift PCB board showing the RC circuit used to decouple the signal from HV when the detector is read from the bottom of the third GEM foil.

4. The HV voltage cable is connected to the SHV connector on the detector, by inserting a HV low-pass filter in order to cut the high frequency noise from the power supply.
5. The power supply parameters are set as follows: Ramp up = 50 V/s; Ramp down = 250 V/s; Max voltage = 5000 V; Trip time = 0 s, Trip action = *KILL*. The amplifier parameters are set as follows: Coarse gain = $\times 4$, Fine gain = $\times 4.5$, Integrate = 500 ns and Differential = 500 ns.
6. The copper ribbons are used to ground the detector, the pre-amplifier, and the HV filter. This configuration reduces the maximum noise level to ~ 100 mV
7. The discriminator threshold and the scaler clock are set to -140 mV and 60 s, respectively.
8. The total resistance of the HV circuit (including the divider and all the HV filters) are measured by using a digital multimeter. The total resistance is used to calculate the expected current in the resistive high voltage divider for every HV points. At this point the experimental setup is ready and the measurement is started.
9. The current limit I_{set} of the power supply is set according to the expected target value, adding $5 \mu A$, and the corresponding high voltage V_{set} is switched on. When the operating current and voltage is stable (after few seconds), the actual voltage $V_{mon.}$ and the current $I_{mon.}$ provided by the power supply are recorded. Finally, the clock of the scaler unit is started and after 60 s the counts measurement is recorded. The oscilloscope allows to identify possible noise pulse and unusual or repetitive signals in the detector under test.

10. The last two steps are repeated until it is reach 4900 V on the detector (maximum allowed voltage). The HV steps are of 200 V from 0 to 3000 V then the HV steps are of 100 V from 3000 V to 4900 V

The Current-Voltage characteristics (I-V curve) represents the relationship between the current ($I_{mon.}$) through the HV distribution circuit (HV divider + HV filters) and the corresponding voltage ($V_{mon.}$) across it. According to Ohm's Law, the I-V curve exhibits a linear relationship between the applied voltage and the resulting electric current. Therefore, the I-V curve is a straight line through the origin with positive slope. The reciprocal of the slope is equal to the total equivalent resistance of the HV distribution circuit. The experimental data are modeled by the function:

$$I_{mon.}(V_{mon.}) = \left(\frac{1}{R_{equiv.}} \right) \times V_{mon.} \quad (5.18)$$

where $R_{equiv.}$ is the total equivalent resistance of the HV circuit. Then, this value is compared to the measured value by using a digital multimeter: a deviation greater than 2% indicates a loss of linearity and the detector undergoes further investigations.

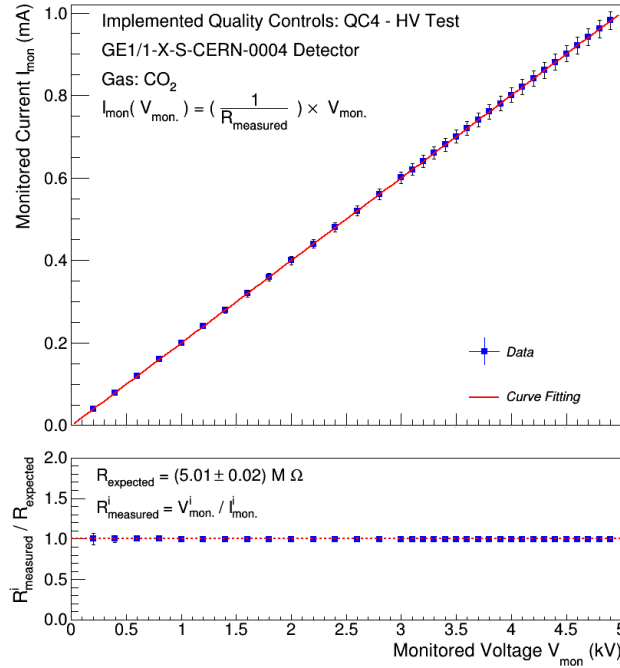
Simultaneous measurement of signal counts is done for every set of high voltage. The rate calculated from these counts is called Intrinsic Noise Rate (R_{noise}), which is defined as the rate of signals which are not originated from the ionization of the gas. The intrinsic noise rate is measured from the bottom of the third GEM-foil as a function of the current through the resistive high voltage divider of the HV distribution circuit. The average intrinsic noise rate of the GE1/1 detectors has been found to be $5 \times 10^{-3} \text{ Hz/cm}^2$ at 4.9 kV , well below the expected background rate at the GE1/1 region in the Moun Spectrometer of the CMS experiment, that is above 1.5 kHz/cm^2 .

Typical results from the QC4 HV test can be seen on Figure 5.61 for a GE1/1 Short detector and Figure 5.62 for a GE1/1 Long detector.

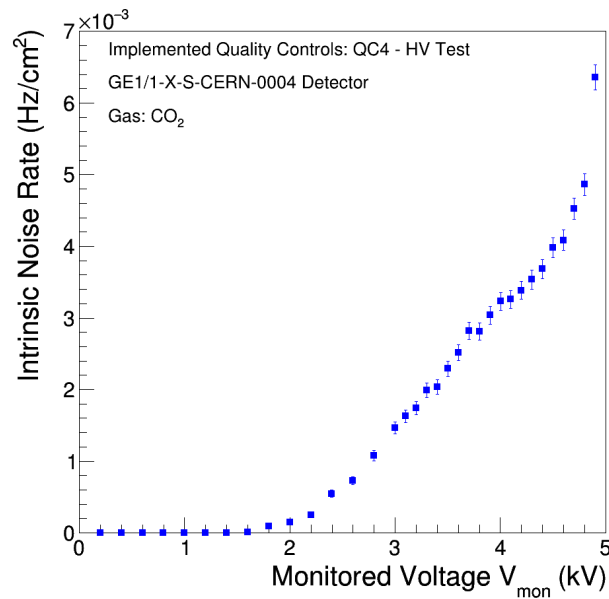
5.4.6 QC5 - Gas Gain measurement in Ar/CO_2 (70/30)

The QC5- effective gas gain measurement is divided into two stages: the measurement of the effective gas gain as a function of the voltage applied on the resistive high voltage divider and the measurement of the response uniformity of the detector through a dedicated readout electronics based on the Scalable Readout System (SRS) which consists of APV25 Front-End ASICs with 128 readout channels connected to the readout board of the detector (see Section 5.4.6.6). Both tests are done in a specific radiation box containing an AMPTEK miniX X-ray source with a silver target emitting $\sim 22 \text{ keV}$ X-ray photons.

5.4. Requirements for GE1/1 Quality Assurance/Quality Control assessment



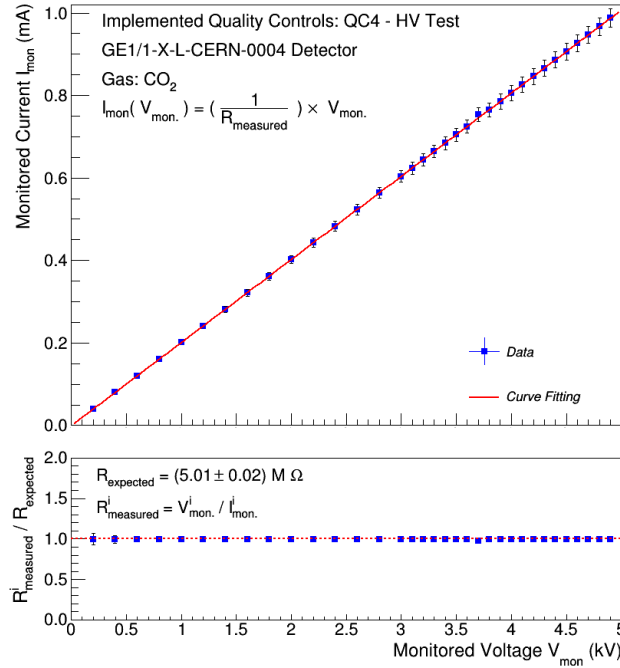
(a)



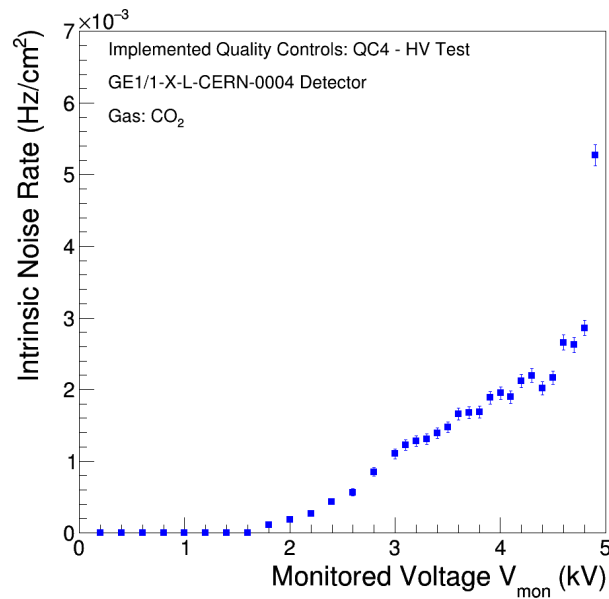
(b)

Figure 5.61: Results from the QC4 HV Test on the GE1/1-X-S-CERN-0004 detector. Top: current through the HV divider as a function of the applied voltage. The linear fit to the experimental data provides an equivalent resistance $R_{equiv.} \sim 4.99 M\Omega$, resulting in a deviation of about 0.4% with respect to the expected value ($R = 5.01 \pm 0.02 M\Omega$). Bottom: intrinsic noise rate N_{noise} as a function of the applied voltage: $N_{noise} \sim 6.4 \times 10^{-3} Hz/cm^2$ at 4.9 kV.

5. The Assembly, Quality Control and Commissioning of the GE1/1 detectors



(a)



(b)

Figure 5.62: Results from the QC4 HV Test on the GE1/1-X-L-CERN-0004 detector. Top: current through the HV divider as a function of the applied voltage. The linear fit to the experimental data provides an equivalent resistance $R_{\text{equiv.}} \sim 4.96 \text{ M}\Omega$, resulting in a deviation of about 1% with respect to the expected value ($R = 5.01 \pm 0.02 \text{ M}\Omega$). Bottom: intrinsic noise rate N_{noise} as a function of the applied voltage: $N_{\text{noise}} \sim 5.3 \times 10^{-3} \text{ Hz/cm}^2$ at 4.9 kV.

5.4.6.1 Preparation and installation of the GE1/1 detector

The procedure for the preparation and installation of the GE1/1 detector on the QC5 test stand is as follows:

1. The GE1/1 detector under test is set up on a laboratory workbench (in horizontal position) and the copper grounding plate is fixed onto the readout board in order to minimize the electronic noise and its contribution to the measurements.
2. The APV25 hybrid cards are connected to the detector, following the map shown in Figure 5.63 and paying attention that the orientation of each APV is identical to the one indicated on the map.

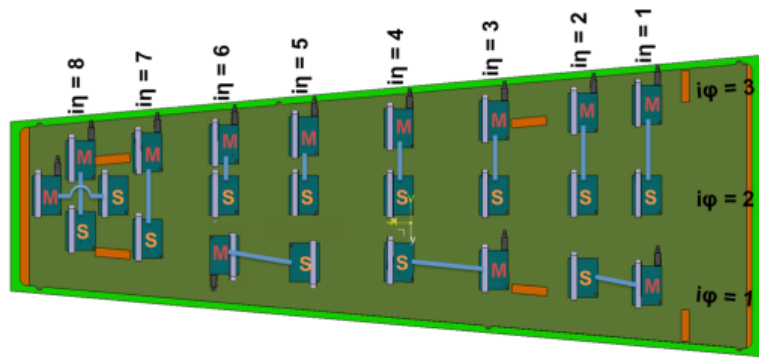


Figure 5.63: QC5 readout sectorization and APV mapping. The dark grey flat cable represent the HDMI connectors on the output of the master APVs. This mapping is valid for both Short and Long detectors.

3. The ground wire of each APV is connected the to the ground plugs already placed on the grounding plate (see Figure 5.64).



Figure 5.64: Close view of an APV25 Front-End ASICs plugged on the detector.

4. The detector is carefully placed inside of the X-ray station: it is oriented in order to have the narrow base of the trapezoid closest to the floor, with the readout board facing away from the X-Ray generator, as shown in Figure 5.65.

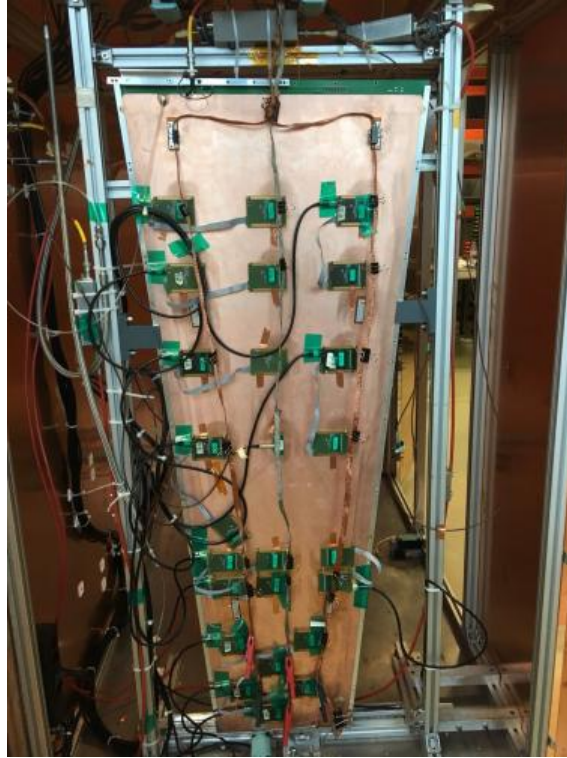


Figure 5.65: Picture of the GE1/1 detector inside of the X-ray station.

5. The detector's inlet (narrow base) and outlet (wide base) are connected to the gas system and the detector is flushed with the CMS-GEM standard gas mixture Ar/CO_2 (70/30). The gas flow rate is set to 5 L/hr and the detector is left to flush for at least 5 hours.
6. While the detector is flushing, the grounding system is prepared by placing three copper ribbons along the $i\phi$ sectors of the detector and making sure that none of the grounding cables are touching the HV circuit or an active part of an APV hybrid. Then, the ground of each APV is connected to the closest copper ribbon, as indicated on Figure 5.66

At this point the detector under test is ready for the the QC5 effective gas gain measurement.

5.4.6.2 Effective gas gain measurement

The effective gas gain is measured in Ar/CO_2 (70/30) gas mixture by comparing the primary current, induced in the drift gap by the X-ray source, and the

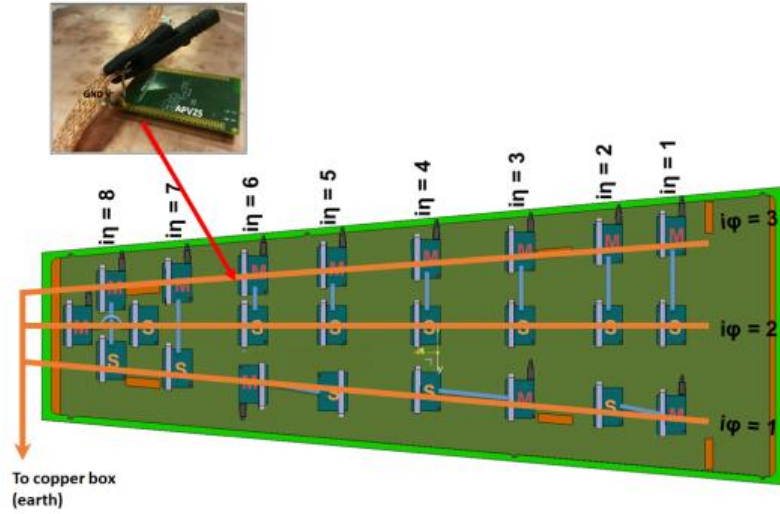


Figure 5.66: QC5 Schematic view of the optimum grounding for QC5 Gas Gain Calibration Test. The orange line represents copper ribbon.

amplified current induced on the readout board. The detectors is irradiated by a AMPTEK miniX X-ray source with a silver target. The X-ray generator uses an electron gun incident on a silver target. The incident X-rays consist of silver K_α and K_β peaks (centered around energy of 22 and 25 keV) over an electron bremsstrahlung continuum background. The X-ray photons are absorbed by the copper atoms of the detector drift electrode which in turn, emits copper X-ray photons of 8 keV energy to come back to the ground state. The X-ray photons emitted by the copper are then converted by photoelectric effect in the active gas volume. The resulting spectrum is thus a convolution of the energies of the incident X-rays photons interacting in the detector active gas volume, the bremsstrahlung continuum background, and a small fraction of unconverted silver K_α and K_β .

Despite the X-ray photons interaction rate is of the order of the kHz, the primary current doesn't exceed several tens of fA. Therefore, it is extremely difficult to measure such primary current directly from the drift plane, which is powered at high voltage and thus subject to noise. This issue is overcome by measuring the interaction rate, i.e. the number of pulses induced by particles per unit time; then, knowing the average ionization energy of the Ar/CO₂ (70/30) gas mixture, the number of primary electrons n_{e^-} per incoming 8 keV X-ray photon is calculated as follows:

$$n_{e^-} = E_\gamma \times \left(\frac{\%Ar}{W_i(Ar)} + \frac{\%CO_2}{W_i(CO_2)} \right) = 8030 \times \left(\frac{0.7}{26} + \frac{0.3}{33} \right) \approx 289 \quad (5.19)$$

where $E_\gamma \approx 8.03\text{keV}$ is the energy of the incident X-ray photons, %Ar and %CO₂ are the percentages of the gases in the mixture, $W_i(Ar)$ and $W_i(CO_2)$ are the work functions of the gases. Finally, the primary current is estimated

by multiplying the X-ray photons interaction rate R , the number of primary electrons n_{e^-} per X-ray photon and the elementary charge e .

On the contrary, the amplified current I_a , induced on the readout board, varies from 10^{-10} to 10^{-8} A depending on the voltage applied on the HV divider. Therefore, its measurement can be performed easily with a pico-ammeter connected to the anode. Finally, the effective gas gain G is expressed as follows:

$$G = \frac{I_a}{R \times n_{e^-} \times e} \quad (5.20)$$

The measurement of the effective gas gain is always performed on a reference readout sector $[(i\eta, i\phi) = (4, 2)]$ and its value is normalized to the pressure and temperature values in the cavern of the CMS experiment, in order to take into account the difference in the environmental conditions across all the different production and quality control sites over the world.

5.4.6.3 Description of the experimental setup

The detector under test is powered using a programmable HV power supply (CAEN N1470) that allows the user to control the current limit (I_{set}), the steps to ramp up and down the voltage, the maximum voltage, and the trip time. The HV power supply is able to deliver a current up to 1 mA with a monitoring resolution of about 50 nA in order to identify possible leaks, sparks, or unusual current fluctuations. The data acquisition setup is shown on Figure 5.67. The readout of the detector is done using a charge sensitive pre-amplifier (ORTEC 142PC module) connected to the reference readout sector $(i\eta, i\phi)=(4, 2)$. The output of the pre-amplifier is then sent to an amplifier+shaper unit (ORTEC 474 module) and then to a discriminator (Lecroy 623A module). The resulting digital pulses directly go to a scaler unit for the interaction rate measurement. This value, multiplied by the number of primary electrons per X-ray photon and by the elementary charge, gives the primary current induced in the drift gap by the X-ray source. The measurement of the output current is simply measured by connecting a pico-ammeter (Keithley 6487) to the same readout sector.

To finalize the connections for the QC5 effective gas gain measurement:

- The Panasonic-to-LEMO adapter with a 50 kΩ protective resistor to ground is connected to the reference readout sector $(i\eta, i\phi)=(4, 2)$. A clamp is used to attach the ground of the Panasonic-to-LEMO adapter to the main copper ribbon, as indicated in Figure 5.68. The LEMO output of this Panasonic-to-LEMO adapter is then connected to the input of the pre-amplifier.
- Additional copper ribbons are used to ground the detector's drift board, the SHV connector, the pre-amplifier and the HV filter. In this configuration the maximum noise level is be of the order of 50-70 mV.

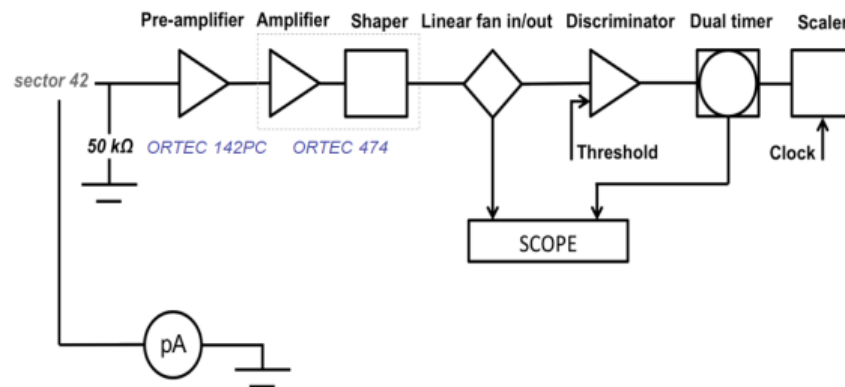


Figure 5.67: QC5 effective gas gain data acquisition setup.

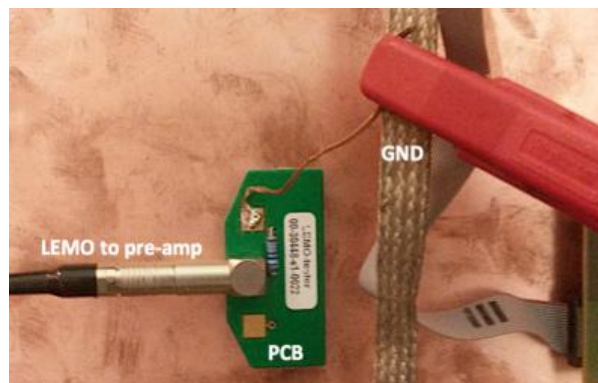


Figure 5.68: Close view of the Panasonic-to-LEMO adapter with a $50\text{ k}\Omega$ protective resistor for the rate measurement.

5.4.6.4 Procedure of the QC5 effective gas gain measurement

The procedure to perform the QC5 effective gas gain measurement is as follows:

1. The HV voltage cable is connected to the SHV connector on the detector through a HV low-pass filter in order to cut the high frequency noise from the power supply.
2. The power supply parameters are set as follows: Ramp up = 50 V/s ; Ramp down = 250 V/s ; Max voltage = 5000 V ; Trip time = 0 s , Trip action = *KILL*. The amplifier parameters are set as follows: Coarse gain = $\times 4$, Fine gain = $\times 4.5$, Integrate = 500 ns and Differential = 500 ns . The discriminator threshold and the scaler clock are set to -140 mV and 60 s , respectively.
3. The X-ray tube powering voltage and current are set to 40 kV and $5\text{ }\mu\text{A}$, respectively. More information about the Amptek miniX X-ray tube and its control software can be found in [80].

5. The Assembly, Quality Control and Commissioning of the GE1/1 detectors

- The effective gas gain is measured for HV_{drift} points between 2585 V and 3290 V, i.e. equivalent currents in the divider between $550 \mu A$ and $700 \mu A$. The measurement starts from the maximum operating point ($700 \mu A$) to the lowest point ($550 \mu A$), by steps of $10 \mu A$.
- The voltage is slowly ramped up on the divider to reach the equivalent current of $700 \mu A$. For each HV step, the current limit I_{set} is set to the expected target value plus $5 \mu A$.
- After few seconds of stabilization, the clock of the scaler is loaded to start counting the events. At this step the X-ray tube is still switched OFF. After 60 s, the counts measurement without X-ray source is recorded. Then, the X-ray tube is switched ON and the counts measurement is repeated in the same conditions.
- The Panasonic-to-LEMO adapter with a $50 k\Omega$ protective resistor for the rate measurement is replaced with a Panasonic-to-LEMO adapter without protective resistor for the readout current measurement, as indicated in Figure 5.69. The LEMO output of this Panasonic-to-LEMO adapter is then connected to the input of the pico-ammeter.

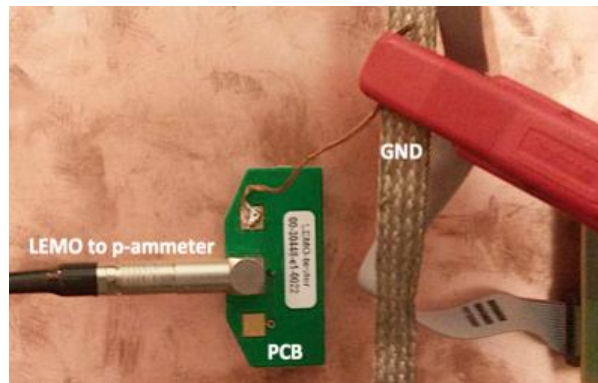


Figure 5.69: Close view of the Panasonic-to-LEMO adapter for the readout current measurement.

- The readout current is recorded by using a Keithley pico-ammeter with the X-ray tube switched OFF. Then, the X-ray tube is switched ON and the readout current measurement is repeated in the same conditions.
- The steps 6 through 8 are repeated for operating points $690 \mu A$ down to $550 \mu A$ point in steps of $10 \mu A$.

5.4.6.5 Results of the QC5 effective gas gain measurement

Typical results of the QC5 effective gas gain measurement are shown on Figure 5.70 for a GE1/1 Short detector and Figure 5.71 for a GE1/1 Long detector:

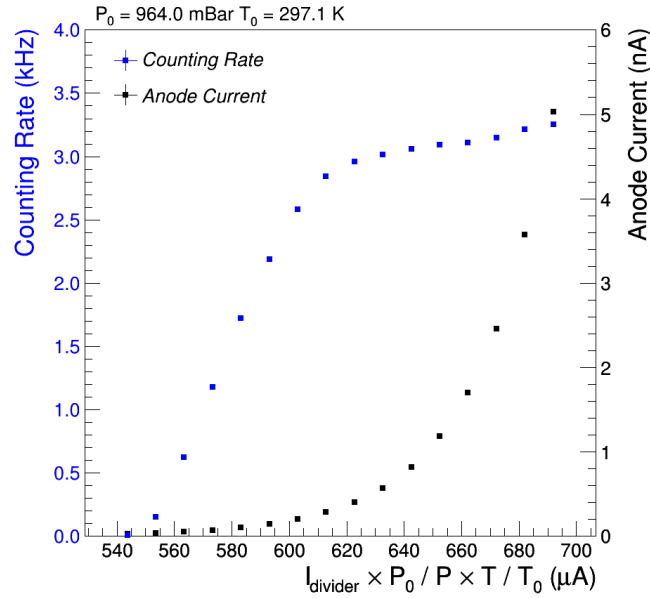
the effective gas gain of the GEM detector exponentially increases with increase in the detector voltage. The maximum measured rate is $\sim 4 \text{ kHz}$; with corresponding measured gas gain of 3.5×10^4 at divider current of $700 \mu\text{A}$.

5.4.6.6 Response Uniformity

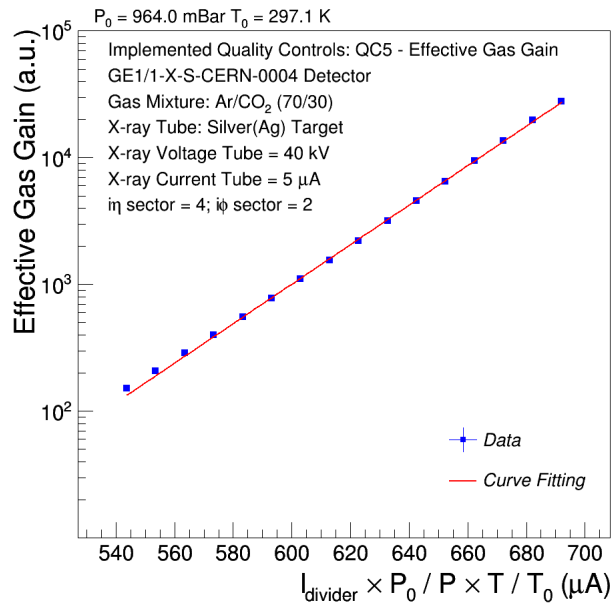
The clear understanding of the influence of the gas composition, GEM-holes geometry and electric field strength inside and between the charge amplification stages on the gas gain of the detector and the quality of the readout board are crucial in the study of detection performances of the GE1/1 detectors. Several factors, such as non-uniformity of the GEM-holes geometry, local contamination, incorrect stretching technique or presences of defects on the readout board could affect the uniformity of gas gain all over the detector active area. Due to the fact that the gas gain determines the detector performances (e.g. efficiency, responding time and spatial resolutions, etc.), the monitoring of the gas gain uniformity across the entire detector active area is fundamental. For this reason, for a large detector, the gas gain variations over its surface is a serious concern and testing the gas gain uniformity is one of the crucial steps of the quality control procedures.

A possible technique to study the gas gain uniformity consists of the measuring the effective gas gain sector-by-sector by moving the X-Ray generator along the detector active area. Such technique mainly consists of the repeating the effective gas gain measurement on the 24 readout sectors by following the procedure described in the previous Section 5.4.6. The main limitations identified in sector-by-sector gas gain uniformity measurement are the following:

- *Time consumption:* the effective gas gain measurement requires several hours per readout sector and several days to scan all the readout sectors of the detector. From the past experiences, the maximum number of sectors that one would be able to test per day should not exceed four sectors per day. With a rate of about four readout sectors per day, it would take a whole week to complete only a single GE1/1 detector, i.e about 4-5 detector per month. This is not suitable for the mass production of large numbers of GE1/1 detectors.
- *Physical conditions:* since the duration of the effective gas gain measurement on each readout sector is quite long, significant fluctuations of the environmental parameters (temperature, pressure and humidity) could be occur during the measurements. This could lead to the variations of gas gain between the readout sectors. Moreover, the readout system and the grounding must be moved manually between one sectors to another, resulting in possible changes of the experimental conditions during the test. These variations of physical conditions could revert in a non-uniformity on the effective gas gain measurements.



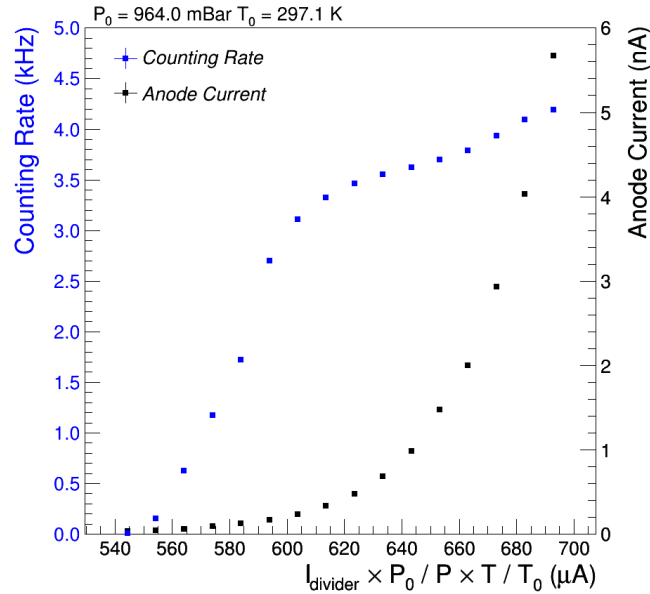
(a) Counting rate and Anode current as a function of the current through the HV divider.



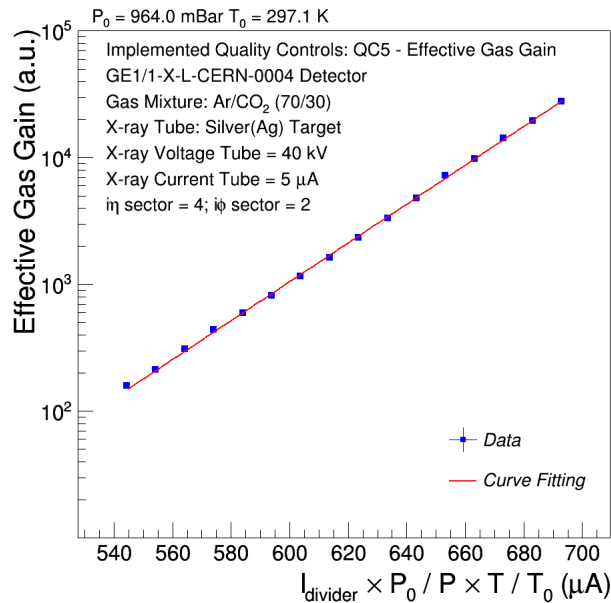
(b) Effective gas gain measurement as a function of the operating current through the HV divider.

Figure 5.70: Results from the QC5 - Effective Gas Gain Measurement on the GE11-X-S-CERN-0004 assembled with GEM-foils based on the single-mask photolithography technique produced by the CERN PCB Workshop. The detector under test has been operated in Ar/CO_2 (70/30) gas mixture and irradiated by a 22 keV photons X-ray from an X-ray tube with an interaction rate of $\sim 3.2 \text{ kHz}$.

5.4. Requirements for GE1/1 Quality Assurance/Quality Control assessment



(a) Counting rate and Anode current as a function of the current through the HV divider.



(b) Effective gas gain measurement as a function of the operating current through the HV divider.

Figure 5.71: Results from the QC5 - Effective Gas Gain Measurement on the GE11-X-L-CERN-0004 assembled with GEM-foils based on the single-mask photolithography technique produced by the CERN PCB Workshop. The detector under test has been operated in Ar/CO_2 (70/30) gas mixture and irradiated by a 22 keV photons X-ray from an X-ray tube with an interaction rate of ~ 4.0 kHz.

- *Gas gain map resolution:* since a LS2 GE1/1 triple-GEM detector is divided into 24 readout sectors and for the standard effective gas gain measurement all the 128 strips of each readout sectors are connected together, there are only 24 measurement points for the entire detector active area, while the total number of readout strips in the LS2 GE1/1 triple-GEM detector is equal to 3072. This implies a drastic loss of granularity of the gas gain measurement. Such drastic loss of granularity could be improved by reading out smaller groups of strips, but it would increase the duration of the entire test as well as the requirements of electronics significantly.

An alternative technique has been developed to overcome the limitations on the sector-by-sector measurement technique. In this method all the 3072 readout strips of a detector are fully irradiated by a large X-ray beam simultaneously and the readout signal is collected through an analog Front-End electronics. Therefore, the time taken to complete the gas gain uniformity test of whole detector is drastically reduced and also the effect of environmental fluctuations during the measurement are suppressed. Moreover, since all the connections are prepared before the data acquisition, the setup is not manipulated during the test. The first attempt of this technique was successfully conducted in 2012 with a GE1/1 detector of the 3rd generation.

Description of the experimental setup. The QC5 response uniformity test consists of measuring the pulse height distribution all over the active surface of a GE1/1 detectors. The QC5 response uniformity test takes place on the same test stand as the QC5 effective gas gain described in Section 5.4.6. The detector is powered using a programmable HV power supply (CAEN N1470 module) that allows the user to control the current limit (I_{set}), the steps to ramp-up and ramp-down the voltage, the maximum voltage, and the trip time. This power supply must be able to deliver a current up to 1 mA with a monitoring resolution lower than 1 μ A in order to identify possible leaks, sparks, or unusual current fluctuations. The detector is flushed with the gas mixture Ar/CO₂ (70 : 30) at least for 5 hours at 5 L/hr in order to guarantee the uniform distribution of the correct gas mixture in the entire detector gas volume. Figure 5.72 shows the complete experimental setup for the QC5 response uniformity test with a GE1/1 detector in place and ready for the data acquisition.

The readout electronics is based on the Scalable Readout System (SRS) [74] designed by the RD51 collaboration [75]. It consists of APV25 Front-End ASICs [76] with 128 readout channels connected to the readout board of the detector (see Figure 5.73). Each channel contains a pre-amplifier and a shaper working at a frequency of 40 MHz. The analog information of the pulses is sent to an ADC card via HDMI cables, itself connected to the Front End Card (FEC) which is responsible for the communication with the external devices and the control of the chips. Then, a Gigabit Ethernet link connects the small-system SRS electronics to a Linux PC running the Alice DAQ software named

5.4. Requirements for GE1/1 Quality Assurance/Quality Control assessment



Figure 5.72: Picture of the experimental setup for the QC5 response uniformity test showing the X-ray generator, the DAQ stations (left) and the inside of the copper box with the electronics in place on the GE1/1 detector (right).

DATE [77] (Data Acquisition and Test Environment). The configuration of the SRS registers is possible through the web interface SCRIBE [79] (Slow Control and Run Initialization Byte-wise Environment) designed by Florida Institute of Technology. The event reconstruction is performed by ROOT-based AMORE SRS package [78] with the final analysis handled by the CMS GEM analysis framework.

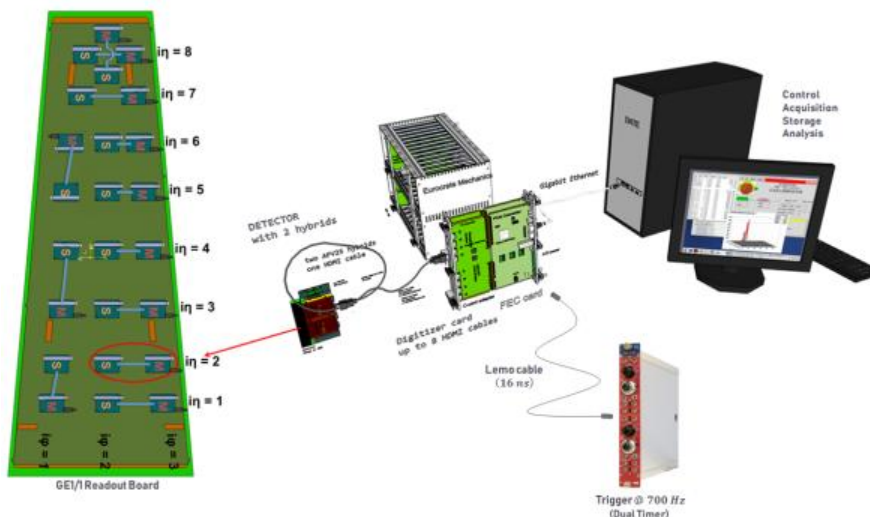


Figure 5.73: Schematic overview of the experimental setup for the QC5 response uniformity test showing the DAQ electronics and the trigger line.

An external trigger is required by the SRS system to send out the data packets.

Since the detector is irradiated by 22 keV X-ray photons, it is not possible to use scintillators in order to generate trigger signals. To overcome this limitation, an external random trigger with rate $\sim 700\text{ Hz}$ is provided by a timing unit (Dual Timer 2255B CAEN module) in oscillator mode. The trigger signal is directly sent to the FEC cards as a trigger to start the acquisition. When the FECs receives a trigger, all the APV25 chips open an acquisition window of 375 ns during which the signals on all the channels are sampled every 25 ns . Figure 5.74 shows the typical raw data read from an APV25 (left), containing the ADC charge of all the channels inside of the acquisition window (top right) and the typical cluster size at a gain of ~ 600 with X-rays (bottom right).

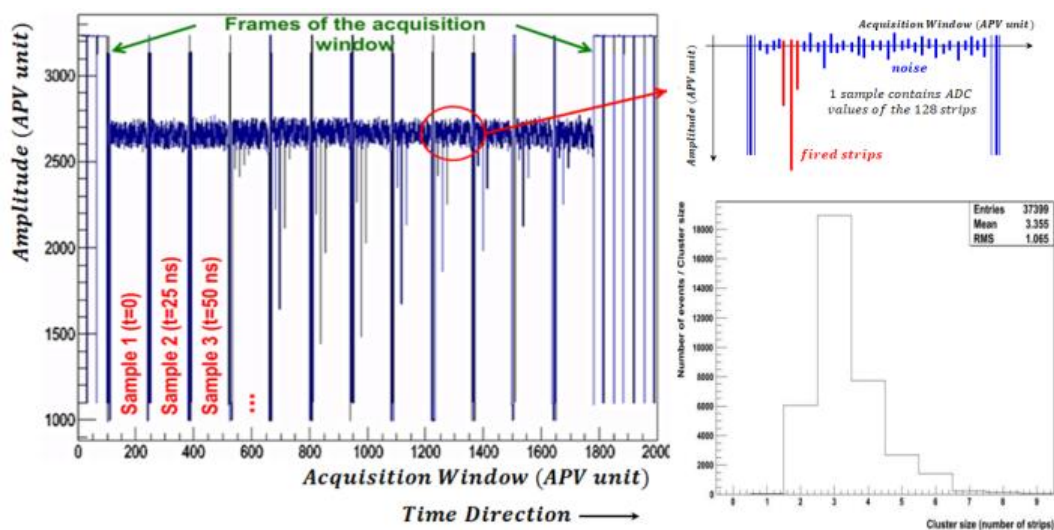


Figure 5.74: Raw data of an APV25 triggered by an X-ray photons. The acquisition window contains 12 samples delayed by 25 ns . Each sample includes the ADC values of all the 128 strips, fired or not by the particles. The average number of strips fired by a 8 keV X-ray is ~ 3 (cluster size) at a gas gain of 600.

Preparation of the detector. After the QC5 effective gas gain test, the detector is already in position in the X-ray station, filled with the gas mixture Ar/CO_2 (70 : 30) and already grounded and equipped with the APV25 chips (see Figure 5.65). The preparation of the detector for the QC5 response uniformity test simply consists of connecting the APV hybrids to the FEC cards with HDMI cables, making sure the SRS system is switched OFF before starting the intervention on the APV chips. The HDMI connections are secured by putting kapton tape or a cable tie near the APV connector, as shown on Figure 5.75, making sure not applying too much stress on the cable itself, under the penalty of breaking the HDMI connector on the APV hybrid.

Additionally, X-ray generator is placed in front of the GE1/1 detector under test, pointing the centre of the detector surface, with no cap, no collimator, and no filter. Taking into account that the opening of the X-ray generator

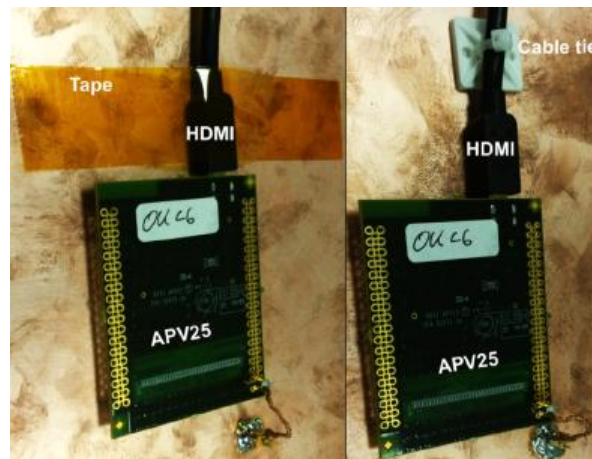


Figure 5.75: QC5 picture of the HDMI cable connected to its APV25 hybrid.

is of the order of 120° , the active area of the detector is fully irradiated at a distance of ~ 1.2 m from the source. At this step the detector is ready for the measurement.

Data Acquisition procedure. The dynamic range of the ADC of the APV25 Front-End ASICs limits the choice of the working point for the response uniformity test. To minimize the saturation in read out signals, which will not allow to appreciate possible gas gain variation between different zone of the same detector, it is necessary to operate the detector under test at reduced charge gain factors. For this region, before starting the response uniformity measurement, the appropriate operating point of the detector under test is defined by using the results obtained with the effective gas gain measurement: the effective gas gain curve is fitted with an exponential function to determine the working point for the response uniformity test. The current through the resistive high voltage divider which corresponds to a gas gain of 600 is estimated. This value of the gas gain ensures that the maximum amplitude of the readout signals is just below the saturation level of the readout electronics. The first step is the so-called *pedestal run*, which is performed with a random trigger signal by keeping the X-ray generator switched OFF in order to measure the average noise and the possible offset of every readout channel. Then, the X-ray generator is switched ON in order to perform the *physics run*.

Analysis procedure. The first phase of the analysis procedure is based on the AMORE framework designed by the ALICE collaboration and adapted to the SRS + APV25 readout system. It consists of three main steps:

1. Zero-Suppression: an appropriate threshold is defined by analyzing the data collected during the pedestal run (X-ray generator switched OFF). The AMORE framework builds the noise distribution and extract the corresponding mean value and standard deviation for each readout channel in order to perform pedestal subtraction from the recorded pulse

heights event-by-event during physical run (X-ray generator switched ON). The subtraction is programmed as a multiple of the sigma from the pedestal mean value. Only data above threshold are transmitted and recorded by the DAQ.

2. Clusterization: for a single event, the hits in neighbor strips are binded as a single object, a cluster, which contains the total charge induced by the particle. The clusterization algorithm allows to applied additional cuts, such as the maximum and the minimum cluster charge, maximum and the minimum cluster sizes, cluster multiplicity, etc. in order to reject noise, fake events and cross talk between adjacent strips.
3. Data storing in a ROOT tree. For every event a ROOT tree are created. It contains all the relevant information which characterize the cluster defined in the previous step, such as the number of clusters, the total charge, the size, the position and the timing information of the clusters.

The second phase of the analysis procedure is the estimation of the gas gain uniformity by extracting the information from the ROOT files through a dedicated algorithm defined in the CMS GEM analysis framework. The algorithm for the offline data analysis consists of three main stpes:

1. Definition of the GE1/1 detector geometry, including the position of all the strips in the η and the ϕ directions, and generation of slice on to which the detector gas gain is avaluated; in the standard analysis procedure 768 sliced are defined, i.e. each η -partition is ideally divided into 96 slices, each slide consisting of 4 strips.
2. For a given slice, the cluster charge for each cluster occurring in this slice is added to a charge histogram. A further selection is performed at this step: the events with the minimum charge and a cluster size lower than 3 strips are interpreted as noise and they are rejected at this step. Additionally, the events with the maximum charge in the first or the last sample of the acquisition window are also rejected since the correct value of the signal charge sampled by the ADC could be outside of the DAQ time window. Figure 5.76 shows a schematic representation of the second phase of the analysis procedure.
3. The spectrum of the charge collected by a cluster of strips, measured in ADC units, is fit to extract the position of the copper fluorescence photopeak. Figure 5.77a shows an example of the spectrum superimposed to the fit function for one of the η sectors of one GE1/1 detector. The data is fitted with Cauchy distribution, to model the copper fluorescence photopeak, plus a 5th order polynomial, to model the combination of electron bremsstrahlung continuum background and small fraction of

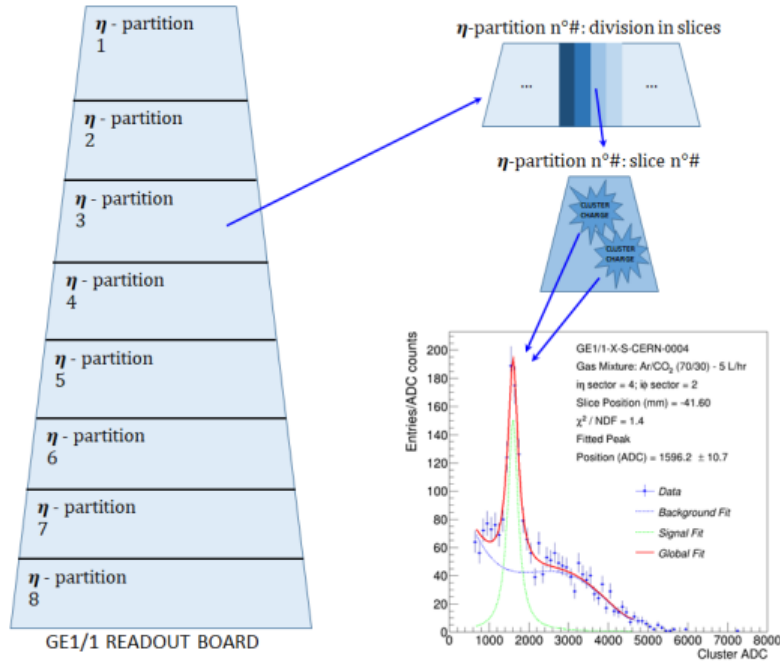


Figure 5.76: Schematic overview of the GE1/1 detector built in the analysis code. The η -partitions are divided in 96 slices. For each slice, the maximum cluster charge for all the events occurring in this slice is added to a charge histogram related to the energy deposited by the particles.

unconverted K_α and K_β photons coming from silver target of the X-ray generator.

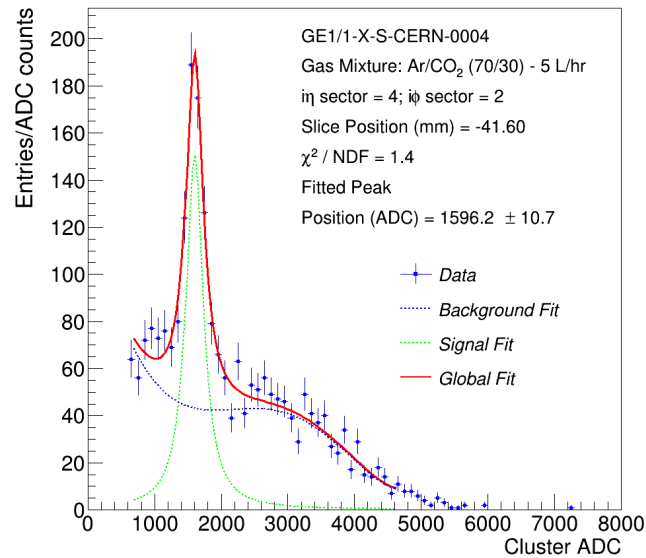
The mean of the copper fluorescence spectrum extracted from the fit of the cluster charge ADC spectrum from each slice is assigned to slice's coordinate point in the detector's local coordinates (see Figure 5.77b).

The copper fluorescence photopeak mean position value of each slice is used to generate a distribution for the entire detector active area. A gaussian function is used to fit this distribution in order to extract the mean μ and the sigma σ (see Figure 5.78a). Figure 5.78b shows the map of the normalized copper fluorescence photopeak energy.

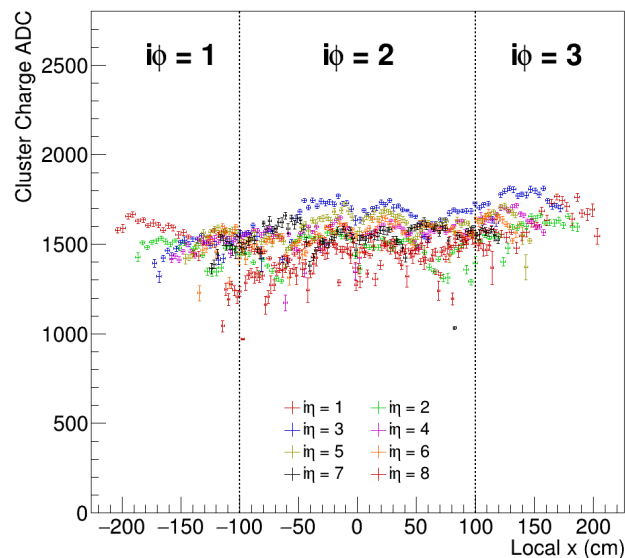
The Response Uniformity ($R.U.$) of a GE1/1 detector is defined as:

$$R.U. = \frac{\sigma}{\mu} \times 100\% \quad (5.21)$$

where μ and σ parameters are the mean and standard deviation taken from a Gaussian fit of the data set of all fixed copper fluorescence peak positions from an entire GE1/1 detector. Ideally, the response uniformity across all the sectors of a given detector should not exceed the 30% value, in order to guarantee a stable operation efficiency (98%) and time resolution (< 10 ns) on the entire detector active area.

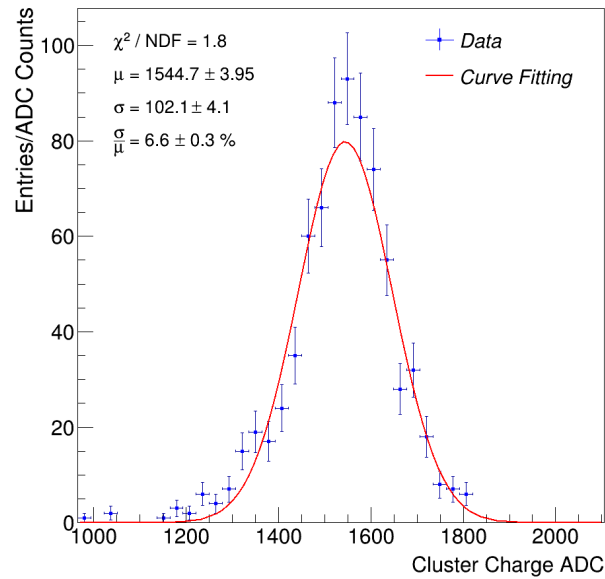


(a)

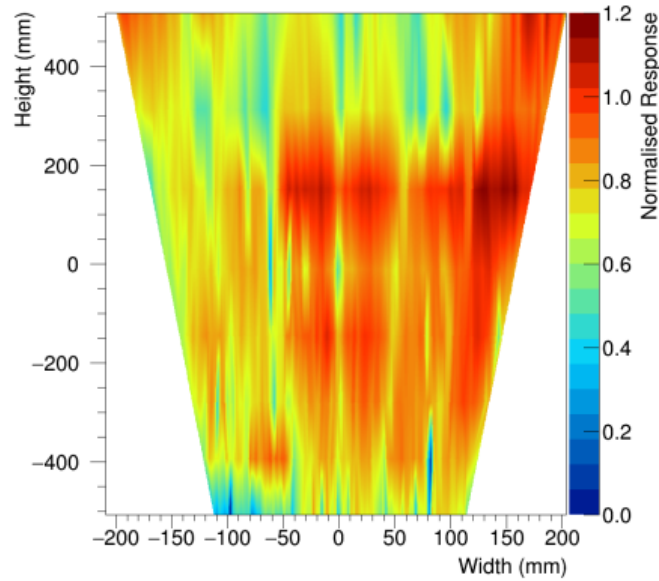


(b)

Figure 5.77: Top: Example of energy spectrum from a slice (four strips) of the GE1/1 triple-GEM detector under test operated at an average gain around 600 with Ar/CO₂ (70/30) fully illuminated by a 22 keV X-ray. The solid line represents a fit to the experimental data using a Cauchy distribution to model the copper fluorescence photopeak plus a fifth order polynomial that models the background. Bottom: The mean of the copper fluorescence spectrum extracted from the fit of each slice is assigned to coordinate point of the slice in the local coordinates of the detector.



(a)



(b)

Figure 5.78: Top: Distribution of fitted photopeak positions obtained from GE1/1 triple-GEM detector under test: the experimental points represent each photopeak position and the solid line is a Gaussian fit to the data. The response uniformity for this detector is $R.U. = 6.6 \pm 0.3\%$. Bottom: Map of the detector response (i.e. the normalized photopeak energy) across the detector under test.

5.4.7 Summary of QA/QC test results at CERN

This section summarizes the results related to the QC3 - Gas Leak Test, QC4 - HV Test and QC5 - Gas Gain Measurement performed on the GE1/1 triple-GEM detectors assembled at CERN production and quality control site.

5.4.7.1 QC3 - Gas Leak Test in CO_2

Type of QA/QC test - The QC3 gas leak test is the first quality control test performed on a new assembled GE1/1 detector and aims to identify possible gas leak and eventually measuring the gas leak rate by monitoring the drop of the internal over-pressure as a function of the time. The LS2 GE1/1 triple-GEM detector under test is validated if the pressure drop in the detector + gas system does not exceed 7 mBar per hour, which corresponds to a gas leak time constant of about $\tau \approx 3.04$ hr.

Acceptance criteria - The gas leak threshold has been established to be for a single GE1/1 triple-GEM detector (see Section 5.4.4):

$$\Delta P \leq 7 \text{ mBar/hr}$$

or in terms of the gas leak time constant:

$$\tau \geq 3.04 \text{ hr}$$

Figure 5.79 shows the summary plots of the QC3 gas leak tests performed on the long GE1/1 detectors (Figure 5.79a) and short GE1/1 detectors (Figure 5.79b) assembled at the CERN production and quality control site.

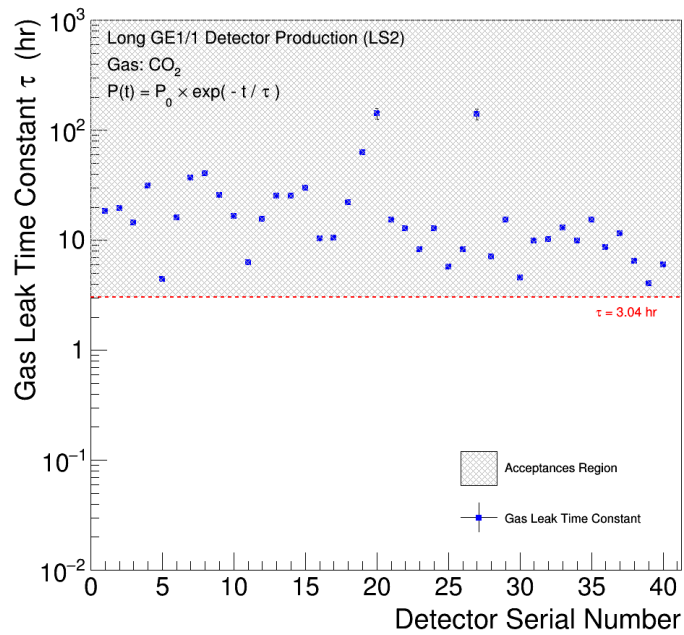
QC3 - gas leak test status at the CERN production and quality control site (latest data as at 31th August 2018):

1. Long GE1/1 triple-GEM detector
 - Number of detectors tested: 40
 - Number of detectors validated: 40
 - Number of detectors rejected: 0

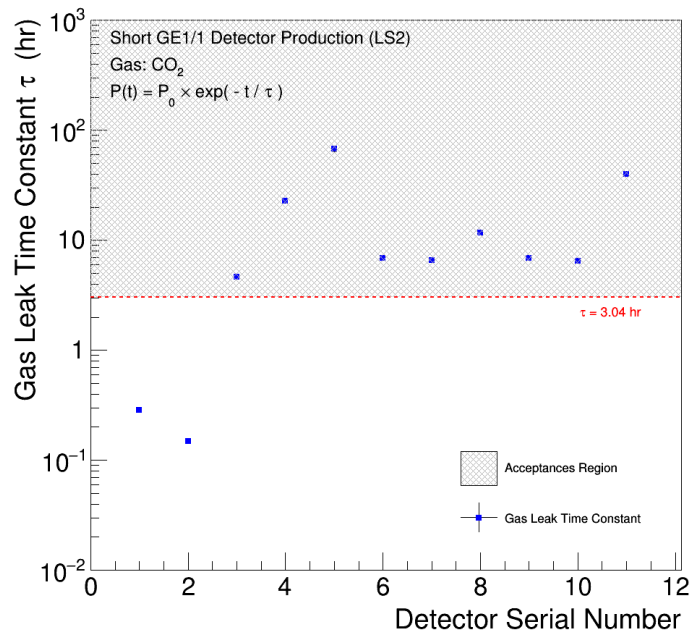
2. Short GE1/1 triple-GEM detector
 - Number of detectors tested: 11
 - Number of detectors validated: 9
 - Number of detectors rejected: 2

Details on rejected detectors:

5.4. Requirements for GE1/1 Quality Assurance/Quality Control assessment



(a)



(b)

Figure 5.79: Summary of QC3 - gas leak tests performed on the long GE1/1 detectors (top) and short GE1/1 detectors (bottom) assembled at the CERN production and quality control site. The horizontal dashed line shows the QC3 acceptance limit in terms of the gas leak time constant $\tau \approx 3.04$ hr, which corresponds to a maximum acceptable gas leak rate of about 7 mBar/hr.

- *GE1/1-X-S-CERN-0001* detector: ~ 60.0 minutes after the starting of the QC3 gas leak test, the pressure drop was about 21.63 *mBar* resulting in a gas leak rate of ~ 0.36 *mBar/min*, i.e. a gas leak rate approximately 3 times higher than the one allowed by the QC3 acceptance criteria for the LS2 GE1/1 mass production.
- *GE1/1-X-S-CERN-0002* detector: ~ 32.5 minutes after the starting of the QC3 gas leak test, the pressure drop was about 22.9 *mBar* resulting in a gas leak rate of ~ 0.70 *mBar/min*, i.e. a gas leak rate approximately 6 times higher than the one allowed by the QC3 acceptance criteria for the LS2 GE1/1 mass production.

The detectors have been assembled using an external frame pre-serie with wrong groove size for the Viton O-ring. Due to an incorrect machining of the external frame, the groove was wider and deeper than the size of the O-ring. The latter was completely inside the groove itself, not allowing proper gas tightness of the detector. The CMS Collaboration decided not to use the two detectors for LS2 GE1/1 mass production, but only for a R&D activities.

5.4.7.2 QC4 - HV Test in CO_2

Type of QA/QC test - The QC4 HV Test aims to determine the Current-Voltage curve of a GE1/1 detector, in order to identify possible malfunctions, defects in the HV circuit and intrinsic noise rate (i.e. pulses not produced by ionizing particle). The detector is ramped up to 3.0 *kV* in step of 200 *V* and up to 4.9 *kV* in step of 100 *V* in pure CO_2 . For each step, the current through the HV circuit and the intrinsic noise rate of the detector are recorded. The detector is accepted if the Current-Voltage curve shows a linear behavior and the intrinsic noise rate is below several hundred of Herz at applied voltage of 4.9 *kV*.

Acceptance criteria - The percentage variation of resistance $\Delta R/R \times 100\%$, which reflects the goodness of the linearity of the experimental Current-Voltage curve, and the intrinsic noise rate R_{noise} threshold have been established to be for a single GE1/1 triple-GEM detector (see Section 5.4.5):

$$\Delta R/R \times 100\% \leq 2\%$$

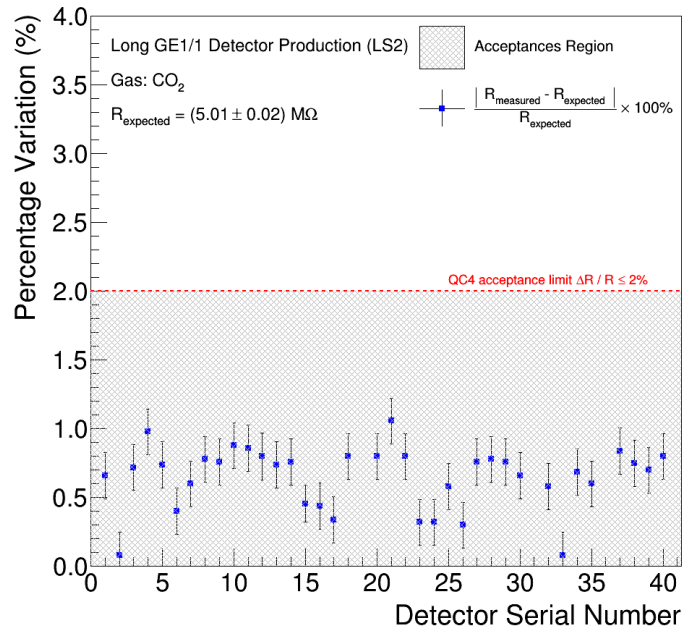
and

$$R_{noise} \leq 0.02 \text{ Hz/cm}^2, \text{ (at } 4.9 \text{ kV)}$$

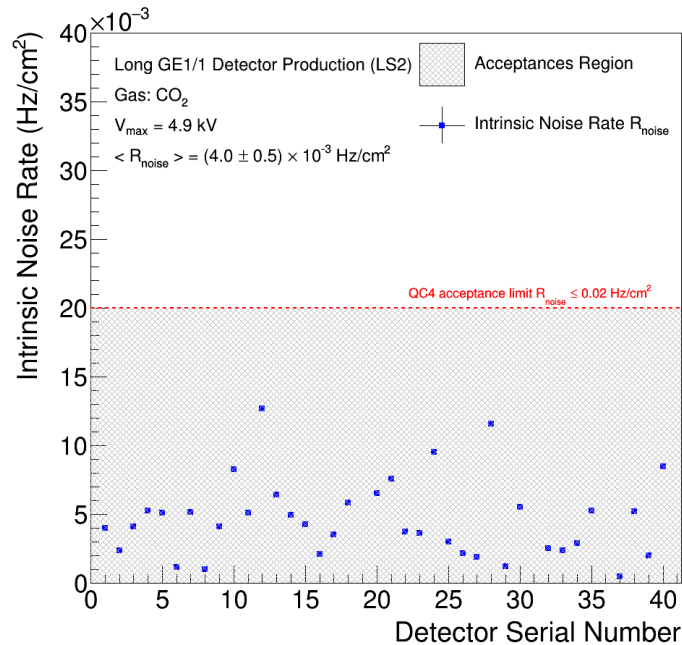
Figure 5.80 and 5.81 show the summary plots of the QC4 HV tests performed on the long and short GE1/1 detectors assembled at the CERN production and quality control site.

QC4 - HV test status at the CERN production and quality control site (latest data as at 31th August 2018):

5.4. Requirements for GE1/1 Quality Assurance/Quality Control assessment



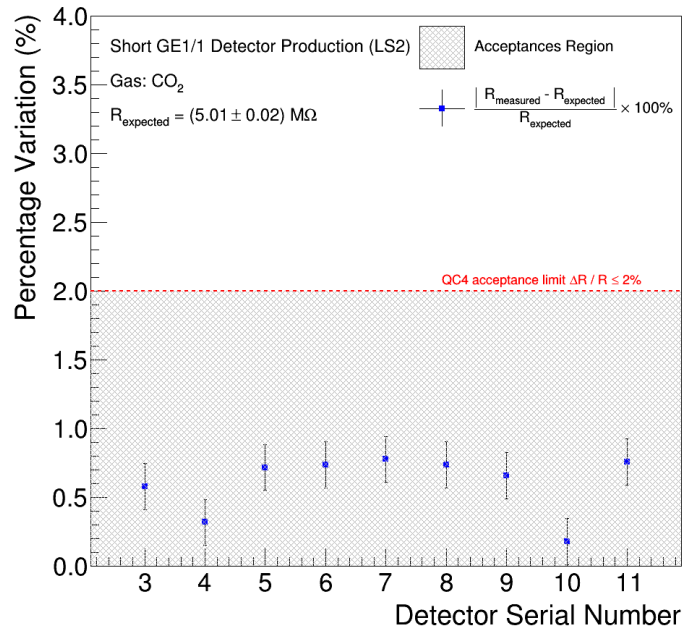
(a)



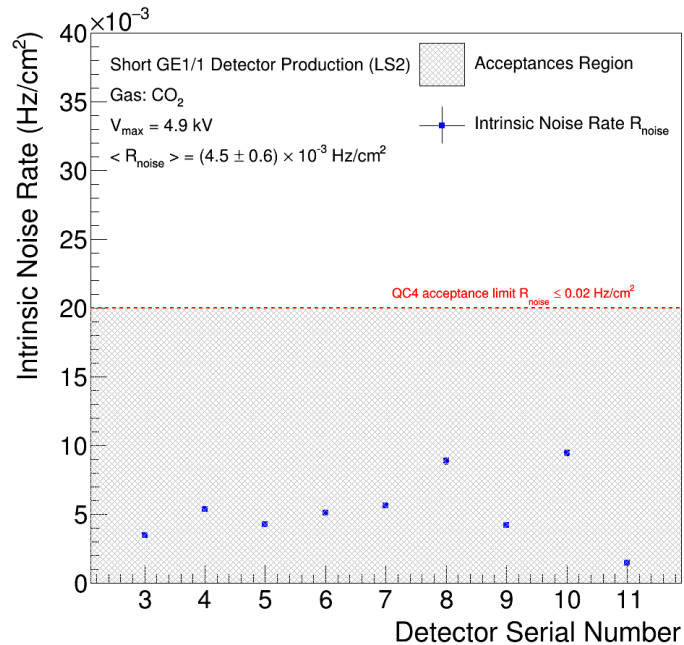
(b)

Figure 5.80: Summary of QC4 - HV tests performed on the long GE1/1 detectors assembled at the CERN production and quality control site: the percentage variation of resistance $\Delta R/R \times 100\%$ (top) and the intrinsic noise rate R_{noise} at applied voltage of 4.9 kV (bottom) are shown as a function of the detectors serial number. The horizontal dashed lines shows the QC4 acceptance limits.

5. The Assembly, Quality Control and Commissioning of the GE1/1 detectors



(a)



(b)

Figure 5.81: Summary of QC4 - HV tests performed on the short GE1/1 detectors assembled at the CERN production and quality control site: the percentage variation of resistance $\Delta R/R \times 100\%$ (top) and the intrinsic noise rate R_{noise} at applied voltage of 4.9 kV (bottom) are shown as a function of the detectors serial number. The horizontal dashed lines shows the QC4 acceptance limits.

1. Long GE1/1 triple-GEM detector
 - Number of detectors tested: 40
 - Number of detectors validated: 37
 - Number of detectors rejected: 3
2. Short GE1/1 triple-GEM detector
 - Number of detectors tested: 9
 - Number of detectors validated: 9
 - Number of detectors rejected: 0

Details on rejected detectors:

- *GE1/1-X-L-CERN-0019* detector: the QC4 - HV test showed the presence of a short circuit fault in one of the HV sectors of the third GEM-foil and several discharges. Intrinsic noise rate $R_{noise} \gg 0.02 \text{ Hz/cm}^2$, (at 4.9 kV).
- *GE1/1-X-L-CERN-0031* detector: the QC4 - HV test showed the presence of a short circuit fault in one of the HV sectors of the second GEM-foil. Intrinsic noise rate $R_{noise} \gg 0.02 \text{ Hz/cm}^2$, (at 4.9 kV).
- *GE1/1-X-L-CERN-0036* detector: the QC4 - HV test showed the presence of multiple short circuit faults on all three GEM-foils.

The multiple short circuit faults and several discharges have not allowed to complete the QC4 - HV Test. Therefore, the quality control data related to the rejected detectors are not present in the Figure 5.80. Further investigations into these detectors rejected in the QA/QC stage have been scheduled over the coming months in order to understand and possibly fix the issues related to the short circuits faults on the GEM-foils.

5.4.7.3 QC5 - Gas Gain Measurement in Ar/CO_2 (70/30)

Type of QA/QC test - The QC5 - Effective Gas Gain Measurement is divided into two stages: the measurement of the effective gas gain as a function of the high voltage applied on the resistive high voltage divider and the measurement of the response uniformity of the detector through a dedicated readout electronics based on the Scalable Readout System (SRS) which consists of APV25 Front-End ASICs with 128 readout channels connected to the readout board of the detector (see Section 5.4.6.6). Both tests are done in a specific radiation box containing an AMPTEK miniX X-ray source with a silver target emitting $\sim 22 \text{ keV}$ X-ray photons.

Acceptance criteria - The acceptance criteria for the QC5 - Effective Gas Gain Measurement derive directly from the required performances of the triple-GEM detector in terms of detection efficiency and time resolution. Figure 5.82 shows the MIP detection efficiency (Figure 5.82a) and time resolution (Figure 5.82b) of a triple-GEM detector in CMS configuration as a function of the detector gas gain, for a Ar/CO_2 (70/30) gas mixture and 3/1/2/1 mm gap configuration. The vertical black dashed line indicates the detector gas gain value of the order of 10^4 (reference value), at which the GE1/1 triple-GEM detectors will be operated in the CMS Muon System and corresponding to 97% detection efficiency and 7 ns time resolution in Ar/CO_2 (70/30) gas mixture. The vertical blue (red) dashed line shows in addition a 37% (50%) variation in the detector gas gain compared to the reference value of the gas gain [82] [83].

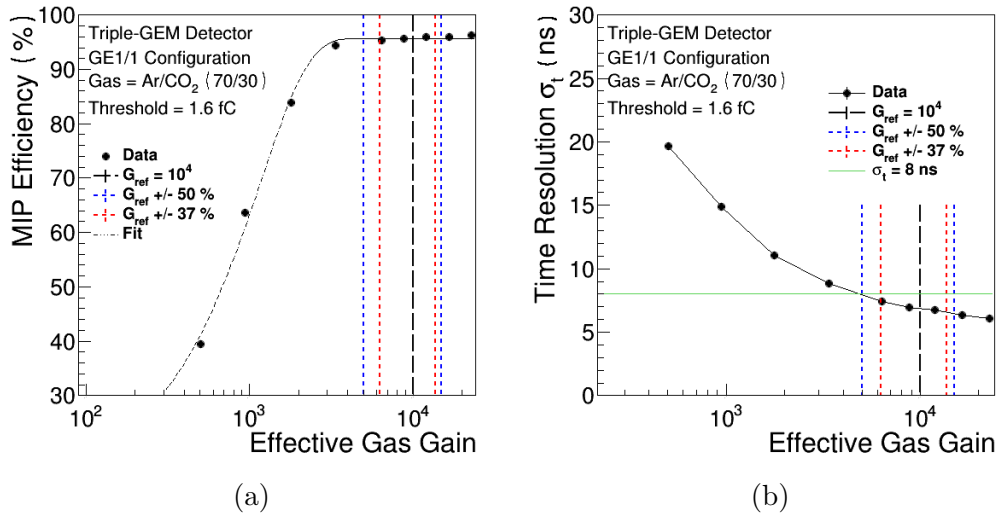


Figure 5.82: MIP detection efficiency (left) and time resolution (right) of a triple-GEM detector in CMS configuration as a function of the detector gas gain, for a Ar/CO_2 (70/30) gas mixture and 3/1/2/1 mm gap configuration [82] [83].

The detection efficiency reach the plateau at about 97% for a gas gain above 4×10^3 . It is also interesting to note the stability of the detector efficiency up to high gas gains of about $2.5 - 3 \times 10^4$. The time resolution of the order of 7 ns is measured at the efficiency plateau for Ar/CO_2 (70/30). It is also interesting to note that the time resolution is improving at higher gas gain up to 6 ns at gas gain of about $2.5 - 3 \times 10^4$. Therefore, a 37% (50%) variation in the detector gas gain should not affect the detector performances.

Due the fact that the gas gain determines the detector performances (e.g. efficiency, responding time and spatial resolutions, etc.), the monitoring of the gas gain uniformity across the entire detector active area is fundamental. Several factors, such as non-uniformity of the GEM-holes geometry, local contami-

nation, incorrect stretching technique or presences of defects on the readout board could affect the uniformity of gas gain all over the detector active area.

Impact of the GEM-foils thickness. According to spec information of the standard GEM-foils which is produced by CERN PCB Workshop, because accuracy of manufacturing of the $50 \mu m$ thick insulator whose material is Polyimide reach $(50 \pm 1) \mu m$, which is about 2%, the intrinsic variation of gas gain will be [55] [58] [81]:

- $\sigma_{single}/G_{single} \approx \pm 2.4\%$ in a single-GEM detector;
- $\sigma_{triple}/G_{triple} = \sqrt{3} \times \sigma_{single}/G_{single} \approx \pm 4.2\%$ in a triple-GEM detector.

A second-order contribution to the intrinsic variation of gas gain ($\pm 0.5\%$) is due to the copper thickness variation on the surface of the GEM-foil.

Impact of the GEM-holes diameter. Local variations in the size, shape, and rim roughness of the GEM-holes could alter the operational characteristics of the GEM-foil. According to spec information of the standard GEM-foils produced at CERN PCB Workshop, because accuracy of etching technique of the polyimide GEM-holes reach $(70 \pm 5) \mu m$ for the their outer diameter, and $(50 \pm 5) \mu m$ for their the inner diameter, the intrinsic variation of gas gain will be [55] [58] [81]:

- $\sigma_{single}/G_{single} \approx \pm 15\%$ in a single-GEM detector;
- $\sigma_{triple}/G_{triple} \approx \pm 26\%$ in a triple-GEM detector.

A second-order contribution to the intrinsic variation of gas gain is also due to the possible asymmetry in the GEM-holes structure.

Impact of the Drift and/or Readout board bending. The bending of the Drift and Readout board could lead to a non-uniform drift and induction gap, respectively. Several factors could determine the bending of the Drift and Readout board:

1. Initial bending from the fabrication process;
2. Bending induced by incorrect stretching technique;
3. Bending caused by mechanical stress on O-ring and internal frame;
4. Bending induced by built-in gas over pressure.

A great effort has been made by the CMS-GEM Collaboration on the detector design and assembly procedure in order to mitigate the Drift and Readout board bending effect. However, for large area GEM-based detector, such as the LS2-GE1/1 triple-GEM detector, one can not completely eliminate the bending of the Drift and/or Readout board.

The maximum variation of the drift gap caused by the the maximum flatness deviation of the Drift board could reach $(3 + 0.6)$ *mm* and leading to a non-uniformity of about 20% in the electric drift field. Similarly, the maximum variation of the induction gap induced by the maximum flatness deviation of the Readout board could reach $(1 + 0.4)$ *mm* and leading to a non-uniformity of about 40% in the electric induction field. Because the Drift and Readout board bending could lead to an electron transparency variation in a GEM-based detector, the intrinsic variation of gas gain will be [55] [58] [81]:

- $\sigma_{triple}/G_{triple} \approx +7.5\%$ caused by the bending of the Drift board;
- $\sigma_{triple}/G_{triple} \approx +25\%$ caused by the bending of the Readout board.

A second-order contribution to the intrinsic variation of gas gain is also due to the thickness Nuvovern[®] polyurethane varnish coating ($\pm 0.5\%$) on the internal frame and/or height of the pull-outs ($\pm 0.7\%$).

Impact of the environmental parameters. The gas gain of a gaseous detector depends approximately through an exponential function, on the gas density, function itself of the ratio temperature over pressure. The measurements have then to be corrected in order to take into account of the temperature and pressure variability in the day–night cycle and/or in the different weather patterns that may occur during the test. Furthermore, the Effective Gas Gain Measurements is normalized to the pressure and temperature values in the cavern of the CMS experiment, in order to take into account the difference in the environmental conditions across all the different production and quality control sites over the world. A second-order contribution to the intrinsic variation of gas gain is also due to the variation in gas mixture composition and/or in gas flow rate.

Expected intrinsic gas gain variation. Although the individual contributions that influence the intrinsic variation of gas gain are not necessarily Gaussian and do not occur independently, nevertheless, as a first approximation, one generally adds these contributions in quadrature to obtain the total gas gain spread as the full width at half maximum:

$$\sigma_{total} = \sqrt{\sigma_{thickness}^2 + \sigma_{diameter}^2 + \sigma_{drift}^2 + \sigma_{readout}^2} \approx 37.1\% \quad (5.22)$$

where:

$\sigma_{thickness}$ contribution induced by the GEM-foils thickness variation;

$\sigma_{diameter}$ contribution induced by the GEM-holes diameter variation;

σ_{drift} contribution induced by the non-uniformity of the Drift board;

$\sigma_{readout}$ contribution induced by the non-uniformity of the Readout board;

Figure 5.83 shows the summary plots of the Effective Gas Gain Measurements (corrected for pressure and temperature variations) performed in a

5.4. Requirements for GE1/1 Quality Assurance/Quality Control assessment

Ar/CO_2 (70/30) gas mixture on the reference readout sector $(i\eta, i\phi) = (4, 2)$ of the Long GE1/1 detectors (Figure 5.83a) and Short GE1/1 detectors (Figure 5.83b) at an applied voltage of 3102 V (660 μA divider current equivalent) as a function of the detectors serial number.

The mean $\langle G \rangle_{Long}$ and standard deviation σ_{Long} of the effective gas gain for the Long GE1/1 triple-GEM detectors are respectively 6495.5 and 1872.8, resulting in detector gas gain variation:

$$G_{Long} = 6495.5 \pm 1872.8 \text{ (mean } \pm \text{ std.)} \Rightarrow \sigma_{Long}/\langle G \rangle_{Long} \approx 28.8\%$$

The mean $\langle G \rangle_{Short}$ and standard deviation σ_{Short} of the effective gas gain for the Short GE1/1 triple-GEM detectors are respectively 7724.1 and 1984.2, resulting in detector gas gain variation:

$$G_{Short} = 7724.1 \pm 1984.2 \text{ (mean } \pm \text{ std.)} \Rightarrow \sigma_{Short}/\langle G \rangle_{Short} \approx 25.7\%$$

The mean value of the effective gas gain for both Long and Short GE1/1 triple-GEM detectors is well below acceptable 50% gas gain variations, which guarantees a stable operation efficiency (97%) and time resolution (< 10 ns) on the entire detector active area.

Figure 5.84 shows the summary plots of the Response Uniformity Measurements performed on the Long GE1/1 detectors (Figure 5.84a) and Short GE1/1 detectors (Figure 5.84b) at an effective gas gain of ~ 600 as a function of the detectors serial number.

The mean $\langle \sigma/\mu \rangle$ and standard deviation $\sigma_{\sigma/\mu}$ of the response uniformity for the Long GE1/1 triple-GEM detectors are respectively 14.2% and 5.4%:

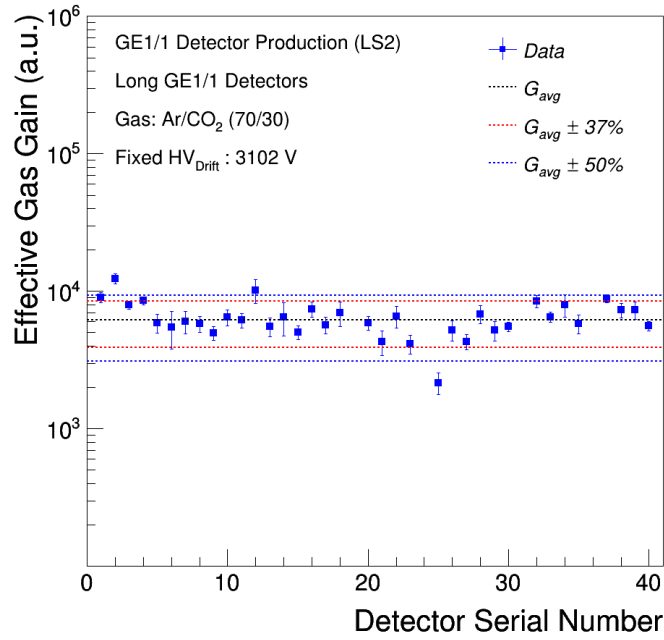
$$(\sigma/\mu)_{Long} = 14.2 \pm 5.4\% \text{ (mean } \pm \text{ std.)}$$

The mean $\langle \sigma/\mu \rangle$ and standard deviation $\sigma_{\sigma/\mu}$ of the response uniformity for the Short GE1/1 triple-GEM detectors are respectively 11.8% and 3.9%:

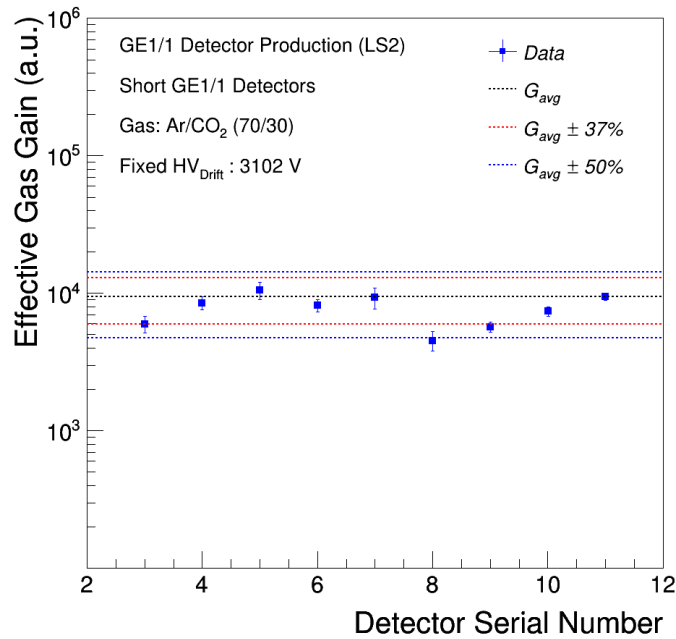
$$(\sigma/\mu)_{Short} = 11.8 \pm 3.9\% \text{ (mean } \pm \text{ std.)}$$

The mean value of the response uniformity for both Long and Short GE1/1 triple-GEM detectors is well below acceptable 50% gas gain variations, which guarantees a stable operation efficiency (97%) and time resolution (< 10 ns) on the entire detector active area.

However, the QC5 - Effective Gas Gain Measurements for both Long and Short GE1/1 triple-GEM detectors, shown in the Figure 5.83, are not representative of the entire detector active area since the measurements are performed only in the reference readout sector $(i\eta, i\phi) = (4, 2)$. To overcome this issue, the uniformity maps, obtained from the QC5 - Response Uniformity Measurements,



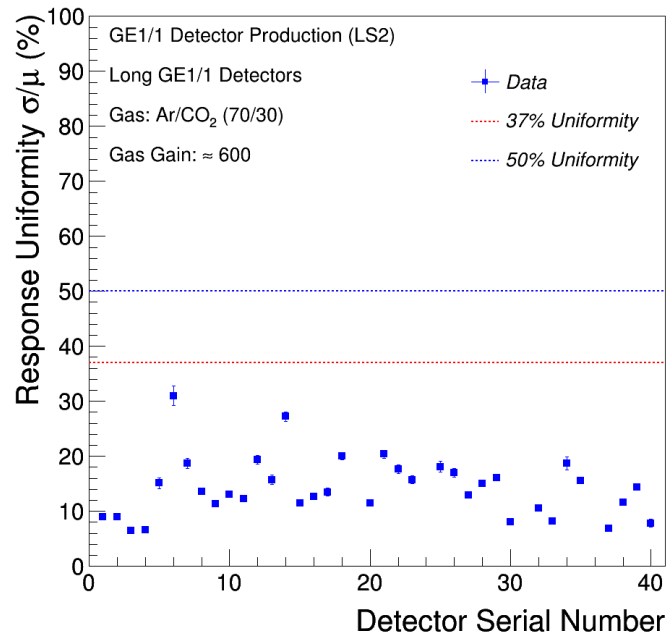
(a)



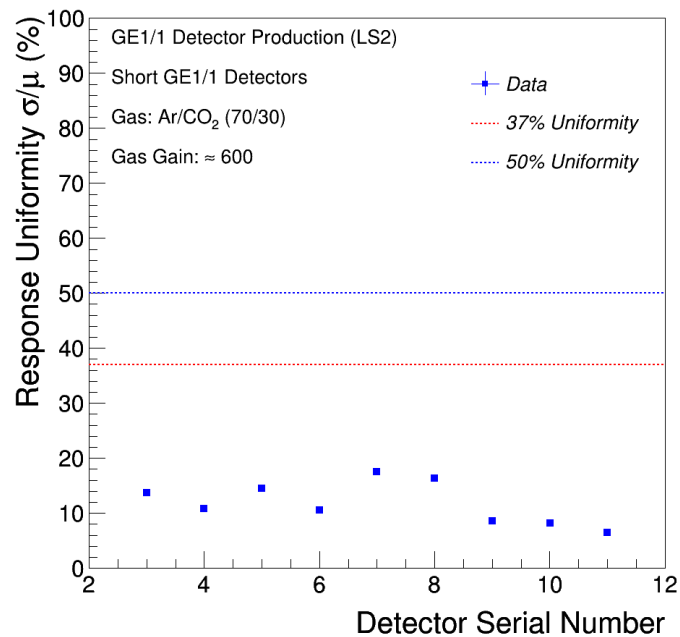
(b)

Figure 5.83: Summary of QC5 - Effective Gas Gain Measurements performed on the Long GE1/1 detectors (top) and Short GE1/1 detectors (bottom) assembled at the CERN production and quality control site. The effective gas gain has been measured in a Ar/CO_2 (70/30) gas mixture on the reference readout sector ($i\eta, i\phi$) = (4, 2) at an applied voltage of 3102 V (660 μA divider current equivalent).

5.4. Requirements for GE1/1 Quality Assurance/Quality Control assessment



(a)



(b)

Figure 5.84: Summary of QC5 - Response Uniformity Measurements performed on the Long GE1/1 detectors (top) and Short GE1/1 detectors (bottom) assembled at the CERN production and quality control site. The response uniformity has been measured in a Ar/CO_2 (70/30) gas mixture at an effective gas gain of ~ 600 .

are used to calculate the average effective gas gain and standard deviation on the entire detector active area. Figure 5.85 shows the summary plots of the Average Effective Gas Gain Measurements (corrected for pressure and temperature variations) performed on Long GE1/1 detectors (Figure 5.85a) and Short GE1/1 detectors (Figure 5.85b) at an applied voltage of 3102 V (660 μ A divider current equivalent) as a function of the detectors serial number.

The mean $\langle G \rangle_{Long}$ and standard deviation σ_{Long} of the average effective gas gain for the Long GE1/1 triple-GEM detectors are respectively 7020.8 and 1555.4, resulting in detector gas gain variation:

$$G_{Long} = 7020.8 \pm 1555.4 \text{ (mean } \pm \text{ std.)} \Rightarrow \sigma_{Long}/\langle G \rangle_{Long} \approx 22.2\%$$

The mean $\langle G \rangle_{Short}$ and standard deviation σ_{Short} of the average effective gas gain for the Short GE1/1 triple-GEM detectors are respectively 7975.0 and 2414.4, resulting in detector gas gain variation:

$$G_{Short} = 7975.0 \pm 2414.4 \text{ (mean } \pm \text{ std.)} \Rightarrow \sigma_{Short}/\langle G \rangle_{Short} \approx 30.3\%$$

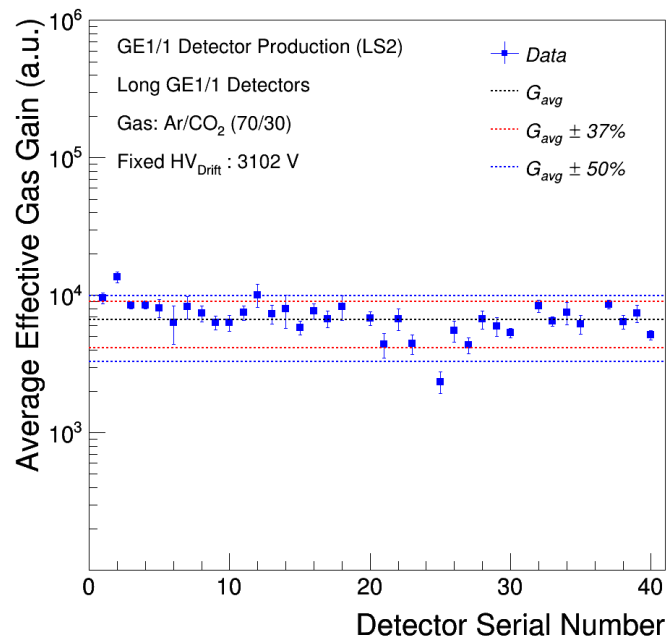
Once again, the mean value of the average effective gas gain for both Long and Short GE1/1 triple-GEM detectors is well below acceptable 50% gas gain variations, which guarantees a stable operation efficiency (97%) and time resolution (< 10 ns) on the entire detector active area. The gain uniformity plays an even greater role than the absolute effective gas gain. Indeed, in order to reduce the differences between detector performances, GE1/1 triple-GEM detectors with similar QA/QC results will be coupled into super-chamber. Each super-chamber will be powered independently. This will allow to tune the high voltage settings and to optimize the working point of each super-chamber, minimising the differences in performances (in particular the effective gas gain).

5.4.8 LS2 - GE1/1 Detector Production Status

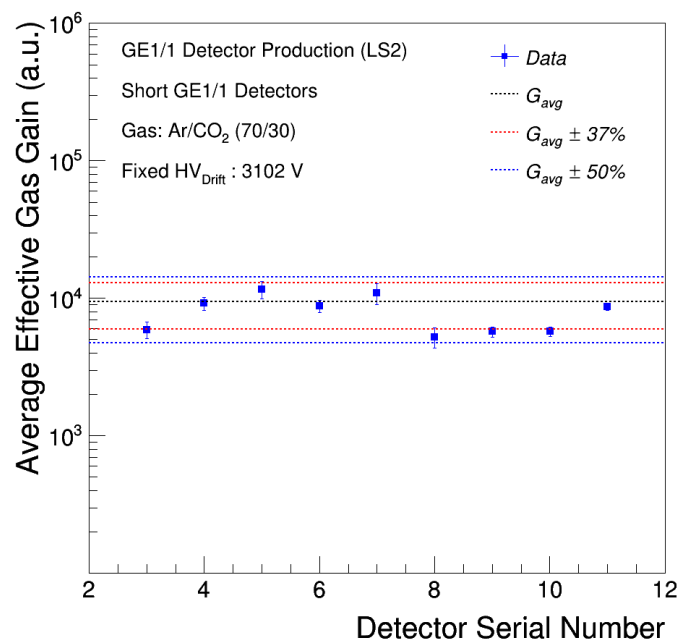
A great effort of whole CMS-GEM Collaboration is under way to complete the assembly and qualification of the GE1/1 triple-GEM detectors, which will be installed in the muon forward region of the CMS experiment during the second Long Shutdown (2019/2020). The assembly and acceptance/qualification testing of the detectors are now proceeding routinely. At the end of August 2018, a total of 140/144 (97%) detectors have been successfully assembled by a massive effort of all production and quality control sites: 103 of those assembled detectors have been completely qualified, while 37 other ones are awaiting or are in different stages of the quality control. In October 2018, the on-detector electronics assembly and the super-chamber production will be launched at the CERN production site.

The LS2 - GE1/1 detectors mass production trend is shown on Figure 5.86. The black solid line shows the level of current production rate, whereas the

5.4. Requirements for GE1/1 Quality Assurance/Quality Control assessment



(a)



(b)

Figure 5.85: Summary of QC5 - Average Effective Gas Gain Measurements performed on the Long GE1/1 detectors (top) and Short GE1/1 detectors (bottom) assembled at the CERN production and quality control site.

5. The Assembly, Quality Control and Commissioning of the GE1/1 detectors

blue dashed line shows the expected detectors based on the average production rates achieved during the GE1/1 Slice Test experience. The red dotted line shows the actual number of validated detectors at different production sites.

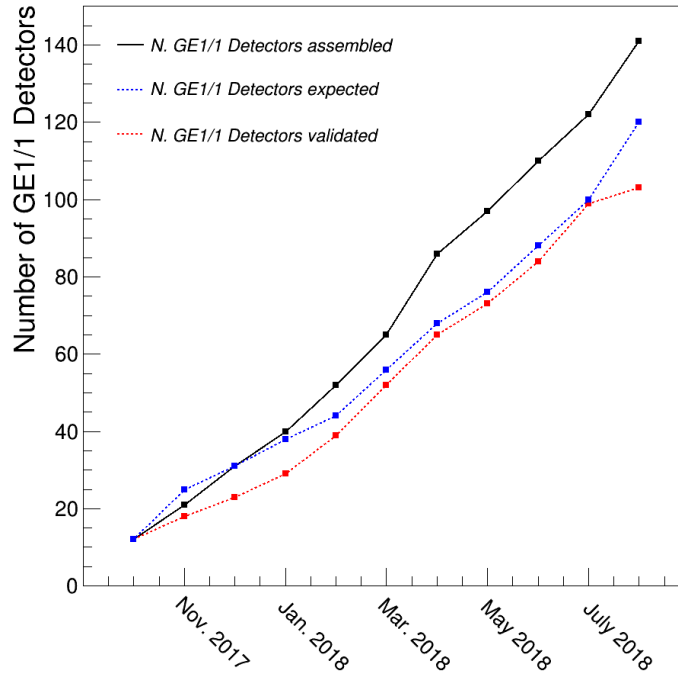


Figure 5.86: LS2 - GE1/1 detectors mass production trend. The black solid line shows the level of current production rate, whereas the blue dashed line shows the expected detectors based on the average production rates achieved during the GE1/1 Slice Test experience. The red dotted line shows the actual number of validated detectors at different production sites (latest data as at 31th August 2018).

Table 5.7 shows the summary status of the LS2-GE1/1 detectors mass production in the different production and quality control sites involved in the CMS-GE1/1 project.

An extensive investigation campaign has been scheduled over the coming months in order to determine the cause of the out of specification results for the rejected detectors. Even if a detector is rejected based on an out of specification result during the QA/QC procedures, the investigation is necessary to identify the causes and possibly recover the detector. Moreover, the detectors which are out of the specification in one production and quality control site will be rechecked in the CERN production site before the final rejection.

5.4. Requirements for GE1/1 Quality Assurance/Quality Control assessment

Production Site	Current state in August 2018		
	Assembled	Validated	Out of Spec.
CERN (from July 2017)	51	46	5
USA (from Aug. 2017)	10	2	1
BE/DE (from Aug. 2017)	21	17	0
ITALY (from Sep. 2017)	26	17	0
INDIA (from Sep. 2017)	17	11	0
PAKISTAN (from May 2018)	15	10	0
Total (August 2018)	140 (69 Long + 71 Short)		

Table 5.7: Summary status of the LS2-GE1/1 detectors mass production in the different production and quality control sites involved in the CMS-GE1/1 project (latest data as at 31th August 2018).

5. The Assembly, Quality Control and Commissioning of the GE1/1 detectors

Long-term operation study

6.1 Introduction

The high-luminosity LHC (HL-LHC) upgrade is setting a new challenge for particle detector technologies. The increase in luminosity will produce a particle background in the gas-based muon detectors ten times higher than the current background produced by LHC. The detailed knowledge of the detector performance in the presence of such a high background is crucial for an optimized design and efficient operation after the HL-LHC upgrade. A precise understanding of possible aging effects of detector materials and gases is of extreme importance. Aging is one of the most critical limitations of the use of gaseous detectors in strong radiation environments; it includes all the processes that lead to a significant and permanent degradation of the performances: gain drop, non-uniformity, dark current, discharge, etc. To evaluate the potential detector performance deterioration over the lifetime of an experiment, detector prototypes are subject to accelerated aging tests performed at a higher instantaneous radiation rate.

The radiation exposure tests aim to accumulate an amount of charge comparable to the values that will be integrated during the lifetime of the HL-LHC. The estimation of the total charge produced at the HL-LHC in the muon chambers of CMS experiment includes the maximum interaction rate R_{max} , the primary charges deposited by particles n_{pair}^{tot} , the gas gain of the detector G and the exposure time at the HL-LHC t_{LHC} . Using the numbers given in Table 6.1, the most probable energy loss by a Minimum Ionizing Particle (MIP) in the Ar/CO_2 (70/30) gas mixture is given by the Bragg additivity law:

$$\left\langle \frac{dE}{dx} \right\rangle_{tot} = \left\langle \frac{dE}{dx} \right\rangle_{Ar} \times w_{Ar} + \left\langle \frac{dE}{dx} \right\rangle_{CO_2} \times w_{CO_2} \approx 2.61 \text{ keV/cm} \quad (6.1)$$

where $\langle dE/dx \rangle_{Ar}$, $\langle dE/dx \rangle_{CO_2}$ and w_{Ar} , w_{CO_2} are respectively the most probable energy loss by a MIP in Ar and CO_2 and the weight fraction of the Ar and CO_2 in the gas mixture.

6. Long-term operation study

Gas	Z	A	Density 10^{-3} (g/cm ³)	E_x (eV)	E_i (eV)	W_i (eV)	$\langle dE/dx \rangle_{MIP}$ (keV cm ⁻¹)	n_p (cm ⁻¹)	n_t (cm ⁻¹)	Radiation Leight (m)
<i>He</i>	2	2	0.178	19.8	24.5	41	0.32	4.2	8	745
<i>Ar</i>	18	39.9	1.782	11.6	15.7	26	2.44	23	94	110
<i>Ne</i>	10	20.2	0.90	16.67	21.56	36.3	1.56	12	43	345
<i>Xe</i>	54	131.3	5.86	8.4	12.1	22	6.76	44	307	15
<i>CF₄</i>	42	88	3.93	12.5	15.9	54	7.0	51	100	92.4
<i>DME</i>	26	46	2.2	6.4	10.0	23.9	3.9	55	160	222
<i>CO₂</i>	22	44	1.98	5.2	13.7	33	3.01	35.5	91	183
<i>CH₄</i>	10	16	0.71	9.8	15.2	28	1.48	25	53	646
<i>C₂H₆</i>	18	30	1.34	8.7	11.7	27	1.15	41	111	340
<i>i - C₄H₁₀</i>	34	58	2.59	6.5	10.6	23	5.93	84	195	169

Table 6.1: Physical Properties of gases at normal temperature and pressure (NTP): E_x and E_i are the excitation and ionization energy, respectively, n_p and n_t are the number of primary electron-ion pairs per cm and the total number of electron-ion pairs per cm, respectively, W_i is the average energy required to produce one electron-ion pair in the gas, $\langle dE/dx \rangle_{MIP}$ is the most probable energy loss by a minimum ionizing particle (MIP) [84].

In a 0.3 cm triple-GEM conversion gap of *Ar/CO₂* (70/30) gas mixture, the energy deposited by a MIP is approximately $E_{MIP} \approx 0.78$ keV. Considering the detector gas gain G , the charge produced by each incident particle at the HL-LHC is given by:

$$Q_{MIP} = \frac{E_{MIP}}{W_i} \times q_e \times G = n_{pair}^{tot} \times q_e \times G \quad (6.2)$$

where $W_i \approx 28.1$ eV and $n_{pair}^{tot} \approx 28$ pair/0.3 cm are respectively the average energy required to produce one electron-ion pair and the total number of electron-ion pairs in a 0.3 cm triple-GEM conversion gap of *Ar/CO₂* (70/30) gas mixture. Since the particles crossing the detector arrive with a maximum angle of 23° at ($\eta = 1.5$), the maximum path length in the triple-GEM conversion gap is 0.33 cm. Therefore the maximum number of primary charges deposited by MIPs in a triple-GEM conversion gap of *Ar/CO₂* (70/30) gas mixture is approximately $n_{pair}^{tot} \approx 31$ pair/0.33cm. Taking into account a nominal gas gain of 2×10^4 , the charge produced per MIP yields is approximately $Q_{MIP} \approx 98.26$ fC.

Assuming the expected background components and their corresponding maximum hit rates R_{max} in the *GE1/1*, *GE2/1* and *ME0* detectors (see Table 6.2), the primary charge induced by particles n_{pair}^{tot} , the gas gain of the detector G and the effective exposure time at the LHC t_{LHC} , the total integrated charge generated in 10 years of HL-LHC operation is given by:

$$Q_{tot} = Q_{MIP} \times R_{max} \times t_{LHC} = n_{pair}^{tot} \times q_e \times G \times R_{max} \times t_{LHC} \quad (6.3)$$

Based on the previous operation of the LHC, the effective exposure time after 10 years is estimated to be 6×10^7 s [69]. Therefore, at a nominal gas gain of 2×10^4 , the total accumulated charge after 10 HL-LHC years in the *Ar/CO₂* (70/30) gas mixture is ~ 6 mC/cm², ~ 3 mC/cm² and ~ 283 mC/cm² for the *GE1/1*, *GE2/1* and *ME0* detectors, respectively.

6.1. Introduction

GEM Station	Max. Neutron Flux [Hz/cm ²]	Max. Neutron Induced Hit Rate [Hz/cm ²]	Max. Photon Hit Rate [Hz/cm ²]	Max. e ⁺ /e ⁻ Hit Rate [Hz/cm ²]	Max. Total Hit Rate [Hz/cm ²]	Tot. Accum. Charge after 10 HL-LHC years [mC/cm ²] – no safety factor –
<i>GE1/1</i>	0.277×10^6	499	847	123	1469	6
<i>GE2/1</i>	0.191×10^6	343	273	56	672	3
<i>ME0</i>	3.280×10^6	5910	33900	7700	47510	283

Table 6.2: Expected background components and their corresponding hit rates in the *GE1/1*, *GE2/1*, and *ME0* detectors. The total accumulated charge is calculated from the total hit rate at a typical detector gas gain of 2×10^4 after 10 HL-LHC years which correspond an effective exposure time of about 6×10^7 s [69].

The aim of the longevity studies is to reproduce in laboratory this lifetime with a safety factor 3 before the final installation in the CMS experiment, by accumulating a charge of ~ 18 mC/cm², ~ 9 mC/cm² and ~ 850 mC/cm² for the *GE1/1*, *GE2/1* and *ME0* detectors, respectively.

6.1.1 Aging phenomena of gaseous detectors

Aging phenomena, a permanent degradation of operating performances under the exposure to ionizing radiation, constitute one of the most complex and serious potential problems which could limit, or severely impair, the use of gas-based detectors in high-energy physics experiments. The *classical aging* [85] [101] [87] effects, primarily observed on the Multi-Wire Proportional Chambers, are the result of the polymerization phenomena due to the chemical reactions occurring in avalanche plasma surrounding the amplification region. Such hypothesis is based on the fact that the dissociation energies of typical molecules (3 – 4 eV) are much lower than the ionization energies (> 10 eV). Since it is necessary to reach the ionization energies in order to generate the final avalanche, it was argued that the avalanche produce even higher concentration of molecular fragments and/or free radicals than that of ions, as is typical in plasma chemistry. Since most of the free radicals are chemically very active, they will either recombine back to form the original molecules or other new volatile species (monomers), or could start to form new cross-linked molecular structures of increasing molecular weight (polymers) [101]. When the polymerized chain becomes large enough for condensation to occur, it will start to diffuse inside the active gas volume of the detector. These polymerized chains will be then either carried away by a gas flow, or could deposit on the electrode surfaces due to their charge or dipole moment. Figure 6.1 shows a Scanning Electron Microscope (SEM) analysis of typical wire deposits after

sustained irradiation of a Multi-Wire Proportional Chambers [87].

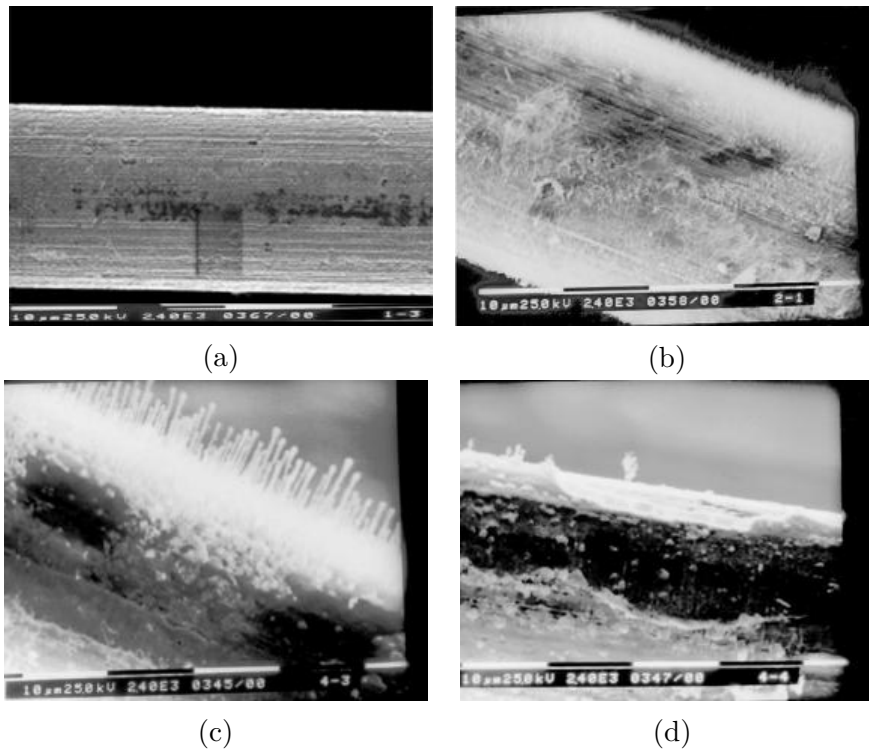


Figure 6.1: Example of SEM micrographs of a clean gold plated tungsten wire (a) and damaged wires (b, c, d) used in a Multi-Wire Proportional Chambers after sustained irradiation, showing a different type of polymer deposits on the wire surface [87].

The formation of these polymer deposits, conductive or insulating, on the anode and/or cathode surface could lead to a number of different operational problems, such as a decrease of the gas gain and energy resolution, excessive currents, self-sustained discharges, or sparking, voltage instability, wire corrosion or wire rupture.

- **Anode Aging.** The accumulation of the polymeric deposit, insulating and/or conductive, on the anode surface could lead to a significant distortion of the electric field in the amplification region [88]. The result of such distortions of the electric field strength is a permanent decrease of the gas gain and/or energy resolution loss (see Figure 6.2).
- **Cathode Aging.** The deposition of polymers at the surface's cathode could lead even more dramatic effects on the detector performances. An example of a particularly disastrous aging effect related to the formation of the polymeric deposit on the cathode surface, is the so-called *Malter effect* [89]. The products of the chemical process could create a thin

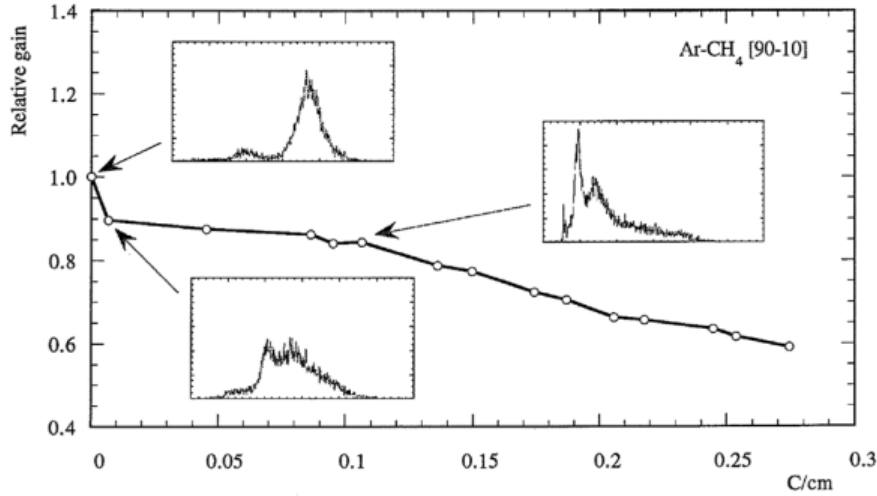


Figure 6.2: Example of *Classical Aging* of a wire chamber exposed to an X-rays flux from a *Cu*-target X-ray tube at a rate of about 1.4 MHz/cm . The detector has been operated at a gas gain of $\sim 2 \times 10^4$ and has been flushed with the *Ar/CH₄* (90/10) gas mixture. The curve represents the variation of the relative gas gain normalized with the initial value as a function of the accumulated charge per unit wire length (*C/cm*). The energy spectrum of the X-ray source has been performed at different value of accumulated charge to quantify the the energy resolution loss [88].

insulating coating on the cathode surface which could inhibit the neutralization of positive ions drifting from the avalanches plasma at the anode (see Figure 6.3).

Therefore, since the polymeric layer is insulating, the positive ions do not readily reach the cathode surface, and since the layer is very thin, the positively charged layer, together with the induced charge on the cathode surface produces a very large electric dipole field which could exceed the threshold for field emission ($\sim 10^7 \text{ V/cm}$). The result is that electrons could be extracted from the cathode surface. These electrons could more successfully penetrate the insulating layer with respect to the positive ions, and some of them will neutralize the positive charge. However, most of these electrons will enter in the active gas volume, drift to the anode, and produce more positive ions, which then drift back to the cathode and enhance the strength of the dipole field emission of electrons. Such positive feedback between the electron emission at the cathode and anode amplification is responsible for an increase of the dark current and/or rate of noise pulses in the detector, self-sustained discharges and the electrical breakdown of the gas.

- **Electronegative Impurities.** Another potentially serious aging effect is the production of long-lived and highly electronegative radicals which

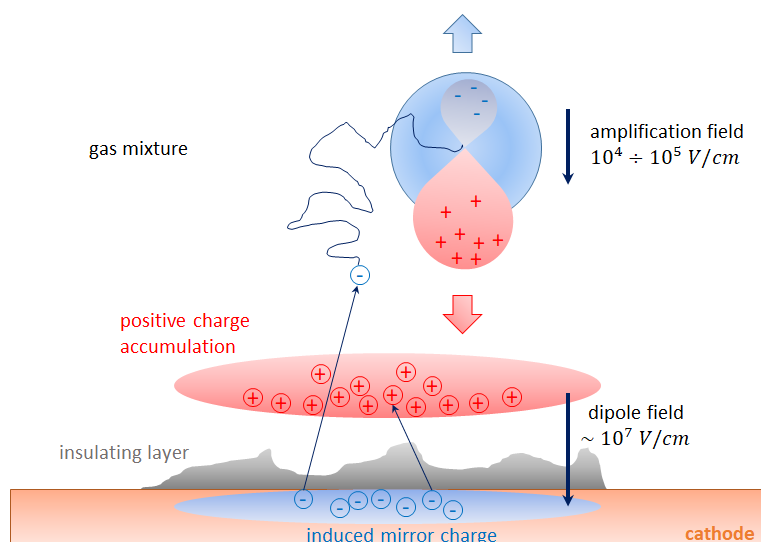


Figure 6.3: Schematic of the mechanism leading to the Malter effect [90].

could significantly degrade the performance of the detector by absorbing the electrons induced by a particle and drastically leading to a decrease of the effective gas gain of the detector [101].

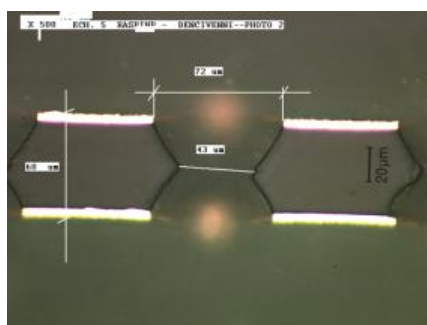
Several aging laboratory test on gaseous detectors have demonstrated that the gas mixtures containing hydrocarbon molecules ($C_2H_2F_4$, CF_4/CH_4 , $Ar/CF_4/CH_4$, etc.) are not trustable for long-term operation in high rate application. Such gas mixtures can lead to the formation of a large variety of hydrogen-deficient radicals that can easily make bonds with other molecular fragments and form large polymer chains (this effect is more pronounced in presence of pollution or under discharges, sparks and Malter effect) [101] [91] [92]. It is generally accepted that oxygen-containing additives can improve the detector life-time in such gas mixture [93] [94] [95]: the resulting oxygen-based radicals can reduce the polymerization processes by absorbing the hydrocarbon molecules and leading to the formation of relatively stable and volatile products (CO , CO_2 , H_2 , H_2O , etc.) that can be easily carried away from the active gas volume of the detector by the gas flow. The hydrogen-free mixtures such as Ar/CO_2 are particularly suitable for the modern high-energy physics experiments: the Ar/CO_2 gas mixture has been adopted by CMS GEM Collaboration for the GE1/1, GE2/1 and ME0 triple-GEM detectors proposed for the future upgrade of the innermost muon spectrometer of the CMS experiment.

A vast literature exists describing the dramatic aging effects on the life-time of the gaseous detectors due to certain traces of pollutants either as contaminants initially present in the gas system or as the result from outgassing of solid construction materials in contact with the gas volume. A large amount of aging and outgassing data have been accumulated in the framework of the RD-10 [96]

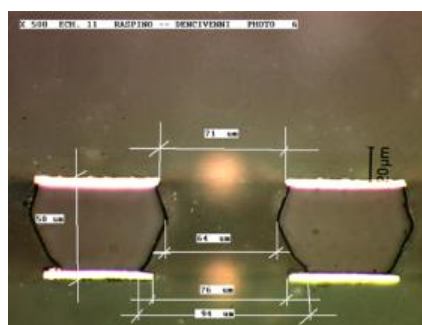
[97] and RD-28 [98] projects at CERN in the last decade: it contains test results for epoxy compounds, adhesive tapes, leak sealers, solid materials, O-rings, plastic gas pipes, etc. This list, summarized at *2001 International Workshop on Aging Phenomena in Gaseous Detectors* (DESY - Hamburg) [99] is useful for pre-selecting assembly materials and components that will then be used in the construction of the detector. In particular, it has been shown in many experiments that the presence of even minute traces of *Si*-based molecules in the active gas volume of a detector readily leads to the production of a large variety and a high concentration of free radicals resulting in polymer deposits which could destroy the entire detector [100] [101]. This has been confirmed by the plasma chemistry where it has been observed that the polymerization rate of silicon-based compounds by far exceeds that of carbon-base molecules, despite their identical valence shell structure [85]. Indeed, silicon-based radicals can react both with hydrocarbons and oxygen-based radicals and can lead to the formation of the rather heavy polymers which cannot be easily evacuated by gas flow. Unfortunately, the silicon-based compounds are present in many grease and/or lubricants, various oils, adhesives and rubber, O-ring and in the standard gas system components such as diffusion pumps, flow regulators, dust filter, etc. Moreover, the halogens contamination has been shown to shorten detector life-times considerably and must be banned from the active gas volume. Because of their low dissociation energy, the compounds containing halogens can lead to the formation of large quantities of free radicals in the avalanche plasma and accelerate greatly certain polymerization reactions. A probable source of these halogen pollution could be from solvents commonly used during manufacture to degrease and clean various materials and/or the outgassing of rubber and some plastic materials. This solvent residue can later contaminate the active gas volume of the detector.

The CF_4 -based mixtures have been proposed as the most attractive candidate for future experiments at high-luminosity colliding beam machines. This is primarily due to their high-drift velocity, high primary ionization and low electron diffusion. Moreover, CF_4 is used as an excellent etching gas for *Si* and *Si*-containing compounds, which react with fluorine to form volatile *Si-F* based products that can be evacuated from the active gas volume [102] [103]. On the other hand, since the $F-F$ bond in the CF_4 molecules is extremely weak (~ 1.6 eV) and easily broken in the plasma avalanche, the CF_4 dissociation can lead to the production of highly reactive CF_x and F radicals which react violently with exposed electrode surfaces to form metal fluorides or cause etching phenomena. Moreover, the products of CF_4 disintegration, in association with H_2O present in the gas mixture, can lead to the formation of the hydrofluoric acid that can chemically attack *HF*-soluble materials existing in the detection system [103] [104]. In the particular case of triple-GEM detectors, several aging laboratory tests have shown that the use of the CF_4 -based gas mixture can lead to a not negligible gas gain variations. The decrease of the electric field intensity inside the GEM-holes, resulting in a gas gain drop,

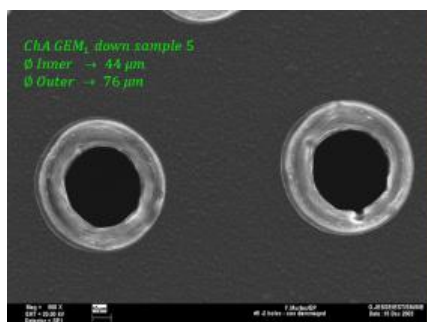
has been attributed to the CF_4 etching of copper and kapton in proximity of GEM-hole edges (see Figure 6.4). Further Scanning Electron Microscope (SEM) analysis have shown the appearance of a thin non conductive layer (a Cu-F compound) on the surface of the GEM-foils in proximity of the holes edge resulting in a significant distortion of the electric field inside the GEM-holes themselves [105]. The solution to this problem consists of increasing the gas flow rate, since this tends to "sweep away" the harmful radicals and ions that could result in surface coatings and/or damage the GEM-foils irreversibly. In general, radiation damage to the triple-GEM technology operating in CF_4 -based gas mixture has been found to be the most significant around the rims of the GEM-holes (where the electric fields intensity exceeds the average value) and for the third GEM-foils in series (where number and density of avalanche electrons is the largest).



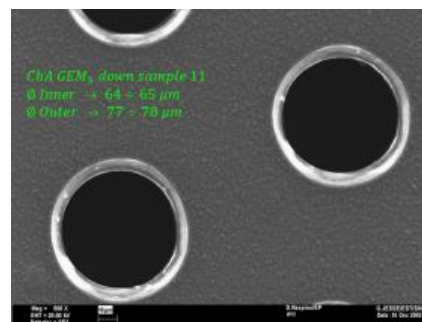
(a) Cross section of the first GEM-foil of a triple-GEM detector



(b) Cross section of the third GEM-foil of a triple-GEM detector



(c) Surfaces of the first GEM-foil of a triple-GEM detector



(d) Surface of the third GEM-foil of a triple-GEM detector

Figure 6.4: Example of SEM micrographs of GEM holes of a triple-GEM detector, showing the etching induced by HF acid [105].

6.1.2 Past experience on the aging of GEM-based detector

The GEM-based detector is rather insensitive to the classical aging processes compared to wire-type detectors. Two geometrical particularities were found to be a major factors which increases the reliability and radiation hardness of a GEM technology. The first advantage is a full decoupling of the amplification stage (GEM-foils) and the readout board (PCB). In the GEM-based detector the gas amplification is localized inside GEM-holes and the absence of a strong amplification field close to the readout plane drastically reduces the rate of polymerization and, therefore, the polymer deposition on the readout strips system. In the same way, the possibility of polymer formation and their deposits on the cathode drift plane is significantly reduced, as well as the resulting Malter effect. The second advantage is the sharing of the gas amplification into multiple cascade stages; in this way each stage will give rise a not very intense plasma avalanche with a lower energy available for the dissociation of the molecules of the active gas. Therefore, the production of free radicals and monomers is significantly suppressed as well as the resulting formation of complex polymer chains and polymeric deposits on the detector structures. Moreover, splitting the amplification in multiple cascaded stages permits to achieve very high gas gain already at relatively moderate voltages across individual GEM-foils. As a consequence, the risk of discharge occurring when a heavily ionizing particle enters the active gas volume, is strongly reduced.

However, similarly to other gaseous detector, the GEM technology might be subject to classical aging effect due to the polymer depositions when operating in a high rate environment. The aging of GEM-based detectors has been extensively studied in the last decade for different sizes, geometries, and configurations:

- A longevity study on the double-GEM technology has been performed in 2000 by COMPASS Collaboration [106], exposing a small double-GEM prototype to a 6 keV X-rays flux from an X-ray tube at a rate of about 4.75 MHz/cm^2 . The detector has been operated at a gas gain of 2.2×10^3 ($\Delta V_{gem1} = \Delta V_{gem2} \sim 410\text{ V}$) and has been flushed with the Ar/CO_2 (70/30) gas mixture. After ~ 900 hours of continuous operation, the detector accumulated a total charge of 1.2 C/cm^2 without showing any loss in gain or instability, demonstrating its relative insensitivity to the classical aging phenomena [107].
- A Longevity study on the triple-GEM technology has been performed in 2001 by COMPASS Collaboration, exposing a full-size triple-GEM prototype to a 8.9 keV X-rays flux from an X-ray tube. The detector under irradiation test was a standard triple-GEM detector proposed for the COMPASS experiment, i.e. a $31 \times 31\text{ cm}^2$ triple-GEM prototype with a gas gap configuration $3/2/2/2\text{ mm}$. The detector has been operated at

a gas gain of 8.5×10^3 ($\Delta V_{gem1} \sim 425$ V, $\Delta V_{gem2} \sim 380$ V, $\Delta V_{gem3} \sim 340$ V) and has been flushed with the Ar/CO_2 (70/30) gas mixture at 80 cc/min. After ~ 240 hours of X-ray irradiation at 630 kHz/cm² and ~ 240 hours at 2.5 MHz/cm², the detector accumulated a total charge of 700 mC/cm² without any reduction of the gain and/or energy resolution [108]. A second longevity test has been performed in 2002 with a triple-GEM detector operating in Ar/CO_2 (70/30) gas mixture at a gas gain of 6.0×10^3 ($\Delta V_{gem1} \sim 400$ V, $\Delta V_{gem2} \sim 390$ V, $\Delta V_{gem3} \sim 380$ V) and a gap configuration $5.5/1.5/3/3.5$ mm. After ~ 750 hours of X-ray irradiation at 6 MHz/cm², the detector accumulated a total charge of about 2.7 C/cm² with no visible classical aging effects. These observations confirm the results of the previous longevity studies, demonstrating the relative insensitivity of GEM-based detectors to classical aging when operated with Ar/CO_2 (70/30) gas mixture [109].

- A longevity study on the triple-GEM technology has been performed in 2004 by LHCb Collaboration [110] at Calliope facility of the ENEA-Casaccia [111] with an intense 1.25 MeV γ -ray flux from a ^{60}Co source. The detectors under irradiation test were three full-scale triple-GEM detectors proposed for the innermost region of the muon spectrometer of the LHCb experiment, i.e. a 20×24 cm² triple-GEM prototypes with a gas gap configuration $3/1/2/1$ mm. The detectors have been operated at a gas gain of 6×10^3 and have been flushed with the $Ar/CO_2/CF_4$ (45/15/40) gas mixture. At the end of the longevity test campaigns, the highest irradiated detector accumulated a total charge of ~ 2.2 C/cm² and a gas gain drop of about 80% have been observed. The final result obtained during the irradiation test has been attributed to the low gas flow rate (350 cm³/min) with respect to the very high gamma ray flux (20 MHz/cm²): in such experimental conditions, the GEM-foils were attacked and etched by HF-acid produced in the avalanche plasma by the fragmentation of the CF_4 molecules, and not quickly removed by the gas flow. Further laboratory analysis confirmed such hypothesis: the aged detectors have been dismantled and some GEM-foil samples have been analyzed with a Scanning Electron Microscope (SEM). The SEM analysis confirmed the enlargement of GEM-holes and also the etching of the kapton inside the holes itself due to the presence of the fluorine-based compounds, leading to a significantly decrease of the gas gain and enhancing charging-up effects [105] [112].
- A longevity study has been performed in 2004 by PHENIX Collaboration [114], exposing a small triple-GEM(CsI) prototype detector to a high $UV - photons$ flux from a $Hg - UV$ lamp. The detector under irradiation test was a small triple-GEM $UV - photon$ detector proposed for the PHENIX experiment, i.e. 10×10 cm² triple-GEM detector with reflective CsI photocathode and a gas gap configuration $1.5/1.5/1.5/2$ mm.

The detector has been operated at a gas gain of $\sim 10^4$ ($\Delta V_{gem} \sim 510$ V) and has been flushed with pure CF_4 . After a total accumulated charge of about 10 mC/cm^2 , no aging effects or etching of the holes have been observed in the GEM-foils [113].

Although the previous longevity studies confirmed that the GEM technology is particularly resistant to typical aging phenomena that can occur in gaseous detectors, it is of paramount importance to carefully validate all materials actually used in the assembly of the *GE1/1*, *GE2/1* and *ME0* detectors. Indeed, the mechanical structure designed to stretch the GEM-foils involves new materials and components that have not been validated from the aging point of view. Moreover, the production of the CMS GEM-foils is based on the new single-mask photolithography technique (see Section 5.2.5) which has never been tested in the previous longevity tests.

The assembly materials and procedure as well as the operating conditions of the triple-GEM detector proposed for the CMS experiment are significantly different from the configurations used in other high energy physics experiments and the results obtained in the previous longevity studies are not sufficient to ensure the long-term operation of the *GE1/1*, *GE2/1* and *ME0* triple-GEM detector in the CMS experiment. For this reason, several outgassing and longevity test campaigns have been performed at the CERN irradiation facilities to prove that the triple-GEM detector in the CMS configuration can operate in the harsh CMS end-cap environment for over 10 years at HL-LHC without suffering any gain drop or instability.

- **Outgassing Studies.** The aging phenomena depend not only on the active gas mixture composition but also on the presence or not of traces of contaminants, either initially present in the gas mixture, or appearing at a later stage as a result of outgassing of some materials used in the assembly of the detectors and/or of the gas system. The materials which are in direct contact with the active gas volume could have dramatic effects on the life-time of the detectors, limiting, or severely impairing, their use in unprecedented harsh radiation environments.

For this reason, the CMS GEM Collaboration investigated the outgassing property of all materials present in the *GE1/1* triple-GEM detectors to ensure that none of them release pollutants during their life-time in CMS experiment [90]. No additional outgassing studies have been needed for the *GE2/1* and *ME0* triple-GEM detectors since they will use the material components adopted for the *GE1/1* detector. The materials have been carefully selected and validated in two main stages:

1. In a first stage, a preliminary selection of materials has been performed on the basis of their chemical, mechanical, electrical, radiation hardness and outgassing properties provided by the manufacturers.

2. In a second stage, the preselected materials have been tested for potentially harmful outgassing and radiation hardness. The experimental setup consists of four parallel and independent testing channels. Each channel contains a gas supply line for the CMS gas mixture, a stainless steel outgassing box containing the materials that allowed to heat the samples under test up to $150\text{ }^{\circ}\text{C}$ and to enhance its outgassing rate. The active gas mixture passed through the outgassing box and then through a Single-Wire Proportional Counter continuously irradiated by a radioactive source in order to measure the possible outgassing effects. The Figure 6.5 shows a schematic overview of the outgassing setup.

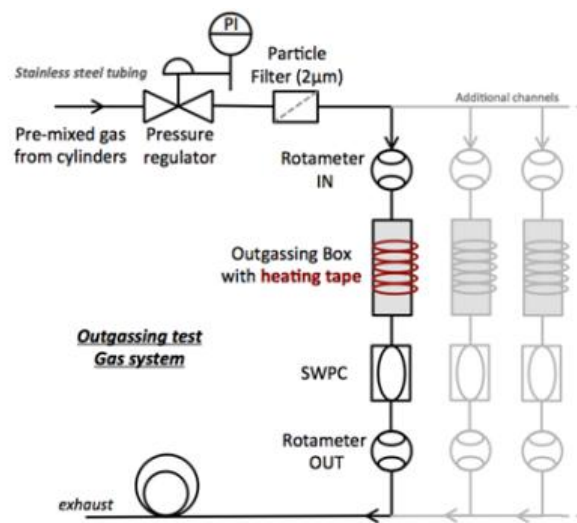


Figure 6.5: Schematic overview of the experimental setup for the outgassing studies showing the outgassing box that contains the material under test and the Single Wire Proportional Counter (SWPC) placed downstream [90].

In case of material outgassing, the contaminants released in the gas mixture will enter the active gas volume of the SWPC. Such contaminants could react with the gas molecules during detector operation and trigger the polymerization on the wire leading to inevitable degradation of the energy resolution and/or to a drop in detector gas gain.

The preselected materials under outgassing test are listed below:

- coating materials: **2-component polyurethane (PU) Nuvovern[®] LW** and **PU CellPack URETHAN[®] Art. n[°]124017**;
- printed circuit board components: **Coverlay film Krempel KDF[®] 0/25/25 HT** and **Soldering mask Elpemer[®] 2467**.
- gas-sealing components: **VITON O-rings** and **Polyamide washers**;

6.1. Introduction

– glues: **silver glue MSDS-Polytec-EC®**;

A detailed list of materials and their properties together with a complete description of the outgassing studies is given in [90]. The final outgassing test results are summarized in Table 6.3.

Triple-GEM element	Material	Aging	Comments
O-rings	VITON	No	Baked two hours in vacuum
PU layer	CellPack Nr. 124017	Yes	20% gain drop due to Si deposits
PU layer	NUVOVERN LW	No	-
Soldering mask	Elpemer 2467	No	-
Sealing coverlay	Krempel AKAFLEX KDF HT	No	-
Silver glue	MSDS-Polytec-EC	No	-
Washer	Polyamide	No	-
Tape	Kapton	No	Energy resolution worsens by 4%
Gas sealing tape	Teflon	No	-

Table 6.3: Outgassing test campaign results showing the list of the materials under test, their role in the detector, and the effect of their presence on the irradiated Single Wire Proportional Counter [90].

As a conclusion, only the PU CellPack URETHAN Art. $n^{\circ}124017$ has been rejected from the final detector design because it displays a large amount of outgassing before and after irradiation. Therefore, it has been considered as polluting material, which could lead to a degradation of the detection performance, and it has been replaced by the PU Nuvovern LW, already used in other applications and validated during the outgassing test campaign.

- **2012/2014 Longevity Studies in $Ar/CO_2/CF_4$ (45/15/40)**

A first longevity test campaign has been performed by the CMS GEM Collaboration at the Gamma Irradiation Facility (GIF) [115] at CERN, exposing a full-size GE1/1 triple-GEM detector to an high 662 keV γ -ray flux from a 566 GBq ^{137}Cs source. The detector under irradiation test was a GE1/1 triple-GEM prototype detector of the 4th generation, including the geometry and construction materials very close to those used in the final version of the GE1/1 detectors which will be installed in the CMS Muon System during the LS2. The detector has been operated at a gas gain of 2×10^4 and has been flushed with a $Ar/CO_2/CF_4$ (45/15/40) gas mixture at 5 L/hr .

After twelve months of continuous operation at GIF facility, the detector accumulated a total charge of $\sim 53 mC/cm^2$, which represents ten years of GE1/1 operation at the HL-LHC with a safety factor 8.8 and ten years of GE2/1 operation with a safety factor 17.7. The result for the normalized anode current, as parameter of the gas gain variation (corrected for pressure and temperature fluctuations) shown in Figure 6.6 indicates that the CMS triple-GEM detector does not suffer from any kind of aging effects or long-term degradation [90].

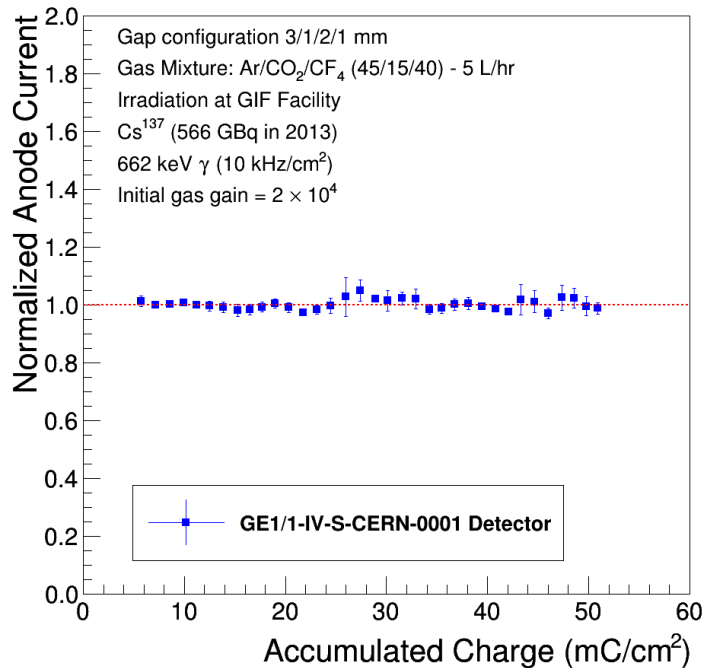


Figure 6.6: Result of the longevity studies at the GIF facility: normalized and corrected anode current as a function of the accumulated charge. The detector under test is a GE1/1 triple-GEM detector of the 4th generation operated in $Ar/CO_2/CF_4$ (45/15/40) gas mixture at an initial gas gain of 2×10^4 [90].

- **2015/2016 Longevity Studies in Ar/CO_2 (70/30)**

A second longevity test campaign has been performed by the CMS GEM Collaboration at the new Gamma Irradiation Facility (GIF++) [116] at CERN (see Section 6.2.1), exposing a full-size GE1/1 triple-GEM detector to an high 662 keV γ -ray flux from a 14 TBq ^{137}Cs source. The detector under irradiation test was a GE1/1 triple-GEM prototype detector assembled in 2014, which is representative of the detectors that will be installed in the CMS-Muon end-caps. The detector has been operated at a gas gain of 2×10^4 and has been flushed with the Ar/CO_2 (70/30) gas mixture at 5 L/hr.

The detector accumulated a total charge of $\sim 55 mC/cm^2$ after six months of continuous irradiation test, i.e. 10 years of real operation in the GE1/1 environment with a safety factor 9.2. and 10 years of real operation in the GE2/1 environment with a safety factor 18.3. The normalized and corrected anode current as a function of the accumulated charge is shown on Figure 6.7 [90].

In addition to monitoring the anode current during the irradiation test, the energy spectrum of the ^{137}Cs source has been continuously measured

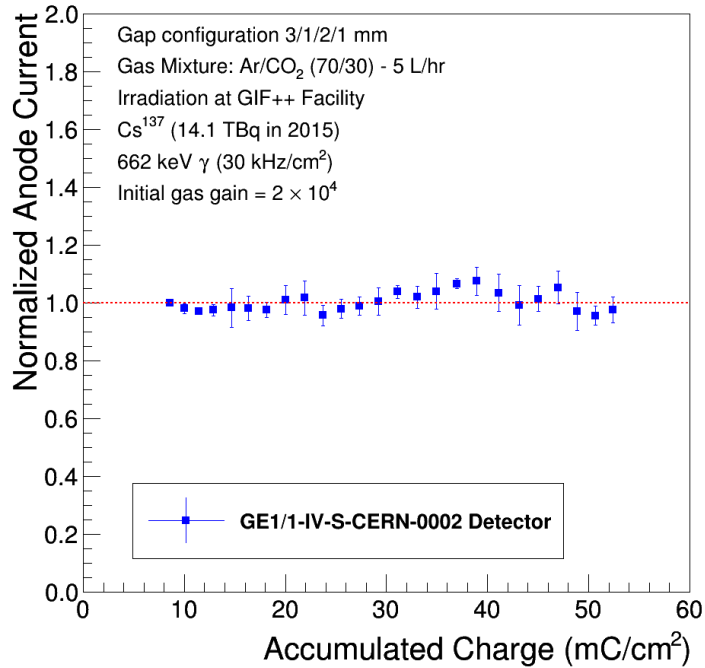


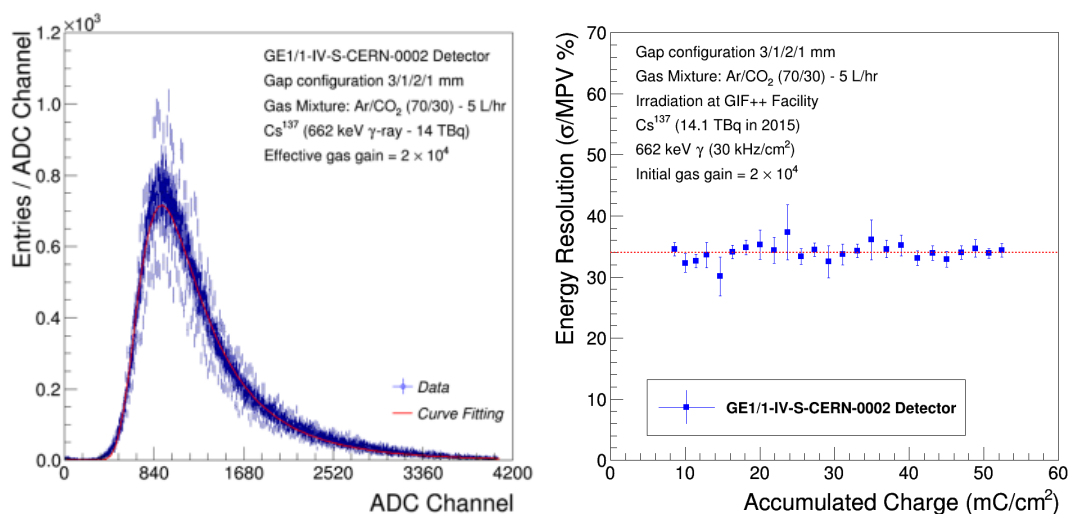
Figure 6.7: Result of the longevity studies at the GIF++ facility: normalized and corrected anode current as a function of the accumulated charge. The detector under test is a GE1/1 triple-GEM detector of the 4th generation operated in Ar/CO_2 (70/30) gas mixture at an initial gas gain of 2×10^4 [90].

every week, i.e. every about $2 \text{ mC}/\text{cm}^2$ of accumulated charge (see Figure 6.8a) and the corresponding energy resolution remained stable during the entire irradiation test (see Figure 6.8b) [90].

The 2012/2016 longevity test campaigns demonstrated that the operation of the triple-GEM technology in the CMS GE1/1 configuration is not affected by the classical aging. The CMS GE1/1 detectors will be able to survive in the harsh CMS-GE1/1 environmental for over 10 HL-LHC years with safety factor 8.8 in $Ar/CO_2/CF_4$ (45/15/40) gas mixture and safety factor 9.2 in Ar/CO_2 (70/30) gas mixture.

6.1.3 Motivation for additional aging studies

The aging properties of CMS triple-GEM detectors operated with the standard Ar/CO_2 (70/30) gas mixture have been extensively studied by the CSM Collaboration since 2012 to cover the CMS GEM projects $GE1/1$, $GE2/1$, and $ME0$. It includes the understanding of the classical aging processes described in Section 6.1.1, and the investigations of possible outgassing of the materials that compose the triple-GEM detectors proposed for the future upgrade of the innermost muon spectrometer of the CMS experiment.



(a) Energy spectrum from the ^{137}Cs source at the GIF++ facility. (b) Energy resolution as a function of the accumulated charge.

Figure 6.8: Result of the longevety studies at the GIF++ facility. Left: Typical ADC spectrum of the GIF++ facility of ^{137}Cs . The experimental data have been fitted by a Landau distribution, convoluted with a normal distribution. Right: energy resolution as a function of the accumulated charge. The detector under test is a GE1/1 triple-GEM detector of the 4th generation operated in Ar/CO₂ (70/30) gas mixture at an initial gas gain of 2×10^4 [90].

The results of the previous CMS GEM longevety studies indicate that the operation of triple-GEM detectors in the CMS configuration is not affected by the classical aging processes up to a total accumulated charge per unit area of about 55 mC/cm^2 (see Section 6.1.2). Therefore, the CMS triple-GEM detectors are expected to survive a minimum of 10 years of real operation with Ar/CO₂ (70/30) gas mixture in the CMS GE1/1 environment (safety factor 9.1) and in the CMS GE2/1 environment (safety factor 18.3) at HL-LHC. The next step consists in measuring the long-term stability of the CMS triple-GEM detector in order to make sure that the detector performance will be stable during the entire life-time of the detectors in the CMS-ME0 environment at HL-LHC.

In the CMS ME0 region a CMS triple-GEM detector must tolerate, without damage or performance losses, an integrated charge of $\sim 283 \text{ mC/cm}^2$ in 10 years of operation at a gain of $\sim 2 \times 10^4$ and an average particle flux of $\sim 48 \text{ kHz/cm}^2$ for an average machine luminosity of $\sim 5 \times 10^{34} \text{ cm}^{-2} \text{ s}^{-1}$ [69]. For this reason, new longevety studies on full size CMS-GE1/1 triple-GEM detectors have been carried out in parallel at CERN Gamma Irradiation Facility (GIF++), using for the irradiation an intense 14 TBq (2015) ^{137}Cs source emitting 662 keV γ rays, and at the CMS-GEM QA/QC Lab. using as irradiation source a 22 keV X-rays tube. Both detectors were operated with

Ar/CO_2 (70/30) gas mixture at an effective gas gain of 2×10^4 .

6.2 Triple-GEM Aging Studies at GIF++ facility

6.2.1 The GIF++ facility at CERN for aging studies

The Gamma Irradiation Facility (GIF++) [116] at CERN is an unique test area in which an high-energy muon beam ($100 \text{ GeV}/c$), from the secondary SPS beam line H4 in EHN1, is combined with a gamma photons from a radioactive ^{137}Cs source. Located in the CERN SPS North Area [117], the facility has been designed in order to provide a high intensity gamma field for high rate and longevety studies. The ^{137}Cs isotope, with an activity $\sim 14.1 \text{ TBq}$ (December 2015), has been chosen instead of ^{60}Co isotope due to its long half-life of 30.08 years, leading to a smaller decrease of the photon rate over the expected life-time of facility. Further, the spectrum of the ^{137}Cs source, composed of the primary 662 keV photons and lower energetic scattered photons. The main source of the interaction background in the CMS muon system are neutron-induced photons, with an energy in the range $0.1\text{-}10 \text{ MeV}$. The GIF++ photons have an energy fairly representative of the energy of LHC/HL-LHC photons seen by the muon detectors [69]. The intense gamma field background, which is a factor 30 more intense than that at original GIF facility, allows to simulate the conditions that detectors will suffer in their future operating environment at the HL-LHC

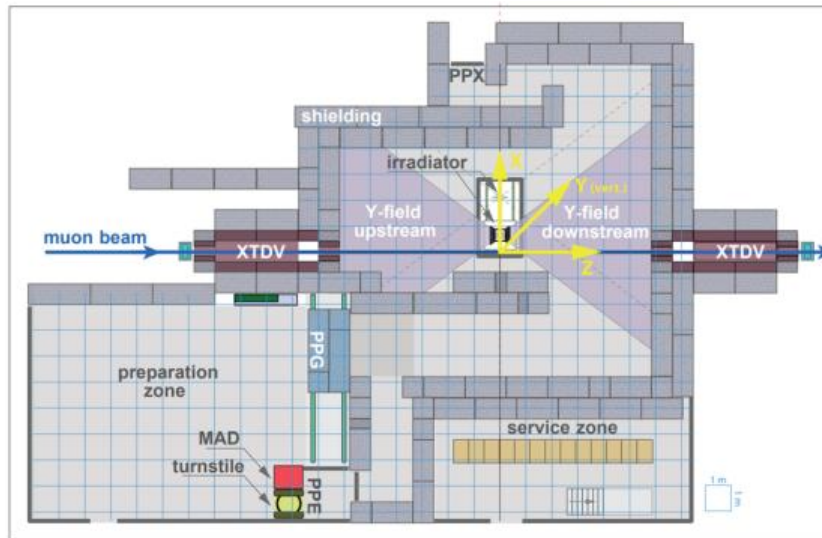


Figure 6.9: Floor plan of the GIF++ facility [116].

The GIF++ irradiation area has a total surface of 100 m^2 divided in two different radiation zones: the Upstream zone (30 m^2) and the Downstream

zone (70 m^2). It has been realized in order to host and test simultaneously full-size detectors and to allow their positioning at different distances from the source point. The irradiation area is shielded by 1.6 m thick concrete walls; it is equipped with a raised floor allowing effective distribution of gas lines and high voltage and/or signal cables. The free height between the floor of the facility and the raised floor is $\sim 0.42 \text{ m}$. The schematic overview of the GIF++ facility is shown in Figure 6.9. Close to the irradiation area, is present a two-floor service zone for hosting the gas (*gas zone*) and the electronic services (*rack zone*). In addition, a preparation zone (80 m^2) is available for preliminary tests on the detectors and their electronics before installing them inside the irradiation area.

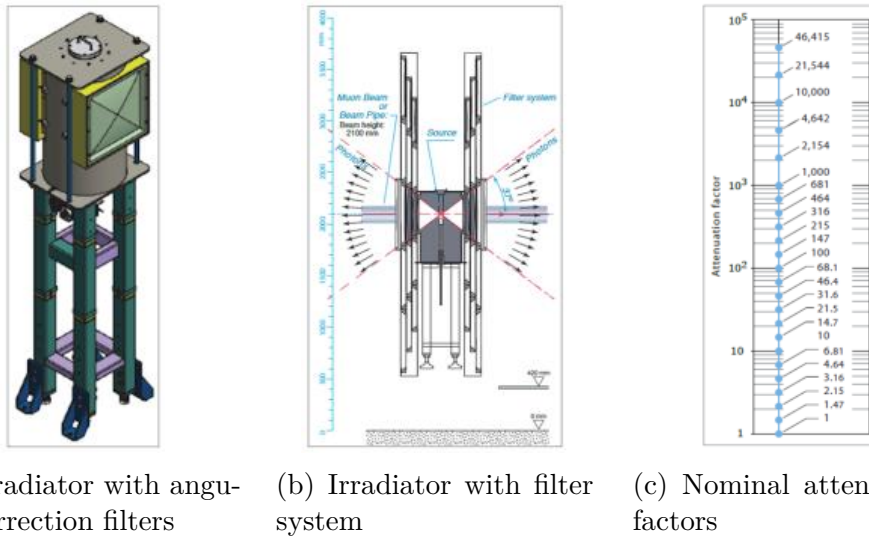


Figure 6.10: (a) Schematic structure of the irradiator at GIF++ facility with angular correction aluminium filters and independent filter systems at both sides. (b) On both sides a set of independently movable and remotely controlled attenuation lead filters and collimator frames permits to fine tune the intensity of emitted photons. (c) Each set of 3×3 movable attenuation filters, with 27 combinations of filters, leads to 24 different attenuation factors between 1 and 46415 [116].

The radioactive source in the irradiation position is at $2.06 \pm 0.01 \text{ m}$ from the floor of the facility, and it is located at the same height of the muon beam, or at $1.64 \pm 0.01 \text{ m}$ from the raised floor where the detectors under irradiation test are placed. The wide opening angle of both areas is 37° on the horizontal and vertical planes in order to cover a large part of the irradiation area, both in the Downstream and Upstream zones. Both irradiation windows are equipped with lens shaped angular correction aluminium filter to provide an uniform photons flux in order to fully irradiate the flat large area detectors, allowing to study the effects of different background radiations on the detector rate capability. In Figure 6.10a, one of the two irradiation windows equipped

6.2. Triple-GEM Aging Studies at GIF++ facility

with the aluminum angular correction lens is shown. For each irradiation zone, the photons flux can be independently fine tuned using two complete and independent attenuation systems (Figure 6.10b), each consisting of an array of 3×3 convex lead attenuation filters. In total, 24 different nominal attenuation factors between 1 and 46415 can be selected according to the 27 possible combinations of the filters (Figure 6.10c).

The irradiation field inside the GIF++ irradiation area has been simulated: Figure 6.11 shows the simulation of the 662 keV photons flux inside the irradiation area in the xz plane without any attenuation applied; this is thus the highest photons flux obtainable at GIF++ facility. The simulation has been validated with experimental measurement, both in Upstream and in Downstream zones. The position of the experimental measurement D1-to-D5 (in Downstream zone) and U1-to-U6 (in Upstream zone) are also marked in Figure 6.11 and 6.12.

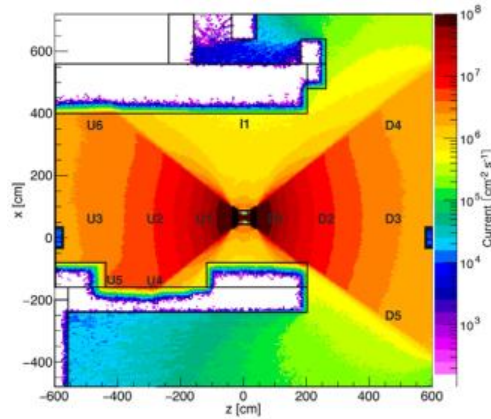


Figure 6.11: Simulated photons current in air [$cm^{-2}s^{-1}$] in xz plane at $y = 0.0 \text{ m}$; attenuation filters system at factor 1 [116].

Figure 6.12 shows the simulated absorbed dose rate in air in the xz plane of the GIF++ irradiation zone. In Figure 6.12a the irradiator is fully opened downstream (i.e. attenuation factor 1) and fully closed upstream (i.e. attenuation factor of 46415), whereas in Figure 6.12b the irradiator is fully closed downstream and fully opened upstream. For instance, in Figure 6.12b it is clearly possible to see the presence of scattered photon from the shielding walls, floor and roof of the irradiation area on the downstream zone. In any case the radiation is almost a factor 10^4 lower than the radiation on the upstream, where the irradiator is completely open. Nevertheless, the two figures confirm that the downstream and upstream zones of the GIF++ facility are basically independent.

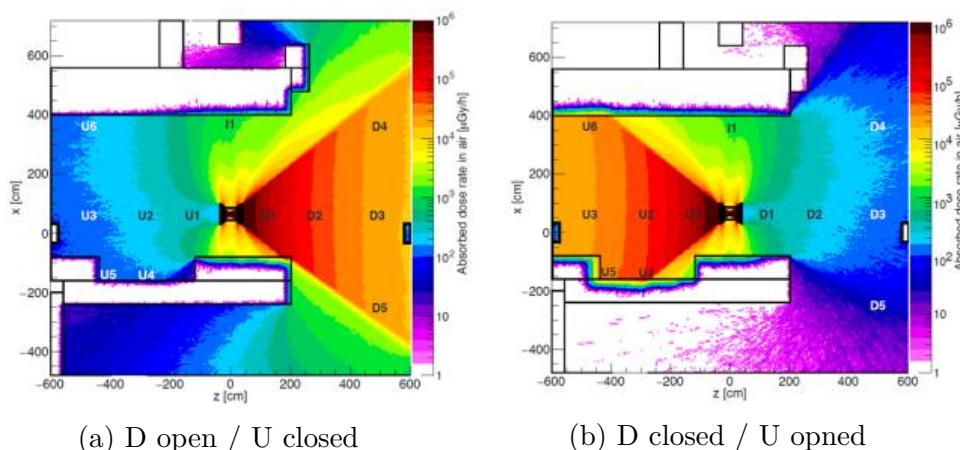


Figure 6.12: Absorbed dose rate in air [$\mu\text{Gy}/\text{h}$] in xz plane at $y = 0.0\text{ m}$ of the facility [116].

6.2.2 Aging Test on triple-GEM technology for the ME0 project of the GIF++ facility

This section describes the studies of long-term irradiation effects on the CMS triple-GEM detectors after long sustained operation in a high-rate environment at the GIF++ facility. The aim of these new longevity tests is to validate the triple-GEM technology developed for the GE1/1 project also for CMS-ME0 project by integrating a minimum of charge per unit area of about $850\text{ mC}/\text{cm}^2$, which represent a 10 years of the total ME0 operation at HL-LHC with a safety factor of three; at the time of the finalization of this Doctoral Thesis, the irradiation tests at the GIF++ facility are still ongoing.

6.2.2.1 The CMS GE1/1 triple-GEM detector under test and quality control

The longevity test campaign at the GIF++ facility are performed with a full-size CMS GE1/1 triple-GEM detector prototype of the 4th generation assembled in 2014, which is representative of the detectors that will be installed in the CMS Muon end-caps, including the geometry and adopted material components. The assembly and sealing of the detector are entirely mechanical (see Section 5.3.4). No glue is applied during assembly, which makes it possible to open a detector again for repairs if needed and to avoid possible gas contamination from glues. A picture of the CMS GE1/1 triple-GEM detector, that is now under test at the GIF++ facility, can be seen on Figure 6.13.

The GE1/1 triple-GEM detector, operated in Ar/CO_2 (70/30) gas mixture with a gas flow rate of $\sim 7\text{ L}/\text{hr}$, has been powered through an HV divider corresponding to the CMS configuration described in Figure 5.23. The gas gain of the detector has been kept constant at an effective value of 2×10^4 during the entire irradiation test.

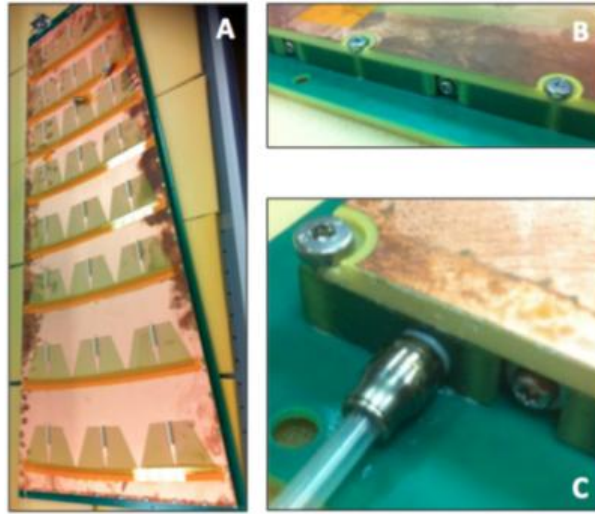


Figure 6.13: Figure A: The detector under test is a GE1/1 triple-GEM detector of the 4th generation operated in Ar/CO_2 (70/30) gas mixture at an initial gas gain of 2×10^4 . Figure B: close lateral view of the external frame. The frame is fixed to the PCB with vertical screws. Figure C: close view of the gas input [90].

It is worth noticing that the detector under irradiation test is the same used in the aging test campaign described in Section 6.1.2, where the detector has already been exposed to the intense gamma radiation in the GIF++ facility during the 2015/2016 longevity test campaign, accumulating a total charge of $\sim 55 \text{ mC/cm}^2$ after 6 months of continuous irradiation. In 2016, at the end of the previous longevity test campaign, the experimental setup at the GIF++ facility has been dismantled and the aged detector has been moved to the laboratory for further measurements in order to study the detector performances in post-irradiation condition.

Before to move back to the GIF++ facility, for the new longevity test campaign, the detector has been fully re-characterised following the standard QA/QC procedures developed for the LS2 GE1/1 detectors qualification:

- **QC3 - Gas Leak Test.** The QC3 Gas Leak Test has been performed in order to verify the gas tightness and quantify the possible gas leak rate of the aged GE1/1 triple-GEM detector by monitoring the drop of the internal over-pressure as a function of the time. The results from the QC3 Gas Leak Test on the aged detector is shown in Figure 6.14.

The detector was found not to be gas-tight: ~ 30 minutes after the starting of the QC3 Gas Leak Test, the pressure drop was about 22.7 mBar resulting in a gas leak rate of $\sim 0.89 \text{ mBar/min}$, i.e. a gas leak rate approximately 8 times higher than the one allowed by the QC3 acceptance criteria for the LS2 GE1/1 mass production (see Section 5.4.4). As result of accurate inspection, no faulty screws or deformed washers have been

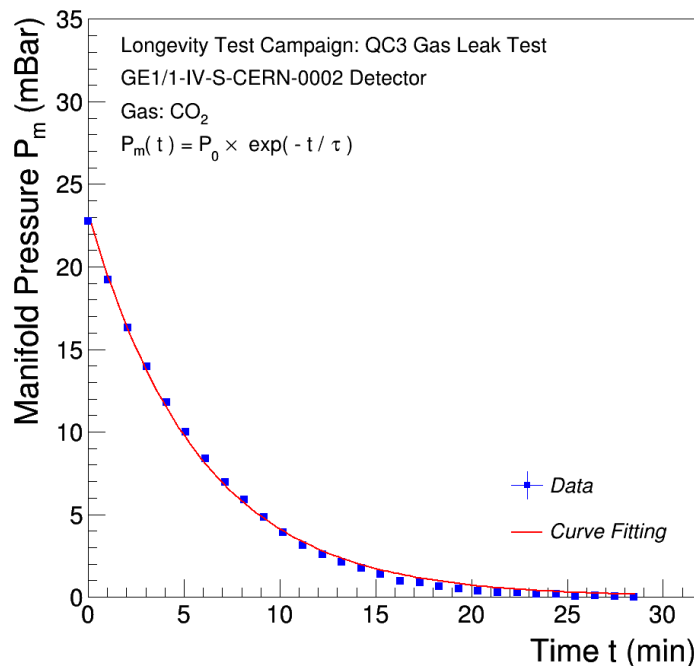


Figure 6.14: Results from the QC3 Gas Leak Test on the aged GE1/1 triple-GEM detector. The pressure drop is modeled by the function $P_m(t) = P_0 \times \exp(-t/\tau)$. The parameter P_0 is a constant that takes into account the initial overpressure of the detector. The parameter τ is the gas leak time constant and quantifies how fast the overpressure inside the detector decreases as a function of the time. The exponential fit to the experimental data provides a gas leak time constant $\tau \sim 6 \text{ min}$.

identified; in this case in order to solve the gas leak issue is necessary to re-open the detector in order to verify and possibly to replace the two rubber O-rings embedded in the external frame and the polyamide washers against the Drift and Readout Board which ensure the gas-tightness of the detector (see Section 5.3).

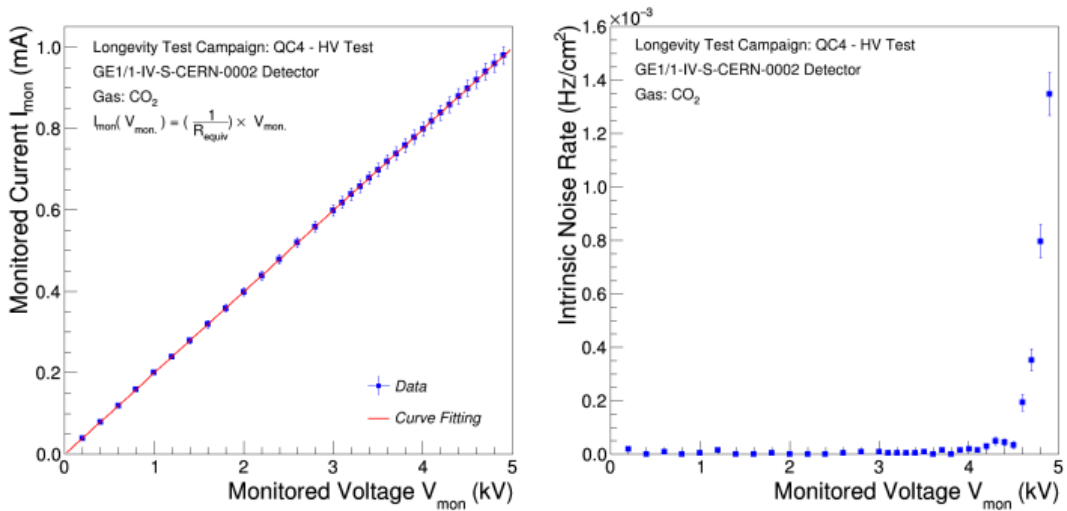
The most important problem with the re-opening of the GE1/1 triple-GEM detector prototype of the 4th generation is that the GEM-foils are stretched purely mechanically against the external detector frame. Such kind of problem has been rectified in the GE1/1 triple-GEM prototype design of the 5th generation by tensioning the GEM-foils against independent "pull-out" pieces (see Section 5.3). Because of this, it is extremely delicate to re-open a GE1/1 triple-GEM detector prototype of the 4th generation and un-stretch its GEM-foils in order to replace the external frame and the O-rings.

For this reason, the CMS GEM Collaboration decided not to re-open the detector in order to reduce the possibility to damage the detector irre-

6.2. Triple-GEM Aging Studies at GIF++ facility

versibly and proposed to increase the input gas flow rate from 5 L/hr to about 7 L/hr allowing the detector to operate even in very high particle rates properly.

- **QC4 - HV Test.** The HV divider has been replaced with a new one at the end of the previous longevity test and the QC4 HV Test has been performed in order to identify possible defects in the HV circuit and to measure the intrinsic noise rate of the aged CMS GE1/1 triple-GEM detector. The results from the QC4 HV test on the aged detector is shown in Figure 6.15.



(a) Current through the HV divider as a function of the applied voltage. (b) Intrinsic noise rate as a function of the applied voltage.

Figure 6.15: Results from the QC4 HV Test on the aged GE1/1 triple-GEM detector. Left: current through the HV divider as a function of the applied voltage. The linear fit to the experimental data provides an equivalent resistance $R_{equiv} \sim 5.00 M\Omega$, resulting in a deviation of about 0.2% with respect to the expected value ($R = 5.01 \pm 0.02 M\Omega$). Right: intrinsic noise rate R_{noise} as a function of the applied voltage: $R_{noise} \sim 1.3 \times 10^{-3} Hz/cm^2$ at 4.9 kV.

The intrinsic noise rate has been found to be $\sim 1.3 \times 10^{-3} Hz/cm^2$ at 4.9 kV (expected background in the ME0 detectors $\sim 47 kHz/cm^2$, see Table 6.2).

- **QC5 - Effective Gas Gain Measurement.** The effective gas gain of the aged GE1/1 triple-GEM detector in Ar/CO_2 (70/30) gas mixture has been measured as a function of the applied HV with a 22 keV $X - ray$ photons from an $X - ray$ tube with $Ag - target$ at a relatively low particle flux of $\sim 20 Hz/cm^2$. Therefore, it was possible to compare the performances of the detector before and after the 2015/2016 longevity

test campaign. In Figure 6.16 the comparison between the effective gas gain of the GE1/1 triple-GEM detector measured before and after the 2015/2016 longevity test campaign is shown; no significant difference in the values of the gas gain have been observed before and after the intense irradiations.

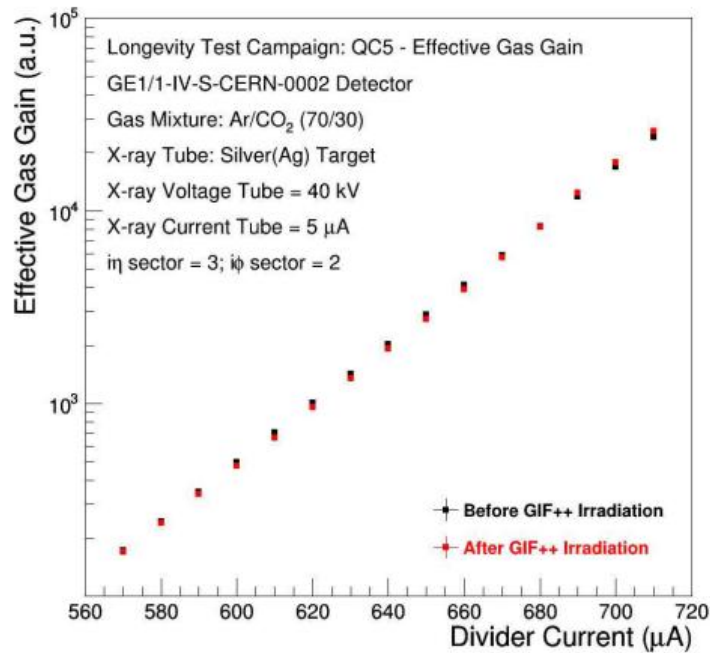


Figure 6.16: Comparison between the effective gas gain of the GE1/1 triple-GEM detector measured before (black dots) and after (red dots) the 2015/2016 longevity test campaign.

- **QC5 - Response uniformity.** The QC5 Response Uniformity test on the aged GE1/1 triple-GEM detector has been performed in order to measure the pulse height distribution all over the active surface of the detector. The data acquisition system and the analysis procedures are identical to those used for the QC5 - Response Uniformity test within the standard QA/QC procedures developed to qualify all the GE1/1 detectors which will be installed in the Muon System of the CMS experiment during the LS2 (see Section 5.4.6.6). The result for the QC5 - Response Uniformity test performed on the aged GE1/1 triple-GEM detector under test are presented in Figure 6.17.

At the end of the detector characterization in post-irradiation conditions, the GE1/1 triple-GEM detector has been moved back into the GIF++ facility for a new longevity test campaign.

6.2. Triple-GEM Aging Studies at GIF++ facility

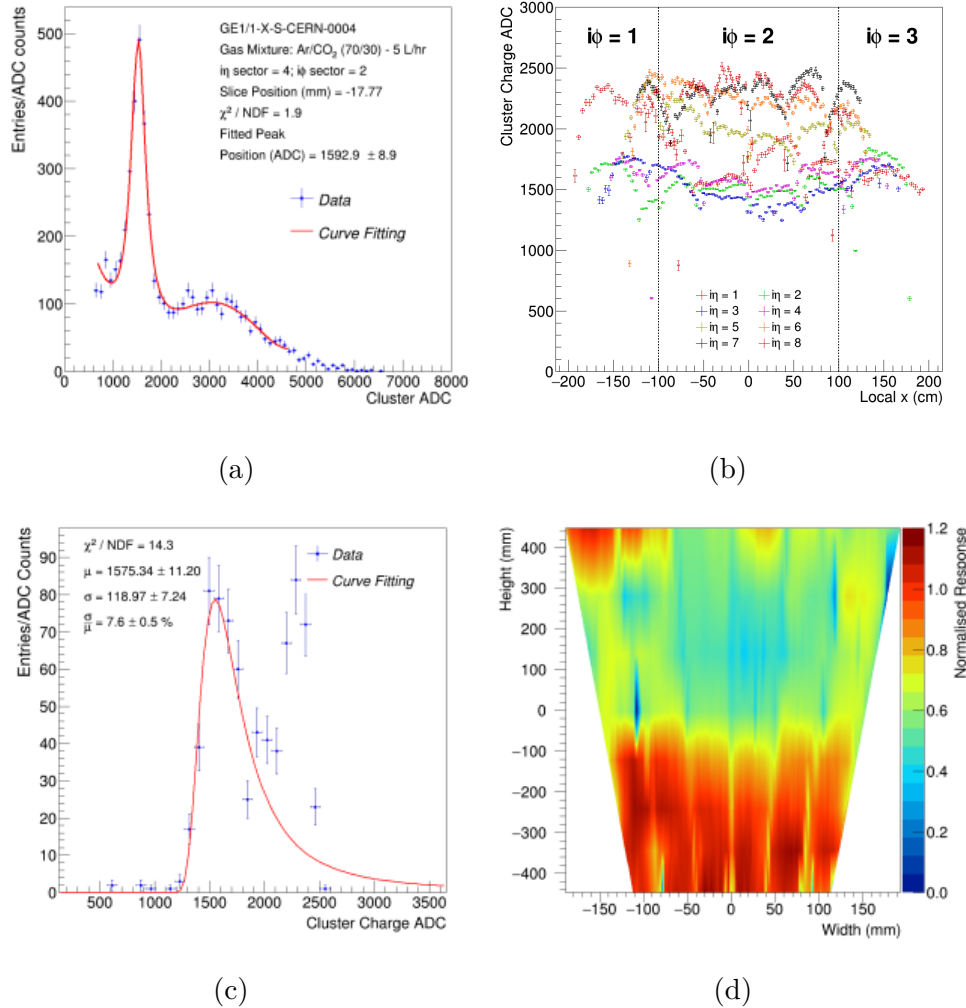


Figure 6.17: (Figure 6.17a) Example of energy spectrum from a slice (four strips) of the GE1/1 triple-GEM detector under test operated at an average gain around 600 with Ar/CO_2 (70/30) fully illuminated by a 22 keV X-ray. The solid line represents a fit to the experimental data using a Cauchy distribution to model the copper fluorescence photopeak plus a fifth order polynomial that models the background. (Figure 6.17b) The mean of the copper fluorescence spectrum extracted from the fit of each slice is assigned to coordinate point of the slice in the local coordinates of the detector. (Figure 6.17c) Distribution of fitted photopeak positions obtained from GE1/1 triple-GEM detector under test: the experimental points represent each photopeak position and the solid line is a Landau fit to the data. The response uniformity for this detector is $R.U. = 7.6 \pm 0.5\%$. (Figure 6.17d) Map of the detector response (i.e. the normalized photopeak energy) across the detector under test.

6.2.2.2 The CMS GE1/1 triple-GEM detector at GIF++ facility

The CMS GE1/1 triple-GEM detector has been installed in the downstream area γ - field downstream at ~ 1 m from the source point (*position D1*) exposed to a photons flux up to 10^8 Hz/cm², see Section 6.2.1. The schematic drawing of the new CMS triple-GEM experimental setup installed in the GIF++ irradiation area is shown in Figure 6.18. It consists of a light and versatile stand in aluminium bosh-profiles, that allows the installation of several GE1/1 triple-GEM detectors up to a maximum of four detector at the same time. The The Data Acquisition System is placed below the detector structure outside the irradiation cone of the ¹³⁷Cs source and is located inside a shielding box with 1 cm thick lead walls in order to be protected by the low-energy photon component that develops due to the multiple scattering of primaries photons within the irradiator and the concrete walls of the irradiation area.

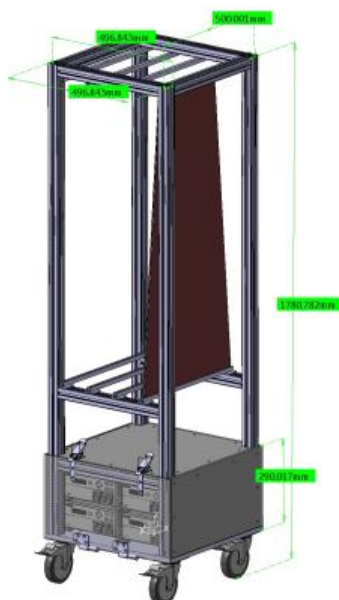


Figure 6.18: Schematic drawing of the CMS triple-GEM stand designed in aluminium bosh-profiles for the longevety studies at GIF++ facility.

The high voltage is provided by a CAEN module N1470 (negative polarity) installed outside the irradiation area in the apposite rack zone. Cables, 30 meters long, have been routed under the concrete walls and the raised floor inside the irradiation area to power the GE1/1 triple-GEM detector. The high voltage line has a low-pass filter to attenuate high frequency ripple in the HV. The CAEN HV power supplier can be remotely controlled and an apposite data acquisition program using LabVIEW has been developed in order to monitor and record the high voltage and the current through the HV divider during the entire radiation exposure test. The LabVIEW-software has been developed to:

6.2. Triple-GEM Aging Studies at GIF++ facility

- increase (ramp-up) and/or decrease (ramp-down) gradually the high voltage applied to the GE1/1 triple-GEM detector with programmable consecutive steps. The high voltage output ramp-up and ramp-down rates can be selected independently in the range 1-500 V/s in 1 V steps.
- to set the operating current limit I_{set} value and the maximum time T_{wnd} which an "overcurrent" is allowed to last. The high voltage channel in "overcurrent" works as a current generator; the output high voltage varies in order to keep the output current lower than the programmed value I_{set} . The "overcurrent" lasting more than set value T_{wnd} causes the high voltage channel to "TRIP" and the output high voltage is drop to zero at the programmed ramp-down rate.
- monitor and record the operating current and high voltage at a programmable rate expressed in seconds.

The LabVIEW-software has been developed to avoid damages to triple-GEM detectors during unexpected situations (discharges, variation in gas mixture composition, for example) and also provided a basic interface for an easy monitoring (see Figure 6.19).

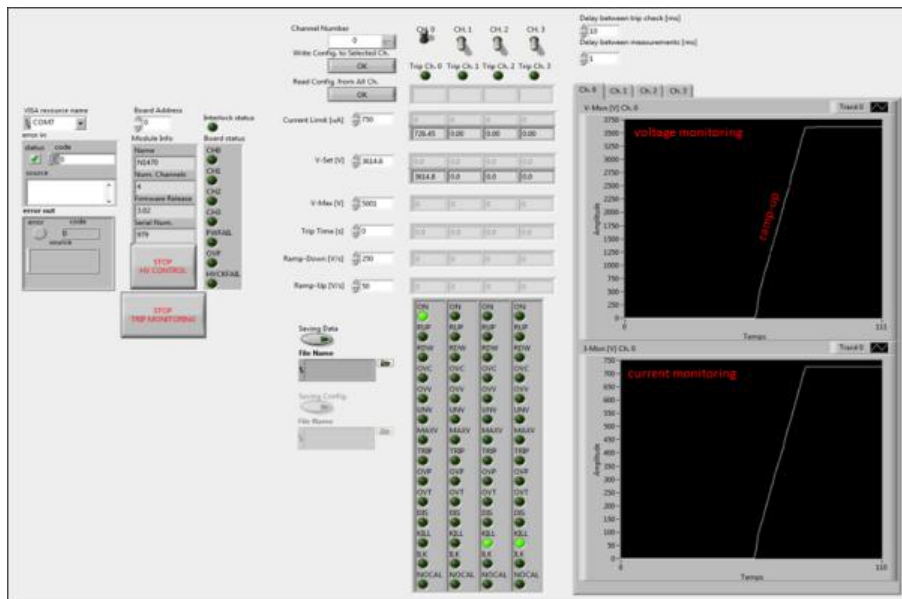


Figure 6.19: LabVIEW-software interface for the N1470 CAEN power supply to control and monitor the high voltages and current of detector. It is possible to see the high voltage real-time monitoring (top right) and the current real-time monitoring (bottom right).

The gas system was designed and built in 2014 by the CERN Gas Group, following strict guidelines concerning the materials to be used, and cleanliness conditions in general. The gas system, schematically shown in Figure 6.20, in

the last 2015 version, is constructed in stainless-steel tube. All the parts, glass tube flow-meters and connectors were previously cleaned with alkaline soap and de-ionized water. In 2017, before to restart the activities at the GIF++ facility, the whole gas line has been flushed in the Ar/CO_2 (70/30) gas mixture without the detectors with gas flow rate of ~ 5.0 L/h for a week in order to clean the gas pipe after a long term of non-operation.

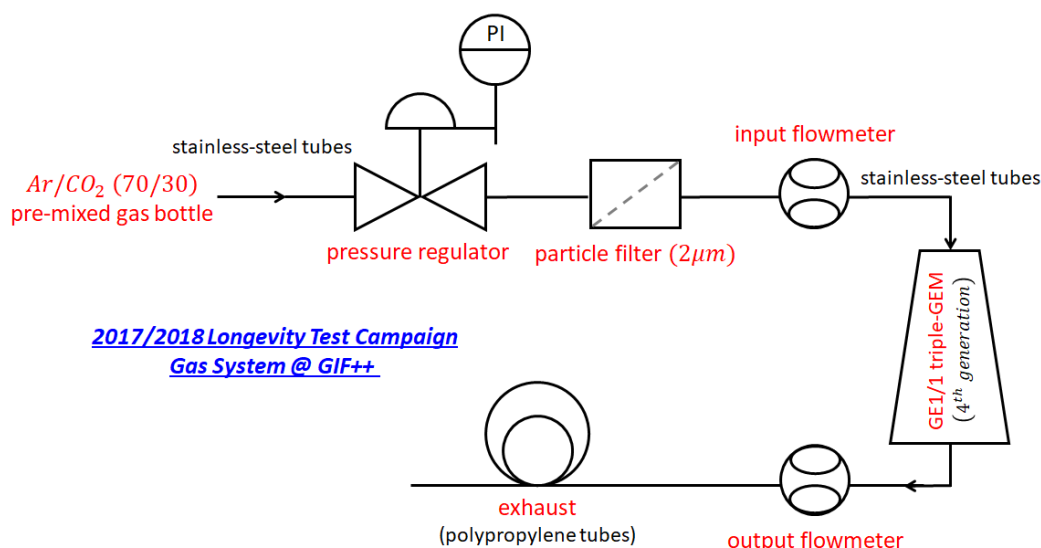


Figure 6.20: Schematics of the gas system in the GIF++ facility. The whole gas inlet line is made of stainless-steel tubes, while the exhaust gas line is made of polypropylene tubes (not hygroscopic).

The parameters of the high voltage power supply and data acquisition system are remotely controlled from outside of the GIF++ irradiation area via USB cables. All data are collected in an appropriate server installed in the rack zone accessible from the CERN network, minimizing the need of stopping the irradiation to access inside the irradiation area. The picture of the experimental setup at GIF++ facility can be seen on Figure 6.21.

6.2.2.3 Data acquisition and analysis procedure

The aim of the long-term stability test has been to detect variation in gas gain, measured as the anode current of the detector exposed to very high rate. Any large variation of the anode current could indicate an instability in the gas gain of the detector under irradiation test. Moreover, in order to monitor fluctuation of the gas gain of the detector under test not correlated with the aging phenomena but with the environmental condition, temperature, atmospheric pressure and relative humidity have been also measured and recorded continuously during the whole irradiation period

A Data Acquisition System has been developed in order to monitor the response of the GE1/1 triple-GEM detector under irradiation at GIF++ facility.

6.2. Triple-GEM Aging Studies at GIF++ facility



Figure 6.21: Picture of the longevity test at GIF++ facility. The GE1/1 triple-GEM detector is placed directly in front of the ^{137}Cs source irradiator. The DAQ electronics is placed below the detector structure and is protected inside the lead shielding box. The entire system is connected to the DAQ station via USB cables.

Figure 6.22 shows the electronics chain, the read-out and the device to store and analyse the data. The readout system for the longevity studies consists of two main readout channels:

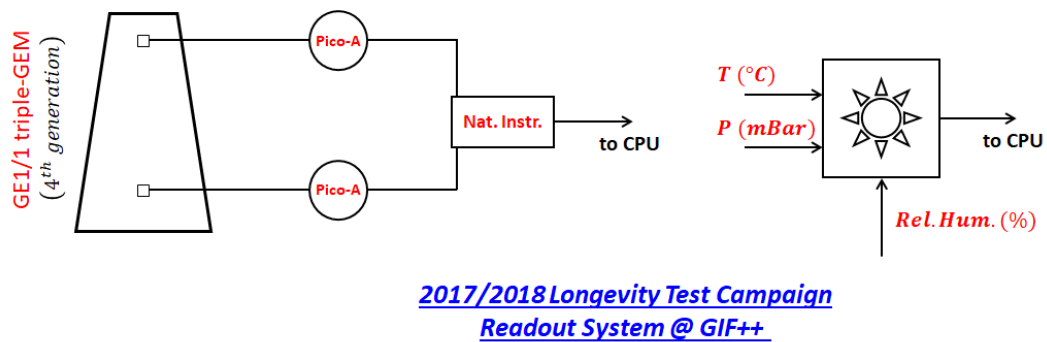


Figure 6.22: Scheme of the electronic chain and data acquisition system used during the longevity test at GIF++ facility.

- Two KEITHLEY 6487 pico-ammeters connected to the R/O sectors of the readout board to measure the anode current, which reflects the effective gas gain of the detector. The read-out of such devices is made through a GPIB interface between the pico-ammeters and the computer station. Every 5 minutes: the GPIB module, in listen mode, receives

1000 different measurements from the pico-ammeters; the LabVIEW acquisition program converts them to their mean value and stores it in a data file. Figure 6.23 shows the main panel of LabVIEW-software to control and monitor the anode current of the GE1/1 triple-GEM detector under irradiation.

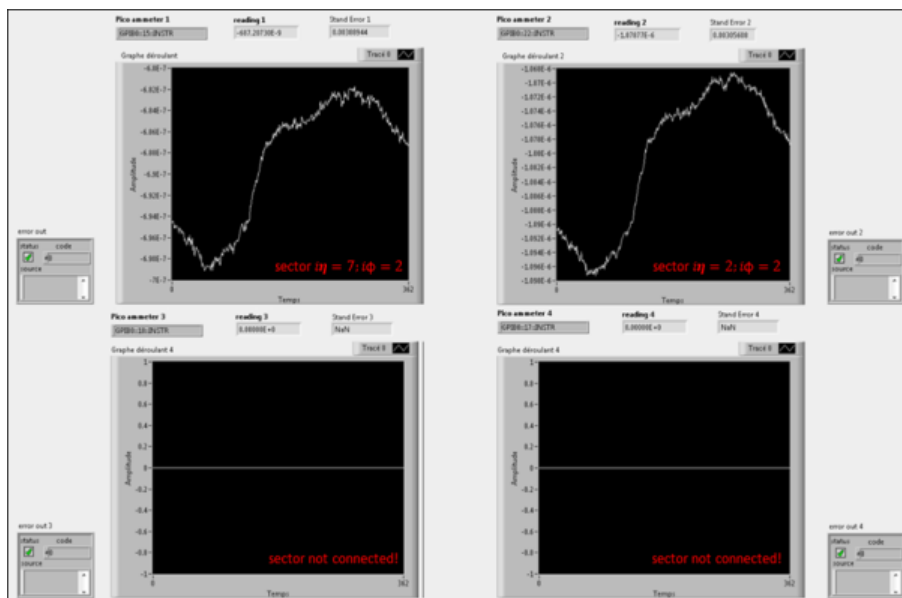


Figure 6.23: LabVIEW-software interface for the KEITHLEY 6487 pico-ammeters to control and monitor the anode current on the R/O sectors under irradiation. The software has been developed to read a maximum of four pico-ammeters at the same time. It is possible to see the anode current real-time monitoring for the R/O sector $i\eta = 7; i\phi = 2$ (top left) and for the R/O sector $i\eta = 2; i\phi = 2$ (top right), as defined in Section 5.2.2.

- An Enviromental Monitoring System to monitor the environmental parameters (atmospheric pressure, temperature, relative humidity) within the experimental irradiated area. Each minute: the system monitors and records the atmospheric pressure through a *GEFRAN TSA* sensor [118], the temperature and relative humidity through a *Michell PCMini 70* sensor [119].

During the longevity test, all relevant parameters in the GE1/1 triple-GEM detector are recorded and the corresponding data files are transferred to a dedicated server outside the GIF++ facility for backup saving and analysis.

The long-duration tests needed to carry out longevity studies exposes the detectors under irradiation to gas gain fluctuations due to the variations provoked by the ambiantal conditions (pressure, temperature, humidity); also variation in gas mixture composition and/or the particle flux could mask the longevity effects, or be wrongly interpreted as sign of the deterioration of the detector

performances. Additionally, the temperature variations can slightly affect the operation of readout electronics and induce baseline fluctuations in the data. It is therefore, essential to take into account the environmental fluctuations in order to isolate the possible aging effects.

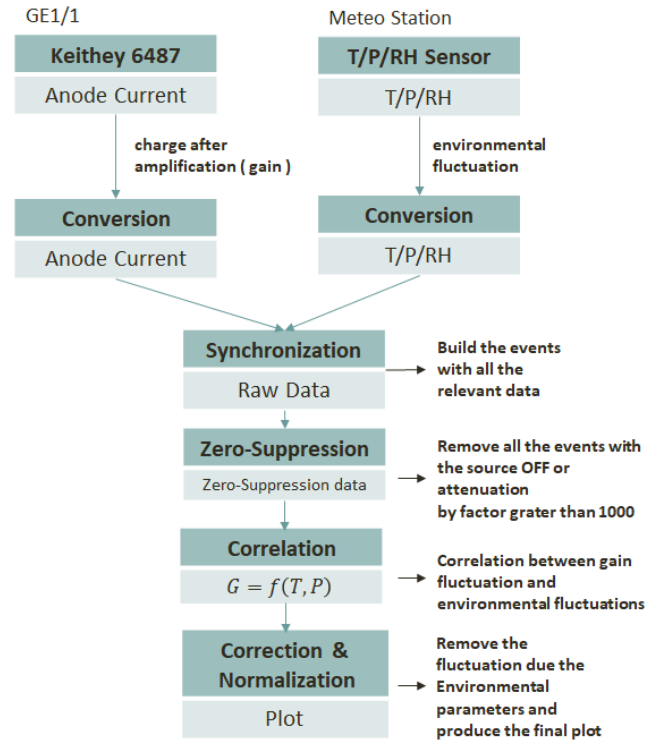


Figure 6.24: Schematic representation of the analysis steps for the longevity studies.

The analysis procedures aim to extract information of gas gain variations as a function of time and/or as a function of accumulated charge, using the data obtained during the irradiation tests. An overview of the analysis procedures is shown in Figure 6.24 It comprises four main steps:

- **Data Conversion.** The data files from the various DAQ-systems are converted into the same format (.txt and .root file), including the relative time of each measurement, the average value of the anode current and the environmental parameters.
- **Time Synchronization and Marging Data.** The relative timestamp of each data point is compared to a reference time common to all the DAQ systems in order to do the synchronization of the data and to assign the correct environmental parameters to each anode current measurement. All the relevant information is stored into single data event, including the gas gain indicator (i.e. the anode current), the environmental parameters and the absolute timestamp.

- **Data Cleaning.** All the events corresponding to the source OFF or the detector not powered are removed from the data set;
- **Correlation with the environmental parameters.** The purpose of the correlation step is to parameterize the influence of the environmental variations on the response of the detector. During the long-term longevity studies, the temperature and the pressure have been monitored in order to establish the correlation with the value of gas gain. The variations of the ambient parameters during the longevity test campaign are plotted in Figure 6.25.

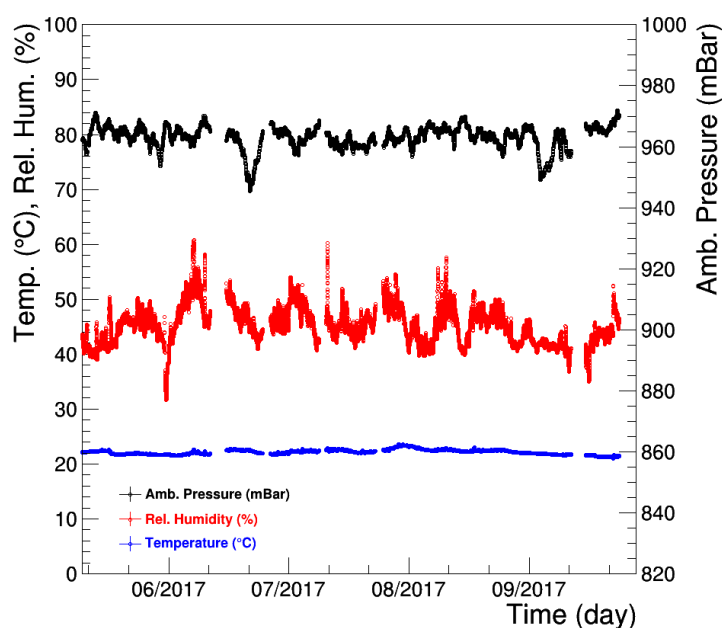


Figure 6.25: Ambient parameters versus time (The accuracy is ± 0.2 °C for temperature, $\pm 2\%$ for relative humidity, and ± 2 mBar for atmospheric pressure).

The influence of the variations of temperature and pressure on the anode current are not negligible and had to be considered. Figure 6.26 shows a sample of data collected at GIF++ facility with the GE1/1 triple-GEM detector during three weeks of continuous irradiation. The anode current fluctuations, of the order of 30%, follow the ratio temperature over pressure (T/P).

In gaseous detector the anode current, which reflects the effective gas gain of the detector, depends approximately through an exponential function, on the gas density, function itself of the ratio temperature over pressure (T/P). Therefore, the corrected and normalized anode current (I_{real}) has been computed from the measured and normalized anode current

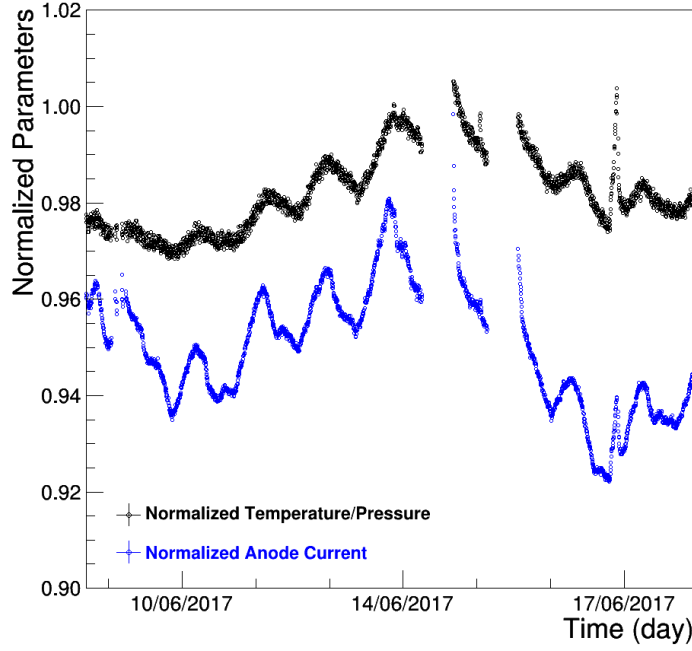


Figure 6.26: Result of the 2017/2018 longevity test campaigns at the GIF++ facility: the normalized anode current and the ratio temperature over pressure of the gas mixture as a function of time. The large fluctuations of the anode current are essentially correlated to the variations of the environmental conditions.

($I_{measured}$) according to the equation:

$$I_{real} = \frac{I_{measured}}{A \cdot \exp(B \cdot T/P)} \quad (6.4)$$

where A and B are fit parameters, determined by fitting the exponential function:

$$I_{measured}(T/P) = A \cdot \exp(B \cdot T/P) \quad (6.5)$$

to the correlation plot shown in Figure 6.27: the scatter plot correlates the value of normalized anode current $I_{measured}$, measured at high rate and fixed voltage with the GE1/1 triple-GEM detector at the GIF++ facility, to the ratio (T/P).

Past experiences [88] show that in some cases the correlation with the environment condition is better described by power functions of pressure and temperature. The previous relation 6.4 becomes:

$$I_{real} = I_{measured} \times (P_i \times \langle 1/P_i \rangle)^{F_1} \times (\langle T_i \rangle / T_i)^{F_2} \quad (6.6)$$

where $\langle T_i \rangle$ and $\langle 1/P_i \rangle$ are the mean values of the temperature and inverse of pressure during the entire irradiation period. The exponents F_1 and F_2

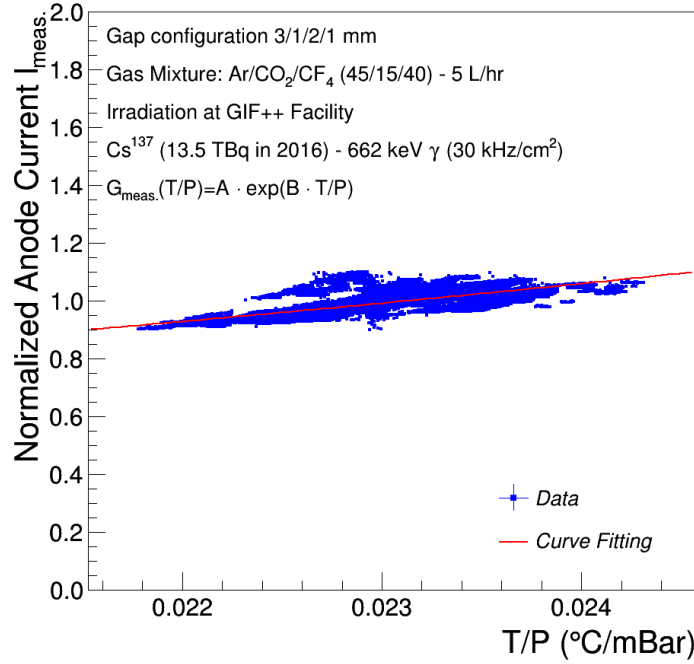


Figure 6.27: Correlation plot: measured and normalized anode current as a function of the ratio temperature over pressure. A best fit to the data with the Equation 6.5 gives for the slope parameter B the value of $\sim 56.22 \text{ mBar}/^\circ\text{C}$. The dependence can be used in the experiment to actively correct the value of the measured anode current in order to maintain it constant in varying ambient conditions.

reflect the goodness of the correlation between the detector anode current and the temperature and pressure fluctuations. The exponents F_1 and F_2 represent the strength of the detector anode current dependency with temperature and pressure, including not only the gas density effects but also other effects such as the influence of the environment parameters on the DAQ electronics.

The value of the first exponent F_1 is selected by fitting the power function:

$$I_{measured}(P_i, T_i) = (P_i \times \langle 1/P_i \rangle)^{F_1} \quad (6.7)$$

$$\ln(I_{measured}(P_i, T_i)) = F_1 \times [\ln(P_i) + \ln(\langle 1/P_i \rangle)] \quad (6.8)$$

to the correlation plot shown in Figure 6.28: the scatter plot correlates the logarithm value of the normalized anode current $\ln(I_{meas.}(P_i, T_i))$, measured at high rate and fixed voltage with the GE1/1 triple-GEM detector at the GIF++ facility, to the logarithm value of the pressure $\ln(P_i)$.

The value of the second exponent F_2 is selected by fitting the power

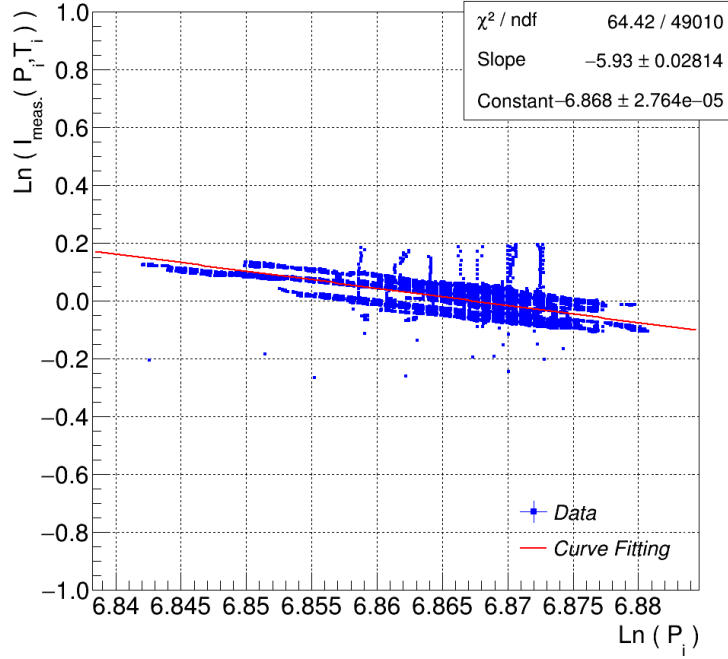


Figure 6.28: Correlation plot: logarithm value of the measured and normalized anode current as a function of the logarithm value of the pressure. A best fit to the data with the Equation 6.8 gives for the slope parameter F_1 the value of -5.93 and for the mean values of the inverse of pressure $\langle 1/P_i \rangle$ the value of $\sim 0.001 \text{ mBar}^{-1}$. The dependence has been used in the experiment to actively correct the value of the measured anode current in order to maintain it constant in varying ambient conditions.

function:

$$I_{measured}(T_i) = (\langle T_i \rangle / T_i)^{F_2} \quad (6.9)$$

$$\ln(I_{measured}(T_i)) = -F_2 \times [\ln(T_i) - \ln(\langle T_i \rangle)] \quad (6.10)$$

to the correlation plot shown in Figure 6.29: the scatter plot correlates the logarithm value of the normalized anode current $\ln(I_{meas.}(T_i))$, already corrected in order to remove fluctuations due to the pressure changes, to the logarithm value of the temperature $\ln(T_i)$.

In order to verify the stability of the detector response under continuous irradiation, the corrected and normalized anode current has been studied as a function of the total accumulated charge per unit irradiated area of the detector, that is directly proportional to exposure time.

In order to estimate the total accumulated charge, the average anode current $(I_i + I_{i+1})/2$ of two adjacent time intervals, (t_i) and (t_{i+1}) , has been taken and multiplied by the time interval $(t_i - t_{i+1})$. The total accumulated charge will

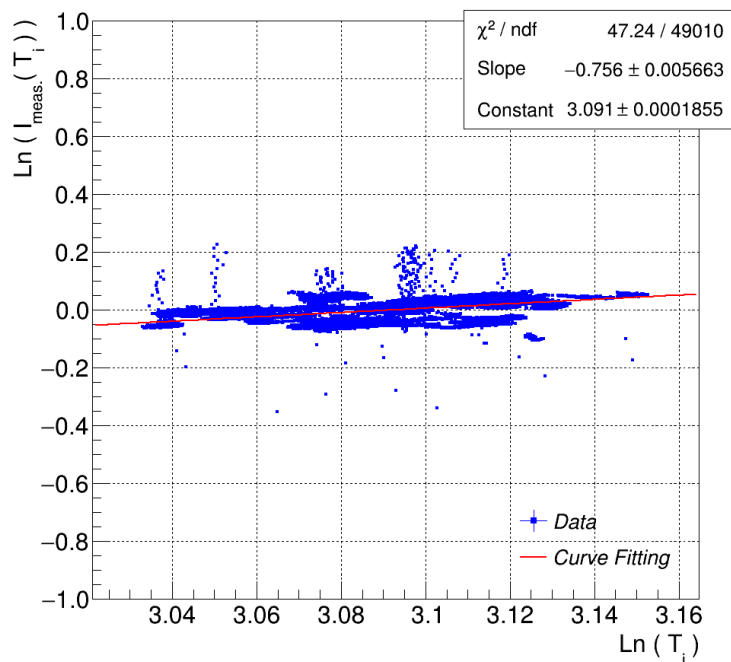


Figure 6.29: Correlation plot: logarithm value of the measured and normalized anode current, already corrected in order to remove fluctuations due to the pressure changes, as a function of the logarithm value of the temperature. A best fit to the data with the Equation 6.10 gives for the slope parameter F_2 the value of -0.756 and for the mean values of the temperature $\langle T_i \rangle$ the value of ~ 22.0 °C. The dependence has been used in the experiment to actively correct the value of the measured anode current in order to maintain it constant in varying ambient conditions.

be the sum of the accumulated charge over all the intervals during every two consecutive readings Q_i . To get the total accumulated charge per unit area, the total accumulated charge has been then divided by the irradiated area. So mathematically the total accumulated charge per unit irradiated area is given by:

$$Q_{tot} = \sum_{i=1}^N Q_i / S = \left[\sum_{i=1}^N \frac{I_i + I_{i+1}}{2} \cdot (t_{i+1} - t_i) \right] / S \quad (6.11)$$

where S is the irradiated area of the detector under irradiation test.

6.2.2.4 Aging Test Results for CERN GEM-foils

The GE1/1 triple-GEM detector of the 4th generation operated with Ar/CO_2 (70/30) gas mixture at an effective gas gain of 2×10^4 has been exposed to the radiation in the GIF++ facility for several months. Figure 6.30 shows the accumulated charge per unit of detector area (mC/cm^2) as a function of time

6.2. Triple-GEM Aging Studies at GIF++ facility

from May 2017 to the beginning of August 2018. During this time, the detector under irradiation test integrated about 126.92 mC/cm^2 after 5.7 months of continuous irradiation of sustained operation in front of the ^{137}Cs source.

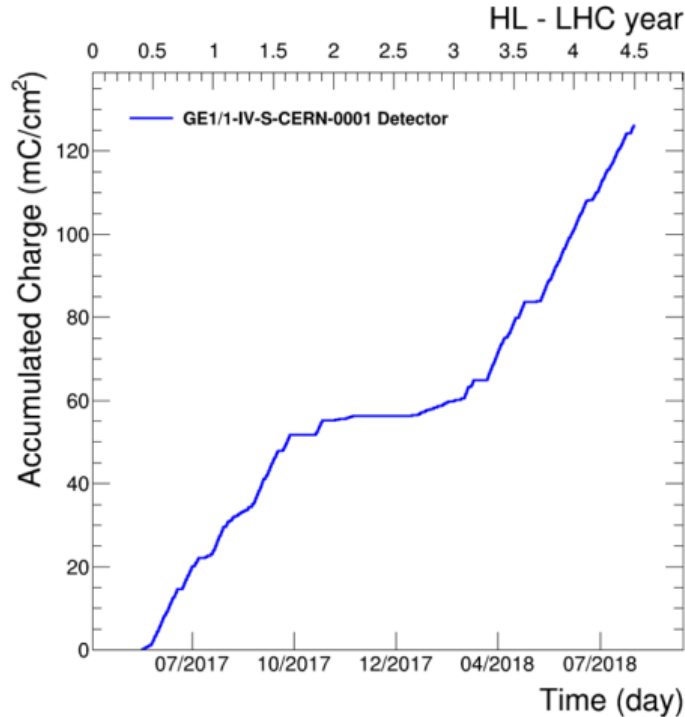


Figure 6.30: Result of the longevity studies at the GIF++ facility: accumulated charge per unit of detector area (mC/cm^2) as a function of time. Different slopes account for different attenuation factors during data taking.

The result for the normalized anode current (corrected for pressure and temperature variations) indicates that the CMS triple-GEM detector does not suffer from any kind of longevity effects or long-term degradation. The anode current, which reflects the effective gas gain of the detector, is stable during the entire irradiation test and only fluctuates within 2 – 3% of its initial value (see Figure 6.31).

Taking into account that the GE1/1 triple-GEM detector under test accumulated a charge of $\sim 55 \text{ mC/cm}^2$ during the previous longevity studies performed at GIF ++ facility between March 2015 and September 2016 (see Section 6.1.2), the final accumulated charge is about 181.9 mC/cm^2 , which represents only 64.3% of the total *ME0* operation. The final normalized and corrected anode current as a function of the accumulated charge for both longevity test campaigns is shown on Figure 6.32.

The 2015/2016 and 2017/2018 longevity test campaigns demonstrated that the operation of the GE1/1 triple-GEM detectors in the CMS configuration is not affected by the aging phenomena up to an integrated charge of 181.9 mC/cm^2 .

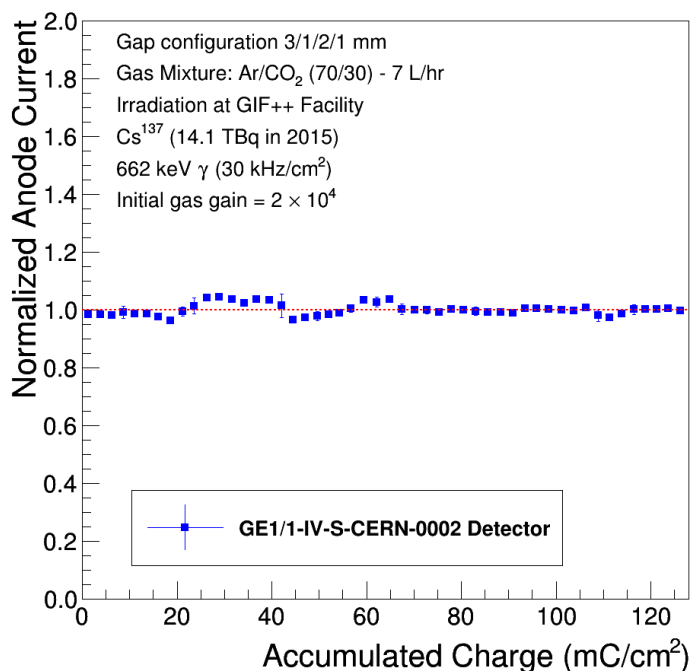


Figure 6.31: Result of the longevity studies at the GIF++ facility: normalized and corrected anode current as a function of the accumulated charge. The detector under test is a GE1/1 triple-GEM detector of the 4th generation operated in Ar/CO_2 (70/30) gas mixture at an initial gas gain of 2×10^4 .

The longevity studies will continue at the GIF++ facility under the same conditions until the detector accumulates a total charge equivalent to ten HL-LHC years in the ME0 environment with a safety factor 3. This will take additional 5-5.5 years of exposure due to the duty factor of the GIF++ facility and its concurrent use by other experiments. To overcome the extremely long time required at the GIF++ facility to assess the triple-GEM technology as suitable choice for the ME0 detector, an additional longevity test has been setup in summer 2017 exposing a GE1/1 triple-GEM detector to 22 keV X-rays from an X-ray source with *Ag*-target at a higher rate (see Section 6.3).

6.2.3 Aging Test on triple-GEM technology for GE2/1 project

6.2.3.1 Introduction

The Korean CMS group (KCMS) has made a consortium with *Mecaro* [120], a Korean company producing component and material of semiconductor production located in Chungcheongbuk-do, Republic of Korea, for the production of large GEM-foils. As the CERN is only one supplier of large size GEM-foils and GEM-based detectors are getting popularity in experimental high-energy

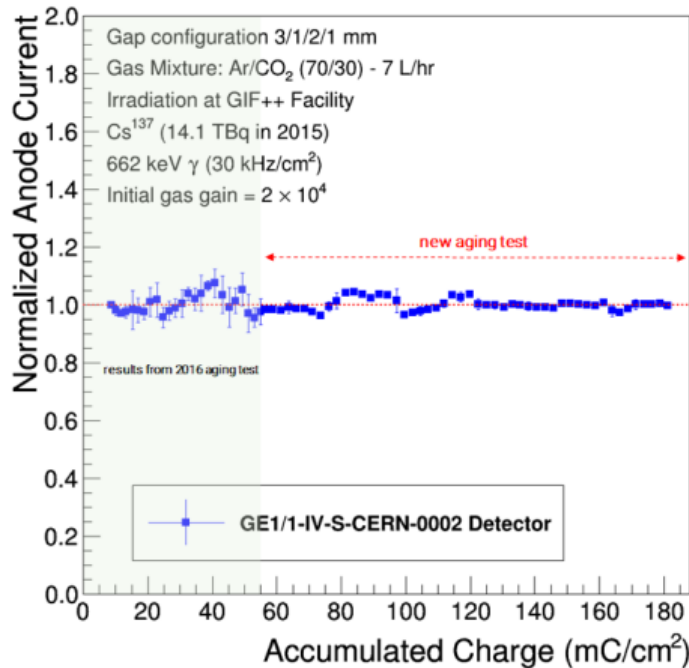
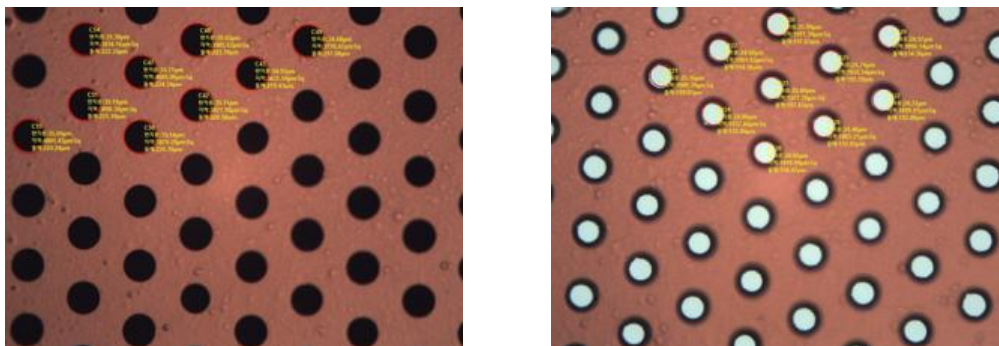


Figure 6.32: Result of the 2015/2016 and 2017/2018 longevity test campaigns at the GIF++ facility: normalized and corrected anode current as a function of the accumulated charge. No gas gain degradation is observed. The detector under test is a GE1/1 triple-GEM detector of the 4th generation operated in Ar/CO_2 (70/30) gas mixture at an initial gas gain of 2×10^4 .

physics community, the supply of GEM-foils could not satisfy its demand even because the primary mission of CERN is in the field of research and development (R&D) and not the mass production. Single source supply also increases the risk due to a single point of failure such as inability to meet increased demand, or product quality issues. This has been the strategy adopted for the GEM-foils mass production for the GE1/1 project, which the CMS-GEM community want to avoid for the future GEM upgrade projects. Consequently, it's necessary to find another supplier of large size GEM-foils. The Korean consortium has been made to be second supplier of large size GEM-foils for the CMS-GE2/1 and CMS-ME0 upgrade project.

The Korean consortium aims to produce large size GEM-foil with standard geometry via double-mask photolithography technique (see Section 5.2.5). The pattern and the GEM-holes size is expected to be similar to those of the GEM-foils produced with the single-mask photolithography technique developed by CERN PCB Workshop. Due to the double-mask technique, the shape of the hole is symmetric and bi-conical compared to the asymmetric and bi-conical shape obtained with single-mask technique (see Figure 6.33). The Korean group will be the first large size GEM foils supplier using double-mask tech-

nique. Thanks to the double-mask photolithography technique and fully automated machineries, much faster production rate is expected to be achieved. The foil production process from lamination of dry film resist (DFR) to etching of polyimide is done by the automated machineries.



(a) Top layer of the double-mask korean GEM-foil. (b) Bottom layer of the double-mask korean GEM-foil.

Figure 6.33: Scanning Electron Microscope (SEM) picture of double-mask korean GEM-foil, the top layer (left) and the bottom layer (right). The outer diameters of the hole are $68\text{-}72\ \mu\text{m}$. (design goal = $70\ \mu\text{m}$) and the inner diameter is $48\text{-}52\ \mu\text{m}$. (design goal = $50\ \mu\text{m}$); the hole pitch is $140\ \mu\text{m}$.

In the double-mask technique, masks alignment become extremely crucial. The large bipolar UV exposure machine handles not only the DFR development, but also the alignment. A four-view bifocal microscope is used to align the top and bottom masks; the residual misalignment is measured less than $3\ \mu\text{m}$. The size of producible GEM-foils is limited by the dimension of the UV exposure machine: $1300\ \text{mm} \times 610\ \text{mm}$ is the maximum size of GEM-foils which can be produced by the Korean consortium.

An intense R&D activity is currently underway in the CMS-GEM QA/QC facility on small- and full-size triple GEM prototypes detectors which have been assembled using GEM-foils developed and produced with the double-mask photolithography technique by the Mecaro company. The aim of this R&D activity, carried out in collaboration with Korea CMS group, is to determine the possible differences between the two different production techniques and measure the absolute characteristics of the double-mask foils produced by the Mecaro company compared to the single-mask foils produced by the CERN PCB workshop, which are currently used in the large CMS triple-GEM detectors for the LS2 GE1/1 detectors mass production. It includes the study of the effective gas gain, the energy response to an X-ray source and the typical behavior when irradiated by an intense flux of particles, such as the rate capability, the discharge probability and the long-term stability.

As for the GEM-foils produced at CERN PCB Workshop with the single-mask photolithography technique, the GEM-foils produced at Mecaro com-

6.2. Triple-GEM Aging Studies at GIF++ facility

pany with the double-mask photolithography technique have to undergo and pass longevity studies to be qualified as suitable components for the GE2/1 triple-GEM detectors. Indeed, the large GEM-foils based on the double-mask technique are not yet tested from the aging point of view. The aim of these longevity tests is to validate the large Korean GEM-foils, based on the double-mask photolithography technique produced by the Mecaro company for CMS-GE2/1 project by integrating a minimum of charge per unit area of about 9 mC/cm^2 , which represent 10 years of the total GE2/1 operation at HL-LHC with a safety factor of three.

6.2.3.2 The triple-GEM detector with korean GEM-foils quality control

The longevity test campaign has been conducted at the GIF++ facility and has been performed with a detector assembled using a full-size LS2 - CMS GE1/1 mechanics of 10th generation and korean GEM-foils based on the double-mask photolithography technique produced by the Mecaro company. The detector has been assembled in 2017. The picture of CMS GE1/1 triple-GEM detector, that is now under test at the GIF++ facility, can be seen on Figure 6.34.



Figure 6.34: The detector under test is a triple-GEM detector equipped with korean GEM-foils based on the double-mask photolithography technique produced by the Mecaro company and operated in Ar/CO_2 (70/30) gas mixture at an initial gas gain of 2×10^4 .

The triple-GEM detector, operating in Ar/CO_2 (70/30) gas mixture with a gas flow rate of $\sim 5 \text{ L/hr}$, has been powered through an HV divider corresponding to the CMS configuration described in Figure 5.23. The gas gain of

the detector has been kept constant at an effective value of 2×10^4 during the entire irradiation test.

Quality control procedures and the detector performances measurements have been carried out on the detector before the installation inside the GIF++ facility, following the same techniques developed to qualify all the GE1/1 detectors which will be installed in the Muon System of the CMS experiment during the LS2.

- **QC3 - Gas Leak Test.** The detector was perfectly gas-tight: ~ 60 minutes after the starting of the QC3 Gas Leak Test, the pressure drop was about 0.99 mBar resulting in a gas leak rate of $\sim 0.02 \text{ mBar}/\text{min}$, i.e. a gas leak rate allowed by the QC3 acceptance criteria for the LS2 GE1/1 mass production (see Section 5.4.4). The results from the QC3 Gas Leak Test on the detector under test is shown in Figure 6.35.

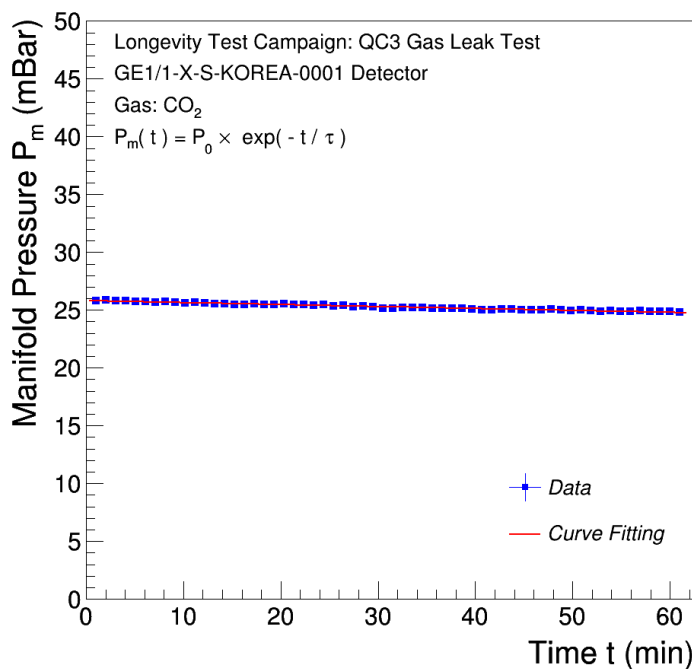
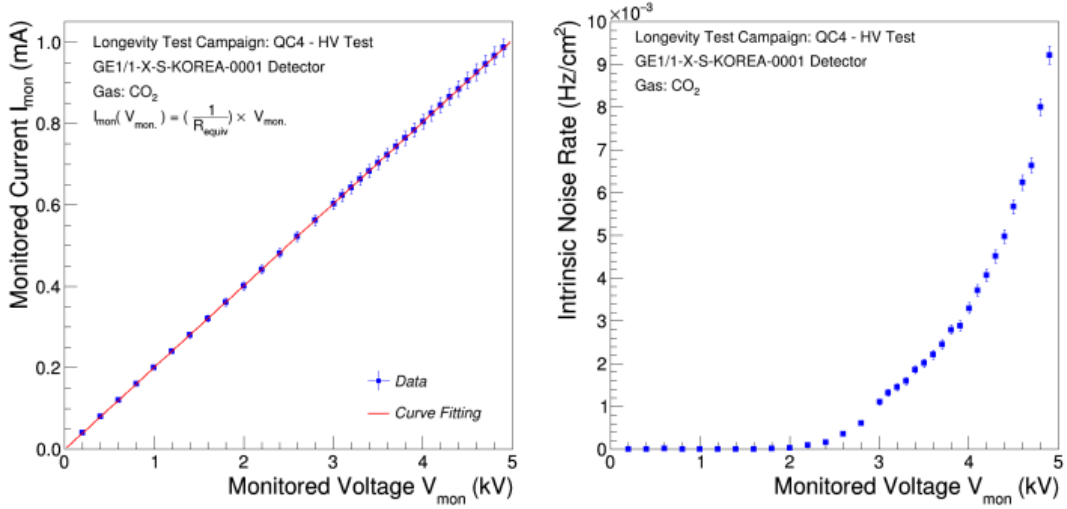


Figure 6.35: Results from the QC3 Gas Leak Test for the triple-GEM detector assembled with korean GEM-foils. The pressure drop is modeled by the function $P_m(t) = P_0 \times \exp(-t/\tau)$. The parameter P_0 is a constant that takes into account the initial overpressure of the detector. The parameter τ is the gas leak time constant and quantifies how fast the overpressure inside the detector decreases as a function of the time. The exponential fit to the experimental data provides a gas leak time constant $\tau \sim 25 \text{ hr}$.

- **QC4 - HV Test.** The intrinsic noise rate has been measured to be $\sim 9.2 \times 10^{-3} \text{ Hz}/\text{cm}^2$ at 4.9 kV (expected background in the GE21/

6.2. Triple-GEM Aging Studies at GIF++ facility

detectors $\sim 1.5 \text{ kHz/cm}^2$, see Table 6.2). The results from the QC4 HV test on the detector under test are shown in Figure 6.36.

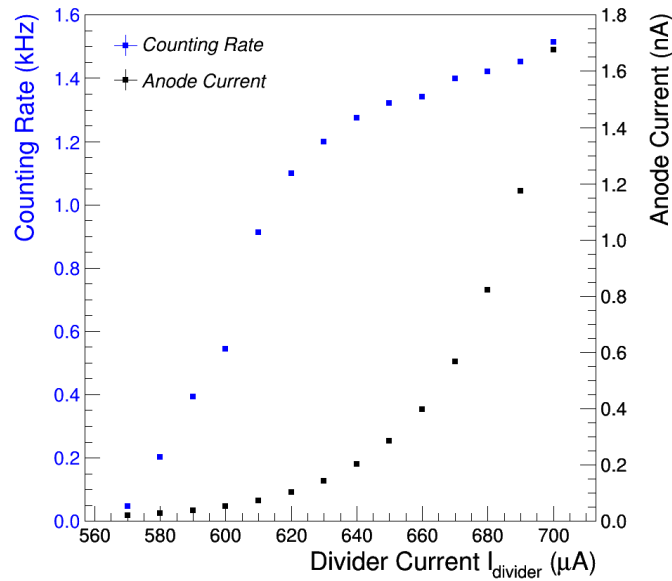


(a) Current through the HV divider as a function of the applied voltage. (b) Intrinsic noise rate as a function of the applied voltage.

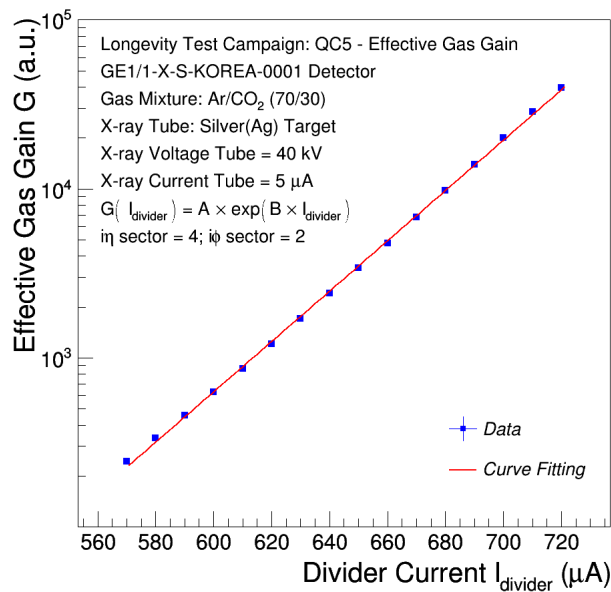
Figure 6.36: Results from the QC4 HV Test for the triple-GEM detector assembled with korean GEM-foils. Left: current through the HV divider as a function of the applied voltage. The linear fit to the experimental data provides an equivalent resistance $R_{equiv} \sim 4.97 \text{ M}\Omega$, resulting in a deviation of about 0.8% with respect to the expected value ($R = 5.01 \pm 0.02 \text{ M}\Omega$). Right: intrinsic noise rate R_{noise} as a function of the applied voltage: $R_{noise} \sim 9.2 \times 10^{-3} \text{ Hz/cm}^2$ at 4.9 kV.

- **QC5 - Effective Gas Gain Measurement.** The effective gas gain of the triple-GEM detector assembled with the korean GEM-foils based on the double-mask photolithography technique developed by the Mecaro company, shows the same behavior of the effective gas gain measured with the LS2 GE1/1 detector assembled with GEM-foils produced with the single-mask photolithography technique developed by CERN PCB Workshop. The results from the QC5 - Effective Gas Gain Measurement on the detector under test are shown in Figure 6.37.
- **QC5 - Response uniformity.** Results from the QC5 - Response uniformity for the triple-GEM detector equipped with GEM-foils based on the double-mask photolithography technique produced by the Mecaro company are presented in Figure 6.38.

At the end of the quality control and the detector characterization, the triple-GEM detector has been installed into the GIF++ facility for a first longevity test campaign.



(a) Counting rate and Anode current as a function of the current through the HV divider.



(b) Effective gas gain measurement as a function of the operating current through the HV divider.

Figure 6.37: Results from the QC5 - Effective Gas Gain Measurement on the triple-GEM detector assembled with GEM-foils based on the double-mask photolithography technique produced by the Mecaro company. The detector under test has been operated in Ar/CO₂ (70/30) gas mixture and irradiated by a 22 keV photons X-ray from an X-ray tube with an interaction rate of 1.5 kHz.

6.2. Triple-GEM Aging Studies at GIF++ facility

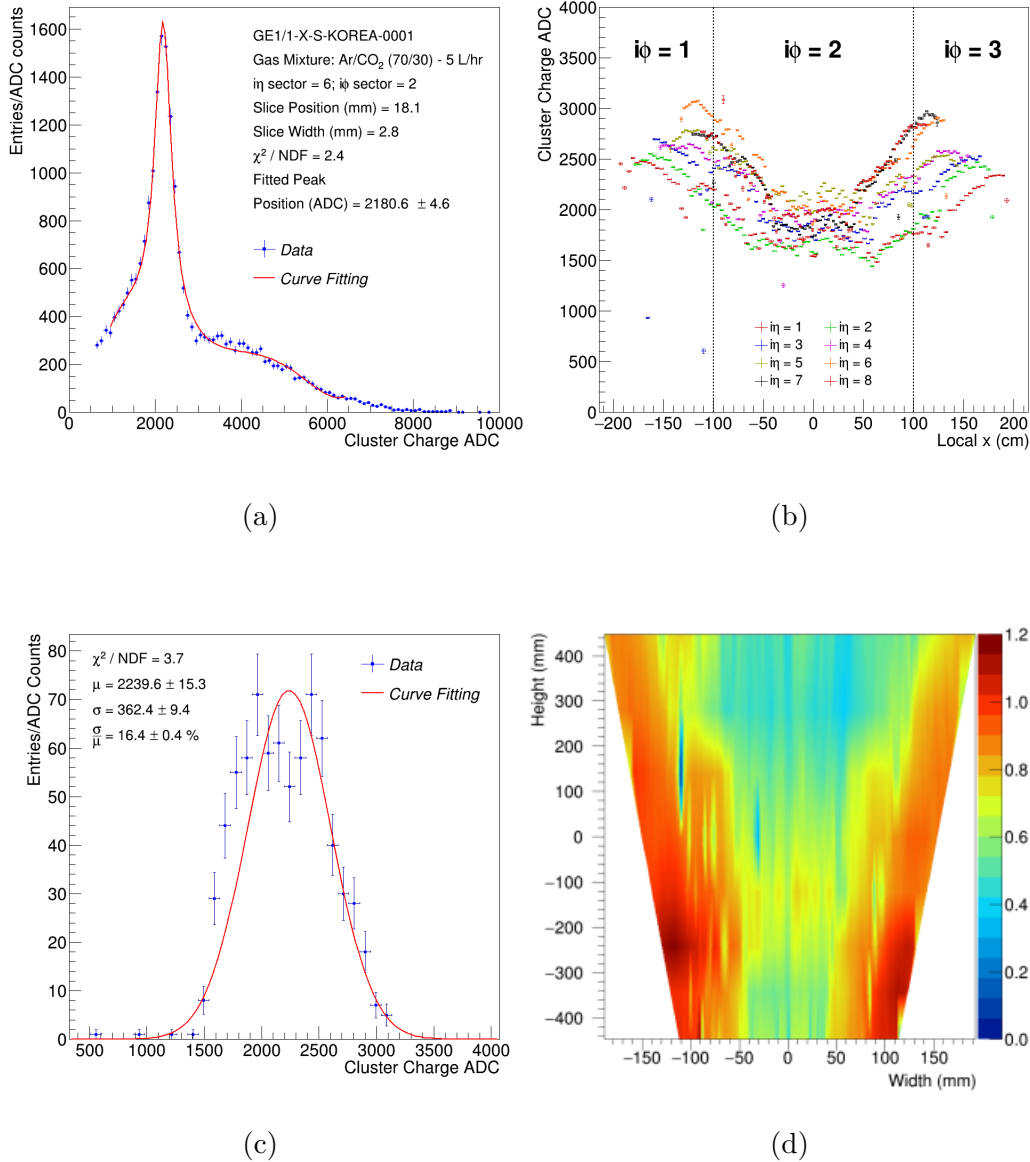


Figure 6.38: (Figure 6.38a) Example of energy spectrum from a slice (four strips) of the triple-GEM detector under test operated at an average gain about 600 with Ar/CO_2 (70/30) fully illuminated by a 22 keV X-ray. The solid line represents a fit to the experimental data using a Cauchy distribution to model the copper fluorescence photopeak plus a fifth order polynomial that models the background. (Figure 6.38b) The mean of the copper fluorescence spectrum extracted from the fit of each slice is assigned to coordinate point of the slice in the local coordinates of the detector. (Figure 6.38b) Distribution of fitted photopeak positions obtained from GE1/1 triple-GEM detector under test: the experimental points represent each photopeak position and the solid line is a Gaussian fit to the data. The response uniformity for this detector is $R.U. = 16.4 \pm 0.4\%$. (Figure 6.38d) Map of the detector response (i.e. the normalized photopeak energy) across the detector under test.

6.2.3.3 Aging Test Results on Korean GEM-foils

The triple-GEM detector equipped with korean GEM-foils based on the double-mask photolithography technique developed by the Mecaro company and operated with Ar/CO_2 (70/30) gas mixture at an effective gas gain of 2×10^4 has been exposed to the radiation in the GIF++ facility for several months. Figure 6.39 shows the accumulated charge per unit of detector area (mC/cm^2) as a function of time from January 2018 to the beginning of August 2018. During this time, the detector under irradiation test integrated about $54.27 mC/cm^2$ after 3.1 months of continuous irradiation of sustained operation in front of the ^{137}Cs source, which represents ten years of $GE2/1$ operation at the HL-LHC with a safety factor 18.1, and 19.2% of the total $ME0$ operation.

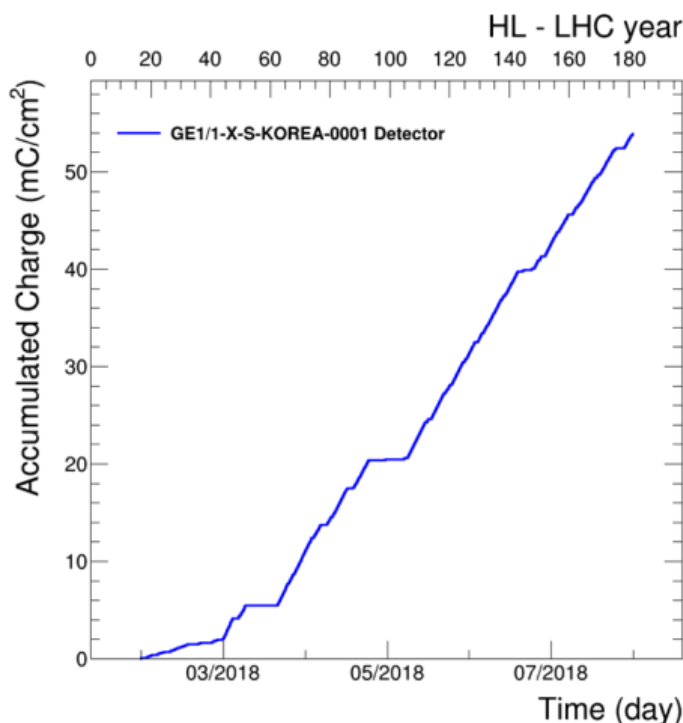


Figure 6.39: Result of the longevity studies at the GIF++ facility: accumulated charge per unit of detector area (mC/cm^2) as a function of time. Different slopes account for different attenuation factors during data taking.

The result for the normalized anode current, which reflects the effective gas gain of the detector (corrected for pressure and temperature variations) indicates that the triple-GEM detector, with korean GEM-foils based on the double-mask photolithography technique produced by the Mecaro company, does not suffer from any kind of longevity effects or long-term degradation. The gas gain is stable during the entire irradiation test and only fluctuates within 2% of its initial value (see Figure 6.40).

The 2017/2018 longevity test campaigns demonstrated that the operation

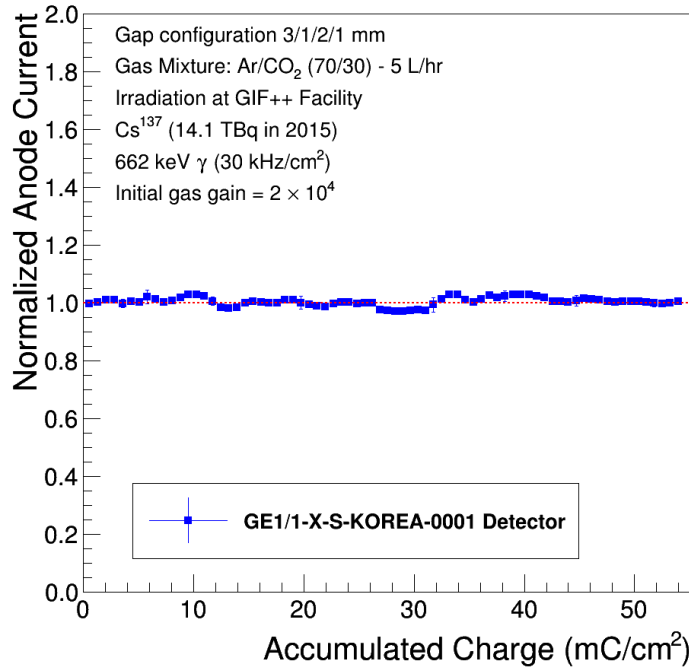


Figure 6.40: Result of the longevity studies at the GIF++ facility: normalized and corrected anode current as a function of the accumulated charge; no gas gain degradation is observed. The detector under test is a triple-GEM detector assembled with korean GEM-foils based on the double-mask photolithography technique developed by the Mecaro company and operated in Ar/CO_2 (70/30) gas mixture at an initial gas gain of 2×10^4 .

of the triple-GEM detectors assembled with korean GEM-foils based on the double-mask photolithography technique developed by the Mecaro company and operated in the CMS configuration is not affected by the aging phenomena; they are then expected to survive a minimum of 10 years of real operation (safety factor 18) with Ar/CO_2 (70/30) in the CMS end-cap environment at HL-LHC. Therefore, the large GEM-foils based on the double-mask photolithography technique are fully validated for CMS-GE2/1 upgrade project from a radiation hardness assurance point of view. The longevity studies will continue at the GIF++ facility under the same conditions until the detector accumulates a total charge equivalent to ten HL-LHC years in the ME0 environment.

6.3 Triple-GEM Aging Studies at CMS-GEM QA/QC facility with X-ray source

6.3.1 Aging Test on triple-GEM technology for ME0 project

This section describes the studies of long-term irradiation effects on the CMS triple-GEM detectors after long sustained operation under intense X-ray radiation at the CMS-GEM QA/QC facility. The aim of these new longevity tests is to validate the triple-GEM technology developed for the GE1/1 project also for CMS-ME0 project by integrating a minimum of charge per unit area of about 850 mC/cm^2 , which represent a 10 years of the total ME0 operation at HL-LHC with a safety factor of three.

As previously mentioned, the longevity studies, restarted at the GIF++ facility in 2017, will continue under the same conditions until the detector accumulates a total charge equivalent to ten HL-LHC years in the ME0 environment with safety factor of 3. This will take additional 5-5.5 years of exposure due to the γ -photons rate provided by the ^{137}Cs source and the duty factor of the GIF++ facility. To overcome the extremely long time required at the GIF++ facility to assess the triple-GEM technology as suitable choice for the ME0 detector, an additional longevity test has been setup in summer 2017 at CMS-GEM QA/QC that exposes a GE1/1 triple-GEM detector to 22 keV X-rays from an X-ray source with Ag-target at a higher rate. Based on the particular characteristic of the X-ray generator available in the CMS-GEM QA/QC facility and the expected duty factor for the experimental setup operation, the exposure time needed to accumulated 850 mC/cm^2 in GE1/1 detector is expected to be ~ 10 times shorter than the GIF++ time (5/6 months of continuous irradiation).

6.3.1.1 GE1/1 detector under test and quality control

The longevity test campaign at the CMS-GEM QA/QC facility has been performed with a full-size CMS GE1/1 triple-GEM detector. One of the first detectors assembled in 2017 for the LS2 GE1/1 installation has been devoted specifically to R&D activities and it has been labelled to as *GE1/1-X-S-CERN-0002* following the standard format of the serial numbers used for the LS2 GE1/1 detectors. Picture of CMS GE1/1 triple-GEM detector under test at the CMS-GEM QA/QC facility, can be seen on Figure 6.41.

The GE1/1-X-S-CERN-0002 detector, operating in Ar/CO_2 (70/30) gas mixture with a gas flow rate of $\sim 5 \text{ L/hr}$, has been powered through an HV divider corresponding to the CMS configuration described in Figure 5.23. The gas gain of the detector has been kept constant at an effective value of 2×10^4 during the entire irradiation test.

The standard GE1/1 LS2 detectors quality control procedures and performances measurements have been performed on the GE1/1-X-S-CERN-0002

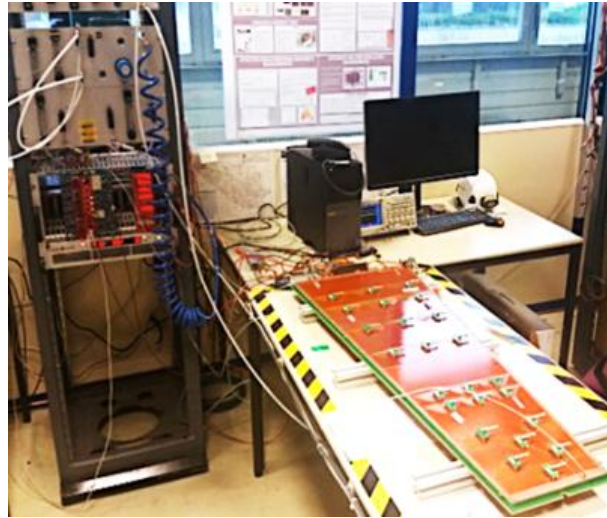


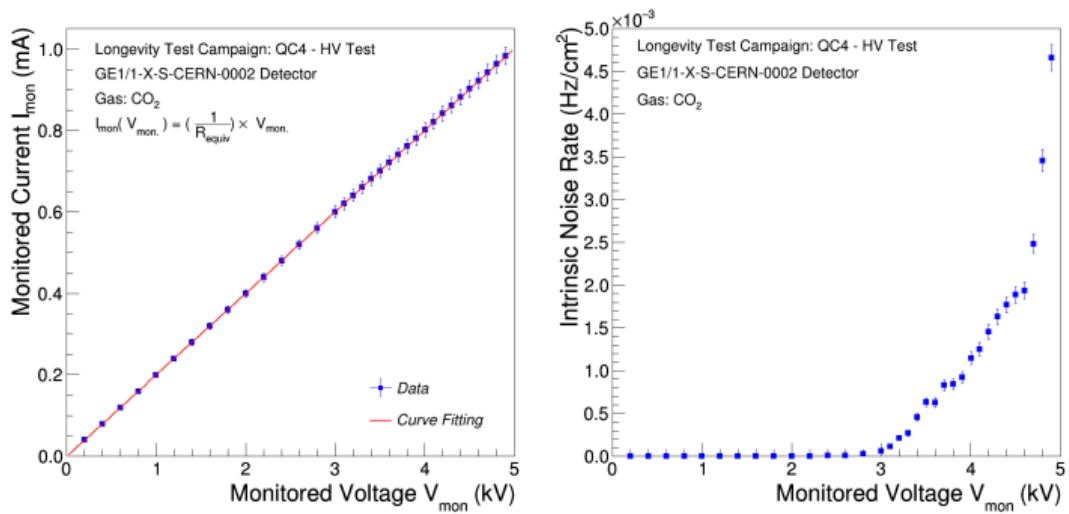
Figure 6.41: The detector under test is a GE1/1 triple-GEM detector of the 10th generation operated in Ar/CO_2 (70/30) gas mixture at an initial gas gain of 2×10^4 for the longevity studies at the CMS-GEM QA/QC facility.

detector before starting the irradiation test. As usual, the Gas Leak Test (QC3), the HV Test (QC4) and the Effective Gas Gain and Response Uniformity measurement (QC5) have been performed. Results in the average of the GE1/1 mass production QA/QC tests have been found. The results from the QC4 HV test on the detector under test are shown in Figure 6.43. The intrinsic noise rate of the GE1/1 triple-GEM detector under test has been measured to be $\sim 4.7 \times 10^{-3} \text{ Hz/cm}^2$ at 4.9 kV (expected background in the ME0 detectors 47 kHz/cm², see Table 6.2).

Due to the fact that the GE1/1-X-S-CERN-0002 detector was expected to be devoted to the longevity studies, the QC5 - Effective Gas Gain measurement has been performed not only on the usual readout sector $i\eta = 4, i\phi = 2$, but also in several readout sectors in order to create a better map of the detector efficiency at several operationg working points. The QC5 - Effective Gas Gain measurement has been performed on thirteen different readout sectors. The Figure 6.43a shows the schematic overview of the detector readout board and the thirteen readout sectors upon which the effective gas gain measurement has been performed. An example of a QC5 - Effective Gas Gain measurement is shown in the Figure 6.43b.

As a graphical representation, Figure 6.44 shows the effective gas gain values for the thirteen readout sector of the GE11-X-S-CERN-0002 detector at an applied voltage of 3390 V (676.6 μA divider current equivalent) as a function of spatial location.

In addition to perform the effective gas gain measurements, the energy resolution of the detector has been studied using a low-intensity ^{109}Cd source (mainly $\sim 22 \text{ keV}$ X-ray photons) with a rate of $\sim 2 \text{ Hz/mm}^2$. For the these

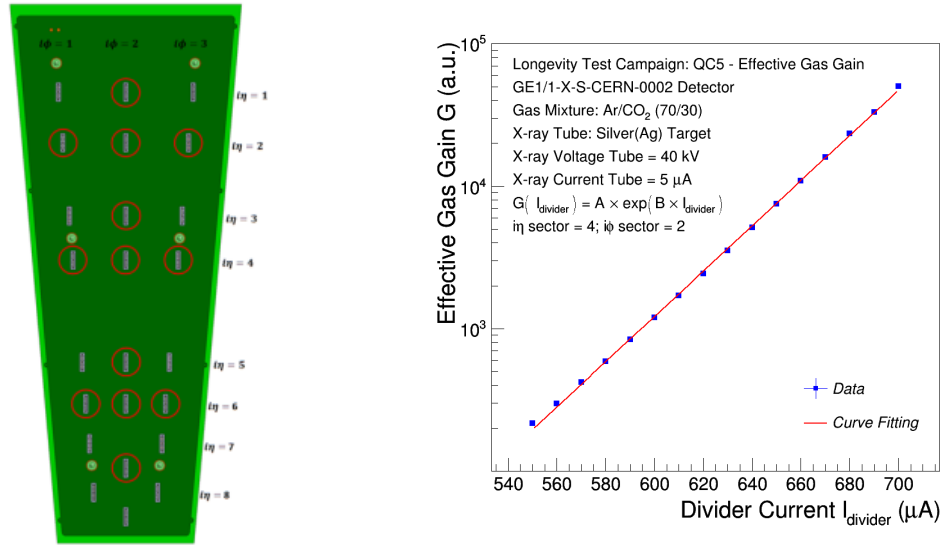


(a) Current through the HV divider as a function of the applied voltage.

(b) Intrinsic noise rate as a function of the applied voltage.

Figure 6.42: Results from the QC4 HV Test on the GE1/1 triple-GEM detector. Left: current through the HV divider as a function of the applied voltage. The linear fit to the experimental data provides an equivalent resistance $R_{\text{equiv}} \sim 4.98 \text{ M}\Omega$, resulting in a deviation of about 0.4% with respect to the expected value ($R = 5.01 \pm 0.02 \text{ M}\Omega$). Right: intrinsic noise rate R_{noise} as a function of the applied voltage: $R_{\text{noise}} \sim 4.7 \times 10^{-3} \text{ Hz/cm}^2$ at 4.9 kV.

6.3. Triple-GEM Aging Studies at CMS-GEM QA/QC facility with X-ray source



(a) Schematic overview of the CMS GE1/1 triple-GEM detector R/O board. (b) Example of QC5 - Effective Gas Gain measurement.

Figure 6.43: Results from the QC5 - Effective Gas Gain Measurement. Left: Schematic overview of the CMS GE1/1 triple-GEM detector readout board showing the readout sectors under test for the effective gas gain measurement (red circle). Right: Example of QC5 - Effective Gas Gain measurement performed on the readout sector $i\eta = 4$, $i\phi = 2$ of the GE11-X-S-CERN-0002 detector.

measurements the detector has been operated at an applied voltage of 3390 V (676.6 μA divider current equivalent), which corresponds to an effective gas gain of about 2×10^4 . In each readout sector under test, a clean separation of the main photopeak and the Ar escape peak is achieved (see Figure 6.45a). The energy resolution, defined by the ratio of the $FWHM$ value and the mean value μ of the main photopeak, is of about 17%. By measuring the ^{109}Cd energy spectrum in thirteen different readout sectors, a map of the energy resolution as a function of spatial location has been obtained (see Figure 6.45b).

Finally, the QC5 Response Uniformity test on the GE11-X-S-CERN-0002 detector has been performed in order to measure the pulse height distribution all over the active surface of the detector. The data acquisition system and the analysis procedures are identical to those used for the QC5 - Response Uniformity test within the standard QA/QC procedures developed to qualify all the GE1/1 detectors which will be installed in the Muon System of the CMS experiment during the LS2. The result for the QC5 - Response Uniformity test performed on the GE11-X-S-CERN-0002 detector under test are presented in Figure 6.46.

At the end of the quality control and the detector characterization, the GE11-X-S-CERN-0002 detector has been installed inside a high intensity X-ray gen-

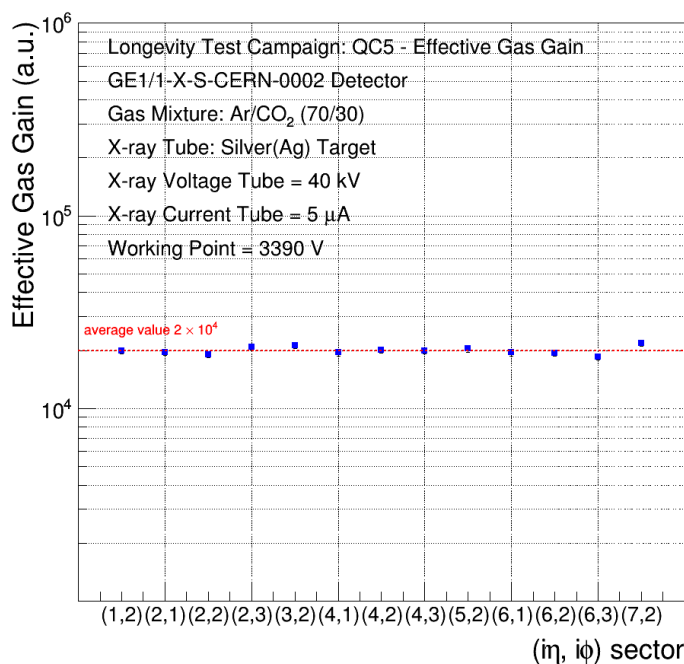


Figure 6.44: Results from the QC5 - Effective Gas Gain Measurement showing the gas gain values for the thirteen readout sector of the GE11-X-S-CERN-0002 detector at an applied voltage of 3390 V (676.6 μ A divider current equivalent) as a function of spatial location.

erator cage for a longevity test campaign.

6.3.1.2 Experimental setup

The GE1/1-X-S-CERN-0002 detector under test is placed in front of a high intensity X-ray generator. The X-ray generator installed in the CMS-GEM QA/QC facility is a conventional X-ray tube with a silver target (AMPTEK mod. Mini-X X-ray Tube [80]), which consists of an electron gun with an accelerating power of the order of tens of kV and electron currents up to 200 μA (see Figure 6.47a). The electron gun is pointing to a metallic cathode which is excited and emits X-rays, the energy of which depends on the cathode material (22 keV for Ag -target). Figure 6.47b shows the energy spectrum for the X-rays emitted by the Ag -target X-ray generator operating at tube voltage of 50 kV and a tube current of 25 μA ; a Cadmium Telluride ($CdTe$) detector has been used to record it [121].

The X-ray generator is fixed on a movable support in the horizontal and vertical direction with high accuracy. The entire system is located inside a large copper box which acts both as a radiation shielding and a Faraday cage (see Figure 6.48), this allows for the irradiation of the detector in any position and the

6.3. Triple-GEM Aging Studies at CMS-GEM QA/QC facility with X-ray source

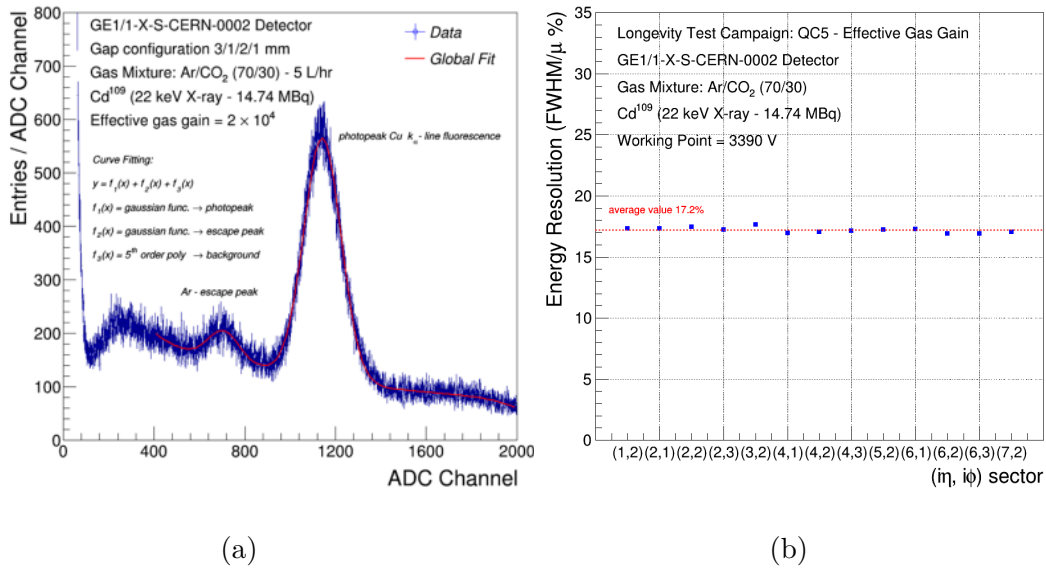


Figure 6.45: Results from the Energy Resolution Measurement. Left: ^{109}Cd energy spectrum taken with the GE11-X-S-CERN-0002 detector at an applied voltage of 3390 V (676.6 μA divider current equivalent). The solid line represents a fit to the experimental data using a sum of two gaussian distributions, to model the copper fluorescence photopeak and the Ar escape peak, plus a fifth order polynomial that models the background. The energy resolution (FWHM value of the photopeak divided by the mean value μ) is 17.2%. Right: Energy resolution as a function of spatial location for the GE11-X-S-CERN-0002 detector at an applied voltage of 3390 V (676.6 μA divider current equivalent).

effective gas gain measurement on the entire active area can be performed in order to control the gas gain stability and uniformity before the intense irradiation and during the longevity test campaign.

The gas system for the CMS-GEM QA/QC installation is substantially identical to the longevity experimental setup at GIF++ facility. The schematic overview of the gas system used for the X-ray longevity test is shown in Figure 6.49. However, the Ar/ CO_2 pre-mixed cylinder has been replaced by the mass flow controllers (MFCs) and gas mixer unit, which supplies the entire CMS-GEM QA/QC facility. Three mass flow controllers F-210CM, provided by Bronkhorst company [122], adjust the proportion of each component (Ar, CO_2 and possibly CF_4) in order to inject a constant and fresh gas mixture into the main gas line. The Ar flow rate is set to 0.52 L/min, the CO_2 flow rate is 0.22 L/min, whereas the CF_4 flow rate is equal to 0 L/min: the resulting gas mixture has a composition of 70% Ar and 30% CO_2 .

Figure 6.50 shows the complete experimental setup for the X-ray longevity test campaign at CMS-GEM QA/QC facility.

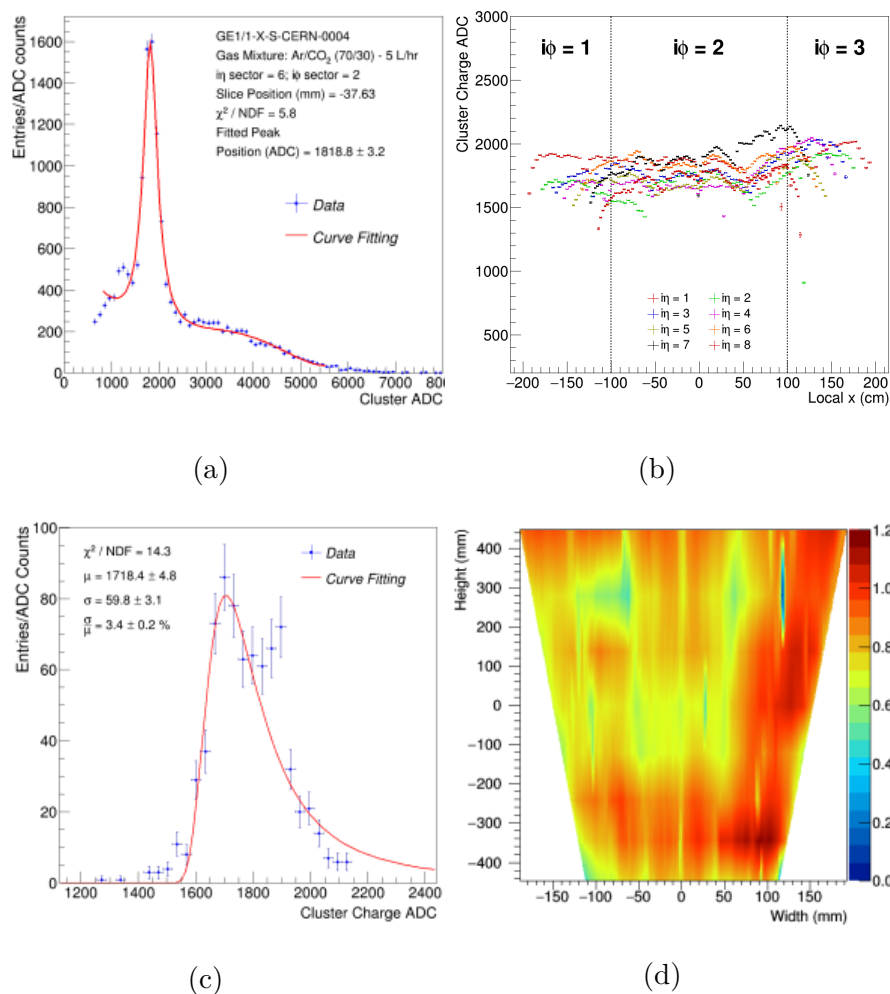
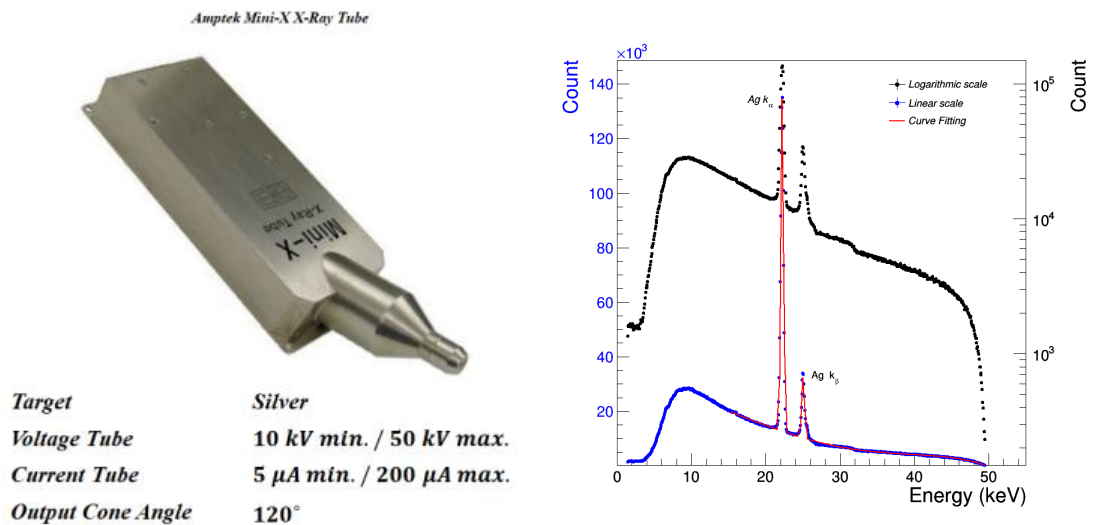


Figure 6.46: (Figure 6.46a) Example of energy spectrum from a slice (four strips) of the GE1/1-X-S-CERN-0002 detector under test operated at an average gain around 800 with Ar/CO₂ (70/30) fully illuminated by a 22 keV X-ray. The solid line represents a fit to the experimental data using a Cauchy distribution to model the copper fluorescence photopeak plus a fifth order polynomial that models the background. (Figure 6.46b) The mean of the copper fluorescence spectrum extracted from the fit of each slice is assigned to coordinate point of the slice in the local coordinates of the detector. (Figure 6.46c) Distribution of fitted photopeak positions obtained from GE1/1 triple-GEM detector under test: the experimental points represent each photopeak position and the solid line is a Gaussian fit to the data. The response uniformity for this detector is $R.U. = 3.4 \pm 0.2\%$. (Figure 6.46d) Map of the detector response (i.e. the normalized photopeak energy) across the detector under test.

6.3. Triple-GEM Aging Studies at CMS-GEM QA/QC facility with X-ray source



(a) Schematic overview of the AMPTEK mod. Mini-X X-ray Tube (b) Energy spectrum of the X-ray tube with silver target

Figure 6.47: (left) Picture of the AMPTEK mod. Mini-X X-ray Tube with the main specifications shown in the table. (right) Energy spectrum of the X-ray emitted by the *Ag*-target X-ray tube operated at tube voltage of 50kV and a tube current of 25 μ A. It has been registered with a *CdTe* detector [121].

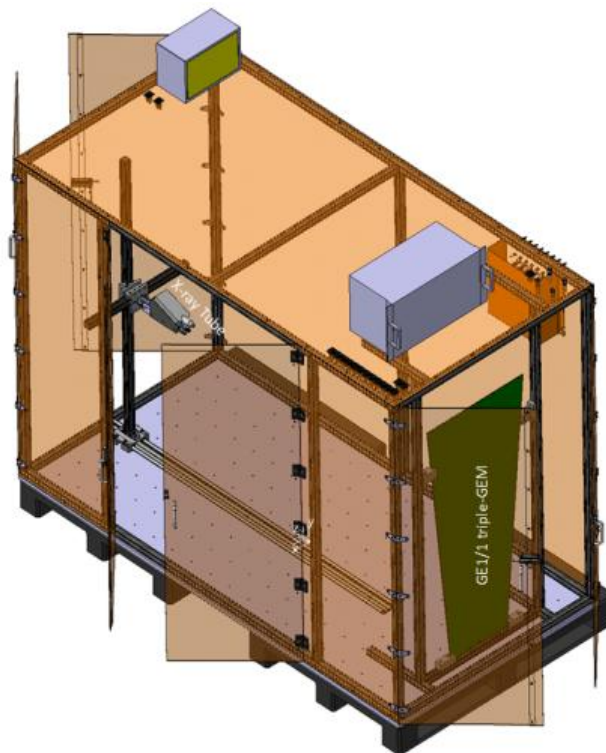


Figure 6.48: Schematic overview of the X-ray copper box showing the detector under test irradiated by the silver X-ray source.

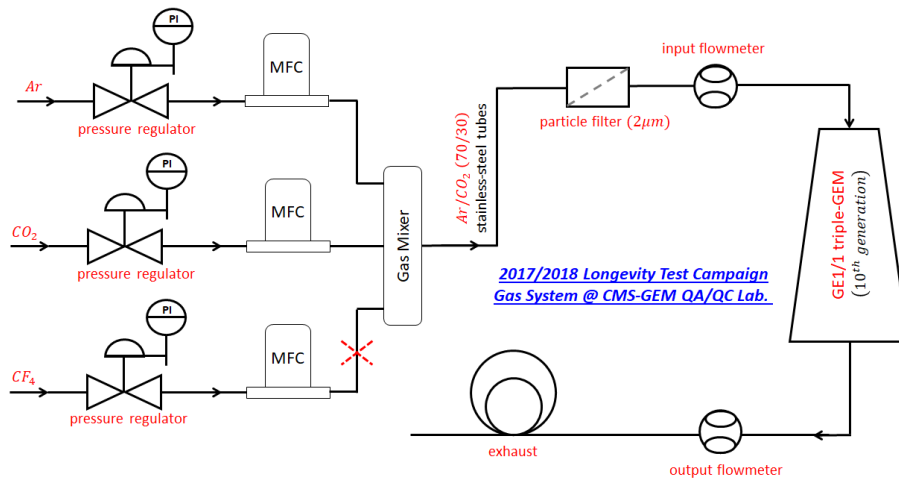


Figure 6.49: The schematic overview of the gas system used during the X-ray longevity test at the CMS-GEM QA/QC facility. The whole gas line is made of stainless-steel tubes.



(a) The X-ray generator in front of the detector under test. (b) The detector under test equipped with the readout electronics.

Figure 6.50: Pictures of the longevity test stand showing the X-ray generator in front of the detector under test (left) and the detector equipped with the readout electronics (right).

6.3.1.3 X-ray generator set-up and working parameters definition

The X-ray generator settings (powering current and voltage) have been studied in order to determine the irradiation properties that the detector would be subjected to, and to decide the final X-ray generator settings to be used which allow to tune its illumination rate and the energy spectrum, and therefore the absolute value of anode current of the GE1/1-X-S-CERN-0002 under irradiation test. For this purpose, the X-ray generator settings have been studied in order to maximize the anode current of the detector under test, and therefore to accelerate the longevity studies.

The procedure for the definition of the X-ray generator settings can be summarized as follows:

- 1^{st} step: The GE1/1-X-S-CERN-0002 detector under test has been placed in front of the AMPTEK miniX X-ray generator and flushed with Ar/CO_2 (70/30) gas mixture at gas flow rate of the order of $5L/hr$ for one and half day. Then, the high voltage has been switched ON and the operating voltage has been selected in order to work at a gas gain of about 2×10^4 . The detector has been kept for several hours at the selected high voltage of $\sim 3390 V$ ($676.6 \mu A$ divider current equivalent) without radiation.
- 2^{sd} step: the X-ray generator has been positioned in the direction of the readout sector $i\eta = 6$, $i\phi = 2$, at $\sim 80.0 cm$ from the detector under test and $\sim 32.5 cm$ from the floor of the X-ray copper box (see Figure 6.51). Since the aperture of the X-ray tube is of the order of 120° , the detector was fully irradiated at a distance of $80.0 cm$ from the source.
- 3^{rd} step: a scan of the X-ray tube powering current has been performed for several powering voltage of the X-ray tube, in order to maximize the anode current from the readout sector under test. The typical tube voltage offers a tunable range from approximately 10 to 50 kV . The highest tube current attainable is dependent on the wattage of the tube, which is restricted in handheld units to 4 W . The tube current is restricted on the basis of the ideal iso-power curve [80] associated with the AMPTEK miniX X-ray. Therefore, based on the iso-power curve, the possible range of values allowed to the tube current for each tube voltage are shown in the table of Figure 6.52.
- 4^{th} step: The anode current collected from the irradiated readout sector $i\eta = 6$, $i\phi = 2$ has been measured using a KEITHLEY 6487 picoammeters for all possible configurations of the powering current and voltage allowed to the X-ray tube. Figure 6.53 shows the anode current monitored on the irradiated readout sector $i\eta = 6$, $i\phi = 2$ at different operating point of the X-ray tube.

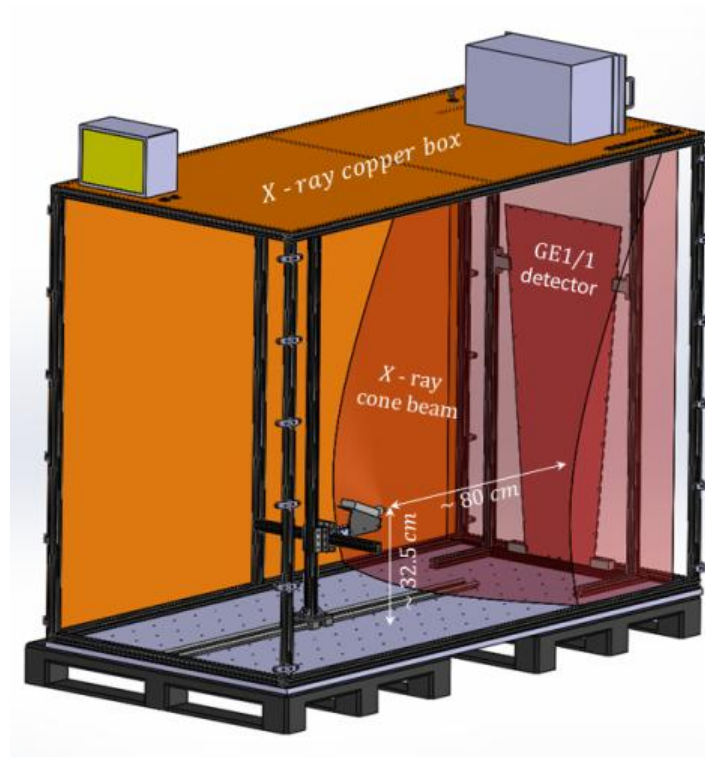


Figure 6.51: Schematic overview of the X-ray copper box showing the detector under test irradiated by the silver X-ray source. The X-ray generator has been initially placed at ~ 80.0 cm from the detector under test and ~ 32.5 cm from the floor of the X-ray copper box

Two possible configurations of the X-ray generator parameters, that maximize the anode current of the irradiated detector, have been selected (see Table 6.4).

Considering that the active area of the irradiated readout sector is about 111 cm², the resulting anode current flow was about 6.66 nA/cm² in the first configuration and 7.83 nA/cm² in the second configuration, i.e. a factor 0.8 and 0.9 compared to the anode current flow observed on the detector under test at GIF++ facility (~ 7.95 nA/cm²). On equal duty factor of the facilities, this working settings lead to an exposure time needed to accumulated 850 mC/cm² in the GE1/1 triple-GEM detector essentially equivalent to the GIF++ time.

- 5th step: Since the X-ray photons flux from the X-ray source is increased by reducing the distance from the source according to the inverse square law, the X-ray tube has been moved as close as possible to the detector under test in order to optimize the X-ray photons flux and thus maximize the anode current collected from the irradiated readout sector. Therefore, for the two previous selected configurations of the X-ray tube parameters, the anode current has been measured as a function of the

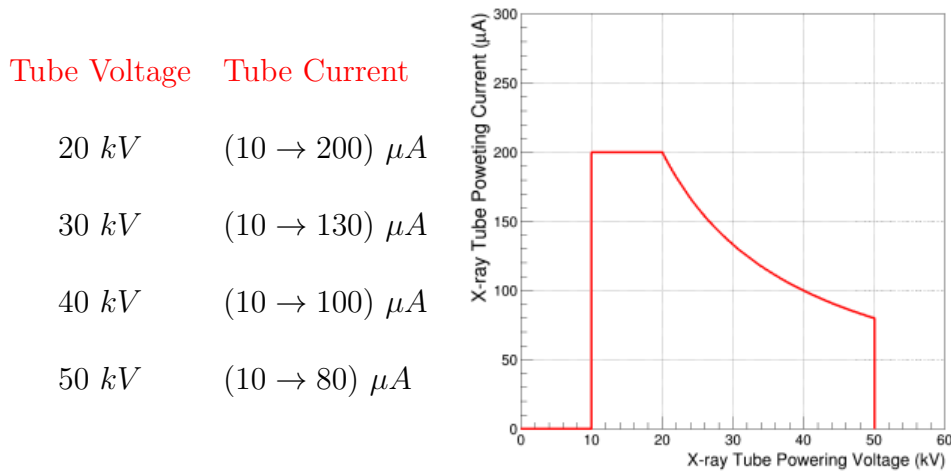


Figure 6.52: AMPTEK miniX X-ray iso-power curve: the tube current and the voltage must be set in accordance with this curve in order to avoid severely damage of the device [80].

x-axis	y-axis	tube voltage	tube current	anode current
80.0 cm	32.5 cm	40 kV	100 μA	~ 739 nA
80.0 cm	32.5 cm	50 kV	70 μA	~ 802 nA

Table 6.4: Configurations which maximize the anode current in the GE1/1-X-S-CERN-0002 detector for the X-ray generator placed at 80cm from the irradiated detector. The anode current has been measured from the readout sector $i\eta = 6$, $i\phi = 2$.

distance of X-ray tube from the detector (see Figure 6.54).

Two new possible configurations of the X-ray generator parameters, that maximize the anode current of the irradiated detector, have been selected (see Table 6.5)

Considering that the active area of the irradiated readout sector is about 111 cm^2 , the resulting anode current flow was about 74.6 nA/cm^2 in the first configuration and 79.0 nA/cm^2 in the second configuration, i.e. a factor 9.4 and 9.9 compared to the anode current flow observed on the detector under test at GIF++ facility (~ 7.95 nA/cm^2).

However, both selected configurations were at the operating limit of the X-ray generator (see Figure 6.52) and therefore, in order to avoid stressing or damaging the X-ray tube during the expected long period of irradiation, the powering current has been reduced at 70 μA and the powering voltage at 40 kV. Furthermore, the distance between the X-ray tube

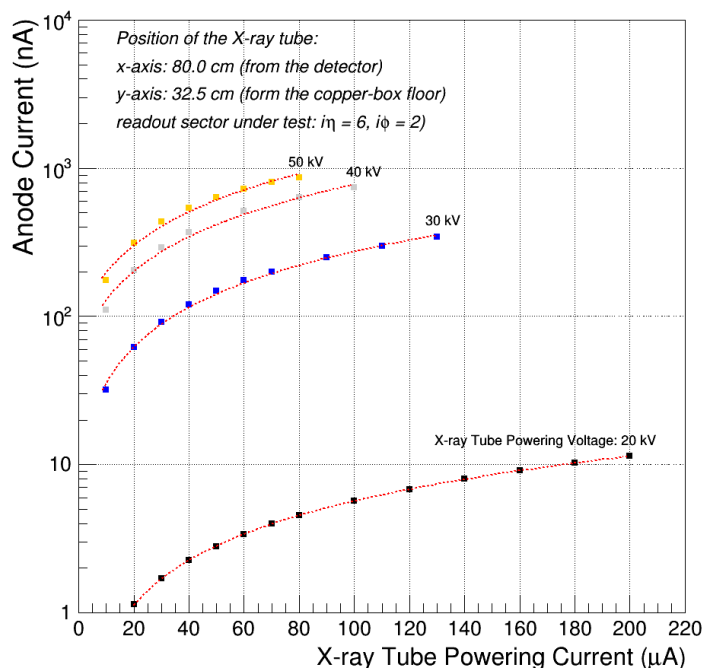


Figure 6.53: Anode current measured on the irradiated readout sector $i\eta = 6$, $i\phi = 2$ at different operating point of the X-ray tube. The X-ray generator has been placed at ~ 80.0 cm from the detector under test and ~ 32.5 cm from the floor of the X-ray copper box. The GE1/1-X-S-CERN-0002 detector has been operated in Ar/CO_2 (70/30) gas mixture at gas gain of 2×10^4 .

and the detector has been optimized in order to allow the source cone to cover the perimeter and frames of the detector, so that to evaluate the aging process on all the detector material and components (GEM foils, internal and external frame, O-ring, etc.) during the irradiation test. The distance between the X-ray tube and the drift plate of the detector under test has been fixed at 12 cm (see Figure 6.55).

As a conclusion, in order to maximize the anode current and therefore, in order to accelerate the longevity studies and preserve the integrity of the X-ray generator, it has been set at a tube current of 70 μA and tube voltage of 40 kV and placed at ~ 12.0 cm from the detector under test: these values resulted in an initial anode current flow, measured in the irradiated readout sector $i\eta = 6$, $i\phi = 2$ using a KEITHLEY 6487 picoammeter, of about 64.2 nA/cm², which corresponds to about a factor of 8.1 compared to the anode current flow measured on the detector under test at GIF++ facility. With the X-ray generator at 12 cm from the GE1/1-X-S-CERN-0002 detector under irradiation test and considering the X-ray cone of about 120°, only 40% of the active area of the detector under test was directly irradiated. The interaction particle flux, as result

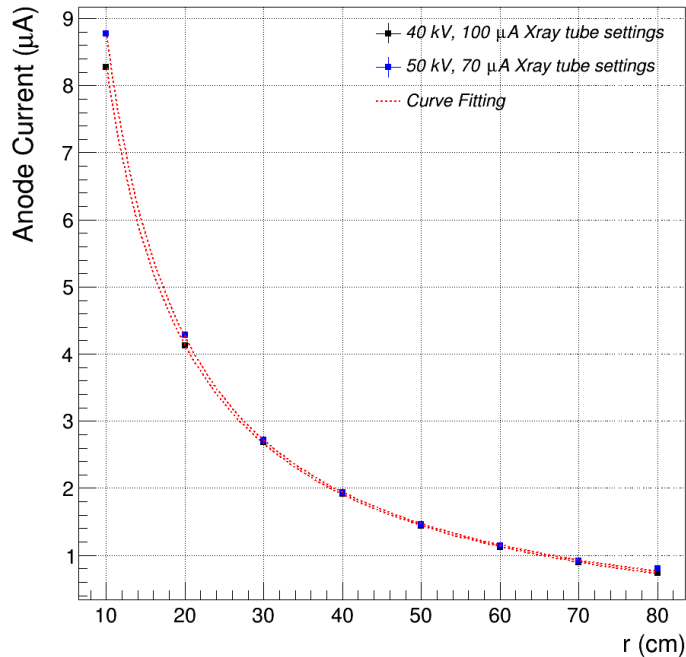


Figure 6.54: Anode current measured on the irradiated readout sector $i\eta = 6$, $i\phi = 2$ at different positions of the X-ray tube from the detector under test. The experimental data are modeled by the function $I_{anode} = A \times r^B$. The X-ray generator settings have been selected at 40 kV and 100 μA (black dots) and at 50 kV and 70 μA (blue dots). The GE1/1-X-S-CERN-0002 detector has been operated in Ar/CO_2 (70/30) gas mixture at gas gain of 2×10^4 .

of the conversion of the X-ray photons flux in the hottest region of the detector, has been evaluated to be about 140 kHz/cm^2 in the readout sector $i\eta = 6$, $i\phi = 2$, while the other 60% was almost not irradiated. Figure 6.56 shows a map of the anode current flow in several readout sectors both in the irradiated and in the non-irradiated zone using the final configuration of the X-ray settings: tube powering current of 70 μA , tube powering voltage of 40 kV and distance between the X-ray tube and the detector of 12 cm.

Such configuration allowed to reduce the exposure time by a factor of ~ 8 compared to the one expected at the GIF++ facility. Therefore, the expected accumulated charge in the ME0 region during 10 years of HL-LHC operation (with a safety factor 3) has been integrated in ~ 6 months of continuous irradiation compared to 5-5.5 years of exposure time expected to the GIF++ facility.

The final step of the experimental setup characterization consisted in the measurement of the X-ray photons interaction rate. However, the X-ray photons

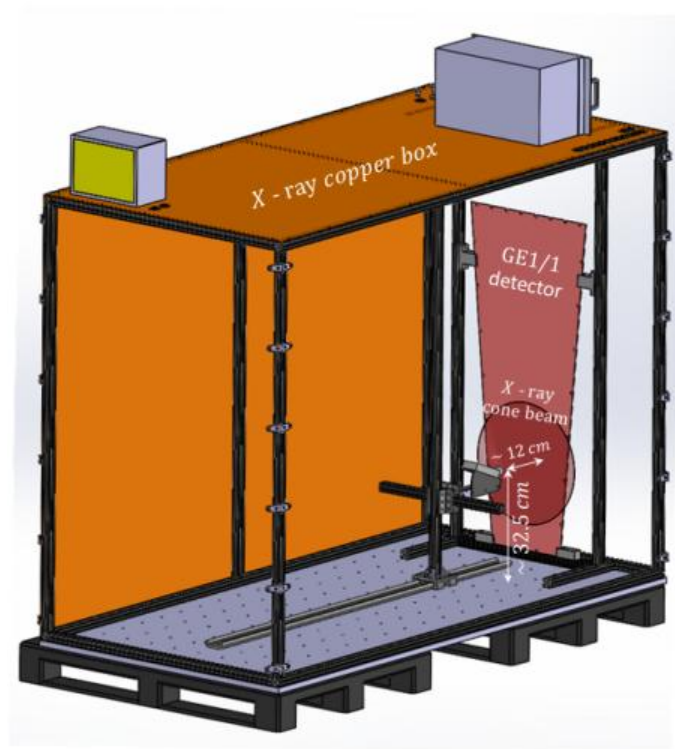


Figure 6.55: Schematic overview of the X-ray copper box showing the detector under test irradiated by the silver X-ray source. The X-ray generator has been placed at ~ 12.0 cm from the detector under test and ~ 32.5 cm from the floor of the X-ray copper box

6.3. Triple-GEM Aging Studies at CMS-GEM QA/QC facility with X-ray source

x-axis	y-axis	tube voltage	tube current	anode current
10.0 <i>cm</i>	32.5 <i>cm</i>	40 <i>kV</i>	100 μA	$\sim 8.28 \mu A$
10.0 <i>cm</i>	32.5 <i>cm</i>	50 <i>kV</i>	70 μA	$\sim 8.77 \mu A$

Table 6.5: The two intermediate working settings for which the anode current has been measured on the readout sector $i\eta = 6$, $i\phi = 2$.

x-axis	y-axis	tube voltage	tube current	anode current
12.0 <i>cm</i>	32.5 <i>cm</i>	40 <i>kV</i>	100 μA	$\sim 7.13 \mu A$

Table 6.6: The final working settings for which the anode current has been measured on the readout sector $i\eta = 6$, $i\phi = 2$.

flux would be too high to measure directly the interaction rate with the detector itself since the signal pulses passing through the pre-amplification stage, available in the CMS-GEM QA/QC facility, overlap in time at rates higher than $\sim 50 \text{ kHz}$. In order to measure the interaction rate, a combination of the two following steps has been used:

- The first step consisted of measuring the interaction rate with a copper attenuators. By introducing a 2.40 *mm* thick copper attenuator, it was possible to reduce the total interaction rate to a few kHz. Therefore, knowing the attenuation factor, it would be possible to extrapolate the real interaction rate without attenuation. For this measurement the powering voltage of the X-ray generator has been fixed at 40 *kV*. Figure 6.57 shows the measured interaction rates with and without the copper attenuator at different current settings for the X-ray generator at 10 *cm* from the detector under test.
- The second step consisted of measuring the interaction rate without copper attenuator as a function of the distance of the X-ray generator from the detector under test. For this measurement the X-ray generator settings have been set at 40 *kV* and 5 μA in order to obtain the lowest possible X-ray photons flux. The interaction rate has been measured for five different positions of the X-ray tube in which the measured rate was always below 50 *kHz* and therefore measurable by the electronics. Figure 6.58a shows the interaction rate measured as a function of the inverse square distance between the X-ray tube and the detector: the linear fit to the experimental data allows to extrapolate the interaction rate at 10 *cm* from the detector in the X-ray generator configuration: 40 *kV*, 5 μA and without copper attenuator. Therefore, knowing the interaction rate measured in the same configuration (40 *kV*, 5 μA , 10 *cm* from the detector) with 2.40 *mm* thick copper attenuator, it was possible to esti-

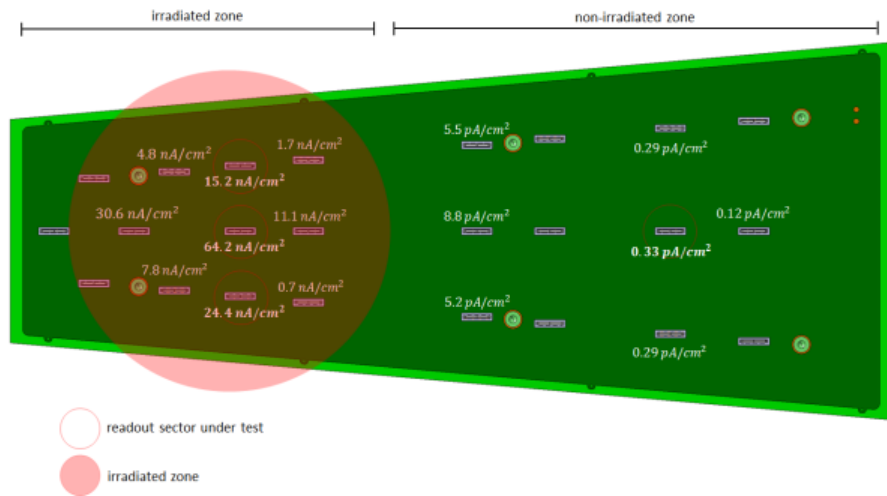


Figure 6.56: Anode current flow map in the final configuration of the X-ray settings: tube powering current of $70 \mu A$, tube powering voltage of $40 kV$ and distance between the X-ray tube and the detector of $12 cm$. The GE1/1 triple-GEM detector has been operated in Ar/CO_2 (70/30) gas mixture at an initial gas gain of 2×10^4 .

mate the attenuation factor of $\sim 1.2 \times 10^4$ and then to extrapolate the interaction rate without attenuation. Figure 6.58b shows the measured and the extrapolated interaction rates at different current settings for the X-ray generator at $10 cm$ from the detector under test.

Considering that the inverse square law describes the photon flux, fixing the X-ray generator settings at $40 kV$, $70 \mu A$ and $12 cm$ from the detector under test, the extrapolated interaction X-ray photons flux at the detector level was about $\sim 140 kHz/cm^2$ at an effective gas gain of 2×10^4 .

When the X-ray generator is switched-on, the current through the resistive high-voltage divider is larger than the current observed when the source is switched-off. This is basically due to the high number of ions collected on the top of the GEM-foils and drift plate in presence of high background radiation. This extra current flowing through the $10 M\Omega$ protection resistance (see Section 5.3) will induce a significant voltage drop on the top electrode, resulting in a decrease of the effective gas gain of the detector under irradiation test. Therefore, using a high impedance HV-probe, the voltage drop has been measured during the irradiation and the voltage on the resistive high-voltage divider has been slightly increased in order to compensate the high rate-induced voltage drop in the GEM-foils.

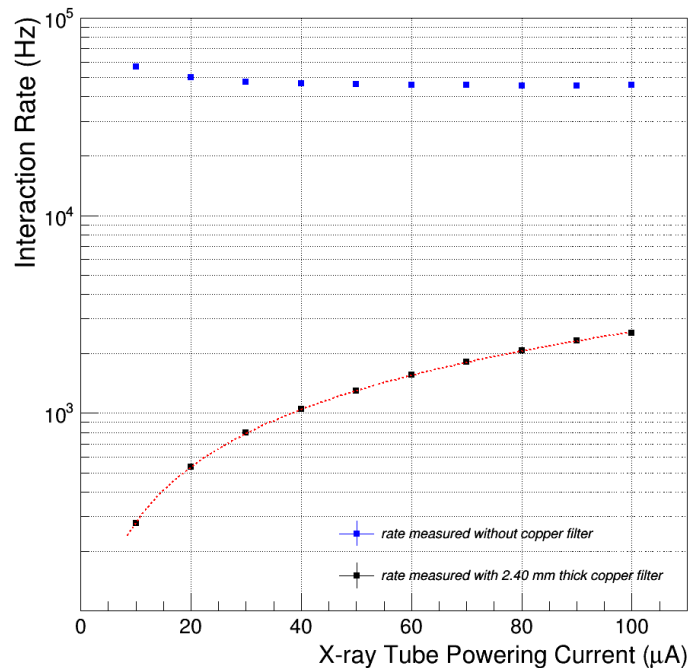


Figure 6.57: Measured interaction rates with and without the copper attenuator at different current settings for the X-ray generator at 10 *cm* from the detector under test. The measured rate without copper attenuators clearly shows the pile-up effect on the preamplifier stage from starting ~ 50 *kHz*. The GE1/1-X-S-CERN-0002 detector has been operated in *Ar/CO*₂ (70/30) gas mixture at an initial gas gain of 2×10^4 .

6.3.1.4 Data acquisition and analysis procedure

The DAQ system and the analysis procedure for the X-ray longevity test are substantially identical to the GIF++ experimental setup:

- Four KEITHLEY 6487 pico-ammeters are connected to several R/O sectors of the readout board in order to monitor the anode current, which reflects the effective gas gain of the GE1/1-X-S-CERN-0002 detector under test: three pico-ammeters are connected in the irradiated zone and another in the non-irradiated zone as a reference. The devices are connected in series with a GPIB protocol and controlled with a LabView interface. The anode current is recorded every 5 minutes for each sector;
- An Environmental Monitoring System based on ARDUINO Mega 2560 microcontroller in order to monitor the environmental parameters (temperature, atmospheric pressure and relative humidity) responsible for the temperature and pressure variations of the gas mixture within the experimental irradiation area. Each minute: the system monitors and

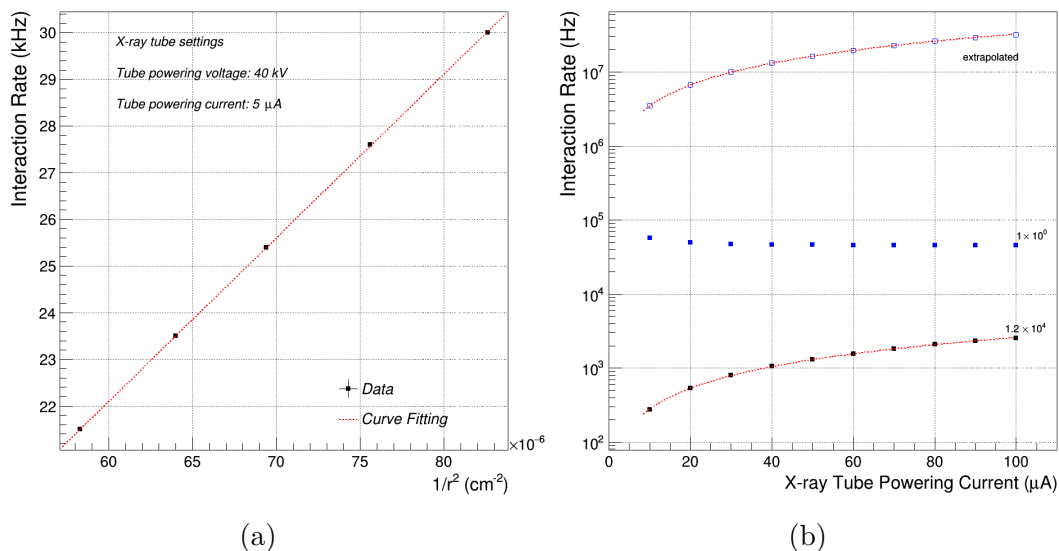


Figure 6.58: (left) Interaction rate measured as a function of the inverse square distance between the X-ray tube and the detector. The experimental data are modeled by the function $R = A \times \frac{1}{r^2} + B$. (right) Measured and extrapolated interaction rates at different current settings for the X-ray generator at 10 cm from the detector under test.

records the the temperature through a LM335Z/NOPB sensor [123], atmospheric pressure through a MPXA61/15AC6U sensor [124] and the relative humidity through a HIH-4000-003 sensor [125].

Figure 6.59 shows the electronics chain, the read-out and the device to store and analyse the data.

All the relevant parameters of the detector under test and the environmental parameters (temperature, pressure and relative humidity) have been recorded during the entire irradiation test. The evolution of the detector under test has been constantly monitored. The data analysis follows the same procedures presented in previous Section 6.2.2.3. It consists of four main steps:

1. **Data Conversion:** the data files from the various DAQ systems are converted into the same format (.txt and .root file), including the relative timestamp of each measurement, the average value of the anode current and the environmental parameters;
2. **Time Synchronization and Marging Data:** the relative timestamp of each data point is compared to a reference time common to all the DAQ systems in order to do the synchronization of the data and to assign the correct environmental parameters to each anode current measurement. All the relevant information is stored into single data event, including the

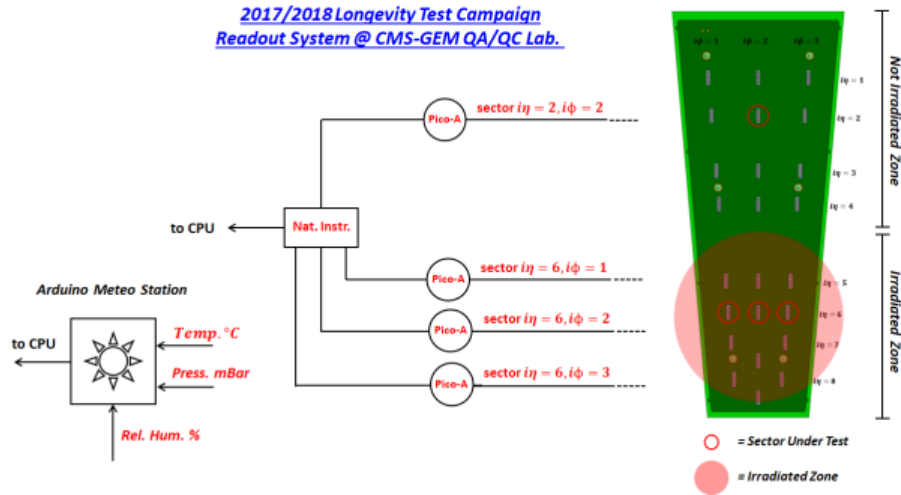


Figure 6.59: Scheme of the electronic chain and data acquisition system used during the longevity test at CMS-GEM QA/QC facility.

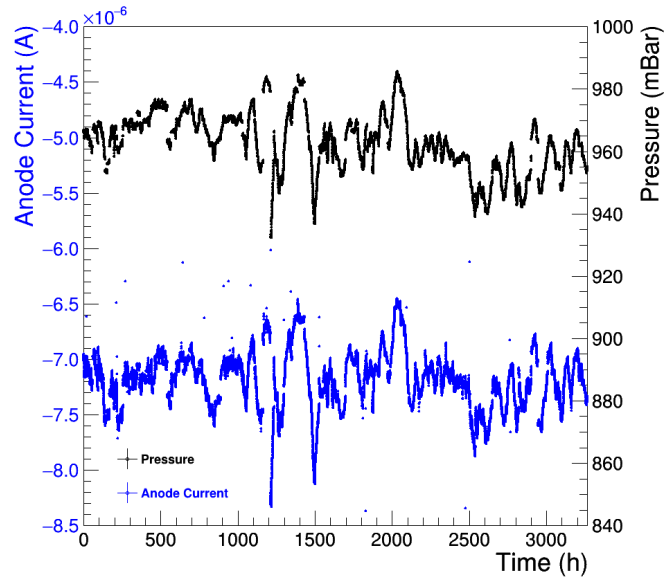
gas gain indicator (i.e. the anode current), the environmental parameters and the absolute timestamp;

3. **Data Cleaning:** all the events corresponding to the X-ray generator OFF or the detectors not powered are removed from the data set;
4. **Correlation with the environmental parameters and P/T Correction:** to parameterize and remove the influence of the environmental variations on the response of the detector.

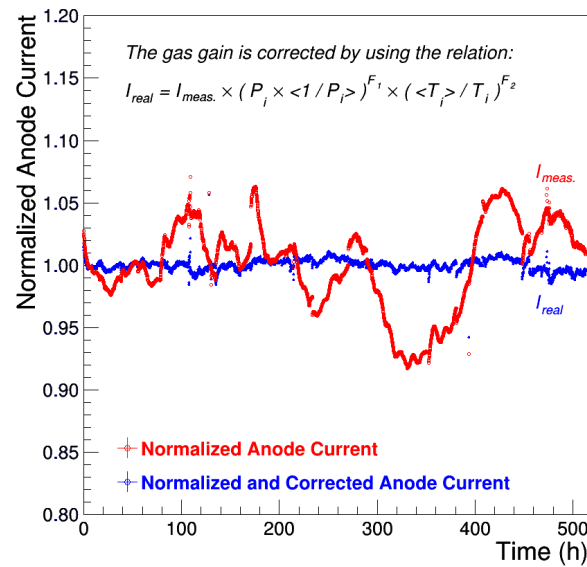
As mentioned, the gas gain of a gaseous detector, and therefore its anode current, is a function of the density of the gas mixture. The measurements have then to be corrected in order to take into account of the temperature and pressure variability in the day–night cycle and/or in the different weather patterns that may occur during the irradiation test. Figure 6.60a shows the clear correlation between the anode current of the GE1/1-X-S-CERN-0002 detector and the atmospheric pressure during the entire irradiation test. Figure 6.60b shows the normalized anode current ($I_{meas.}$) measured as a function of the time on the detector under test during the irradiation period (~ 1 month). The figure shows also the normalized and corrected anode current (I_{real}) after applying the temperature and pressure correction expressed in the Equation 6.6.

During the irradiation test, in addition to the monitoring of the anode current:

- The effective gas gain and the energy resolution have been continuously measured every week (i.e. every about 30 mC/cm^2 of accumulated charge) on the readout sectors under test.



(a)



(b)

Figure 6.60: (top) Correlation between the anode current of the GE1/1-X-S-CERN-0002 detector and the atmospheric pressure during the entire irradiation test (~ 5 months). (bottom) Normalized anode current ($I_{meas.}$) of the GE1/1-X-S-CERN-0002 detector under test, over the irradiation period (~ 1 month). I_{real} is the normalized and corrected anode current after the applying the correction expressed in Equation 6.6. All the data points have been normalized with the initial value of the anode current.

6.3. Triple-GEM Aging Studies at CMS-GEM QA/QC facility with X-ray source

- the gas gain map uniformity measurements have been performed every month (i.e. every about $100\text{-}120\text{ mC/cm}^2$ of accumulated charge) in order to check for the gas gain variation between the irradiated and non irradiated detector active area.

6.3.1.5 Aging Test Results for CERN GEM-foils

The GE1/1-X-S-CERN-0002 detector operated with Ar/CO_2 (70/30) gas mixture at an effective gas gain of 2×10^4 has been exposed to the X-ray radiation in the CMS-GEM QA/QC facility for several months. Figure 6.61 shows the accumulated charge per unit of detector area (mC/cm^2) as a function of time from August 2017 to the beginning of May 2018 for the irradiated sector $i\eta = 6, i\phi = 2$. During this time, the detector under irradiation test integrated about 875.05 mC/cm^2 after ~ 3767 hours of continuous irradiation with 22 keV X-ray photons from an X-ray tube with *Ag-target*. Such accumulated charge represents ten years of *ME0* operation with safety factor 3.1.

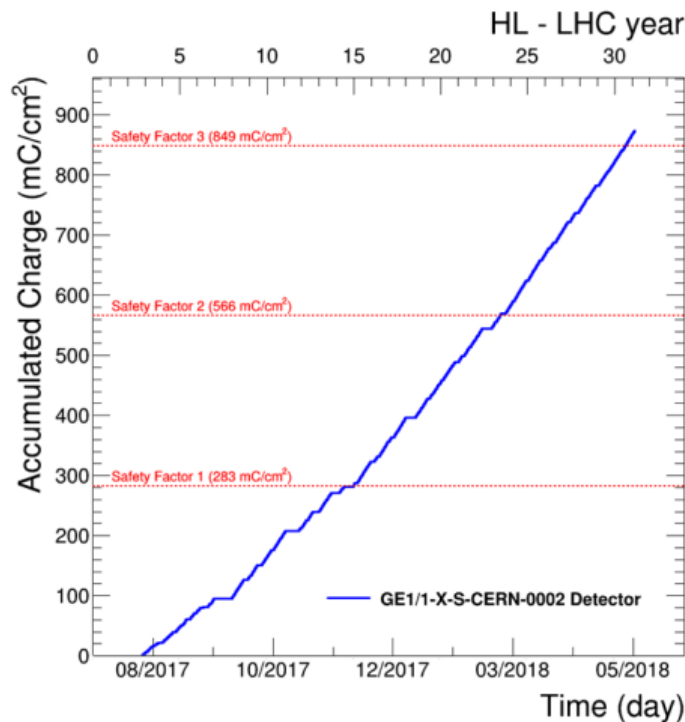


Figure 6.61: Result of the longevity studies at the CMS-GEM QA/QC facility: accumulated charge per unit of detector area (mC/cm^2) as a function of time for the irradiated $i\eta = 6, i\phi = 2$.

Figure 6.62 shows the accumulated charge per unit of detector area as a function of time in two different periods of continuous irradiation. The linear fit to the experimental data allows to extrapolate the accumulated charge rate

expressed as accumulated charge per unit irradiated area and per unit time ($mC/cm^2 \cdot day$).

- 1st period: 1.7 days of continuous irradiation test

$$R(Q_{int})_{X-ray} = 5.52 mC/cm^2 \cdot day$$

- 2nd period: 2.0 days of continuous irradiation test

$$R(Q_{int})_{X-ray} = 5.50 mC/cm^2 \cdot day$$

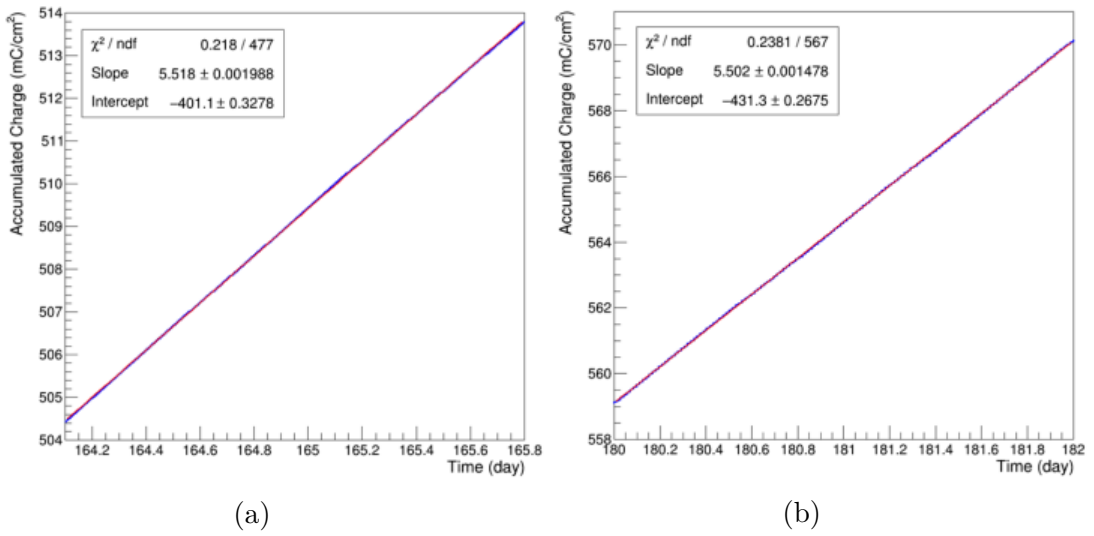


Figure 6.62: Accumulated charge per unit of detector area as a function of time in two different periods of continuous irradiation. The linear fit to the experimental data provides the average integrated charge rate: $R(Q_{int})_{X-ray} = 5.5 \pm 0.1 mC/cm^2 \cdot day$

The average integrated charge rate achieved during the irradiation test at the CMS-GEM QA/QC facility has been estimated to be $R(Q_{int})_{X-ray} = 5.5 \pm 0.1 mC/cm^2 \cdot day$. Considering that the expected accumulated charge rate in ME0 detectors during the HL-LHC operation is $R(Q_{int})_{ME0} = 28.3 mC/cm^2 \cdot year$, the resulting Aging Acceleration Factor (A.A.F.) has been calculated as follows:

$$A.A.F. = \frac{R(Q_{int})_{X-ray}}{R(Q_{int})_{ME0}} = 55.5 \pm 0.7 \quad (6.12)$$

The normalized anode current (corrected for pressure and temperature variations) provides a good indication that the CMS GE1/1-X-S-CERN-0002 detector does not suffer from any kind of longevity effects or long-term degradation.

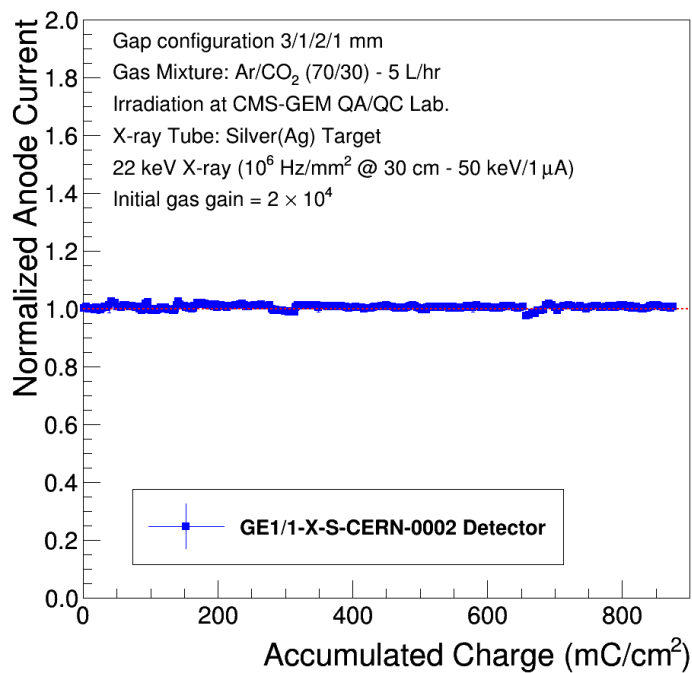


Figure 6.63: Result of the longevity studies at the CMS-GEM QA/QC facility: normalized and corrected anode current as a function of the accumulated charge for the irradiated sector $i\eta = 6, i\phi = 2$. The GE1/1-X-S-CERN-0002 has been operated in Ar/CO_2 (70/30) gas mixture at an initial gas gain of 2×10^4 .

The anode current measured on the hottest irradiated sector $i\eta = 6, i\phi = 2$ is stable during the entire irradiation test and only fluctuates within 2% of its initial value (see Figure 6.63).

The other two irradiated sectors $i\eta = 6, i\phi = 1$ and $i\eta = 6, i\phi = 3$ have accumulated 363.38 mC/cm^2 and 178.46 mC/cm^2 , respectively. Figure 6.64 shows the accumulated charge per unit of detector area (mC/cm^2) as a function of time and the normalized and corrected anode current as a function of the accumulated charge for the other two readout sectors under test. The normalized anode current is stable over the entire irradiation test, with fluctuations within 2-3% of its initial value.

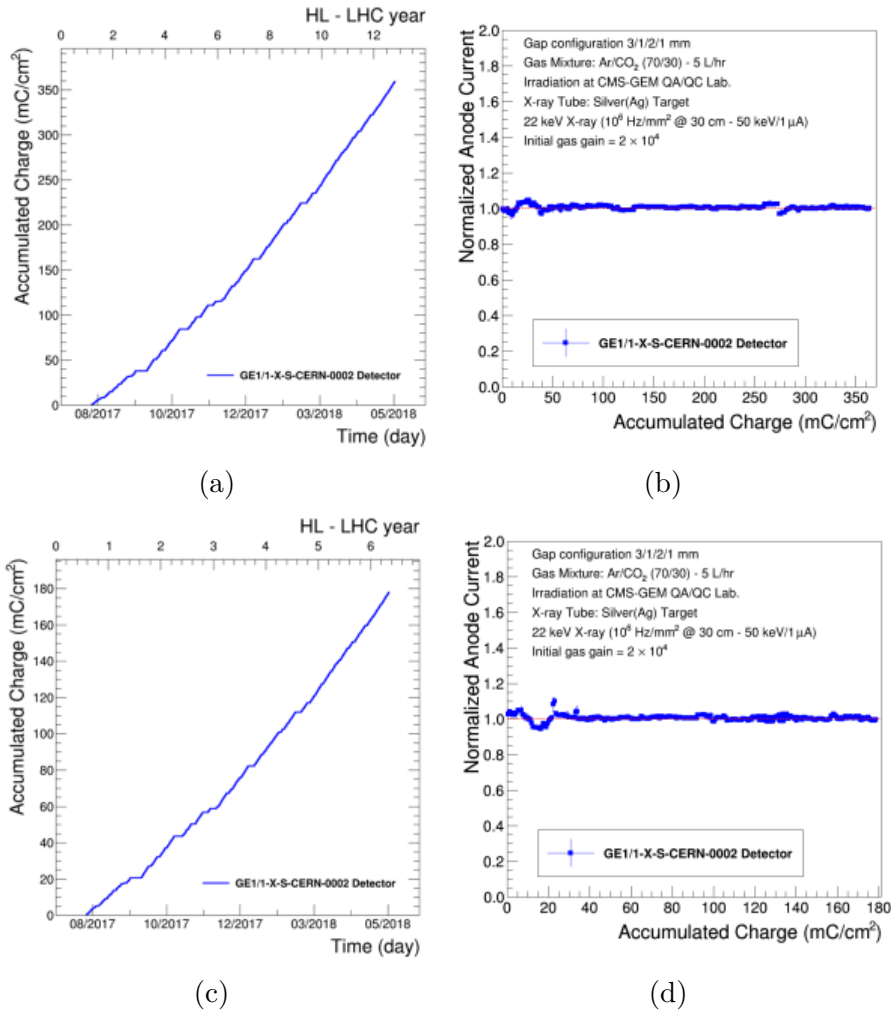


Figure 6.64: Result of the longevity studies at the CMS-GEM QA/QC facility: accumulated charge per unit of detector area (mC/cm^2) as a function of time (6.64a, 6.64c) and normalized and corrected anode current as a function of the accumulated charge (6.64b, 6.64d) for the readout sectors $i\eta = 6, i\phi = 1$ (top) and $i\eta = 6, i\phi = 3$ (bottom).

Effective gas gain measurements campaign. The effective gas gain of the CMS GE1/1-X-S-CERN-0002 detector in Ar/CO_2 (70/30) gas mixture has been measured as a function of the applied HV with a 22 keV X-ray photons from an X-ray tube with *Ag-target* approximately every 30 mC/cm^2 of integrated charge

The Figure 6.65 shows the effective gas gain measurement performed on the readout sectors $i\eta = 6, i\phi = 2$ for different accumulated charge value: 0 mC/cm^2 , 326.06 mC/cm^2 (safety factor ~ 1.2), 570.31 mC/cm^2 (safety factor ~ 2.0) and 874.16 mC/cm^2 (safety factor ~ 3.1). The complete campaign of all effective gas gain measurements performed every week for the selected HV divider current can be seen on Figure 6.66a ($I_{divider} = 660 \mu A$) and Figure 6.66b ($I_{divider} = 680 \mu A$).

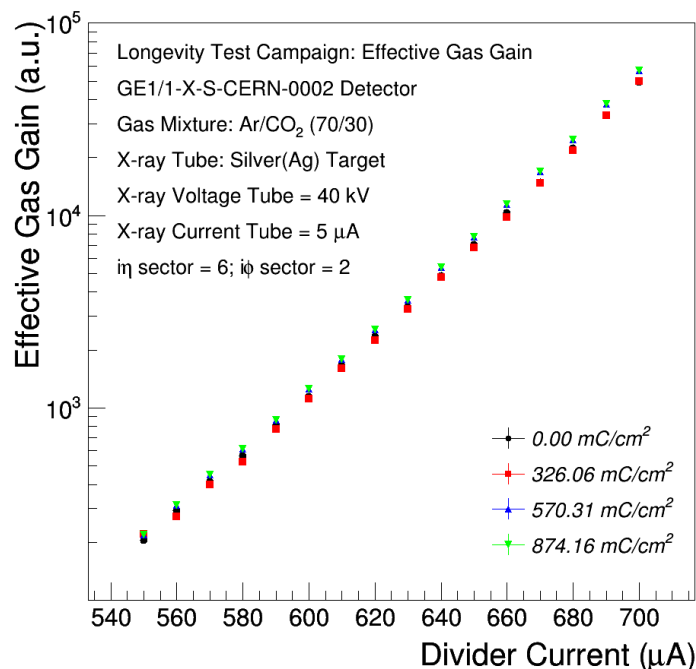
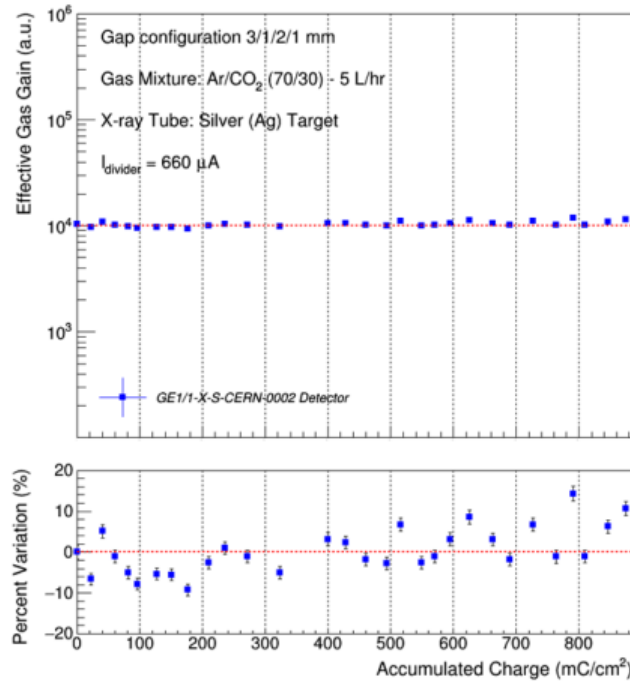


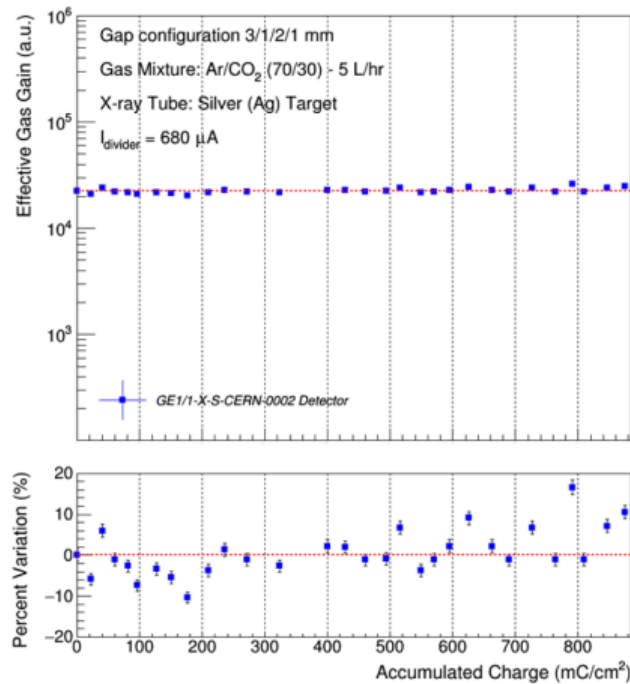
Figure 6.65: Effective gas gain measurement as a function of the divider current performed on the readout sectors $i\eta = 6, i\phi = 2$ for different accumulated charge value: 0 mC/cm^2 , 326.06 mC/cm^2 (safety factor ~ 1.2), 570.31 mC/cm^2 (safety factor ~ 2.0) and 874.16 mC/cm^2 (safety factor ~ 3.1).

The effective gas gain is stable during the entire irradiation test and only fluctuates within 10% of its initial value. Such gas gain fluctuations include also the variations induced by the environmental conditions.

Energy resolution measurements campaign. The energy resolution of the GE1/1 triple-GEM detector in Ar/CO_2 (70/30) gas mixture has been



(a)



(b)

Figure 6.66: Results from the effective gas gain measurement campaign. Effective gas gain measurements performed every week (i.e. every about $30 mC/cm^2$ of accumulated charge) on the readout sectors $i\eta = 6, i\phi = 2$ for the selected HV divider current $I_{divider} = 660 \mu A$ (left) and $I_{divider} = 680 \mu A$ (right).

measured using a low-intensity ^{109}Cd source (mainly $\sim 22\text{ keV}$ X-ray photons) with a rate of $\sim 2\text{ Hz/mm}^2$. For these measurements the detector has been operated at an applied voltage of about 3390 V ($676.6\text{ }\mu\text{A}$ divider current equivalent). The effective gas gain of the detectors for these measurements was at the beginning of the irradiation test campaign, and as demonstrated in this section during the entire radiation exposure period, about 2×10^4 . Figure 6.67a shows the typical ^{109}Cd energy spectrum for the readout sectors $i\eta = 6, i\phi = 2$: a clean separation of the main photopeak and the Ar escape peak is achieved. The energy resolution, defined by the ratio of the $FWHM$ value and the mean value μ of the main photopeak, is on the order of 17%. The complete campaign of all energy resolution measurements performed every week for the selected applied voltage can be seen on Figure 6.67b.

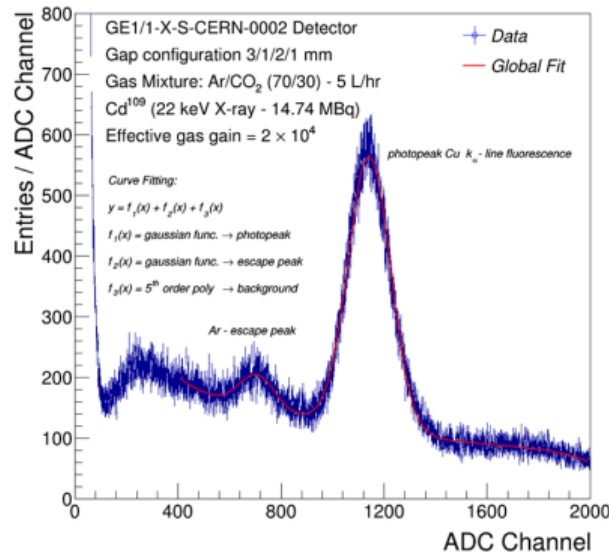
The energy resolution is stable during the entire irradiation test and only fluctuates within 2-3% of its initial value. Such energy resolution fluctuations include also the variations induced by the environmental conditions.

The effective gas gain and the energy resolution measurements campaign performed every week on the other two irradiated readout sectors can be seen on Figure 6.68.

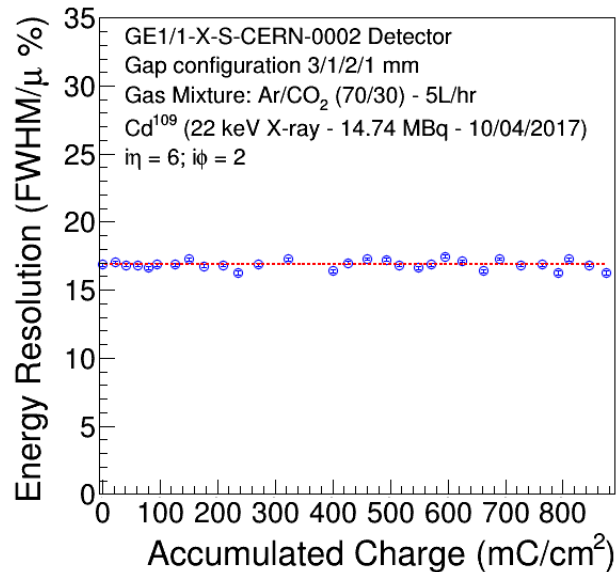
Response Uniformity Finally, the uniformity of the gas gain across the entire detector active area has been continuously measured every month (i.e. every about $100\text{-}120\text{ mC/cm}^2$ of accumulated charge). The DAQ system and the analysis procedure for the response uniformity measurements are identical to the QC5 - Response Uniformity setup adopted in the quality control for the LS2 GE1/1 detectors mass production (see Section 5.4.6.6). Figure 6.69 - Figure 6.73 show the map of the detector response (i.e. the normalized photopeak energy) across the detector under irradiation test for different accumulated charge value. Figure 6.74 shows the Response Uniformity of the GE1/1-X-S-CERN-0002 detector under irradiation test, normalized to the initial value, as a function of the accumulated charge.

The results of the effective gas gain measurements, together with the results obtained from the energy resolution and response uniformity measurements demonstrated that the performances of the triple-GEM detectors, assembled with the GEM-foils based on the single-mask photolithography technique produced by the CERN PCB workshop, are not affected by any classical aging phenomena and the detector remains fully operational after 875 mC/cm^2 of accumulated charge.

The online monitoring of the operating high voltage and current drawn by the detector can reveal the instantaneous problems, like GEM-discharges and/or shorts in the GEM foils. The detector under test has been supplied by a HV power supply CAEN N1470. This module allowed to fix a protection against overcurrent, operating current limit with a precision of 50 nA . The protection threshold has been fixed at $10\text{ }\mu\text{A}$ above the operating current measured at the beginning of the irradiation test campaign. The environmental variation



(a)



(b)

Figure 6.67: Results from the energy resolution measurement campaign. Top: ¹⁰⁹Cd energy spectrum taken with the GE11-X-S-CERN-0002 detector at an applied voltage of 3390 V (676.6 μ A divider current equivalent). The solid line represents a fit to the experimental data using a sum of two gaussian distribution, to model the copper fluorescence photopeak and the Ar escape peak, plus a fifth order polynomial that models the background. The energy resolution (FWHM value of the photopeak divided by the mean value μ) is 17%. Bottom: Energy resolution as a function of accumulated charge for the readout sectors $i\eta = 6$, $i\phi = 2$ at an applied voltage of 3390 V (676.6 μ A divider current equivalent).

6.3. Triple-GEM Aging Studies at CMS-GEM QA/QC facility with X-ray source

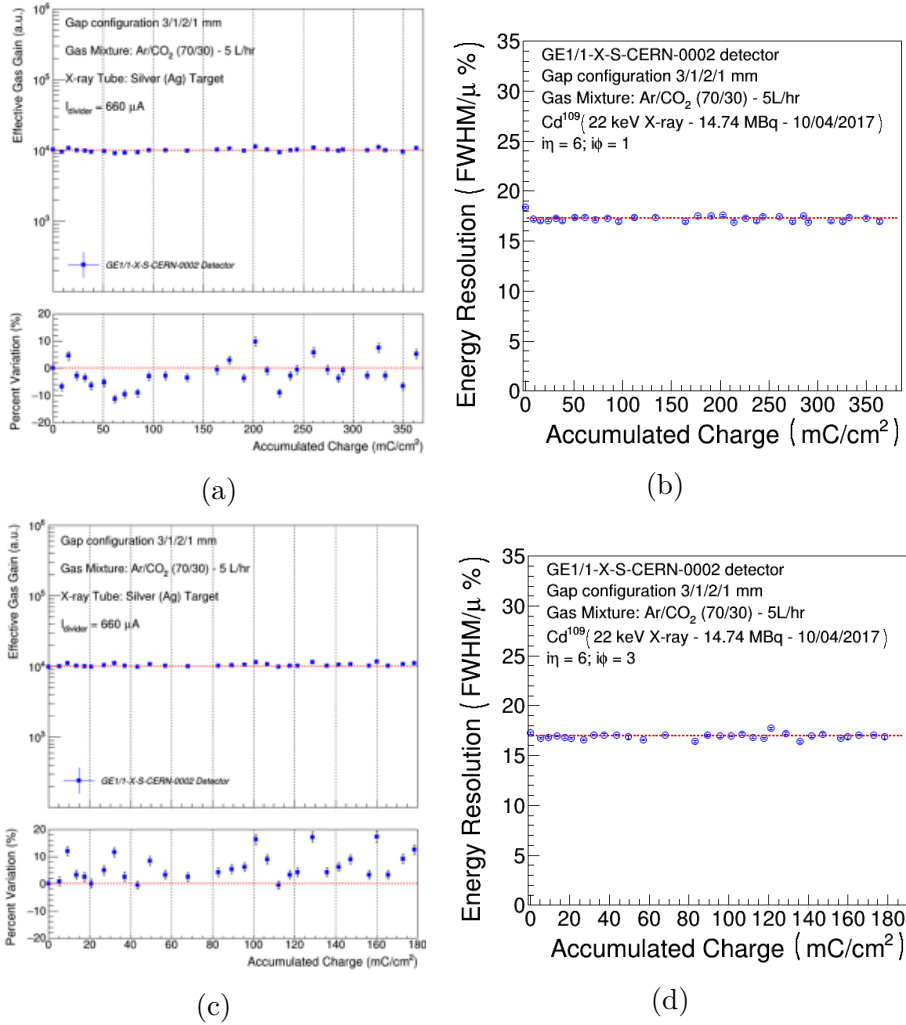
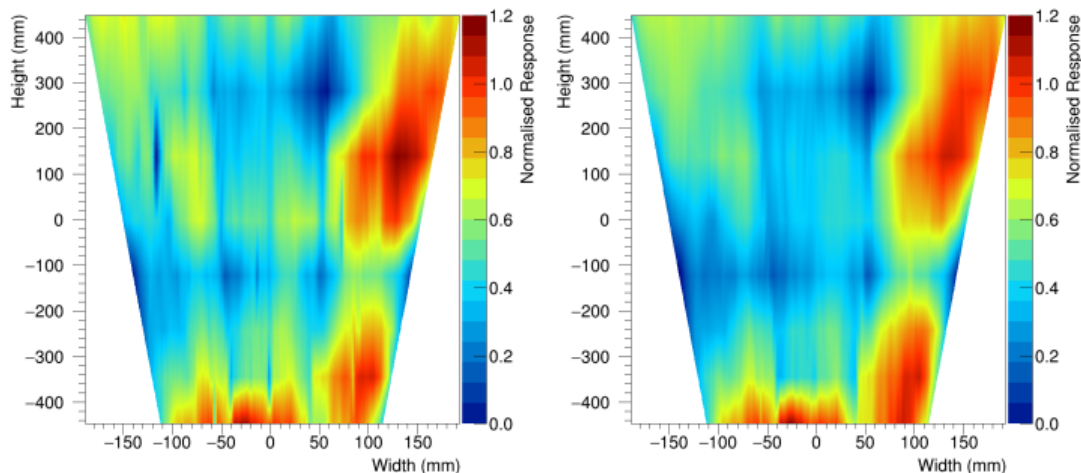


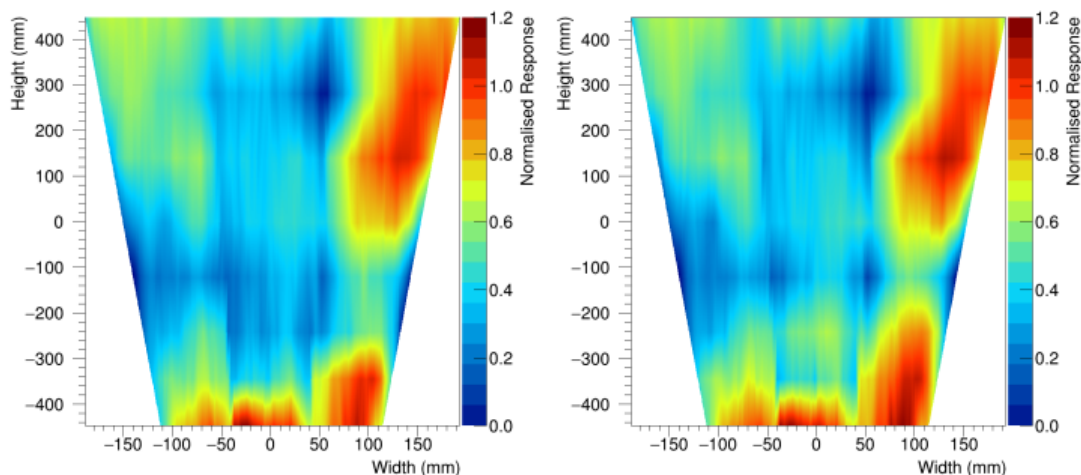
Figure 6.68: Results of the effective gas gain and the energy resolution measurements campaign: effective gas gain and the energy resolution measurements campaign performed every week (i.e. every about 30 mC/cm^2 of accumulated charge) on the readout sectors $i\eta = 6, i\phi = 1$ (top) and $i\eta = 6, i\phi = 3$ (bottom).



(a) Map of the detector response at 80 mC/cm^2 ($\sim 29\%$ of the total ME0 operation).

(b) Map of the detector response at 209.20 mC/cm^2 ($\sim 74\%$ of the total ME0 operation).

Figure 6.69: Results from the response uniformity measurement campaign. The detector under test is a GE11-X-S-CERN-0002 detector operated in Ar/CO_2 (70/30) gas mixture at an effective gas gain of ~ 600 .

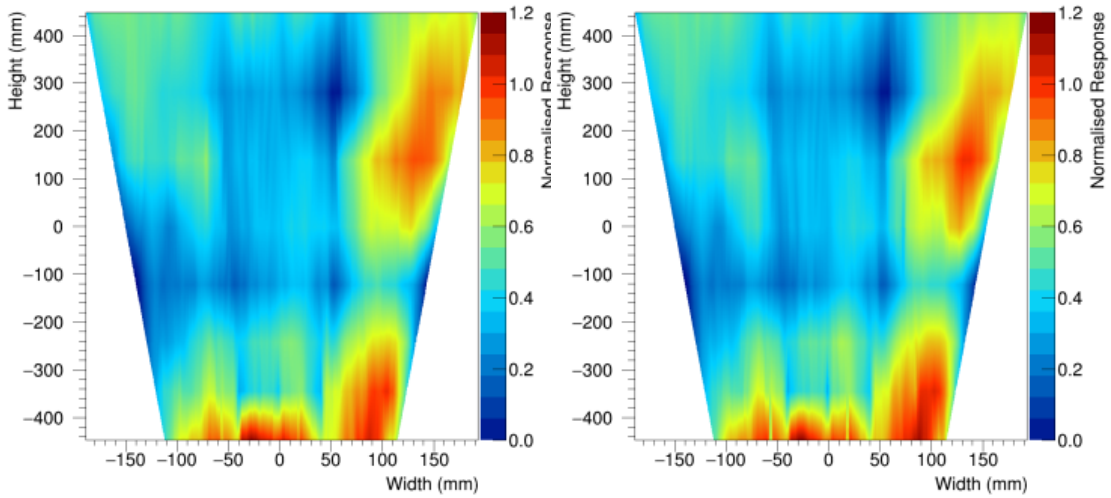


(a) Map of the detector response at 271.20 mC/cm^2 ($\sim 96\%$ of the total ME0 operation).

(b) Map of the detector response at 323.06 mC/cm^2 (safety factor ~ 1.1).

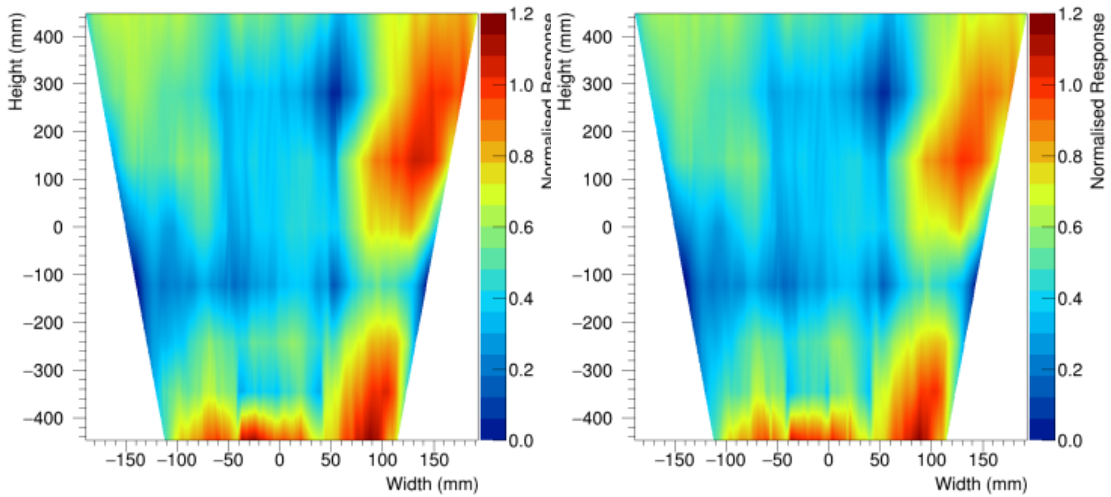
Figure 6.70: Results from the response uniformity measurement campaign. The detector under test is a GE11-X-S-CERN-0002 detector operated in Ar/CO_2 (70/30) gas mixture at an effective gas gain of ~ 600 .

6.3. Triple-GEM Aging Studies at CMS-GEM QA/QC facility with X-ray source



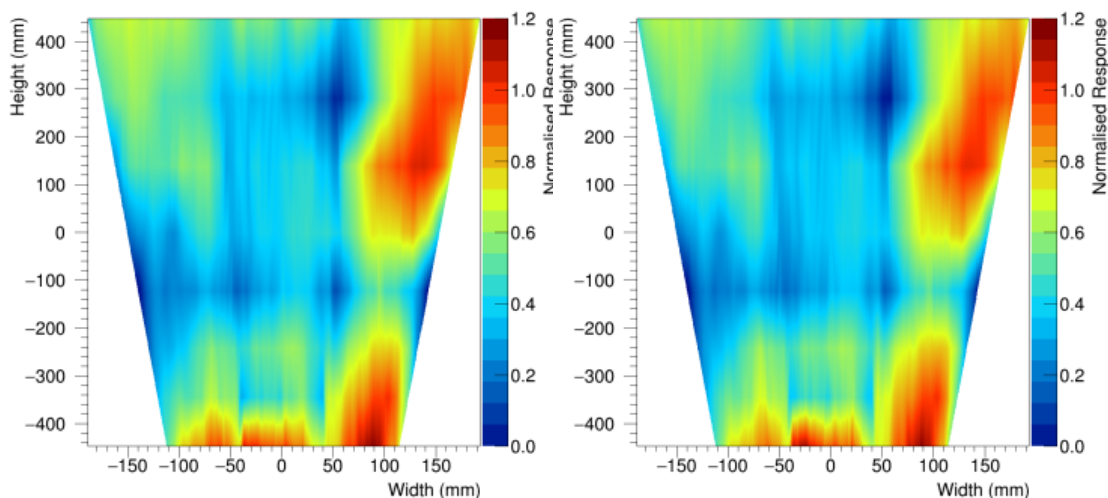
(a) Map of the detector response at 400.18 mC/cm^2 (safety factor ~ 1.4). (b) Map of the detector response at 492.89 mC/cm^2 (safety factor ~ 1.7).

Figure 6.71: Results from the response uniformity measurement campaign. The detector under test is a GE11-X-S-CERN-0002 detector operated in Ar/CO_2 (70/30) gas mixture at an effective gas gain of ~ 600 .



(a) Map of the detector response at 570.31 mC/cm^2 (safety factor ~ 2.0). (b) Map of the detector response at 662.27 mC/cm^2 (safety factor ~ 2.3).

Figure 6.72: Results from the response uniformity measurement campaign. The detector under test is a GE11-X-S-CERN-0002 detector operated in Ar/CO_2 (70/30) gas mixture at an effective gas gain of ~ 600 .



(a) Map of the detector response at 736.51 mC/cm^2 (safety factor ~ 2.6). (b) Map of the detector response at 875.50 mC/cm^2 (safety factor ~ 3.1).

Figure 6.73: Results from the response uniformity measurement campaign. The detector under test is a GE11-X-S-CERN-0002 detector operated in Ar/CO_2 (70/30) gas mixture at an effective gas gain of ~ 600 .

induced operating current fluctuations in the range between $694.70 \mu A$ and $698.65 \mu A$. The $10 \mu A$ was enough to cause a trip in the HV power supply when a sustained discharge occurred in a single GEM.

During the entire irradiation test, four trips of the power supply have been recorded: considering them as discharges, the upper limit of the 22 keV X-ray photons induced discharge probability $P_{Disch.}$ has been calculated as follows:

$$P_{Disch.} = \frac{N_{Disch.}}{R_{meas.} \times \Delta T_{meas.}} \quad (6.13)$$

where $R_{meas.}$ is the measured X-ray photons interaction rate and $\Delta T_{meas.}$ is the irradiation period. In the case of the gas gain used in the measurement, since $R_{meas.} \sim 15.5 \text{ MHz}$ (see Section 6.3.1.3), $N_{Disch.} = N_{trip} = 4$ and $\Delta T_{meas.} \sim 1.3 \times 10^7 \text{ s}$ of continuous irradiation, $P_{Disch.} \sim 1.9 \times 10^{-14}$ at gas gain of $\sim 2 \times 10^4$.

As result of the 2017/2018 longevity test campaigns, the triple-GEM technology is fully validated for CMS-ME0 upgrade project.

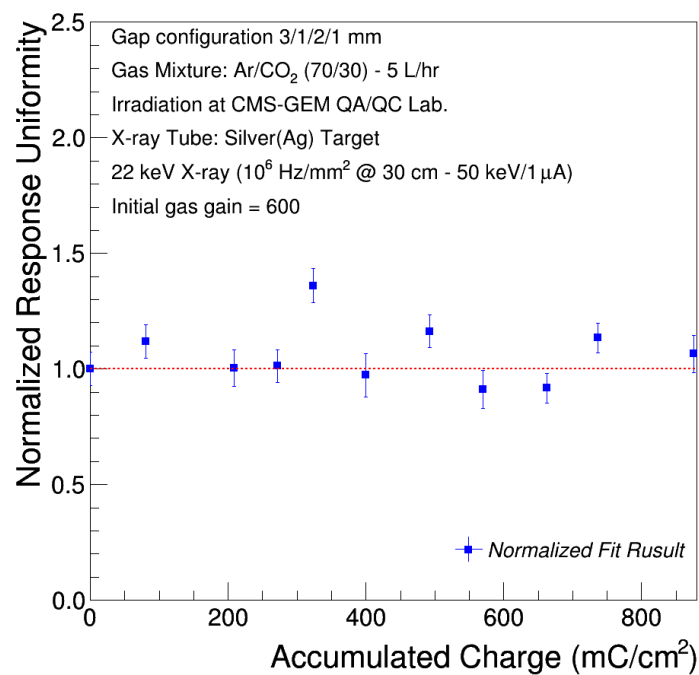


Figure 6.74: Result from the response uniformity measurement campaign showing the response uniformity of the detector under irradiation test, normalized to the initial value, as a function of the accumulated charge. The detector under test is a GE11-X-S-CERN-0002 detector operated in Ar/CO_2 (70/30) gas mixture at an initial gas gain of 2×10^4 .

Discharge Probability Studies in triple-GEM detectors

7.1 Introduction

The increase of the energy and luminosity during the future upgrades of the LHC machine will adversely affect the performance of the CMS Muon System due to the harsh background environment and the high pile-up. Among the innovative detector techniques, Micro-Pattern Gaseous Detectors, and in particular the Gas Electron Multiplier, should be good alternatives for the muon detector upgrade in the high luminosity LHC framework because of a good spatial and time resolutions, high-rate capability, possibility to build large active areas, radiation hardness, ageing resistance and stability against electrical discharges. In particular, the discharge damages represent a serious limitation to the integrity of the gas-based detectors, as they could cause irreversible damages to the detector itself, ranging from enhanced leakage currents to permanent electric short circuits that render the detector effectively blind. Moreover, the discharges are not only a problem concerning the detector robustness or their electronics on which one can had a suitable protection, but the discharge of the whole electrode could induces a dead time on the order of *ms* to recover the nominal voltage.

The occurrence of discharges in a gas-based detector is generally correlated to the transition from the avalanche-multiplication regime to the streamer regime. This transition is highly dependent on the gas gain and primary ionization density. In studies with parallel-plate counters, the transition from avalanche to streamer regime and the resulting discharge have been measured to occur when the total charge in the avalanche-multiplication process exceeds a critical value of the order of 10^7 - 10^8 electron-ion pairs (the so-called Raether's limit) [65] [126].

As for the GEM-based detectors, the typical high-rate capabilities for these detectors are of the order of several MHz/cm^2 . Considering the geometry of

such detectors (few mm drift gaps) and gas mixtures (Ar -based), a single MIP particle crossing the gas-filled conversion gap generates an average primary charge density of a few electrons per cm^2 . Even at a rate of the order of $1\text{ MHz}/cm^2$, taking into account the electron drift time, no pile-up effects are expected. Therefore, the resulting primary charge density is far below the Raether's limit, even if amplified by gas gain values of $O(10^4)$ at which such detectors are typically operated. However, an accidental release of larger amounts of ionization could lead the total charge above the Raether's limit and trigger possible destructive discharges. Large and high charge densities could be released in the closest vicinity of the GEM-foils by heavily ionising particles, such as nuclear fragments, gamma and neutron that appear due to hadronic interactions in the detector materials exposed to high energy hadron beam.

The triple-GEM technology has two main benefits regarding the mitigation of the induced discharge probability and the damage caused by it. The first advantage is the sharing of the gas amplification into multiple cascade multiplication stages; this allows to achieve gas gains as high as 10^5 without approaching the Raether's limit on each single GEM-foil. In the same time, the spread of the multiplication electrons during the transport between adjacent foils allows to dilute the charge densities over more than a single hole, reducing the probability of reaching the Raether's limit in the third multiplication stage. The second advantage is a full decoupling of the amplification stage (GEM-foils) and the readout board (PCB). In the GEM-based detector the gas amplification is localized inside GEM-holes and the absence of a strong amplification field close to the readout plane drastically reduce the discharge probability.

Extensive studies on the induced discharge probability of the GEM-based detectors have been investigated since 2000, which provide a set of recommendations to minimize the discharge probability [127]. These recommendations, adopted in the CMS triple-GEM detector, include a sectorization of the GEM-foils in several partition whose area is restricted to $\sim 100\text{ cm}^2$ and the use of $10\text{ M}\Omega$ protection resistors (see Section 5.3) to limit the energy available in case of a discharge process. In the case of a discharge, the current flowing through the protection resistance will induce a voltage drop on the upper electrode of the GEM-foil preventing the propagation of the discharge. Moreover, an asymmetric distribution of the voltage difference across the GEM electrodes, in which the highest amplification occurs in the first foil in the stack and successively decreases towards the readout board, allows to minimize significantly the induced discharge probability even for a total gas gain of the order of 10^5 . Such configuration has been successfully adopted by the GEM-based trackers of COMPASS experimental [128] [129] and LHCb experiment [130] at CERN-LHC.

Several measurements of the discharge probability have been performed by CMS-GEM Collaboration in order to confirm the robustness of the CMS triple-

GEM detectors, by estimating the total number of discharges detected by the detector, and evaluating the effect of discharge processes on the long-term detector operation [69] [90]. In 2014, a CMS triple-GEM detector has been irradiated by a 5.6 MeV α -particles from an ^{241}Am source in order to replicate the Heavily Ionizing Particle (HIP) interactions induced by the high-energy neutron background during the operation in the Muon Spectrometer of the CMS experiment. The discharges have been identified via the transient fluctuations of the high voltage power supply and anode current by using a pico-ammeter. Additionally, the signals induced on the lower electrode of last GEM-foil have been used to count the total number of particles crossing the active gas volume of the detector under test and to identify the α -particles. Since the discharge probability for a triple-GEM detector is expected to be less than of $10^{-10}/HIP$ at the normal CMS operation, the gas gain has been set to the extreme values $3\text{-}6\times 10^5$. These extreme operating conditions are not realistic, but they allow to accumulate a sufficient number of discharges in order to evaluate the discharge probability in a reasonable time. Finally, the data has been extrapolated to obtain the discharge probability at the effective gas gain of $1\text{-}2\times 10^4$. The results demonstrated that the discharge probability for a CMS triple-GEM detector operating in the CMS configuration is on the order of $10^{-10}/HIP$.

7.2 Discharge probability studies on triple-GEM technology at CHARM facility

More recently, a series of discharge probability studies have been performed by the CMS-GEM Pavia group in the harsh mixed-radiation fields available at the CHARM facility [131] [132] [133] at CERN in order to estimate the discharge probability of the CMS triple-GEM detectors in more realistic conditions.

7.2.1 The CHARM facility at CERN

The CERN High Energy Accelerator Mixed-field (CHARM) facility is situated in the CERN PS (Proton Synchrotron) East Experimental Area hall [117] at the Meyrin Site of CERN in Switzerland. The purpose of CHARM facility is to have a dedicated experimental area for testing particle detectors, electronic equipment and systems in a mixed-radiation fields, which can replicate a wide number of real radiation environments that are typical of the CERN accelerator complexes and other applications of interest such as space, atmosphere, etc.

Starting with the 24 GeV/c proton beam from the Proton Synchrotron, the beam is directed along a number of beam-lines to various test area. The CHARM facility is located at the end of the T8 beam-line, that is shared with the IRRAD facility [134], located up-stream of CHARM facility. A 3D Catia drawing of the PS East Experimental Area hall is shown in Figure 7.1.

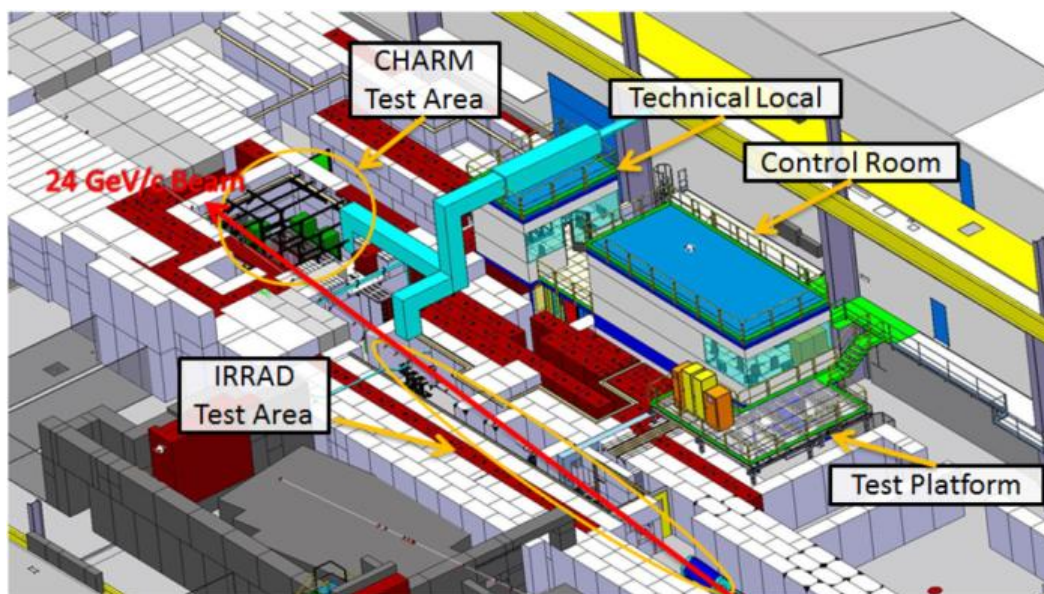


Figure 7.1: A 3D Catia schematic overview for the T8 beam-line on the PS East Experimental Area hall showing the position of the IRRAD and CHARM facilities along the T8 beam-line [132].

The beam structure is in "spills" (or bunches) of length 325 m.s , separated by 1.2 seconds and ordered in a "super-cycle" usually of around 30 spills. This gives the beam a "burst" like nature, as opposed to a constant beam without interruption. Once the proton beam passes through IRRAD facility, it enters the CHARM experimental area where it impinges on a massive cylindrical copper or aluminium target. A horizontal view of the CHARM experimental area is shown in Figure 7.2.

In addition, there are four movable blocks of shielding installed in the middle of the experimental area between the target and the test positions, which can be moved in and out of place in order to modulate the energy, composition and intensity of the mixed-radiation field. The outer two layers of 40 cm thick concrete surround two layers of 40 cm thick iron in a "sandwich" arrangement (see Figure 7.2). Since the secondary mixed-irradiation field, produced from the interaction between the $24\text{ GeV}/c$ proton beam and the copper or aluminium target penetrates the movable shielding blocks, the energy is reduced, the particle field composition is modified (more neutrons are produced and the quantity of charged hadrons are reduced) and the dose rate and fluxes are decreased. The "concrete-iron-iron-concrete" layout is referred to as "CIIC" for the facility configuration, while partial or null shielding is referred to as "CIOO" (concrete-iron-open-open) and "OOOO" (all four open).

Within the CHARM experimental area there are a total of thirteen possible test positions, which are referred to as "r1" to "r13" (see Figure 7.2): the devices under irradiation test can be placed either directly in the proton beam,

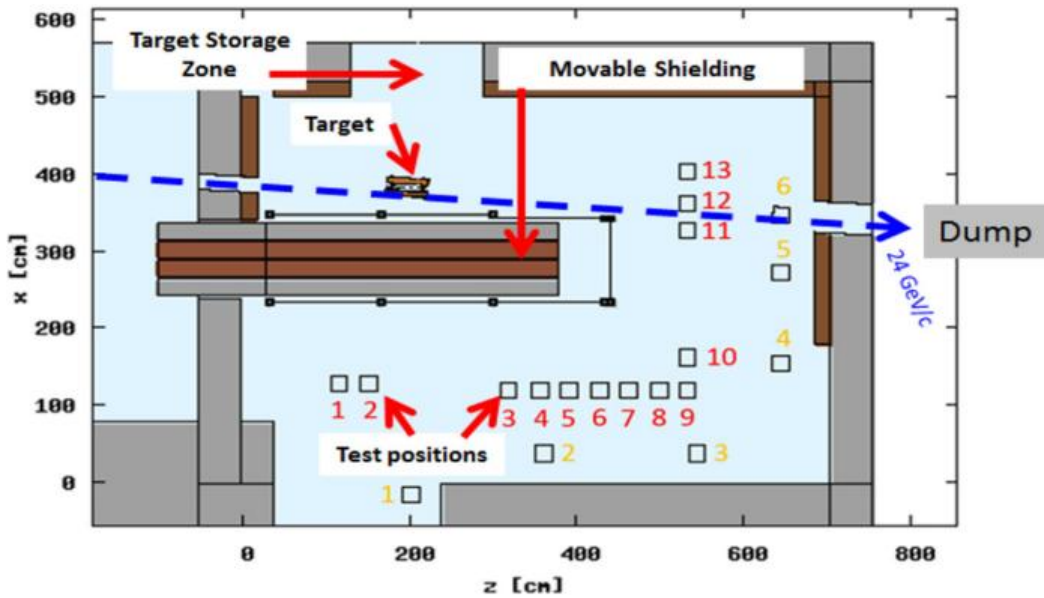


Figure 7.2: FLUKA Monte Carlo geometry simulations of the experimental area, cut at beam-height. The racks 1 to 13 are the regions that correspond to the test position. The grey and brown plates are concrete and iron movable blocks of shielding respectively [132].

behind shielding or at various angles and distances from the target. Depending on the target and the test position selected, the device under test will be exposed to different mixed-radiation field. In order to understand it, dedicated FLUKA Monte Carlo simulations [135] [136] and experimental dose measurements have been performed for the various target/shielding configurations and test positions. A detailed list of the available information related to the radiation spectra, total ionising dose, 1 MeV equivalent neutron fluence in Silicon, etc. is given in [131] [132] [133].

An example plot of the radiation spectra seen at the R1 test position is shown in Figure 7.3. The FLUKA Monte Carlo analysis has been used in order to perform the radiation field calculations for the copper target configuration without shielding (copper-OOOO). The plot shows the relative particle fluences for several type of particles expressed in lethargy form. The lethargy is defined as the differential flux multiplied by the geometrical mean of the bin energy. Of particular interest is the neutron spectrum which typically has a much larger energy range than the other particles, and is strongly influenced by the shielding configuration and test position.

Figure 7.4a and 7.4b show the dose and fluence of the High Energy Hadrons (HEH) mapped out at the proton beam height for the whole experimental area. The plots show the presence of large gradients at the test positions close to the beam axis and some "shadows" in the HEH fluence due to the interaction with structural supports of the shielding.

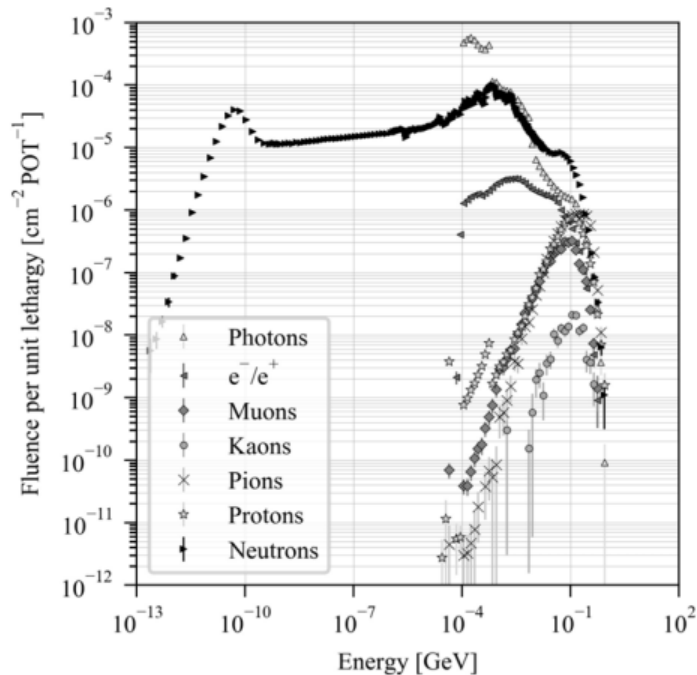


Figure 7.3: An example plot of the radiation spectra seen at the R1 test position for the facility configuration copper-OOOO. The artificial lower thresholds seen for electrons and photons at ~ 1 MeV is due to the threshold settings used for the FLUKA Monte Carlo simulations and is not strictly a physical phenomena [137].

7.2.2 The triple-GEM detector prototype under test and characterization

A triple-GEM detector prototype, consisting of $10\text{ cm} \times 10\text{ cm}$ GEM-foils developed and produced with single-mask photolithography technique, obtained from CERN PCB Workshop has been assembled with the drift gap, two transfer gaps and induction gap of 3/1/2/1 mm respectively. Differently from the GE1/1 detector assembly technique the $10\text{ cm} \times 10\text{ cm}$ GEM-foils have been directly glued on Fiberglass (FR4) frames, defining the drift gap, the two transfer regions and induction gap between GEM-foils themselves, then sandwiched between a cathode and anode PCBs. The read-out board consist of 81 pads of $1 \times 1\text{ cm}^2$ size. All the readout pads were routed to a 128 signal-pins Panasonic connector. To power a triple-GEM, a total of seven different high-voltage potentials have to be applied to its layers. During the R&D phases, these voltages have been typically achieved with a single high voltage channel using an on-chamber resistive divider circuit. However, using the high voltage resistive divider is not possible to appreciate the fluctuation of the current induced by the discharge (few μA) on the single GEM-foil due the high current absorbed by the resistive divider ($\sim 700\ \mu\text{A}$). To overcome these issues, the seven channels have been powered individually using the CAEN A1515TG multi-channel HV

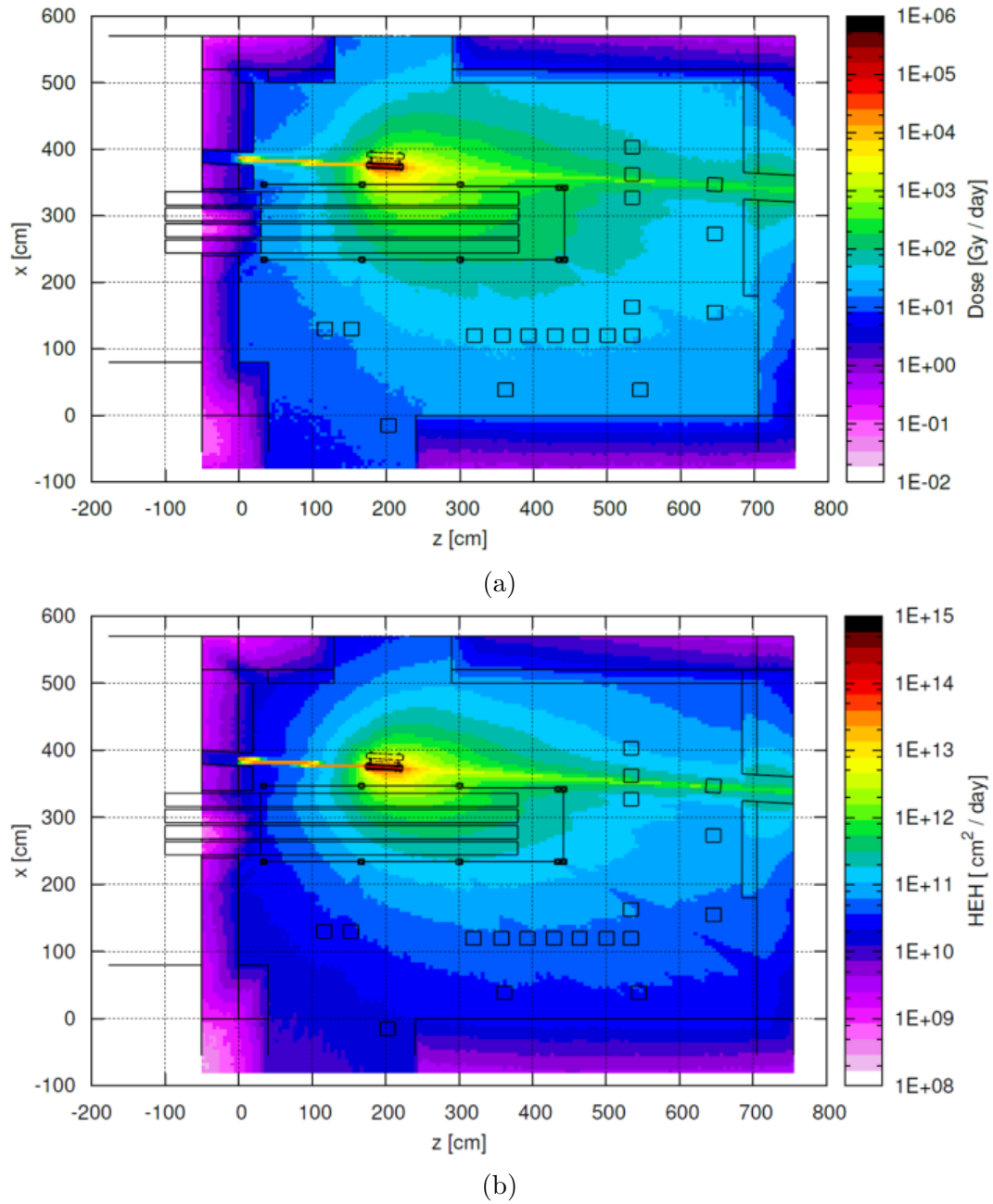


Figure 7.4: An example plot of the dose (left) and high energy hadrons fluence (right) normalised per day inside the experimental area at beam height. (1.5×10^{15} protons per day) [132].

power supply [138], specifically designed for triple-GEM detectors. This board has been developed through a collaboration of CAEN and INFN Napoli, based on the experience in LHCb experiment with a triple-GEM multi-channel high-voltage power supply [139]. One A1515TG module provides fourteen floating HV channels, grouped in two complex channels. Within a complex channel, the seven channels can be configured individually. The floating design assures that the failure of one channel shall not result in an increase of the potential on the neighboring layer. The A1515TG module allows for 1 *kV* and 1 *mA* per channel. The voltage for each channel can be set and read with a 20 *mV* resolution, and an accuracy of $0.2\% \pm 0.2 V \pm 50 \text{ ppm}/^\circ C$, and current limits can be set with a 20 *nA* resolution. Below 100 μA , the current can be monitored with a resolution of 100 *pA*, and in the range of 100 μA to 1 *mA*, the resolution becomes 1 *nA* with accuracy $0.5\% \pm 5 nA \pm 50 \text{ ppm}/^\circ C$. The ramp-up and ramp-down rates can be selected independently for each channel in the range 1-100 *V/s* in 1 *V* steps and the reaction to an overcurrent (trip time) can be delayed from 0 *s* to 1000 *s* in steps of 0.1 *s*. The configuration of potentials in the triple-GEM detector is shown in Figure 7.5. A 10 *M Ω* protection resistors have been mounted on the upper electrode of each GEM-foils, while a HV low-pass filters composed of 100 *k Ω* resistors and 2.2 *nF* capacitors have been employed on the lower electrode of each GEM-foils in order to cut the high frequency noise from the HV power supply. The details of the values for electric potentials on the seven electrodes and for voltages and electric fields across the drift, induction and two transfer gaps and the three GEM-foils are summarized in Figure 7.6.

Before to start the studies for the discharge probability measurement, the detector prototype has been fully characterized.

7.2.2.1 Effective gas gain measurement

The effective gas gain has been measured in *Ar/CO₂* (70/30) gas mixture by comparing the primary current, induced in the drift gap by a X-ray source, and the amplified current induced on the readout board. The detectors has been irradiated by a ⁵⁵*Fe* source producing X-ray photons with an average energy of 5.9 *keV* that fully convert into the drift gap via photoelectric effect.

Despite the X-ray photons interaction rate was of the order of *kHz*, the primary current doesn't exceed several tens of *fA*. Therefore, it was extremely difficult to measure such primary current directly from the drift plane or from the first GEM-foil, which were powered at high voltage and thus subject to noise. This issue is overcome by measuring the interaction rate *R*, i.e. the number of pulses induced by particles per unit time. The readout of the detector was done using a charge sensitive pre-amplifier (ORTEC 142A model) connected to the bottom electrode of the third GEM-foil. This connection was made through a decoupling RC circuit already present on the detector's frame. The output of the pre-amplifier was then sent to an amplifier+shaper unit (ORTEC

7.2. Discharge probability studies on triple-GEM technology at CHARM facility

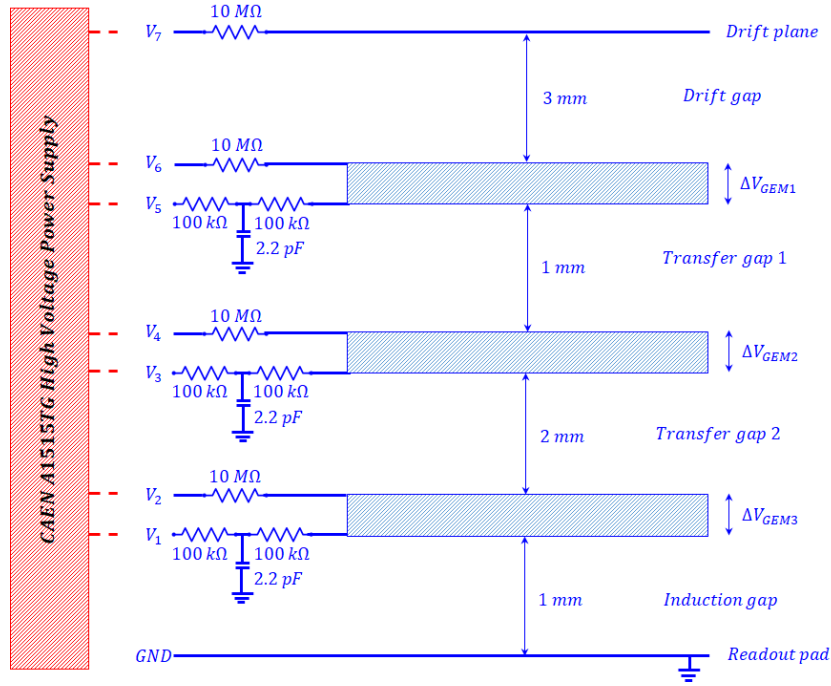


Figure 7.5: Voltage distribution in the triple-GEM detector prototype under test at CHERM facility.

474 model) and then to a discriminator (Lecroy 623A model). The resulting digital pulses went through a dual timer and then to a scaler unit for the rate measurement. Knowing the average ionization energy of the Ar/CO_2 (70/30) gas mixture, the number of primary electrons n_{e^-} per incoming 5.9 keV X-ray photon was calculated as follows:

$$n_{e^-} = E_\gamma \times \left(\frac{\%Ar}{W_i(Ar)} + \frac{\%CO_2}{W_i(CO_2)} \right) = 5900 \times \left(\frac{0.7}{26} + \frac{0.3}{33} \right) \approx 212 \quad (7.1)$$

where $E_\gamma \approx 5.9$ keV is the energy of the incident X-ray photons, $\%Ar$ and $\%CO_2$ are the percentages of the gases in the mixture, $W_i(Ar)$ and $W_i(CO_2)$ are the work functions of the gases. Finally, the primary current was estimated by multiplying the X-ray photons interaction rate R , the number of primary electrons n_{e^-} per X-ray photon and the elementary charge e .

On the contrary, the amplified current I_a , induced on the readout board, varied from 10^{-10} to 10^{-8} A depending on the voltage applied on the GEM-foils. Therefore, its measurement can be performed easily with a pico-ammeter connected to the anode. Even though the readout is segmented, in the effective gas gain measurement the signals obtained from all pads were fed into a single channel 6487 Keithley pico-ammeter and analyzed with LabVIEW based data acquisition system. Finally, the effective gas gain G is expressed as follows:

$$G = \frac{I_a}{R \times n_{e^-} \times e} \quad (7.2)$$

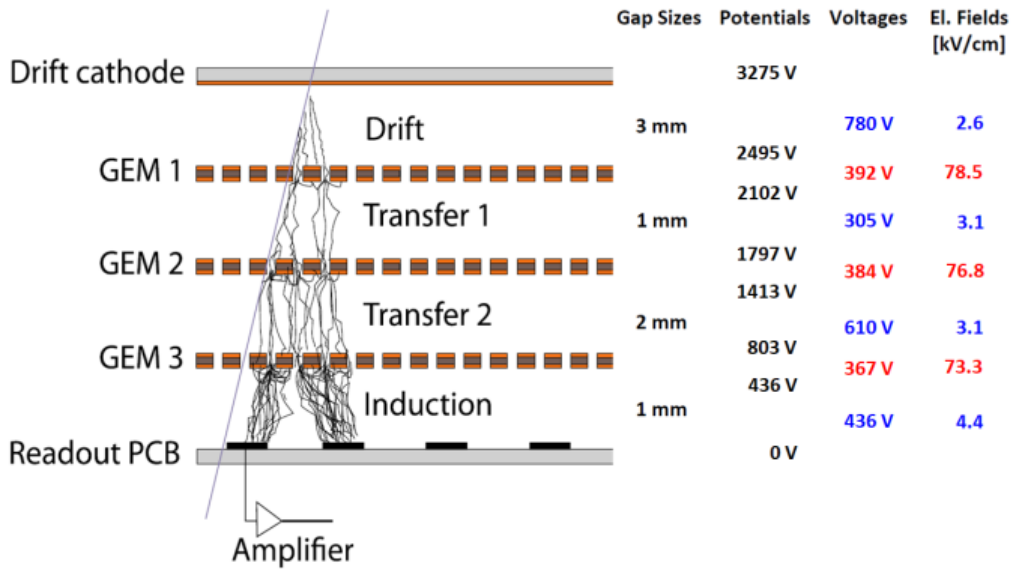


Figure 7.6: Principle of operation of the triple-GEM detector prototype and definition of drift, transfer, and signal induction gap regions within the detector. The columns on the right give the actual gap sizes in the detector. They also list typical values for electric potentials on the seven electrodes and typical values for voltages and electric fields across the four gaps (blue) and the three GEM-foils (red) if the nominal potential of 3275 V in Ar/CO_2 (70/30) is applied to the drift cathode (696.8 μA divider current equivalent).

The experimental setup for the effective gas gain measurements is shown on Figure 7.7. The detector and the readout elements were shielded with copper plates to minimize the electronic noise and its contribution to the measurements.

Figure 7.8 shows the measured particle interaction rate (black dots) and the effective gas gain (blue dots) as function of the voltage difference applied to the drift cathode V_{Drift} for a Ar/CO_2 (70/30) gas mixtures. A clear exponential relation between the gas gain and the high voltage can be seen. The maximum gas gain can reach 3.5×10^4 when the voltage difference applied to the drift cathode V_{Drift} is 3300 V (702.1 μA divider current equivalent).

7.2.2.2 Energy resolution measurement

The energy resolution was measured in Ar/CO_2 (70/30) gas mixture at an initial gas gain of 2×10^4 by using a multi-channel analyzer (MCA) in order to record the pulse height induced on the readout pads. The detector is irradiated by a ^{55}Fe isotope producing X-ray photons with an average energy of 5.9 keV that fully convert into the drift gap via photoelectric effect. As previously mentioned, although there was a segmented readout pads, in the energy resolution measurement the induced signal was obtained from all the pads added by a sum up connector (Panasonic to LEMO connector) and a sin-

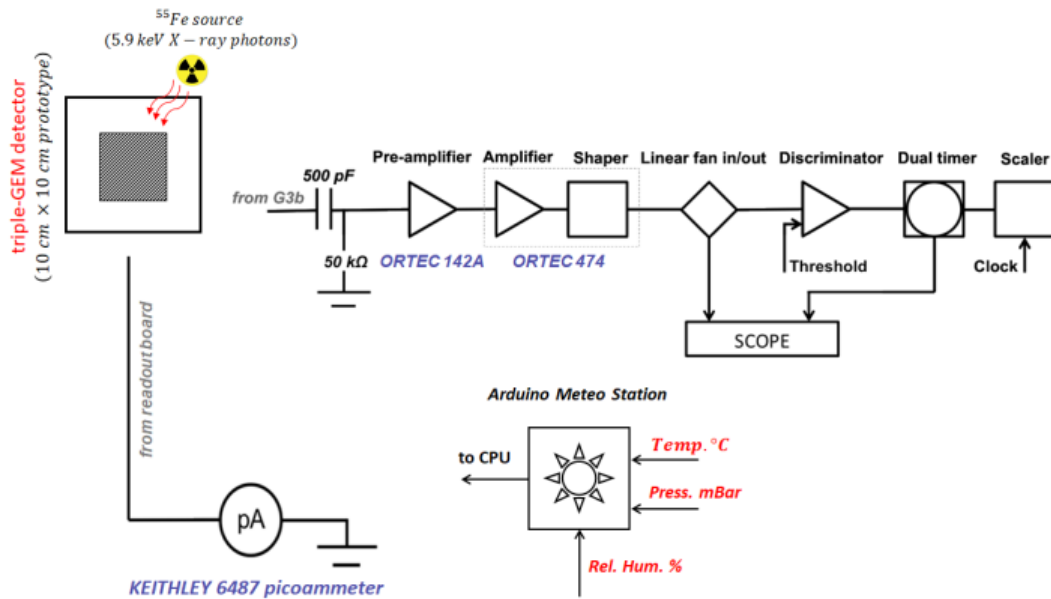


Figure 7.7: Schematic overview of the experimental set-up used for the effective gas gain measurement on the $10\text{ cm} \times 10\text{ cm}$ triple GEM detector prototype.

gle input was fed to a charge sensitive preamplifier (ORTEC 142A model). The output of the pre-amplifier was then sent to an amplifier+shaper unit (ORTEC 474 model) and then to a multi-channel analyzer (MCA-8000D Amptek). Since multi-channel analyzer requires positive pulse, hence the polarity of the induced signal was inverted by the amplification stage. The experimental setup for the energy resolution measurements is shown on Figure 7.9.

Figure 7.10 shows the typical ^{55}Fe energy spectrum: a clean separation of the main photopeak and the Ar escape peak is achieved. The energy resolution, defined by the ratio of the $FWHM$ value and the mean value μ of the main photopeak, is on the order of $25.9 \pm 0.1\%$.

At the end of the detector characterization, the triple-GEM detector has been installed into the CHARM facility for a first discharge probability test campaign.

7.2.3 The triple-GEM detector prototype at the CHARM facility

The triple-GEM detector prototype under test has been situated in a dedicated test location within the CHARM experimental area, as shown in Figure 7.11.

As previously mentioned, a 24 GeV proton beam coming from the PS extraction line hits a target and the resulting particle shower irradiates the whole experimental area, with energies ranging from thermal neutrons (meV) up to tens of GeV . The environment is dominated by hadrons, mainly protons and

7. Discharge Probability Studies in triple-GEM detectors

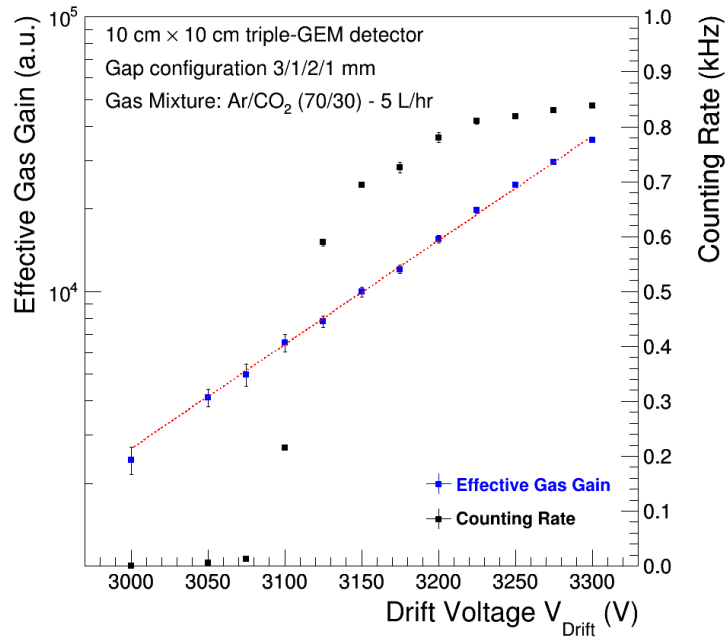


Figure 7.8: Measured particle interaction rate (black dots) and the effective gas gain (blue dots) as function of the voltage difference applied to the drift cathode V_{Drift} . The detector under test is a single-mask GEMs in tripple stack configuration of $10\text{ cm} \times 10\text{ cm}$ operated in Ar/CO_2 (70/30) gas mixture.

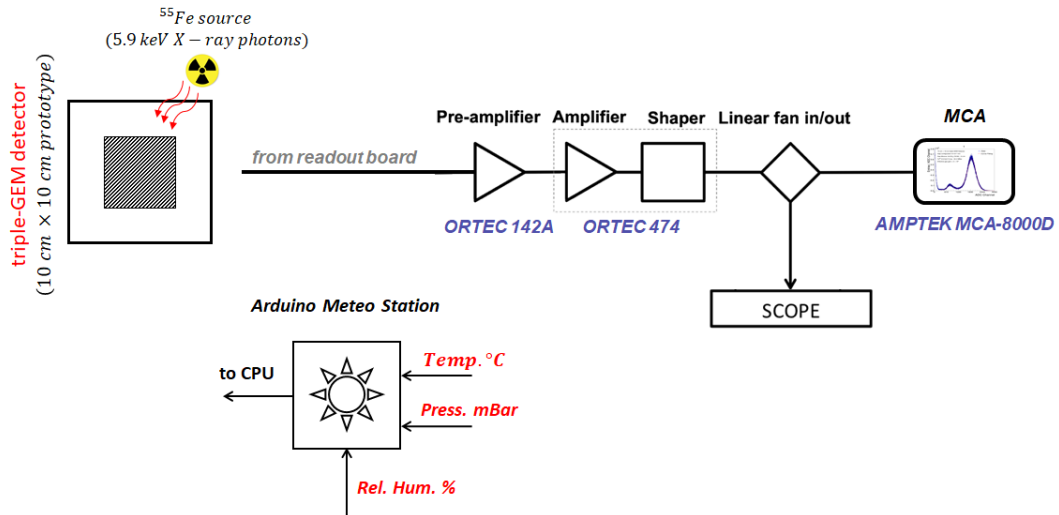


Figure 7.9: Schematic overview of the experimental set-up used for the energy resolution measurement on the $10\text{ cm} \times 10\text{ cm}$ triple GEM detector prototype.

neutrons. Four movable shieldings can be placed in the experimental area to realize different environment spectra. The expected dose rate and High Energy

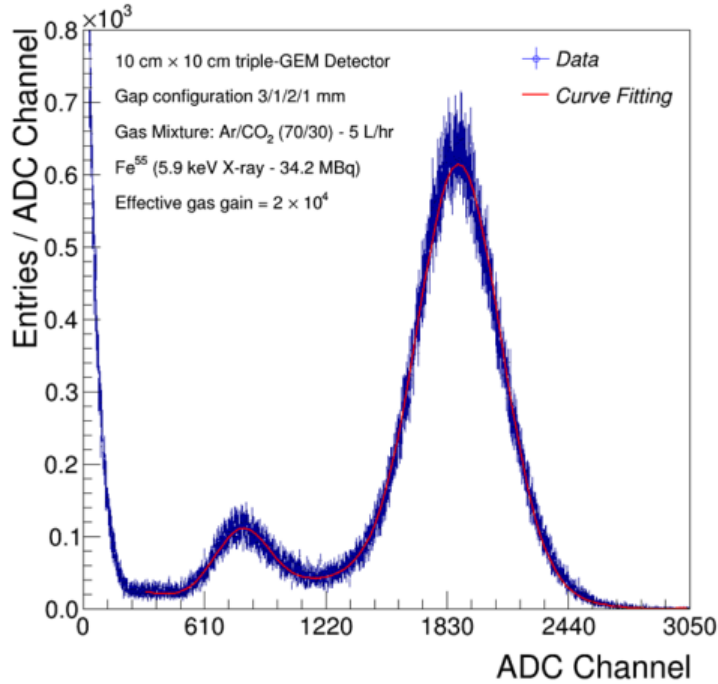


Figure 7.10: ^{55}Fe energy spectrum taken with single-mask GEMs in tripple stack configuration of $10\text{ cm} \times 10\text{ cm}$ operated in Ar/CO_2 (70/30) gas mixture at an $V_{\text{Drift}} = 3275\text{ V}$ ($696.8\ \mu\text{A}$ divider current equivalent). The solid line represents a fit to the experimental data using a sum of two gaussians distribution, to model the main photopeak and the Ar escape peak, plus a fifth order polynomial that models the background. The energy resolution ($FWHM$ value of the main photopeak divided by the mean value μ) is $25.9 \pm 0.1\%$.

Hadron (HEH) flux depend on the chosen test location, target material and shielding.

During the discharge probability test campaign, the triple-GEM detector prototype has been placed in the R3 test location and copper target and shielding configuration Copper-CIIC has been selected in order to achieve a neutron energy spectrum which is representative of the neutron energy spectrum in the CMS Muon System. The particles lethargy spectra obtained by Fluka simulation for the this configuration is shown on Figure 7.12. On Table 7.1 the different type of particles with the relative contribution is shown [137].

As a comparison, Figure 7.13 shows the simulated CMS energy spectra for the ME0 detector for different background particles at instantaneous luminosity of $5 \times 10^{34}\text{ cm}^2\text{s}^{-1}$ [69]. One can see that the neutron energy spectrum closely resembles that in the innermost region of the Muon Spectrometer of the CMS experiment.

The gas system has been designed and built in 2016 by the CERN Gas Group,

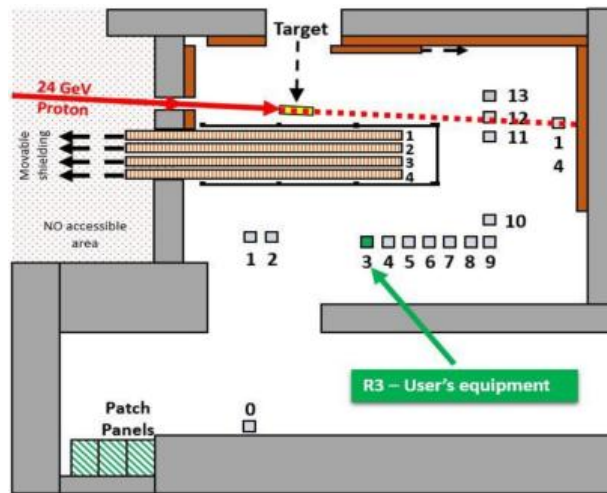


Figure 7.11: Layout of CHARM configuration with copper target with shielding (copper-CIIC). The position used during the discharge probability test campaign is highlighted in green.

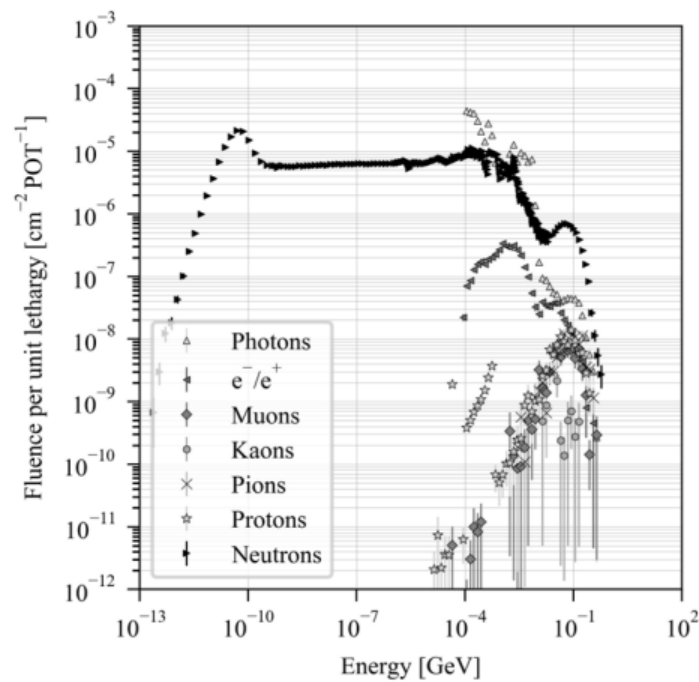


Figure 7.12: Particles lethargy spectra obtained by Fluka simulation for the CuCIIC configuration in the R3 test position, i.e. the available particle fluence for the configuration copper-CIIC in the R3 test position normalized over primary Protons On (copper-)Target (POT) [137].

following strict guidelines concerning the materials to be used, and cleanliness conditions in general. The gas system, schematically shown in Figure 7.14, is constructed in stainless-steel tube. The whole gas line has been flushed in

Particle type	Fluence ($cm^{-2}/Spill$)
<i>Neutrons</i>	8.30×10^7
<i>HEH</i>	1.31×10^6
e^+/e^-	6.29×10^5
<i>Muons</i>	2.29×10^4
<i>Pions</i>	3.97×10^4
<i>Protons</i>	4.80×10^4

Table 7.1: Different type of particles with the relative contribution for the configuration copper-CIIC in the R3 test position. *HEH* refers to "High Energy" Hadrons, i.e. all hadron particles with energy above 20 *MeV* [137].

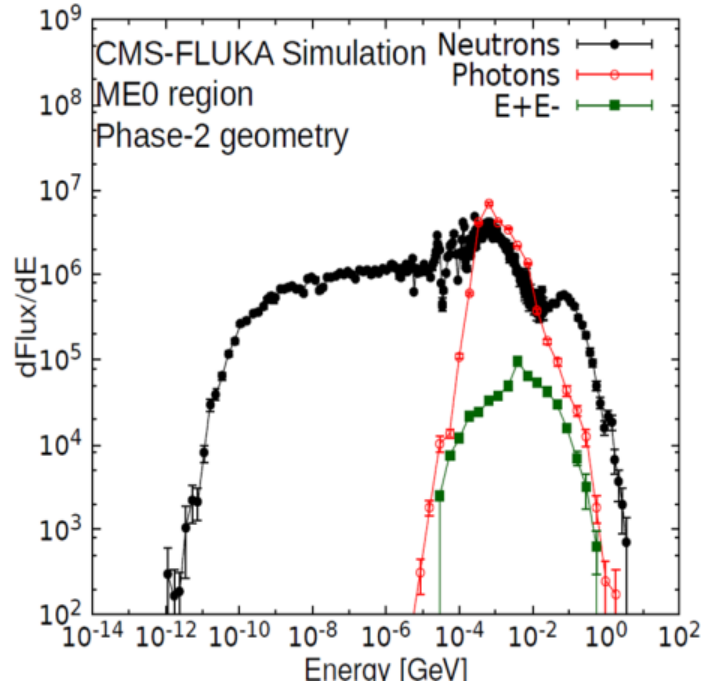


Figure 7.13: Simulated energy spectra for different background particles considering CMS-FLUKA Phase-2 geometry and an instantaneous luminosity of $5 \times 10^{34} cm^2 s^{-1}$ for the upgrade ME0 detector [140].

the Ar/CO_2 (70/30) gas mixture without the detectors with gas flow rate of $\sim 5.0 L/h$ for several days in order to clean the gas pipe after a long term of non-operation.

The control and monitoring equipment of the full experimental set-up is installed in an appropriate technical-locale, where the operating point, the parameters of the Data Acquisition Systems and the collection of the data are remotely controlled from outside of the CHARM irradiation area via CERN network, minimizing the need of stopping the irradiation to access the detec-

7. Discharge Probability Studies in triple-GEM detectors

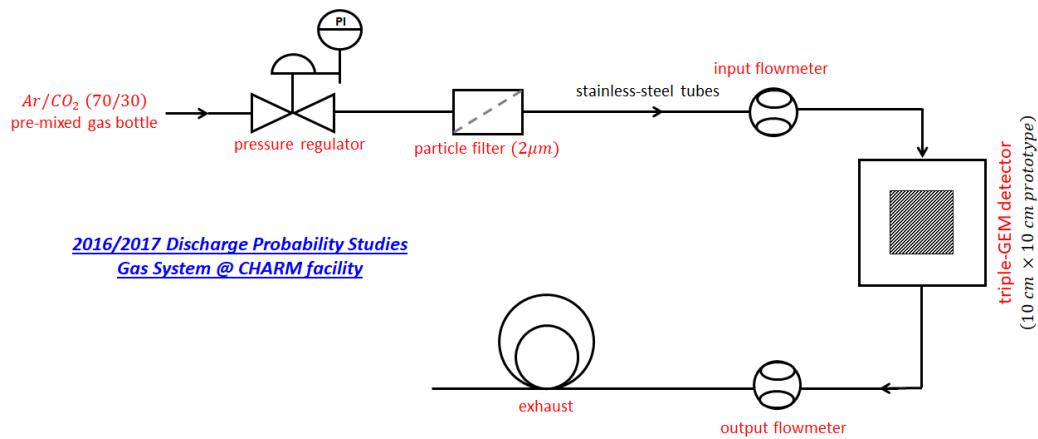


Figure 7.14: Schematic overview of the gas system used during the irradiation test at CHARM facility. The whole gas line is made of stainless-steel tubes.

tor. The picture of experimental setup at CHARM facility can be seen on Figure 7.15.

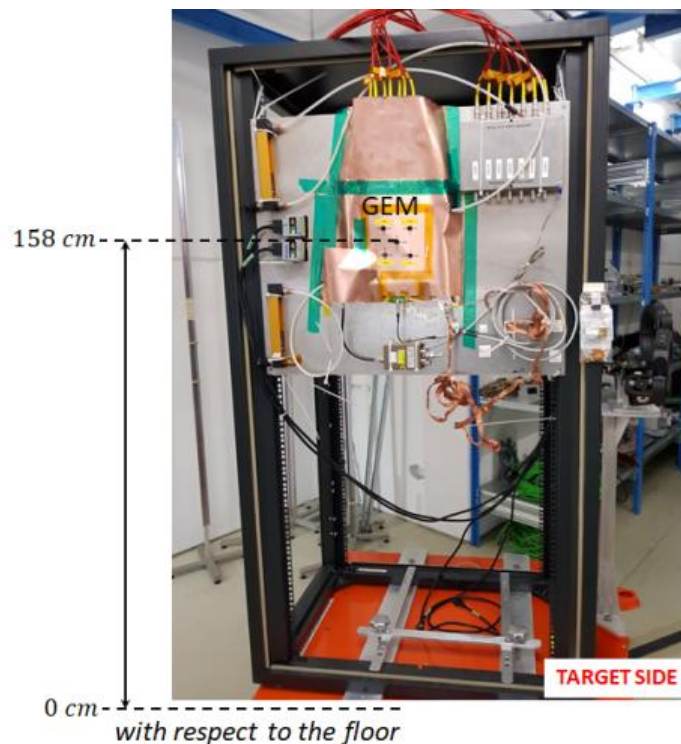


Figure 7.15: Pictures of the experimental set-up for the discharge probability studies at CHARM facility. The triple-GEM detector prototype is placed in the R3 test location and the copper target in the shielding configuration copper-CIIC has been selected.

7.2.4 The data acquisition system and discharge monitoring at the CHARM facility

A data acquisition system has been developed in order to monitor the response of the triple-GEM detector prototype under irradiation at CHARM facility. Figure 7.16 shows the electronics chain, the read-out and the device to store and analyse the data. The readout system for the discharge probability studies consists of four main readout channels:

- CAEN A1515TG multi-channel HV power supply is used to monitoring the operating current and the high voltage in all the individual channels: the drift plane and the upper and lower electrode of the three GEM-foils. The A1515TG board, housed in a CAEN SY1527 HV mainframe, is read-out through a Ethernet interface between the mainframe and the computer station. A custom software written in C++ programming language has been developed in order to record the operating current and the high voltage information provided by the A1515TG board during the entire radiation exposure test. The software has been developed to monitor the operating current and the high voltage every second and store the raw data in a file for subsequent analysis.
- KEITHLEY 6487 pico-ammeter is connected to the readout board to measure the anode current, which reflects the effective gas gain of the detector. The read-out of such device is made through a RS232 interface between the pico-ammeter and the computer station. The pico-ammeter is configured to sample the anode current: 40 sequential measurements at a rate of about 80 Hz , i.e. an anode current measurement every $\sim 12.5 ms$ for a total sampling time of $\sim 500 ms$ in order to cover the whole PS spill length.
- NIM+VME based data acquisition system is employed to measure the interaction rate. The readout of the detector is done using a charge sensitive pre-amplifier (ORTEC 142A model) connected to the bottom electrode of the third GEM-foil. This connection is made through a decoupling RC circuit already present on the detector's frame. The output of the pre-amplifier is then sent to an amplifier+shaper unit (ORTEC 474 model) and then to a timing single channel analyzer unit (ORTEC 551 model). The timing single channel analyzer unit is operated in integral mode and the lower level in the unit is used as the threshold to the signal. The threshold is set at 0.5 V to reject the noise. The resulting digital pulses go through a NIM/ECL adapter (CAEN V538A model) then to a scaler unit (CAEN V560E model) for the rate measurement. The acquisition is made through a CAEN V1718 controller with an USB interface between the electronic chain and the computer station.
- Enviromental Monitoring System based on ARDUINO Mega 2560 micro-controller has been designed to monitor the environmental parameters

7. Discharge Probability Studies in triple-GEM detectors

(atmospheric pressure, temperature) within the experimental irradiated area. Each minute: the system monitors and records the atmospheric pressure through a MPXA61/15AC6U sensor, the temperature through a LM335Z/NOPB sensor.

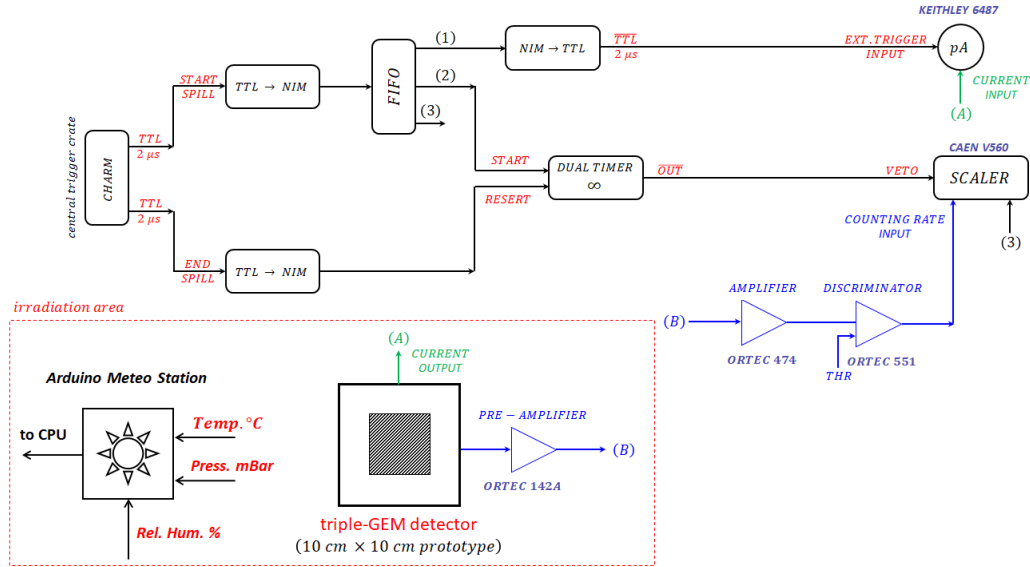


Figure 7.16: Scheme of the electronic chain and data acquisition system used during the discharge probability studies at CHARM facility.

The picoammeter is configured in external trigger mode in order to measure the anode current from the detector readout board in sync with the 24 GeV proton beam extracted from the PS accelerator and directed on the copper target inside the CHARM experimental area. The synchronization with the PS spill structure is achieved distributing across the experiment two signals, received from the PS accelerator and available in the central trigger crate inside the control room of the facility: the Start-Of-Spill (SOP) and the End-Of-Spill (EOS). The Start-Of-Spill and the End-Of-Spill signals from the central trigger crate, which are TTL nature, are fed to a TTL-NIM adapter and then converted from TTL to NIM signals. The Start-Of-Spill signal, converted from TTL to NIM signal, is split by using a linear Fan-in-Fan-out. A first NIM output signal (1) of the Fan-in-Fan-out is converted back to a TTL signal through a NIM-TTL adapter and the resulting output TTL signal is used to trigger the picoammeter which accepts a TTL signal as a digital trigger signal. Therefore, the picoammeter is configured to receive the Start-of-Spill from the central trigger crate, read out and buffer events during the spill, and between the spills it send the event "blobs" to the computer station. A second NIM output signal (2) of the Fan-in-Fan-out is sent together with the End-Of-Spill, converted from TTL to NIM signal, to a dual timer unit in order to build a proper gating signal used as a digital veto signal to disable the scaler unit in

the out-of-spill period. A third NIM output signal (3) of the Fan-in-Fan-out is directly sent to the scaler unit in order to record the total number of spill during the entire irradiation test.

In order to measure the discharge probability under neutron irradiation, the anode current, readout from the readout pads (connected all together) using a KEITHLEY 6487 pico-ammeter, has been combined with the operating current and voltage information provided by the CAEN A1515TG multi-channel HV power supply: if a discharge occurs in one of the three GEM-foils, the corresponding potential difference will drop to zero. As a consequence, the gas gain of one of the three GEM-foils is temporarily reduced and a lower anode current is measured on the anode. Alternatively, the possible occurrence of a discharge in the triple-GEM detector under test can be identified through a drop in the counting rate of the signals induced on the lower electrode of the third GEM-foil. During a discharge, a sudden drop in the electric field inside a GEM-holes reduces the overall gas gain and thus the counting rate in the triple-GEM detector. Additionally, measuring the operating current from the individual channels and observing an increase in the current value particularly from the upper electrode of the three GEM-foils is another way to determine the occurrence of a discharge during a spill. Thus, the occurrence of a discharge can alternatively be determined from such a sudden operating current increase on any one of the electrodes of the three GEM-foils. The latter method to detect a discharge can be implemented through a built-in feature of the A1515TG multi-channel HV power supply. The board comprises a special function called *overcurrent detection* [138] when a channel attempts to exceed the programmed current limit, it is signalled to be in "overcurrent" and the channel enter in a TRIP status. The output voltage is varied to keep the operating current below the programmed limit for a programmable TRIP time. The overcurrent lasting more than set value, causes the TRIP of the channel: the channel is switched off and the output high voltage is drop to zero at the programmed ramp-down rate. A TRIP current threshold (I_{thr}) and a TRIP time window (T_{wnd}) can be properly set so that the board together with the data acquisition software can register the number of times (N_{TRIP}) that the operating current readings has gone beyond the specified threshold value. Considering the TRIPs of the HV power supply as possible discharges, with a high current threshold value, a count of the N_{TRIP} yields an estimate the number of discharge that occurred during the radiation exposure test. An increase in N_{TRIP} indicates in increase in the number of discharge. This method has one particular advantage: it not only yields the number of discharge in a particular supply channel, but also points to the particular GEM-foil where the discharge occurred.

7.2.5 Measurement of the discharge probability

A triple-GEM detector in CMS configuration has been placed near the CHARM target and has been irradiated up to a neutron fluence close to $2.5 \times 10^8 \text{ n/cm}^2$ and a dose of about 9.4 Gy , i.e. a dose rate of about 1 Gy/day has been collected at the R3 test location. The detector has been operated at a gas gain of 3.5×10^4 in Ar/CO_2 (70/30) gas mixture. As previously mentioned, the GEM-foils have been powered independently with a multi-channel power supply in order to monitor the operating current and high voltage induced on each electrode and to detect possible discharge signals. Additionally, the signals induced on the bottom electrode of third GEM-foil have been used to count the total number of particles crossing the detector active volume and to identify the high-charge signals induced by highly ionizing particle (*HIPs*). A pico-ammeter connected to the readout electrode also measured the total charge generated in the triple-GEM detector prototype under test.

The aim of the discharge probability test at CHARM facility has been to count the number of discharges that could induce a TRIP in the high voltage system. The TRIP current threshold for each GEM-foils and for the drift cathode has been set $1 \mu\text{A}$ higher than the normal operating current seen by each one within a spill. The discharge probability has been defined as the ratio of the total number of discharge produced in the detector to the total number of particles interacting with the detector under test:

$$P_{Disch.} = \frac{N_{Disch.}}{R_{meas.} \times \Delta T_{SPILL} \times N_{spill}} = \frac{N_{TRIP}}{R_{meas.} \times \Delta T_{SPILL} \times N_{spill}} \quad (7.3)$$

where $R_{meas.}$ is the counting rate per spill, i.e the rate of interacting particles per spill, ΔT_{SPILL} the spill length, N_{spill} the total number of spills recorded during the entire radiation exposure test and $N_{Disch.}$ the total number of discharge produced in the triple-GEM detector under irradiation test, which is equivalent to the total number of TRIPs N_{TRIP} in the high voltage system.

Figure 7.17 shows the average counting rate per spill as a function of the voltage difference applied to the drift cathode V_{Drift} measured by the triple-GEM detector under irradiation test within the spill at a discriminator threshold value of 500 mV . The "average net" counting rate per spill, defined as the average counting rate inside the spill to which the average counting rate outside the spill has been subtracted, is also plotted and shows a plateau in the region of the working point $V_{Drift} = 3350 \text{ V}$ ($712.8 \mu\text{A}$ divider current equivalent). The average counting rate outside the spill is affected by the neutron activation of the materials and varies with time.

The irradiation test with the triple-GEM detector prototype operated in stable condition lasted for a total of 18524 spills during which none of the high voltage power supply trips or disruptive events have been observed. To set an upper limit the rule of the *three-sigma rule* [141] [142] has been used for the discharge

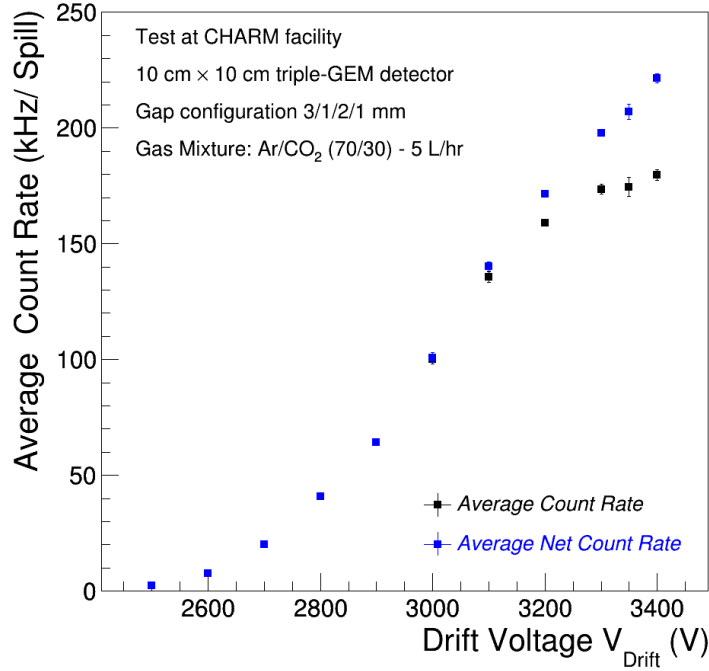


Figure 7.17: Average counting rate per spill from the lower electrode of the third GEM-foil as a function of the voltage difference applied to the drift cathode V_{Drift} measured by the triple-GEM detector under irradiation test at CHARM facility a discriminator threshold value of 500 mV. The average counting rate inside the spill (black dots) has been corrected by the average counting rate outside the spill and the average net counting rate per spill (blue dots) has been obtained. The working point corresponding to a $V_{Drift} = 3350$ V (712.8 μA divider current equivalent) has been used to calculate the discharge probability.

probability at 95% C.L.:

$$\begin{aligned}
 P_{Disch.} &= \frac{N_{Disch.}}{R_{meas.} \times \Delta T_{SPILL} \times N_{spill}} = \\
 &= \frac{3}{1.75 \times 10^5 \text{ s}^{-1}/spill \times 0.325 \text{ s} \times 18524 \text{ spill}} \approx 2.85 \times 10^{-9}/HIP \quad (7.4)
 \end{aligned}$$

Finally, the irradiation test at CHARM facility has enabled to estimate the neutron sensitivity of the triple-GEM detectors directly. Since charged hadrons, electrons/positrons, and other particles are also present in this mixed-radiation field, the neutron signals have been selected in the triple-GEM detector under test by requiring hits with large charge using an appropriate discriminator threshold. The signal from the lower electrode of the last GEM-foil has been picked-up, pre-amplified and sent to the control room of the facility where it has

been amplified and discriminated for counting purposes. Figure 7.18 shows the typical counting rate per spill measured from this channel as a function of the discriminating threshold at working point corresponding to a $V_{Drift} = 3350 V$ ($712.8 \mu A$ divider current equivalent).

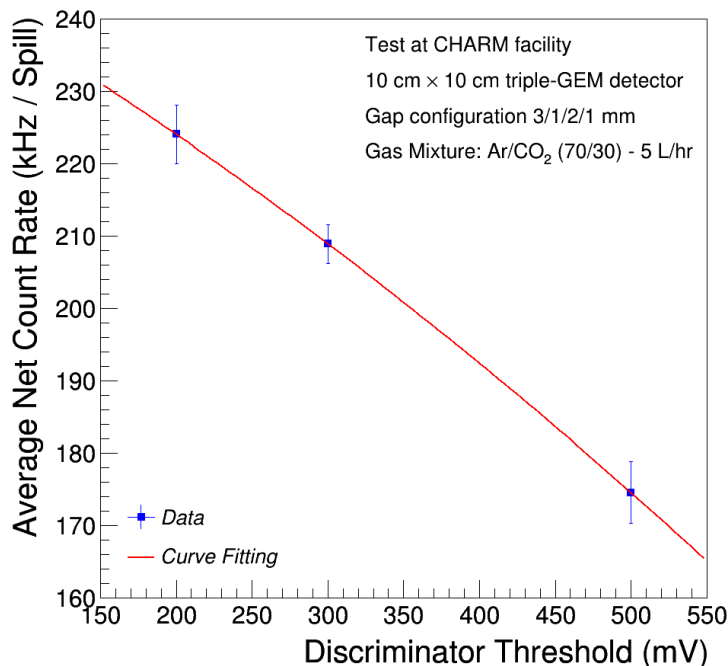


Figure 7.18: Average net counting rate per spill from the lower electrode of the third GEM-foil as a function of the applied discriminating threshold at working point corresponding to a $V_{Drift} = 3350 V$ ($712.8 \mu A$ divider current equivalent). The point corresponding to a threshold value of $500 mV$ has been used to calculate the triple-GEM neutron sensitivity.

By changing the threshold value, a minimum amount of charged released into the triple-GEM detector can be identified. As the threshold increases, the counting rate decreases signaling that high charge releasing events have been selected. It has been relied on this approach for identify neutron-like events since, due to the characteristic of the CHARM facility, a pure neutron beam could not be selected. By considering Figure 7.18, the point corresponding to a threshold of $500 mV$ has been used in order to calculate the triple-GEM neutron sensitivity. From the ratio of measured counts above threshold and incident neutron fluence, the neutron sensitivity for the triple-GEM detector has been measured to be 7.5×10^{-4} . A comparison of the measured triple-GEM neutron sensitivity with the simulated triple-GEM neutron sensitivity 2.6×10^{-4} obtained for the spectrum showed in Figure 7.12 and for the triple-GEM used materials, showed an agreement within a factor 3, which represents

a significant result given the complexity of the neutron interactions with the triple-GEM detectors and the dearth of experimental studies on this topic.

7.2.5.1 Expected number of discharges during detector operation

The expected background components and their corresponding hit rates in the GE1/1, GE2/1, and ME0 regions in the CMS Muon System has been computed using the CMS-FLUKA simulation software. Additionally, the sensitivity of triple-GEM detectors to the different background components and energies has been simulated with the GEANT4 framework. The results of the simulation, shown in Table 6.2 (Section 6.1), indicate that the background hit rate is mainly dominated by neutrons and photons: neutrons are produced by the hadronic interactions in the inner part of the detector and by the interactions of protons of the beam with the collimators, with energies between few meV and hundreds of GeV ; photons instead come from neutron capture, with typical energies between few keV and tens of MeV . Based on the neutron hit flux presented in Table 6.2, it can be estimated the total number of discharges per detector after ten years of operation at the HL-LHC. However, only neutrons with an energy above 1 MeV are expected to produce HIPs and trigger possible discharges, which represents about 20% of the total neutron spectrum in the innermost region of the forward CMS Muon Spectrometer. Therefore, the expected number of discharges in GE1/1, GE2/1, and ME0 detectors after ten years of operation at HL-LHC is given by:

$$N_{Disch.} = P_{Disch.} \times R_{max} (> 1 MeV) \times t_{LHC} \quad (7.5)$$

where $P_{Disch.}$ is the discharge probability estimated with the alphas source test ($P_{Disch.} \approx 10^{-10}/HIP$) and with harsh mixed-radiation fields at the CHARM facility using the upper limit for the discharge probability ($P_{Disch.} \approx 2.85 \times 10^{-9}/HIP$), $R_{max} (> 1 MeV)$ is the maximum expected neutron fluence in the hottest region of the detector assuming that all neutrons with energy higher than 1 MeV can induce heavily ionising particles, and t_{LHC} is the effective exposure time after ten HL-LHC years.

Table 7.2 shows the expected number of discharges per cm^2 after ten years of operation at HL-LHC, considering the discharge probabilities estimated both with the alphas source test and with the harsh mixed-radiation fields at the CHARM facility. Due to the high background rate in the innermost ME0 region, the largest number of discharges is expected in that station: $\sim 225 Disch./cm^2$. However, this number is to be compared against a discharge test with alpha particles in which $\sim 450 Disch./cm^2$ discharges have been observed. Those discharges did neither damage the GEM-foils, nor did they degrade the detector performance [69] [90].

GEM Station	Expected number of discharges (using $P = 10^{-10}/HIP$ from test with alphas) [$1/cm^2$]	Expected number of discharges (using $P = 2.85 \times 10^{-9}/HIP$ from CHARM test) [$1/cm^2$]
GE1/1	0.6	17.0
GE2/1	0.4	11.7
ME0	7.9	224.8

Table 7.2: Expected number of discharges in GE1/1, GE2/1, and ME0 triple-GEM detectors after ten years of operation at HL-LHC.

7.2.5.2 Effects of the discharges on the detector operation

The triple-GEM detector prototype based on the single-mask photolithography technique developed by the CERN PCB Workshop and operated with Ar/CO_2 (70/30) gas mixture at an effective gas gain of 2×10^4 has been exposed to the radiation in the CHARM facility. Figure 7.19 shows the accumulated charge per unit of detector area (mC/cm^2) as a function of time. During this time, the detector under irradiation test integrated about $0.9 mC/cm^2$ after ~ 120 hours of continuous irradiation of sustained operation in the harsh mixed-radiation fields, which represents the 15% of the total GE1/1 operation and the 30% of the total GE2/1 operation at the HL-LHC.

No performance degradation or unstable operation has been observed during the entire irradiation test at CHARM facility. An effective gas gain measurement has been performed before and after the irradiation test in order to identify a possible degradation of the GEM-foils. Figure 7.20 shows the comparison of effective gas gains of the triple-GEM detectors under test at the CHARM facility in pre- and post-irradiation conditions with the irradiated electronics. It has not been observed any significant gain differences before and after the intense irradiations.

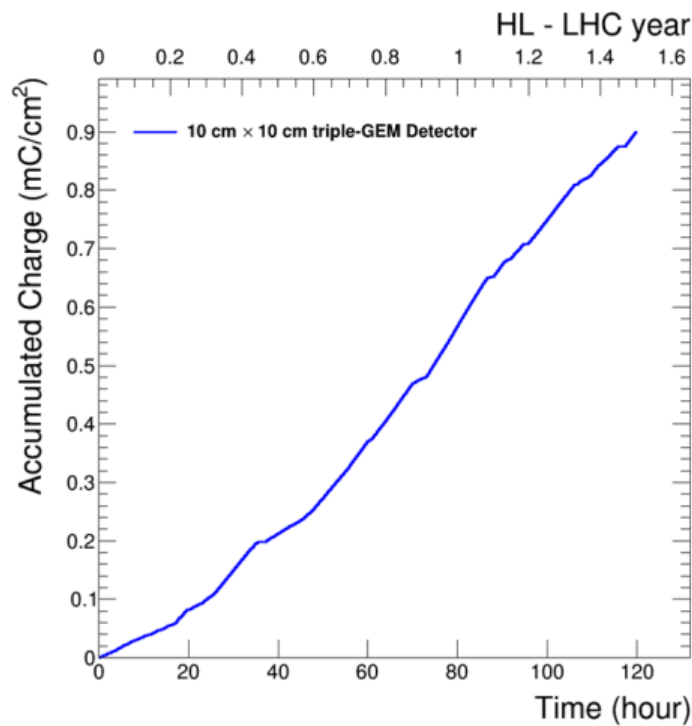


Figure 7.19: Result of the discharge probability studies at the CHARM facility: accumulated charge per unit of detector area (mC/cm^2) as a function of time. The detector under irradiation test integrated about $0.9 mC/cm^2$ after ~ 120 hours of continuous irradiation of sustained operation in the harsh mixed-radiation fields, which represents about 1.5 years of operation in GE1/1 environment at the HL-LHC.

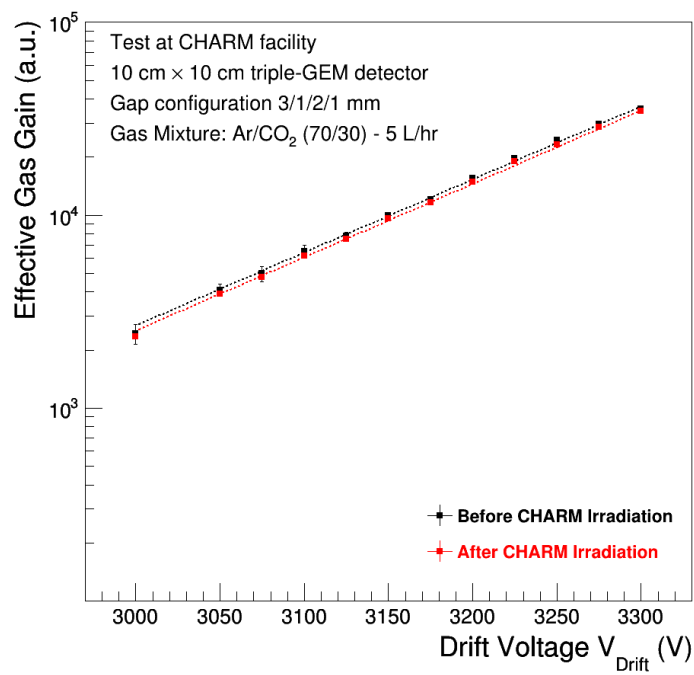


Figure 7.20: Comparison of effective gas gains of the triple-GEM detectors under test at the CHARM facility in pre- and post-irradiation conditions with the irradiated electronics.

General conclusions

The Compact Muon Solenoid (CMS) is a general purpose experiment measuring proton-proton and heavy-ion collisions at Large Hadron Collider (LHC) at CERN laboratory, in Geneva. The detector has been running successfully at unprecedented proton-proton center-of-mass energies up to 13 TeV , with an LHC luminosity exceeding $10^{34}\text{ cm}^{-2}\text{s}^{-1}$. The missing key particle of the Standard Model, the Brout-Englert-Higgs boson, was discovered through its two-photon and four-lepton decay modes in 2012. To extend the sensitivity for new physics searches, a major upgrade of the LHC machine has been decided and is being prepared, the High Luminosity LHC (HL-LHC). The center-of-mass energy for proton-proton collisions is expected to be raised from the current 13 TeV up to 14 TeV and the instantaneous luminosity of LHC is expected to exceed the nominal value and reach $2.5 \times 10^{34}\text{ cm}^{-2}\text{s}^{-1}$, after the second Long Shutdown (LS2) foreseen in 2019-2020. A further increase is planned during the third Long Shutdown (LS3) in 2024-2026, up to $5 \times 10^{34}\text{ cm}^{-2}\text{s}^{-1}$, i.e. a yield five times greater than the initially design value of the current LHC. The increase of the center-of-mass energy and instantaneous luminosity during the future upgrades of the LHC machine will deeply affect the performance of the CMS detectors as well as their data acquisition system due to the harsh background environment and the high pile-up. To cope with very high operation condition, high pile-up and background environment the CMS experiment and the muon detectors in particular need major upgrades.

This Doctoral Thesis has been carried out in the framework of the upgrade of the forward muon spectrometer of the CMS experiment. One of the future major CMS upgrade is the addition of new detector layers in the forward muon spectrometer of CMS experiment. The detector technology that has been chosen by the CMS Collaboration for this upgrade is the triple Gas Electron Multiplier (triple-GEM) technology. The triple-GEMs are gaseous detectors, characterized by a detection efficiency more than 98% even for rate exceeding few MHz/cm^2 , high spacial resolution of order $\sim 100\text{ }\mu m$, and good time resolution of order $\sim 8\text{ ns}$ and $\sim 5\text{ ns}$ at the efficiency plateau for Ar/CO_2 (70/30)

and $Ar/CO_2/CF_4$ (45/15/40) gas mixture, respectively. Additionally, the gas gain is observed to be stable up to a several MHz/cm^2 of incident particle rate by demonstrating that the triple-GEM detectors have a high rate capability and will be suitable to operate in the forward muon region of CMS experiment, where a maximum rate on the order of $50 kHz/cm^2$ is expected. Despite being invented just in 1997 by F. Sauli, the triple-GEM technology has become a widely used detection technology for high-rate experiments like COMPASS, LHCb or TOTEM and are foreseen for new experiments or upcoming upgrades, such as the CMS Muon System or the ALICE TPC upgraded.

The triple-GEM detectors are approved to instrument two forward region of the Muon System of the CMS experiment at $1.6 < \eta < 2.4$, called GE1/1 and GE2/1 station during the second and third Long Shutdown, respectively. The GE1/1 and GE2/1 detectors are "super-chambers", each made of a double layer of trapezoidal triple-GEM detector. They will cover slightly more than 10° in GE1/1 station and 20° in GE2/1 station, overlapping in φ just like the corresponding CSC detectors in ME1/1 and ME2/1 stations, complementing them and providing redundancy and enhanced triggering and tracking capabilities in the region which currently suffering from the highest background rates and a non uniform magnetic field. Therefore, 36 super-chambers will be installed for the GE1/1 station and 18 for the GE2/1 station in each muon endcap in order to ensure the full azimuthal coverage. In addition to GE1/1 and GE2/1 station, the ME0 station is approved to be instrumented with triple-GEM detector. Indeed, with pixel tracking extension close to $\eta < 4$ and the replacement of the endcap of the electromagnetic and hadronic calorimeters during the third Long Shutdown, comes the opportunity to extend the muon coverage beyond the present limit of $\eta < 2.4$ with the addition of a muon gas-based detector installed in a space of $\sim 30 cm$ freed behind the new end-cap calorimeters. The ME0 detector station comprises 36 module stacks (18 per endcap), each composed of six layers of triple-GEM detectors, compared to the two-layer design of GE1/1 and GE2/1, covering the region $2 < \eta < 2.8$, in order to allow proper rejection of neutron background, particularly intense in that region. The large η coverage foreseen would lead to an improvement of the acceptance, with a consequent boost in the signal over noise ratio in the signature with muons, especially with the multiple-muon final states, and better hermeticity for signature without muons.

The Doctoral Thesis subject has been proposed by the CMS GEM Collaboration and three main research projects have been conducted in this context:

The first project, conducted in the framework of the LS2 GE1/1 detector mass production, has been focused on the production and quality control of the triple-GEM detectors for the CMS-GE1/1 station, to be installed in the CMS Muon System during the second Long Shutdown in 2019/2020. The aim of the LS2 GE1/1 detector mass production was to assembly, certify and characterize the CMS GE1/1 triple-GEM detectors using the large amount of data

acquired during the 18 months of quality certification tests at the CERN production site. The Quality Assurance (QA) and the Quality Control (QC) are key elements to ensure the delivery of fully efficient GE1/1 detectors yielding their best performance when installed in the Muon Spectrometer of the CMS experiment. The final detector quality and performance depend on the production quality and on the accuracy of the detector assembly procedures. For this reason, a standardized QA and QC protocol for the GE1/1 chamber and super-chamber assembly and certification has been carefully prepared for each level of the mass production in order to prevent any mechanical or electrical issues that might affect the detector performance. The quality control tests involved all the principal GE1/1 detector components and focused on the following main aspects: Gas Tightness, Electric Test, Noise, Effective Gas Gain and Response Uniformity Measurement. The LS2 GE1/1 triple-GEM detectors mass production and quality control is carried out by several universities and research institutes, distributed around the world and led by CERN which is the headquarters of the production collaboration. Among the production and quality control sites, CERN implemented the most exhaustive quality assurance/quality control tests, since the production headquarters takes care of both raw materials and integration of the detectors. As for the raw materials, CERN is the only production site that deals with verifying the integrity and specifications of the detector components. As for the integration of the detectors, CERN, being the final recipient of the detectors assembled externally at the other production sites, implemented additional quality control tests to verify and test the performance of received detectors. A great effort of whole CMS-GEM team is under way to complete the assembly and qualification of the GE1/1 triple-GEM detectors, which will be installed in the muon forward region of the CMS experiment during the second Long Shutdown. The assembly and acceptance/qualification testing of the GE1/1 triple-GEM detectors are now proceeding routinely. At the end of August 2018, a total of 140/144 (97%) detectors have been successfully assembled by a massive effort of all production and quality control sites: 103 of those assembled detectors have been completely qualified, while 37 other ones are awaiting or are in different stages of the quality control. In October 2018 the on-detector electronics assembly and the super-chamber production will be launched at the CERN production site.

The second project has been focused on the long-term operation of triple-GEM detectors, in particular the study of the aging phenomena. Similarly to several gaseous detector, the triple-GEM detector might be subject to aging effect when operating in a high-rate environment. For this reason, several aging tests of full size CMS-GE1/1 triple-GEM detectors have been carried out in parallel at CERN Gamma Irradiation Facility (GIF++), using for the irradiation an intense 14 TBq (2015) ^{137}Cs source emitting 662 keV γ -rays, and at the CMS-GEM QA/QC facility using as irradiation source a 22 keV X-rays source. Both detectors have been operated with Ar/CO_2 (70/30) gas mixture at an

effective gas gain of 2×10^4 . The aim of this aging test campaign was to validate the triple-GEM technology developed for the CMS-GE1/1 project, using large GEM-foils based on the single-mask photolithography technique produced by the CERN PCB workshop, also for CMS-ME0 project which is expected to integrate an accumulated charge of 283 mC/cm^2 in 10 years of HL-LHC.

- *Gamma exposure at GIF++ facility*

After twelve months of continuous operation, the detector accumulated charge was about 182 mC/cm^2 , which represents only 64% of the total ME0 operation. The longevity test campaigns at the GIF++ facility demonstrated that the operation of the triple-GEM detectors in the CMS configuration is not affected by the aging phenomena up to an integrated charge of $\sim 182 \text{ mC/cm}^2$. The longevity studies will continue at the GIF++ facility under the same conditions until the detector accumulates a total charge equivalent to ten HL-LHC years in the ME0 environment with a safety factor 3. This will take additional 5-5.5 years of exposure due to the duty factor of the GIF++ facility and its concurrent use by other experiments. To overcome the extremely long time required at the GIF++ facility to assess the triple-GEM technology as suitable choice for the ME0 detector, an additional longevity test has been setup in summer 2017 exposing a GE1/1 triple-GEM detector to 22 keV X-rays from an *X-ray* source with *Ag*-target at a higher rate.

- *X-ray exposure at CMS-GEM QA/QC facility*

After five months of continuous irradiation with *X-ray*, the detector accumulated a total charge of about 875 mC/cm^2 , thus providing a safety factor of more than 3 with respect to 10 years of HL-LHC operations in the CMS-ME0 environment. The anode current remained stable, proving the detector gas gain was not affected on the whole irradiation period. In addition to monitoring the anode current during the irradiation, the effective gas gain and the energy resolution were continuously measured every week, i.e. every about 30 mC/cm^2 of accumulated charge. The results of the effective gas gain measurements, together with the results obtained from the energy resolution measurements demonstrated that the performances of the triple-GEM detectors in the CMS configuration are not affected by any classical aging phenomena and the detector remains fully operational after 875 mC/cm^2 of accumulated charge.

An additional aging test on the triple-GEM technology based on the double-mask photolithography technique developed by the Mecaro company (Korea) has been carried out in parallel at GIF++ facility. The detector is operated with *Ar/CO₂* (70/30) gas mixture at an effective gas gain of 2×10^4 . The aim of this aging test campaign was to validate the large double-mask GEM-foils for CMS-GE2/1 project by integrating a minimum of charge per unit area of about 9 mC/cm^2 , which represent a 10 years of the total GE2/1 operation at

HL-LHC with a safety factor three, and future applications. The detector under irradiation integrated about 54 mC/cm^2 after three months of continuous irradiation of sustained operation in front of the ^{137}Cs source at the GIF++ facility, which represents ten years of GE2/1 operation at the HL-LHC with a safety factor 18.1, and 19.2% of the total ME0 operation. The longevity test demonstrated that the operation of the triple-GEM detectors assembled with large double-mask GEM-foils in the CMS configuration is not affected by the aging phenomena up to an integrated charge of $\sim 54 \text{ mC/cm}^2$

The third project included a systematic investigation of the discharge probability with the triple-GEM detectors under neutron irradiation in Ar/CO_2 (70/30) gas mixture. Still on the subject of the capability of the new detectors of working in intense neutrons and photons environment, the CMS-GEM Pavia group performed a neutron test at CERN CHARM (Cern High energy AccelERator Mixed Field facility): it provides neutrons, produced in spallation reaction of the Proton Synchrotron (PS) beam with a copper target, with an energy spectrum similar to CMS Muon System. The aim of these neutron tests has been the study of neutron sensitivity and neutron-induced discharge probability of a triple-GEM detector irradiated by neutrons. These measurements have been crucial in the choice of technology to be installed on the detector in order to preserve adequate detector performance and its discovery potential in high luminosity environment of the HL-LHC era. A triple-GEM detector in CMS configuration was placed near the CHARM target and was irradiated up to a neutron fluence close to $2.5 \times 10^8 \text{ n/cm}^2$ and an integrated charge of about 0.9 mC/cm^2 . The detector was operated at a gas gain of 3.5×10^4 in Ar/CO_2 (70/30). The GEM foils were powered independently with a multi-channel power supply in order to monitor the current induced on each electrode and to detect possible discharge signals. Additionally, the signals induce on the bottom electrode of third GEM-foil were used to count the total number of particles crossing the detector and to identify the high-charge signals induced by HIPs. A pico-ammeter connected to the readout electrode also measured the total charge generated in the GEM detector. No trips of the power supply or disruptive events were recorded during the entire test. As a results, considering the average interaction rate at the CHARM facility, an upper limit for the discharge probability of $2.85 \times 10^{-9}/\text{HIPs}$ at 95% C.L. has been established.

The aging and the discharge probability studies have been performed in the framework of an R&D activity on detectors for the innermost region of the forward muon spectrometer of the CMS experiment. These long-term operation test campaigns have demonstrated the robustness and the radiation hardness of the triple-GEM technology, which could tolerate the radiation dose foreseen in 10 HL-LHC years of operation in the ME0 environmental of the CMS experiment. Therefore, the triple-GEM technology, based on the single-mask photolithography technique produced by the CERN PCB workshop, is fully validated for CMS-ME0 upgrade project. The results obtained during the three years of Ph.D. have been contributed to the success of the CMS-ME0

upgrade project and its approval by the CMS and LHCC Collaboration.

Appendix A

CMS-GEM QA/QC facility in CERN

The CMS-GEM QA/QC facility is located in CERN building 904 at the Prévessin site. This facility includes a Clean Room for the GE1/1 triple-GEM detector assembly and a laboratory where the assembled detectors are tested through multiple stages of strict quality control.

The Clean Room for the GE1/1 detectors assembly. Given the complexity of triple-GEM detectors and the quantity needed to instrument the CMS GE1/1 muon station, several assembly and quality control lines have been established to perform the GE1/1 detector mass production using a progressive assembly approach. In accordance with this approach, the GE1/1 detector design relies on interchangeable parts added in sequence until the final assembly. The entire detector assembly takes place in a class 1000 Clean Room fully equipped with all the necessary tooling and assembly devices. The Clean Room is necessary to meet the environmental purity requirements for the detectors assembly and to have the ability to retrofit them if it turns out to be necessary during the production phase. Figure A.1 shows the plan of the Clean Room installed at the CMS-GEM QA/QC facility at CERN.

The Clean Rooms are classified according to the number and size of particles permitted per volume of air. This Clean Room installed at the CMS-GEM QA/QC facility is classified as ISO 6 (Class 1000), with an internal area of about 40 m^2 limited by moveable curtain, with improved quality. The Clean Room facility comprises the clean room proper, the SAS Pass Through (Safety Access System) area for the entrance of the users and two SAS Pass Through zone for the entrance and exit of the material. The SAS Pass Through are chambers with an independent filtration air system that ensure the entrance of the users or the transfer of objects and materials in a safe way, avoiding any kind of contamination in both directions. The complete facility is equipped with vertical laminar walls and roof producing a vertical airflow extracted by the lateral wall. The total flow rate is distributed through 42 housings with

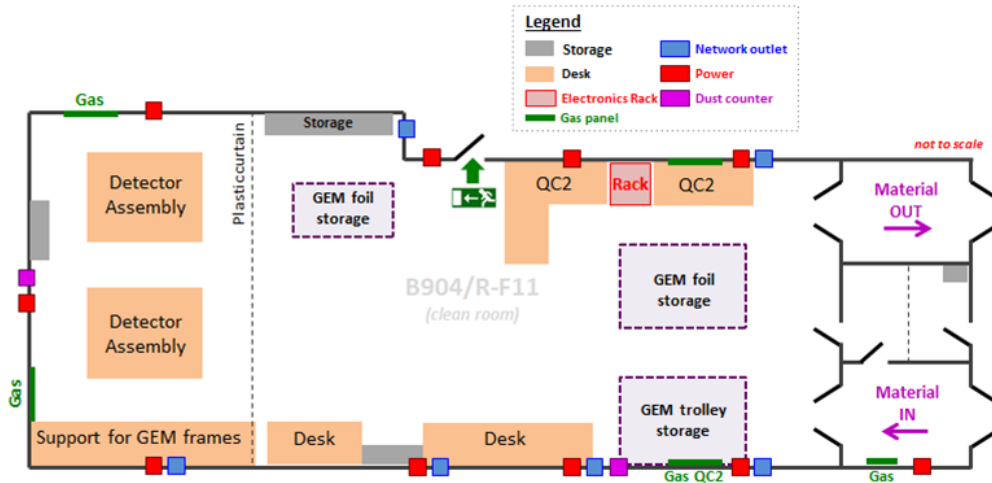


Figure A.1: Plan of the Clean Room installed at the CMS-GEM QA/QC facility at CERN.

absolute filtration $1220 \times 610 \times 70 \text{ mm}^3$ (each one $1200 \text{ m}^3/\text{h} = 180$ air cycles per hour). Additionally, the Clean Room is equipped with a temperature and humidity control and a related monitoring system. The Clean Room is able to host two GE1/1 detector production lines (QC2 Long - Current Leakage Test and GE1/1 detectors assembly).

Technical Specifications:

- An available surface area of about 102 m^2 (Clean Room) + 18 m^2 (SAS);
- Clean room proper: ISO 6 (CLASS 1000) according to ISO 14644-1 over-pressurized for simultaneously 6-7 people working inside;
- SAS Pass Through zone for the entrance of the users;
- SAS Pass Through zone for the material in/out from the room before entering the proper clean room;
- SAS Pass Through zone on over pressure of $\Delta P = 10 \text{ Pa}$ with respect to the main building. The clean room over pressure is $\Delta P = 20 \text{ Pa}$;
- Clean room is equipped with sub-area, delimited by curtain;
- Two Local Exhaust Ventilation systems (LEV) to extract fumes eventually produced by soldering activities;
- Interlock system to the entrance doors to avoid possible clean room contamination;
- Temperature and the relative humidity controlled: Relative Humidity $40\% \pm 10\%$ and Temperature $23 \text{ }^\circ\text{C} \pm 2 \text{ }^\circ\text{C}$.

Pictures of the Clean Room installed at the CMS-GEM QA/QC facility at CERN are shown on Figure A.2, A.3, A.4 and A.5.



Figure A.2: The view of the CMS-GEM QA/QC facility at CERN.



Figure A.3: The internal view of the Clean Room installed at the CMS-GEM QA/QC facility at CERN.

The GEM Laboratory for the GE1/1 detectors quality control. Any industrial mass production implies the adoption of several Quality Assurance (QA) and Quality Control (QC) procedure in order to verify the manufacturing output against the requirements set by the specification. Following this principle, the GE1/1 detectors are also systematically subjected to a series



Figure A.4: The view of the assembly zone in the Clean Room installed at the CMS-GEM QA/QC facility at CERN.

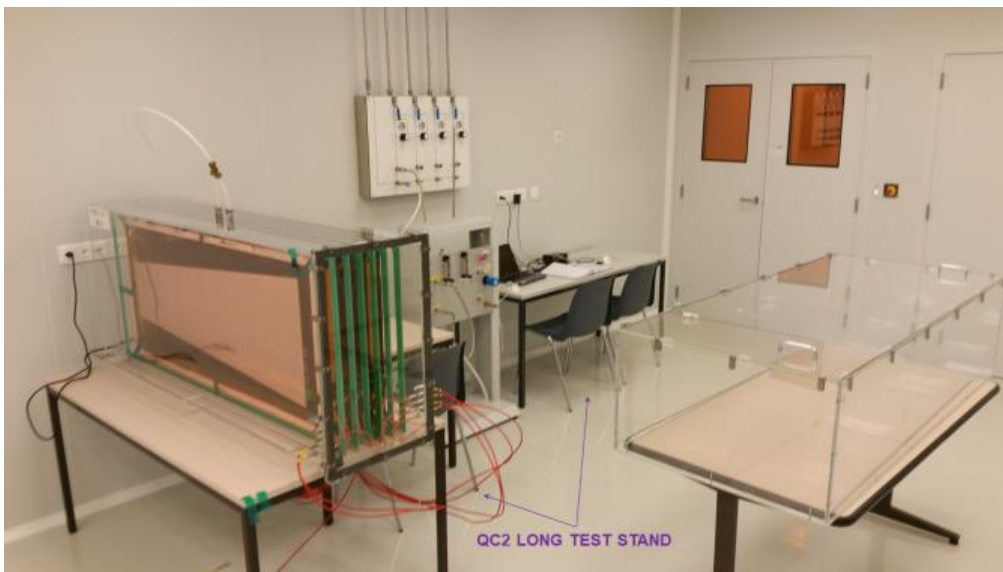


Figure A.5: The view of the QC2 Long - Current Leakage Test in the Clean Room installed at the CMS-GEM QA/QC facility at CERN.

of rigorous tests in order to prevent any mechanical or electrical issues that might affect the detector performance during their operation at CMS Muon System. Figure A.6 shows the plan of the GEM Laboratory installed at the CMS-GEM QA/QC facility at CERN for the GE1/1 detectors certification and qualification.

Technical Specifications:

- An available surface area of about about $284 m^2$;

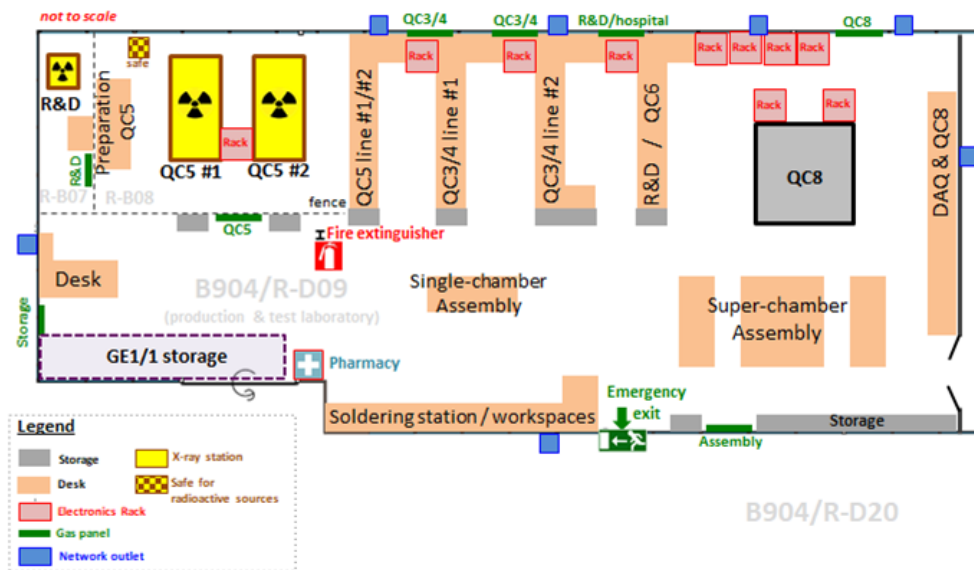


Figure A.6: Plan of the GEM Laboratory installed at the CMS-GEM QA/QC facility at CERN.

- Controlled environment parameters (temperature and relative humidity);
- The GEM Laboratory can handle a minimum of two quality control lines:
 1. QC3 - Gas Leak Test
 2. QC4 - HV test
 3. QC5 - Effective Gas Gain Measurement
 4. QC5 - Response Uniformity
- The GEM Laboratory can handle the final steps of the production and quality control phase:
 1. QC6 - HV test with multichannel power supply
 2. Superchamber assembly
 3. QC8 - Cosmic Stand
- About 18 m^3 available for GE1/1 detectors storage (6 m^2 footprint).

Pictures of the GEM Laboratory installed at the CMS-GEM QA/QC facility at CERN are shown on Figure A.7 and A.8 .



Figure A.7: The view on the QC3/4 stands in the CMS-GEM QA/QC facility at CERN.



Figure A.8: The view on the QC5 stands in the CMS-GEM QA/QC facility at CERN.

Bibliography

- [1] CERN, Home Page - <https://home.cern/>
- [2] The LHC Study Group, *The Large Hadron Collider Conceptual Design Report*. CERN/AC 95-05, 1995.
- [3] O. S. Brüning, P. Collier, P. Lebrun, S. Myers, R. Ostojic, J. Poole, and P. B. Proudlock, *LHC Design Report Vol. 1: The LHC Main Ring*. CERN-2004-003-V1, 2004.
- [4] O. S. Brüning, Poole, P. Collier, and P. B. Proudlock, P. Lebrun, S. Myers, R. Ostojic, J. *LHC Design Report Vol. 2: The LHC Infrastructure and General Services*. CERN-2004-003-V2, 2004.
- [5] M. Benedikt, P. Collier, V. Mertens, J. Poole, and K. Schindl, *LHC Design Report Vol. 3: The LHC Injector Chain*. CERN-2004-003-V3, 2004.
- [6] Lep Injector Study Group, *LEP Design Report Vol. 1: The LEP Injector Chain*. CERN-LEP-TH-83-29, CERN-PS-DL-83-81, CERN-SPS-83-26, LAL-RT-83-09, 1983.
- [7] Lep Injector Study Group, *LEP Design Report Vol. 2: The LEP Main Ring*. CERN-LEP/8-01, 1984.
- [8] Lep Injector Study Group, *LEP Design Report Vol. 3: LEP2*. CERN-AC-96-01-LEP2, 1996.
- [9] The ATLAS Collaboration, *ATLAS: A Toroidal LHC ApparatuS Technical Proposal*. CERN/LHCC 94-18, LHCC/P1, December, 1994.
- [10] CMS Collaboration, *The CMS experiment at LHC*, JINST 08 (2008) 03.
- [11] The ALICE Collaboration, *A Large Ion Collider Experiment Technical Proposal Design*. CERN/LHCC 95-71, LHCC/P3, 1995.
- [12] The LHCb Collaboration, *A Large Hadron Collider Beauty Experiment for Precision Measurements of CP-Violation and Rare Decays LHCb Technical Proposal*, CERN/LHCC 98-04, LHCC/P4, 1998.

-
- [13] A. W. Chao, K. H. Mess, M. Tigner, F. Zimmermann, *Handbook of Accelerator Physics and Engineering*, ed. World Scientific (2013).
- [14] CMS Collaboration, *CMS Luminosity - Public Results*, <https://twiki.cern.ch/twiki/bin/view/CMSPublic/LumiPublicResults>.
- [15] F Halzen and A D Martin. *Quarks and Leptons*. John WILEY and SONS, 1985.
- [16] The Review of Particle Physics, Home Page - URL <http://pdg.lbl.gov>.
- [17] K A Olive. (*PDG*) *Chin. Phys.*, C(38), 2014.
- [18] LHC/LC Study Group Collaboration. *Physics Interplay of the LHC and the ILC*. Phys. Rep., 426(hep-ph/0410364. ANL-HEP-PR-2004-108. CERN-PH-TH-2004-214. DCPT-2004-134. DESY-04-206. DESY-2004-206. IFIC-2004-59. IISc-CHEP-2004-13. IPPP-2004-67. SLAC-PUB-10764. UB-ECM-PF-2004-31. UCD-2004-28. UCI-TR-2004-37. 2-6):47–358. 472 p, Oct 2004. URL <https://cds.cern.ch/record/800650>.
- [19] S. Dittmaier et al. *Handbook of LHC Higgs Cross Sections: 1. Inclusive Observables*. CERN, Geneva, 2011. URL <https://cds.cern.ch/record/1318996>. Comments: 153 pages, 43 figures, to be submitted to CERN Report. Working Group web page: <https://twiki.cern.ch/twiki/bin/view/LHCPhysics/CrossSections>.
- [20] F. Gianotti. *Collider physics: LHC*. (CERN-OPEN-2000-293), 2000. URL <https://cds.cern.ch/record/458489>.
- [21] *Combination of standard model Higgs boson searches and measurements of the properties of the new boson with a mass near 125 GeV*. Technical Report CMS-PAS-HIG-13-005, CERN, Geneva, 2013. URL <https://cds.cern.ch/record/1542387>.
- [22] ATLAS Collaboration, *The ATLAS Experiment at the CERN Large Hadron Collider*, JINST 3 (2008)
- [23] CMS Collaboration, *The CMS experiment at the CERN LHC*, JINST 3 (2008)
- [24] ALICE Collaboration, *The ALICE experiment at the CERN LHC*, JINST 3 (2008)
- [25] LHCb Collaboration, *The LHCb Detector at the LHC*, JINST 3 (2008)
- [26] V. Karimäki, *The CMS tracker system project: Technical Design Report*. Technical Design Report CMS. CERN, Geneva, 1997.
- [27] *The CMS tracker: addendum to the Technical Design Report*. Technical Design Report CMS. CERN, Geneva, 2000.

BIBLIOGRAPHY

- [28] Vardan Khachatryan et al. *CMS Tracking Performance Results from Early LHC Operation*. Eur. Phys. J. C, 70(arXiv:1007.1988. CERN-PH-EP-2010-019. CMS-TRK-10-001):1165. 29 p, Jul 2010. URL <https://cds.cern.ch/record/1277738>.
- [29] *The CMS electromagnetic calorimeter project: Technical Design Report*. Technical Design Report CMS. CERN, Geneva, 1997.
- [30] P. Bloch, R. Brown, P. Lecoq, and H. Rykaczewski, *Changes to CMS ECAL electronics: addendum to the Technical Design Report*. Technical Design Report CMS. CERN, Geneva, 2002.
- [31] CMS Collaboration, *Energy calibration and resolution of the CMS electromagnetic calorimeter in pp collisions at $\sqrt{s} = 7$ TeV*, JINST 8 (2013) P09009, arXiv:1306.2016 [hep-ex]
- [32] *The CMS hadron calorimeter project: Technical Design Report*. Technical Design Report CMS, CERN-LHCC-97-031. CERN, Geneva, 1997.
- [33] *The CMS muon project: Technical Design Report*. Technical Design Report CMS, CERN-LHCC-97-032. CERN, Geneva, 1997.
- [34] A. Colaleo et al., CERN-LHCC-2017-012, CMS-TDR-016, 12 September 2017.
- [35] *CMS TriDAS project: Technical Design Report; 1, the trigger systems*. Technical Design Report CMS, CERN-LHCC-2000-038. CERN, Geneva, 2000.
- [36] CMS Collaboration. *CMS. The TriDAS project. Technical design report, vol. 1: the trigger sistem*. CMS-TDR-6-1, 2000. <http://cds.cern.ch/record/706847ln=it>.
- [37] CMS Collaboration, *CMS: The TriDAS project. Technical design report, Vol. 2: Data acquisition and high-level trigger*, CMS-TDR-6, 2002. <http://cds.cern.ch/record/578006l>
- [38] CMS Collaboration. *Technical proposal for the upgrade of the CMS detector through 2020*. Technical Report CERN-LHCC-2011-006. LHCC-P-004, CERN, Geneva, Jun 2011. URL <https://cds.cern.ch/record/1355706>.
- [39] CMS Collaboration, *Technical proposal for the phase II upgrade of the Compact Muon Solenoid*, CERN-LHCC-2015-10, CMS-TDR-15-02.
- [40] G. Charpak et al., Nucl. Instr. and Meth. **A 62** (1968) 262.
- [41] F. Sauli, *Principle of operation of multiwire proportional and drift chamber*, Yellow Report, CERN 77-09, 1977.

-
- [42] A. Oed et al., Nucl. Instr. and Meth. **A 263** (1988) 351.
- [43] F. Angelini et al., Nucl. Instr. and Meth. **A 283** (1989) 755.
- [44] F. Angelini et al., Nucl. Instr. and Meth. **A 382** (1996) 461.
- [45] R. Bouclier et al., Nucl. Instr. and Meth. **A 369** (1996) 328.
- [46] Bouclier et al., Nucl. Instr. and Meth. **A 381** (1996) 289.
- [47] F. Angelini et al., Nucl. Instr. and Meth. **A 335** (1993) 69.
- [48] S. Biagi et al., Nucl. Instr. and Meth. **A 361** (1995) 72.
- [49] F. Bartol et al., J. Phys. III France 6 (1996) 337.
- [50] I. Giomataris et al., Nucl. Instr. and Meth. **A 376** (1996) 29.
- [51] R. Bellazzini et al., Nucl. Instr. and Meth. **A 424** (1999) 444.
- [52] R. Bellazzini et al., Nucl. Instr. and Meth. **A 423** (1999) 125.
- [53] F. Sauli, Nucl. Instr. and Meth. **A 386** (1987) 531.
- [54] J. Benlloch et al., Nucl. Instr. and Meth. **A 419** (1998) 410.
- [55] F. Sauli, Nucl. Instr. and Meth. **805** (2016) 2–24
- [56] A. Gandi, *Laboratory of Photomechanical Technique and Printed Circuits*, EST SM-CI Section, CERN, Geneva, Switzerland.
- [57] J. Benlloch et al., *Development of the Gas Electron Multiplier (GEM)*, CERN-PPE/97-146.
- [58] S. Bachmann et al., Nucl. Instr. and Meth. **A 438** (1999) 376.
- [59] R. Veenhof, Nucl. Instr. and Meth. **A 419** (1998) 726.
- [60] Maxwell 3D Field Simulator. User's refence. Ansoft Corporation.
- [61] J. Townsend, *Electron in gases*, Hutchinson, Londra 1947.
- [62] C. Richter et al., Nucl. Instrum. and Meth. **A 461** (2001) 38.
- [63] D. Pinci PhD. Thesis, *A triple-GEM detector for the muon system of the LHCb experiment*, (2002).
- [64] G. Bencivenni et al., Nucl. Instrum. and Meth. **A 488** (2002) 493.
- [65] H. Raether, *Electron avalanches and breakdown in gases*, Butterworths (1964)

BIBLIOGRAPHY

- [66] F. Sauli et al., Nucl. Instrum. and Meth. **A 479** (2002) 294.
- [67] S. Ramo, *Currents induced in electron motion*, Proc. IRE 27 (1934) 584.
- [68] A. Colaleo, A. Safonov, A. Sharma, and M. Tytgat. CMS TECHNICAL DESIGN REPORT FOR THE MUON ENDCAP GEM UPGRADE. Technical Report CERN-LHCC-2015-012. CMS-TDR-013, CERN, Geneva, Jun 2015.
- [69] A. Colaleo et al., CERN-LHCC-2017-012, CMS-TDR-016, 12 September 2017.
- [70] S. D. Pinto et al., *A large area GEM detector*, 2008 IEEE Nuclear Science Symposium Conference Record, Dresden, Germany, 2008, pp. 1426-1432.
- [71] S. Duarte Pinto and R. De Oliveira. *A method of manufacturing a gas electron multiplier*. Patent Wipo WO/2009127220.
- [72] F. Paschen. *Wied. Ann.*, 37:69, 1889.
- [73] Jitschin, Wolfgang. (2004). *Gas flow measurement by the thin orifice and the classical Venturi tube*. Vacuum. 76. 89-100. 10.1016/j.vacuum.2004.05.014.
- [74] S. Martoiu et al., *Front End Electronics for the Scalable Readout System of RD51*, in 2011 Proc. IEEE Nucl. Sci. Symp., pp 2036-2038.
- [75] S. Duarte Pinto (on behalf of the RD51 coll.), *RD51 - An R&D collaboration for micropattern gaseous detectors*, presented at 2009 47th International Winter Meeting on Nuclear Physics, Bormio, Italy, arXiv:0907.2673 [physics.ins-det].
- [76] M. Raymond et al., *The APV25 0.25 μm CMOS readout chip for the CMS tracker*, IEEE Nucl. Sci. Symp. Conf. Rec. 2 (2000) 9/113.
- [77] V. Altini, et al., *Commissioning and initial experience with the ALICE on-line*, 2009 Proc. 17th International Conference on Computing in High Energy and Nuclear Physics, J. Phys. Conf. Ser. 219:022022, 2010, Prague, Czech Republic.
- [78] B. V. Haller, et al., *The ALICE data quality monitoring*, 2009 Proc. 17th International Conference on Computing in High Energy and Nuclear Physics, J. Phys. Conf. Ser. 219:022023, 2010, Prague, Czech Republic.
- [79] S. Colafranceschi, *A new Slow Control and Run Initialization Byte-wise Environment (SCRIBE) for the quality control of mass-produced CMS GEM detectors*. IEEE Nucl. Sci. Symp. Med. Imag. Conf. Rec. (2016).
- [80] *Amptek, Mini-X X-Ray Tube System* - <http://amptek.com/products/mini-x-ray-tube/>

-
- [81] J. A. Merlin, *Analysis Report on GE1/1 QC5 Gain Calibration*. General Muon Meeting. August 2018, CERN, Geneva (Switzerland). <https://indico.cern.ch/event/742724/contributions/3115401/attachments/1705486/2747859/>
- [82] Martina Ressegotti, *Study on a new design of a GEM-based technology detector for the CMS experiment*. Instr17: Instrumentation for Colliding Beam Physics Parallel Talk. Budker Institute of Nuclear Physics and Novosibirsk State University, Novosibirsk (Russian Federation).
- [83] Martina Ressegotti, *Current state of the R&D on Micropattern Gaseous Detectors for the CMS muon system upgrade*. Posters at LHCC, CERN, Geneva, CH: Students' Poster Session at the 2017 Winter LHCC meeting Poster CERN, Geneva (Switzerland).
- [84] A. Sharma A, *Properties of some gas mixtures used in tracking detectors*. SLAC-JOURNAL-ICFA-16-3. 1988
- [85] C. Niebuhr. *Aging effects in gas detectors*. Nucl. Instrum. Methods Phys. Res., **A 566** (2006) 118–122
- [86] J A Kadyk. *Wire chamber aging*. Nucl. Instrum. Methods Phys. Res., **A 300** (LBL-29852):436-479. 78 p, Mar 1990.
- [87] M. Titov, *Radiation damage and long-term aging in gas detectors*, in arXiv: physics/0403055; also in Proc. of the Workshop of the INFN ELOISATRON Project **Innovative Detectors For Super-Colliders**, Erice, Italy (2003).
- [88] M. Capeáns and J. M. G. Cuadrado. *Study of Ageing of Gaseous Detectors and Solutions for the Use of MSGCs in High Rate Experiments*. Ph.D Thesis, Santiago de Compostela U., Santiago de Compostela, 1995.
- [89] L. Malter. *Thin film field emission*. Physics Review, (50):48, 1936.
- [90] J. A. Merlin, *Study of long-term sustained operation of gaseous detectors for the high rate environment in CMS*, CERN, May 2016.
- [91] *Proceedings of the international workshop on aging phenomena in gaseous detectors*. Nuclear Instruments and Methods in Physics Research, **A(515)**, 2003.
- [92] M. Capeáns et al., *Aging and materials: Lessons for detectors and gas systems*. Nucl. Instrum. Methods Phys. Res., **A 515**:73-88, 2003.
- [93] D. Bailey and R. Hall-Wilton. *Proceedings of the International Workshop on Aging Phenomena in Gaseous Detectors*. Nucl. Instrum. Methods Phys. Res., **A 515**:37, 2003.

BIBLIOGRAPHY

- [94] C. Niebuhr. *Proceedings of the International Workshop on Aging Phenomena in Gaseous Detectors*. Nucl. Instrum. Methods Phys. Res., **A 515**:43, 2003.
- [95] M. Binkley. *Proceedings of the International Workshop on Aging Phenomena in Gaseous Detectors*. Nucl. Instrum. Methods Phys. Res., **A 515**:53, 2003.
- [96] CERN/DRDC/90-40 (8 November, 1990).
- [97] M. Capeáns, C. Garabatos, R. D. Heuer, R. Mackenzie, T. C. Meyer, F. Sauli, T. Mashimo, G. Pfister, M. Simona, M. Fraga, MS. Leite, E.d. Lima, R. Marques, A. Policarpo and K. Silander, CERN/DRDC/93-52 (1993).
- [98] RD-28 Collaboration, CERN/DRDC/92-30 (1992).
- [99] M. Hohlmann, C. Padilla, N. Tesch, M. Titov (Eds.), *Proceedings of the International Workshop on Aging Phenomena in Gaseous Detectors*, DESY, Hamburg, October 2-5, 2001. Nucl. Instrum. Methods Phys. Res., **A 515**: 1-385, 2003.
- [100] J. Vavra. *Review of wire chamber aging*. Technical Report SLAC-PUB-3882, SLAC, Stanford, CA, Feb 1986.
- [101] J. A. Kadyk. *Wire chamber aging*. Nucl. Instrum. Methods Phys. Res., **A**, 300(LBL-29852):436-479. 78 pp., Mar 1990.
- [102] S. Chatrchyan et al. *The CMS experiment at the CERN LHC. The Compact Muon Solenoid experiment*. J. Instrum., **3**:S08004. 361 p, 2008.
- [103] J. Wise, J A Kadyk, D W Hess, and M C S Williams. *Effects of freons on wire chamber aging*. Technical Report LBL-29252, Lawrence Berkeley Nat. Lab., Berkeley, CA, Jun 1990.
- [104] T. Åkesson et al. *Aging studies for the ATLAS Transition Radiation Tracker (TRT)*. Nucl. Instrum. Methods Phys. Res., **A 515**:166–179, 2003.
- [105] M. Alfonsi, G. Bencivenni, P. De Simone, F. Murtas, M. P. Poli Lener, W. Bonivento, A. Cardini, D. Raspino, B. Saitta, D. Pinci, and S. Baccaro. *Aging measurements Bibliography on triple-GEM detectors operated with CF₄-based gas mixtures*. Nucl. Phys. B, Proc. Suppl 150:159–163, 2006.
- [106] P. Abbon et al., *The COMPASS Experiment at CERN*. Nucl. Instrum. Methods Phys. Res., **A 577** (2007) 455-518.
- [107] S. Bachmann, A. Bressan, A. Placci, L. Ropelewski, and F. Sauli. *Development and test of large size GEM detectors*. IEEE Trans. Nucl. Sci., **47**(4, pt.1):1412–15, 2000.

- [108] M. C. Altunbas, K. Dehmelt, S. Kappler, B. Ketzer, L. Ropelewski, F. Sauli, and F. Simon. *Aging measurements with the gas electron multiplier (GEM)*. Nucl. Instrum. Methods Phys. Res., **A 515** (CERN-EP-2001-091. 1-2):249–254. 6 p, Dec. 2001.
- [109] L. Guirl, S. Kane, J. May, J. Miyamoto, and I. Shipsey. *An aging study of triple GEMs in Ar/CO₂*. Nucl. Instrum. Methods Phys. Res., **A 478** (1-2):263–266, 2002.
- [110] A. Augusto Alves Jr. et al. *The LHCb Detector at the LHC - LHCb Collaboration*. JINST 3 (2008) S08005.
- [111] S. Baccaro, A. Cemmi, G. Ferrara, S. Fiore. (2015). *Calliope gamma irradiation facility at ENEA -Casaccia R.C.* (Rome). Rome, Italy: ENEA. (RT/2015/13/ENEA).
- [112] M. Alfonsi, G. Bencivenni, P. De Simone, F. Murtas, M. Poli-Lener, W. Bonivento, A. Cardini, C. Deplano, D. Raspino, and D. Pinci. *High-rate particle triggering with triple-GEM detector*. Nucl. Instrum. Methods Phys. Res., **A**, 518:106–112, 2004.
- [113] A. Kozlov, I. Ravinovich, L. I. Shekhtman, Z. Fraenkel, M. Inuzuka, and I. Tserruya. *Development of a triple GEM UV-photon detector operated in pure CF₄ for the PHENIX experiment*. Nucl. Instrum. Methods Phys. Res., **A 523** (physics/0309013. 3):345–354. 14 p, Aug. 2003.
- [114] Z. Fraenkel, B. Khachaturov, A. Kozlov, A. Milov, D. Mukhopadhyay, D. Pal, I. Ravinovich, I. Tserruya and S. Zhou, *PHENIX Technical Note* 391.
- [115] S. Agosteo et al., *A facility for the test of large area muon chambers at high rates*, Nuclear Instruments and Methods in Physics Research **A 452** (2000) 94-104.
- [116] D. Pfeiffer et al., *The radiation field in the Gamma Irradiation Facility GIF++ at CERN*. Nucl. Instrum. Meth. **A 866** (2017). 91-103 arXiv:1611.00299
- [117] CERN, Super Proton Synchrotron (SPS) Home Page - <http://ab-dep-op-sps.web.cern.ch/ab-dep-op-sps/>
- [118] *Recision Absolute and Gauge Pressure Transmitter*. DTS-TSA-05-2016-ENG. GEFran spa. May 2016.
- [119] *Relative Humidity and Temperature Mini Probe PCMini70 97177 V3 UK* 0616. Michell Instruments. 2016.
- [120] *MECARO Company* - <http://www.mecaro.com/>

BIBLIOGRAPHY

- [121] *Amptek, CdTe X-ray and gamma ray detector* - <http://amptek.com/products/xr-100cdte-x-ray-and-gamma-ray-detector/>
- [122] Bronkhorst, F-210CM Mass flow controllers - <http://www.bronkhorst.com/files/downloads/brochures/folder-el-flow.pdf/>
- [123] *LM135/LM235/LM335, LM135A/LM235A/LM335A Precision Temperature Sensors*. DS005698. National Semiconductor Corporation. November 2000.
- [124] *High Temperature Accuracy Integrated Silicon Pressure Sensor for Measuring Absolute Pressure, On-Chip Signal Conditioned, Temperature Compensated and Calibrated*. Rev 4. Freescale Semiconductor. October 2007.
- [125] *HIH-4000 Series Humidity Sensors* - <https://sensing.honeywell.com/honeywell-sensing-hih4000-series-product-sheet-009017-5-en.pdf> l.
- [126] F.E. Taylor, Nucl. Instrum. Meth. **A 289** (1989) 283
- [127] S. Bachmann et al., *Discharge studies and prevention in the gas electron multiplier (GEM)*, Nucl. Instrum. Meth. **A 479** (2000) 294.
- [128] C. Altunbas et al., *Construction, test and commissioning of the triple-GEM tracking detector for COMPASS*, NIM A **490** (2002) 177.
- [129] B. Ketzer, *Micropattern gaseous detectors in the COMPASS tracker*, NIM A **494** (2002) 142.
- [130] G. Bencivenni et al., *A triple GEM detector with pad readout for high rate charged particle triggering*, NIM **A 488** (2002) 493.
- [131] CERN, CHARM facility Home Page - <http://charm.web.cern.ch/>
- [132] J. Mekki, M. Brugger, R. Alia, A. Thornton, N. Dos Santos Mota and S. Danzeca, *CHARM: A Mixed Field Facility at CERN for Radiation Tests in Ground, Atmospheric, Space and Accelerator Representative Environments* IEEE Trans. Nucl. Sci., vol. 63, no. 4, pp. 2106-2114, 2016.
- [133] S. Bonaldo, *CHARM - A new mixed-field facility for ionizing radiation test of electronics at CERN* Università degli studi di Padova, Padova, Italy, 2016.
- [134] CERN, IRRAD facility - <https://ps-irrad.web.cern.ch/>

- [135] Giuseppe Battistoni, F Cerutti, A Fassò, A Ferrari, S Muraroi, J Ranft, S Roesler, and P R Sala. *The FLUKA code: Description and benchmarking*. AIP Conf. Proc., 896(SLAC-REPRINT-2007-184):31-49. 19 p, 2007.
- [136] A Ferrari, Paola R Sala, A Fassò, and Johannes Ranft. *FLUKA: A multiparticle transport code* (program version 2005). CERN, Geneva, 2005.
- [137] A. Infantino, CERN-ACC-NOTE-2017-0059, *FLUKA Monte Carlo Modelling of the CHARM Facility's Test Area: Update of the Radiation Field Assessment*, 14 November 2017.
- [138] *A1515 1-1.3kV/1-3mA HV Reversible Ch. Boards*, rev. 6 - 8 March 2018. CEAN S.p.a.
- [139] G. Corradi, F. Murtas, and D. Tagnani, *A novel High-Voltage System for a triple GEM detector*, Nucl. Instrum. Meth. **A 572** (2007) 96.
- [140] <https://twiki.cern.ch/twiki/bin/view/MPGD/Phase2BkgFLUKA> (CMS-FLUKA simulation for the background condition during Phase-2 for the muon upgrade subsystems).
- [141] Leonard Kazmier, *Schaum's Outline of Business Statistics*. McGraw Hill Professional, Sep. 24, 2003, p. 359.
- [142] Erik W. Grafarend, *Linear And Nonlinear Models: Fixed Effects, Random Effects, And Mixed Models*. Walter de Gruyter, 2006, p. 553.

Acknowledgements

Un sentito ringraziamento va ad Archana Sharma, Cristina Riccardi, Alessandro Braghieri, Jeremie A. Merlin, Marcus Hohlmann, Michele Bianco e Paolo Vitulo per avermi dato l'opportunità di approfondire lo studio di argomenti che hanno suscitato in me grande interesse e per avermi trasmesso il loro grande entusiasmo e la loro sete di conoscenza, al punto da fornirmi le motivazioni che mi hanno spinto ad affrontare questo lavoro, non privo di difficoltà, con suggerimenti e consigli.

Ad Archana Sharma, Jeremie A. Merlin, Michele Bianco e Paolo Vitulo, esprimo ancora sentimenti di gratitudine per l'accoglienza riservatami e per aver messo a mia disposizione tutta la strumentazione necessaria per la realizzazione del progetto. La mia stima per loro è dovuta, oltre che alla loro profonda esperienza e conoscenza nel campo della Fisica, alla grande umanità con la quale hanno saputo incoraggiarmi in tutti i momenti di difficoltà. L'entusiasmo e l'impegno che ho mantenuto durante il mio lavoro di tesi trovano giustificazione nella sapiente direzione profusa dai miei relatori.

Un grazie di cuore va a Michele Bianco e Paolo Vitulo per la disponibilità dimostratami durante il periodo di preparazione della mia tesi. Grazie per il tempo e l'attenzione che mi hanno dedicato e per aver instaurato con me un rapporto non solo professionale, ma anche di fiducia e amicizia.

Ai miei amici Alice Magnani, Chiara Giroletti, Davide Fiorina, Gianfranco Morello, Marek Michal Gruchala, Pratik Jawahar, Lisa Borgonovi, Muhammad Sohaib Hassan, Yong Hoon Lee e Vanessa Pallozzi che mi hanno sempre ascoltato, appoggiato e spronato nei momenti di sconforto e hanno sempre gioito per me nei momenti felici, per aver sempre creduto in me fin dall'inizio, per avermi supportato in questo mio percorso formativo e per essere rimasti il mio punto di riferimento sempre presente.

Infine ringrazio la mia famiglia che mi ha sostenuto con quell'affetto che ritengo sia fondamentale nella mia vita. Un sentito ringraziamento ai miei genitori che, con il loro incrollabile sostegno morale ed economico, mi hanno permesso di raggiungere questo traguardo. A mia sorella Teresa, sempre pronta ad ascoltarmi e a darmi consigli. A cercare in ogni occasione di far salire la

mia autostima, insegnandomi a camminare ogni giorno a testa alta senza aver paura dei giudizi degli altri. Ogni volta che ho bisogno di lei, nonostante i chilometri che ci separano, è sempre presente.

Un ringraziamento speciale va alla mia fidanzata Elena Voevodina che, nonostante lo stress e a volte il mio cattivo umore, ha accettato di diventare mia moglie.

Grazie perché senza di voi non sarei mai arrivato fino in fondo a questo difficile, lungo e tortuoso cammino. Questa tesi la dedico a voi che siete la mia famiglia, il mio più grande sostegno e la mia guida.